

PROGRESS IN RESEARCH

April 1, 2014 - March 31, 2015

CYCLOTRON INSTITUTE

Texas A&M University

College Station, Texas

PROGRESS IN RESEARCH

APRIL 1, 2014- MARCH 31, 2015

Prepared By

The Cyclotron Institute Staff

Texas A&M University

College Station, TX 77843-3366

Phone: (979) 845-1411

Fax: (979) 845-1899

Web: <http://cyclotron.tamu.edu>

June 2015

TABLE OF CONTENTS

Introduction	X
S.J. Yennello, Director	
SECTION I: NUCLEAR STRUCTURE, FUNDAMENTAL INTERACTIONS AND ASTROPHYSICS	
Isoscalar E1-E3 strength in Mo isotopes.....	I-1
D.H. Youngblood, Y.-W. Lui, Krishichayan, J. Button, G. Bonasera, and S. Shlomo	
Beta-asymmetry measurement with the TRIUMF neutral atom trap.....	I-5
B. Fenker, M. Mehlman, D. Melconian, and P.D. Shidling	
Polarization by optical pumping – the β-asymmetry of ^{37}K.....	I-8
B. Fenker, M. Mehlman, D. Melconian, and P.D. Shidling	
Production studies of proton-rich T=2 nuclei.....	I-10
E. Bennett, R. Burch, B. Fenker, M. Mehlman, D. Melconian, and P.D. Shidling	
α-cluster asymptotic normalization coefficients from sub-Coulomb ($^6\text{Li,d}$) reaction: benchmark measurement.....	I-12
G.V. Rogachev, E. Koshchiy, M.L. Avila, L.T. Baby, J. Belarge, K.W. Kemper, A.N. Kuchera, and D. Santiago-Gonzalez	
Constraining the cascade transitions in the astrophysically important $^{12}\text{C}(\alpha,\gamma)^{16}\text{O}$ reaction.....	I-15
G.V. Rogachev, E. Koshchiy, E. Uberseder, A.M. Mukhamedzhanov, M.L. Avila, L.T. Baby, J. Belarge, K.W. Kemper, A.N. Kuchera, and D. Santiago-Gonzalez	
α asymptotic normalization coefficient of the sub-threshold $1/2^+$ state at 6.356 MeV in ^{17}O.....	I-18
G.V. Rogachev, E. Koshchiy, M.L. Avila, L.T. Baby, J. Belarge, K.W. Kemper, A.N. Kuchera, and D. Santiago-Gonzalez	
Structure of ^{10}N via $^9\text{C}+p$ resonance scattering.....	I-22
G.V. Rogachev, J. Hooker, E. Koshchiy, E. Uberseder, H. Jayatissa, C. Hunt, and B. Roeder	
Experimental study of ^9He through the isobaric analog states in ^9Li.....	I-25
E. Uberseder, G.V. Rogachev, V.Z. Goldberg, E. Koshchiy, B.T. Roeder, G. Chubarian, J. Hooker, H. Jayatissa, D. Melconian, R.E. Tribble, M. Alcorta, B. Davids, and C. Fu	

Elastic scattering of ^{28}Si on ^{13}C	I-28
M. Dag, A. Spiridon, B.T. Roeder, A. Saastamoinen, R. Chyzh, V.Z. Goldberg, and R.E. Tribble	
Search for quasi molecular states in interaction of ^{40}Ar with light nuclei	I-30
V.Z. Goldberg, M.S. Golovkov, I. Ivanov, M. Kisieliński, S. Kliczewski, M. Kowalczyk, N. Munbayev, A. Nurmukhanbetova, E. Piasecki, G. Tiourin, S. Torilov, W. Trzaska, A. Trzcińska, R. Wolski, V. Zhrebchevski, and R.E. Tribble	
Data from the $^{13}\text{C}+\alpha$ interaction for the studies of the cluster structure and for astrophysics	I-33
A. Kock, V.Z. Goldberg, G.V. Rogachev, E. Uberseder, N.A. Mynbayev, A.K. Nurmukhanbetova, M.S. Golovkov, M. Koloberdin, I. Ivanov, D.K. Nauruzbayev, and R.E. Tribble	
Study of the lowest states in ^9He as a test of unusual nuclear structure beyond nuclear stability ..	I-35
R. Chyzh, A. Saastamoinen, M. McCleskey, V.Z. Goldberg, G.V. Rogachev, Y. Koshchiy, E. Simmons, A. Spiridon, M. Dag, and R.E. Tribble	
Study of excited states of ^{35}Ar through β-decay of ^{35}K for nucleosynthesis in novae and X-ray bursts.....	I-39
A. Saastamoinen, G.J. Lotay, A. Kankainen, B.T. Roeder, R. Chyzh, M. Dag, E. Simmons, A. Spiridon, and R.E. Tribble	
Superallowed beta decay	I-41
J.C. Hardy, I.S. Towner, V.E. Jacob, H.I. Park, L. Chen, V. Horvat, N. Nica, M. Bencomo, and R.E. Tribble	
Improvement in the precision of the ^{34}Ar half-life	I-46
V.E. Jacob, J.C. Hardy, M. Bencomo, H.I. Park, L. Chen, V. Horvat, N. Nica, B.T. Roeder, and A. Saastamoinen	
Update on the superallowed branching ratio in the ^{34}Ar	I-48
V.E. Jacob, J.C. Hardy, M. Bencomo, H.I. Park, L. Chen, V. Horvat, N. Nica, B.T. Roeder, and A. Saastamoinen	
Precise measurement of branching ratios in the β decay of ^{38}Ca	I-50
H.I. Park, J.C. Hardy, V.E. Jacob, M. Bencomo, L. Chen, V. Horvat, N. Nica, B.T. Roeder, E. McCleskey, R.E. Tribble, and I.S. Towner	
Superallowed β-decay branching-ratio measurement of ^{26}Si.....	I-53
M. Bencomo, J.C. Hardy, V.E. Jacob, H.I. Park, L. Chen, V. Horvat, N. Nica, B.T. Roeder, A. Saastamoinen, R.E. Tribble, and I.S. Towner	

United States nuclear structure data program (USNDP) and evaluated nuclear structure data file (ENSDF) at Texas A&M University	I-56
N. Nica and J.C. Hardy	
Tests of internal-conversion theory with precise γ- and x-ray spectroscopy: Selection of new cases	I-58
N. Nica, J.C. Hardy, and M.B. Trzhaskovskaya	
Tests of internal-conversion theory with precise γ- and x-ray spectroscopy: The case of ^{111m}Cd.....	I-62
N. Nica, L. Pineda, J.C. Hardy, V.E. Iacob, H.I. Park, and M.B. Trzhaskovskaya	
Superaligned $0^+ \rightarrow 0^+$ nuclear β decays: 2014 critical survey, with precise results for V_{ud} and CKM unitarity	I-65
J.C. Hardy and I.S. Towner	
Progress in measuring GMR in unstable nuclei: Decay detector calibration and inverse reaction experiment	I-68
J. Button, Y.-W. Lui, and D.H. Youngblood	
Spin physics with STAR at RHIC	I-73
Z. Chang, C.A. Gagliardi, M.M. Mondal, R.E. Tribble, and the STAR Collaboration	

SECTION II: HEAVY ION REACTIONS

Isospin equilibration in Fermi-energy heavy-ion nuclear collisions	II-1
L.W. May, P. Cammarata, L. Heilborn, Z. Kohley, A. McIntosh, M. Youngs, A. Zarrella, and S.J. Yennello	
N/Z transport within a deformed nuclear system	II-3
A. Jedele, A.B. McIntosh, L. Heilborn, M. Youngs, A. Zarrella, E. McCleskey, L.W. May, and S.J. Yennello	
Exploring the limits of the thermodynamic model of heavy-ion collisions with respect to particle ratios	II-6
M. Youngs, A.B. McIntosh, L. Heilborn, A. Jedele, L.W. May, E. McCleskey, S.J. Yennello, and A. Zarrella	
Incomplete fusion reactions measured with the QTS	II-10
A.B. McIntosh, L. Heilborn, M. Youngs, L.A. Bakhtiari, M. Chapman, A. Jedele, L.W. May, E. McCleskey, A. Zarrella, and S.J. Yennello	

Constraining supernova equations of state.....	II-13
M. Hempel, K. Hagel, J.B. Natowitz, G. Roepke, and S. Typel	
Exploring clusterization in $^{28}\text{Si}+^{12}\text{C}$ collisions at 35MeV/u with the NIMROD-ISiS array	II-16
X.G. Cao, K. Schmidt, E.-J. Kim, K. Hagel, M. Barbui, S. Wuenschel, J.B. Natowitz, H. Zheng, N. Blando, A. Bonasera, G. Giuliani, M. Rodrigues, R. Wada, M. Huang, C. Botosso, G. Liu, G. Viesti, S. Moretto, G. Prete, S. Pesente, D. Fabris, Y. El Masri, T. Keutgen, S. Kowalski, Z. Kohley, and A. Kumar	
The clusterization of alpha-conjugate nuclei.....	II-21
K. Hagel, K. Schmidt, S. Wuenschel, E.J. Kim, M. Barbui, J.B. Natowitz, H. Zheng, N. Blando, A. Bonasera, G. Giuliani, M. Rodrigues, R. Wada, M. Huang, C. Botosso, G. Liu, G. Viesti, S. Moretto, G. Prete, S. Pesente, D. Fabris, Y. El Masri, T. Keutgen, S. Kowalski, Z. Kohley, and A. Kumar	
Exploring clustering in alpha-conjugate nuclei using the thick target inverse kinematic technique for multiple alpha emission	II-24
M. Barbui, K. Hagel, J. Gauthier, S. Wuenschel, R.T. deSouza, S. Hudan, D. Fang, V.Z. Goldberg, H. Zheng, G. Giuliani, G. Rapisarda, E.-J. Kim, X. Liu, and J.B. Natowitz	
Progress on campaign surveying deep inelastic multi-nucleon transfer for creation of super- and hyper-heavy elements	II-26
S. Wuenschel, M. Barbui, X. Cao, J. Gauthier, K. Hagel, S. Kowalski, Z. Majka, J.B. Natowitz, K. Schmidt, Z. Sosin, A. Wieloch, and H. Zheng	
Analysis of $^{124}\text{Sn}+^{112,124}\text{Sn}$ at 264 MeV reaction data taken on NIMROD.....	II-29
J. Gauthier, M. Barbui, X. Cao, K. Hagel, J.B. Natowitz, R. Wada, and S. Wuenschel	
Observations from evaporation residue cross sections in ^{45}Sc- and ^{44}Ca-induced reactions	II-32
T.A. Werke, D.A. Mayorov, M.C. Alfonso, E.E. Tereshatov, and C.M. Folden III	
Ion exchange separation of indium and thallium.....	II-35
E.E. Tereshatov, M.Yu. Boltoeva, and C.M. Folden III	
Ionic liquid-based extraction of indium and thallium	II-38
E.E. Tereshatov, M.Yu. Boltoeva, and C.M. Folden III	
Signals of Bose Einstein condensation and Fermi quenching in the decay of hot nuclear systems.....	II-41
P. Marini, H. Zheng, G. Verde, A. Chbihi, and A. Bonasera	
Toward understanding relativistic heavy-ion collisions with the STAR detector at RHIC.....	II-43
M. Cervantes, Y. Liu, S. Mioduszewski, N. Sahoo, and the STAR Collaboration	

Inelastic scattering of alphas on ^{24}Mg as a surrogate for stellar carbon burning.....	II-46
J.M. Munson, E.B. Norman, J.T. Burke, R.J. Casperson, E. McCleskey, M. McCleskey, R. Hughes, S. Ota, A. Czeszumaska, A. Saastamoinen, and A. Spiridon	

SECTION III: NUCLEAR THEORY

Neutron stars in the framework of Landau's theory	III-1
H. Zheng, J. Sahagun, and A. Bonasera	

Asymptotic normalization coefficients and spectroscopic factors from deuteron stripping reactions.....	III-3
D.Y. Pang and A.M. Mukhamedzhanov	

Big bang nucleosynthesis revisited via Trojan Horse method measurements.....	III-4
R.G. Pizzone, R. Sparta, C.A. Bertulani, C. Spitaleri, M. La Cognata, J. Lalmansingh, L. Lamia, A. Mukhamedzhanov, and A. Tumino	

Constraining the 6.05 MeV 0^+ and 6.13 MeV 3^- cascade transitions in the $^{12}\text{C}(\alpha,\gamma)^{16}\text{O}$ reaction using the asymptotic normalization coefficients	III-5
M.L. Avila, G.V. Rogachev, E. Koshchiy, L.T. Baby, J. Belarge, K.W. Kemper, A.N. Kuchera, A.M. Mukhamedzhanov, D. Santiago-Gonzalez, and E. Uberseder	

Determination of the asymptotic normalization coefficients for the $^{14}\text{C} + n \leftrightarrow ^{15}\text{C}$, $^{14}\text{C}(n,\gamma)^{15}\text{C}$ reaction rate and evaluation of a new method to determine spectroscopic factors.....	III-6
M. McCleskey, A.M. Mukhamedzhanov, L. Trache, R.E. Tribble, A. Banu, V. Eremenko, V.Z. Goldberg, Y.-W. Lui, E. McCleskey, B.T. Roeder, A. Spiridon, F. Carstoiu, V. Burjan, Z. Hon, and I.J. Thompson	

Indirect techniques in nuclear astrophysics: A review	III-7
R.E. Tribble, C.A. Bertulani, M. La Cognata, A.M. Mukhamedzhanov, and C. Spitaleri	

Low-energy R-matrix fit for the $^6\text{Li}(d,\alpha)^4\text{He}$ S factor.....	III-8
J. Grineviciute, L. Lamia, A.M. Mukhamedzhanov, C. Spitaleri, and M. La Cognata	

Measurement of the 10 keV resonance in the $^{10}\text{B}(p, \alpha_0)^7\text{Be}$ reaction via the Trojan Horse method.....	III-9
C. Spitaleri, L. Lamia, S.M.R. Puglia, S. Romano, M. La Cognata, V. Crucilla, R.G. Pizzone, G.G. Rapisarda, M.L. Sergi, M. Gimenez Del Santo, N. Carlin, M.G. Munhoz, F.A. Souza, A. Szanto de Toledo, A. Tumino, B. Irgaziev, A. Mukhamedzhanov, G. Tabacaru, V. Burjan, V. Kroha, Z. Hons, J. Mrazek, Shu-Hua Zhou, Chengbo Li, Qungang Wen, Y. Wakabayashi, H. Yamaguchi, and E. Somorjai	

New determination of the ${}^2\text{H}(d,p){}^3\text{H}$ and ${}^2\text{H}(d,n){}^3\text{He}$ reaction rates at astrophysical energies.....	III-10
A.Tumino, R. Spartà, C. Spitaleri, A.M. Mukhamedzhanov, S. Typel, R.G. Pizzone, E. Tognelli, S. Degl'Innocenti, V. Burjan, V. Kroha, Z. Hons, M. La Cognata, L. Lamia, J. Mrazek, S. Piskor, P.G. Prada Moroni, G.G. Rapisarda, S. Romano, and M.L. Sergi	
Optical model potential of $A = 3$ projectiles for 1p-shell nuclei.....	III-11
D.Y. Pang, W.M. Dean, and A.M. Mukhamedzhanov	
Surface-integral formalism of deuteron stripping	III-12
A.M. Mukhamedzhanov, D.Y. Pang, C.A. Bertulani, and A.S. Kadyrov	
Trojan Horse particle invariance in fusion reactions	III-13
R.G. Pizzone, C. Spitaleri, C. Bertulani, A. Mukhamedzhanov, L. Blokhintsev, M. La Cognata, L. Lamia, R. Spartà, and A. Tumino	
Investigating discrepancy of the isoscalar giant octupole resonance in ${}^{92,96,98,100}\text{Mo}$.....	III-14
D.H. Youngblood, Y.-W. Lui, Krishichayan, J. Button, G. Bonasera, and S. Shlomo	
Isoscalar giant quadrupole resonances in select spherical nuclei and the effective mass	III-17
M.R. Anders, G. Bonasera, and S. Shlomo	
Measured difference between ${}^{206}\text{Pb}$, ${}^{205}\text{Tl}$ charge distributions and the proton $3s_{1/2}$ wave function.....	III-19
M.R. Anders, S. Shlomo, and I. Talmi	
Properties of high-energy isoscalar monopole excitations in medium-heavy mass spherical nuclei.....	III-22
M.L. Gorelik, S. Shlomo, B.A. Tulupov, and M.H. Urin	
Unitarity of the particle-hole dispersive optical model.....	III-24
M.L. Gorelik, S. Shlomo, B.A. Tulupov, and M.H. Urin	
Jet fragmentation via recombination of parton showers in vacuum.....	III-27
K. Han, R. Fries, and C.M. Ko	
Spinodal instability in baryon-rich quark matter.....	III-29
F. Li and C.M. Ko	
Medium modification of pion production threshold in heavy ion collisions and the nuclear symmetry energy	III-32
T. Song and C.M. Ko	

Dilepton production from quark-gluon plasma in the PNJL model.....	III-34
Y.F. Sun and C.M. Ko	
Heavy quark correlations and the effective volume for quarkonia production in heavy ion collisions.....	III-36
J.P. Liu, C.M. Ko, and F. Li	
Searching for photons from jets in quark gluon plasma using jet triggers.....	III-38
R.J. Fries and Collaborators	
Heavy flavor at the large hadron collider in a strong coupling approach.....	III-40
M. He, R.J. Fries, and R. Rapp	
Pseudo-critical enhancement of thermal photons in relativistic heavy-ion collisions?	III-43
H. van Hees, M. He, and R. Rapp	
Universal parameterization of thermal photons in hadronic matter	III-45
M. Heffernan, P. Hohler, and R. Rapp	
Realistic implementation of massive Yang-Mills theory for ρ and a_1 Mesons	III-47
P.M. Hohler and R. Rapp	
Weak branches in ^{34}Ar and ^{38}Ca β^+ decay	III-49
I.S. Towner and J.C. Hardy	
Spectrum shape functions in first-forbidden beta transitions	III-51
I.S. Towner	

SECTION IV: SUPERCONDUCTING CYCLOTRON, INSTRUMENTATION AND RIB UPGRADE

K500 operations and development	IV-1
D.P. May, G.J. Kim, B.T. Roeder, H.L. Clark, and F.P. Abegglen	
Texas A&M cyclotron radiation effects facility April 1, 2014 – March 31, 2015.....	IV-3
H.L. Clark, J. Brinkley, L. Chen, G. Chubarian, V. Horvat, B. Hyman, B. Roeder, and G. Tabacaru	
Plans for new ECR4 ion source	IV-5
D.P. May and L.E. Henderson	
Axially-mounted, high-temperature oven for ECR2	IV-7
H. Peeler, F.P. Abegglen, B.T. Roeder, and D.P. May	

Texas A&M cyclotron K150 broad beams for foil irradiation	IV-10
L.E. Henderson and H.L. Clark	
A new radiation effects facility beam line.....	IV-12
B. Hyman, H.L. Clark, G.J. Kim, B. Roeder, and S. Russell	
Repair of the H⁻ ion source.....	IV-13
H. Clark, B.T. Roeder, D.P. May, G. Kim, F. Abegglen, H. Peeler, and G. Tabacaru	
Cyclotron Institute upgrade project.....	IV-15
H.L. Clark, F. Abegglen, G. Chubaryan, G. Kim, D.P. May, B. Roeder, and G. Tabacaru	
Cyclotron computing	IV-24
R. Burch and K. Hagel	
MARS status report for 2014-2015.....	IV-25
B.T. Roeder, A. Saastamoinen, and A. Spiridon	
Update on the upgrade of the Oxford detector	IV-29
A. Spiridon, R. Chyzh, M. Dag, E. McCleskey, M. McCleskey, B.T. Roeder, A. Saastamoinen, R.E. Tribble, L. Trache, E. Pollacco, and G. Pascovici	
Construction and commissioning of the AstroBox2 detector.....	IV-33
A. Saastamoinen, B.T. Roeder, A. Spiridon, R.E. Tribble, E. Pollacco, L. Trache, and G. Pascovici	
Commissioning the TAMUTRAP RFQ cooler/buncher.....	IV-36
E. Bennett, R. Burch, B. Fenker, M. Mehlman, D. Melconian, and P.D. Shidling	
Texas active target (TexAT) detector – part 1: Design and construction progress	IV-42
E. Koshchiy, G.V. Rogachev, E. Uberseder, and E. Pollacco	
Texas active target (TexAT) detector - part 2: Monte Carlo simulations	IV-47
E. Uberseder, G.V. Rogachev, E. Koshchiy, and E. Pollacco	
Texas active target (TexAT) detector - part 3: Acquisition and analysis infrastructure	IV-51
E. Uberseder, G.V. Rogachev, E. Koshchiy, and E. Pollacco	
FAUST upgrade (FAUSTUPS) for experimental proton-proton correlation functions	IV-54
L. Heilborn, A.B. McIntosh, M. Youngs, K. Hagel, L. Bakhtiari, P.J. Cammarata, M. Chapman, A. Jedele, J. Mabilia, L.W. May, A. Zarrella, and S.J. Yennello	

The ParTI array for studying pionic fusion	IV-58
A. Zarrella, A. Bonasera, L. Heilborn, A. Jedele, L.W. May, A.B. McIntosh, M. Youngs, and S.J. Yennello	
Upgrades and characterization of the Texas A&M quadrupole triplet spectrometer (QTS).....	IV-62
A.B. McIntosh, L. Heilborn, M. Youngs, L.A. Bakhtiari, M. Chapman, A. Jedele, L.W. May, E. McCleskey, A. Zarrella, and S.J. Yennello	
A LabVIEW solution for coupling an automated gamma-ray counter and software for spectra analysis	IV-66
E.E. Tereshatov and C.M. Folden III	
Shape discrimination of digitized pulses	IV-75
V. Horvat, L. Chen, and J.C. Hardy	
Tests on digital system for precise half-life measurement of ⁴²Ti.....	IV-79
H.I. Park, L. Chen, and J.C. Hardy	

SECTION V: PUBLICATIONS

Papers published	V-1
-------------------------------	------------

SECTION VI: APPENDIX

Talks presented	VI-1
Research personnel and engineering staff	VI-9
Students.....	VI-10
Organizational chart.....	VI-11
Graduate degree students.....	VI-12
Institute colloquia and seminars	VI-13

Introduction

April 1, 2014 – March 31, 2015

Progress in research and operations at the Texas A&M Cyclotron Institute is summarized in this report for the period April, 1, 2014 through March 31, 2015. The format follows that of previous years. Sections I through III contain reports from individual research projects. Operation and technical developments are given in Section IV. Section V lists the publications with Cyclotron Institute authors and outside users and the Appendix gives additional information including talks presented by members of the Institute during the past year. Once again, the full volume of this year's Progress in Research is available only on our web site (<http://cyclotron.tamu.edu>). *Since most of the contributions presented here are truly reports on progress in research, results and conclusions should not be quoted from the report without the consent of the authors.*

We are pleased to announce that we have successfully completed a search for a new tenure track faculty position. We had a number of outstanding candidates and were fortunate to convince the University to allow us to hire two of them. We will be joined by Dr. Gregory Christian and Dr. Ania Kwiatkowski in the fall. Both are outstanding young experimentalists that will be relocating from TRIUMF. We also have been given permission to search for a theorist to complement our local experimental efforts, and that search is underway.

The K150 cyclotron provided 2,917 hours of beams including strip extracted protons, alpha particles, ^{12}C , ^{13}C , ^{16}O , ^{20}Ne , ^{28}Si beams for science experiments and for the development of the light-ion guide system, despite 8 weeks of downtime for the repairs on the cooling-water heat exchanger and the deflector spark shields. Over 2,300 hours of beams from the K150 cyclotron were provided during simultaneous operation with the K500 cyclotron. This demonstrates that once the ion guides are fully functional, the laboratory is operationally ready for radioactive beam production. The light-ion guide project continued to advance with a campaign of experiments designed to improve the transport efficiency of radioactive ions from the gas cell to the charge-breeding ECR (CB-ECR) ion source. The single sextupole transport device was replaced with two shorter sections that offered finer control but also improved the pumping speed in the region of poor vacuum. In the experiments, 15 MeV proton beams on natural Zinc targets were used to produce ^{64}Ga and ^{66}Ga radioactive ions as test ions and were successfully transported through the CB-ECR ion source. Diagnostic detectors are now being added to the system in order to tune the beam line sections before and after the CB-ECR ion source. Also the main components of the heavy-ion guide gas cell have been assembled and testing with a Cf source will begin in the fall

As in previous reports, I include here some highlights of work carried out over the past year.

- An in-depth analysis of the applicability of popular astrophysical equations of state for describing the neutrino sphere region in a supernova, using heavy ion collision data from the NIMROD detector, clearly indicates that a description of nuclear matter at the densities and temperatures of interest

requires: (i) consideration of *all* relevant particle degrees of freedom, (ii) mean-field effects of the unbound nucleons, and (iii) a suppression mechanism for bound clusters at high densities.

- We have published a new critical survey of world data for superallowed $0^+ \rightarrow 0^+$ β decays, the seventh in a series that began in 1973 and the first in six years. The value obtained for V_{ud} , the up-down quark-mixing element of the Cabibbo-Kobayashi-Maskawa matrix, is consistent with, but more precise than, values we have obtained previously. A new limit was also set on the possible existence of scalar interactions.
- Strong evidence that the super-heavy helium isotope, ${}^9\text{He}$, is unbound by about 3 MeV instead of ~ 0.2 MeV, as suggested previously, has been found through the measurement of the $T=5/2$ isobaric analog states in ${}^9\text{Li}$.
- The first unambiguous high statistics observation of ${}^{10}\text{N}$ ground states were observed in ${}^9\text{C}+p$ elastic scattering, resulting in a definitive spin-parity assignment.
- Efficient separation of the group 13 elements In and Tl was achieved using a cation exchange column indicating a possible means of investigating the liquid-phase chemistry of element 113.
- The upgraded RFQ cooler and buncher for the TAMUTRAP facility has been commissioned with a demonstrated 60% efficiency in continuous mode.
- Analysis of the polarimetry results from the June 2014 TRINAT data is complete, with an average nuclear polarization of $\langle P \rangle = 99.1(2)\%$. We expect in our next experiment to reduce the uncertainty to below the 0.1% threshold needed for the angular distribution measurement.
- The FAUSTUPS-QTS experimental line has been fully commissioned.
- Measured xn cross sections of ${}^{45}\text{Sc}$ and ${}^{44}\text{Ca}$ with various lanthanides, and demonstrated that the survivability of the compound nucleus is strongly affected by small changes in its fission barrier and neutron binding energy.
- HF-RPA calculations with the KDE0v1 interaction (the overall best in an independent test of 240 Skyrme interactions) gave energies of the GMR in ${}^{96,98,100}\text{Mo}$ and ISGDR in ${}^{92,96,98,100}\text{Mo}$ in agreement with experiment, but for each of the isotopes the measured GQR energies were somewhat lower than predicted and the measured HEOR energies were substantially lower ($\sim 1.5\text{MeV}$) than predicted.
- Stringent constraints on the values of nuclear matter properties, needed for determining the next generation energy density functional, were obtained by carrying out extensive calculations of isoscalar and isovector giant resonances of multipolarities $L=0$ to 3 for a wide range of nuclei using over 30 commonly employed Skyrme type interactions.
- The energy-averaged double transition densities for giant resonances were determined, for the first time, within the particle-hole optical model and compared with the quasi-classical collective model forms commonly used in experimental analysis of excitation of giant resonances.
- Made the first-ever observations of the Collins effect, which convolutes quark transversity with the spin-dependent Collins fragmentation function, in $p+p$ collisions.
- Performed the first measurements of the longitudinal double-spin asymmetry for inclusive jet production in $p+p$ collisions at 510 GeV, thereby obtaining sensitivity to gluon polarization down to $x > 0.02$.

- The theory of the deuteron stripping to resonance states based on the surface-integral formalism and CDCC was developed.
- Review of indirect methods in nuclear astrophysics was published.
- The dependence of the ratio of positively to negatively charged pions produced in heavy ion collisions on the stiffness of nuclear symmetry energy at high densities has been better understood after including in a relativistic transport model the effect due to medium modification of the pion production threshold in these collisions.
- The implementation of ρ and a_1 mesons into the chiral pion lagrangian using the local Massive-Yang Mills gauging procedure has been achieved with a fully resummed ρ propagator in the a_1 selfenergy, which enables a simultaneous description of the vacuum vector and axialvector spectral functions (as measured in hadronic τ decays) within a local-gauge approach.
- The nonperturbative framework for heavy-flavor diffusion and hadronization in QCD matter, implemented into a hydrodynamic modeling for Pb-Pb collisions at the LHC, has resulted in fair agreement with ALICE and CMS data for charm and bottom observables at low and intermediate transverse momenta implying a diffusion coefficient of $D_s \cong 4/(2\pi T)$.
- A novel idea to measure high energy photons from jets, using jets at opposite azimuthal angle (around the beam axis) from the photon as triggers, has been proposed to allow direct access to the interaction mechanism of jets with quark gluon plasma.

Institute scientists remain active in a number of collaborative research efforts around the world. Major programs include: mass measurements using the Penning Trap at the University of Jyväskylä; continued work with the STAR collaboration at RHIC; measurements of beta decays with the TRINAT collaboration at TRIUMF; ANASEN at MSU; and participation in the SAMURAI collaboration at RIBF in Tokyo, Japan.

I am indebted to Dr. Y.-W. Lui for assembling this report.

S.J. Yennello
June 17, 2015

SECTION I

NUCLEAR STRUCTURE, FUNDAMENTAL INTERACTIONS AND ASTROPHYSICS

Isoscalar E1-E3 strength in Mo isotopes

D.H. Youngblood, Y.-W. Lui, Krishichayan,^{1,2} J. Button, G. Bonasera, and S. Shlomo

¹*Department of Physics, Duke University, Durham, North Carolina 27708*

²*Triangle Universities Nuclear Laboratory, Durham, North Carolina 27708*

Isoscalar giant resonances in $^{92,96,98,100}\text{Mo}$ have been studied with inelastic scattering of 240 MeV α particles at small angles including 0° . We have reported the results obtained for the E0 distributions in these nuclei as well as in $^{90,92,94}\text{Zr}$ [1]. However, a significant fraction of the EWSR was also found for isoscalar E1(71%, 71%, 70%, 55%), E2(73%, 69%, 85%, 79%) and high energy octupole E3(52%, 65%, 61%, 53%) resonances in $^{92,96,98,100}\text{Mo}$, respectively. The techniques used for the experiments, data analysis, and DWBA calculations are described in Ref. [1] and references therein. The E0-E3 distributions obtained for ^{92}Mo and ^{96}Mo are shown in Fig.

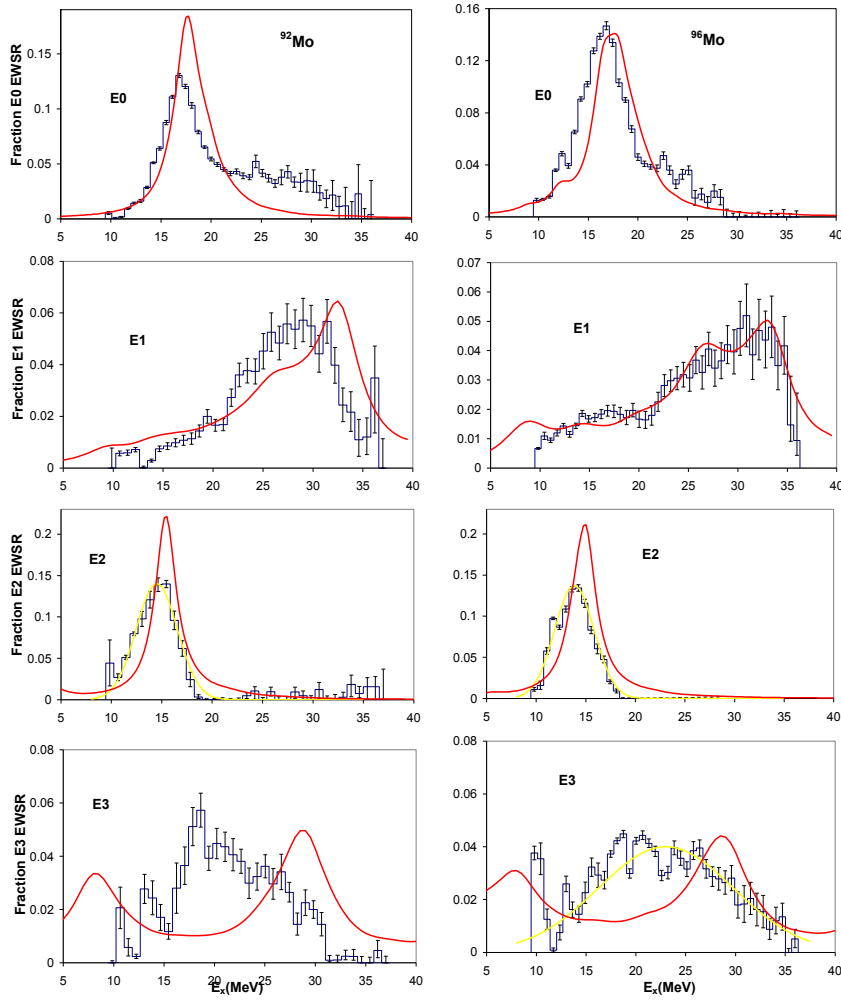


FIG. 1. Strength distributions obtained for ^{92}Mo and ^{96}Mo are shown by the histograms. The thin (red) lines are the strength distributions obtained with the HF-RPA calculations using the KDE0v1 interaction.

1 and those for ^{98}Mo and ^{100}Mo are shown in Fig. 2. Spherical Hartree-Fock-based random-phase approximation calculations[2] were made for each multipole using the KDE0v1 Skyrme-type effective interaction. This interaction was the only one to pass a test of 240 Skyrme interactions, published in the literature, analyzed [3,4] for their ability to pass constraints relating to experimental data on properties of nuclear matter and nuclei, such as incompressibility coefficient, symmetry energy, effective mass, binding energies, radii and fission barriers and observational data of neutron stars. The calculated distributions, using smearing widths of $\Gamma = 10$ MeV for the ISGDR and $\Gamma = 5$ MeV for the other multipoles, are shown superimposed on the experimental results in Figs. 1 and 2.

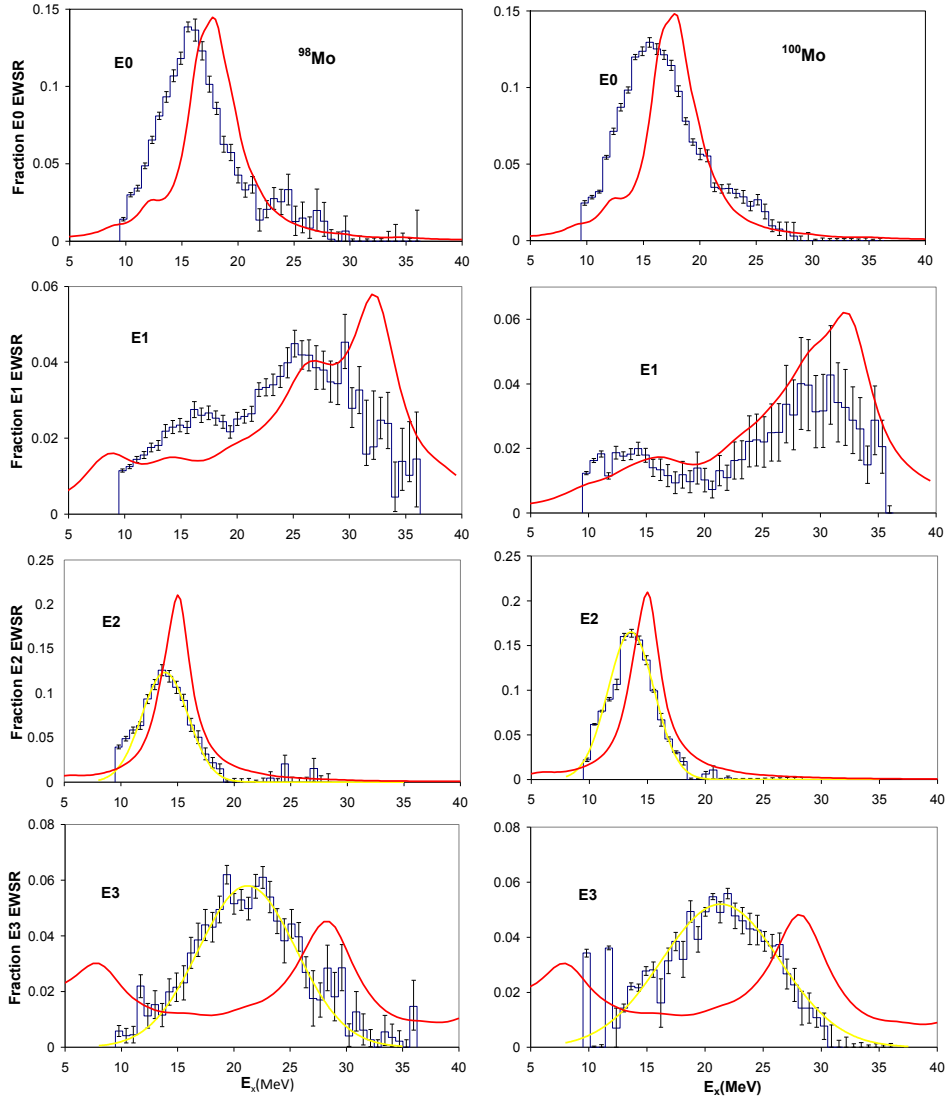


FIG. 2. Strength distributions obtained for $^{98,100}\text{Mo}$ are shown by the histograms. See Fig.1 caption.

Moalem *et al.* [5] studied the isoscalar giant quadrupole resonance (GQR) with inelastic scattering of 110 MeV ^3He in all of the stable Mo isotopes while Duhamel *et al.* [6] reported results for the GQR and the isoscalar giant monopole resonance (GMR) in ^{92}Mo obtained by inelastic scattering of 152 MeV α particles. Our results for the energies of the GQR in these nuclei are compared to those studies and the KDE0v1 calculations in Fig. 3. Our results for strength observed, the energy and width of the GQR agree within the errors with the Moalem *et*

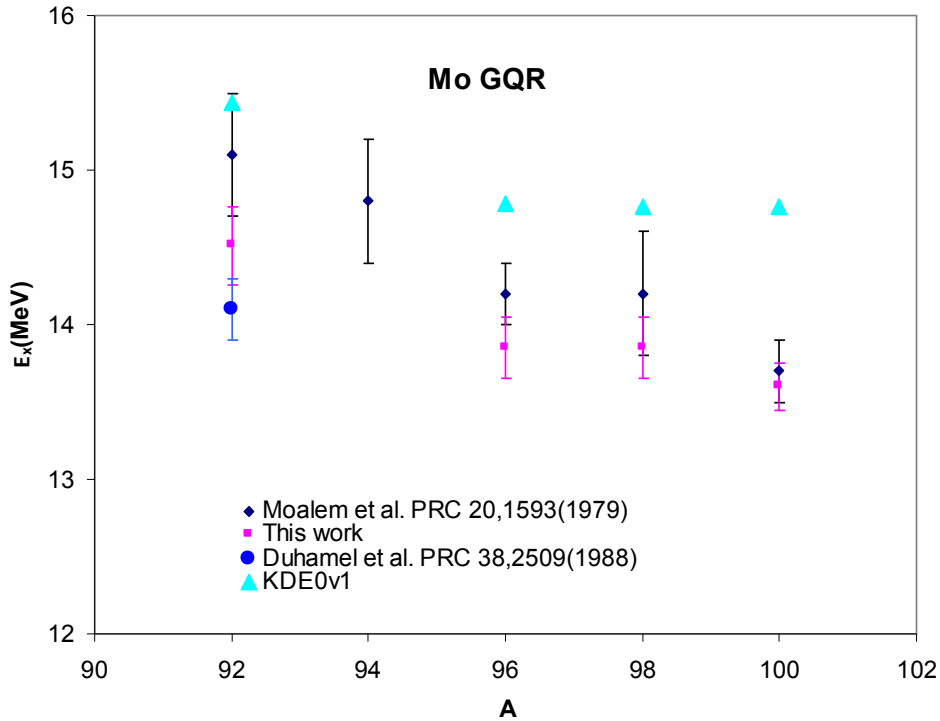


FIG. 3. The centroid of the E2 strength in each of the Mo isotopes obtained in this work [red squares] is plotted vs. A. The error bars indicate the uncertainty obtained using the errors shown in Figs. 1 and 2. Also shown with error bars are centroids reported in Ref. [3] (black diamonds) and a measurement for ^{92}Mo [4] (blue circle). The light blue triangles show the centroid of the E2 strength obtained from HF-RPA calculations with the KDE0v1 interaction.

al. work. The energy and width obtained for the GQR in ^{92}Mo by Duhamel *et al.* also agree within the errors with our result, but they only identified $23\pm 5\%$ of the E2 EWSR strength compared to our $73\pm 13\%$.

- [1] D.H. Youngblood, Y.-W. Lui, Krishichayan, J. Button, M.R. Anders, M.L. Gozeli, M.H. Urin, and S. Shlomo, Phys. Rev. C **88**, 021301(R) (2013).
- [2] M. Anders, S. Shlomo, Tapas Sil, D.H. Youngblood, Y.-W. Lui, and Krishichayan, Phys. Rev. C **87**, 024303 (2013).
- [3] M. Dutta, O. Lourenco, J.S. Sa Martins, A. Delfino, J.R. Stone, and P.D. Stevenson, Phys. Rev. C **85**, 035201 (2012).

- [4] P.D. Stevenson, P.D. Goddard, J.R. Stone, and M. Dutta, arXiv:1210.1592v1 [nucl-th] 2012
- [5] A. Moalem, Y. Gaillard, A.M. Bemolle, M. Buenerd, J. Chauvin, G. Duhamel, D. Lebrun, P. Martin, G. Perrin, and P. de Saintignon, *Phys. Rev. C* **20**, 1593(R) (1979).
- [6] G. Duhamel, M. Buenerd, P. de Saintignon, J. Chauvin, D. Lebrun, Ph. Martin, and G. Perrin, *Phys. Rev. C* **38**, 2509 (1988).

Beta-asymmetry measurement with the TRIUMF neutral atom trap

B. Fenker, M. Mehlman, D. Melconian, and P.D. Shidling

Along with collaborators at the TRIUMF Neutral Atom Trap (TRINAT), we have taken data for a measurement of the polarized beta-asymmetry parameter in ^{37}K . The apparatus uses a magneto-optical trap (MOT) to confine and cool neutral ^{37}K atoms and optical pumping to achieve spin-polarization of 99%. The trapped atoms, localized in space and nearly at rest, undergo positron decay and the angular distribution of decay positrons with respect to the spin-polarization axis provides the experimental signature. Furthermore, the polarization is precisely measured using techniques described in our other report. Compared to our 2012 run, we have implemented a number of technical improvements resulting in an increased number of trapped atoms, a longer trap lifetime, and improved detector performance. With these improvements we have collected data with enough statistics for a 0.3% precision measurement. This measurement will be used to constrain physics beyond the Standard Model.

Using a newly developed high-power Titanium-carbide target, TRIUMF was able to deliver more than twice the yield of ^{37}K than during our previous run. Additionally, our own technical improvements increased the trapping and cooling efficiency of the MOT. As a result, we increased the number of trapped atom to almost 9000 and increased the MOT lifetime from 1s in 2012 to 4s in 2014.

The main detectors in the experiment are a pair of plastic scintillators coupled via light guides to photomultiplier tubes (PMT). These record the full energy of the positron but have no position information and are very sensitive to a large gamma-ray background from positrons annihilating in the apparatus. To both provide position information and suppress this background, each scintillator is placed directly behind a thin double-sided silicon-strip detector. The low efficiency of these detectors for detecting gamma-rays suppresses their background and the segmentation provides position sensitivity. A typical positron energy spectrum with and without the coincidence requirement is shown in the Fig. 1. In our run last year, we continuously monitored the gain of each PMT using a stabilized LED. This allows us to measure and correct for any drifts in gain over the roughly three weeks during which the data was taken. Additionally, we added a forced-air cooling system to the silicon detector to combat the heating induced by the AC magnetic fields of the MOT. Operating the silicon detectors at a lower temperature directly reduces the noise inherent in these detectors. Also, in 2012, half the strips on one of these detectors were not functioning which resulted in large complications in the analysis and therefore a significant systematic uncertainty in how best to approach this problem. We have fixed this issue and therefore eliminated this large systematic for the 2014 data set. Finally, we have added position sensitivity to the shake-off electron micro-channel plate. This detector provides an extremely clean signal that a detected beta-decay occurred from within the trap rather than after escaping the trap and perhaps depolarizing. The position sensitivity shown in Fig. 2 has demonstrated that very few of these electrons miss the detector, which confirms that this is not a significant source of systematic uncertainty.

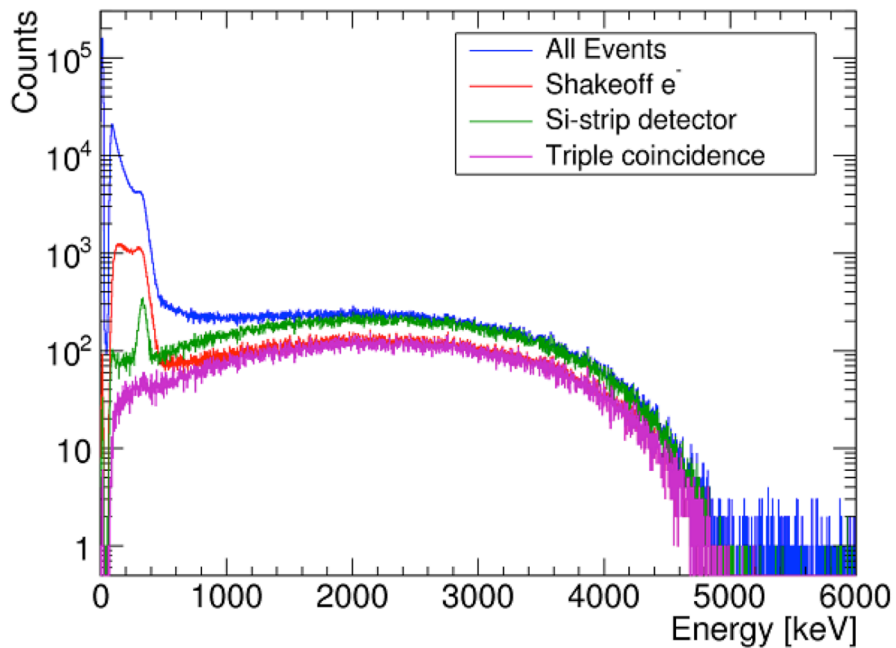


FIG. 1. Positron energy spectrum in the plastic scintillator. Requiring a coincidence with the shake-off electron detector (green) eliminates background from untrapped atoms and requiring a silicon-strip detector coincidence (green) reduces the gamma-ray background. Final analysis is done with the three-fold coincidence (magenta).

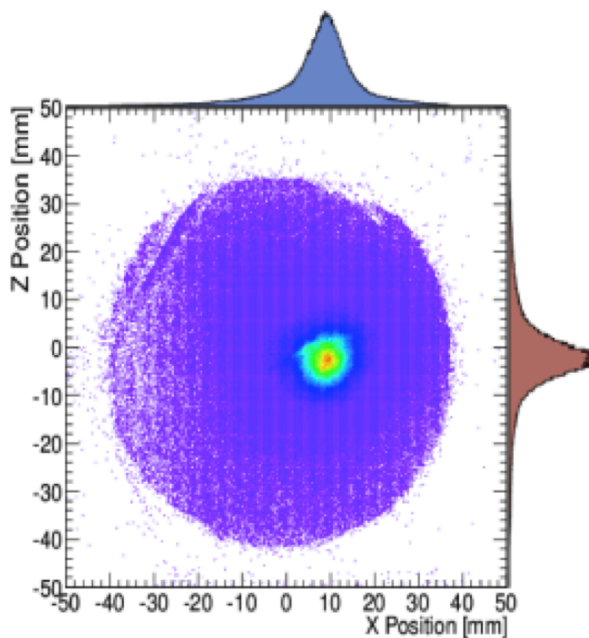


FIG. 2. Position spectrum of atomic electrons shaken off from the recoiling daughter nucleus as a result of the sudden change in nuclear charge. That few events are registered near the detector edges confirms that the possible systematic effect from electrons missing the detector is quite small.

With the upgrades and larger number of atoms, the current data set has a higher statistical sensitivity and better control over systematic uncertainties. The total statistical uncertainty is expected to be about 0.3%, half as large as the 2012 data set. We have also reduced all the main sources of systematic uncertainty. The proper functioning of all regions of the silicon detectors has already been discussed and having more trapped atoms allows a more precise determination of trap parameters such as size and average velocity. Also, the larger number of trapped atoms has resulted in a very clean polarization signal which allows a much more precise measurement than before and is discussed in our other report. Combining systematic and statistical uncertainties, we expect the final uncertainty to be $\lesssim 0.5\%$, making it the most precise determination of the beta-asymmetry in a nucleus and of similar precision to measurements in the neutron. The results will be used to constrain possible Standard Model extensions and in particular search for a possible $V+A$ (vector + axial-vector) component in the charged weak interaction.

Polarization by optical pumping – the β -asymmetry of ^{37}K

B. Fenker, M. Mehlman, D. Melconian, and P.D. Shidling

As described in Ref. [1], we have collected data for a $\lesssim 0.5\%$ measurement of the polarized beta-asymmetry parameter in ^{37}K . The observed positron asymmetry is equal to the physics parameter of interest multiplied by the nuclear polarization. Therefore, a precise beta-asymmetry measurement requires a precise polarization measurement. To achieve the high polarization, we use a technique called optical pumping. In this process, we illuminate the atoms with circularly polarized laser light to select a particular Zeeman sublevel, called the “stretched state,” which corresponds to complete atomic and nuclear polarization. However, not all of the atoms accumulate in the desired state, leaving the polarization slightly imperfect.

We can monitor the total population of non-stretched states by photoionizing and detecting a small fraction of atoms that have been excited by the laser light. The frequency of the photoionization laser is chosen such that it can only photoionize atoms after they have been excited by the optical pumping laser. Since atoms in the stretched state cannot be excited by the optical pumping light, they cannot be photoionized. Therefore, this technique produces a signal proportional to the total population of all the non-stretched states. As atoms accumulate in the stretched state they are no longer available to be photoionized and the time evolution of the photoionization rate, shown in Fig. 1, provides a clean measurement of the polarization.

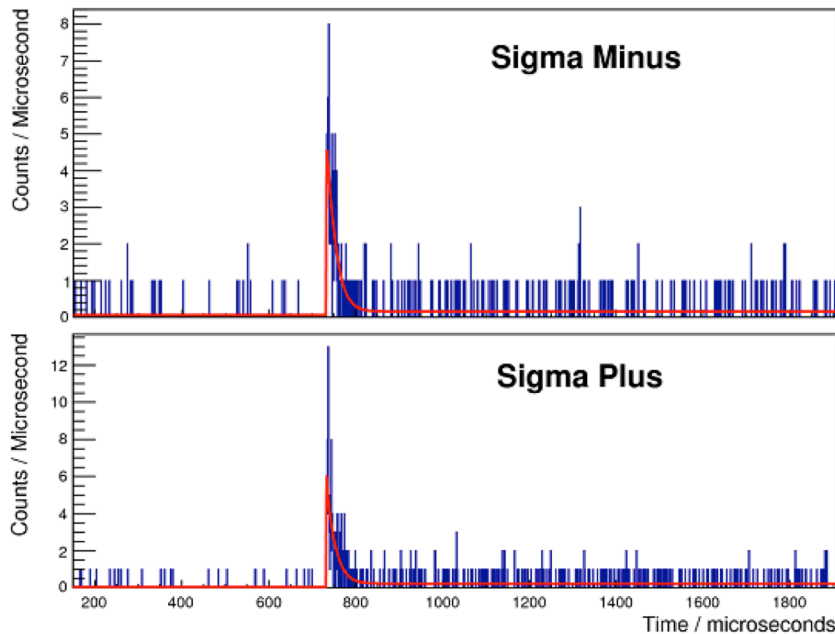


FIG. 1. Photoionization signal as a function of time. The photoionization signal is proportional to the total non-stretched population. Therefore, if the photoionization were completely extinguished the polarization would be 100% as all the atoms would be stretched. The degree to which the photoionization is not completely extinguished can be used to infer the nuclear polarization.

However, because it only measures the total non-stretched population and not the distribution among these states, the photoionization signal is an indirect measurement of the polarization. We have used a numerical model of optical pumping to infer this distribution and calculate the polarization. It includes two mechanisms by which the polarization can be imperfect: imperfect polarization of the laser light and a magnetic field transverse to the polarization axis. These two depolarizing mechanisms are completely indistinguishable in the data and so represent a systematic uncertainty in the polarization. To reduce this uncertainty, we have used off-line measurements of the light ellipticity and transverse magnetic field to constrain these parameters. While not eliminating the effect, this has allowed us to reduce the uncertainty to acceptable values, similar to the statistical uncertainty.

The polarization analysis is nearly complete with the result expected to have $P \approx 99.1\%$ and $< 0.3\%$ total uncertainty. This is a factor of 3 more precise than previous analyses by our group and represents significant progress towards the most precise determination of the beta-asymmetry in a nucleus.

[1] B. Fenker, M. Mehlman, D. Melconian, and P.D. Shidling, *Progress in Research*, Cyclotron Institute, Texas A&M University (2014-2015), p. I-5.

Production studies of proton-rich T=2 nuclei

E. Bennett, R. Burch, B. Fenker, M. Mehlman, D. Melconian, and P.D. Shidling

We have continued our investigations of efficiently producing the nuclei of interest to the TAMUTRAP facility using the K150 Cyclotron with the heavy-ion guide. As part of this effort, we performed a ^{24}Si production experiment using the K500 Cyclotron in combination with the MARS spectrometer.

^{24}Si was produced in fusion-evaporation reaction in an inverse kinematic mode. A primary beam of ^{24}Mg at 23 MeV/u was bombarded on a 1 atm ^3He gas target cooled to liquid nitrogen temperature. The reaction products were analyzed using the MARS spectrometer, which was operated with a total momentum acceptance of $\Delta p/p = 1.92\%$. Identification of the reaction products was made in the usual way: via a position-sensitive Si-strip detector in the focal plane of MARS. Fig. 1 shows the energy deposited in this detector versus the vertical position in the strip detector, with the isotope of interest, ^{24}Si , clearly separated from the other reaction products.

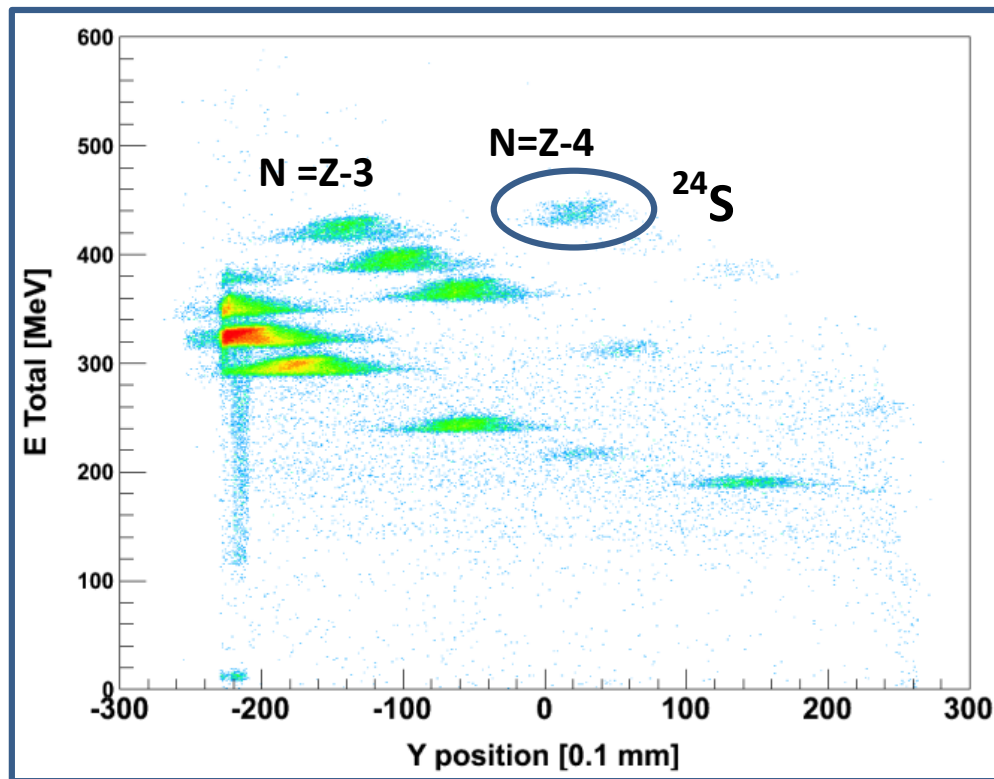


FIG. 1. Results of ^{24}Si production run, The 2D plot of the energy loss versus Y position in the strip detector separates the different reaction products.

The yield of different reaction products and isobars ($A=24$) produced in this reaction were determined by optimizing the rigidity settings of MARS. The production rate for ^{24}Si observed at the focal plane was twice the production rate of ^{32}Ar [1] which was also produced in fusion-evaporation reaction. Theoretical cross-section calculations for nuclei of interest were

carried out using PACE4 code [2]. The calculations predict a factor of two between the production cross-sections ^{32}Ar and ^{24}Si , in agreement with the experiment.

The efficiency of MARS spectrometer needs to be known for determining the absolute cross section experimentally. In this connection, we performed an experiment for determining the transport efficiency of MARS by bombarding ^{36}Ar beam at 17 MeV/u on ^{27}Al target of thickness 75 μm . The reason for using this target was to match the rigidity setting of ^{36}Ar primary beam with the ^{32}Ar secondary beam. This leads us to determine the transport efficiency of MARS for a particular rigidity setting. In this experiment, the current of ^{36}Ar after reacting with ^{27}Al target was measured at the target chamber Faraday cup and at the focal plane Faraday cup. We are currently analyzing the data and also trying to estimate the transport efficiency using LISE++ code [3].

In addition to this, we have looked into using a projectile fragmentation reaction for producing beta-delayed super allowed proton emitters. We performed an experiment for producing ^{32}Ar in this mode by bombarding a primary beam of ^{36}Ar at 17MeV/u on ^9Be , $^{\text{nat}}\text{Ni}$ and ^{27}Al targets of thickness 150 μm , 6 μm , and 76 μm respectively. In the coming year, we will be analyzing the data of projectile fragmentation reaction, estimate the transport efficiency of MARS spectrometer and compare it with the prediction made using LISE++ code [3].

- [1] O.B. Tarasov and D. Bazin, Nucl. Instrum. Methods Phys. Res. **B204**, 174 (2003), (Modified version of Julian code incorporated in LISE++ package).
- [2] R.S. Behling *et al.*, *Progress in Research*, Cyclotron Institute, Texas A&M University (2013-2014), p. I-58.
- [3] O. Tarasov, D. Bazin, M. Lewitowicz, and O. Sorlin, Nucl. Phys. **A701**, 661 (2002).

**α -cluster asymptotic normalization coefficients from sub-Coulomb (${}^6\text{Li},d$) reaction:
Benchmark measurement**

G.V. Rogachev, E. Koshchiy, M.L. Avila,¹ L.T. Baby,¹ J. Belarge,¹ K.W. Kemper,¹
A.N. Kuchera,¹ and D. Santiago-Gonzalez¹

¹*Department of Physics, Florida State University, Tallahassee, Florida 32306*

Nuclear reaction rates that involve α particles are often key nuclear physics inputs required for stellar models. There are many examples of reactions that involve α particles on both stable and radioactive nuclei that are critical for nuclear astrophysics. To name a few: the ${}^{12}\text{C}(\alpha,\gamma)$ reaction that determines the carbon to oxygen ratio in the Universe, the ${}^{13}\text{C}(\alpha,n)$ and ${}^{22}\text{Ne}(\alpha,n)$ neutron source reactions for s-process in AGB stars, the αp -chain reactions ${}^{18}\text{Ne}(\alpha,p)$ and ${}^{22}\text{Mg}(\alpha,p)$ that play an important role during x-ray bursts, etc. Yet, direct measurements of the α induced reaction cross sections at energies that are relevant for stellar environments have not been possible. The product of the reaction cross section and the Maxwell-Boltzmann energy distribution for α particles in a stellar environment defines the energy range at which the specific reaction is most efficient. This energy range, known as the Gamow window, is typically far below the Coulomb barrier, where the Coulomb repulsion dominates, and therefore the nuclear reaction cross section is very small and drops exponentially with energy. Since the cross section is often too small to be measured directly we are forced to rely on extrapolation of measurements done at higher energies down to the energies of interest. However, the reliability of these extrapolations is handicapped by the unknown nuclear structure of the systems involved. For example, direct measurements of the ${}^{12}\text{C}(\alpha,\gamma)$ reaction cross section have been performed only down to 900 keV in the center-of-mass frame (c.m.), while the Gamow window for the helium-burning stage is around 300 keV. The extrapolation is strongly affected by the sub-threshold states in ${}^{16}\text{O}$. Indirect methods can be used to constrain the properties of these resonances and therefore reduce the uncertainties related to low energy extrapolations.

One such method is the α -transfer reaction performed at sub-Coulomb energy. By measuring the α -transfer reaction cross section at energies low enough to be below the Coulomb barrier in both entrance and exit channels the dependence of the result on the optical model parameters is significantly reduced. Moreover, if the asymptotic normalization coefficients (ANCs) are extracted instead of the spectroscopic factors (SFs) then the dependence on the shapes of the α -cluster form factors and the number of nodes of the cluster wave function is also eliminated. Therefore, this technique yields an almost model independent result, as long as the peripheral direct reaction mechanism dominates.

The approach has already been applied to determine the α -ANCs for the astrophysically important states in ${}^{16}\text{O}$, ${}^{17}\text{O}$ and ${}^{18}\text{O}$ [1-3]. However, the benchmark measurement that allows to verify the technique using resonances with known partial α -width close to the α -decay threshold has not been performed so far and is the main goal of this work. The key to proving this technique is the choice of a specific case that can serve as its verification. The nearly ideal opportunity to test the sub-Coulomb α -transfer approach is provided by the 1^- state at 5.79 MeV in ${}^{20}\text{Ne}$. It is a

purely α -cluster state with a partial α -width close to the single-particle (SP) limit. This state is above the ^{20}Ne α -decay threshold by 1.06 MeV. Its natural width is known with good accuracy to be 28(3) eV [4] and it equals to partial α width.

We measured the α -ANC for the 1^- state at 5.79 MeV in ^{20}Ne using the $^{16}\text{O}(^6\text{Li},d)$ reaction performed at sub-Coulomb energy and related it to the partial α -width following the prescriptions of Ref. [5]. Measurements were performed at the John D. Fox Superconducting Linear Accelerator Laboratory at Florida State University. The differential cross section for the $^6\text{Li}(^{16}\text{O},d)^{20}\text{Ne}(1^-, 5.79 \text{ MeV})$ reaction at 12.57 MeV energy of ^{16}O beam is shown in Fig. 1. The theoretical analysis of the cross section is done using the finite-range DWBA approach via the

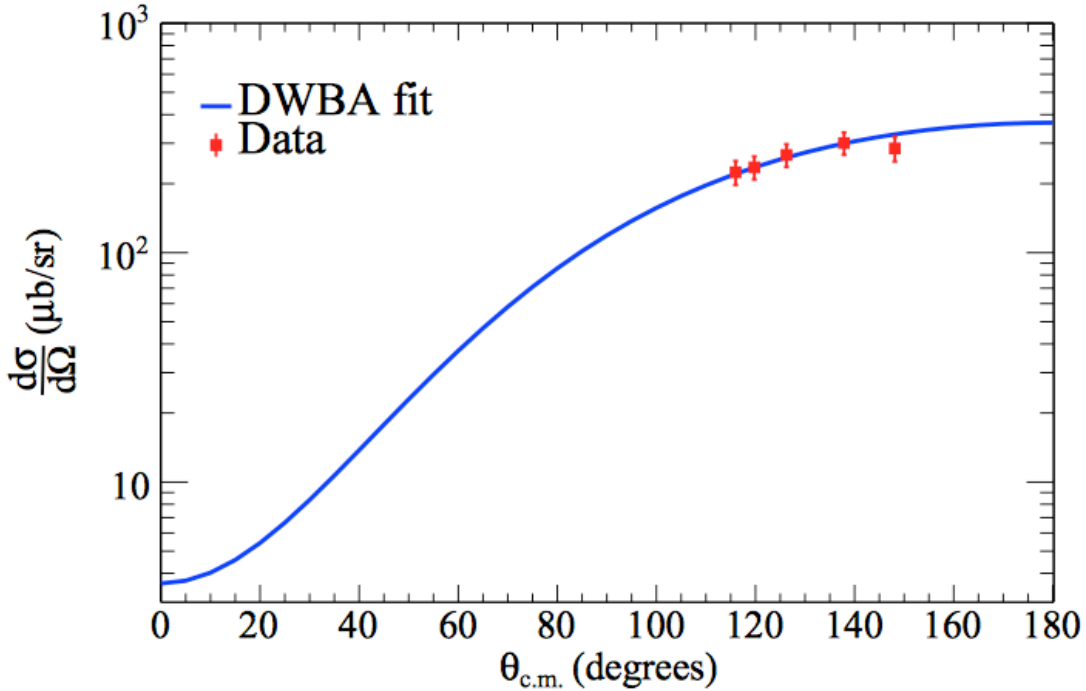


FIG. 1. Angular distribution of deuterons from the $^6\text{Li}(^{16}\text{O},d)$ reaction populating the $1^-(5.79 \text{ MeV})$ state in ^{20}Ne and DWBA fit for $E(^{16}\text{O})=12.57 \text{ MeV}$.

computer code FRESKO. Due to sub-Coulomb regime,

dependence of the final result on the optical model parameters is very weak (<13%). The FRESKO code is designed for calculating transfer cross section into the bound states and since the 1^- at 5.79 MeV is an unbound resonance an artificial binding energy was used in the calculations. The fit shown in Fig. 1 is obtained using a binding energy of 0.1 MeV. The value of the ANC and partial α width calculated from it depend on the choice of binding energy so that the partial α width for different binding energies was calculated and a nearly linear dependence on the binding energy was found as shown in Fig. 2. Linear extrapolation allows the partial α width for the correct binding energy of -1.06 MeV for this unbound state to be determined. The Whittaker function and penetrability factor are calculated using a channel radius of $R = 5.1 \text{ fm}$

(the result is almost independent of this parameter as well). The final result obtained for the

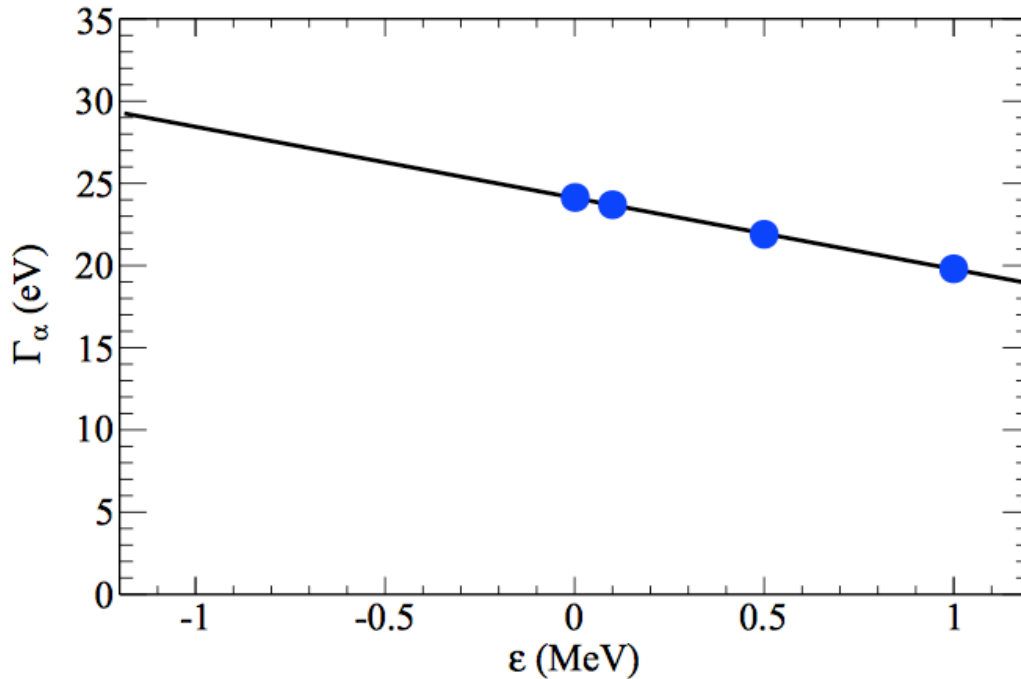


FIG. 2. Partial α width as a function of binding energy for the 1^- (5.79 MeV) state in ^{20}Ne .

partial α width for the unbound 1^- state at excitation energy of 5.79 MeV in ^{20}Ne is 28(6) eV. This is in perfect agreement with the known partial α width for this state [4].

We have verified that an α -transfer reaction performed at sub-Coulomb energies can produce an accurate and model-independent determination of the alpha asymptotic normalization coefficients of the near-threshold resonances and sub-threshold states. These model independent ANCs can be used to constrain key astrophysical reaction rates. The results of this work are published in Ref. [6].

- [1] C.R. Brune, W.H. Geist, R.W. Kavanagh, and K.D. Veal, Phys. Rev. Lett. **83**, 4025 (1999).
- [2] E.D. Johnson, G.V. Rogachev *et al.*, Phys. Rev. Lett. **97**, 192701 (2006).
- [3] E.D. Johnson, G.V. Rogachev *et al.*, Phys. Rev. C **80**, 045805 (2009).
- [4] D.R. Tilley, C.M. Cheves, J.H. Kelley *et al.*, Nucl. Phys. **A636**, 249 (1998).
- [5] A.M. Mukhamedzhanov and R.E. Tribble, Phys. Rev. C **59**, 3418 (1999).
- [6] M.L. Avila, G.V. Rogachev, E. Koshchiy *et al.*, Phys. Rev. C **90**, 042801 (R) (2014).

Constraining the cascade transitions in the astrophysically important $^{12}\text{C}(\alpha,\gamma)^{16}\text{O}$ reaction

G.V. Rogachev, E. Koshchiy, E. Uberseder, A.M. Mukhamedzhanov, M.L. Avila,¹ L.T. Baby,¹
J. Belarge,¹ K.W. Kemper,¹ A.N. Kuchera,¹ and D. Santiago-Gonzalez¹

¹*Department of Physics, Florida State University, Tallahassee, FL 32306*

The radiative capture of α -particles on ^{12}C plays a fundamental role in astrophysics. The $^{12}\text{C}(\alpha,\gamma)^{16}\text{O}$ reaction cross section at 300 keV determines the relative abundance of $^{12}\text{C}/^{16}\text{O}$ in the stellar core as a result of helium burning. Not only this ratio determines the relative carbon-oxygen abundance in the Universe, but it has important implications for the sequence of later quiescent and explosive burning stages in stars, including nucleosynthesis and production of long-lived radioactive isotopes, such as ^{26}Al , ^{44}Ti and ^{60}Fe in core collapse supernova [1]. It also has direct influence on the composition of white dwarfs, and therefore plays an important role in the type Ia supernova ignition process (see Ref. [2] and references therein).

Significant progress in constraining the $^{12}\text{C}(\alpha,\gamma)^{16}\text{O}$ reaction rate has been achieved over the last 40 years, however, the astrophysically required precision of better than 10% [3] is still out of reach. It was assumed in the past that the ground state transition through the tails of sub-threshold states and above threshold resonances plays a dominant role and that cascade transitions (transitions by capture to the sub-alpha-threshold excited states in ^{16}O with subsequent decay to the ground state) are relatively unimportant. This assumption was called into question in [4] where the S-factor at 300 keV for the 0^+ state at 6.05 MeV cascade transition was determined to be 25 ± 16 keV b (this is 15% of the total S-factor). Contradicting conclusion was made in Refs. [5, 6], where the upper limit for the cascade transitions was set at <1 keV b. The main goal of this work was to constrain the 6.05 MeV 0^+ and 6.13 MeV 3^- cascade transitions using an independent technique.

We measured the Asymptotic Normalization Coefficients (ANCs) of all sub-alpha-threshold states in ^{16}O using the $^{12}\text{C}(^6\text{Li},d)$ alpha-transfer reaction at sub-Coulomb energy. Measurements were performed at the John D. Fox Superconducting Accelerator Laboratory at Florida State University. The advantage of using the sub-Coulomb energies for α -transfer reactions is that the extracted ANCs are practically independent of the optical model potentials. Extracting the ANC instead of the spectroscopic factor eliminates uncertainties associated with the shape of the cluster form factor potential and the number of nodes of the cluster wave function. Therefore, results of these measurements are nearly model independent and do not require any additional normalization as long as the reaction mechanism is dominated by peripheral single-step α -capture. The technique was benchmarked using the $^{16}\text{O}(^6\text{Li},d)$ reaction and the results of this test are described in a separate report [7] and published in Ref. [8].

All four sub-alpha-threshold excited states in ^{16}O have been populated (see Fig. 1) and the ANCs for these states have been measured. Table I contains the squared ANCs for these states determined in this work in comparison with previous results for the 2^+ at 6.92 MeV and 1^- at 7.12 MeV. The ANCs for the 0^+ at 6.05 MeV and the 3^- at 6.13 MeV have been measured for the first time.

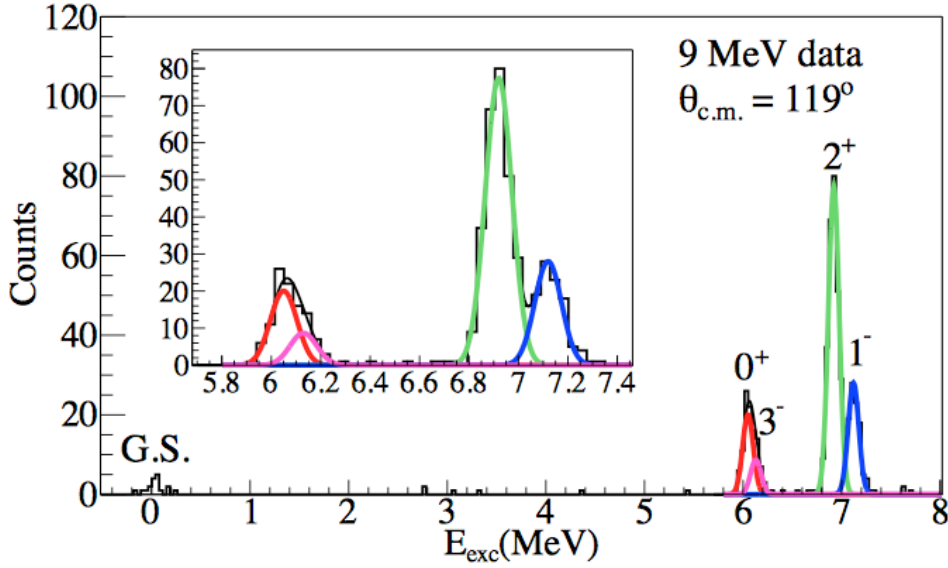


FIG. 1. Spectrum of deuterons from the $^{12}\text{C}(^6\text{Li},d)^{16}\text{O}$ reaction. The ^{12}C effective beam energy is 8.7 MeV (energy in the middle of the ^6Li target) and the deuteron scattering angle is 119° in the center of mass.

Table I. Squared ANCs (in fm^{-1}) for the 0^+ (6.05 MeV), 3^- (6.13 MeV), 2^+ (6.92 MeV) and 1^- (7.12 MeV) sub-threshold states in ^{16}O , compared to previous measurements.

0^+ at 6.05 MeV	3^- at 6.13 MeV	2^+ at 6.92 MeV	1^- at 7.12 MeV	Ref.
		$2.07(80)\times 10^{10}$	$4.0(14)\times 10^{28}$	[9]
		$1.29(23)\times 10^{10}$	$4.33(84)\times 10^{28}$	[10]
		$2.0(13)\times 10^{10}$	$3.5(20)\times 10^{28}$	[11]
$2.43(30)\times 10^6$	$1.93(25)\times 10^4$	$1.48(16)\times 10^{10}$	$4.39(59)\times 10^{28}$	This work

Using the measured alpha ANCs the cross section for direct capture can be calculated unambiguously using the approach outlined in [12] for all cascade transitions. The strongest one is the E2 transition through the 0^+ state at 6.05 MeV with the corresponding S-factor 3.2(4) keV b. However, in addition to the direct capture component, capture through the high energy tail of the 2^+ state at 6.92 MeV into the 0^+ at 6.05 MeV is also possible. Since ANC for the 2^+ is also known the corresponding resonance amplitude can be calculated. The interference sign between

these two amplitudes (direct capture into 0^+ and capture through the tail of the 2^+ state) is not known and cannot be determined in present work. Taking into account interference, the total S-factor at 300 keV for the 0^+ cascade transition can be either 4.36(45) keV b for constructive or 1.96(30) keV b for destructive interference. Similar situation is observed for the 3^- cascade transition, for which the direct E2 capture interferes with capture through the tail of 1^- state at 7.12 MeV. The total S-factor for the 3^- cascade transition is 1.44(12) keV b for the constructive and 0.12(04) keV b for the destructive interference.

The main conclusion of this work is that while interference sign is still the source of uncertainty, the maximum contribution of the 0^+ and 3^- cascade transitions can be determined by assuming positive interference in both cases and the combined contribution of these cascade transitions does not exceed 4% of the total $^{12}\text{C}(\alpha,\gamma)^{16}\text{O}$ S-factor. Significant uncertainty for the $^{12}\text{C}(\alpha,\gamma)^{16}\text{O}$ reaction S-factor have been dramatically reduced. The results of this work are published in Ref. [13].

- [1] C. Tur, A. Heger, and S.M. Austin, *Astrophys. J.* **718**, 357 (2010).
- [2] M. Wiescher, F. Käppeler, and K. Langanke, *Ann. Rev. Astron. Astrophys.* **50**, 165 (2012).
- [3] T.A. Weaver and S.E. Woosley, *Phys. Rep.* **227**, 65 (1993).
- [4] C. Matei, L. Buchmann, W.R. Hannes *et al.*, *Phys. Rev. Lett.* **97**, 242503 (2006).
- [5] D. Schurmann, A.D. Leva, L. Gialanella *et al.*, *Phys. Lett. B* **703**, 557 (2011).
- [6] D. Schurmann, L. Gialanella, R. Kunz, and F. Strieder, *Phys. Lett. B* **711**, 35 (2012).
- [7] G.V. Rogachev, E. Koshchiy, M.L. Avila *et al.*, *Progress in Research*, Cyclotron Institute, Texas A&M University (2014-2015), p. I-12.
- [8] M.L. Avila, G.V. Rogachev, E. Koshchiy *et al.*, *Phys. Rev. C* **90**, 042801 (2014).
- [9] N. Oulebsir, F. Hammache, P. Roussel *et al.*, *Phys. Rev. C* **85**, 035804 (2012).
- [10] C.R. Brune, W.H. Geist, R.W. Kavanagh, and K.D. Veal, *Phys. Rev. Lett.* **83**, 4025 (1999).
- [11] A. Belhout, S. Ouichaoui, H. Beaumevieille *et al.*, *Nucl. Phys.* **A793**, 178 (2007).
- [12] A.M. Mukhamedzhanov, H.L. Clark, C.A. Gagliardi *et al.*, *Phys. Rev. C* **56**, 1302 (1997).
- [13] M.L. Avila, G.V. Rogachev, E. Koshchiy *et al.*, *Phys. Rev. Lett.* **114**, 071101 (2015).

α asymptotic normalization coefficient of the sub-threshold $1/2^+$ state at 6.356 MeV in ^{17}O

G.V. Rogachev, E. Koshchiy, M.L. Avila,¹ L.T. Baby,¹ J. Belarge,¹ K.W. Kemper,¹
A.N. Kuchera,¹ and D. Santiago-Gonzalez¹

¹*Department of Physics, Florida State University, Tallahassee, Florida 32306*

The slow neutron capture process, or s process, occurs in a relatively low neutron density environment in asymptotic giant branch (AGB) stars. This process is essential for the nucleosynthesis of heavier elements. It is believed that the s process is responsible for nearly half of the heavy elements observed in the universe [1]. The main characteristic of this process is that neutron capture is slower than β decay. At low temperature ($<10^8$ K) for low-mass stars the $^{13}\text{C}(\alpha,n)^{16}\text{O}$ reaction plays the major role and is considered to be the main source of neutrons for the s-process in such stars [2]. Thus, this reaction rate is a necessary ingredient for constraining the models of AGB stars. Direct measurements are only available for center-of-mass (c.m.) energies above 279 keV. This is 100 keV above the energy for which α -capture is most efficient (Gamow energy). Below this energy the cross section has to be extrapolated. Extrapolation to lower energies causes a large uncertainty due to the presence of a sub-threshold $1/2^+$ resonance in ^{17}O at excitation energy of 6.356 MeV (3 keV below the $^{13}\text{C}+\alpha$ threshold energy). This sub-threshold resonance enhances the cross section at low energies, making an important contribution to the astrophysical S factor.

There have been several attempts to use various α -transfer reactions to constrain the contribution of the $1/2^+$ state to the low energy $^{13}\text{C}(\alpha,n)^{16}\text{O}$ cross section [3-7]. However, significant discrepancy still remains. In particular, previous measurement of the asymptotic normalization coefficient for the $1/2^+$ state using the $^{13}\text{C}(^6\text{Li},d)^{17}\text{O}$ reaction at sub-Coulomb energy [4] produced the squared Coulomb-modified ANC of $0.89\pm 0.23 \text{ fm}^{-1}$. While α -transfer measurements at above barrier energies in Refs. [5] and [6] indicate much larger ANC values, 4.5 ± 2.2 and $4.0\pm 1.1 \text{ fm}^{-1}$ respectively. The most recent measurements using the Trojan Horse Method indicate even larger ANC of $7.7\pm 0.3\pm 1.5 \text{ fm}^{-1}$ [7]. The main goal of this work is to remeasure the corresponding ANC using the sub-Coulomb α -transfer reaction and resolve the discrepancies between the ANC measured at sub-Coulomb energies and the ANC measured at above Coulomb barrier energies.

Measurements were performed at the John D. Fox Superconducting Accelerator Laboratory at Florida State University. The spectrum of deuterons from the $^6\text{Li}(^{13}\text{C},d)^{17}\text{O}$ reaction at 8 MeV of ^{13}C beam at 144° in c.m. is shown in Fig. 1. The $1/2^+$ state at 6.356 MeV is clearly observed. The DWBA calculations using code FRESKO were used to extract the ANC from the experimental angular distribution shown in Fig. 2. The squared Coulomb-modified ANC that we determined in this work for the $1/2^+$ state at 6.356 MeV in ^{17}O is $3.6\pm 0.7 \text{ fm}^{-1}$. The ANCs reported in Refs. [4-7] and the value obtained in this work are shown in Fig. 3. The cross section measured in Ref. [4] is about a factor of three smaller than the cross section measured in the present work. The main reason for this difference is the target deterioration effect that was not taken into account in [4]. The target thickening due to material buildup was observed in this

experiment, causing the beam energy in the middle of the target to decrease. The effect was mitigated by frequent target change and also by monitoring of the target condition using

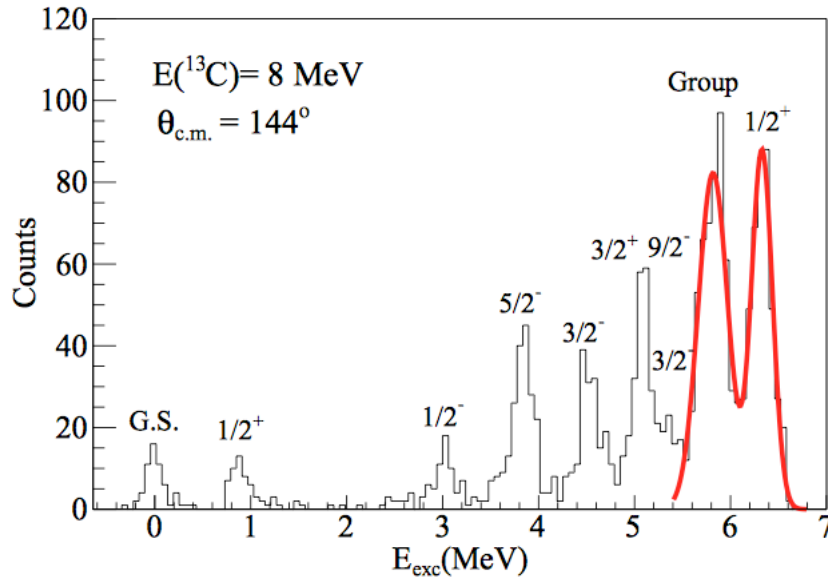


FIG. 1. Spectrum of deuterons from ${}^6\text{Li}({}^{13}\text{C},d){}^{17}\text{O}$ reaction at 8 MeV (7.72 MeV effective energy after energy-loss corrections) of ${}^{13}\text{C}$ beam at 144° in c.m.

elastic scattering of the Li beam. This was not done in the previous experiment [4]. Therefore, the beam energy in the middle of the target was decreasing during measurements that used the same target over extended periods of time in Ref. [4]. As a result, the measured cross section is

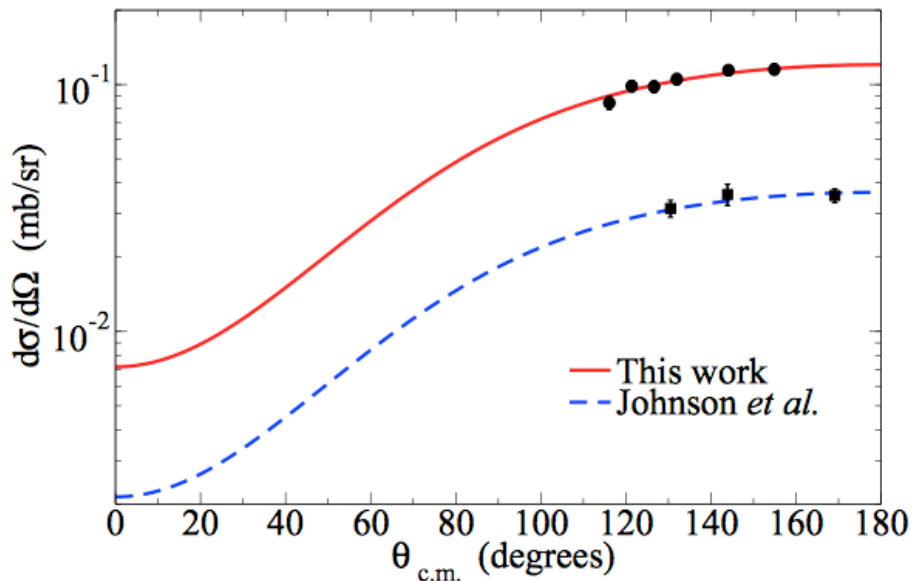


FIG. 2. Cross section and DWBA fit as a function of center-of-mass angle for the ${}^6\text{Li}({}^{13}\text{C},d){}^{17}\text{O}$ reaction populating the $1/2^+$ sub-threshold state at 6.356 MeV in ${}^{17}\text{O}$. Solid curve is the present work and the dashed curve is that from Ref. [5] (dashed line).

significantly lower than it should have been. One of the characteristic features of sub-Coulomb transfer reactions (unlike the reactions performed at higher energies) is the strong dependence of the reaction cross section on the energy of the beam. The lower reaction cross section measured in Ref. [4] naturally led to the smaller ANC.

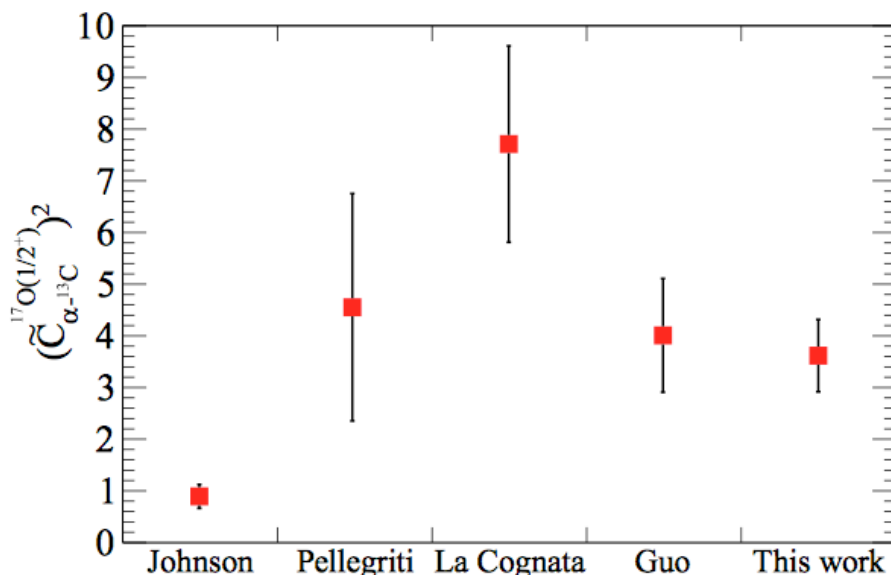


FIG. 3. Squared Coulomb-modified ANC value obtained in this work, for the $1/2^+$ at excitation energy of 6.356 MeV in ^{17}O , compared with previous results from Johnson et al. [4], Pellegriti et al. [5], Cognata et al. [7], and Guo et al. [6].

In summary, we used the direct α -transfer reaction $^6\text{Li}(^{13}\text{C},d)^{17}\text{O}$ at a sub-Coulomb energy to extract the α ANC for the $1/2^+$ state at 6.356 MeV in ^{17}O . This parameter is the major source of uncertainty for the astrophysically important $^{13}\text{C}(\alpha,n)^{16}\text{O}$ reaction rate at temperatures relevant for the s process in AGB stars (<100 MK). The Coulomb-modified square ANC for the $1/2^+$ state is measured to be $3.6 \pm 0.7 \text{ fm}^{-1}$. This is the most precise value to date but in good agreement with the results of Refs. [5,6]. The main value of this work is that the discrepancy between the present results obtained by α -transfer reactions at higher energy and the sub-Coulomb energies is now removed. Both give similar values but the advantage of sub-Coulomb transfer is that this technique is much less model dependent. The discrepancy (although a much smaller one than before) still remains between the Trojan Horse method measurements [7] and the sub-Coulomb ANC results. It is important to investigate the source of this discrepancy further in order to improve the reliability of both indirect methods, which promise to be important tools for nuclear astrophysics. The more accurate ANC for the $1/2^+$ at 6.356 MeV state in ^{17}O and the new low-energy $\alpha+^{13}\text{C}$ elastic scattering data [8] can now be used to impose tighter constraints than before on the $^{13}\text{C}(\alpha,n)^{16}\text{O}$ reaction rate (see also discussion in Ref. [9]). The results of this work are published in Ref. [10].

- [1] A.G.W. Cameron, *Astrophys. J.* **121**, 144 (1955).
- [2] I. Iben and A. Renzini, *Ann. Rev. Astron. Astrophys.* **21**, 271 (1983).
- [3] S. Kubono, K. Abe, S. Kato *et al.*, *Phys. Rev. Lett.* **90**, 062501 (2003).
- [4] E.D. Johnson, G.V. Rogachev *et al.*, *Phys. Rev. Lett.* **97**, 192701 (2006).
- [5] M.G. Pellegriti, F. Hammache, P. Roussel *et al.*, *Phys. Rev. C* **77**, 042801 (2008).
- [6] B. Guo, Z.H. Li, M. Lugaro *et al.*, *Astrophys. J.* **756**, 193 (2012).
- [7] M.L. Cognata, C. Spitaleri, O. Trippella *et al.*, *Astrophys. J.* **777**, 143 (2013).
- [8] N. Mynbayev, A. Nurmukhanbetova, V. Goldberg *et al.*, *J. Exp. Theor. Phys.* **119**, 663 (2014).
- [9] A. Kock, V.Z. Goldberg, G.V. Rogachev *et al.*, *Progress in Research*, Cyclotron Institute, Texas A&M University (2014-2015), p.I-33.
- [10] M.L. Avila, G.V. Rogachev, E. Koshchiy *et al.*, *Phys. Rev. C* **91**, 048801 (2015).

Structure of ^{10}N via $^9\text{C}+p$ resonance scattering

G.V. Rogachev, J. Hooker, E. Koshchiy, E. Uberseder, H. Jayatissa, C. Hunt, and B. Roeder

The new era of rare isotope beams in nuclear physics started by the discovery of unusually large matter radii in some exotic nuclei by Tanihata, et al. [1]. The most striking example is ^{11}Li which has a nuclear matter radius as large as that of ^{208}Pb . This is due to the two-neutron halo of ^{11}Li - the wave function of two valence neutrons extends far beyond the ^9Li core. Important role in explaining the halo structure of ^{11}Li was played by three-particle models that describe ^{11}Li as $^9\text{Li}-n-n$ system. These models rely on accurate knowledge of neutron- ^9Li interaction, that can be established from the known states in ^{10}Li . However, in spite of much effort (see [2-8] and references therein), uncertainty in spin-parity assignments and excitation energies of some low-lying states in ^{10}Li still remains. Even less is known about the mirror nucleus - ^{10}N . There has been only one experiment that claimed observation of the ground state of ^{10}N as a broad resonance using multi-nucleon transfer reaction $^{10}\text{B}(^{14}\text{N}, ^{14}\text{B})^{10}\text{N}$ [9]. The goal of this work is to provide a spin-parity assignment for the ground state and search for the excited states in this exotic, proton drip-line nitrogen isotope - ^{10}N .

States in ^{10}N , including the ground state, were populated in resonance elastic scattering of ^9C on protons. The rare isotope beam of ^9C was produced by recoil spectrometer MARS using $^{10}\text{B}(p,2n)$ reaction. Intensity of ^9C beam was 10^3 pps and total energy after the entrance window was 85 MeV. The ^9C beam had purity of 90% with small admixtures of mostly ^3He (about 10%). The excitation function for the $^9\text{C}+p$ scattering was measured using the new time projection chamber (TexAT-P1). The general design of TexAT-P1 is shown in the Fig. 1. We used planar

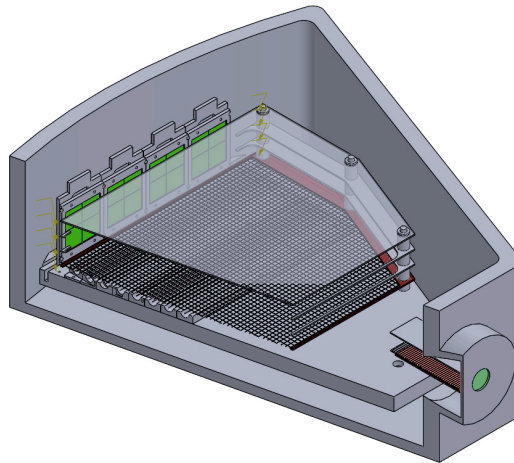


FIG. 1. The layout of the time projection chamber TexAT-P1.

geometry of the field cage to create a uniform electric field for electron drift. In order to achieve high sensitivity in horizontal direction the carbon fiber wires (8 wires in total) were used as anodes for the readout. Due to high resistivity of these wires we were able to achieve 2 mm resolution in the horizontal direction perpendicular to the beam axis. Sensitivity along the vertical axis was achieved by measuring time of electron drift from the location of the track to the anode wire. Resolution of better than 2 mm was achieved in vertical direction. The time projection chamber allowed for accurate proton track reconstruction and particle ID (using specific energy losses). The total energy of protons was measured in the silicon array located at the forward angles (with respect to the beam direction). The scattering chamber was filled with methane gas. Pressure was adjusted to stop the ${}^9\text{C}$ beam ions before the first anode wire. The ionization chamber installed at the entrance of the scattering chamber was used to identify the events associated with ${}^9\text{C}$ ions. Also, the time and energy signal from two PMTs observing the scintillator foil placed in front of the scattering chamber, before the 5 μm Havar entrance window, was used to provide additional selection of ${}^9\text{C}$ related events.

The excitation function for ${}^9\text{C}+p$ elastic scattering at a scattering angle around 165° in c.m.s. is shown in Fig. 2. Only the first half of the measured excitation energies are shown and the analysis of the higher energy region is still in progress. Preliminary R-matrix calculations are shown as a black curve in Fig. 2. These calculations indicate presence of a broad s-wave state at energy of 2.25 MeV with a width of 1.5 MeV. The red curve in Fig. 2 shows the pure Coulomb scattering cross section, which obviously does not describe the data. The s-wave state is needed to reproduce the shape of the excitation function. This is the first high statistics observation of the ${}^{10}\text{N}$ ground states with definitive assignment of the proton orbital angular momentum. The specific spin-parity assignment will be done after complete excitation function is extracted from the experimental data and the R-matrix analysis is performed for the higher energy range as well.

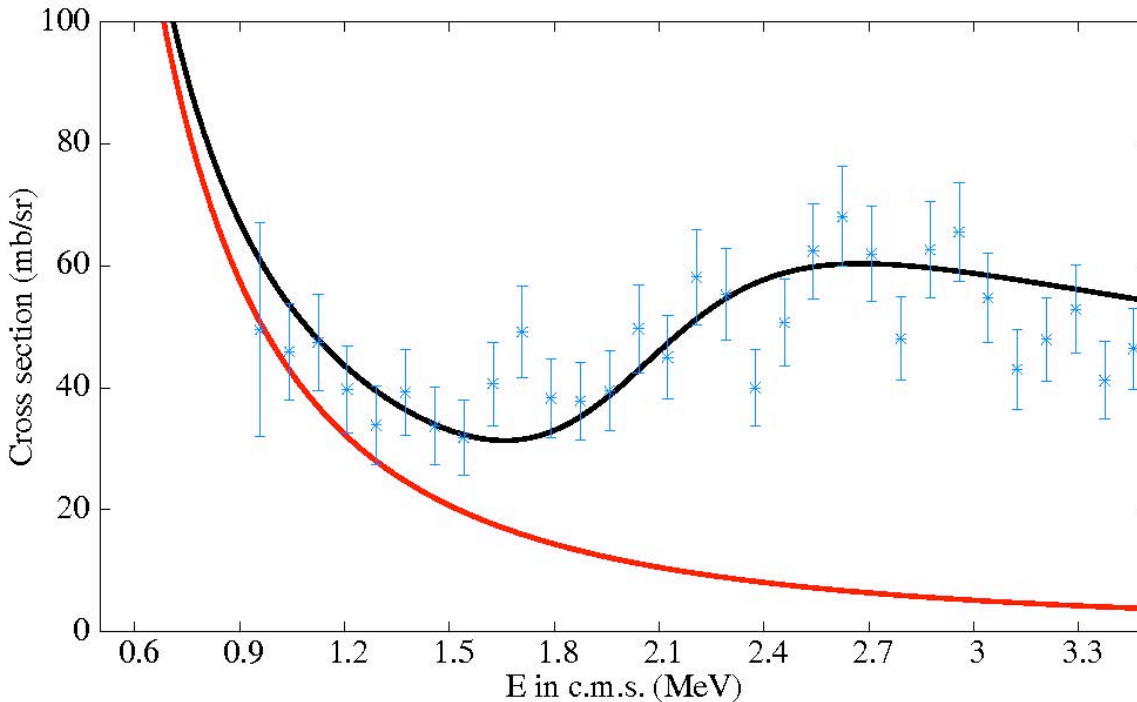


FIG. 2. The excitation function for ${}^9\text{C}+p$ elastic scattering measured at around 165° in c.m.s. The red curve is pure Coulomb scattering cross section. The black curve is a preliminary R-matrix calculation with a single $L=0$ resonance at 2.25 MeV above the proton separation energy and a width of 1.5 MeV.

- [1] I. Tanihata, H. Hamagaki, O. Hashimoto *et al.*, Phys. Rev. Lett. **55**, 2676 (1985).
- [2] H.G. Bohlen, B. Gebauer, M. von Lucke-Petsch *et al.*, Z. Phys. A **344**, 381 (1993).
- [3] B.M. Young, W. Benenson, J.H. Kelley *et al.*, Phys.Rev. C **49**, 279 (1994).
- [4] M. Zinser, F. Humbert, T. Nilsson *et al.*, Phys. Rev. Lett. **75**, 1719 (1995).
- [5] J.A. Caggiano, D. Bazin, W. Benenson *et al.*, Phys. Rev. C **60**, 064322 (1999).
- [6] P. Santi, J.J. Kolata, V. Guimaraes *et al.*, Phys. Rev. C **67**, 024606 (2003).
- [7] H. Jeppesen, F. Ames, U.C. Bergmann *et al.*, Nucl. Phys. **A738**, 511 (2004).
- [8] B.A. Chernyshev, Yu.B. Gurov, V.S. Karpukhin *et al.*, Eur. Phys. J. A **49**, 68 (2013).
- [9] A. Lepine-Szily, J.M. Oliveira, V.R. Vanin *et al.*, Phys. Rev. C **65**, 054318 (2002).

Experimental study of ${}^9\text{He}$ through the isobaric analog states in ${}^9\text{Li}$

E. Uberseder, G.V. Rogachev, V.Z. Goldberg, E. Koshchiy, B.T. Roeder, G. Chubarian, J. Hooker,

H. Jayatissa, D. Melconian, R.E. Tribble, M. Alcorta,¹ B. Davids,¹ and C. Fu²

¹*TRIUMF, Vancouver, Canada*

²*Shanghai Jiao Tong University, Shanghai, China*

The unbound neutron-rich ${}^9\text{He}$ isotope has been studied extensively over the past two decades, and many unusual experimental claims have been put forth that stand in contradiction to our understanding of nuclear structure in this mass region. Specifically, several works in the literature have argued for the existence of two narrow low lying states in ${}^9\text{He}$: a $l=0$ virtual state just above the neutron separation energy with a strongly negative scattering length and an $l=1$ state at approximately 1.3 MeV above the neutron separation energy with a width on the order of 100 keV [1-7]. Such narrow widths for these states have not been successfully reconciled with nuclear theory, and in each case the argument for their existence is not supported by a strong statistical significance above background due to the small cross sections involved in the individual techniques.

We have performed a search for low-lying states in ${}^9\text{He}$ by looking for evidence of their $T=5/2$ isobaric analogs in ${}^9\text{Li}$ populated through the elastic scattering of protons from ${}^8\text{He}$. The experiment was performed at the ISAC facility at TRIUMF using a reaccelerated ${}^8\text{He}$ beam produced through the ISOL technique, and excitation functions were measured using the thick target inverse kinematics (TTIK) method [8]. The beam impinged on a scattering chamber filled with 990 Torr of methane gas, and protons from elastic scattering were detected in three quad-segmented forward Si detectors. For particle identification and scattering angle determination, two layers of position-sensitive proportional counter cells were placed just before the Si detectors. Absolute normalization of the data and beam-contaminant identification was provided by an ionization chamber located just after the entrance to the scattering chamber. The excellent quality of the ${}^8\text{He}$ beam produced at TRIUMF allowed for good energy resolution across the excitation energy region of interest.

To verify the experimental setup, technique, and analysis, proton elastic scattering was also measured from incident ${}^{12}\text{C}$ ions in a separate experiment performed at the Cyclotron Institute as well as at TRIUMF just before the main ${}^8\text{He}$ run. Due to varying experimental conditions, these runs provided data over differing energy regions. The combined results can be seen in Fig. 1, and the excellent resolution is clearly visible over the state at 1.6 MeV. Also shown is an R-matrix calculation produced after fitting resonance parameters to the data of Meyer et al. [9].

The ${}^8\text{He}(p,p){}^8\text{He}$ experiment yielded a relatively featureless spectra with an isotropic distribution (see Fig. 2). The only notable feature in the spectra is a low energy rise, detectable at the most forward angles in the lab frame and attributed to the closing of the neutron decay channel to $T=2$ states in ${}^8\text{Li}$. This decay channel is most preferred by $T=5/2$ resonances, and taken

together with the isotropic distribution is strong evidence for a broad $T=5/2$ $l=0$ contribution to the cross section. The solid red curve in Fig. 2 shows the best R-matrix description of the cross section, and includes only a broad $T=5/2$

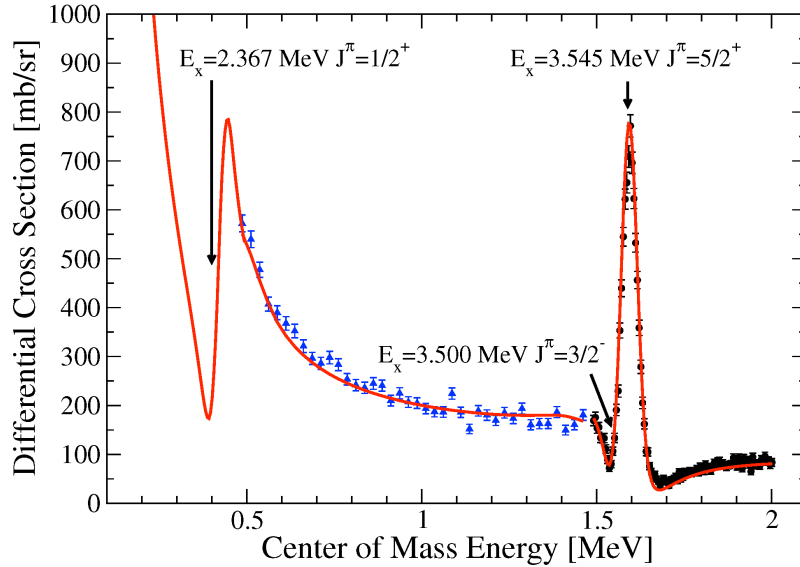
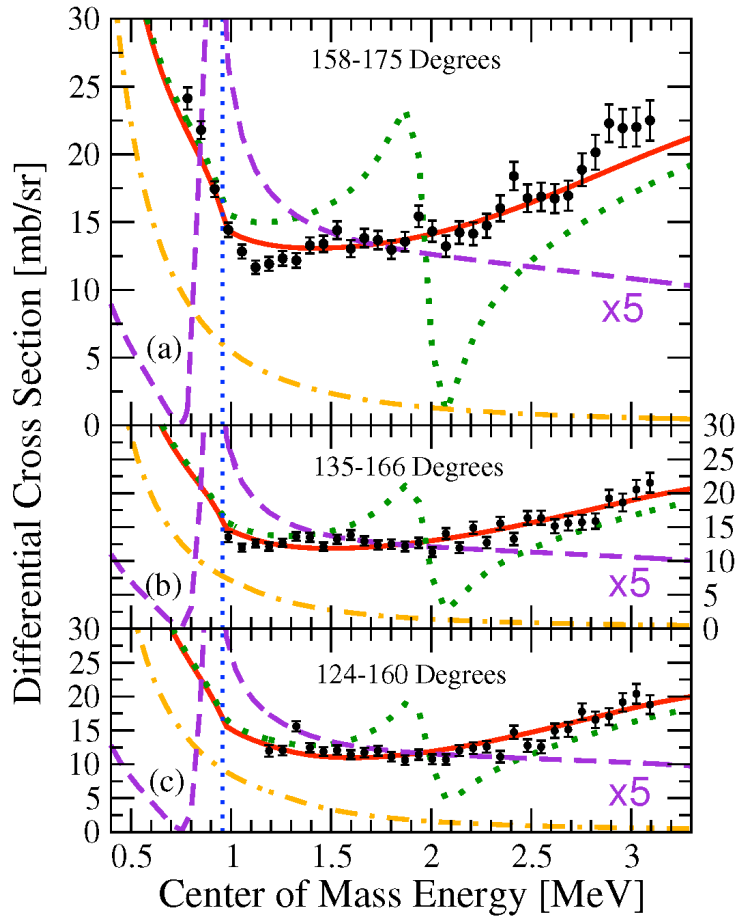


FIG. 1. Present measurement of the $^{12}\text{C}(p,p)^{12}\text{C}$ reaction. The blue points were taken at the Cyclotron Insitute while the black points were measured at TRIUMF. The red line is a calculation based on a fit to Meyer.

s-wave resonance at approximately 3 MeV combined with a $T=3/2$ s-wave background



contribution arising from a potential model calculation. Most striking in the present spectrum is the absence of any evidence for either a narrow $l=0$ state near the neutron decay threshold to the first $T=2$ state in ${}^8\text{Li}$ or a narrow $l=1$ state approximately 1.3 MeV above this threshold. The calculated effect of these states is shown by the dotted green and dashed purple lines, respectively. The orange dash dotted line in Fig. 2 show the contribution to the cross section arising from Coulomb scattering only.

We have performed a high resolution study with low statistical uncertainty searching for $T=5/2$ isobaric analogs of the low-lying states in ${}^9\text{He}$. We find no evidence of any narrow structures, instead observing only a broad, isotropic $T=5/2$ s-wave contribution to the elastic scattering cross section at an energy of approximately 3 MeV. Results of the present experiment have been submitted to Physical Review Letters for publication and are currently under review [10].

- [1] K. Seth *et al.*, Phys. Rev. Lett. **58**, 1930 (1987).
- [2] W. von Oertzen *et al.*, Nucl. Phys. **A588**, 129 (1995).
- [3] K.M. Bohlen *et al.*, Prog. Part. Nucl. Phys. **42**, 17 (1999).
- [4] L. Chen *et al.*, Phys. Lett. B **505**, 21 (2001).
- [5] S. Fortier *et al.*, AIP Conf. Proc. **912**, 3 (2007).
- [6] H.T. Johansson, Nucl. Phys. **A842**, 15 (2010).
- [7] T. Al Kalanee *et al.*, Phys. Rev. C **88**, 034301 (2013)
- [8] K.P. Artemov *et al.*, Sov. J. Nucl. Phys. **52**, 408 (1990)
- [9] H. Meyer *et al.*, Zeit. Phys. A **279**, 41 (1976)
- [10] E. Uberseder *et al.*, Phys. Rev. Lett. (submitted); [arXiv:1504.00879](https://arxiv.org/abs/1504.00879).

Elastic scattering of ^{28}Si on ^{13}C

M. Dag, A. Spiridon, B.T. Roeder, A. Saastamoinen, R. Chyzh, V.Z. Goldberg, and R.E. Tribble

Elastic scattering is a basic process of all nuclear interactions since it accompanies any reactions, and the analysis of elastic scattering by means of optical model provides for basic information about the properties of nuclear interactions as well as the distorted waves which in turn may be used as ingredients in theoretical description of non-elastic reactions. One of the great strengths of the optical model is also that it is possible to obtain global potential fitting the elastic scattering by many nuclei over a range of energies with very similar parameters, and use them to generate distorted waves for energies and target nuclei for which no elastic scattering measurements are available.[1,2]

In present work we aim to study elastic scattering ^{28}Si on ^{13}C to determine optical potential parameters which may be used to yield distorted waves for nuclei in same region for which no elastic scattering measurements are available. In an experiment carried out at Texas A&M Cyclotron Institute, a beam of 336 MeV ^{28}Si ions from K150 cyclotron bombarded self-supporting ^{13}C target foil in the chamber of the multipole-dipole-multipole (MDM) spectrometer. Reaction products were separated using the MDM spectrometer and were observed by means of the Oxford detector. Elastic scattering of ^{28}Si on ^{13}C was measured from 2° up to 15° in the lab frame (corresponded to $6^\circ - 49^\circ$ in the center-of-mass frame). As shown on Fig.1, for example, the elastic scattering of ^{28}Si on ^{13}C measured at 4° was plotted onto $\Delta E1$ - E_{RESIDUAL} histogram

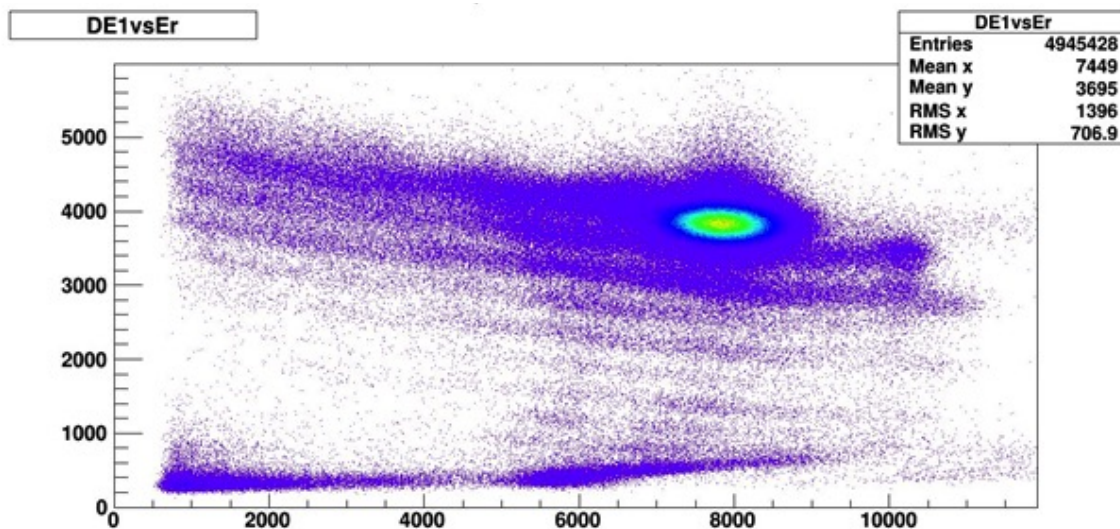


FIG. 1. $\Delta E1$ - E_{RESIDUAL} measured with the Oxford detector centered at 4 deg.

using the energy loss measured by the first two plates (named as $\Delta E1$) and the residual energy left in the scintillator, respectively. As an alternative way for the detection of the reaction products using Micromegas [3], the same data set, as shown Fig.2, was also plotted onto $E_{\text{MICROMEGAS}}$ -

E_{RESIDUAL} histogram using the energy loss measured by Micromegas and the residual energy left in the scintillator, respectively. An analysis of elastic scattering at 13° is currently proceeding, and the experiment will be repeated in near future due to lack of data at 10° .

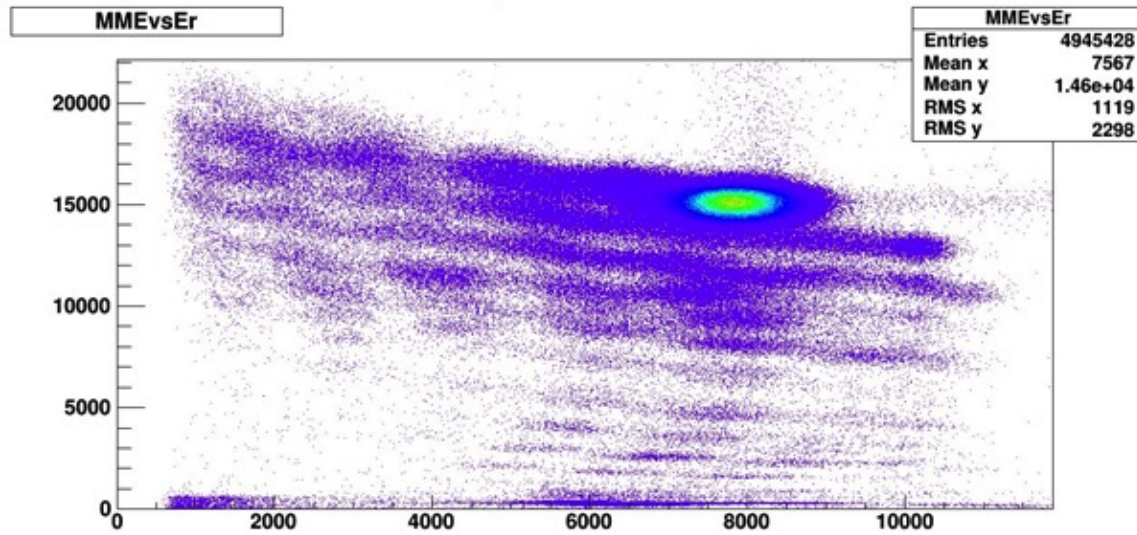


FIG. 2. $E_{\text{MICROMEGAS}}-E_{\text{RESIDUAL}}$ measured with the Oxford detector centered at 4 deg.

- [1] P.E. Hodgson, *The Nuclear Optical Model Introductory Overview*, Nuclear Physics Lab., Dept. Of Physics, University of Oxford, Oxford, United Kingdom.
- [2] P.E. Hodgson, *Nuclear Heavy-Ion Reactions*, Oxford University Press (1978).
- [3] Y. Giomataris *et al.*, Nucl. Instrum. Methods Phys. Res. **A376**, 29 (1996).

Search for quasi molecular states in interaction of ^{40}Ar with light nuclei

V.Z. Goldberg, M.S. Golovkov,¹ I. Ivanov,² M. Kisieliński,³ S. Kliczewski,⁴ M. Kowalczyk,³ N. Munbayev,⁵ A. Nurmukhanbetova,⁵ E. Piasecki,^{3,6} G. Tiourin,⁷ S. Torilov,⁸ W. Trzaska,⁷ A. Trzcińska,³ R. Wolski,¹ V. Zhrebchevski,⁸ and R.E. Tribble

¹*JINR, Dubna, Russia*

²*L.N. Gumilyov Eurasian National University, Astana, Republic of Kazakhstan*

³*Heavy Ion Laboratory, University of Warsaw, Warsaw, Poland*

⁴*IFJ PAN, Kraków, Poland*

⁵*Nazarbayev University Research and Innovation System, Astana, Republic of Kazakhstan*

⁶*National Center for Nuclear Research, Świerk, Poland*

⁷*University of Jyväskylä, Finland*

⁸*Saint-Petersburg State University, Saint-Petersburg, Russia*

During last few years, one can observe a renewed interest to the manifestations of the α clustering in the atomic nuclei. New possibilities of using rare beams, together with the permanent astrophysical interest to nuclear reactions involving helium and expectations of new effects of Bose-Einstein condensation make this field very broad and promising. One would expect similar developments for a very popular previously field of studies of quasi molecular states, which is also of the current astrophysical interest. However, after the controversy of the $^{16}\text{O}+^{40}\text{Ca}$ case [1], there is no evident progress in the studies of the quasi molecular resonances in the systems heavier than $^{16}\text{O}+^{16}\text{O}$.

Many recent achievements in the investigations of the α cluster structure (see [2], for example) are related with the application of the Thick Target Inverse Kinematics method (TTIK) [3] which has the advantage of measuring excitation functions for the elastic scattering with a single beam energy. In this technique, the incoming ions (^{40}Ar) are slowed in the thick target (a gas as the target can be used) and the recoil lighter ions of the target are detected from a scattering event. These recoils emerge from the interaction with the beam and hit Si detector telescope located at forward angles while the beam ions (^{40}Ar) are stopped in the target, as the lighter recoils have smaller energy losses than the ions of the beam. A very important feature of this approach is an easy access to measurements at zero degrees in the lab. system corresponding to 180 CM degree. At the extreme, CM backward, angles the potential scattering should be small and the resonance scattering should reach its maximum. It is especially important for the resonances with heavy ions, because one can expect a population of the high spin states in such cases. In this experiment the 220 MeV ^{40}Ar beam from the Warsaw Cyclotron, with intensity of 30 – 160 enA after collimating to 5 mm diam. (C1, see the Fig. 1), bombarded the $100\ \mu\text{g}/\text{cm}^2$ Au foil placed in the vacuum reaction chamber. Two semiconductor detectors (R1, R2) were placed upstream of the main scattering chamber and were used to monitor the beam intensity. Then, the beam passed through a window made of the $4\ \mu\text{m}$ Havar foil (H) and entered the main scattering chamber. In the main chamber we placed a solid carbon target (T) of $50\ \mu\text{m}$ thickness or 600 mm long cylinder filled with a gas (^4He , ^{20}Ne or CO_2). The target-like reaction products were detected

by a telescope consisting of Si detectors of 10 μ m, 250 μ m and 1350 μ m thickness, placed on the beam axis, at zero degrees. The telescope provided for

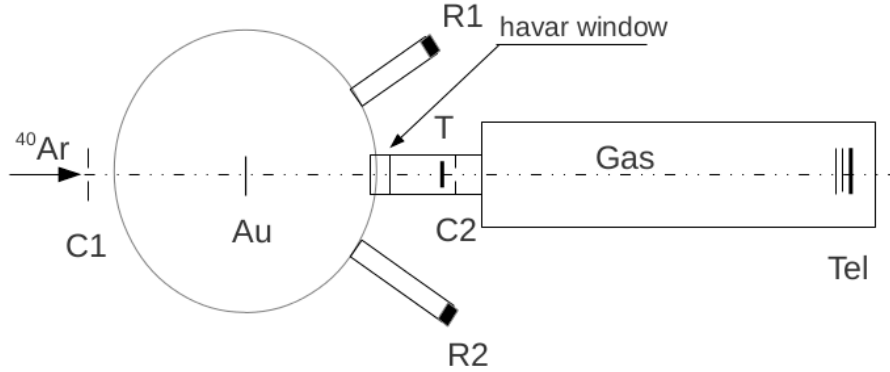


FIG. 1. Scheme of experimental setup.

resolution needed to separate elements up to Mg, but not good enough to separate the heavier isotopes (starting with A=12). As a result we have obtained thick target spectra of different light elements at the extreme CM angle (180⁰) using targets of ⁴He, ¹²C, ²⁰Ne and CO₂ and the beam of ⁴⁰Ar. We observed sharp resonances (with CM resolution of 50 keV) in the interaction of ⁴⁰Ar with ⁴He which were an evidence of the manifestations of the alpha cluster structure at the conditions of high density of the compound states and many open decay channels.

We did not observe evident resonances in any other studied cases as it is seen in Fig. 2.

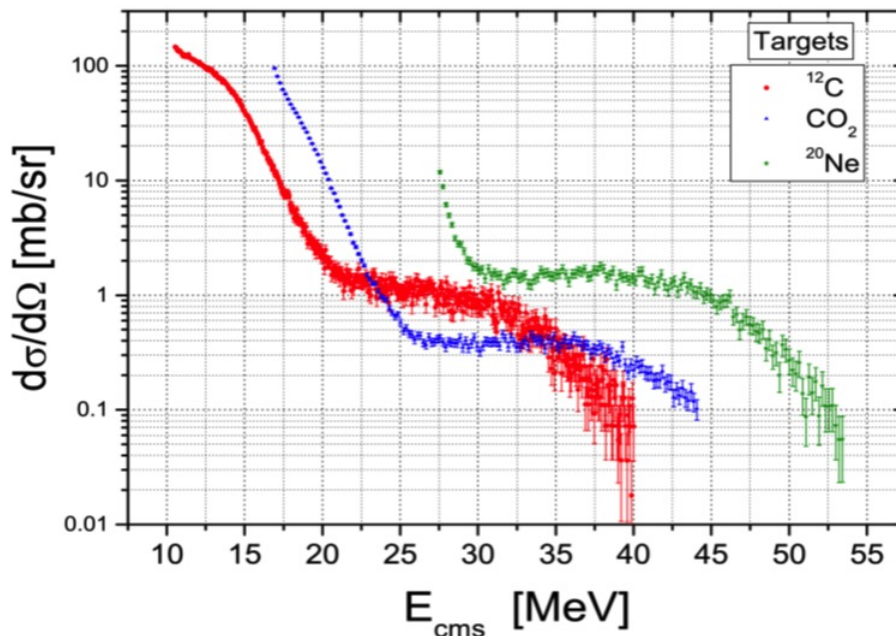


FIG. 2. Experimental excitation functions.

Fig 2 demonstrates the excitation functions for the interaction of Ar with C, CO₂, and Ne correspondingly.

At present we are trying to understand the origin of the continuous spectra of elements obtained in the unusual conditions of the present experiment.

[1] K.O. Groeneveld *et al.*, Phys. Rev. C **6**, 805(1972).

[2] M.L. Avila *et al.*, Phys. Rev. C **90**, 024327 (2014).

[3] K.P. Artemov *et al.*, Sov. J. Nucl. Phys. **52**, 406 (1990).

Data from the $^{13}\text{C}+\alpha$ interaction for the studies of the cluster structure and for astrophysics

A. Kock, V.Z. Goldberg, G.V. Rogachev, E. Uberseder, N.A. Mynbayev,¹ A.K. Nurmukhanbetova,¹ M.S. Golovkov,² M. Koloberdin,³ I. Ivanov,³ D.K. Nauruzbayev,¹ and R.E. Tribble

¹*National Laboratory Astana, Astana, Kazakhstan*

²*Joint Institute for Nuclear Research, Dubna, Russia*

³*L.N. Gumylov Eurasian National Institute, Astana, Kazakhstan*

Our knowledge of the α -cluster structure in atomic nuclei is mainly based on the investigation of self-conjugate $4N$ nuclei, like ^8Be , ^{12}C , ^{16}O , and so on (for the most recent review see [1]). The available data on the α -cluster states in neutron rich nuclei are scarce [2–6], but they give indications for the developed cluster structures with very large moments of inertia. The study of non-self-conjugate nuclei has an additional advantage in that one can investigate isobaric analog states in mirror systems. Comparison of the results for the mirror systems can bring new spectroscopic information. The Coulomb energy differences can be used to get reliable estimations for the radii of the cluster states.

It is well known that reactions induced by α particles play an important role in the development of stars. The reaction $^{13}\text{C}(\alpha,n)^{16}\text{O}$ is considered to be the main source of neutrons for the s process at low temperatures in low mass stars in the asymptotic giant branch (AGB) [1]. About half of all elements heavier than iron are produced in a stellar environment through the s process, which involves a series of subsequent neutron captures and α decays. Two factors determine the efficiency of this reaction: the abundance of ^{13}C and the rate of the $^{13}\text{C}(\alpha,n)^{16}\text{O}$ reaction (see [2], and references therein). The rate of the $^{13}\text{C}(\alpha,n)^{16}\text{O}$ reaction at temperatures of $\sim 10^8$ K is uncertain by $\sim 300\%$ [3] due to the prohibitively small reaction cross section at energies below 300 keV, therefore the nuclear models are helpful to make the theoretical predictions.

Therefore, even if astrophysical reactions involving helium do not proceed through strong α -cluster states (because of their high excitation energy), the properties of the α -cluster states can provide for the knowledge to the region of astrophysical interest through configuration mixing. Teams of the Cyclotron Institute and Nazyrbaeyev University (Astana) develop a joint program of the study of the α -cluster states in $N \neq Z$ light nuclei which can be of interest for their nuclear structure and for astrophysics. A new DC-60 Astana cyclotron accelerating heavy ions up to energies of 1.75 MeV/A appeared to be a useful instrument in these studies.

The resonance elastic $^{13}\text{C}+\alpha$ elastic scattering was studied by Thick Target Inverse Kinematics method [10] at the ^{13}C initial beam energy of 1.75 MeV/A. The excitation functions were obtained at different angles in the forward hemisphere (including zero degrees) and at cm energies down to 1.5 MeV. The details are given in [11]. At present we are close to finishing the complete R-matrix analysis of the $^{13}\text{C}+\alpha$ elastic scattering with information on over 25 levels in ^{17}O (the example of the fit for the zero degrees data (180° cm) is given in Fig.1). The parameters obtain in this fit are used to describe the $^{13}\text{C}(\alpha,n)^{16}\text{O}$ and $^{13}\text{O}(n,n)^{16}\text{O}$ data. Then we plan to test

the parameters in the description of the available $^{16}\text{O}(p,\alpha)^{13}\text{N}$ and $^{16}\text{O}(p,p)$ data. The found parameters together with recent ANC measurements[12] for the ^{17}O resonances close to the threshold for decay to $^{13}\text{C}+\alpha$, should provide for very exact knowledge of the data needed calculation of the s process in stars.

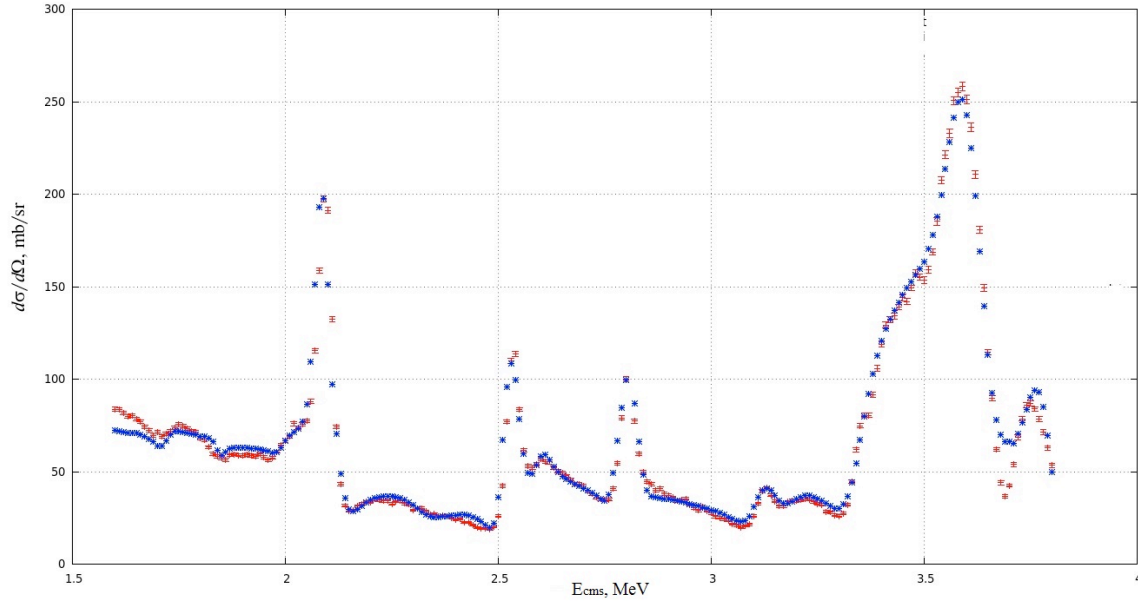


FIG. 1. Excitation function for the $^{13}\text{C}+\alpha$ elastic scattering at 180° degrees cm. Blue points -R matrix fit, red points-experimental data.

- [1] M. Freer, Rep. Prog. Phys. **70**, 2149 (2007).
- [2] M. Freer *et al.*, Phys. Rev. Lett. **96**, 042501 (2006).
- [3] A.A. Korshennikov *et al.*, Phys. Lett. B **343**, 53 (1995).
- [4] V.Z. Goldberg *et al.*, Phys. Rev. C **69**, 024602 (2004).
- [5] L. Buchmann, *et al.*, Phys. Rev. C **75**, 012804(R) (2007)
- [6] E. Johnson *et al.*, Eur. Phys. J. A **42**, 135 (2009).
- [7] I. Iben, Astrophys. J. **196**, 525 (1975).
- [8] S. Goriely and L. Siess, Astron. Astrophys. **378**, L25 (2001).
- [9] C. Angulo *et al.*, Nucl. Phys. **A656**, 3 (1999).
- [10] K.P. Artemov *et al.*, Yad. Fiz. **52**, 634 (1990); Sov. J. Nucl. Phys. **52**, 408 (1990).
- [11] N. Mynbayev *et al.*, J. Exp. Theo. Phys. **119**, 663 (2014); Zh. Eksp. Teor. Fiz. **146**, 754 (2014).
- [12] M.S. Avila *et al.*, Phys. Rev. C **91**, 048801 (2015).

Study of the lowest states in ${}^9\text{He}$ as a test of unusual nuclear structure beyond nuclear stability

R. Chyzh, A. Saastamoinen, M. McCleskey, V.Z. Goldberg, G.V. Rogachev, Y. Koshchiy, E. Simmons, A. Spiridon, M. Dag, and R.E. Tribble

Examining nuclear matter under extreme conditions makes the most demanding test of our understanding of nuclear structure. A well known opportunity is provided by the study of nuclei which are far from the valley of stability. Indeed, it looks like we encounter a case of very light neutron rich nuclei: ${}^9\text{He}$, ${}^{10}\text{He}$, and ${}^7\text{H}$ which challenges our current knowledge of nuclear structure. A controversy between different experimental results and predictions for ${}^7\text{H}$ and ${}^{10}\text{He}$ is broadly discussed (see [1,2] and references therein). However, the most evident contradiction between the theoretical predictions and experimental results is for ${}^9\text{He}$.

The structure of ${}^9\text{He}$, with its 2 protons and 7 neutrons could be expected to be simple: two protons fill the s shell, while six neutrons fill the $p_{3/2}$ sub shell and the extra neutron should be in $p_{1/2}$ state. The most sophisticated modern calculations ([3,4] and references therein) support this “naive” view on the ${}^9\text{He}$ structure. This means that the reduced neutron decay width for the $1/2^-$ state should be close to the Wigner limit and the state should be rather broad (all calculations predict the ${}^9\text{He}$ to be unstable to a neutron decay to ${}^8\text{He}$). However several high resolution measurements of spectra of products of complicated binary or quasi binary reactions induced by heavy ions by a group in the Hahn-Meitner Institute [5, 6] brought interesting data with rather small uncertainties. They found the $1/2^-$ state of ${}^9\text{He}$ at 1.27 ± 0.10 MeV above the ${}^8\text{He} + n$ threshold with $\Gamma = 0.10 \pm 0.06$ MeV. The width appeared to be more than ten times smaller than it can be expected [4]. The narrow width of the $1/2^-$ state could be considered as a direct evidence for its complicated, non shell model structure, and could be a sign of an unusual structure appearing at the neutron drip line. Several groups tried to obtain detailed information on the lowest states in ${}^9\text{He}$ (including using the ${}^8\text{He}(d,p)$ reaction[7]), but low counting statistics or inadequate energy resolution did not give a possibility to test results [5,6].

We began an experimental study of the lowest states in ${}^9\text{He}$ using the ${}^9\text{Be}({}^{18}\text{O}, {}^{18}\text{Ne}){}^9\text{He}$ reaction. Different to other similar investigations we used coincidence between ${}^{18}\text{Ne}$ and the products of the ${}^9\text{He}$ decay, ${}^8\text{He}$ and ${}^6\text{He}$. This should provide for the attribution of the correct excitation energy to the reaction products because there are excited states in ${}^{18}\text{Ne}$ which are stable to a nucleon decay, and improve the effect/background ratio. The first stage of study was to understand counting conditions in the MDM chamber and to test a possible time resolution in the experiment. The experiment was made using ${}^{18}\text{O}$ beam of 11.5 MeV/A energy of K150 cyclotron. Heavy ions were detected using MDM spectrometer [8] in the angular interval $5^\circ \pm 2^\circ$. Detection system of the MDM spectrometer [8] provided for the needed angular ($\pm 0.3^\circ$) and energy resolution (~ 200 keV). The charged products of ${}^9\text{He}$ decay: ${}^8\text{He}$, ${}^6\text{He}$ or ${}^4\text{He}$ should be detected by Si detectors placed in the scattering chamber of the MDM spectrometer (a scheme of the setup is given in Fig.1). As tests of the setup and the experimental parameters we used reactions of the ${}^{18}\text{O}+{}^9\text{Be}$ elastic scattering and the ${}^9\text{Be}({}^{18}\text{O}, {}^{20}\text{Ne}){}^7\text{He}$ reaction.

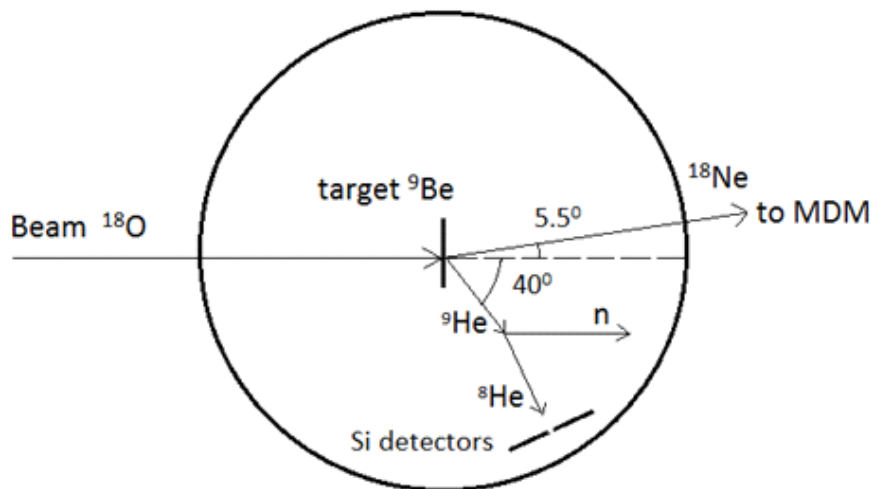


FIG. 1. Scheme of setup of the experiment.

In the first part of the data analysis we looked at the coincidences between ^{18}O and ^9Be in the process of elastic scattering. ^{18}O was registered in the Oxford detector and ^9Be in the silicon detectors. Coincidence scheme did prove to work fine in the case of elastic scattering with the best time resolution 5 ns for the energy 3 MeV in the silicon detector (Fig. 2).

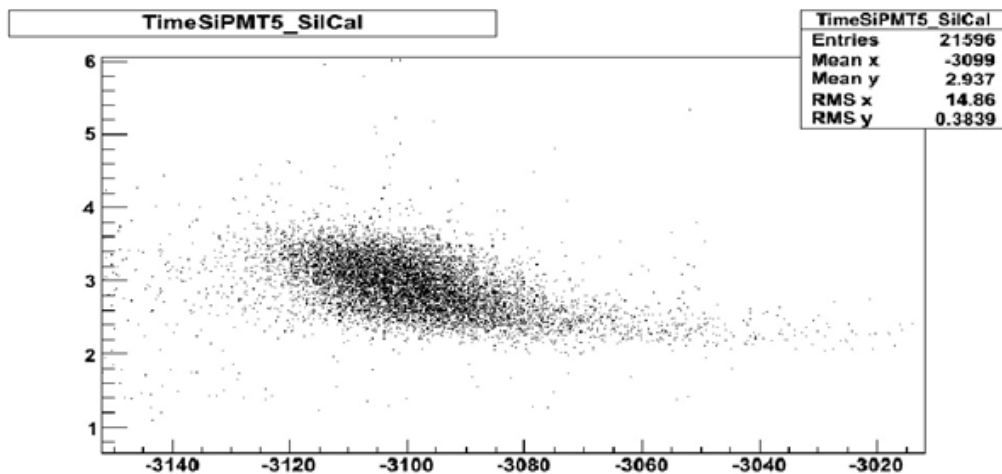


FIG. 2. Energy in the silicon in MeV (y-axis) versus time between the silicon detector and PMT in the Oxford (x-axis) 200ps/channel.

The following Fig.3 presents two dimensional dE-E spectrum for the reaction ${}^9\text{Be}({}^{18}\text{O}, {}^{20}\text{Ne}){}^7\text{He}$. The magnetic field of the MDM was tuned to detect ${}^{20}\text{Ne}$ in the Oxford detector. It can be seen that Oxygen and Carbon isotopes produced relatively narrow stripes which we assume are related to ${}^{12}\text{C}$ and ${}^{16}\text{O}$. In the Ne region we observed a broad distribution which we think includes isotopes of Ne (and probably F) with comparable intensities. We could not select ${}^{20}\text{Ne}$ using coincidences with Si detectors placed in the MDM target chamber.

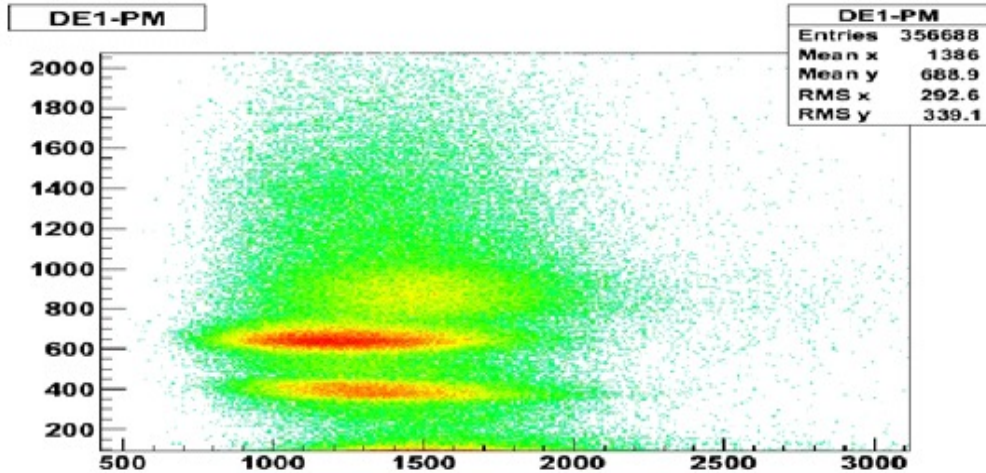


FIG. 3. In y-axis energy loss in dE1 plate of the Oxford detector versus energy in the PMT x-axis.

Time resolution of coincidence scheme in this case was 16 ns. It can be seen in the Fig.4 as the time-width of the most intense spot in the picture.

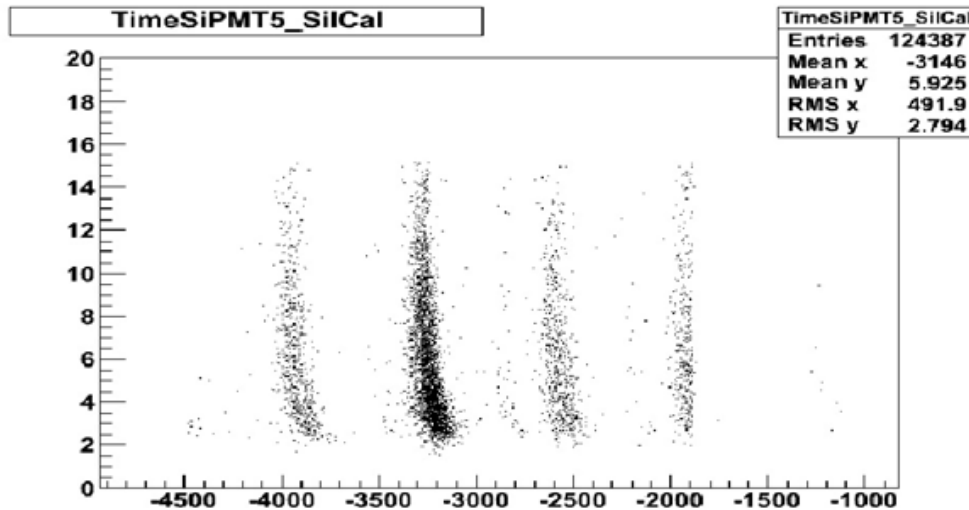


FIG. 4. Energy in the silicon detector in MeV (y-axis) versus time between the silicon detector and PMT in the Oxford (x-axis) 200ps/channel.

- [1] Z. Kohley *et al.*, Phys. Rev. Lett. **109**, 232501 (2012).
- [2] E.Yu. Nikolskii *et al.*, Phys. Rev. C **81**, 064606 (2010).
- [3] B.R. Barrett, Prog. Part. Nucl. Phys. **67**, 521 (2012).
- [4] K.M. Nollett, Phys. Rev. C **86**, 044330 (2012).
- [5] H.G. Bohlen *et al.*, Prog. Part. Nucl. Phys. **42**, 17 (1999).
- [6] W. von Oertzen *et al.*, Nucl. Phys. **A588**, 129c (1995).
- [7] T. Al Kalanee. Phys. Rev. C **88**, 034301 (2013).
- [8] D.M. Pringle *et al.*, Nucl. Instrum. Methods Phys. Rev **A245**, 230 (1986).

Study of excited states of ^{35}Ar through β -decay of ^{35}K for nucleosynthesis in novae and X-ray bursts

A. Saastamoinen, G.J. Lotay,¹ A. Kankainen,² B.T. Roeder, R. Chyzh, M. Dag, E. Simmons, A. Spiridon, and R.E. Tribble

¹*Department of Physics, University of Surrey, Guildford, GU2 7XH, United Kingdom*

²*School of Physics and Astronomy, University of Edinburgh, Edinburgh, EH9 3JZ, United Kingdom*

The thermonuclear runaway in close binary systems such as novae and X-ray bursts proceeds through proton-rich nuclei and many of the radiative proton capture reactions (p,γ) involving sd-shell nuclei close to the drip-line are dominated by resonant capture. The key parameters in understanding the astrophysical reaction rates are the energies, decay widths and spins of these resonances. One of the reactions for which improved data are needed and which determines the synthesis of nuclei beyond sulfur and chlorine is the radiative proton capture $^{34}\text{Cl}(p,\gamma)^{35}\text{K}$. At the moment the properties of the excited states of ^{35}Ar above the proton separation threshold are rather poorly known and the astrophysical reaction rate is based on statistical Hauser-Feshbach calculations.

In a recent experiment we have studied the excited states of ^{35}Ar selectively through the β -decay of the $3/2^+$ ground state of ^{35}K . A beam of ^{35}K was made at the Cyclotron Institute in inverse kinematics through reaction $^1\text{H}(^{36}\text{Ar},^{35}\text{K})2\text{n}$ by bombarding LN₂ cooled H₂ gas cell with 36-MeV/u ^{36}Ar beam. The reaction products were separated by using the Momentum Achromat Recoil Spectrometer (MARS), resulting a 70% pure beam as shown in Fig 1. The beam was

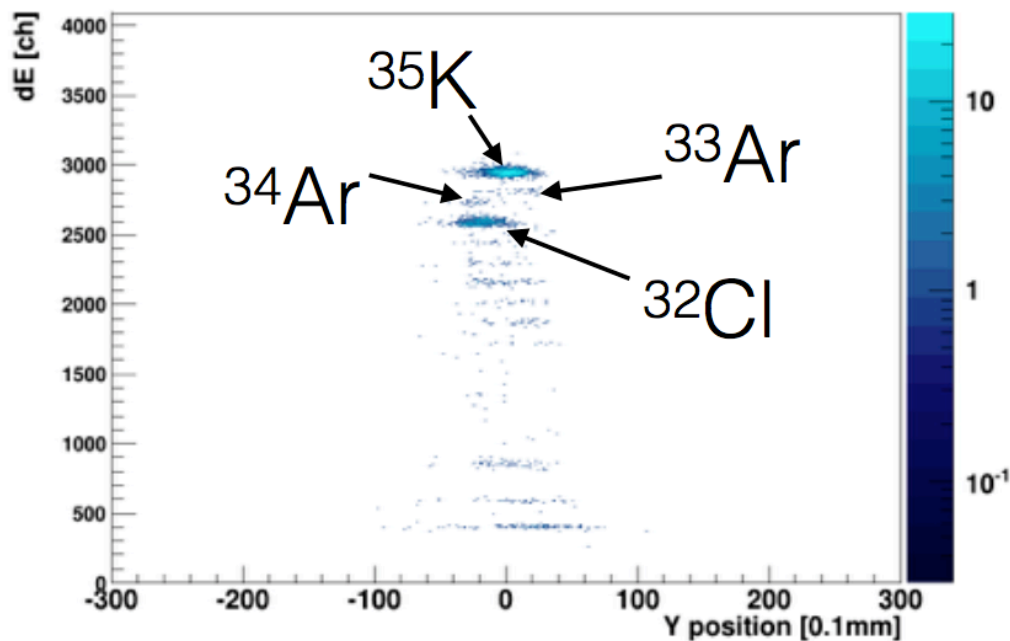


FIG. 1. Particle ID of the separated ^{35}K beam.

implanted into the Si implantation setup [1], consisting of a stack of Si detectors accompanied by two 70% HPGe detectors. This setup allows measuring β -delayed protons and γ -rays simultaneously, including coincidences. The setup was calibrated with standard offline sources and with ^{32}Cl and ^{36}K beams produced with the same primary beam.

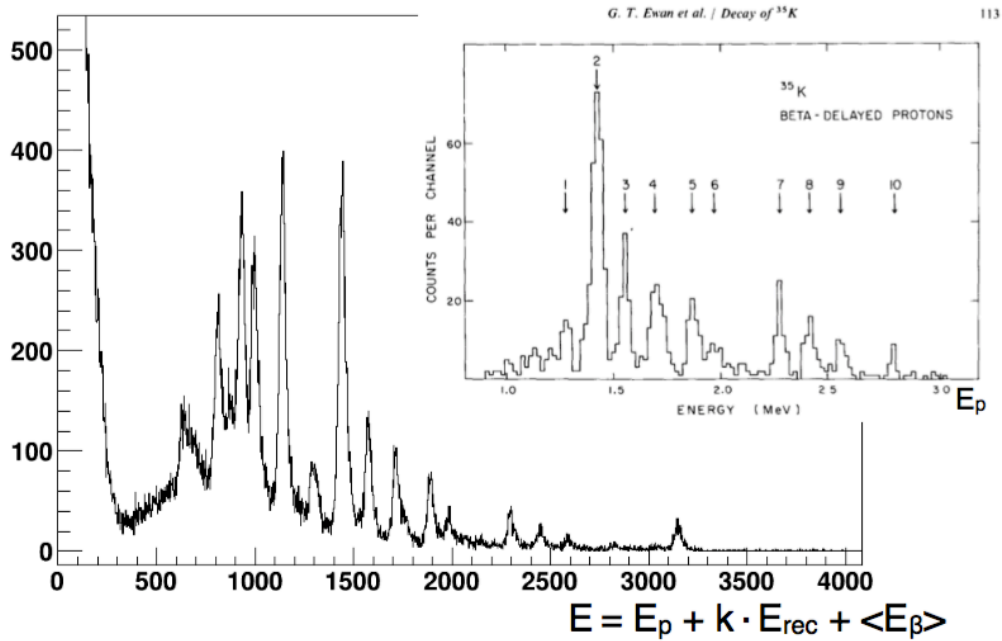


FIG. 2. Beta-delayed particles from ^{35}K decay. Inset shows previously known data (taken from from [2]).

In this experiment, we observed several new proton groups as shown in Fig. 2, first direct observation of the Isobaric Analogue State of ^{35}K ground state in ^{35}Ar in β -decay and determined an improved half-life of ^{35}K . The analysis of the data is in progress.

[1] M. McCleskey *et al.*, Nucl. Instrum. Methods Phys. Res. **A700**, 124 (2013).

[2] G.T. Ewan *et al.*, Nucl. Phys. **A343**, 109 (1980).

Superallowed beta decay

J.C. Hardy, I.S. Towner, V.E. Jacob, H.I. Park, L. Chen, V. Horvat, N. Nica,
M. Bencomo, and R.E. Tribble

Superallowed $0^+ \rightarrow 0^+$ beta decay between T=1 analogue states has been a subject of continuous and often intense study for five decades. The ft values of such transitions are nearly independent of nuclear-structure ambiguities and depend uniquely on the vector part of the weak interaction. Their measurement gives us access to clean tests of some of the fundamental precepts of weak-interaction theory, and, over the years, this strong motivation has led to very high precision being achieved in both the experiments and the theory used to interpret them. We have a major program at the Cyclotron Institute to study superallowed beta decay.

To obtain the ft value for any transition, three quantities must be measured: the half-life $t_{1/2}$ of the parent, the Q_{EC} value for the transition of interest, and the branching ratio R for that transition. Our most recent complete survey of world data on these superallowed decays, just published [1], provides a critical evaluation of all the experimental data and final ft values obtained from the averaged results, to which radiative and isospin-symmetry-breaking corrections have been applied in order to derive a final set of “corrected ft values”, denoted $\mathcal{F}t$, for 14 transitions known to $\sim 0.1\%$ precision (see Fig. 1). Excellent consistency among the average $\mathcal{F}t$ values for all 14 transitions – an expected consequence of the conservation of vector current (CVC) – confirms the validity of the correction terms; and our recent measurement of ^{38}Ca decay [2], which closely compares a pair of mirror superallowed transitions with $A = 38$, further supports that validity.

The resultant average $\mathcal{F}t$ value, when combined with the muon lifetime, yields the up-down quark-mixing element of the Cabibbo-Kobayashi-Maskawa (CKM) matrix, $V_{ud} = 0.97417$ (21), a result that is consistent with, but more precise than, values we have obtained in previous analyses of superallowed β decay. The unitarity test on the top row of the matrix becomes $|V_{ud}|^2 + |V_{us}|^2 + |V_{ub}|^2 = 0.99978$ (55) if the Particle Data Group recommended value for V_{us} is used. However, recent lattice QCD calculations, not included yet in the PDG evaluation, have introduced some inconsistency into kaon-decay measurements of V_{us} and V_{us}/V_{ud} . In ref. [1], we have examined the impact of these new results on the unitarity test and conclude that there is no evidence of any statistically significant violation of unitarity. Finally, from the $\mathcal{F}t$ -value data we also set limits on the possible existence of scalar interactions.

This result is not only a significant verification of the standard model but the uncertainty quoted on the sum provides a tight limit on any possible new physics beyond the standard model, such as right-hand currents, extra Z bosons or supersymmetric models. In short, superallowed $0^+ \rightarrow 0^+$ beta decay provides a high-profile application of nuclear-physics measurements to the study of fundamental symmetries, a subject of vital interest to both nuclear and particle physicists. Although much has already been achieved in this field by nuclear physicists, improvements are

still possible. Reducing the uncertainty on the unitarity sum – and, with it, the scope for new physics – remains the primary goal of our research program.

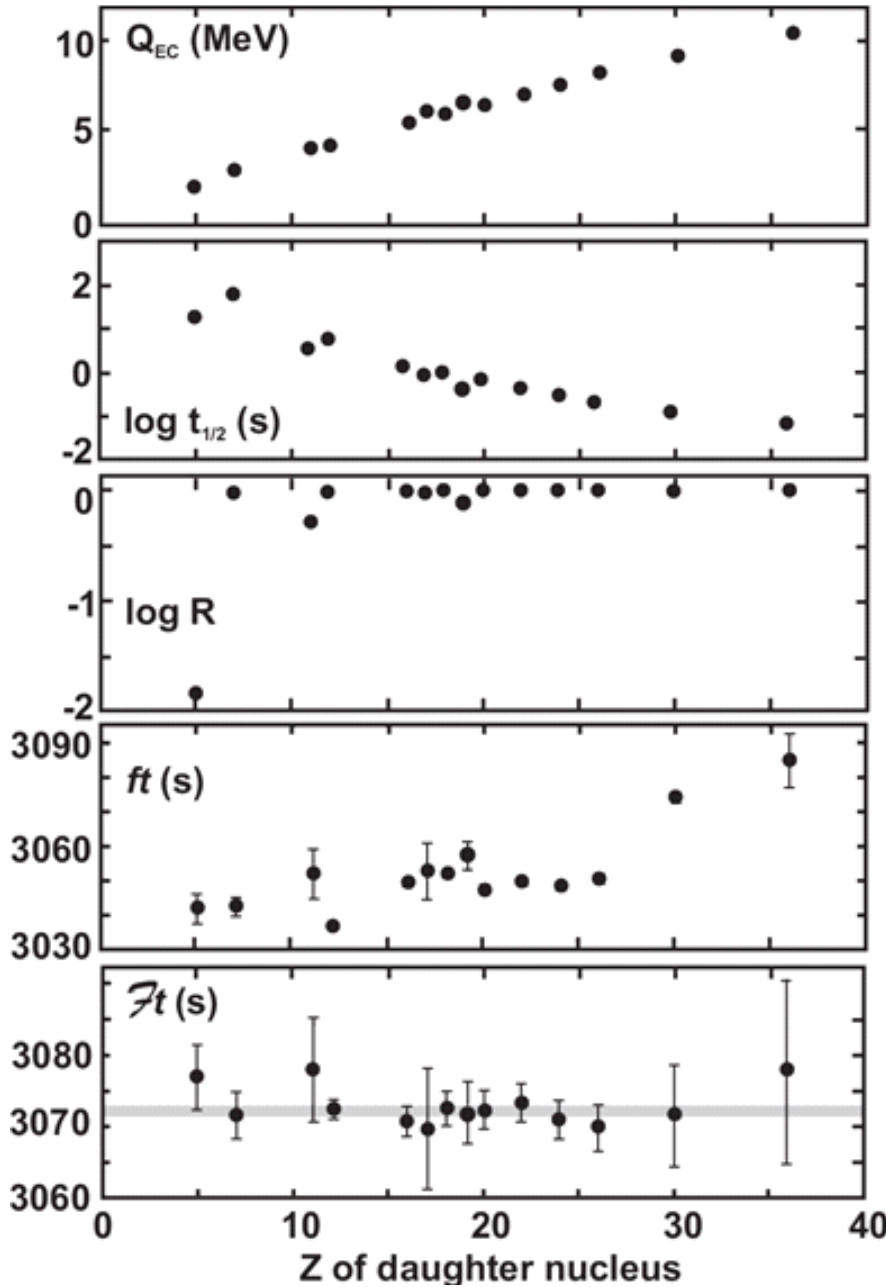


FIG. 1. Results from the most recent survey of 14 precisely measured superallowed $0^+ \rightarrow 0^+$ β transitions [1]. The parents of these transitions, from left to right, are ^{10}C , ^{14}O , ^{22}Mg , ^{26m}Al , ^{34}Cl , ^{34}Ar , ^{38m}K , ^{38}Ca , ^{42}Sc , ^{46}V , ^{50}Mn , ^{54}Co , ^{62}Ga and ^{74}Rb . The top three panels present the average of measured Q_{EC} , $\log t_{1/2}$ and $\log R$ values for each transition. The bottom two panels give the corresponding ft and Ft values. The shaded horizontal line in the bottom panel represents the overall average Ft value for all transitions. All error bars are shown: in the cases where none are visible, they are smaller than the data point.

Our approach follows from the observation [1] that the second largest contributor to the uncertainty in V_{ud} is the theoretical uncertainty in the nuclear-structure-dependent corrections, δ_{NS} and δ_C , used in the derivation of the $\mathcal{F}t$ values. Though these corrections are only of order 1%, their effect is very significant: The bottom two panels of Fig. 1 show the result of applying δ_{NS} and δ_C , (together with δ'_R , which is nearly independent of Z). Obviously they act very well to remove the considerable “scatter” in ft values apparent in the second panel from the bottom, replacing it with the consistent set of corrected $\mathcal{F}t$ values appearing in the bottom panel. Since these corrections were determined [3] completely independently of the superallowed decay data, this consistency in $\mathcal{F}t$ values is already a powerful validation of these calculated corrections, but obviously the remaining uncertainty still influences the final result for V_{ud} .

Even though the 2015 survey [1] included more than 222 individual measurements relating to 14 precisely known ft values, it is still possible for well-selected experiments to make real improvements in the validation tests of the nuclear-structure-dependent correction terms. At TAMU we are currently focusing on adding to the ft -value list new superallowed transitions, selected from amongst those with large calculated corrections. If the ft values measured for cases with large calculated corrections also turn into corrected $\mathcal{F}t$ values that are consistent with the others, then this must verify the calculations' reliability for the existing cases, which have smaller corrections. We are studying decays from $T_z = -1$ parent nuclei, which consistently have higher predicted structure-dependent correction terms than the well-known $T_z = 0$ cases.

Of particular importance are the four $T_z = -1$ parent nuclei – ^{26}Si , ^{34}Ar , ^{38}Ca and ^{42}Ti – whose decays are mirrors to well-known superallowed decays from $T_z = 0$ parents. Specifically, the mirror-decay pairs are $^{26}\text{Si} \rightarrow ^{26m}\text{Al} \rightarrow ^{26}\text{Mg}$, $^{34}\text{Ar} \rightarrow ^{34}\text{Cl} \rightarrow ^{34}\text{S}$, $^{38}\text{Ca} \rightarrow ^{38m}\text{K} \rightarrow ^{38}\text{Ar}$ and $^{42}\text{Ti} \rightarrow ^{42}\text{Sc} \rightarrow ^{42}\text{Ca}$. Their importance stems from our observation that the ratio of mirror ft values for such cases is very sensitive to the model used to calculate the small isospin-symmetry-breaking corrections δ_{NS} and δ_C . The details have been described in our report on the first measurement of a mirror pair, with $A = 38$ [2]. Until very recently, none of the $T_z = -1$ parent decays was known precisely enough to provide a statistically significant constraint on the correction terms via the ratio of mirror ft values, but we are now well on our way to rectifying this situation.

After a long period of incremental upgrades to our experimental techniques, we succeeded in pushing our precision in branching ratio measurements close to $\pm 0.1\%$, our ultimate goal. This is crucial for the characterization of $T_z = -1$ parent decays, which – unlike $T_z = 0$ decays – exhibit a number of strong Gamow-Teller branches that compete with the superallowed Fermi branch. A demonstration of our success in this endeavor is our measurement of the superallowed branching ratio for the decay of ^{38}Ca ($t_{1/2} = 444$ ms) to a precision of $\pm 0.2\%$, where that precision was actually limited by counting statistics, not systematics [2,4]. An important aspect of these decays is the possibility of weak beta decays to highly excited states in the daughter, which are too weak to be observed individually but in total could constitute sufficient strength to affect the branching ratio obtained for the superallowed branch. These have been investigated theoretically for ^{34}Ar and ^{38}Ca decay, and found to be negligibly small [5].

To our knowledge, this is the most precise direct branching-ratio measurement ever made for short-lived beta emitter. It also provides the first mirror pair of $0^+ \rightarrow 0^+$ superallowed emitters (^{38}Ca and $^{38}\text{K}^m$) that is precise enough to distinguish meaningfully between the Saxon-Woods-based radial-overlap correction, δ_{C2} , and the one based on Hartree-Fock radial wave functions. It favors the former over the latter, but we must await results from the other mirror pairs before we can be confident of the verdict. We are now well embarked on the measurement of the remaining three accessible pairs: We have already made a measurement of the branching ratio for the superallowed decay of ^{34}Ar , the data from which are currently being analyzed [6]; and we have also re-measured its half-life [7]. In addition, we have also made a successful measurement of the ^{26}Si beta-decay branching ratios, which is under analysis as the thesis project of M. Bencomo [8]. Finally, successful test measurement of the half-life of ^{42}Ti [9] has led to a full-blown measurement now scheduled for June 2015.

We are also endeavoring to improve our data acquisition techniques for half-life measurements by a variety of means, including a digital-pulse-analysis system for the signals from our 4π proportional gas counter. We have been exploring a variety of algorithms for distinguishing real beta pulses from spurious ones [10,11] and have been testing our results on the data from an experiment to measure the half-life of another $T_z = -1$ superallowed emitter, ^{30}S , in which we have used three different methods for taking data from the proportional gas counter: our standard analog technique, a TDC-based approach, and the digital-pulse-analysis system. The results, which are still under study, will determine whether we can improve our half-life precision in future and, if so, by which path. It will also yield the first precise study of this previously neglected superallowed emitter.

- [1] J.C. Hardy and I.S. Towner, Phys. Rev. C **91**, 025501 (2015); J.C. Hardy and I.S. Towner, *Progress in Research*, Cyclotron Institute, Texas A&M University (2014-2015), p. I-65.
- [2] H.I. Park, J.C. Hardy, V.E. Jacob, M. Bencomo, L. Chan, V. Horvat, N. Nica, B.T. Roeder, E. Simmons, R.E. Tribble, and I.S. Towner, Phys. Rev. Lett. **112**, 102502 (2014).
- [3] I.S. Towner and J.C. Hardy, Phys. Rev. C **77**, 025501 (2008).
- [4] H.I. Park, J.C. Hardy, V.E. Jacob, M. Bencomo, L. Chan, V. Horvat, N. Nica, B.T. Roeder, E. Simmons, R.E. Tribble, and I.S. Towner, Phys. Rev. C, accepted for publication (2015); H.I. Park *et al.*, *Progress in Research*, Cyclotron Institute, Texas A&M University (2014-2015), p. I-50.
- [5] I.S. Towner and J.C. Hardy, *Progress in Research*, Cyclotron Institute, Texas A&M University (2014-2015) p. III-49.
- [6] V.E. Jacob *et al.*, *Progress in Research*, Cyclotron Institute, Texas A&M University (2014-2015), p. I-48.
- [7] V.E. Jacob *et al.*, *Progress in Research*, Cyclotron Institute, Texas A&M University (2014-2015), p. I-46.
- [8] M. Bencomo *et al.*, *Progress in Research*, Cyclotron Institute, Texas A&M University (2014-2015), p. I-53.

- [9] H.I. Park *et al.*, *Progress in Research*, Cyclotron Institute, Texas A&M University (2013-2014), p. I-23.
- [10] V. Horvat, L. Chen, and J.C. Hardy, *Progress in Research*, Cyclotron Institute, Texas A&M University (2014-2015), p. IV-75.
- [11] H.I. Park, L. Chen, and J.C. Hardy, *Progress in Research*, Cyclotron Institute, Texas A&M University (2014-2015), p. IV-79.

Improvement in the precision of the ^{34}Ar half-life

V.E. Iacob, J.C. Hardy, M. Bencomo, H.I. Park, L. Chen, V. Horvat, N. Nica,
B.T. Roeder, and A. Saastamoinen

Our recent ^{34}Ar branching-ratio measurement [1] along with a more precise half-life would yield an ft value for the ^{34}Ar decay whose accuracy would match that of the well-known cases [2] used in generating the corrected $\mathcal{F}t$ values that are instrumental in extracting V_{ud} and testing the unitarity of the CKM matrix [2].

The measurement was similar to the one reported in [3]. The radioactive beam was produced in the $^1\text{H}(^{35}\text{Cl}, 2n)$ reaction with a primary ^{35}Cl beam at 30A MeV from the K500 cyclotron. The hydrogen target was kept at liquid nitrogen temperature and at a pressure of ~ 2 atm. A pure ($>99\%$) ^{34}Ar beam separated by the MARS spectrograph was extracted in air, degraded and eventually implanted in the center of the 76- μm -thick Mylar tape of our fast transport system. Then the beam was turned off and the implanted ^{34}Ar samples were moved into the center of a 4π proportional counter, from which the signals were multiscaled. In repeated collect-move-detect cycles we recorded more than 3×10^8 combined β^+ -events. The time-settings for the collect-move-detect intervals were 0.7 s-0.15 s-16 s.

We performed a variety of checks to test for possible systematic effects caused by the electronic setup: We changed the critical settings for:

- detector biases (2450, 2500, 2550, 2600, 2650, 2700, and 2750V),
- discriminator thresholds (150, 200, and 250mV), and
- dead-times: (3, 4, 6, 8, 10, and 12 μs).

The parent ^{34}Ar ($t_{1/2}=0.84$ s) decays to ^{34}Cl , which itself is β^+ -unstable ($t_{1/2}=1.53$ s). As the 4π proportional counter is unable to distinguish between the β^+ 's generated by the parent and daughter nuclei, only a combined decay spectrum can be acquired. As discussed in Ref. [3], a precision half-life result cannot be obtained using a free fit: For cases like this one, with a parent-to-daughter half-life ratio close to 0.5, the composite decay curve shows very little deviation from a single exponential with the characteristic half-life of the daughter. Therefore a key ingredient in the fit must be the imposition of the independently determined parent-to daughter link based on the parent's implantation and decay history. Qualitatively, higher precision is achieved because use of the parent-to-daughter link reduces by one the number of parameters to be fit: A free fit would seek the amplitudes for the two components, the half-life of the parent and possibly the background. Using the parent-to daughter link, one of the two decay-amplitudes is fully expressed in terms of the other fit-parameters. Nevertheless, this gain results in an increase in the nonlinearity of the fit.

Quantitatively, to determine the parent-to-daughter link requires knowledge of the beam-profile (implantation history), the tape move-time and the ratio of the detection-efficiencies for the two components. At the time of the measurements reported in [3] the experimental setup was in its infancy. In the meantime, our experimental set-up has been subject to a series of upgrades and as such it is expected to allow an increased precision in the ^{34}Ar half-life. Most important

from this perspective are more precise controls over the implantation profile and the timing of the cycle: We now monitor (and record) for each cycle the corresponding beam-profile [4] and move-time. Thus, the data analysis can exactly account for instantaneous changes in the beam current in each cycle; likewise it exactly accounts for “in-flight” adjustments in the move-times. These added features increase the accuracy of the ratio of the parent-to-daughter activities.

Moreover, to better control the dead-time corrections we have increased the number of multiscaler channels used to record the decay curve from 500 to 15,000, essentially removing the need to account for a variable rate during each channel’s time-window.

The data analysis is in progress.

- [1] V.E. Iacob *et al.*, *Progress in Research*, Cyclotron Institute, Texas A&M University (2013-2014), p. I-20.
- [2] J.C. Hardy and I.S. Towner, *Phys. Rev. C* **91**, 025501 (2015); J.C. Hardy and I.S. Towner, *Progress in Research*, Cyclotron Institute, Texas A&M University (2014-2015), p. III-49.
- [3] V.E. Iacob, J.C. Hardy, J.F. Brinkley, C.A. Gagliardi, V.E. Mayes, N. Nica, M. Sanchez-Vega, G. Tabacaru, L. Trache, and R.E. Tribble, *Phys. Rev. C* **74**, 055502 (2006).
- [4] V.E. Iacob *et al.*, *Progress in Research*, Cyclotron Institute, Texas A&M University (2008-2009), p. V-43.

Update on the superallowed branching ratio in the ^{34}Ar

V.E. Iacob, J.C. Hardy, M. Bencomo, H.I. Park, L. Chen, V. Horvat, N. Nica,
B.T. Roeder, and A. Saastamoinen

Last year we reported a measurement of the branching ratios in the decay of ^{34}Ar [1]. This experiment, along with a more precise half-life value [2] is expected to yield an ft value for the superallowed transition from ^{34}Ar whose accuracy matches that of the well-known superallowed decays used in generating the corrected $\mathcal{F}t$ values that are instrumental in extracting V_{ud} and testing the unitarity of the CKM matrix [3].

The experiment described in Ref. [1] measured β - γ coincidences and β singles from cyclotron-produced ^{34}Ar sources placed between a 1-mm-thick plastic scintillator (located 2.5 mm from the source) and our efficiency-calibrated HPGe detector [4] (151 mm from the source). Since then, we have analyzed the data to obtain the precise photopeak areas for all the γ rays observed (at 461, 666, 2580, and 3129 keV). The statistical uncertainties range from 0.8% to 2.5%, the higher ones being associated with the γ rays generated by the weaker β -decay branches ($\sim 1\%$ or less).

These areas have to be corrected for losses. All observed γ rays de-excite an excited state directly to the ^{34}Cl ground state. Any γ -cascades, if they occur at all, are too weak to be detected. Thus, true γ -ray coincidences in the HPGe detector cannot occur. However, the γ rays and the decay positrons are coincident on the timescale of our electronics and there are two mechanisms by which those positrons can generate coincident photons: (a) bremsstrahlung and (b) annihilation, either in flight or at rest. If these photons appear in the HPGe detector in coincidence with a γ ray, then the total energy recorded in the detector is increased, thus resulting in some of the γ -ray photopeak events being lost. The combined correction associated with photon losses due to true coincidences with bremsstrahlung and positron annihilation is 2.4%.

The branching ratio for the β -decay branch k , which leads to emission of a γ_k photon, can be expressed as the ratio between the β_k - γ_k coincidences and the total number of decays (or β 's). Highly simplified, this can be expressed as:

$$BR_k = \frac{N_{\beta_k-\gamma_k}}{\varepsilon_{\beta_k} \varepsilon_{\gamma_k}} \bigg/ \frac{N_{\beta_{tot}}}{\langle \varepsilon_{\beta} \rangle} \quad (1)$$

Here $N_{\beta_k-\gamma_k}$ is the number of observed β_k - γ_k coincidence events (the γ_k photopeak area), $N_{\beta_{tot}}$ is the total number of observed β 's associated with the ^{34}Ar decay, ε_{γ_k} is the absolute photopeak efficiency for γ_k , ε_{β_k} is the absolute detection efficiency for a branch- k positron in the plastic scintillator, and $\langle \varepsilon_{\beta} \rangle$ is the average detection efficiency for all decay positrons in the plastic scintillator.

The parent ^{34}Ar ($t_{1/2}=0.84$ s) decays to ^{34}Cl , which itself is β^+ -unstable ($t_{1/2}=1.53$ s). Obviously, it is only the β 's associated with the ^{34}Ar decay alone that must be used in Eq. (1). Taking the known half-lives of the two nuclei, the measured time-profile of the ^{34}Ar beam implantation, and the collect-move-

detect time-values, we determined that 47% of the total β singles recorded are associated with the parent decay. In addition, small corrections have to be applied to take account of beam impurities ($\sim 0.08\%$).

The plastic-scintillator efficiency for detecting β 's has a small dependence on the β -spectrum energy and, as a result, small corrections related to the ratio $\langle \epsilon_{\beta} \rangle / \epsilon_{\beta_k}$ also must be applied. These corrections were derived from Monte Carlo calculations and range from -3% to $+1\%$; the negative values correspond to weak β branches that populate high-energy excited states. Overall this leads to an average contribution of 0.4% to the final superallowed branching ratio since the whole decay is dominated by the ground-state branch.

Naturally, corrections are required to correct for all forms of dead time: in the singles channels and in the β - γ coincidences. Their combined contribution is 0.4% .

Last, small corrections must be applied to the results to incorporate the very small contribution from electron capture, which affects the decay branching but does not lead to β -coincident γ rays in our measured spectrum. For the branches in ^{34}Ar decay these corrections range from 0.07% to 1.2%

The data analysis continues.

- [1] V.E. Iacob, *et al.*, *Progress in Research*, Cyclotron Institute, Texas A&M University (2013-2014), p. I-20.
- [2] V.E. Iacob, *et al.*, *Progress in Research*, Cyclotron Institute, Texas A&M University (2014-2015), p. I-46.
- [3] J.C. Hardy and I.S. Towner, *Phys. Rev. C* **91**, 025501 (2015).
- [4] J.C. Hardy *et al.*, *Appl. Radiat. Isot.* **56**, 65 (2002) ; R.G. Helmer *et al.*, *Nucl. Instrum. Methods Phys. Res.* **A511**, 360 (2003); R.G. Helmer *et al.*, *Appl. Radiat. Isot.* **60**, 173 (2004).

Precise measurement of branching ratios in the β decay of ^{38}Ca

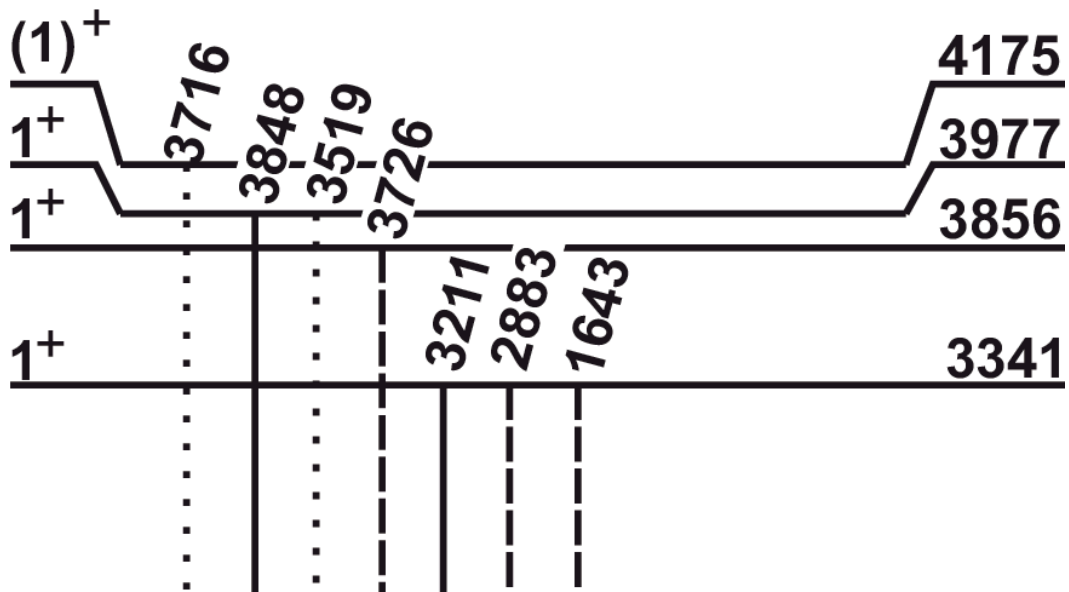
H.I. Park, J.C. Hardy, V.E. Jacob, M. Bencomo, L. Chen, V. Horvat, N. Nica, B.T. Roeder,
E. McCleskey, R.E. Tribble, and I.S. Towner

Last year we published a letter [1] briefly describing our measurement of the branching ratio for the superallowed β -transition from ^{38}Ca and applying the result to a sensitive test of isospin-symmetry-breaking corrections from the mirror superallowed $0^+ \rightarrow 0^+$ decays, $^{38}\text{Ca} \rightarrow ^{38\text{m}}\text{K}$, and $^{38\text{m}}\text{K} \rightarrow ^{38}\text{Ar}$. This year we have written a detailed description of the measurement including results for the branching ratios of all the β -decay transitions from ^{38}Ca . This manuscript has been accepted for publication [2].

Our experimental method is to produce pure samples of ^{38}Ca using the K500 cyclotron and the MARS spectrometer; and then record decay γ rays in coincidence with β 's. Fuller explanations appear in Refs. [1,2]. The coincident γ -ray spectrum has been examined meticulously to determine, or set limits on, the relative intensities of all γ rays that follow the decay of ^{38}Ca ; our search was guided by the results of previous studies [3,4]. Our results appear in Table I and Fig. 1. Also given in Table I are the results from those previous studies [3,4]. Our sensitivity is similar to the most recent previous measurement, by Anderson *et al.* [4], but our results show some significant discrepancies with theirs. The most egregious is for the intensity of the 2883-keV γ transition, which we determine to be an order of magnitude less than their result. It seems very likely that the value quoted by Anderson *et al.* is simply a misprint since it does not seem to be supported by their own γ -ray spectrum (see Fig. 5 in Ref. [4]), in which the 2883-keV peak is clearly not one-half the intensity of the nearby peak at 3211 keV as their tabulated intensity would lead one to believe. There are two other smaller, but still significant, discrepancies between our results and those of Anderson *et al.* for the peaks at 1643 and 3726 keV. These discrepancies give us good reason to use our results exclusively in all subsequent determinations of the Gamow-Teller β -branching ratios from ^{38}Ca .

Table I. Relative intensities of β -delayed γ rays from the β^+ decay of ^{38}Ca .

E_γ (keV)	I_γ		
	Ref. [3]	Ref. [4]	This work
328	0.126(16)	0.159(10)	0.1489(26)
1240	<0.010	0.0024(5)	0.0036(13)
1567	1	1	1
1643	<0.010	0.0040(5)	0.0010(7)
1698	<0.0082	0.0008(4)	<0.0008
2883	<0.0033	0.007(2)	0.0006(4)
3211	0.0139(15)	0.0138(10)	0.0150(9)
3519	<0.0042	0.0004(3)	<0.0003
3716	<0.0045	0.0002(1)	<0.0005
3726	<0.0036	0.0019(2)	0.0007(3)
3848	<0.0081	0.0056(5)	0.0051(7)



By comparing the intensity of the β -coincident 1567-keV γ ray with the singles β intensity – and correcting for dead-time losses, real-coincidence summing and a variety of other smaller effects – we determined the branching ratio for the (β^+ + ec) transition to the 1628-keV state to be 0.1948(13) [2]. Combining this value with the relative γ -ray intensities in Table I, we obtain the final branching ratios and $\log ft$ values listed in Table II. The branching ratio for the superallowed branch was derived by subtracting the total of all the Gamow-Teller branches from 1. The uncertainty budget for this important result is given in Table III.

Table II. Measured β -branching ratios to all the states in ^{38}K populated by the β decay of ^{38}Ca

E_x (keV)	$E_{b\max}$ (keV)	Branching ratio	$\log ft$	Superallowed $\mathcal{F}t$ (s)
130.4	5590.1	0.7728(16)	3.4860(10)	3076.4(72)
458.5	5262.0	0.0281(6)	4.804(1)	
1697.8	4022.7	0.1948(13)	3.426(3)	
3341.2	2379.3	0.0032(3)	4.19(4)	
3856.0	1864.5	0.00014(6)	5.09(19)	
3977.3	1743.2	0.0010(2)	4.11(9)	

Table III. Uncertainty budget for ^{38}Ca branching ratios.

Source	Uncertainty (%)	
	\sum GT branches	$0^+ \rightarrow 0^+$ branch
Counting statistics, γ_{1567} & β singles	0.49	0.14
Contaminant contribution to β singles	0.30	0.09
$\sum \gamma / \gamma_{1567}$	0.25	0.08
Coincidence summing with 5110keV γ 's	0.21	0.06
HPGe detector efficiency	0.20	0.06
Dead time	0.07	0.021
Bremsstrahlung coincidence summing	0.05	0.015
^{38}Ca component of β singles	0.06	0.017
Random preemption of real coincidences	0.04	0.012
Total uncertainty	0.70	0.21

- [1] H.I. Park, J.C. Hardy, V.E. Jacob, M. Bencomo, L. Chan, V. Horvat, N. Nica, B.T. Roeder, E. Simmons, R.E. Tribble, and I.S. Towner, Phys. Rev. Lett. **112**, 102502 (2014).
- [2] H.I. Park, J.C. Hardy, V.E. Jacob, M. Bencomo, L. Chen, V. Horvat, N. Nica, B.T. Roeder, E. McCleskey, R.E. Tribble, and I.S. Towner, Phys. Rev. C (to be published).
- [3] H.S. Wilson, R.W. Kavanagh, and F.M. Mann, Phys. Rev. C **22**, 1696 (1980).
- [4] B.D. Anderson, A.R. Baldwin, P. Baumann, B.A. Brown, F. Didierjean, C.C. Foster, L.A.C. Garcia, A. Huck, A. Knipper, R. Madey, D.M. Manley, G. Marguier, M. Ramdhane, H. Ravn, C. Richard-Serre, G. Walter, and J.W. Watson, Phys. Rev. C **54**, 602 (1996).

Superaligned β -decay branching-ratio measurement of ^{26}Si

M. Bencomo, J.C. Hardy, V.E. Jacob, H.I. Park, L. Chen, V. Horvat, N. Nica, B.T. Roeder,
A. Saastamoinen, R.E. Tribble, and I.S. Towner

We have measured the branching ratio for the superallowed $0^+ \rightarrow 0^+ \beta^+$ emitter ^{26}Si (see Fig. 1). Since the QEC [1] value and half-life [2] have already been measured, the branching ratio will allow us to determine the ft value. This would complete another pair of mirror superallowed transitions, $^{26}\text{Si} \rightarrow ^{26m}\text{Al}$ and $^{26m}\text{Al} \rightarrow ^{26}\text{Mg}$. The first mirror transitions to be precisely measured, $^{38}\text{Ca} \rightarrow ^{38m}\text{K}$ and $^{38m}\text{K} \rightarrow ^{38}\text{Ar}$, showed that the ratio of mirror ft values is very sensitive to the model used to calculate the small isospin symmetry-breaking corrections required to extract V_{ud} . In calculating this correction both Woods-Saxon (WS) and Hartree-Fock (HF) radial wave functions have been used, with the experimental results from the $A = 38$ pair favoring the WS calculation [3]. We are extending this work to the $A = 26$ mirror pair in order to determine if this conclusion is applicable more generally.

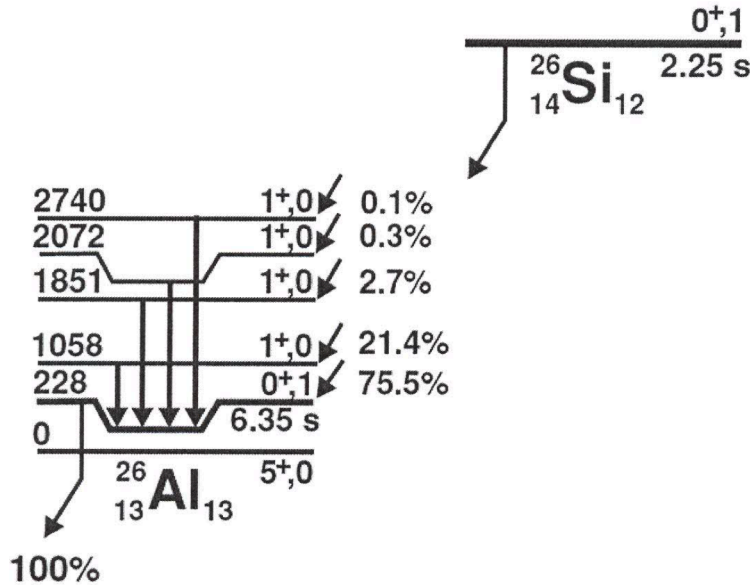


FIG. 1. Decay scheme of ^{26}Si showing only those features of relevance to the superallowed β -decay measurement. All energies are in keV. The data are taken from Ref. [4].

We produced 2.25-s ^{26}Si using a 30A MeV ^{27}Al beam from the Texas A&M K500 superconducting cyclotron to initiate the $p(^{27}\text{Al}, 2n)^{26}\text{Si}$ reaction on a hydrogen gas target cooled to LN2 temperatures. The ejectiles from the reaction were fully stripped and, after passing through the MARS spectrometer, produced a ^{26}Si secondary beam of >98% purity at the extraction slits in the MARS focal plane. The ^{26}Si beam exited the vacuum system through a 50- μm -thick Kapton window, passed

successively through a 0.3-mm-thick BC-404 scintillator and a stack of aluminum degraders, finally stopping in the 76- μm -thick aluminized Mylar tape of our tape transport system. Since the few impurities remaining in the beam had ranges different from that of ^{26}Si , most were not collected on the tape. The only surviving impurities were ^{24}Al , ^{22}Mg and ^{23}Mg .

In a typical measurement, we collected ^{26}Si on the tape for 5 s, then interrupted the beam and triggered the tape-transport system to move the sample in 160 ms to a shielded counting station 90 cm away, where the sample was positioned between a 1-mm-thick BC404 scintillator to detect β^+ particles, and a 70% HPGe detector for γ rays. Data was collected for 5 s after which the cycle was repeated. Essential to our experimental method is the precisely known absolute efficiency of the γ -ray detector [5], which was positioned at 15.1 cm from the collected sample.

Time-tagged β - γ coincidence data were stored event by event. The β and γ -ray energies, the coincidence time between them, and the time of the event after the beginning of the cycle were all recorded, as was the total number of β -singles events for each cycle. The recorded spectrum for β - γ coincidences is shown in Fig. 2.

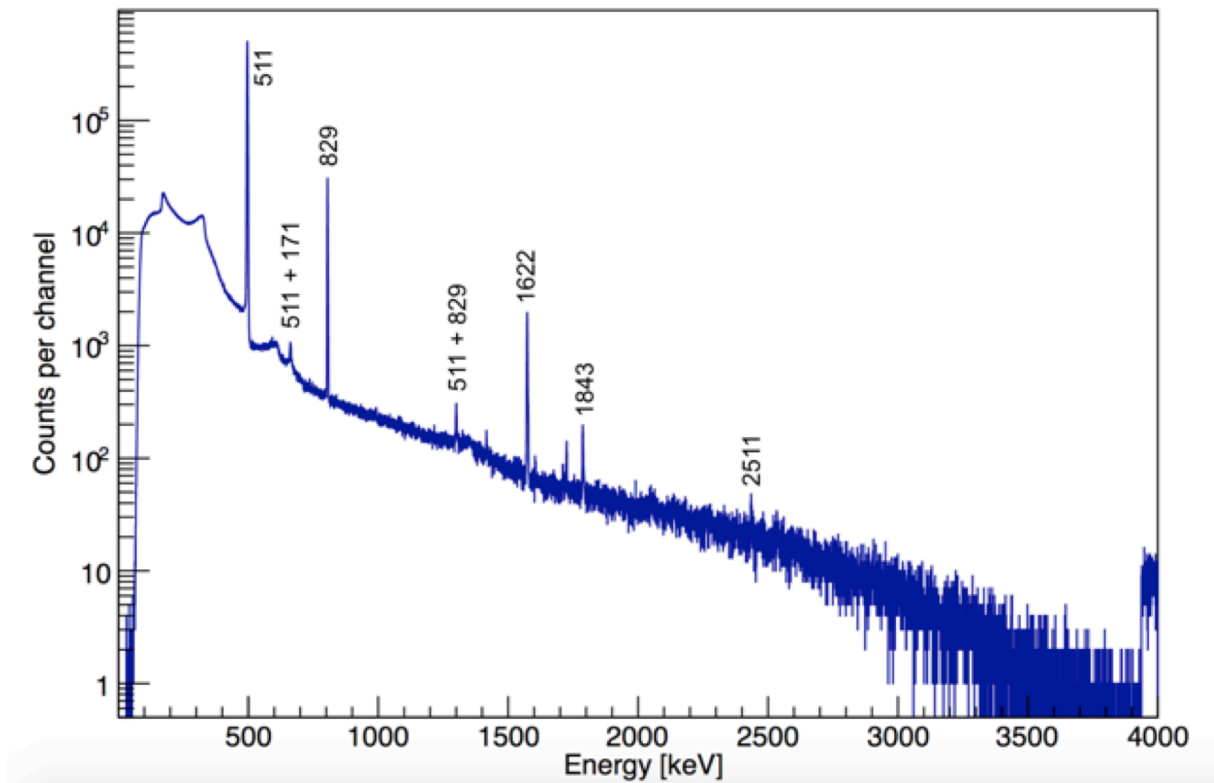


FIG. 2. Spectrum of γ rays coincident with beta particles from the decay of ^{26}Si . Peaks are labeled according to their energy in keV. The peak labeled ‘511+171’ is caused by positron annihilation, from which one 511-keV γ ray sums with a back-scattered γ ray from the second 511-keV γ ray. The ‘511+829’ peak is a result of coincidence summing between a 511-keV γ ray from annihilation and the 829-keV γ ray.

In order to obtain the branching ratio of the superallowed transition we first need to determine the branching ratio to the 1^+ state in ^{26}Al at 829 keV (see Fig. 1). From the relative intensities of all the other γ -ray peaks we can determine the total Gamow-Teller branching ratio to all 1^+ states in ^{26}Al . Subtracting this total from 100% we can then determine the branching ratio to the 0^+ state: i.e.

$$BR_F = 1 - \sum BR_{GT} , \quad (1)$$

where BR_F is the Fermi branching ratio and BR_{GT} the Gamow-Teller branching ratios. We obtain the branching ratio R_i , to a particular state i in ^{26}Al using the following equation:

$$R_i = \frac{N_{\beta\gamma i} \varepsilon_\beta}{N_\beta \varepsilon_{\gamma i} \varepsilon_{\beta i}} \quad (2)$$

where $N_{\beta\gamma i}$ is the total number of β - γ coincidences in the γ_i peak; N_β is the total number of beta singles corresponding to the decay of ^{26}Si ; $\varepsilon_{\gamma i}$ is the efficiency of the HPGe detector for detecting γ_i ; $\varepsilon_{\beta i}$ is the efficiency of the plastic scintillator for detecting the betas that populate the state i ; and ε_β is the average efficiency for detecting the betas from all ^{26}Si transitions.

The analysis of this experiment is still in progress. Corrections for dead time, pile up, random coincidences, summing and other smaller effects still need to be done. If the results from this experiment are consistent with $A = 38$ in favoring the WS radial functions, we would be one step closer to sensitively discriminating between the models used to calculate the isospin-symmetry-breaking correction, δ_C . This could ultimately reduce the uncertainties in both V_{ud} and the unitary sum for the Cabibbo-Kobayashi-Maskawa matrix.

- [1] T. Eronen *et al.*, Phys. Rev. C **79**, 032802(R) (2009).
- [2] V.E. Iacob, J.C. Hardy, A. Banu, L. Chen, V.V. Golovko, J. Goodwin, V. Horvat, N. Nica, H.I. Park, L. Trache, and R.E. Tribble. Phys. Rev. C **82**, 035502 (2010).
- [3] H.I. Park *et al.*, Phys. Rev. Lett. **112**, 102502 (2014).
- [4] J.C. Hardy and I.S. Towner, Phys. Rev. C **79**, 055502 (2009).
- [5] J.C. Hardy *et al.*, Appl. Radiat. Isot. **56**, 65 (2002) ; R.G. Helmer *et al.*, Nucl. Instrum. Methods Phys. Res. **A511**, 360 (2003); R.G. Helmer *et al.*, Appl. Radiat. Isot. **60**, 173 (2004).

United States nuclear structure data program (USNDP) and evaluated nuclear structure data file (ENSDF) at Texas A&M University

N. Nica¹ and J.C. Hardy

¹*Under contract with Brookhaven National Laboratory*

Since 2005 we have been an important partner in the nationwide United States Nuclear Data Program (USNDP), which is part of the Nuclear Structure and Decay Data (NSDD) international nuclear data-evaluation network. USNDP is in fact the backbone of the NSDD network, making the greatest effort in completion of the goals of the nuclear-structure data-evaluation communities. Nuclear data evaluation is a national-interest activity financed by DOE, through which relevant nuclear-science results in virtually all world publications are retrieved and put together in a large Evaluated Nuclear Structure Data File (ENSDF) database according to general policies, a set of rules that make possible a standard approach through which the data are uniformly evaluated.

This activity is carried by a relatively small group of professionals located mostly in national institutes but also hosted by a few universities. The nuclear data network is the nodal point for the wide dissemination of nuclear knowledge to many users, from those in basic science to those engaged in commercial applications in American and international businesses. The output is published in the Nuclear Data Sheets, an Elsevier publication, and also is disseminated by different on-line databases, which can be retrieved at the NNDC site (<http://www.nndc.bnl.gov>), IAEA Vienna's site (<http://www-nds.iaea.org>) and several other locations.

For ten years now at the Cyclotron Institute of Texas A&M we have completed the evaluation of mass chains covering a large part of the nuclear chart. We have published in Nuclear Data Sheets the superheavy $A=252$ mass chain [1]; the very data-rich mid-mass chains, $A=140$ [2], $A=141$ [3], $A=147$ [4] and $A=148$ [5]; the relatively lighter chains, $A=97$ [6] and $A=84$ [7]; and, in collaboration with B. Singh and a group of authors from McMaster University, Canada, we also published the $A=77$ [8], $A=37$ [9], $A=36$ [10], and $A=34$ [11] chains. Another two big mass chains, $A=158$ and $A=157$, have been submitted, the former in 2013 and the latter in 2014; both are still in the review process. Our total effort is 0.67 FTE per year.

Beginning in January 2015 we started a new evaluation of $A=140$, a mass chain that we first evaluated a decade ago. The chain includes Sb, Te, I, Xe, Cs, Ba, La, Ce, Pr, Nd, Pm, Sm, Eu, Gd, Tb, Dy, and Ho, a total of 17 isobars. More than 130 papers have been published since January 2006, when our previous evaluation closed. This work is in progress.

[1] N. Nica, Nucl. Data Sheets **106**, 813 (2005).

[2] N. Nica, Nucl. Data Sheets **108**, 1287 (2007).

[3] N. Nica, Nucl. Data Sheets **122**, 1 (2014).

[4] N. Nica, Nucl. Data Sheets **110**, 749 (2009).

[5] N. Nica, Nucl. Data Sheets **117**, 1 (2014).

- [6] N. Nica, Nucl. Data Sheets **111**, 525 (2010).
- [7] D. Abriola *et al.*, Nucl. Data Sheets **110**, 2815 (2009).
- [8] B. Singh and N. Nica, Nucl. Data Sheets **113**, 1115 (2012).
- [9] J. Cameron, J. Chen, B. Singh, and N. Nica, Nucl. Data Sheets **113**, 365 (2012).
- [10] N. Nica, J. Cameron, and B. Singh, Nucl. Data Sheets **113**, 1 (2012).
- [11] N. Nica and B. Singh, Nucl. Data Sheets **113**, 1563 (2012).

**Tests of internal-conversion theory with precise γ - and x-ray spectroscopy:
Selection of new cases**

N. Nica, J.C. Hardy, and M.B. Trzhaskovskaya¹

¹*Petersburg Nuclear Physics Institute, Gatchina RU-188300, Russia*

After having completed eight precise measurements of Internal Conversion Coefficients (ICCs) at the Cyclotron Institute, we find consistent agreement with the ICCs that are calculated with full account being taken of the atomic vacancy, or hole, left behind by the conversion electron [1]. Before 2004, when we published our first measurement, calculations that ignored the hole were accepted and the code BrIcc [2], which was based on those calculations, was in standard use for the Evaluated Nuclear Structure Data File (ENSDF), the nuclear data base maintained by the US National Nuclear Data Center (NNDC). However, based on our early results, since 2004 the NNDC has adopted the calculations that include the hole and BrIcc has been modified accordingly. Our supplementary measurements have continued to support this decision. This is a rather rare example – perhaps insufficiently popularized – of basic university research serving not only basic science but also broader societal applications.

When we started the series of measurements our interest was to tackle a controversial conclusion coming from an important survey work [3], which compared ICC calculated and measured values. The authors found that the ‘no-hole’ calculations showed better agreement with the measured values. Yet the time for the converted electron to leave the atom can easily be calculated and shown to be much shorter than the known lifetime of a K-shell vacancy (10^{-18} s \ll 10^{-15} – 10^{-17} s). In order to clarify this situation, we chose to measure or re-measure the ICCs of transitions for which the relative difference between ‘hole’ and ‘no hole’ calculations is of several percent. With our experimental precision of $\sim 1\%$ we could convincingly discriminate between the two types of calculation in such cases. Our first measurement was of the most favorable case, that of the 80.2-keV $M4$ transition in ^{192m}Ir , where there is an 11% difference between ‘hole’ and ‘no hole’ calculated values. Our result agreed completely with the ‘hole’ value and disagreed by more than 10 standard deviations from the ‘no hole’ one.

This result also suggested that the problem with the survey result [3] may have lain simply with the overall lack of precision and quality of the experimental set of ICCs available at the time. Indeed, of the 100 experimental cases used, only five had a precision of $< 2\%$, while most were in the range of 5%. In the series of measurements that we have continued since then, we have more than doubled the number of measured ICCs with $\sim 1\%$ precision. In some cases, we corrected previous ICC results; in others we measured the ICCs precisely for the first time. Overall we have chosen transitions that spanned a range of Z and A values, γ -ray energies and multipolarities so as to investigate the efficacy of the ‘hole’ theory under a variety of conditions. So far [1] we have completed measurements of eight transitions in the following nuclei: ^{191}Ir , ^{134}Cs , ^{137}Ba , ^{139}La , ^{197}Pt , ^{119}Sn , ^{127}Te and ^{111}Cd (the last two are still to be published). In all cases, the results support the ICCs calculated with the atomic vacancy included.

In looking to the future we have recently completed a systematic investigation of what cases remain that we can usefully measure with our experimental technique, which depends on there being a single predominant transition that converts in the K shell, allowing us to determine α_K from the ratio of the K x-ray intensity to the corresponding γ -ray intensity, both being measured in the same well-calibrated HPGe detector. The following is an outline of the procedures that we followed:

1. As main guidance for our search, we used Fig. 1, which displays the difference Δ_K between $\alpha_K(\text{hole})$ and $\alpha_K(\text{no hole})$ expressed as a percent and plotted as a function of the kinetic energy of the conversion-electron energy E_K for four multiplicities and four Z values. Evidently the most interesting cases – the ones with the highest Δ_K – have to have the highest multiplicities (E3, M4) and the lowest values of E_K .

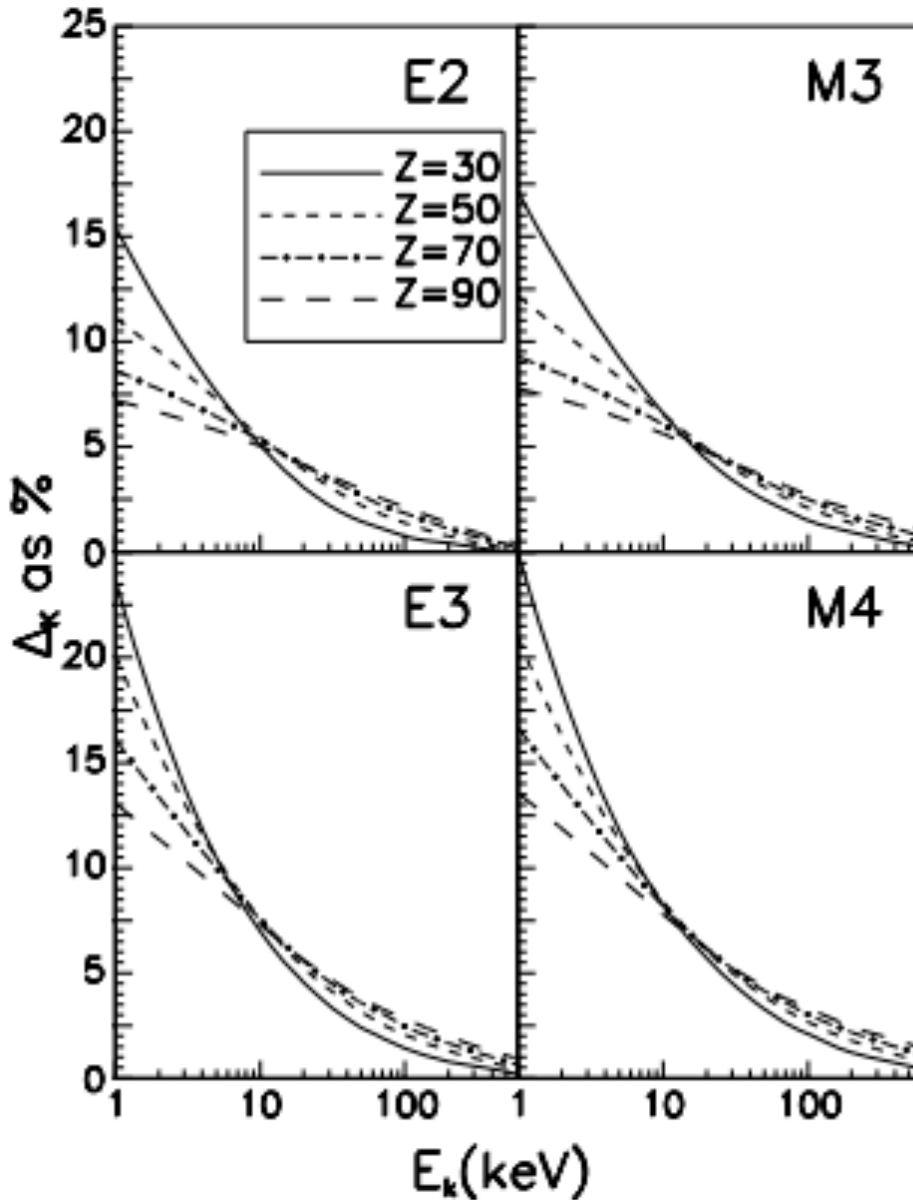


FIG. 1. The difference Δ_K between $\alpha_K(\text{'hole'})$ and $\alpha_K(\text{'no hole'})$ plotted as function of the kinetic energy of conversion electron E_K

2. To achieve sufficient counting rate, we depend upon neutron activation of our sources with the TRIGA reactor at Texas A&M University. Consequently we are limited to relatively long-lived nuclides, $T_{1/2} > 0.5$ h since it takes at least an hour to extract an activated source and transport it to our detector laboratory. With this condition we effectively exclude low multipolarity, $M1$ and $E2$, transitions.

3. With these conditions set we conducted a search with *NuDat*, the NNDC nuclear-data web tool based on the ENSDF database, and found a preliminary set of α_K candidates: 14 $E3$, 9 $M3$, 2 $E4$, and 8 $M4$ transitions, a total of 33 all having Δ_K of between 5 and 13%.

4. Of these, we excluded the nuclides whose production cross sections were too small to ensure enough counting statistics for the peaks of interest.

5. Also from the production point of view, we explicitly filtered out cases in which contaminant activities could play a seriously detrimental role.

6. We also excluded those nuclides in which other strongly converted transitions would contribute to the K x-ray spectrum.

7. We separately examined the 100 experimental α_K cases taken into consideration in the previously mentioned survey [3] looking for cases that disagreed with both ‘hole’ and ‘no hole’ calculations or otherwise showed indications of atypical or abnormal behavior.

8. Of the promising cases that were thus identified, four more had to be excluded for a specific reason:

- ^{58m}Co was eliminated because its 7-8 keV K x rays are too soft to be measured with our HPGe detector; we could use a Si detector but that would necessitate very thorough new efficiency calibration work.
- ^{93m}Nb , while a very good candidate ($\Delta_K = 8\%$, single 30-keV γ ray, clean and easy to measure), is commercially unavailable and we cannot produce it locally.
- ^{130m}I and ^{144m}Pr are also good candidates but have $t_{1/2}$ of 12 min and 17 min respectively and could perhaps be measured close to the reactor used to produce them. However because of the critical role our HPGe detector plays in our precision β -decay measurements we prefer not to move it away from the Cyclotron Institute.

9. Finally the cases that we can measure at this time are:

- ^{125m}Te : 109.2-keV, $M4$ γ ray, whose measured $\alpha_K = 167(7)$ in ref. [3] disagrees with both calculations, $\alpha_K(\text{hole}) = 185$ and $\alpha_K(\text{no hole}) = 179$. It can easily be produced by thermal-neutron activation from the enriched ^{124}Te isotope.
- ^{103m}Rh : 39.8-keV, $E3$ γ ray from ^{103}Ru β^- decay populated by thermal neutron activation of ^{102}Ru . ^{103m}Rh can also be populated from ^{103}Pd ec decay but the enriched ^{102}Pd isotope needed to produce ^{103}Pd is far too expensive. The most precise α_K values previously measured, 127(6) [4], and 138(5) [5] are of no help in distinguishing between the two calculations, $\alpha_K(\text{no hole}) = 127$ and $\alpha_K(\text{hole}) = 135$.

In conclusion, all the six cases, ^{58m}Co , ^{93m}Nb , ^{130m}I , ^{144m}Pr , ^{125m}Te , and ^{103m}Rh , are approachable by our method but the first four offer significant challenges. For now, we plan to measure the last two, ^{125m}Te , and ^{103m}Rh .

- [1] N. Nica *et al.*, Phys. Rev. C **70**, 054305 (2004); Phys. Rev. C **71**, 054320 (2005); Phys. Rev. C **75**, 024308 (2007), Phys. Rev. C **77**, 034306 (2008), Phys.Rev. C **80**, 064314 (2009); Phys. Rev. C **89**, 014303 (2014); J.C. Hardy *et al.*, Appl.Radiat.Isot. **87**, 87 (2014).
- [2] T. Kibédi *et al.*, Nucl. Instrum. Methods Phys. Res. **A589**, 202 (2008).
- [3] S. Raman *et al.*, Phys. Rev. C **66**, 044312 (2002).
- [4] K.H. Czock *et al.*, Int. J .Appl. Radiat. Isotop. **26**, 417 (1975).
- [5] E. Niesdchmidt and D.A. Pearson, Reports IN-1218, p. 87 (1968) and IN-1317, p. 122 (1970); quoted by [4].

**Tests of internal-conversion theory with precise γ - and x-ray spectroscopy:
The case of ^{111m}Cd**

N. Nica, L. Pineda, J.C. Hardy, V.E. Iacob, H.I. Park, and M.B. Trzhaskovskaya¹
¹*Petersburg Nuclear Physics Institute, Gatchina RU-188300, Russia*

Internal conversion is an important component of most nuclear decay schemes. In order to balance decay schemes correctly, one needs to know the internal conversion contribution to each transition as expressed by its internal conversion coefficient (ICC). Nevertheless, ICCs are only rarely measured; instead they are taken from tabulations. As a result, calculated ICCs are essential input to every decay scheme, except those for the lightest nuclei. Unfortunately, over the decades, tabulated ICC values have differed significantly from one calculation to another by a few percent. Although for many applications such differences can be tolerated, transitions used in critical calibrations require very precise and accurate ICC values, precision that has simply been impossible to guarantee at the one-percent level or below.

In order to correct for this deficiency one can only seek guidance from measured ICCs that have sufficient precision to distinguish among the various calculations. However, as recently as a decade ago, when a survey of measured ICCs was made by Raman et al. [1], there were only five published ICC values with precision of the order of $\pm 1\%$, not enough to make any definitive conclusion possible. At that time, one aspect of the ICC calculations remained a particular concern. The final-state electron wave function must be calculated in a field that adequately represents the remaining atom. But should that representation include the atomic vacancy created by the conversion process? Some calculations included it and some did not.

Thus the problem of measuring ICCs at the $\pm 1\%$ precision level became critical and, with our very precisely efficiency-calibrated HPGe detector [2], we found ourselves in a position to be able to address it. Consequently, over the past decade we have been measuring a series of ICCs [3] covering a wide range of atomic numbers, $50 \leq Z \leq 78$. So far, all these results have indicated that the atomic vacancy should be taken into account in the calculations. With $Z = 48$, the new case reported here – the 150.8-keV $E3$ transition in ^{111}Cd – extends the lower end of that range.

The total intensity of an electromagnetic transition is split between γ -ray emission and electron conversion, which can take place in several atomic shells and subshells, and is followed by the corresponding x rays. If only K -shell conversion is considered, then one can use the following formula to determine the K -shell conversion coefficient, α_K :

$$\alpha_K \omega_K = \frac{N_K}{N_\gamma} \cdot \frac{\varepsilon_\gamma}{\varepsilon_K} \quad (1)$$

where ω_K is the fluorescence yield, which we take from Ref. [4]; N_K and N_γ are the respective peak areas of the K x rays and the γ ray; and ε_K and ε_γ are the corresponding detector absolute efficiencies.

The 150.8-keV, $E3$ transition in ^{111}Cd depopulates the 396.3-keV, 49-min isomeric state and is followed by a 245.4-keV $E2$ transition to the stable ground state. Naturally the Cd K x-ray group is the

sum of K x rays following the electron conversion of both transitions. However, the K x-ray contribution from the 245.4-keV transition is relatively small and can be reliably subtracted along with even smaller contributions from other Cd isotopes to yield a clean N_K number for Eq. (1).

Two samples were prepared by electro-deposition of 1 mg of 96%-enriched ^{110}Cd oxide on 10- μm -thick Al foil, 99.999% pure. The CdO layer was 1.7-cm in diameter and about 0.55 μm thick. The 396.3-keV isomeric state in ^{111}Cd was populated by thermal neutron activation at the Nuclear Science Center TRIGA reactor of Texas A&M University at a fluency of 7.5×10^{12} neutron/(cm^2s). The samples were activated at different dates for about 2 h, cooled down for 2 h, and measured for 3 weeks. A total of four spectra were acquired, from which $\alpha_K(150.8)$ was extracted, the final result being the average of the four values. Since the 150.8-keV transition is in cascade with the $E2$ 245.4-keV transition, as a byproduct we could also obtain the total conversion coefficient α of the former transition by measuring the intensity of the latter since the calculated total ICC value of the $E2$ transition is insensitive to the treatment of the vacancy.

As described in Ref. [2], ε_γ for a 150.3-keV γ ray in our detector is known to $\pm 0.15\%$ relative precision; however a special investigation was required in order to get a precise value for ε_K at 23.6 keV, the average energy of the cadmium K x ray group. We accomplished this by measuring a well-known calibration source, ^{109}Cd , which decays by electron capture to ^{109}Ag , followed by a unique 88.0-keV, $M4$ γ transition. The K x rays of silver, following both the electron capture decay and the electron conversion of the 88.0-keV transition, form a prominent K x-ray group situated at 22.1-keV (K_α) and 25.0-keV (K_β). The K x-rays, together with the 88.0 keV γ ray, were then used with a formula similar to eq. (1) to deduce ε_K at the silver K x-ray energies based on the calculated α_K value for the 88.0-keV transition in ^{109}Ag . This α_K value is relatively insensitive to the treatment of the atomic vacancy so we could use the mean value of the calculated 'hole' and 'no hole' α_K values with an uncertainty chosen to encompass both. Then by a short interpolation from the silver K x-ray energies to those of cadmium, we determined the ε_K value for cadmium K x-rays with a total uncertainty of the order of $\pm 1\%$.

From our analysis, we found that the contribution to the cadmium K x rays coming from the electron conversion of the 245.4-keV transition in ^{111}Cd was 11.2% of the contribution from the 150.8-keV transition. In addition, transitions in ^{115}Cd , ^{117}Cd , ^{117}In and ^{116}In were identified as contributing to the K x-ray group, with a total contribution of 3 – 7 % depending on the time after activation.

Our preliminary result, $\alpha_K(150.8) = 1.454(20)$, is in best agreement with the theoretical calculation incorporating the vacancy, $\alpha_K(\text{hole}) = 1.450$, which is in conformity with all our previous results [3]. For comparison, the 'no hole' result is $\alpha_K(\text{no hole}) = 1.425$. For the total conversion coefficient of the same transition, our preliminary result is $\alpha(150.8) = 2.241(30)$, which can be compared with $\alpha(\text{no hole}) = 2.26$ and $\alpha(\text{hole}) = 2.28$. Both our results disagree with less-precise previous measurements [5], $\alpha_K(150.8) = 1.29(11)$ and $\alpha(150.8) = 1.98(5)$, which were significantly lower than both types of calculations.

[1] S. Raman *et al.*, Phys. Rev. C **66**, 044312 (2002).

[2] J.C. Hardy *et al.*, Appl. Radiat. Isot. **56**, 65 (2002); R.G. Helmer *et al.*, Nucl. Instrum. Methods Phys. Res. **A511**, 360 (2003); R.G. Helmer *et al.*, Appl. Radiat. Isot. **60**, 173 (2004).

- [3] N. Nica *et al.*, Phys. Rev. C **70**, 054305 (2004); Phys. Rev. C **71**, 054320 (2005); Phys. Rev. C **75**, 024308 (2007), Phys. Rev. C **77**, 034306 (2008), Phys.Rev. C **80**, 064314 (2009);Phys.Rev. C **89**, 014303 (2014); J.C. Hardy *et al.*, Appl.Radiat.Isot. **87**, 87 (2014).
- [4] E. Schönfeld and H. Janssen, Nucl. Instrum. Methods Phys. Res. **A369**, 527 (1996).
- [5] Zs. Nemeth and A. Veres, Phys. Rev. C **35**, 2294 (1987).

Superaligned $0^+ \rightarrow 0^+$ nuclear β decays: 2014 critical survey, with precise results for V_{ud} and CKM unitarity

J.C. Hardy and I.S. Towner

Beta decay between nuclear analog states of spin-parity, $J^\pi = 0^+$, and isospin, $T = 1$, has been a subject of continuous and often intense study for five decades. The strengths, or ft values, of such transitions are nearly independent of nuclear-structure ambiguities and depend uniquely on the vector part of the weak interaction. Thus, their measurement has given nuclear physicists access to clean tests of some of the fundamental precepts of weak-interaction theory and, over the years, this strong motivation has led to very high precision being achieved in both the experiments and the theory required to interpret them.

As befits such an important issue, we have undertaken periodic surveys of the relevant world data (see, for example, refs [1-6]). Since our last survey closed in September 2008, a large amount of significant new data has appeared, so that survey was already out of date. We have now published a thorough new overview [7], in which we critically survey all relevant measurements formally published before September 2014.

Compared with our last review, we have added results from 24 new publications and eliminated 9 references, the results from which having been superseded by much more precise modern data. We obtained world-average ft -values for each of the eighteen transitions that have a complete set of data, then applied radiative and isospin-symmetry-breaking corrections to extract "corrected" $\mathcal{F}t$ values. Fourteen of these $\mathcal{F}t$ values now have a precision of order 0.1% or better. In the process of obtaining these results we carefully evaluated the available calculations of the isospin-symmetry-breaking corrections by testing the extent to which they lead to $\mathcal{F}t$ values consistent with conservation of the vector current (CVC). Only one set of calculations satisfactorily meets this condition. As shown in Fig. 1, the results for the $\mathcal{F}t$ values are impressively constant.

The resultant average $\mathcal{F}t$ value, when combined with the muon lifetime, yields the up-down quark-mixing element of the Cabibbo-Kobayashi-Maskawa (CKM) matrix, $V_{ud} = 0.97417$ (21), a result that is consistent with, but more precise than, values we have obtained in previous analyses of superallowed β decay. To emphasize the consistency and steady improvement that has characterized the value of V_{ud} as derived from nuclear β decay, in Fig. 2 we plot our new result together with V_{ud} values published at various times over the past two-and-a-half decades.

The unitarity test on the top row of the matrix becomes $|V_{ud}|^2 + |V_{us}|^2 + |V_{ub}|^2 = 0.99978$ (55) if the Particle Data Group recommended value for V_{us} is used. However, recent lattice QCD calculations, not included yet in the PDG evaluation, have introduced some inconsistency into kaon-decay measurements of V_{us} and V_{us}/V_{ud} . In ref. [7], we have examined the impact of these new results on the unitarity test and conclude that there is no evidence of any statistically significant violation of unitarity. Finally, from the $\mathcal{F}t$ -value data we also set limits on the possible existence of scalar interactions.

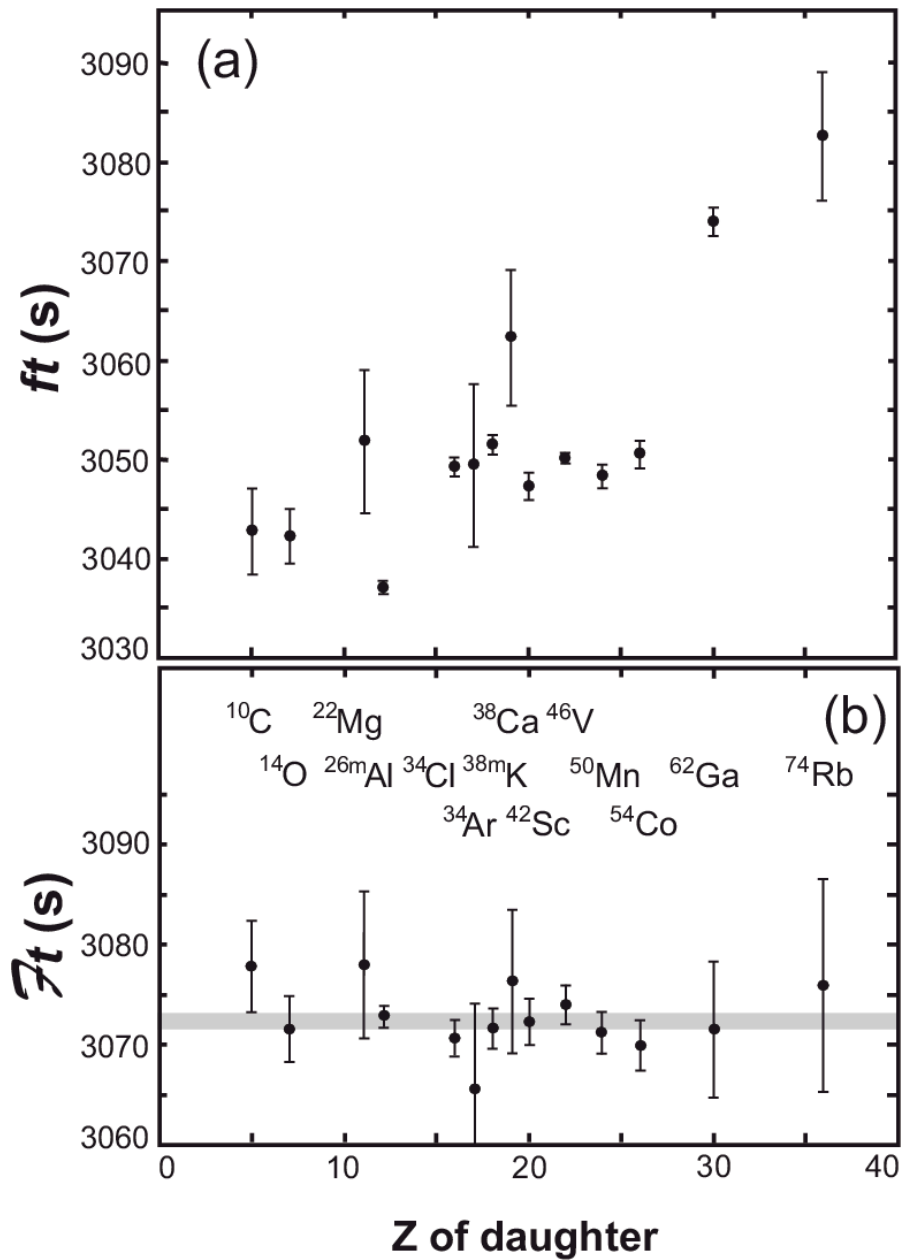


FIG. 1. In the top panel are plotted the uncorrected experimental ft values as a function of the charge on the daughter nucleus. In the bottom panel, the corresponding Ft -values are given; they differ from the top panel simply by the inclusion of the correction terms δ_R^2 , δ_{NS} and δ_C . The horizontal grey band in the bottom panel indicates the average Ft -value with its uncertainty.

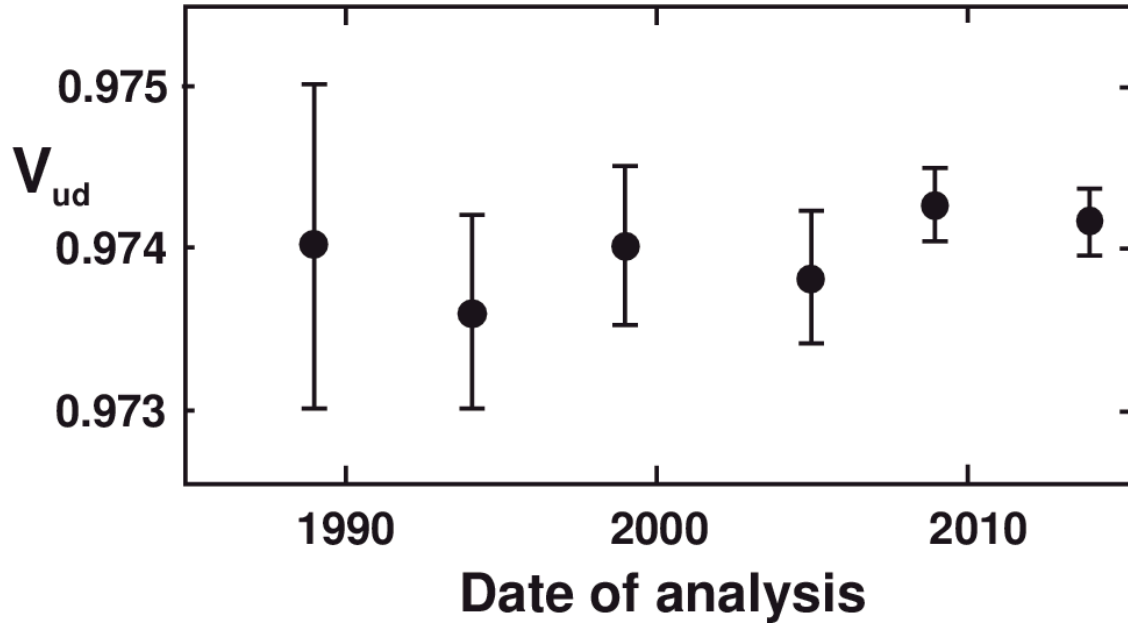


FIG. 2. Values of V_{ud} as determined from superallowed $0^+ \rightarrow 0^+$ β decays plotted as a function of analysis date, spanning the past two-and-a-half decades.

- [1] I.S. Towner and J.C. Hardy, Nucl. Phys. **A205**, 33 (1973).
- [2] J.C. Hardy and I.S. Towner, Nucl. Phys. **A254**, 221 (1975).
- [3] V.T. Koslowsky, E. Hagberg, J.C. Hardy, H. Schmeing, R.E. Azuma, and I.S. Towner, in *Proc. 7th Int. Conf. on atomic masses and fundamental constants, Darmstadt-Seeheim*, ed. O. Klepper (T.H. Darmstadt, 1984), p. 572.
- [4] J.C. Hardy, I.S. Towner, V.T. Koslowsky, E. Hagberg, and H. Schmeing, Nucl. Phys. **A509**, 429 (1990).
- [5] J.C. Hardy and I.S. Towner, Phys. Rev. C **71**, 055501 (2005).
- [6] J.C. Hardy and I.S. Towner, Phys. Rev. C **79**, 055502 (2009).
- [7] J.C. Hardy and I.S. Towner, Phys. Rev. C **91**, 025501 (2015).

Progress in measuring GMR in unstable nuclei: Decay detector calibration and inverse reaction experiment

J. Button, Y.-W. Lui, and D.H. Youngblood

I. Introduction

The Giant Monopole Resonance (GMR) is interesting because its excitation energy is directly related to the incompressibility of the nucleus K_A . K_A can be used to derive the incompressibility of nuclear matter K_{NM} , but this extrapolation from the data for real nuclei is not straightforward due to contributions from surface, Coulomb and asymmetry effects. Thus, improvements to the extrapolated K_{NM} can be made by measuring the GMR for increasing asymmetry $(N-Z)/A$. The incompressibility of nuclear matter is of importance in the nuclear equation of state (EOS) which describes a number of phenomena: collective excitations of nuclei, supernova explosions and radii of neutron stars [1]. The GMR and nuclear incompressibility provide important tests for nuclear effective forces. Additionally, measurement of the ISGMR along isotopic chains with changing nuclear pairing effects may be a useful tool for demonstrating whether or not superfluidity has an effect on nuclear incompressibility [2].

The measurement of the GMR in unstable nuclei was done using inverse kinematics, with a 40 MeV per nucleon beam of the unstable nucleus incident on a ${}^6\text{Li}$ target. X. Chen *et al.* studied the viability of this approach, taking data for elastic scattering and inelastic scattering to low-lying states and giant resonances of 240 MeV ${}^6\text{Li}$ ions on ${}^{24}\text{Mg}$, ${}^{28}\text{Si}$, and ${}^{116}\text{Sn}$ [3]. Also, Krishichayan *et al.* showed that optical potential parameters for ${}^6\text{Li}$ scattering calculated from systematics with respect to changing target mass number can be used to accurately calculate GMR cross-sections [4]. To demonstrate the effectiveness of the inverse kinematics measurement of the GMR, we measured ${}^{28}\text{Si}$ and ${}^{16}\text{O}$ stable nuclei for which the GMR is known. Additionally, we measured the GMR in ${}^{18}\text{O}$, and ${}^{20}\text{Ne}$ stable nuclei for which the GMR is unknown and targets are difficult to make for normal kinematics studies

Nuclei excited to the GMR region are particle unstable and will decay by p, α or n decay shortly after excitation. To reconstruct the event it is necessary to measure the energy and angle of the decay particle and of the residual heavy ion. In many lighter nuclei a few nucleons off stability, and in light proton rich nuclei, the neutron threshold is above the region of interest. There are 3 bodies in the final state (recoiling ${}^6\text{Li}$, decay particle, and residual heavy ion). The recoiling ${}^6\text{Li}$ have low energy and for the most part will not get out of the target. Thus in order to experimentally determine the kinematics, we must measure at least three of the four quantities: decay particle energy and angle, and residual nucleus energy and angle. Thus a ΔE - ΔE -E decay detector composed of plastic scintillator arrays has been built and tested to measure the energy and angle of the light decay particle. The heavy ion is measured using the Oxford detector in the MDM spectrometer. We can calibrate the decay detector elements using the EDSE model for scintillator light output [5]. A hole in the decay detector with a horizontal and vertical opening of 5° allows the residual heavy-ion to enter the MDM spectrometer, which has horizontal and

vertical angular acceptances of $\pm 2.5^\circ$. The energy and angle of the heavy-ion is determined with the Oxford detector. The decay detector can measure decay particles within an angular range of 4° to 35° with respect to the beam direction.

II. Calibration Study of the Decay Detector

We had calibrated the decay detector with a beam of 30 MeV protons scattered from a ^{12}C target. From data of the elastic scattering and inelastic scattering exciting the 2^+ (4.4 MeV) and 3^- (9.6 MeV) levels of ^{12}C [5], we were able to find a set of EDSE fit parameters (ρ , I, F) [6]; these parameters are intrinsic to the type of plastic scintillator used in all three layers of the detector. The last parameter, the normalization constant C, differs between all the strips and varies slightly according to the attenuation behavior along the length of each strip. Therefore, it is necessary to find the normalization constant C for $\Delta\text{E}1$, $\Delta\text{E}2$, and E of all segments of the decay

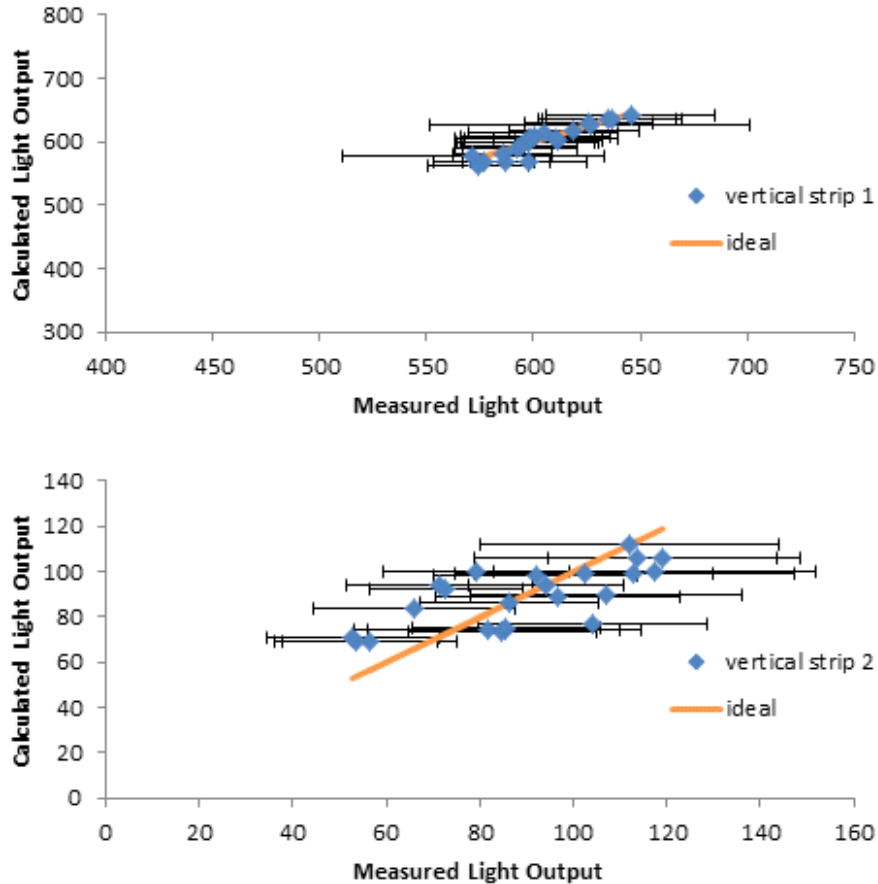


FIG. 1. Comparison of the measured and calculated light outputs of two of the vertical strips in the $\Delta\text{E}1$ layer due to incident 15 MeV, 30 MeV, and 45 MeV protons and 100 MeV α -particles from elastic scatter off ^{12}C target: The calculated light output is obtained by using the EDSE model with these parameters obtained by χ^2 fit to the experimental data: $\rho_1 = 373$ MeV/nm, $F = 1$, and $A = 2.1\text{E-}5$. The normalization constant, C, varies along the length of the vertical strip. The position on the vertical strip is determined by coincidence with the $\Delta\text{E}2$ layer. $C \approx 12.3$ for vertical strip 2, and $C \approx 89.0$ for vertical strip 1

detector. Also the light output of the thin scintillator segments which are used in the two ΔE layers of the decay detector may change over time so that a thorough calibration should be carried out shortly before each data run. All scintillators need to be handled carefully because applied pressure or torque will result in surface cracking (also known as crazing) and reduced efficiency of light transmission. The thin scintillators seem to be more prone to crazing than the scintillator blocks used in the E-layer.

Thus we did a series of calibrations using a ^{12}C target with 15 MeV, 30 MeV, and 45 MeV proton beams and a 100 MeV α beam earlier. Analysis of this calibration data is still ongoing. The procedure for obtaining the light response of the scintillator strips and blocks from the experimental data is outlined in Ref. [5]. The expected light response was calculated by first solving for the energy of the incident proton or α -particle on $\Delta E1$ using relativistic kinematics. The energy deposited in each layer was found by using the SRIM tables, and the EDSE model was used to calculate the expected light response. A comparison of the calculated and measured light outputs from the most recent calibration data is shown in Fig. 1.

III. Faraday Cup and Blocker Plate

A movable Faraday cup and blocker plate were both installed in the space between the MDM Spectrometer and the Oxford detector. The cup consists of a thin layer of brass, in order to stop the beam, and a much thicker layer of tantalum to stop secondary decay particles. The horizontal positions of both the cup and plate can be controlled and read-out remotely. The cup, plate, and drive assembly can be seen in Fig. 2.



FIG. 2. From Top Left moving counter-clockwise: 1) Front-view of the Faraday Cup and Blocker Plate; 2) Back-view of the Cup and Plate, also visible are the tracks which span the length of the spacer section and that the two parts are mounted to; 3) Top-view of the exterior of the spacer section: There are two drive motors, the top motor moves the Cup and the bottom motor moves the Plate; 4) Side-view of the exterior of the spacer section.

The blocker plate completely covers entry into the Oxford detector and is intended to protect the detector from damage while tuning the beam onto the Faraday cup. The Faraday cup stops the beam near the focal plane but allows the heavy decay particle from GR excitation to enter into the detector on the left and right sides of the cup.

IV. Inverse Reaction Experiment

Data were taken using 40 MeV/u beams of ^{28}Si , ^{16}O , ^{18}O , and ^{20}Ne bombarding a ^6Li target. Events were required to be coincident in the decay detector and in the Oxford detector. Signals from the $\Delta E2$ layer were used as a trigger for gates to record signals from the $\Delta E1$, $\Delta E2$, and E layers of the decay detector as well as the 4 proportional counter wires, cathode, and scintillator signals of the Oxford detector. An example illustrating how the new Faraday cup works to block the primary beam and allow the heavy residual ion from proton and α decay can be seen in Fig. 3

When the detector calibration is completed, analysis of the inverse reaction data will

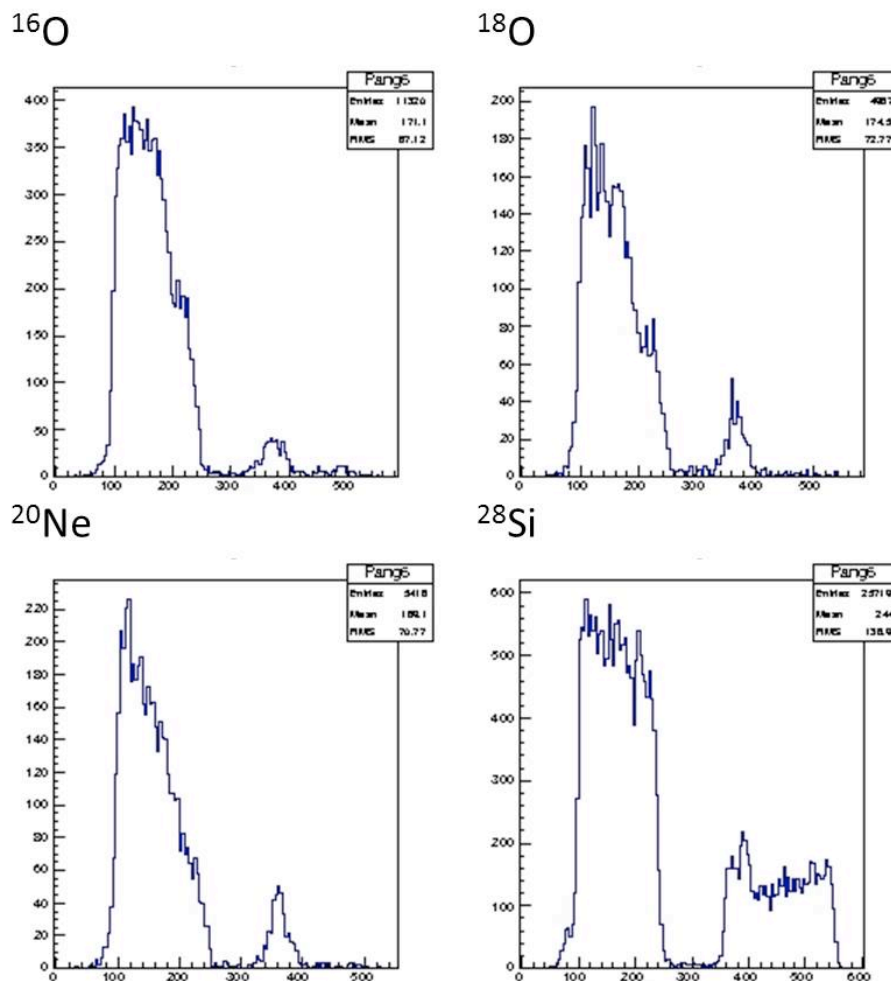


FIG. 3. The spectra for all heavy ions for an uncalibrated angle bin near 0° measured in the Oxford detector in coincidence with the decay detector. The gap in the middle of each spectrum correlates to the position of the Faraday cup before the Oxford detector. The low-side of each spectrum (<300) corresponds to the heavy ion that results from proton decay, and the high-side corresponds to the heavy ion that results from α decay

begin.

- [1] M. Harakeh and A. Van Der Woude, *Giant Resonances: Fundamental High-frequency Modes of Nuclear Excitation* (Clarendon Press, 2001).
- [2] E. Khan, Phys. Rev. C **80**, 011307 (2009).
- [3] X. Chen, Ph.D. Thesis, Texas A&M University, 2008.
- [4] Krishichayan, X. Chen, Y.-W. Lui, J. Button, and D. H. Youngblood, Phys.Rev.C **81**, 044612 (2010).
- [5] J. Button *et al.*, *Progress in Research*, Cyclotron Institute, Texas A&M University (2013-2014), p. IV-56.
- [6] K. Michaelian, A. Menchaca-Rocha, and E. Belmont-Moreno, Nucl. Instrum. Methods Phys. Res. A**356**, 297 (1995).

Spin physics with STAR at RHIC

Z. Chang, C.A. Gagliardi, M.M. Mondal, R.E. Tribble, and the STAR Collaboration

Our group continues to play major roles in STAR investigations of both longitudinal and transverse spin phenomena in polarized pp collisions at RHIC. During the past year, we finalized the STAR results for the longitudinal double-spin asymmetry, A_{LL} , for inclusive jet production in 200 GeV pp collisions based on data that were recorded in 2009, completed a preliminary analysis of A_{LL} for inclusive jets in 510 GeV pp collisions based on data that STAR recorded in 2012, made the first observations of the Collins effect in pp collisions based on data from 500 GeV collisions in 2011 and 200 GeV collisions in 2012, and found further support, in the form of forward-mid-rapidity di-jet correlations, for last year's observation that the large transverse single-spin asymmetries that have been seen for inclusive hadron production at forward rapidities at RHIC are unlikely to arise from conventional $2 \rightarrow 2$ parton scattering.

A major goal of the RHIC spin program is to determine the gluon polarization in the proton over a wide range of x . The longitudinal double-spin asymmetry, A_{LL} , for inclusive jet production is an ideal tool in this effort because the cross section is large and dominated by quark-gluon and gluon-gluon scattering processes, both of which have large partonic

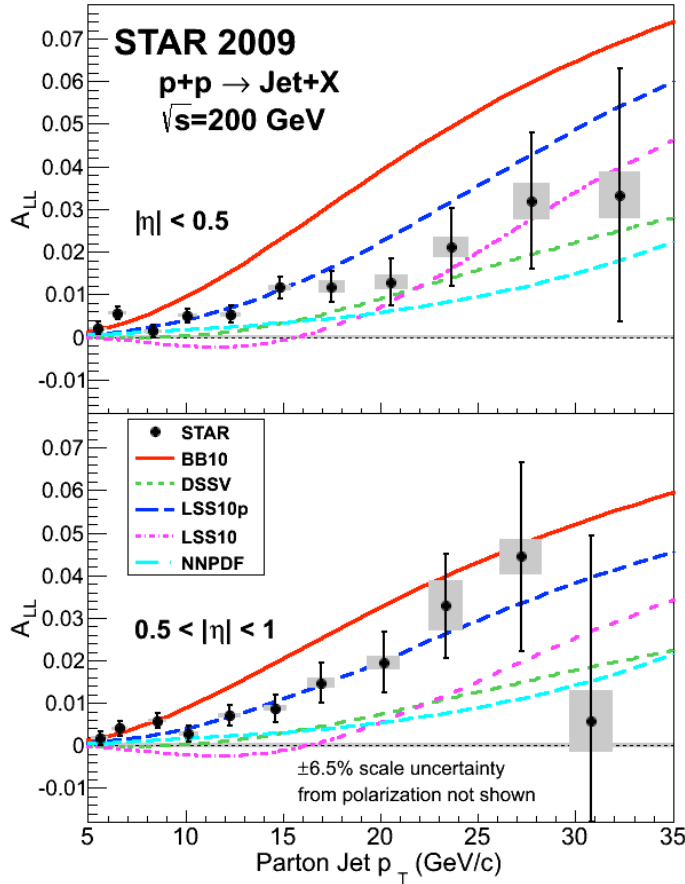


FIG. 1. A_{LL} for inclusive jet production in 200 GeV pp collisions, based on data that STAR recorded in 2009, together with predictions based on several recent polarized parton distribution fits. See [1] for details.

asymmetries. Fig. 1 shows the final STAR results for A_{LL} for inclusive jets in 200 GeV collisions, based on data that were recorded in 2009. The paper describing these results was submitted to Physical Review Letters this past year [1]. These results have now been included in new global analyses of the polarized parton distribution functions by the DSSV [2] and NNPDF groups [3]. Both groups find that the 200 GeV STAR inclusive jet A_{LL} results provide ~ 3 -sigma evidence of positive gluon polarization in the proton within the sampled region, $x > 0.05$.

Since then, we have focused on completing a similar analysis of the inclusive jet data that STAR recorded in 2012 at the higher collision energy of 510 GeV. The higher center-of-mass energy provides access to gluon polarization down to $x \sim 0.02$. The first STAR preliminary results for A_{LL} for inclusive jets in 510 GeV collisions [4], shown in Fig. 2, were presented at the SPIN 2014 conference in Beijing in October, 2014. We find that A_{LL} at 510 GeV is consistent with those global analyses that successfully describe our previous 200 GeV results. It is also consistent with our previous measurements at 200 GeV in the overlapping x_T range. We are now working on the remaining steps necessary to turn these preliminary results into final results.

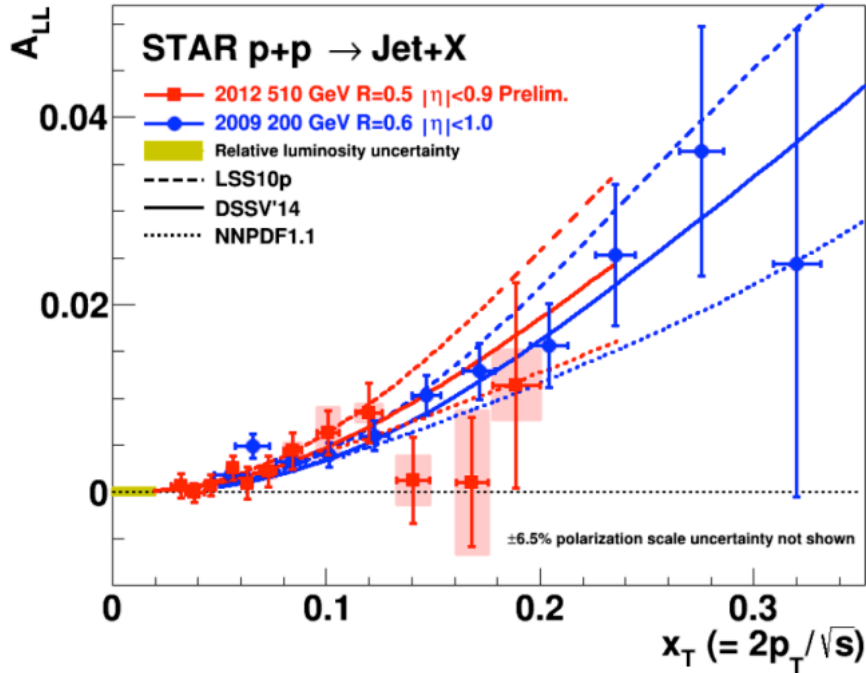


FIG. 2. A_{LL} for inclusive jet production in 510 GeV pp collisions, compared to that for 200 GeV collisions [4]. The curves show three recent polarized parton distribution function fits that describe the 200 GeV results.

Inclusive jets also provide access to a wealth of transverse spin observables. During this past year, STAR reported the first observation of the Collins effect in pp collisions [5], based on the azimuthal distributions of charged pions in mid-rapidity jets. We have now released preliminary results of measurements in both 200 and 500 GeV pp collisions, as shown in Fig. 3 [6]. The results at the two energies agree with each other, and are qualitatively similar to the Collins asymmetries that have been measured at comparable x values in semi-inclusive deep-

inelastic lepton scattering (SIDIS). These data will provide important insights into quark transversity in the range $0.1 < x < 0.3$ where it is only weakly constrained by existing SIDIS measurements, as well as evolution effects in transverse-momentum-dependent fragmentation functions and factorization breaking effects for fragmentation functions in pp collisions.

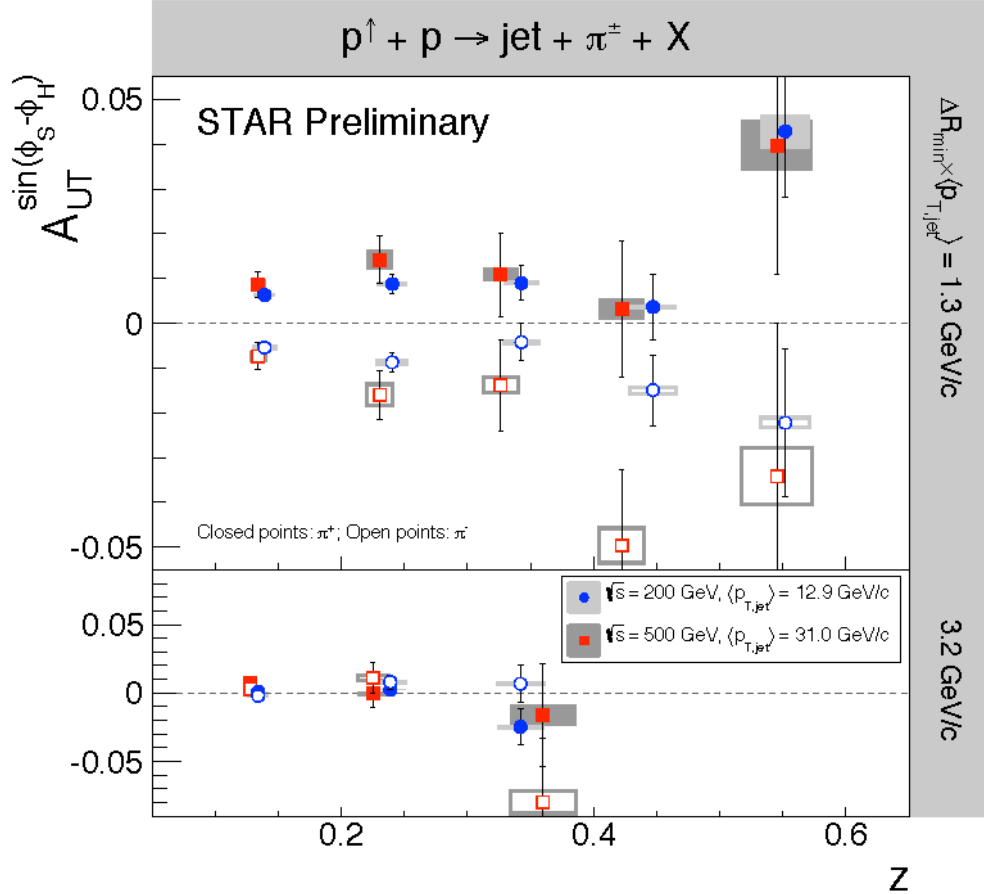


FIG. 3. Collins effect measurements in 200 and 500 GeV pp collisions [6]. The p_T ranges at the two energies have been chosen to sample the same x_T regions. We find that the asymmetries are quite sensitive to j_T , the transverse momentum of the pion relative to its parent jet thrust axis, as demonstrated by the different signal magnitudes in the upper and lower

The 500 GeV results in Fig. 3 focus on the high- p_T region where quark-initiated scattering makes a significant contribution to the cross section. Lower- p_T jets in 500 GeV collisions are more likely to arise from gluon-gluon scattering. Therefore, the 500 GeV Collins effect measurements have been complemented with studies of the total inclusive jet asymmetry, A_N , and the gluon analog of the Collins effect. The former provides information regarding the gluon Sivers function. The latter, sometimes referred to as the ‘‘Collins-like effect’’, involves a convolution of the gluon linear polarization in a transversely polarized proton with the gluon analog of the Collins fragmentation function. The STAR 500 GeV data provide the first ever experimental sensitivity to these novel gluon distributions. A paper describing the measurements of the inclusive jet A_N , the Collins effect, and the Collins-like effect with the 500 GeV data is

currently being written up for publication. It will be followed by a paper describing the 200 GeV results as soon as they are finalized.

The STAR Forward Meson Spectrometer (FMS) provides electromagnetic calorimetry in the pseudo-rapidity region $2.5 < \eta < 4$. But unlike mid-rapidity, the FMS has no charged hadron tracking to complement it. Therefore, in the forward direction STAR can only reconstruct “EM-jets” from the neutral fragments, mostly photons from π^0 decays. We are investigating the transverse single-spin asymmetry, A_N , for forward EM-jet production in 500 GeV pp collisions that were recorded by STAR in 2011. In last year’s *Progress in Research*, we showed that A_N for EM-jets is a strong function of the number of photons in the jet. Most of the 2-photon EM-jets, and a significant fraction of the 1-photon events, arise from an isolated π^0 . They have large asymmetries, consistent with previous STAR measurements. As the number of photons in the jet increases, A_N is seen to decrease, eventually being consistent with zero for EM-jets that contain 5 or more photons. During this past year, we examined the spin asymmetries when the EM-jets are separated according to whether or not a coincident away-side EM-jet is observed by the mid-rapidity STAR calorimeters. As shown in Fig. 4, the asymmetries for isolated π^0 production are found to be substantially smaller when an away-side mid-rapidity jet is seen [7]. Taken together, these observations raise serious question whether the large transverse spin asymmetries that have

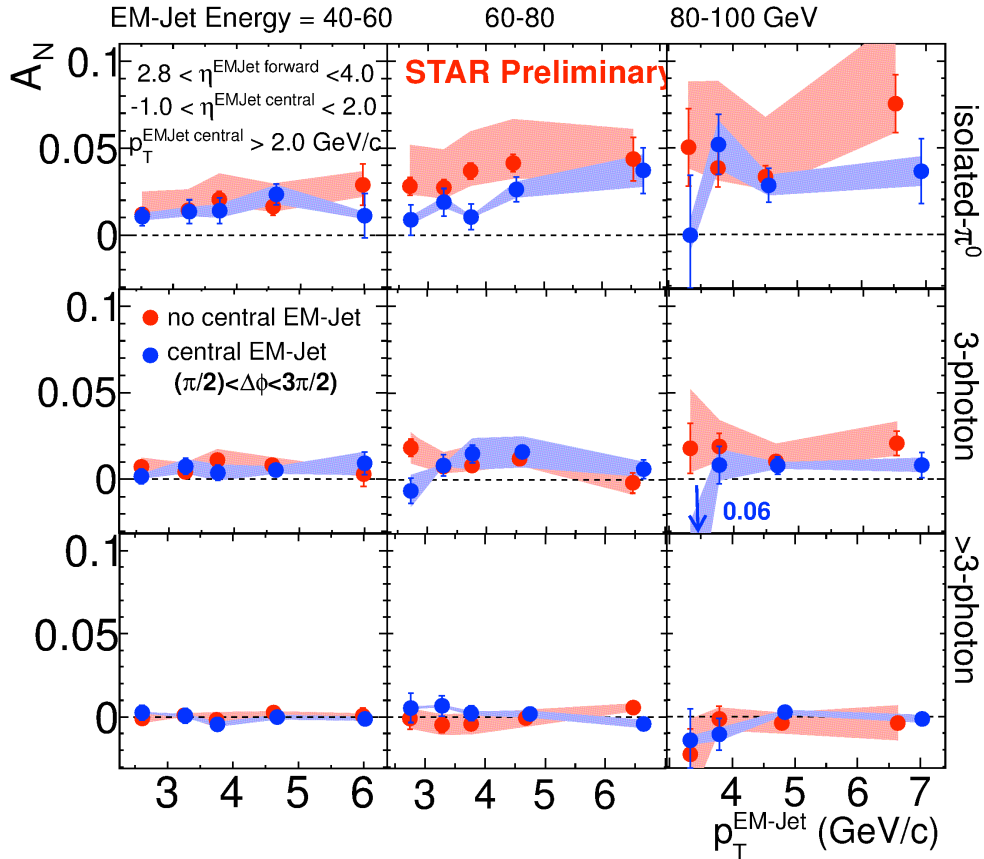


FIG. 4. A_N for forward EM-jet production as a function of energy, p_T , and whether or not a coincident away-side EM-jet is seen at mid-rapidity [7].

been seen for forward inclusive hadron production arise from conventional $2 \rightarrow 2$ parton scattering. At present, we are working on Monte Carlo simulations to finalize the systematic uncertainties for these measurements.

- [1] L. Adamczyk *et al.* (STAR Collaboration), arXiv:1405.5134.
- [2] D. DeFlorian *et al.*, Phys. Rev. Lett. **113**, 012001 (2014).
- [3] E.R. Nocera *et al.* (NNPDF Collaboration), Nucl. Phys. B **887**, 276 (2014).
- [4] Z. Chang, for the STAR Collaboration, invited talk at SPIN 2014.
- [5] J.K. Adkins, for the STAR Collaboration, talk at SPIN 2014.
- [6] E.C. Aschenauer *et al.* (RHIC Spin Collaboration), arXiv:1501.01220.
- [7] M.M. Mondal, for the STAR Collaboration, arXiv:1407.3715.

SECTION II
HEAVY ION REACTIONS

Isospin equilibration in Fermi-energy heavy-ion nuclear collisions

L.W. May, P. Cammarata, L. Heilborn, Z. Kohley, A. McIntosh, M. Youngs,
A. Zarrella, and S.J. Yennello

The nuclear equation-of-state (EoS) has been well studied for symmetric nuclear matter at nuclear saturation densities. However, there are not strong constraints on the density dependence of the symmetry energy at sub-saturation densities. Nucleon transport, which includes isospin drift and diffusion, describes the interaction and movement of nucleons between projectile and target in a nuclear reaction. Isospin diffusion, the transport of nucleons due to differences in isospin content, can be used to further constrain the density dependence of the symmetry energy by examining the degree of isospin equilibration that takes place between projectile and target in nuclear collisions [1,2].

Experimental data was collected for the systems of 35 MeV/nucleon $^{70}\text{Zn}, ^{64}\text{Ni}+^{64}\text{Zn}$ and $^{64}\text{Zn}+^{70}\text{Zn}, ^{64}\text{Ni}$ in order to supplement the 35 MeV/nucleon $^{70}\text{Zn}+^{70}\text{Zn}, ^{64}\text{Zn}+^{64}\text{Zn}$, and $^{64}\text{Ni}+^{64}\text{Ni}$ data collected by Z. Kohley [3]. All experimental data were measured using the NIMROD-ISiS array, briefly described below. With the addition of the previously acquired systems, a complete data set of 7 reaction systems was formed and used to perform the isospin equilibration analysis.

The isoscaling technique scales the yield of individual isotopes from a neutron-rich source relative to the yield of the same isotope from a neutron-poor source. The resulting yield ratios of all isotopes follow the relations seen in Eqs. 1 & 2 where the yield ratio R is exponential with the neutron and proton number of the isotope. The scaling parameters α and β refer to the slope of the fit lines and separation between the fit lines, respectively. The α parameter specifically has been proposed to be linearly dependent on the source asymmetry [2].

$$R_{21}(N, Z) = C \exp(\alpha N + \beta Z) \quad (1)$$

$$R_{21}(N, Z) = Y_2(N, Z) / Y_1(N, Z) \quad (2)$$

Using the fragments from reconstructed quasi-projectiles (QP) [4,5] and by fitting the yields of the most prominent isotopes from $Z=4-8$ (similar to that of Tsang *et al.* in Ref. [2] and shown on the left side of Fig. 1), an α parameter was extracted from the fits. This α value was then used to produce the comparisons seen on the right side of Fig. 1. Here the α value for the fit from the isoscaling of each system relative to the $^{64}\text{Zn}+^{64}\text{Zn}$ (most neutron-poor system) is plotted as a function of the composite system isospin asymmetry. Using the method described by Tsang *et al.* [2] an equilibration value was extracted for the two separate sets of reactions: the $^{70,64}\text{Zn}+^{70,64}\text{Zn}$ reactions and the $^{64}\text{Zn}, \text{Ni}+^{64}\text{Zn}, \text{Ni}$. It was found that the QPs from the $^{70,64}\text{Zn}+^{70,64}\text{Zn}$ set of reaction systems experienced $77\pm 5\%$ equilibration while the QPs from the $^{64}\text{Zn}, \text{Ni}+^{64}\text{Zn}, \text{Ni}$ set of reactions experienced $83\pm 5\%$ equilibration. This compares to a reported equilibration of “about 50%” from the Tsang *et al.* work for 50 MeV/nucleon $^{112,124}\text{Sn}+^{112,124}\text{Sn}$.

While the equilibration seen in this data is higher than that reported by Tsang *et al.* [2] the result is consistent when noting that this work is at a lower beam energy which should experience more equilibration due to longer contact time as shown by Johnston *et al.* [6].

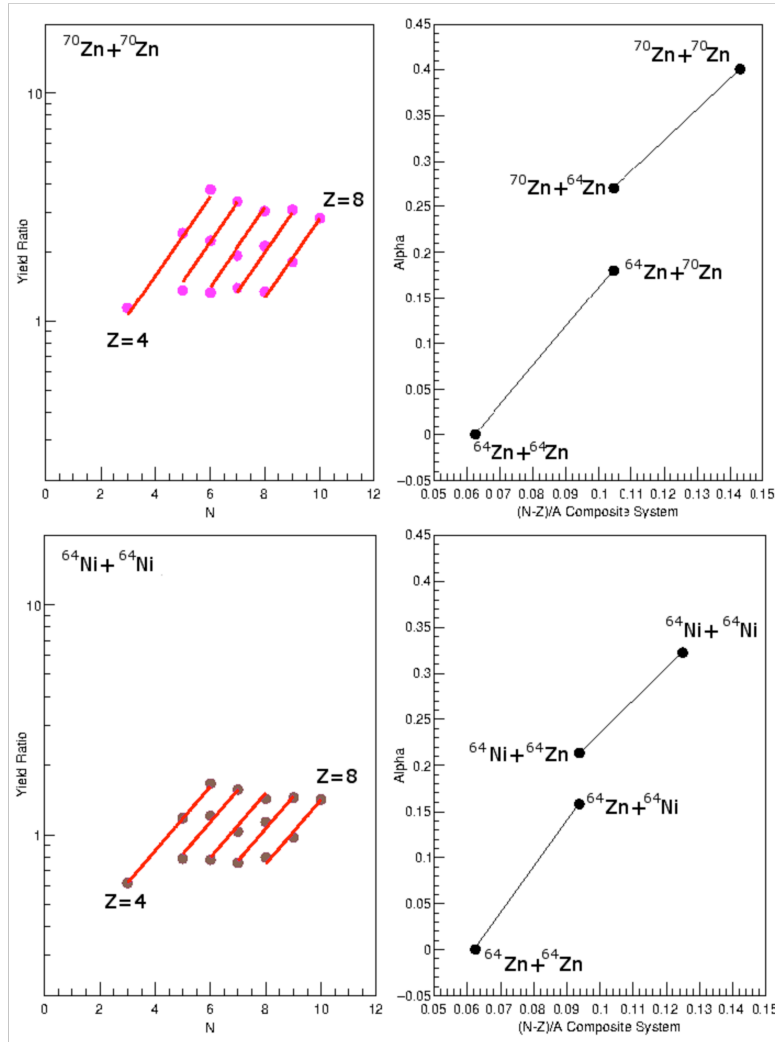


FIG. 1. Top left: Example isoscaling plot for $Z=4-8$ for the $^{70}\text{Zn}+^{70}\text{Zn}$ versus $^{64}\text{Zn}+^{64}\text{Zn}$ reaction systems. Bottom left: Example isoscaling plot for $Z=4-8$ for the $^{64}\text{Ni}+^{64}\text{Ni}$ versus $^{64}\text{Zn}+^{64}\text{Zn}$ reaction systems. Top right: Extracted isoscaling alpha parameter as a function of composite system asymmetry for the $^{70,64}\text{Zn}+^{70,64}\text{Zn}$ reactions. Bottom right: Extracted isoscaling alpha parameter as a function of composite system asymmetry for the $^{64}\text{Zn},^{64}\text{Ni}+^{64}\text{Zn},^{64}\text{Ni}$ reactions.

- [1] A.L. Keksis *et al.* Phys. Rev. C **81**, 054602 (2010).
- [2] M.B. Tsang *et al.* Phys. Rev. Lett. **92**, 062701 (2004).
- [3] Z. Kohley *et al.* Phys. Rev. C **81**, 064601 (2010).
- [4] S. Wuenschel, Ph.D. Thesis, Texas A&M University, 2009.
- [5] L.W. May, Ph.D. Thesis, Texas A&M University 2015.
- [6] H. Johnston *et al.* Phys. Lett. B **371**, 186 (1996).

N/Z transport within a deformed nuclear system

A. Jedele, A.B. McIntosh, L. Heilborn, M. Youngs, A. Zarrella, E. McCleskey,
L.W. May, and S.J. Yennello

Neutron-proton equilibration is sensitive to the asymmetry energy in the nuclear equation of state. The process is governed by the contact time between the colliding nuclei and the gradient of the potential driving the equilibration. Recently, N/Z equilibration within a single dynamically produced and deformed nuclear system has been observed [1-3]. The decaying excited projectile-like fragment (PLF*) has an angular distribution indicative of decay on a timescale shorter than its rotational period. The N/Z composition was observed to depend on the decay angle and thus on the lifetime, consistent with equilibration between regions of the decaying PLF*[4-8]. We present observations that the composition of the heavy fragment changes with decay angle in a consistent manner.

Data from a ^{70}Zn - ^{70}Zn reaction at 35 MeV/nucleon using the NIMROD-ISIS array was analyzed [3]. To focus on N/Z in binary decays, events were selected where two mass identified fragments were detected. The events were sorted based on atomic number followed by mass number, with the heaviest (second heaviest) designated as Z_H (Z_L). In order to ensure the PLF* fragments corresponded to a large fraction of the initial projectile, events were required to have $Z \geq 7$ for Z_H and $Z \geq 3$ for Z_L . A total Z cut of minimum $Z=21$ (70% of beam) and maximum $Z=32$ for all fragments was also included. Fig. 1 shows the Z distribution for the heaviest vs. the second heaviest fragment. The distribution is strongly weighted toward lighter fragments, but extends with significant yield to Z_H and Z_L at near the Z of the beam.

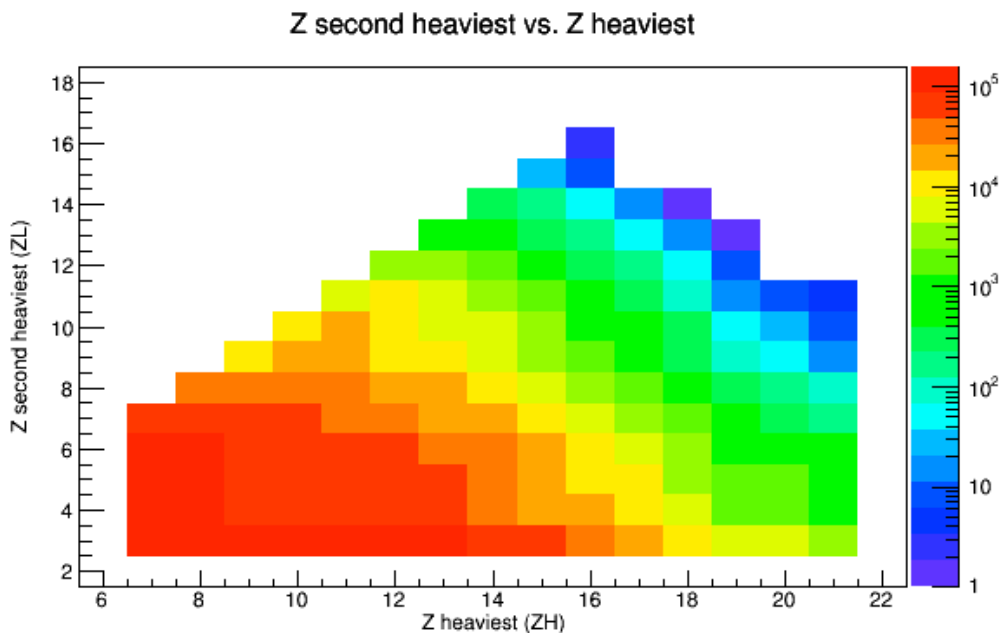


FIG. 1. Z second heaviest vs. Z heaviest distribution.

The decay angle (α) is the angle between the relative velocity (v_{REL}) defined as $v_H - v_L$ and the center-of-mass velocity (v_{CM}) of the two fragments. The angle α was calculated using the formula

$$\alpha = 180 - \cos^{-1}(\vec{v}_{REL} \cdot \vec{v}_{CM} / (\|v_{REL}\| \|v_{CM}\|))$$

Aligned emission of the Z_L in the backward direction (towards the target) corresponds to $\alpha=180^\circ$.

The angular distributions for select pairing of Z_H and Z_L are shown in Fig. 2. A large peak between $160-180^\circ$, seen most clearly in asymmetric pairings, is consistent with previous findings, indicating a timescale of dynamical binary splitting of the PLF* much shorter than its rotational period. For more symmetric splits of the PLF* (i.e. similarly sized Z_H and Z_L), the peak at 180° becomes less pronounced and the peak at 0° becomes more prominent. The width of the peak also

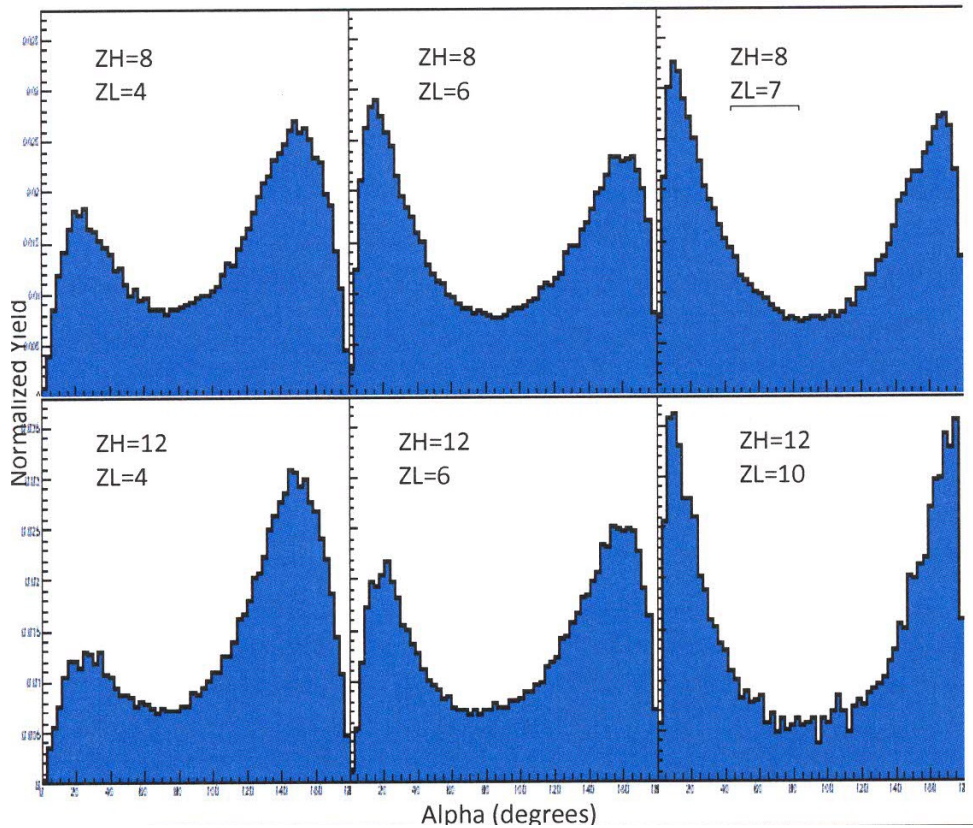


FIG. 2. Angular distributions for select Z_H and Z_L pairing.

narrows indicating stronger alignment, both forward and backward.

Next, the composition of Z_H and Z_L were examined as a function of angle. Fig. 3 depicts a maximum (minimum) $\langle(N-Z)/A\rangle$ at 180° for Z_H (Z_L). As the angle decreases from 180° , indicating a greater contact time, the $\langle(N-Z)/A\rangle$ decreases (increases) for Z_H (Z_L) reaching an

equilibrium value between 20-40°. As the two fragments become more symmetric for constant Z_L , the $\langle(N-Z)/A\rangle$ for Z_H decreases for $\alpha=160-180^\circ$.

Results indicate that when the smaller fragment is emitted in the backward direction (i.e. towards the target, $\alpha=180^\circ$), there is less N/Z equilibration, corresponding to a shorter equilibration time. As α decreases, the N/Z converges towards equilibrium. This effect is strongly dependent on the composition of the second heaviest fragment, although this may be due to greater changes in $\langle(N-Z)/A\rangle$ coming from smaller isotopic range and smaller values for A.

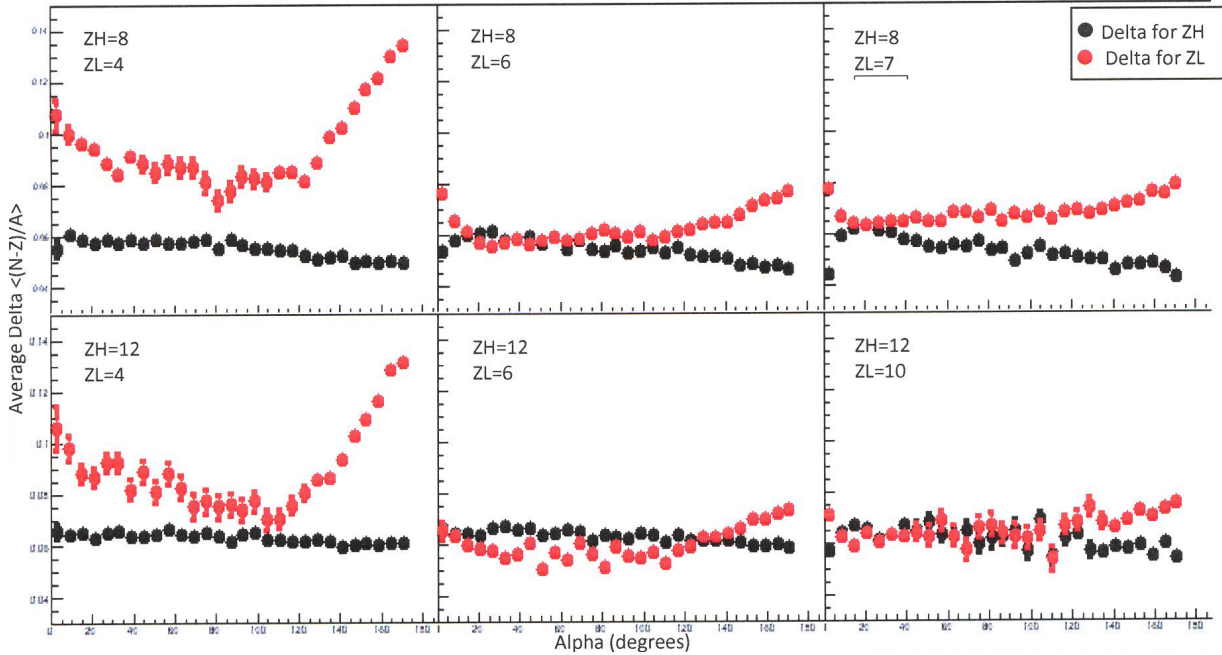


FIG. 3. Average Delta ($\langle(N-Z)/A\rangle$) vs. Alpha. Red points correspond to Delta calculated for the second heaviest fragment (ZL). Black points correspond to Delta calculated for the heaviest fragment (ZH).

Future work will focus on quantifying the effect observed here and determining timescales. The analysis will also be performed on the ^{64}Zn - ^{64}Zn data. Given the good mass resolution and coverage of NIMROD-ISIS, the study of this process using reconstructed PLFs* is an unique opportunity.

- [1] M.B. Tsang *et al.*, Phys. Rev. C **86**, 015803 (2012).
- [2] M.B. Tsang *et al.*, Phys. Rev. Lett. **92**, 062701 (2004).
- [3] Z. Kohley *et al.*, Phys. Rev. C **86**, 044605 (2012).
- [4] A.B. McIntosh *et al.*, Phys. Rev. C **81**, 034603 (2010).
- [5] S. Hudan *et al.*, Phys. Rev. C **86**, 02160 (2012).
- [6] K. Brown *et al.*, Phys. Rev. C **87**, 061601 (2013).
- [7] S. Hudan *et al.*, Eur. Phys. J. A **50**, 36 (2014).
- [8] K. Stiefel *et al.*, Phys. Rev. C **90**, 061605 (2014).

Exploring the limits of the thermodynamic model of heavy-ion collisions with respect to particle ratios

M. Youngs, A.B. McIntosh, L. Heilborn, A. Jede, L.W. May, E. McCleskey,
S.J. Yennello, and A. Zarrella

Many models have been used to predict the shape of particle energy spectra and also to attempt to understand the underlying physics that dictates this shape. The thermodynamic model of heavy-ion collisions as described by das Gupta and Mekjian in Reference [1] predicts the shape of the energy distribution of composite nuclei based on that of protons. To do so they suggest that

$$\frac{d^3 N_A}{d^3 p_A}(p_A) = \exp\left(\frac{\mu_A}{T}\right) g_A \frac{V}{h^3} \exp\left(-\frac{\sqrt{m_A^2 c^4 + p^2 c^2}}{T}\right) \quad (1)$$

where $\mu_A = N\mu_n + Z\mu_p$ for a composite particle A that has N neutrons and Z protons. Here, p_A is the momentum per nucleon of the composite particle, g_A is the spin degeneracy factor of the composite particle, $\mu_{n,p}$ are the chemical potentials for neutrons and protons respectively, V is the volume, and T is the temperature. We would like to investigate the difference in the shape of energy spectra for a given isotope from two different sources under similar conditions. Using Equation (1) we can take the ratio of the energy spectra for a chosen isotope from one reaction system to the energy spectra for the same isotope from a different reaction system. By doing so, we can compare our experimentally determined ratios to the change in chemical potential between the two systems. The reaction systems were chosen to have the same Z (to avoid significant Coulomb differences) and different asymmetries where the asymmetry is defined as $\delta = \frac{N-Z}{A}$. We will refer to the ratio of these energy spectra moving forward as the Isotope Particle Ratio (IPR).

When we investigate the IPR for large systems and at a specific kinetic energy we note that most of the terms cancel out and we are left with

$$\frac{\frac{dN_B}{dE}}{\frac{dN_A}{dE}} = \exp(\Delta\mu/T) \quad (2)$$

where B and A represent the spectra (as a function of center of mass kinetic energy instead of momentum) from two different reaction systems. The resulting $\Delta\mu = N\Delta\mu_n + Z\Delta\mu_p$ implies that the value of this ratio depends only on the neutron and proton content of the emitted isotope as well as the difference in the chemical potentials for neutrons and protons between these two systems.

One of the primary uses of isotope ratios has been isoscaling which is typically performed using integrated particle yields as originally described in Ref. [2]. In most experiments the inability to achieve a large amount of statistics for heavy particles requires the use of integrated yields instead of investigating

the ratio of the spectra. In the thesis experiment performed by Z. Kohley and described in Ref. [3], measurements using the 4π NIMROD array were taken measuring the reaction products from both $^{64}\text{Zn}+^{64}\text{Zn}$ and $^{70}\text{Zn}+^{70}\text{Zn}$ (system *A* and *B* respectively in Eq. (2)) at 35 MeV per nucleon. In this experiment, kinetic energy spectra were measured for a broad range of particle types with isotopic resolution up to $Z=17$ in many detectors with $Z=20$ measured in a select few.

It is important to note that Eq. (1) is intended to use the true differential multiplicity in the calculation and not the measured one. Any losses due to detection efficiency can significantly change the results of the composite spectra. Unfortunately, completing a full efficiency corrected set of data for each isotope would be prohibitive and so to approximate this effect we include only detectors that behaved similarly in both sets of data. This removes the bulk of any differential efficiency that would occur between the two reaction systems. We then construct the kinetic energy spectra per event whereupon taking the ratios of the spectra would cause any efficiency corrections to cancel out to first order.

The primary goal of this analysis is to investigate large composite particles and the different trends these ratios provide. We begin by investigating the isotopes as displayed in Fig. 1 so that each panel represents a different value of $N-Z$. All particles of the given isotope, regardless of detection

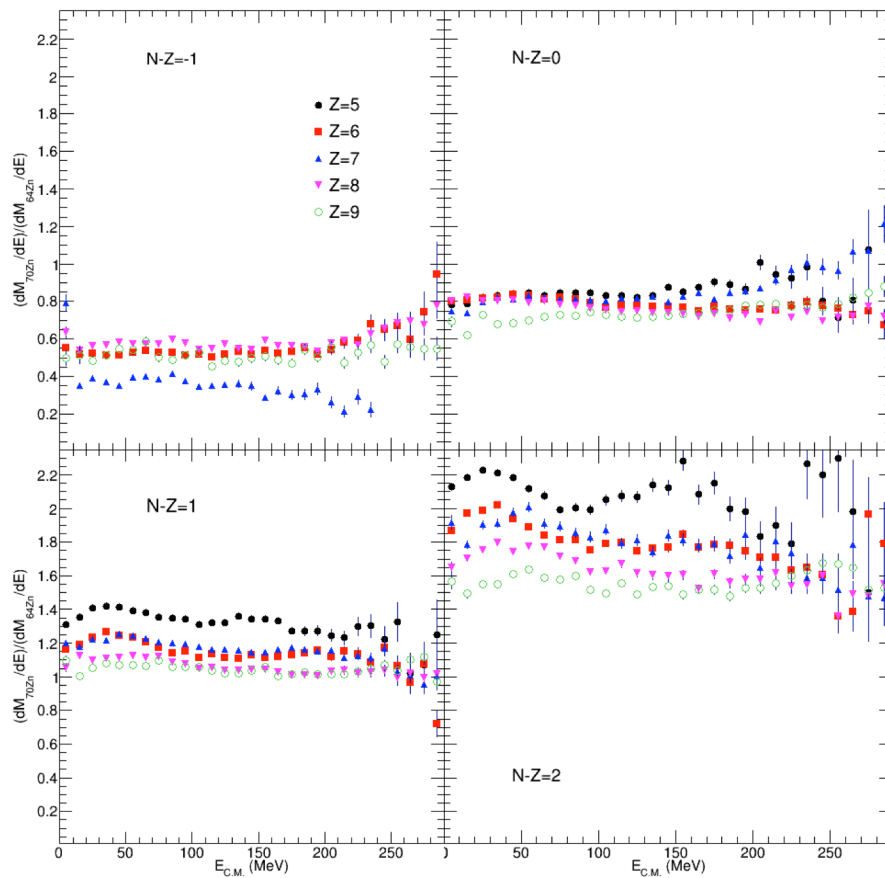


FIG. 1. The IPR for particles with $Z=5$ through $Z=9$. Each panel represents the isotopes that fall into the category $N-Z = -1$ (upper left), 0 (upper right), 1 (lower left) and 2 (lower right). Each plot shows the IPR as a function of center of mass kinetic energy

location or energy, are included in the figure with statistical uncertainties provided as error bars. In the figure, only particles with $4 \leq Z \leq 9$ are provided for demonstration. We omit particles with $Z \leq 4$ due to the expectation that secondary decay is causing an added effect.

Several interesting results of this figure immediately present themselves. As a function of center of mass kinetic energy, the ratio of the spectra for a given fragment is remarkably flat. Assuming that the thermodynamic model is valid, one can understand this by realizing that the average temperature between the two systems is approximately equal. This implies that the ratio in Equation (2) is energy independent.

In addition, as the neutron excess of the isotope increases the value of the ratio also increases. Each class of isotopes (where a class is given by a constant $N-Z$ value) rises together in a consistent manner. This implies that $\Delta\mu_n > 0$, while the value of the ratio of the symmetric isotopes (and proton-like isotopes) suggests $\Delta\mu_p < 0$, and that the magnitude of $\Delta\mu_p$ is greater than that of $\Delta\mu_n$. This result helps to explain an initially unexpected trend primarily visible in the $N-Z=1$ and 2 panels; as Z increases the value of the IPR decreases. This can be explained mathematically based on the results of the sign and magnitude of the chemical potentials. Let X be an isotope with N neutrons and Z protons, with isotope Y having $N+1$ neutrons and $Z+1$ protons so that the value of $N-Z$ remains constant. Simple algebra will show $\Delta\mu_Y < \Delta\mu_X$ implying that the IPR for particle Y would be less than particle X . With a different choice of the two systems this trend may be reversed as the change in chemical potential for protons and neutrons may change, however this trend for the larger values of $N-Z$ is in agreement with the results from the symmetric data.

As mentioned previously, in each panel we see agreement between the different isotopes that have the same value of $N-Z$. This holds quite well with the lone exception of the proton-like ^{13}N . At this time, it is uncertain why this particular isotope behaves in such a way. In order to investigate this trend more, a horizontal line was fit to each isotope and the result was plotted as a function of $N-Z$. In Fig. 2 we can see the fit results for four different groups of Z values over the full range of measured isotopes for that given Z . It appears that within each group of isotopes up through $Z=14$ the fits follow the same general pattern of an exponential increase with the value of $N-Z$ in reasonable agreement with its nearest neighbors. As expected, each group decreases its value relative to the previous set of lower Z values. This trend is seen for all types of isotopes regardless of their $N-Z$ value.

Once the measurements reach approximately $Z=15$, the trend begins to change resulting in the final result presented here. This value of Z represents the value where half of the charge of the beam has been measured in one particle so it is reasonable to assume that the mechanisms that create these isotopes are no longer governed by the chemical potential in the same way that the lighter isotopes are. While $Z=15$ and 16 seem to follow the same general trend that the lighter isotopes do, their values and separation are significantly different. In the $Z=17-20$ region, the pattern changes significantly not only in values of the fits, but also shape. This implies that the limit where the mechanics of the thermodynamic model break down is around half of the charge or mass of the beam. The most reasonable physical explanation is that the large particles most likely represent residues of the emitting source instead of the particles being emitted from the source.

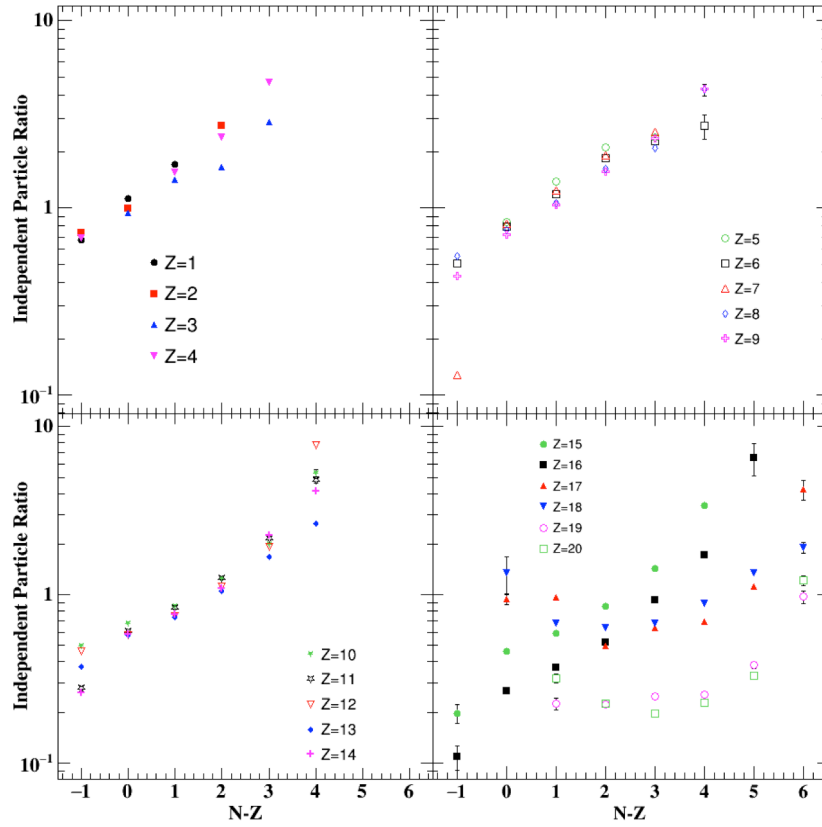


FIG. 2. The fit value for a horizontal line for each isotope from the ratio of spectra. The data is split into four groups where the first three groups (top row and lower left) show agreement within a panel while the lower right panel ($15 \leq Z \leq 20$) shows what appears to be a limit where this agreement breaks down.

- [1] S. Das Gupta and A.Z. Mekjian, Phys. Rep. **72**, 131 (1981).
- [2] M.B. Tsang *et al.*, Phys. Rev. Lett. **86**, 5023 (2001).
- [3] Z. Kohley, Ph.D. Thesis, Texas A&M University, 2010.

Incomplete fusion reactions measured with the QTS

A.B. McIntosh, L. Heilborn, M. Youngs, L.A. Bakhtiari, M. Chapman, A. Jedele, L.W. May,
E. McCleskey, A. Zarrella, and S.J. Yennello

The first observation of the asymmetry dependence of the caloric curve was recently reported [1-3]. This asymmetry dependence can be verified with improved statistical and systematic uncertainties with a new incomplete fusion experiment. By measuring heavy residues produced in fusion reactions and the coincident light charged particles temperatures and excitation energies can be obtained for excited compound nuclei without reliance on a measurement of the free neutrons.

A short measurement of $^{86}\text{Kr} + \text{C}$ at 35 MeV/nucleon was performed to validate our understanding of experimental setup and to provide insight into the reaction mechanisms at work. Light charged particles were measured (dE, E) in FAUSTUPS with $1.6^\circ < \theta < 45^\circ$ and heavy residues were measured (TOF, dE, E) with the Quadrupole Triplet Spectrometer with $0.9^\circ < \theta < 2.3^\circ$. For energies at and below the Fermi energy, fusion reactions constitute a significant part of the nuclear cross section. Complete fusion however is only significant at much lower energies; incomplete fusion, a.k.a. massive transfer, dominates above 10 MeV/nucleon [4].

In order measure a nuclear caloric curve, the excitation energy must be known. In incomplete fusion reactions of $\text{Kr} + \text{C}$, the excitation energy of the compound nucleus depends to first order on the fraction of the carbon that fuses with the krypton. This fraction also determines the velocity of the compound nucleus to first order. If evaporative cooling of the hot nucleus is isotropic, the average residue velocity for a cohort of events then indicates the average excitation energy.

Measured velocity distributions of heavy residues produced in reactions of $^{86}\text{Kr} + \text{C}$ @ 35 MeV/nucleon are shown in Fig. 1. These velocities have been corrected for energy loss in all detectors and in the target. The correction is on the order of 5% or less. Each panel represents a different tune of the Quadrupole Triplet Spectrometer (QTS), used to focus a broad but finite range of reaction products across a $\sim 5.5\text{m}$ flight path. The bottom panel corresponds to the rigidity of the beam, and each other panel to a subsequently lower rigidity. The vertical axis shows the measured counts per minute, which allows immediate comparison of the yield from the five different rigidities. Heavy incomplete fusion residues are dominant around 84% of the rigidity of the beam. In Fig. 1, the upper dashed line indicates beam velocity, and the lower dashed line indicates the velocity a completely fused $^{86}\text{Kr} + 12\text{C}$ system would have. As the rigidity of the beam decreases from 100%, the velocity centroid initially drops. Around 84%, the centroid finds a peak about two-thirds from v_{beam} to v_{CF} , and remains there as the rigidity continues to drop. This suggests that more than eight nucleons of the twelve in the carbon target are rarely picked up in fusion with the krypton. This ratio of two thirds hints that alpha cluster structure of the carbon may be relevant in this process.

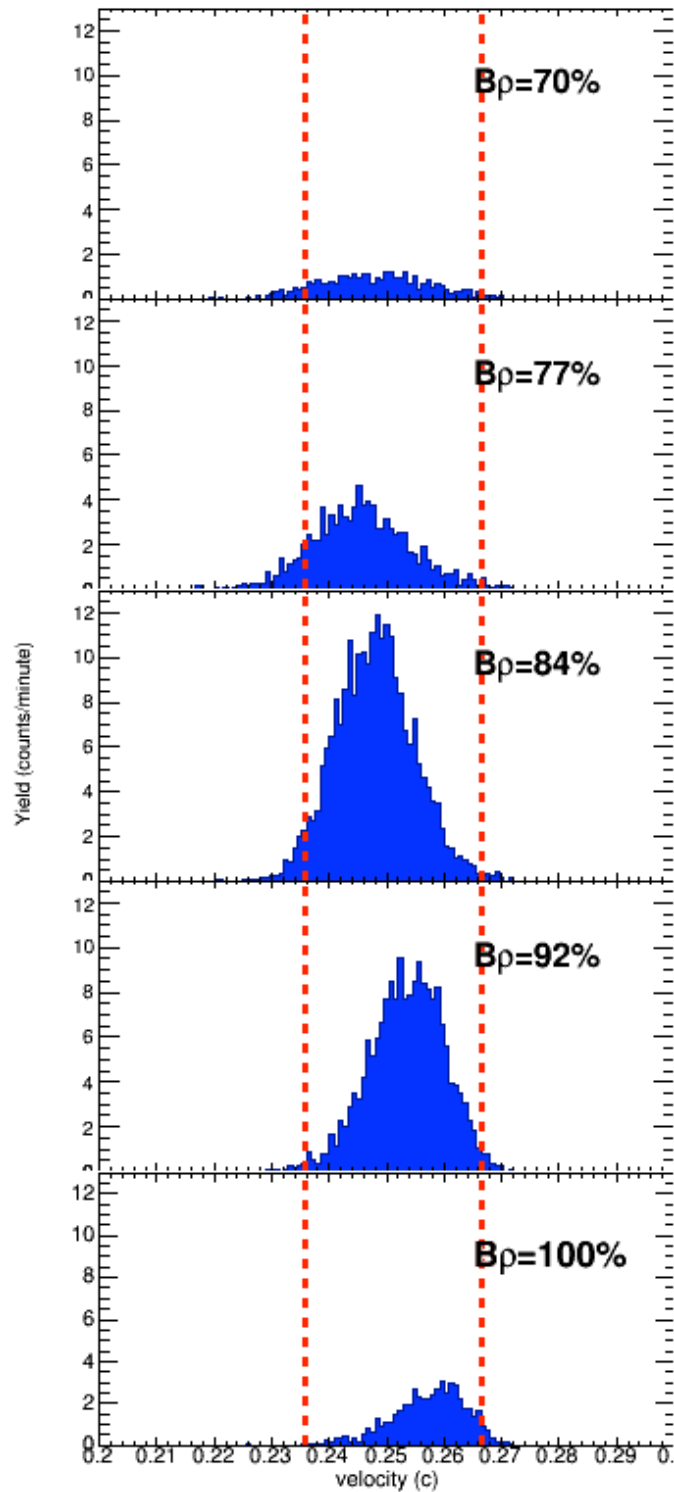


FIG. 1. Velocity distributions measured by time-of-flight. The upper dashed line represents the beam velocity and the lower dashed line corresponds to the velocity of a completely fused $^{86}\text{Kr} + ^{12}\text{C} = ^{98}\text{Mo}$ compound nucleus. The tune of the triplet selects residues with different magnetic rigidities and thus different velocities.

The width of the velocity distributions shown in Fig. 1 arises first from the number of nucleons picked up from the target. However, once the rigidity of the QTS is low enough that the mean is no longer changing, we are selecting only the fusion events with a single value of the momentum transfer; higher momentum transfer is not produced with appreciable yield at this beam energy. Therefore in this regime, variation in the number of nucleons picked up from the target is not a major cause of the width of the velocity distribution. Second, evaporative particle emission from the compound nucleus causes the heavy residue to recoil, causing significant broadening of the velocity distribution. Neither of these effects precludes the use of the centroid as a measure of the excitation energy. However, it is possible that the fraction of the target that did not fuse will have some energy imparted to it, either internal or translational. This effect would cause a systematic error in the calculation of the excitation of the compound nucleus. However, there is precedent for using the average velocity without correction for energy imparted to the un-fused “pre-equilibrium” nucleons [4, 5, 6].

To determine how a different velocity of the pre-equilibrium nucleons will affect the excitation energy, we can utilize the analytical formula of Bohne [Boh90]. The compound nucleus will be at very small angle, and all of the krypton projectile remains in the compound nucleus. Since we are interested not in an absolute value right now but in how a different velocity of pre-equilibrium nucleons will affect the excitation energy. Taking the extreme limit that maximizes the difference of $\cos\theta_{TV_P-V_T}$, there is a 9% difference in the excitation energy if the pre-equilibrium nucleons remain at rest or are boosted to half the residue velocity. Light charged particles boosted to just under this velocity or greater would be measurable, allowing us to constrain this error at the 9% level.

However, it should be considered that the amount of energy imparted to the pre-equilibrium nucleons should not be significantly different between reactions of $^{86}\text{Kr} + ^{12}\text{C}$ and reactions of $^{78}\text{Kr} + ^{12}\text{C}$. Since the goal is to examine relative trends in the caloric curve for systems with different neutron content, an identical shift in the excitation energy of both curves would represent a completely correlated error and thus have no effect on the differences extracted.

- [1] A.B. McIntosh *et al.*, Phys. Rev. C **87**, 034617 (2013).
- [2] A.B. McIntosh *et al.*, Eur. Phys. J. A **50**, 35 (2014).
- [3] A.B. McIntosh *et al.*, *Progress in Research*, Cyclotron Institute, Texas A&M University (2014-2015), p. IV-62.
- [4] H. Morgenstern *et al.*, Phys. Lett. **113B**, 463 (1982).
- [5] H. Nifnecker *et al.*, Nucl. Phys. **A447**, 533 (1986).
- [6] K. Hagel, Ph.D. Thesis, Texas A&M University, 1989.

Constraining supernova equations of state

M. Hempel,¹ K. Hagel, J.B. Natowitz, G. Roepke,² and S. Typel³

¹*Department of Physics, University of Basel, 4056 Basel, Switzerland*

²*University of Rostock, FB Physik, Rostock, Germany*

³*GSI Helmholtzzentrum für Schwerionenforschung GmbH, D-64291 Darmstadt, Germany*

Cluster formation is a fundamental aspect of the equation of state (EOS) of warm nuclear matter such as can be found in supernovae (SNe). Similar matter, with properties comparable to that found in the neutrinosphere region of a supernova, can be studied in heavy-ion collisions (HIC). We have used the experimental data of Qin *et al.*[1] to test calculations of cluster formation and the role of in-medium modifications of cluster properties in SN EOSs. For the comparison between theory and experiment we use chemical equilibrium constants as the main observables. This reduces some of the systematic uncertainties and allows deviations from ideal gas behavior to be identified clearly. In the analysis, we carefully account for the differences between matter in SNe and HICs. At the lowest densities, the experimental data and all

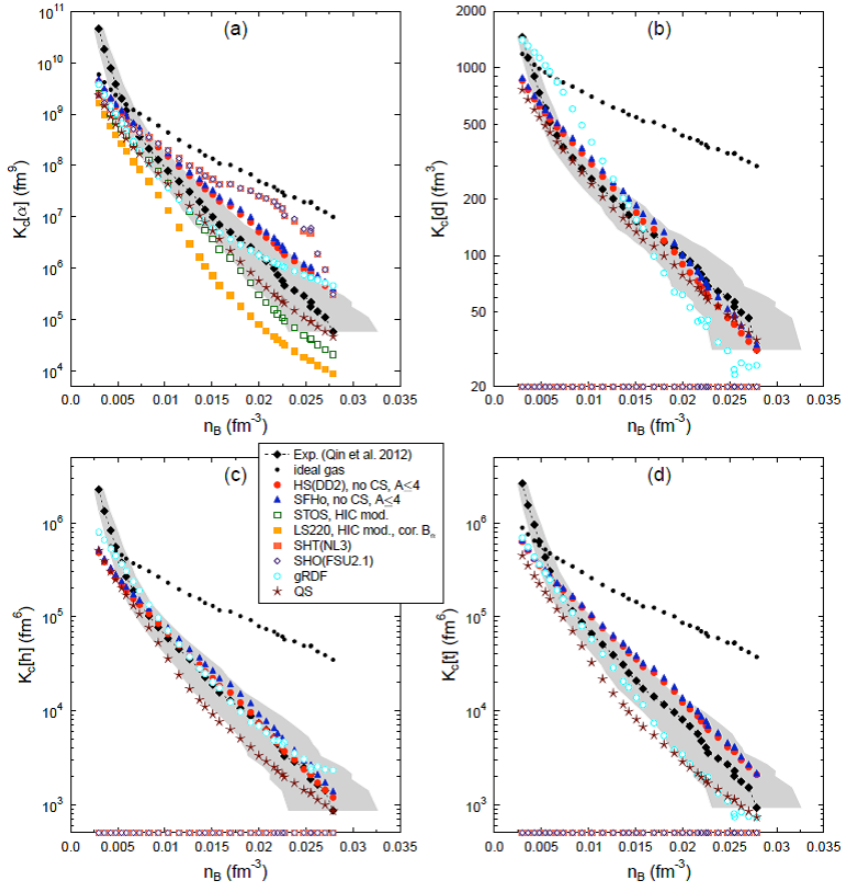


FIG. 1. Equilibrium constants vs density. ECs for (a) α particles, (b) deuterons, (c) helions, and (d) tritons from the experiments (black diamonds) are compared with those from various theoretical models, which are all adapted for the conditions in HIC, as far as possible. The ECs of nuclei which are not included in a specific model are put on the x axis.

theoretical models are consistent with ideal gas behavior. See Fig. 1.

Equilibrium constants should only be independent of composition, density, and asymmetry for ideal Maxwell-Boltzmann gases without interactions. In that case they are only a function of temperature. Fig. 2 presents the equilibrium constants as a function of temperature. As soon as interactions and/or Fermi-Dirac or Bose-Einstein statistics are included, a dependence on composition and density arises. Deviations of ECs from the ideal values measure the strength of interactions. Thus ECs represent very useful and instructive quantities. Furthermore, some of the systematic uncertainties are reduced when one uses ECs instead of particle yields or mass fractions. ECs will depend on the asymmetry of the system, or, equivalently, the total proton fraction $Y_{\text{Tot p}}$. Therefore we chose $Y_{\text{Tot p}} = 0.41$, as determined in the experiments, for all theoretical calculations.

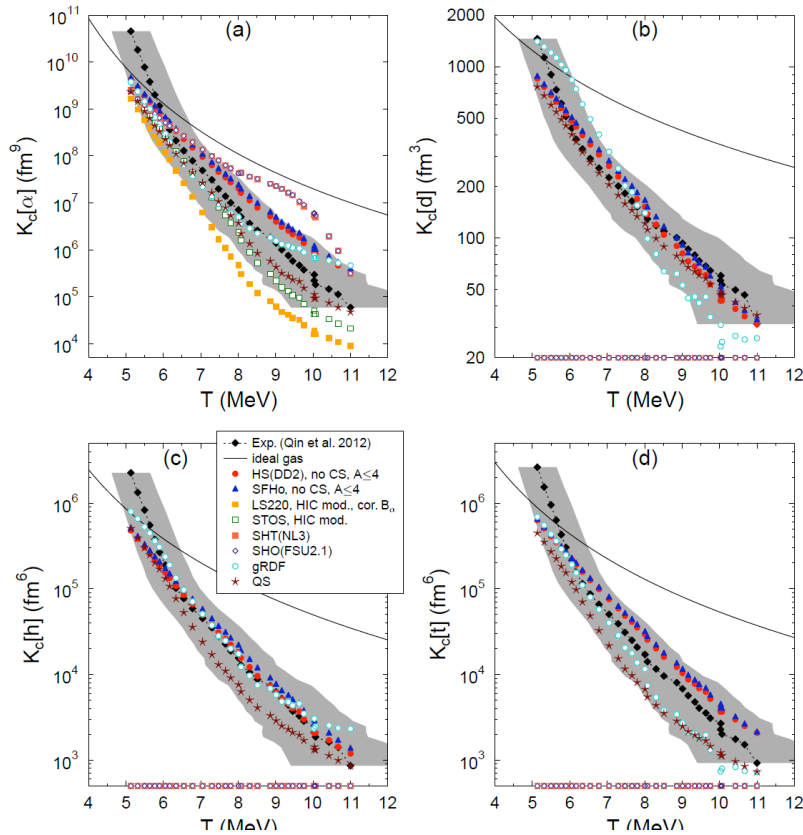


FIG. 2. Equilibrium constants vs temperature. This figure shows the main results of our investigation: EC for (a) alpha particles, (b) deuterons, (c) helions, and (d) tritons as a function of temperature. The grey band represents the experimental uncertainty for the temperature determinations. Experimental data (black diamonds) is compared with various different theoretical models, which are all adapted for the conditions in HIC, as far as possible. The ECs of nuclei which are not included in a model are put on the x-axis. The black lines show the ECs of the ideal gas model, which are solely a function of temperature.

Four of the models which we considered (QS, gRDF, HS(DD2), SFHo) are fully compatible with the experimental data, or show at least only minor deviations from the experiment. We conclude that at the densities and temperatures discussed mean-field interactions of nucleons, inclusion of all relevant light clusters, and a suppression mechanism of clusters at high densities have to be incorporated in the SN EOS. From the comparison with the models that fail to explain the full experimental data set, we can identify the following three ingredients that seem to be necessary for the description of clusterized nuclear matter at the densities and temperatures of interest: (i) consideration of all relevant particle degrees of freedom, (ii) mean-field effects of the unbound nucleons, and (iii) a suppression mechanism for bound clusters at high densities.

[1] L.-J. Qin *et al.*, Phys. Rev. Lett. **108**, 172701 (2012).

Exploring clusterization in $^{28}\text{Si}+^{12}\text{C}$ collisions at 35MeV/u with the NIMROD-ISiS array

X.G. Cao, K. Schmidt, E.-J. Kim, K. Hagel, M. Barbui, S. Wuenschel, J.B. Natowitz, H. Zheng, N. Blando, A. Bonasera, G. Giuliani, M. Rodrigues, R. Wada, M. Huang, C. Botosso, G. Liu, G. Viesti, S. Moretto, G. Prete, S. Pesente, D. Fabris, Y. El Masri, T. Keutgen, S. Kowalski, Z. Kohley, and A. Kumar

Clustering is one of the most fundamental physics aspects, competing with mean field, in light nuclei. In particular, α clusters play more important roles in self-conjugate light nuclei near the α decay threshold because of the high binding energy compared with its neighbors and the strong α - α repulsive interaction. Theoretical study predicted that the self-organizing of α cluster is favored over deuteron below a critical density with moderate temperature [1], where the possible Bose-Einstein condensation (BEC) is expected to occur. Some excited states in ^{12}C and ^{16}O can be reasonably described by condensate type wave functions [2]. The nucleus itself consists of protons and neutrons, both spin up and spin down. Condensation of quartets with four different fermions is still an open question in cold atom physics though manipulating three different fermions has recently succeeded [3].

Specific alpha configurations among the ground and excited states of ^{12}C , ^{16}O , ^{20}Ne , such as triangular, linear-chain, tetrahedral and bent configurations, are predicted by the state-of-the-art nuclear theoretical approaches such as chiral nuclear effective field theory [4], algebraic model [5], orthogonality condition model [6], time-dependent Hartree-Fock theory [7], fermionic molecular dynamics [8], antisymmetrized molecular dynamics [9] and energy-density functionals [10] etc..

However the experimental information about the α states at low density is scarce. It is natural to pursue experiments with α conjugate beams and advanced detection apparatus to explore the collective dynamics of α clustered systems at low density, whether the BEC of quartets exists in the nuclear diagram and how the different α configurations such as the possible toroidal and linear chain configurations made out of α clusters, also recently predicted by very recent calculations, appear [11,12].

The experiments were carried out at the end of 2008 and 2009 with ^{40}Ca and ^{28}Si beams at 10, 25, 35 MeV/u incident on ^{28}Si , ^{12}C , ^{40}Ca and ^{180}Ta targets [13,14]. The combinations of different α conjugate projectiles (^{28}Si and ^{40}Ca) and targets (^{12}C , ^{28}Si and ^{40}Ca) favor the population of α different cluster states and the ^{180}Ta target allows us to study the projectile excitation and decay more clearly. Systematically comparisons of different projectile-target combinations, such as $^{40}\text{Ca} + ^{40}\text{Ca}$, $^{40}\text{Ca} + ^{28}\text{Si}$, $^{28}\text{Si} + ^{40}\text{Ca}$ and $^{28}\text{Si} + ^{12}\text{C}$, will provide insight to unambiguously identify the α emission source and multiple checks to remove the system dependence. The preliminary analysis of raw data was accomplished by C. Botosso [14] and K. Schmidt et al. [13]. K. Schmidt et al. have analyzed the clusterization aspects of $^{40}\text{Ca} + ^{40}\text{Ca}$ in detail [15,16,17]. It is found that there is a strong neck-like emission, which consists mainly of α -like fragments. These α -like fragments also obey the "hierarchy effect" observed in ref [18]. The enhanced emission of α -like fragments from the neck-like region is absent in the systems with the

Ta target [17]. The characteristic of the α emission source is further explored by the multi-particle correlation and quantum fluctuation approach etc..

The $^{28}\text{Si}+^{12}\text{C}$ system at 35MeV/u is analyzed to look for the possible high-spin toroidal isomers made out of α clusters formed in semi-peripheral collisions. Meanwhile this lighter system allows us to check and understand the phenomena, such as quantum fluctuations and correlations found in $^{40}\text{Ca}+^{40}\text{Ca}$ system. Firstly, we calculate the multiplicity of “ α -like fragments” and the total mass of those fragments for each event, which are defined as following.

$$\alpha\text{-like mult} = \alpha \text{ mult} + {}^{12}\text{C} \text{ mult} + {}^{16}\text{O} \text{ mult} + \dots + {}^{28}\text{Si}$$

$$\alpha\text{-like mass} = 4(\alpha \text{ mult}) + 12({}^{12}\text{C} \text{ mult}) + 16({}^{16}\text{O} \text{ mult}) + \dots + 28({}^{28}\text{Si} \text{ mult})$$

We can also define similar observables for “d-like fragments”. Another useful global observable B_j is defined as following,

$$B_j = \frac{1}{M} \sum_{i=1}^M \frac{(-1)^{Z_i} + (-1)^{N_i}}{2},$$

which characterizes events according to the even-odd character of fragments in exit channel and it ranges from -1 to +1. In our case, negative B_j means there is more d-like fragments while positive B_j shows there is more α -like fragments.

Fig. 1 shows the observables defined above for $^{28}\text{Si}+^{12}\text{C}$ at 35MeV/u. We can see there are some abnormal events with mass number larger than 40. This comes from the pileup events,

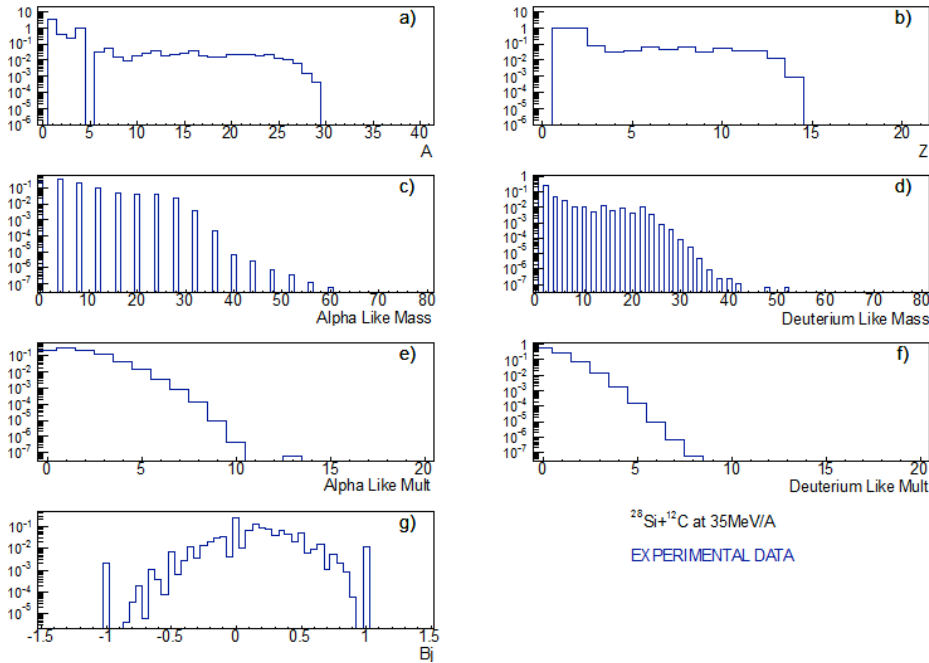


FIG. 1. A, Z, α -like mass, d-like mass, α -like multiplicity, d-like multiplicity, B_j distributions of $^{28}\text{Si}+^{12}\text{C}$ at 35MV/u.

where two reactions occur within the same beam burst and can not be distinguished by DAQ gate. This contamination is very harmful for our physics goal since the events we are interested in are very rare in the whole recorded event set. We found the pileup events are more than 1% just considering total mass number cut. The pileup is a direct result of thick C target (967 mg/cm^2) and high beam intensity ($\sim 2.23 \times 10^8 / \text{s}$).

A significant probability to break up into predominantly α -like masses is observed in Fig. 2. This is the result of strong entrance channel effect of α conjugate projectile and target. The events with α -like mass equals 28 in exit channel occupy about 2% of the total recorded events.

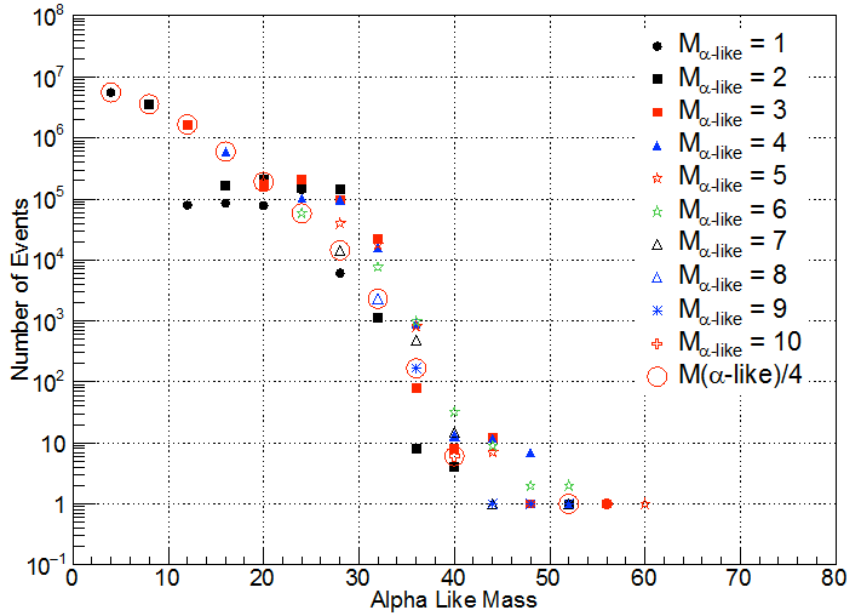


FIG. 2. α -like mass distribution for fixed α -like multiplicities. The open circles indicate that the total detected α -like mass consists of only α particles.

The proportion of various channels in the α -like = 28 cut is plotted in Fig. 3. We can see the breakup channel with one or several α and one remaining heavier fragment has higher cross section compared with the two heavy fragment channel. The seven α breakup channel has a significant proportion, which may originate from possible exotic toroidal configurations or BEC.

The further analysis of α emission source in early stage of collision by correlation and fluctuation approaches will be very interesting. However, the pileup events must be rejected as cleanly as possible considering the rarity of α -like decay events. The mass, charge and total energy conservation are obvious necessary conditions needed to be fulfilled to reject the pileup events. The momentum conservation is hard to apply since we do not detect all the fragments in exit channel

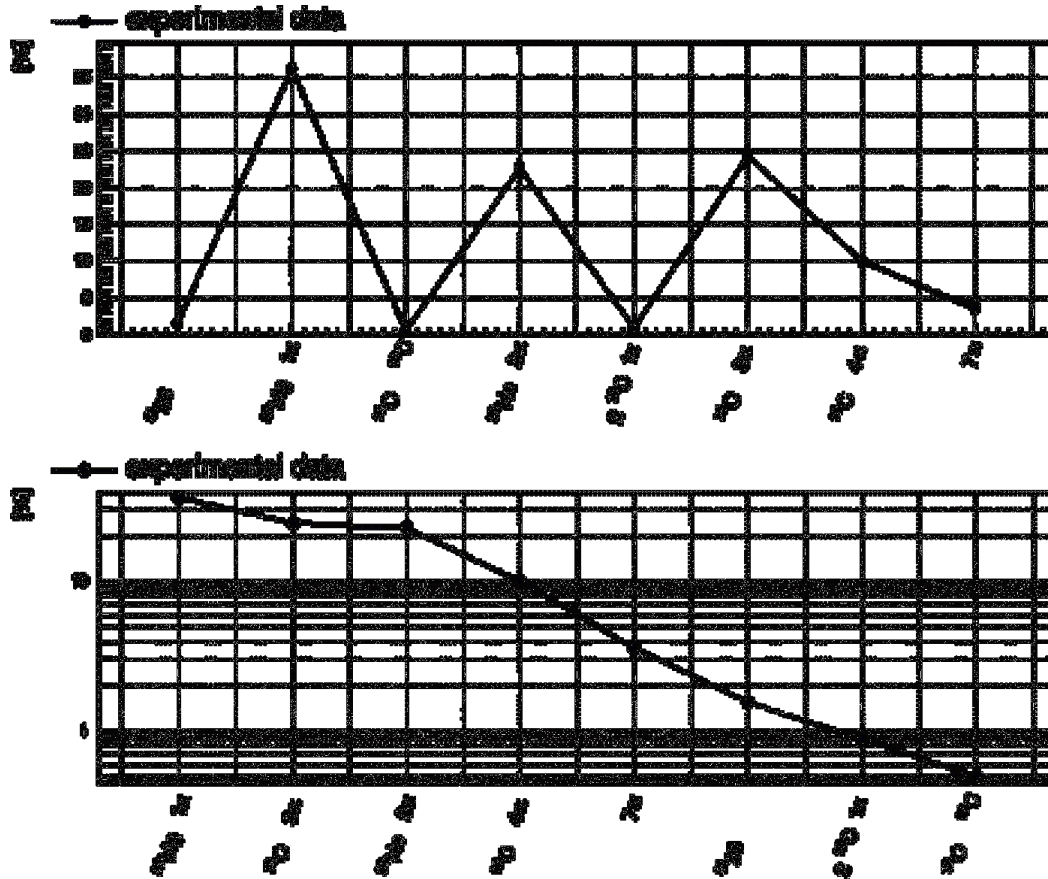


FIG. 3. The proportion of different channels for the α -like = 28 cut. The upper panel is sorted according to the cluster decay threshold in the Ikeda diagram and the lower panel is sorted according to the channel proportion from high to low.

For rare breakup channels such as 7α , more contamination can come from pileup events. Therefore, a reliable assessment of contamination is needed. We are looking for sensitive observables for the pileup events when the time stamp of recorded event is absent in DAQ. The neutron multiplicity, variance velocity, polar distribution, excitation energy and Dalitz plots all do not show distinct differences when applying the total mass, charge and energy conservation cuts. The sensitive observable must be summation quantities based on event by event basis or correlation quantities depicting the characteristic of α -like emission source. The pileup problem must be overcome before moving forward to next step. An analysis of an AMD simulation employing the NIMROD detector filter and artificially mixing two events may provide valuable insight to allow rejection of the pileup events. It is underway.

- [1] G. Roepke *et al.*, Phys. Rev. Lett. **80**, 3177 (1998).
- [2] T. Suhara, Y. Funaki, B. Zhou *et al.*, Phys. Rev. Letts. **112**, 062501 (2014).
- [3] A.N. Wenz, T. Lompe, T.B. Ottenstein, F. Serwane *et al.*, Phys. Rev. A **80**, 040702(R) (2009).
- [4] E. Epelbaum, H. Krebs, A. Lähde Timo *et al.*, Phys. Rev. Letts. **112**, 102501 (2014).

- [5] R. Bijker and F. Iachello, Phys. Rev. Lett. **112**, 152501 (2014).
- [6] T. Yamada, Y. Funaki, T. Myo *et al.*, Phys. Rev. C **85**, 034315 (2012).
- [7] A.S. Umar, J.A. Maruhn, N. Itagaki, and V.E. Oberacker, Phys. Rev. Lett. **104**, 212503 (2010).
- [8] M. Chernykh, H. Feldmeier, T. Neff *et al.*, Phys. Rev. Lett. **98**, 032501 (2007).
- [9] Y. Kanada-Eñyo, M. Kimura, and A. Ono, Prog. Theor. Exp. Phys., 01A202 (2012).
- [10] J.P. Ebran, E. Khan, T. Niksic *et al.*, Nature **487**, 341 (2012).
- [11] Andrzej Staszczak and Cheuk-Yin Wong, Phys. Lett. B **738**, 401 (2014).
- [12] Yoritaka Iwata, Takatoshi Ichikawa *et al.*, arXiv:1409.8012
- [13] K. Schmidt *et al.*, *Progress in Research*, Cyclotron Institute, Texas A&M University (2010-2011), p. II-8.
- [14] C. Bottosso *et al.*, *Progress in Research*, Cyclotron Institute, Texas A&M University (2008-2009), p. II-7
- [15] K. Schmidt *et al.*, *Progress in Research*, Cyclotron Institute, Texas A&M University (2011-2012), p. II-7.
- [16] K. Schmidt *et al.*, *Progress in Research*, Cyclotron Institute, Texas A&M University (2012-2013), p. II-17.
- [17] K. Schmidt *et al.*, *Progress in Research*, Cyclotron Institute, Texas A&M University (2013-2014), p. II-18.
- [18] J. Colin *et al.*, Phys. Rev. C **67**, 064603 (2003).

The clusterization of alpha-conjugate nuclei

K. Hagel, K. Schmidt, S. Wuenschel, E.J. Kim, M. Barbui, J.B. Natowitz, H. Zheng, N. Blando, A. Bonasera, G. Giuliani, M. Rodrigues, R. Wada, M. Huang, C. Botosso, G. Liu, G. Viesti, S. Moretto, G. Prete, S. Pesente, D. Fabris, Y. El Masri, T. Keutgen, S. Kowalski, Z. Kohley, and A. Kumar

We have discussed the analysis of an experiment probing the clusterization of alpha conjugate nuclei in several previous reports [1,2,3]. To recount, data on a number of systems that are composed of alpha conjugate nuclei was collected using the NIMROD-ISiS multidetector array. One experiment was performed using Ca beams of 35, 25 and 10 MeV/u and the other with Si beams at 35 and 15 MeV/u. Data was collected with each of the beams using Ca, Si, C and Ta targets.

The previous report [3] showed results of an analysis of emission patterns for the various decay channels that lead to an alpha-like mass of 40 for all of the systems that were studied with the 35 MeV/u Ca beams and an alpha-like mass of 28 for all of the systems that were studied using the 35 MeV/u Si beams. The emission patterns indicate a neck like origin of the alpha in the reactions where the complete system is composed of alpha-like nuclei. This behavior appears to be inconsistent with statistical behavior. Indeed, recent studies [4] at higher energies have shown various behaviors associated with the breakup of alpha cluster nuclei to have a non-statistical origin.

In order to explore this possible non statistical behavior, we have performed statistical model calculations. These model calculations can indicate whether the observed behavior results from reaction mechanisms having a non statistical origin or whether a simple statistical explanation that includes detector biases might explain the observation.

The procedure used in [3] was to reconstruct the decaying source and plot the velocity spectra of the decaying products in the frame of the decaying source. The extension that we discuss in this work is similar in that the decaying source is reconstructed. The properties (mass, charge, excitation energy) of the reconstructed source are then used as input into the statistical model, GEMINI [5] on an even by event basis. The decays from GEMINI are performed event by event and are filtered through the experimental acceptance. The reaction products passing the filter are then analyzed in the same way as the experimental data.

Fig. 1 shows invariant velocity plots of the products that originate from events selected to have a total detected alpha-like mass of 40 for the systems with Ca beams and a total detected alpha-like mass of 28 for the systems with Si beams. We show the emission patterns for the various decay channels that lead to an alpha-like mass of 40 (28) for all of the systems with the Ca (Si) beam that were studied. The left side of the frame of each system shows the velocity distributions of the heavier alpha like fragments and the right side shows the velocity distributions of the alpha particles associated with those heavier fragments. The vertical lines indicate the location $v_z=0$ which is the frame of the reconstructed decaying system. In contrast to the experimental data [3], this distribution shows a symmetric pattern of the alpha particle emission

relative to the rest frame of the emitting source. The emission pattern of the heavy partner also forms an oval around the rest frame of the emitting source as is expected from statistical behavior.

GEMINI

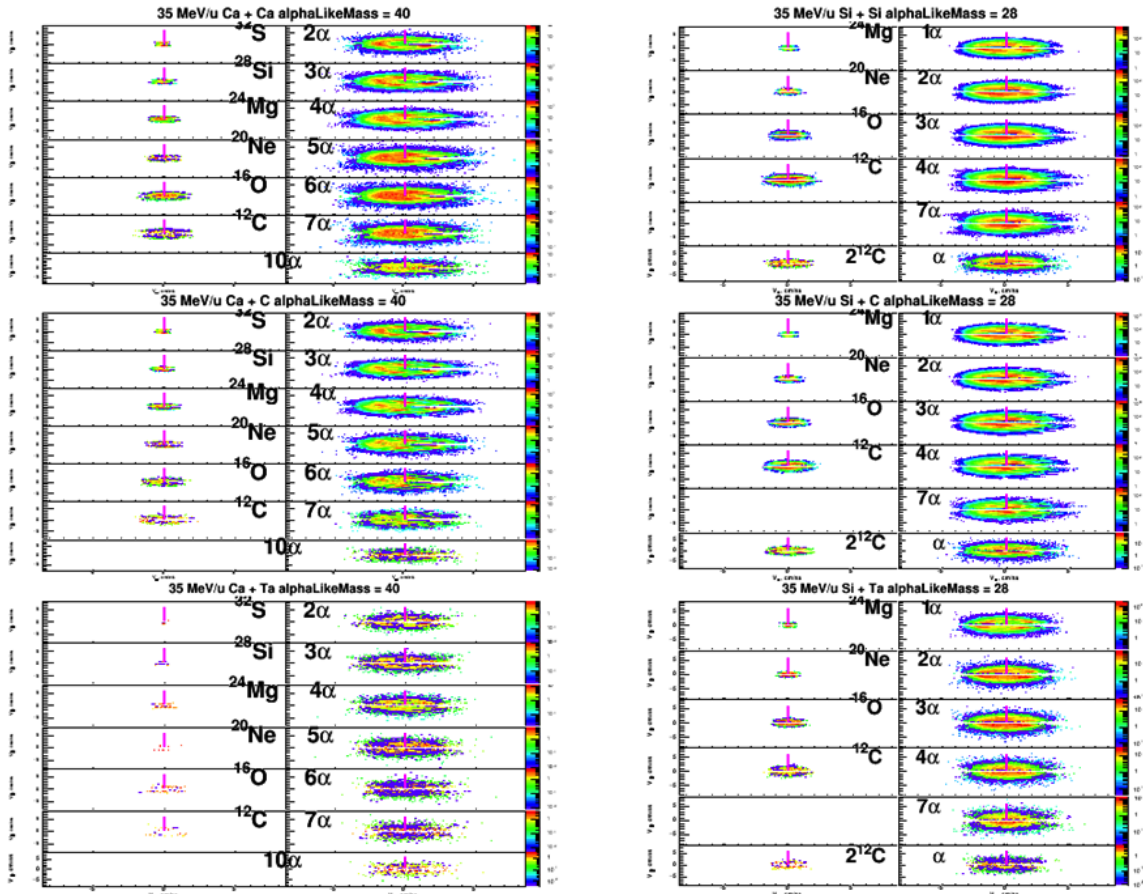


FIG. 1. Invariant velocity distributions of products predicted by GEMINI resulting from the various decay channels of a decaying source reconstructed in events having a detected alpha like mass of 40 for reactions with Ca beams and an alpha-like mass of 28 for the reactions with Si beams. The vertical lines indicate $v_z=0$, the frame of the reconstructed source.

The emission patterns resulting from the model calculations and filtered through the experimental acceptance produce symmetric distributions, ie rings around the emitting source as expected from statistical decay, indicates that the observed behavior in the experimental data [3] is not the result of detector bias. As mentioned in the introduction, clear deviations from statistical behavior have been observed in the $^{12}\text{C} + ^{12}\text{C}$ alpha cluster reactions at higher energies. Branching ratios of multiple alpha particle emission were observed to be much larger than in the experimental data than the statistical would predict. The significant production of multiple alpha particle emission has been discussed in this work [3] and the emission patterns in the

experimental data compared to the statistical predictions are consistent with that non statistical behavior.

We are continuing the analysis of this large body of data. In particular, the calibrations of the same systems mentioned here at 10 and 15 MeV/u are in progress.

- [1] K. Schmidt *et al.*, *Progress in Research*, Cyclotron Institute, Texas A&M University (2012-2013), p. II-20.
- [2] K. Schmidt *et al.*, *Progress in Research*, Cyclotron Institute, Texas A&M University (2011-2012), p. II-9.
- [3] K. Schmidt *et al.*, *Progress in Research*, Cyclotron Institute, Texas A&M University (2012-2013), p. II-9.
- [4] G. Baiocco *et al.*, *Phys. Rev. C* **87**, 054614 (2013); L. Morelli *et al.*, *J. Phys. G* **41** 075108 (2014).
- [5] R.J. Charity *et al.*, *Nucl. Phys.* **A483**, 371 (1988).

Exploring clustering in alpha-conjugate nuclei using the thick target inverse kinematic technique for multiple alpha emission

M. Barbui, K. Hagel, J. Gauthier, S. Wuenschel, R.T. deSouza,¹ S. Hudan,¹ D. Fang,² V.Z. Goldberg,

H. Zheng, G. Giuliani, G. Rapisarda, E.-J. Kim, X. Liu,³ and J.B. Natowitz

¹Indiana University, Bloomington, IN, USA

²Shanghai Institute of Applied Physics (SINAP), Chinese Academy of Sciences, Shanghai, China

³Institute of modern physics, Chinese Academy of Sciences, Lanzhou, China

Searching for alpha cluster states analogous to the ^{12}C Hoyle state in heavier alpha-conjugate nuclei can provide tests of the existence of alpha condensates in nuclear matter. Such states are predicted for ^{16}O , ^{20}Ne , ^{24}Mg , ^{28}Si etc. at excitation energies slightly above the multi-alpha particle decay threshold [1-3].

The Thick Target Inverse Kinematics (TTIK) [4] technique can be successfully used to study the breakup of excited self-conjugate nuclei into many alpha particles. A test run was performed at Cyclotron Institute at Texas A&M University to study the reaction $^{20}\text{Ne}+\alpha$ at 10 AMeV. Here the TTIK method was used to study both single α -particle emission and multiple α -particle decays. Due to the limited statistics, only events with alpha multiplicity up to three were analyzed. The analysis of the three α - particle emission data allowed the identification of the Hoyle state and other ^{12}C excited states decaying into three alpha particles. Some results are reported in Refs. [5, 6] and compared with other data available in the literature.

The experiment has been recently repeated using an improved experimental setup

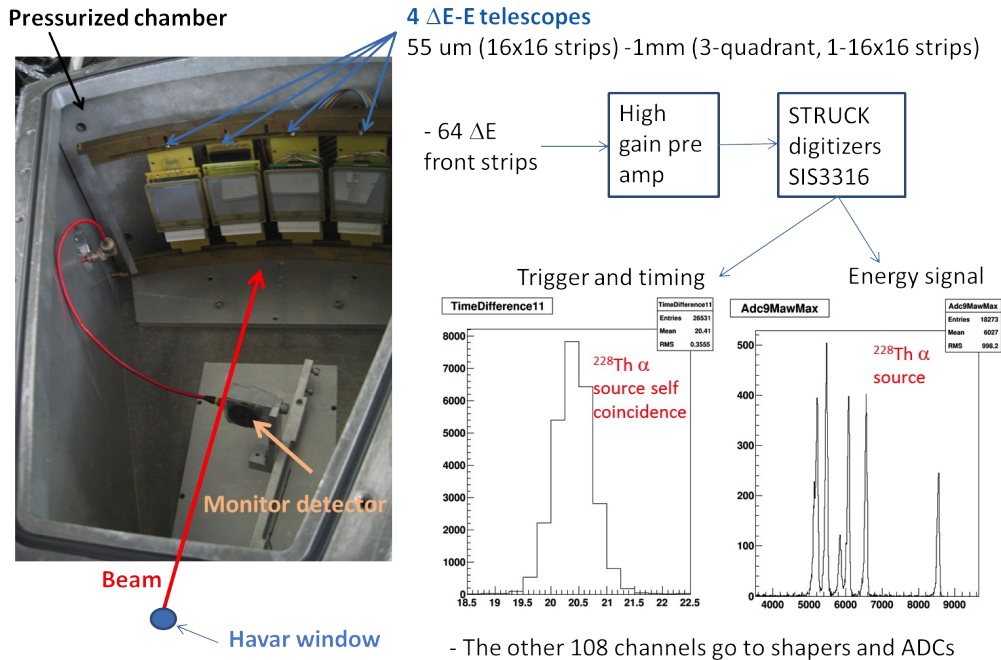


FIG. 1. Experimental setup and scheme of the electronics. Good energy and time resolution are obtained by using the STRUCK digitizers SIS3316.

covering a larger solid angle and having a better granularity. A picture of the new experimental setup is shown in Fig. 1.

In the new setup, four DeltaE-E telescopes placed at the end of the pressurized chamber allow the detection of the reaction products. The DeltaEs consist of 55 micron, double sided, 16x16 strip silicon detectors. The E are 1 mm thick quadrant silicon detectors. The signals from the front strips of the DeltaEs are sent to high gain pre-amplifiers from Indiana University and digitized using Struck SIS1366 Flash ADC. Those digitizers provide energy and time information relative to the cyclotron radio frequency. Particle identification is obtained from the two dimensional scatter plots Time-Energy and DeltaE-E. The signals from the back strips of the DeltaEs and from the E detectors are processed with high gain pre-amplifiers, shaping amplifiers and then acquired with peak sensing ADCs.

The new setup was tested on December 2014 using a ^{20}Ne beam at 13 AMeV provided by the TAMU K150 Cyclotron on ^4He gas at a pressure of 4964 mbar. The data analysis is still in progress. The overall statistics collected during this test run is 1/3 of that collected in the previous run. Fig. 2 shows the spectrum of elastically scattered alpha particles at 1.6 degrees, compared with the spectrum obtained at zero degrees in the previous experiment. The two spectra are consistent with each other. A full implementation of this experiment is being planned for the winter of 2015. Employment of the active target currently under development by the Rogachev group is also under consideration.

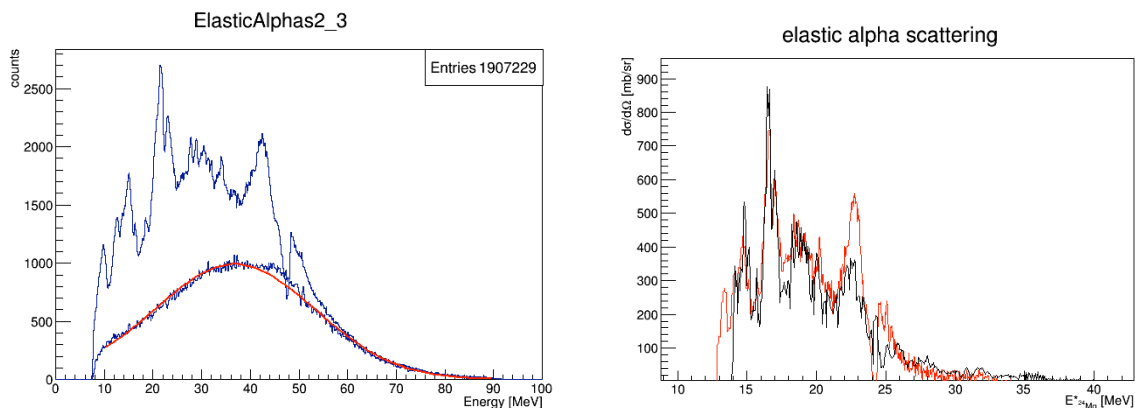


FIG. 2. Elastically scattered alpha particles. Left panel: alpha particle spectrum at 1.6 degrees in the laboratory. The resonances lie on top of a continuous spectrum. This contribution is subtracted using the alpha particle spectrum at 5.6 degrees properly normalized to match the tail of the energy distribution at 1.6 degrees and fitted with a Gaussian (red curve). Right panel: excitation energy of ^{24}Mg at 1.6 degrees after subtraction of the continuum. The red curve shows the result from this experiment the black line shows the spectrum obtained at zero degrees in the previous experiment [5,6].

- [1] K. Ikeda, N. Takigawa, and H. Horiuchi, Prog. Theor. Phys. Suppl. Extra Number, 464 (1968);
- [2] W. von Oertzen, M. Freer, and Y. Kanada-En'yo, Phys. Rep. **432**, 43 (2006);
- [3] C. Beck, J. Phys. Conference Series **436**, 012014 (2013).
- [4] K. Artemov *et al.*, Sov. J. Nucl. Phys. **52**, 406 (1990);
- [5] M. Barbui *et al.*, Eur. Phys. J. Web of Conferences **66**, 03005 (2014);
- [6] M. Barbui *et al.*, Progress in Research, Cyclotron Institute, Texas A&M University (2013-2014), p.II-7.

Progress on campaign surveying deep inelastic multi-nucleon transfer for creation of super- and hyper-heavy elements

S. Wuenschel, M. Barbui, X. Cao, J. Gauthier, K. Hagel, S. Kowalski, Z. Majka, J.B. Natowitz, K. Schmidt, Z. Sosin, A. Wieloch, and H. Zheng

In continuation of our investigations of super heavy element synthesis, we have enhanced our experimental apparatus. In the previous version[1], heavy reaction residues were collected on a passive foil. Alpha particles emitted by the residues were then collected in 8 IC-Si modules located upstream of the target. The passive catcher foil has been replaced by an active catcher: a collection of 63 BC-418 fast plastic scintillator coupled to photomultiplier tubes via light guides (Fig. 1). This design enhancement provides position information for correlation with the alphas detected in the backward direction and may lead to the ability to follow alpha decay chains. In addition, a mounting system was constructed that provides increased control and reproducibility in IC-Si module positioning. Finally, the IC was shortened to increase the fraction of the active

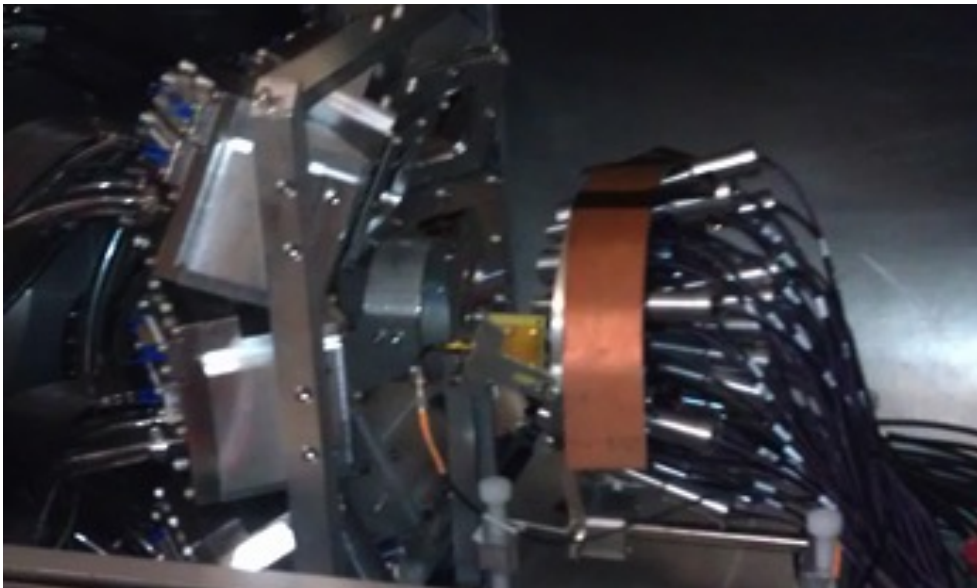


FIG. 1. Experimental setup. Beam enters from the left. Active catcher array is on right hand side.

catcher to which each IC-Si is sensitive.

The fast plastic PMT output was collected using Caen V1742 flash ADCs configured to provide 1 microsecond of waveform in 1 nanosecond buckets (Fig. 2). The waveforms provide the capacity to observe residue implantation, implantation then decay, and fast decay chains. We discovered that gammas emitted during beam/target interaction provide consistent and distinctive peaks in the waveforms. This provides a check of the RF beam time location and a sensitive probe for the presence of beam during nominally beam-off periods.

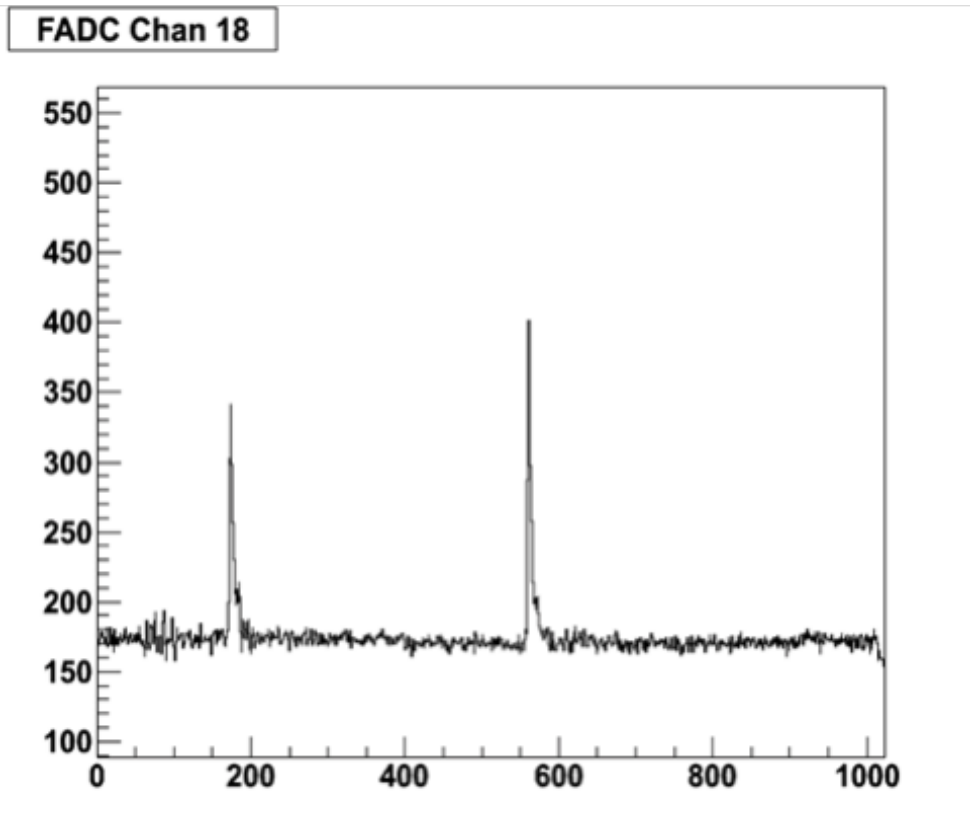


FIG. 2. Active catcher waveform.

The experimental array was used to collect data for nearly two weeks. However, the timing correlation between the IC-Si and the fast plastic was not calibrated to sufficient precision. This caused ambiguity in correlation between signals in the fast plastic and alphas detected in the upstream IC-Si modules. We believe that the correlation can be recovered in future experiments by a very careful time calibration.

Several improvements are being investigated for the next experiment. The fast plastic is unable to independently differentiate alpha particles from fission fragments and residue implantation and has exhibited poor energy resolution in our implementation. We are investigating two options for replacing the current fast plastic. YAP scintillators would retain the fast timing characteristics and allow for pulse shape discrimination based separation of the alphas from heavier fragments [2] because of its two component light output (Fig. 3). Another alternative to the current fast plastic would be the use of scintillating fibers. Scintillating fibers have a fast rise time and would eliminate the need for the light guides that are negatively affecting the fast plastic energy resolution. In addition, active bases will eliminate concerns about overheating in vacuum and increase the gain stability of the PMTs over time.

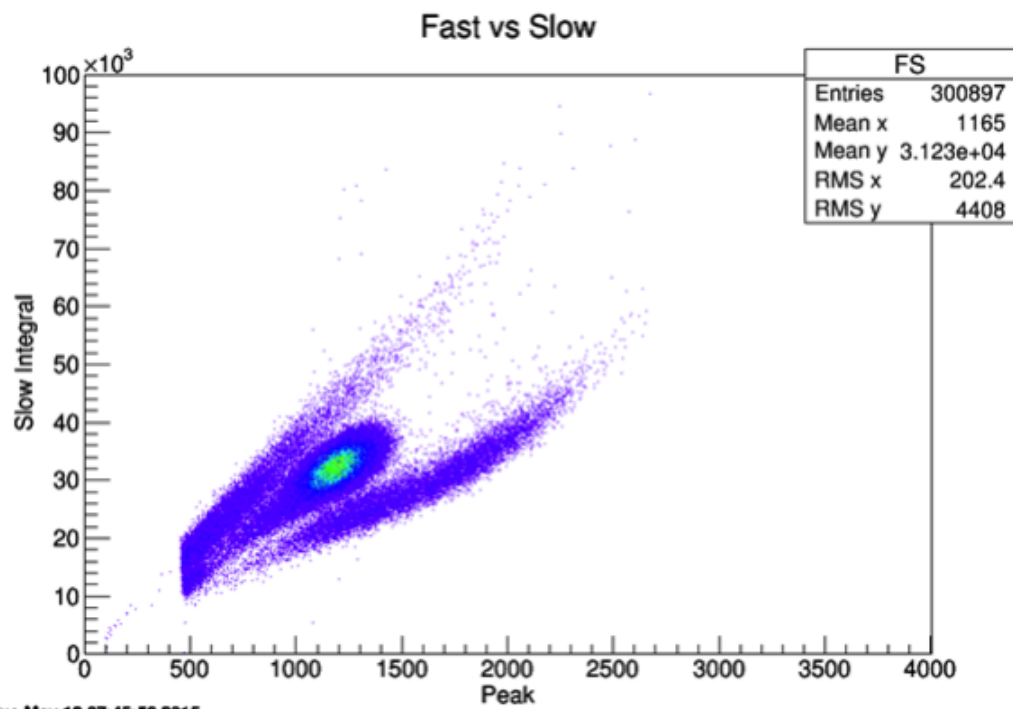


FIG. 3. Test of YAP scintillator with ^{252}Cf . Alphas constitute the peak in the center. The lower band is fission fragments.

- [1] S. Wuenschel *et al.*, *Progress in Research*, Cyclotron Institute, Texas A&M University (2013-2014), p. II-14.
- [2] M. Barbui, Ph. D. Thesis, Università degli studi di Padova, 2005.

Analysis of $^{124}\text{Sn}+^{112,124}\text{Sn}$ at 26A MeV reaction data taken on NIMROD

J. Gauthier, M. Barbui, X. Cao, K. Hagel, J.B. Natowitz, R. Wada, and S. Wuenschel

The analysis of the data set coming from ^{124}Sn beam at 26A MeV on ^{112}Sn and ^{124}Sn targets acquired by the NIMROD heavy ion detector [1] is now underway. These data will be used to perform isotopic study of the reaction products and thus the emission sources [2] in order to better characterize the reaction dynamics and the asymmetry term in the nuclear equation of state [3].

This data set is composed of 33 runs combining 26 000 000 events. To protect the silicon detectors from the heaviest fragment produced by this very heavy system, 229 μm thick aluminum foils were placed in front of the super telescopes in rings 2 to 5 and every other silicon in rings 2 to 7 had a 178 μm thick foil in front of them. There was no foil at all in front of rings 8 and 9.

The linearization of those data is now completed and particle identifications have been generated for every detector. We first performed the linearization of the CsI(Tl) for which a graphical interface has been used to draw four lines per spectra: one for the protons, one for the tritons, another for the alphas and a final one for the heaviest elements in order to make the $Z=2$ identification cleaner. Once the lines are set, the distance between those and the data points is calculated [4] and used to project the data for each element on the x axis to gives a visual evaluation of the isotope separation. At that point, limits are manually set to separate the isotopes. A lower limit is also set to cut the noise and the mixed line part at the very bottom of the slow vs fast spectra. An example of those identification plots is shown in Fig. 1. The lines and limits are then used by the particle identification program to generate PID files. This method allows us to discriminate mass up to $Z=2$ in the case of the CsI(Tl) detectors.

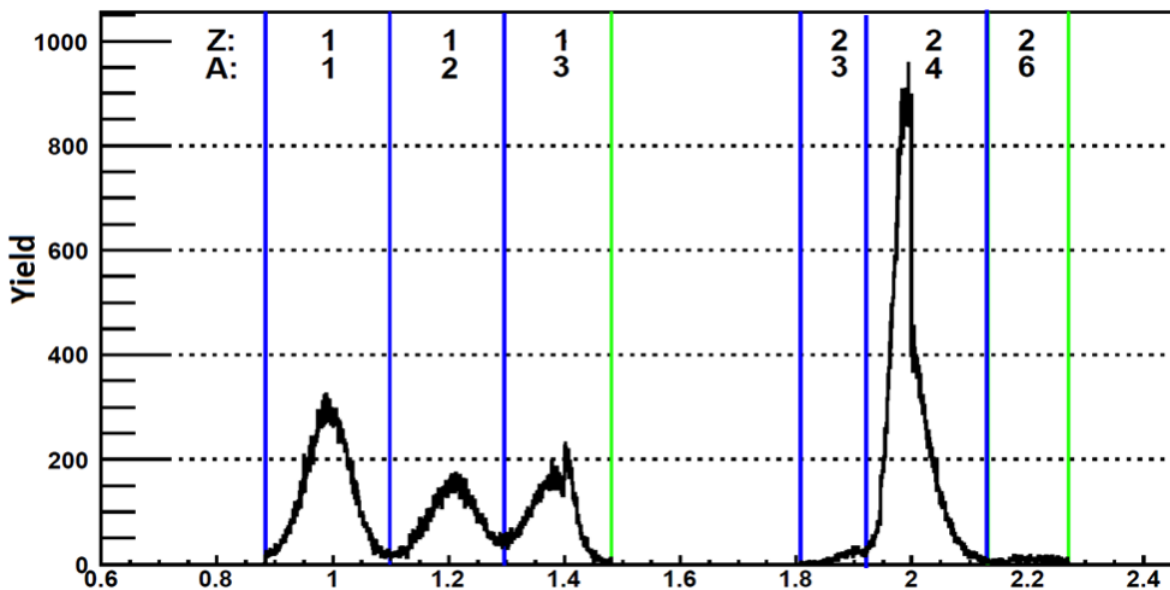


FIG. 1. Linearization plot and identification limits for CsI(Tl) number 54 (ring 6). Isotopic identification is achieved for $Z=1$ and 2 particles.

The same procedure has been used for the Si-Si super telescopes and Si-CsI(Tl) telescopes. The only difference is that we set a line for each visually separable element (that can go up to $Z=42$ in the case of the super telescopes). In both cases, isotopic identification is achievable up to $Z=9$ for the best detectors and all the charges are well separated if there are enough statistics. Fig. 2 shows the identification plot and limits for particles with a charge from $Z=3$ to 9 for the Si-Si super telescope 56-58.

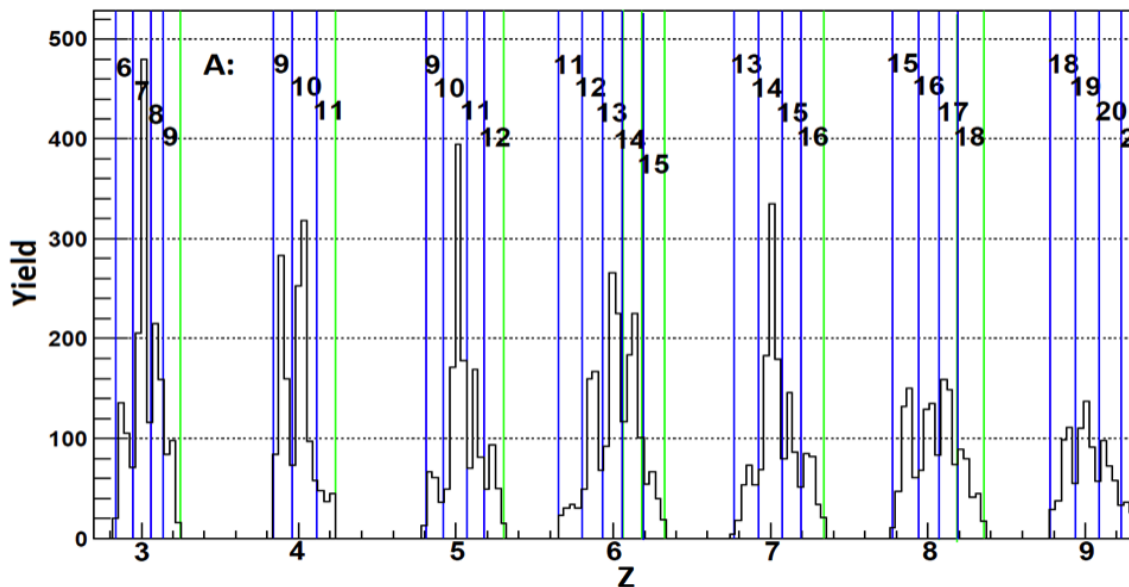


FIG. 2. Linearization plot and identification limits for Si-Si super telescope number 56-58 (ring 5). Isotopic identification is achieved up to $Z=9$.

As indicated above, the linearization is now completed and we are calibrating the Si-Si telescopes. Since we do not have any calibration data, we are using SRIM stopping power calculations [5] to establish the energy. The punch through being equal to the total energy, we can calculate the energy lost into the ΔE . The energy deposited into the E stage is then the total minus ΔE . Since we don't know the mass of the fragments with $Z>9$, we use a N/Z mass attribution factor for SRIM calculations and we compare the calibrated spectra with the energy loss lines calculated by the software.

We can see on Fig. 3 that the procedure is working well for the Si-Si telescope number 38-40. Here, the calibration is made using the punch through energy points from $Z=2$ to 14 and a N/Z mass factor equal to 1.15 is applied for $9<Z<15$, 1.24 for $14<Z<25$ and 1.20 for $Z>24$. This method and these values are working fine for most of the detectors. However, several telescopes don't match with the SRIM calculated lines and we will have to introduce a Si thickness correction in the energy loss calculations. At the end, we will also have to make a correction for the aluminum foil degrader in front of the silicons for rings 2 to 7. For the other detectors, a

calibration run will have to be done in order to be able to calibrate the Si-CsI(Tl) and CsI(Tl) detectors properly.

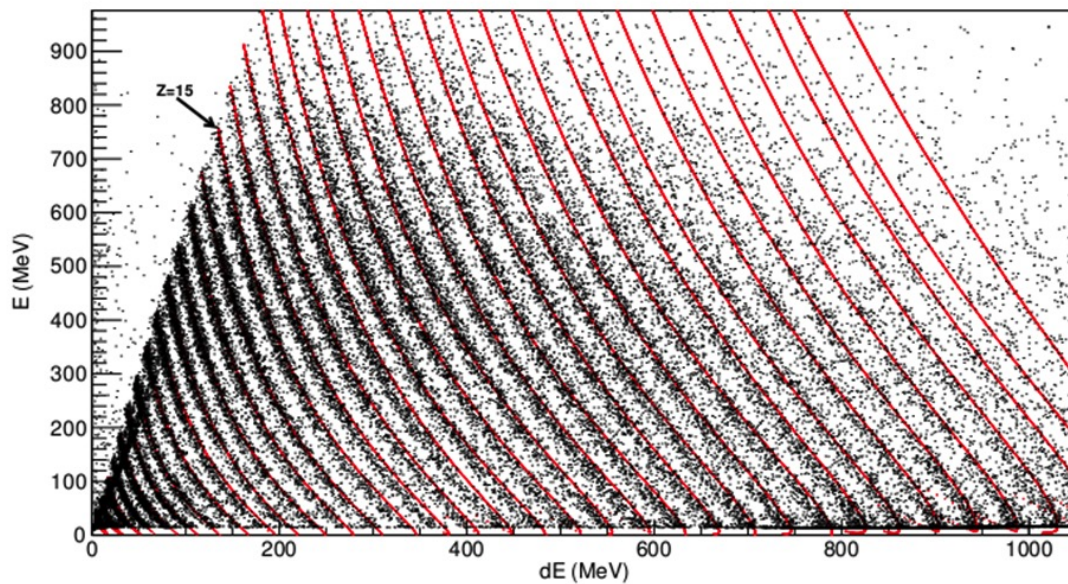


FIG. 3. Calibrated spectra for Si-Si super telescope number 38-40 (ring 4). Red lines are SRIM calculated energy loss data.

- [1] R. Wada *et al.*, Nuclear Physics News, **24**, 28 (2014).
- [2] D.V. Shetty *et al.*, Phys. Rev. C **68**, 054605 (2003).
- [3] M.A. Famiano *et al.*, Phys. Rev. Lett. **97**, 052701 (2006).
- [4] L.W. May *et al.*, *Progress in Research*, Cyclotron Institute, Texas A&M University (2007-2008), p. II-26.
- [5] J.F. Ziegler *et al.*, Nucl. Instrum. Methods Phys. Res. **B268**, 11 (2010).

Observations from evaporation residue cross sections in ^{45}Sc - and ^{44}Ca -induced reactions

T.A. Werke, D.A. Mayorov, M.C. Alfonso, E.E. Tereshatov, and C.M. Folden III

Recent measurements of evaporation residue (EvR) cross sections [1-3] for nuclei near the $N = 126$ shell have emphasized the importance of collective enhancements to the level density (CELD) for spherical ground-state nuclei and may have relevance for new superheavy element (SHE) synthesis. The study of ^{45}Sc -induced reactions on lanthanide targets [3] revealed that proton evaporation competed effectively with neutron evaporation from the compound nuclei (CN) that were produced. The xn cross sections of ^{45}Sc -induced reactions were also three or more orders of magnitude smaller than cross sections of ^{48}Ca -induced reactions on the same targets due to the relative neutron deficiency of ^{45}Sc .

In the last year, we bombarded $^{156, 157}\text{Gd}$ targets with ^{45}Sc projectiles and ^{158}Gd , ^{159}Tb , and ^{162}Dy targets with ^{44}Ca projectiles as part of a systematic study to produce CN near the $N = 126$ shell. The beams of $^{45}\text{Sc}^{6+}$ and $^{44}\text{Ca}^{6+}$ were provided from the K500 cyclotron, and the unreacted beam and other unwanted reaction products were separated using the Momentum Achromat Recoil Spectrometer (MARS) [4]. Full experimental details are given in Refs. [1, 5].

Combined with previous results, reactions of $^{45}\text{Sc} + ^{156-158, 160}\text{Gd}$ have now been studied and $4n$ cross sections are shown in Fig. 1. As expected, the $4n$ cross sections decrease as the neutron number in the target decreases. As the CN become more neutron-deficient, the fission

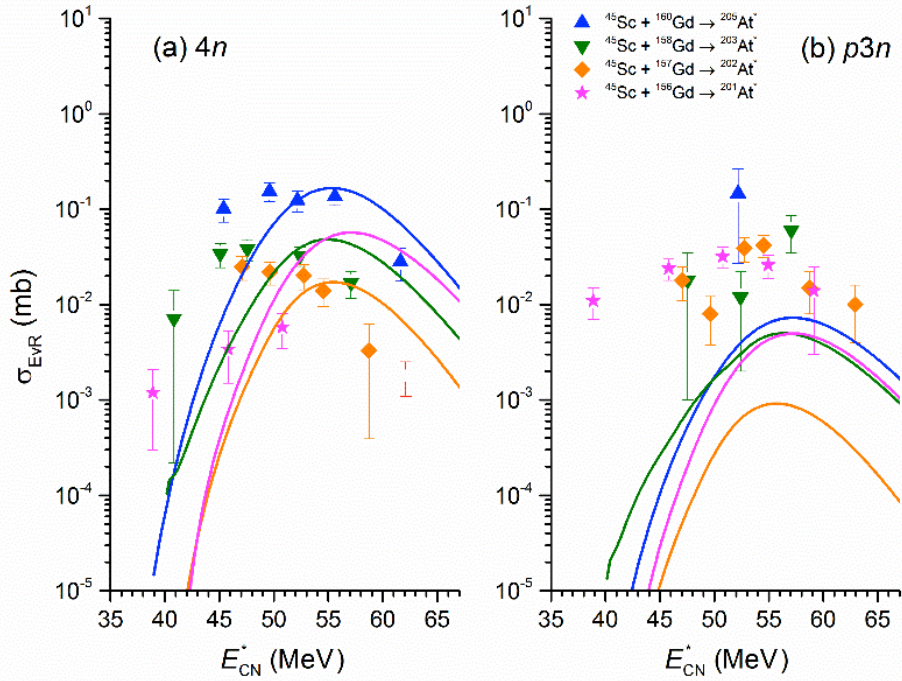


FIG. 1. (a) $4n$ and (b) $p3n$ cross sections for ^{45}Sc -induced reactions on $^{156-158, 160}\text{Gd}$ targets. Symbols indicate experimental data and solid lines indicate theoretical calculations.

barriers decrease and the neutron binding energies increase, leading to a higher probability of fission. ^{44}Ca is of interest because it is only one proton removed from ^{45}Sc (both are $N = 24$ nuclei). Cross sections for the reactions of ^{44}Ca on lanthanide targets are approximately two orders of magnitude larger than for reactions of ^{45}Sc on the same targets as shown in Fig. 2. The pxn cross sections in the ^{44}Ca -induced reactions are also larger than in the ^{45}Sc -induced reactions. This emphasizes the role of the extra proton in ^{45}Sc in creating much more fissile CN which have low survival probabilities. A simple theoretical model based on Ref. [6] was developed, and the inclusion of CELD was necessary to reproduce the experimental data. This may have implications for producing SHEs near the predicted $N = 184$ spherical closed shell, as CELD may negate any possible enhancement to the xn cross section as a result of producing CN on this shell.

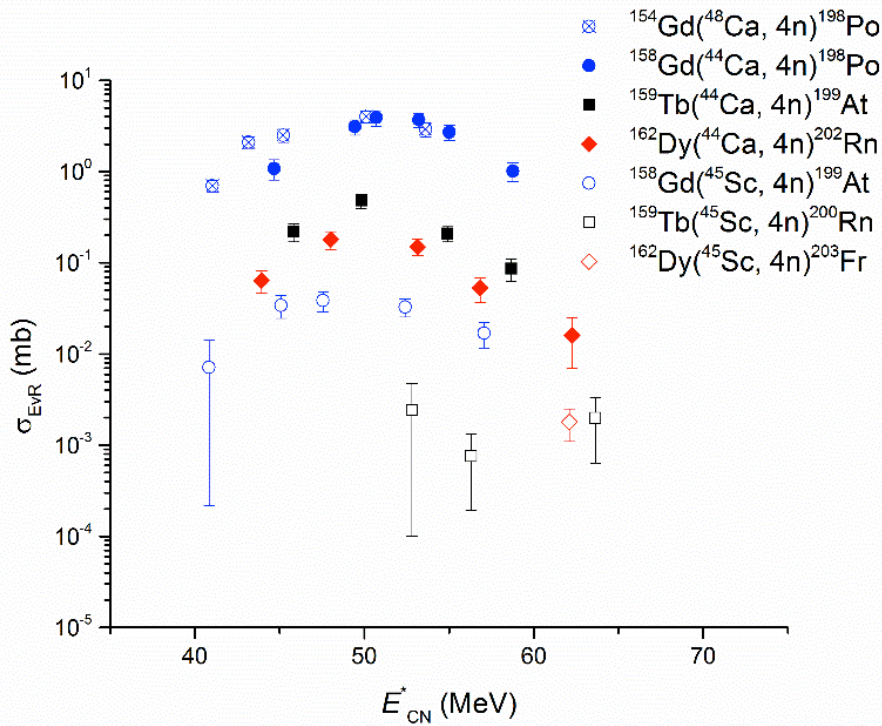


FIG. 2. Comparison of $4n$ cross sections in ^{44}Ca -induced reactions (solid points) and ^{45}Sc -induced reactions (open points) on ^{158}Gd , ^{159}Tb , and ^{162}Dy targets. The cross-bombardment reactions $^{48}\text{Ca}+^{154}\text{Gd}$ (circles with diagonal lines) and $^{44}\text{Ca} + ^{158}\text{Gd}$ (solid circles) are very similar.

Two reactions with ^{44}Ca projectiles were cross bombardments for reactions that had been previously studied using either ^{48}Ca or ^{45}Sc projectiles. Cross sections for the $4n$ EvR of the $^{48}\text{Ca} + ^{154}\text{Gd}$ and $^{44}\text{Ca} + ^{158}\text{Gd}$ reactions which produced the ^{202}Po CN are very similar (see Fig. 2). However, the maximum $4n$ EvR cross section of the $^{44}\text{Ca} + ^{159}\text{Tb}$ reaction which produced the ^{203}At CN is approximately an order of magnitude larger than in the $^{45}\text{Sc} + ^{158}\text{Sc}$ reaction which produced the same CN. Some of this discrepancy should be accounted for by differences in the

fusion probability, but we cannot rule out other effects such as pre-equilibrium emission playing a role [7].

These data demonstrate that the production of neutron-deficient heavy nuclei using ^{44}Ca and ^{45}Sc projectiles is relatively difficult compared to similar reactions using ^{48}Ca projectiles reacting with the same targets.

- [1] D.A. Mayorov, T.A. Werke, M.C. Alfonso, M.E. Bennett, and C.M. Folden III, *Phys. Rev. C* **90**, 024602 (2014).
- [2] D.A. Mayorov, T.A. Werke, M.C. Alfonso, E.E. Tereshatov, M.E. Bennett, M.M. Frey, and C.M. Folden III, *Phys. Rev. C* (submitted).
- [3] T.A. Werke, D.A. Mayorov, M.C. Alfonso, M.E. Bennett, M.J. DeVanzo, M.M. Frey, E.E. Tereshatov, and C.M. Folden III, *Phys. Rev. C* (submitted).
- [4] R.E. Tribble, R.H. Burch, and C.A. Gagliardi, *Nucl. Instrum. Methods. Phys. Res.* **A285**, 441 (1989).
- [5] C.M. Folden III *et al.*, *Nucl. Instrum. Methods. Phys. Res.* **A678**, 1 (2012).
- [6] K. Siwek-Wilczyńska, I. Skwira, and J. Wilczyński, *Phys. Rev. C* **72**, 034605 (2005).
- [7] M.K. Sharma *et al.*, *Phys. Rev. C* **91**, 014603 (2015).

Ion exchange separation of indium and thallium

E.E. Tereshatov, M.Yu. Boltoeva,^{1,2} and C.M. Folden III

¹Université de Strasbourg, IPHC, Strasbourg, 67037 France

²CNRS, Strasbourg, 67037 France

Indium and thallium belong to the same group of the Periodic Table of the Elements and are considered to be light homologues of the last member of this group, element 113. This element is the heaviest odd-Z superheavy element (SHE) that has been chemically investigated. There is only one paper published on this topic so far that confirmed element 113 to be volatile and to have weak adsorption on inert surface such as Teflon [0]. The goal of this work is to develop a simple cation exchange procedure for indium and thallium separation with potential application in future liquid-phase SHE experiments.

Strelow *et al.* studied distribution ratios of In, Tl and other elements between Dowex 50x8 resin and HCl/acetone solutions [0]. We chose pure HCl media and a resin with lower cross-linkage (Dowex 50x4) to simplify the process and minimize the volume of each fraction. Also, zirconium and yttrium were introduced to the system to simulate fission and transfer reaction product behavior, respectively, upon element 113 synthesis [0].

Fig. 1 shows isocratic separations of the light homologues of element 113. Recoveries of In and Tl(I) are $(97.9 \pm 0.5)\%$ and $(98.8 \pm 0.8)\%$, respectively. This result provides a good scheme for SHE investigation in aqueous media. Yttrium remains on the column until the HCl concentration is increased up to 3 M with $(97 \pm 4)\%$ recovery. This yttrium fraction can be analyzed in an experiment with element 113 synthesis to represent actinide transfer reaction

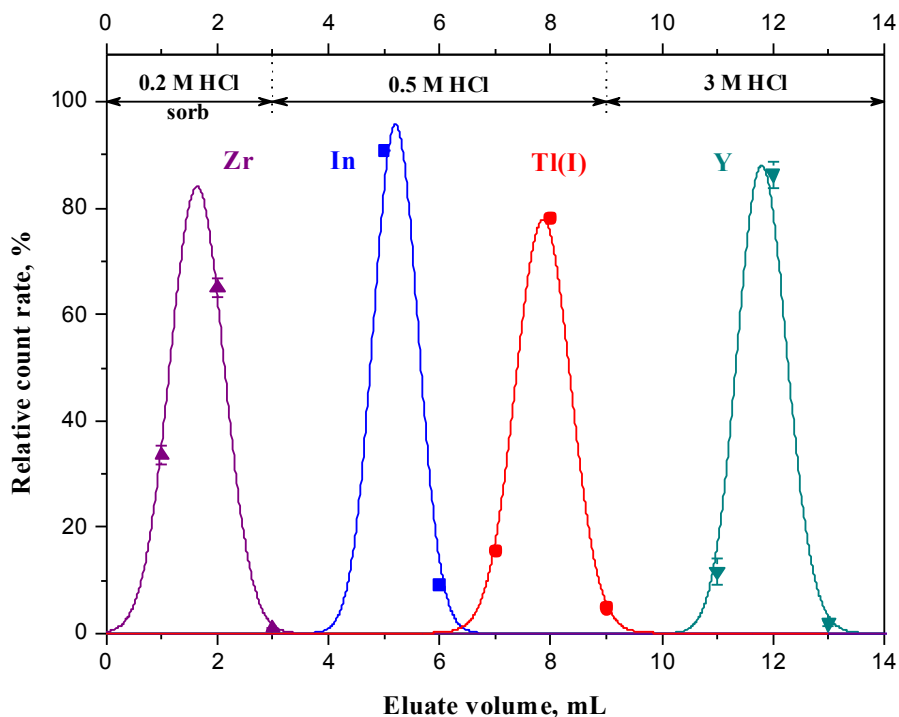


FIG. 1. Separation of Zr, In, Tl(I), and Y (4x80 mm column with Dowex 50x4, 200-400 mesh resin).

products. The zirconium elution position is quite interesting because it should have been strongly adsorbed by the cation exchanger [0]. Based on the shape of its elution curve and $(90 \pm 4)\%$ recovery, we can draw the conclusion that Zr was in the form of a negatively charged compound. The structure of this compound is uncertain because we might deal with chloride and/or oxalate (initial form of Zr product) complexes. Such a hypothesis is confirmed by a previous report [0] that showed large distribution coefficients of Zr on anion exchange resins in the presence of hydrochloric and oxalic acids.

In order to possibly change the elution order of indium and thallium, bromine water was applied to oxidize the latter. Fig. 2 shows stepwise group 13 elements separation and their isolation from zirconium and yttrium. One can see that the Tl(III) and In elution curves are barely overlapped, indicating good peak resolution. Total Tl(III) and In recoveries are $(94.4 \pm 1.0)\%$ and $(79.7 \pm 0.8)\%$, respectively. Lack of full indium elution is probably due to resin degradation because of being in contact with bromine water. Nevertheless, satisfactory separation of Tl(III) and In is achieved within a volume of 8 mL. The behavior of Zr and Y in this experiment is analogous to one described above with $(96 \pm 5)\%$ and $(86.3 \pm 1.8)\%$ recoveries, respectively.

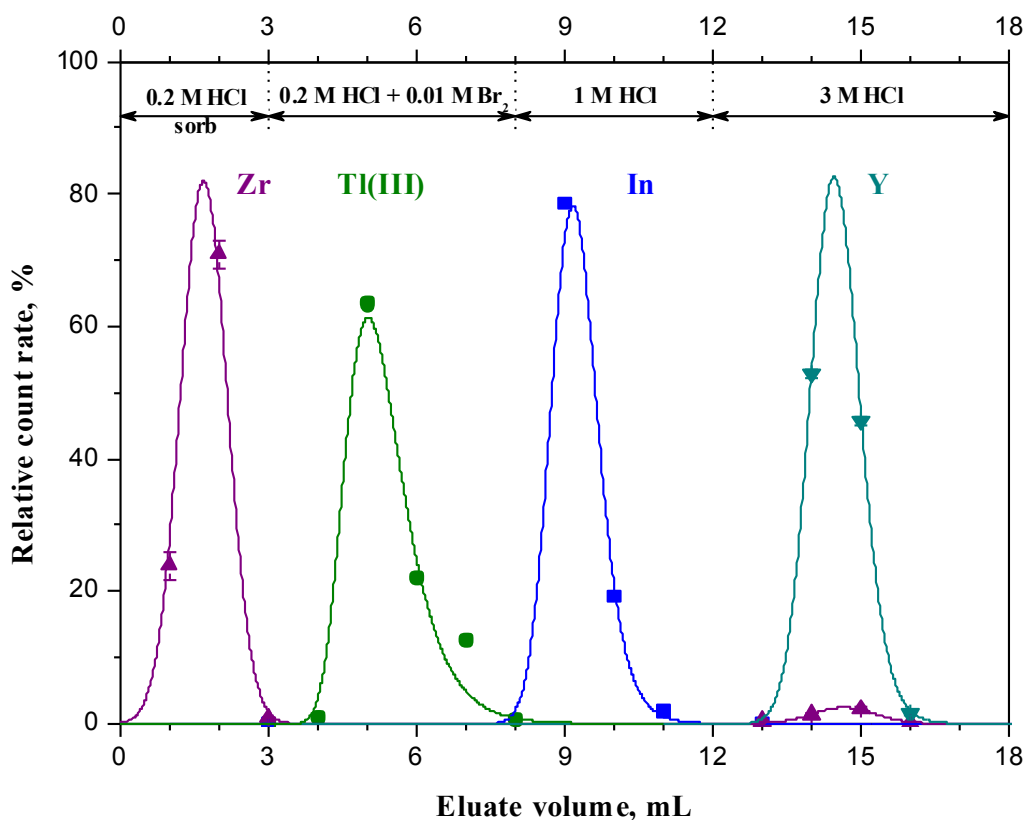


FIG. 2. Separation of Zr, In, Tl(III), and Y (4x80 mm column with Dowex 50x4, 200-400 mesh resin).

These results suggest that this system may be suitable for determining the ion exchange behavior of element 113.

- [1] S.N. Dmitriev, N.V. Aksenov, Yu.V. Albin *et al.*, Mendeleev Commun. **24**, 253 (2014).
- [2] F.W.E. Strelow, A.H. Victor, C.R. van Zyl, and C. Eloff, Anal Chem. **43**, 870 (1971).
- [3] D. Schumann, H. Bruchertseifer, R. Eichler *et al.*, Radiochim Acta. **93**, 727 (2005).
- [4] Z. Szegłowski, L.I. Guseva, Din-Ti-Lien *et al.*, Radiochem. **36**, 289 (1994).

Ionic liquid-based extraction of indium and thallium

E.E. Tereshatov, M.Yu. Boltoeva,^{1,2} and C.M. Folden III

¹Université de Strasbourg, IPHC, Strasbourg, 67037 France

²CNRS, Strasbourg, 67037 France

Indium and thallium are elements of interest for radiopharmaceuticals [1], manufacture of liquid crystal displays [2], and environmental protection [3]. The growing economic needs from high-tech industries support studies on efficient recovery of indium and development of new techniques for trapping of toxic thallium.

The goal of this work is to develop ionic liquid-based extraction procedures for indium and thallium. We investigated the extraction behavior of In and Tl from hydrochloric acid solutions into $[\text{C}_4\text{mim}][\text{Tf}_2\text{N}]$, a well-characterized room temperature 1-butyl-3-methyl imidazolium *bis*(trifluoromethanesulfonyl)imide ionic liquid (IL) [4], with and without the widely used extracting agent tributyl phosphate, TBP (see Fig. 1). To the best of our knowledge, this extraction system has never been examined before for the extraction study of group 13 elements.

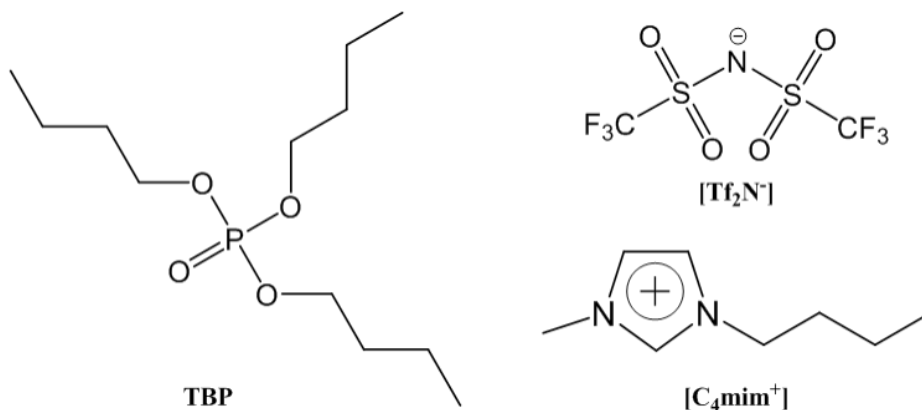


FIG. 1. Molecular structure and abbreviations of extractant and ionic liquid used in this work.

First, we have checked the ability of pure IL to extract Tl and In from the aqueous HCl solutions. Hereinafter, we describe the extraction system as $M/\text{HCl}/L/[\text{C}_4\text{mim}][\text{Tf}_2\text{N}]$ where M is a metal ion and L is an extracting agent. The metal ion distribution between the IL and aqueous phases has been examined by varying the concentration of hydrochloric acid. The results of varying the HCl concentration are shown in Fig. 2. The distribution ratios of trivalent thallium are much higher than those of Tl(I) and In(III) in the whole acidity range. Moreover, the variation of acid concentration in the aqueous phase affects the extraction efficiency of trivalent thallium and indium differently. $D_{\text{Tl(III)}}$ decreases from 300 in 0.2 M HCl to 20 in 6 M, while $D_{\text{In(III)}}$ increases from 1×10^{-5} to 5×10^{-3} , respectively. There is no monotonic dependency on the acid concentration for extraction efficiency of Tl(I). This can indicate that Tl(I) extraction mechanism might be different for $[\text{HCl}] > 1$ M. The high extraction of Tl(III) without any extracting agents indicates that the IL is not an inert solvent and that it participates in the extraction process.

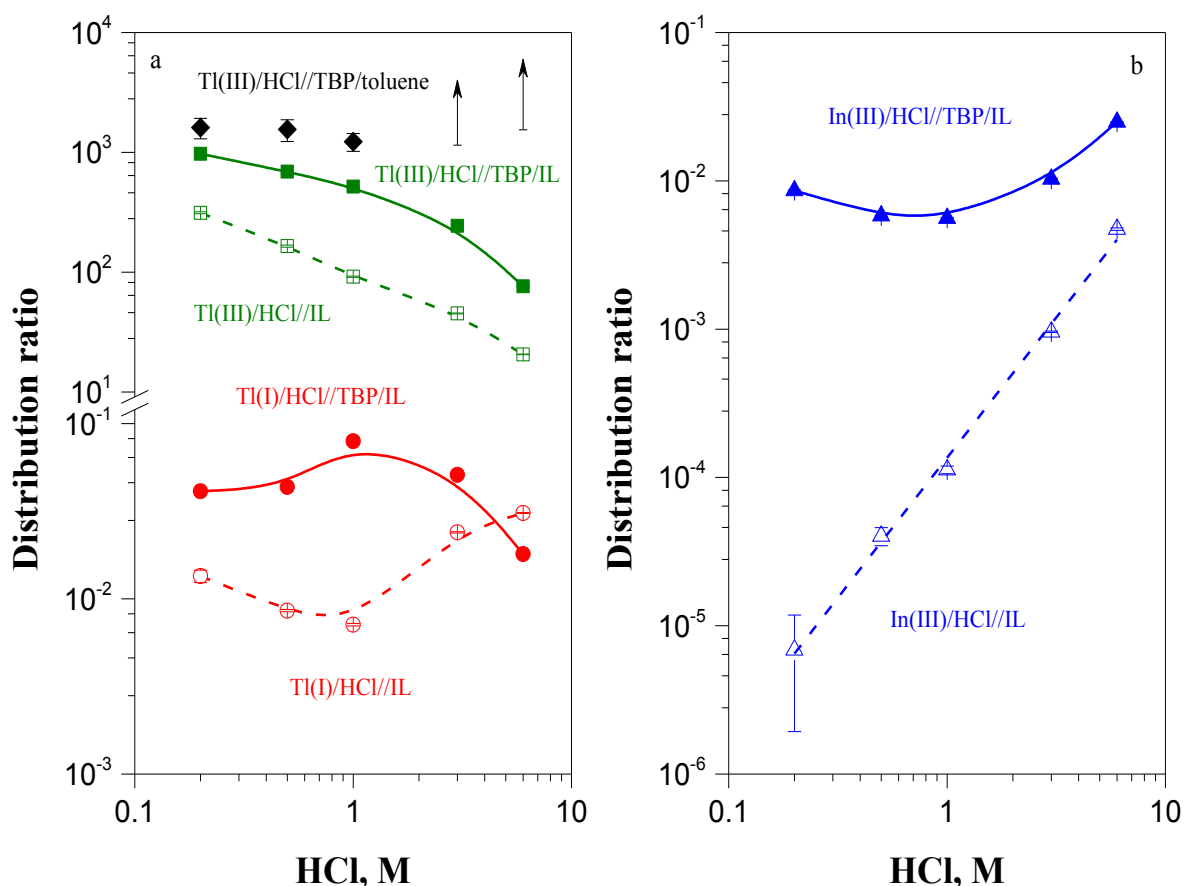


FIG. 2. Distribution ratio of: a – Tl(I) and Tl(III), b – In(III) from HCl solutions into IL (open symbols) and into IL or toluene with 30 % TBP (closed symbols).

The extraction of the individual metal ions has been also carried out in different initial hydrochloric acid concentrations in the aqueous phase (from 0.2 to 6 M HCl) with 30% TBP dissolved in IL or toluene (Fig. 2). As expected, the introduction of TBP, an organic ligand, in the extraction system results in a significant increase in the extraction efficiency of the metals. The extraction efficiencies of Tl(I) and In(III) by TBP and IL are greater than those for pure IL and the latter values are below 0.1. The extraction is quantitative for trivalent thallic ions into IL or toluene over the entire range of HCl concentrations. For the extraction into toluene, the highest $D_{\text{Tl(III)}}$ values have been found for $[\text{HCl}] \leq 1$ M. In the case of further increase of acid concentration, only lower limits of distribution ratios have been measured. Our results are in agreement with literature data on the extraction of thallium and indium ions by TBP dissolved in molecular solvents. For example, De and Sen reported the complete extraction of trivalent thallium from 6 M HCl aqueous solution by 30% TBP in benzene, while In(III) is extracted much less efficiently ($D_{\text{In(III)}} = 3.57$ at $[\text{HCl}] = 2$ M) [0]. Furthermore, the trend similarity of both distribution curves for Tl(III)/HCl/IL and Tl(III)/HCl/TBP/IL may indicate that the nature of extracted complexes stays the same, i.e. there are anionic species in both extraction systems. The

difference in shape of the curves for In(III) and Tl(I) reveals that composition of the extracted species is affected by the presence of TBP.

- [1] V. Drozdovitch, A.B. Brill, R.J. Callahan *et al.*, Health Phys. **108**, 520 (2015).
- [2] W.I. Mortada, I.M. Kenawy, and M.M. Hassanien, Anal. Methods **7**, 2114 (2015).
- [3] A. Miyazaki, A. Kimura, and H. Tao, Bull. Environ. Contam. Toxicol. **89**, 1211 (2012).
- [4] M. Vranes, S. Dozic, V. Djeric, and S. Gadzuric, J. Chem. Eng. Data **57**, 1072 (2012).
- [5] A.K. De and A.K. Sen, Talanta **14**, 629 (1967).

Signals of Bose Einstein condensation and Fermi quenching in the decay of hot nuclear systems

P. Marini,¹ H. Zheng, G. Verde,^{2,3} A. Chbihi,⁴ and A. Bonasera

¹*Centre d'Etudes Nucléaires de Bordeaux Gradignan Chemin du Solarium, Le haut Vigneau,
BP 120, F-33175 Gradignan Cedex*

²*Institut de Physique Nucléaire, IN2P3-CNRS, Université Paris-Sud 11, F-91406 Orsay Cedex, France*

³*INFN-Sezione di Catania, via Santa sofia, 62 95123 Catania, Italy*

⁴*Grand Accélérateur National d'Ions Lourds, Bd Henri Becquerel BP 55027 – 14076 CAEN, France*

We report experimental signals of Bose-Einstein condensation in the decay of hot Ca projectile like sources produced in mid-peripheral collisions at sub-Fermi energies [1]. The experimental setup, constituted by the coupling of the INDRA 4π detector array to the forward angle VAMOS magnetic spectrometer, allowed us to reconstruct the mass, charge and excitation energy of the decaying hot projectile-like sources. Furthermore, by means of quantum fluctuation analysis techniques, temperatures and mean volumes per particle as seen by bosons and fermions separately are correlated to the excitation energy of the reconstructed system. The obtained results are consistent with the production of dilute mixed (bosons/fermions) systems, where bosons experience a smaller volume as compared to the surrounding fermionic gas. Our findings recall similar phenomena observed in the study of boson condensates in atomic traps.

Only peripheral and semi-peripheral collisions, leading to a heavy QP remnant detected in VAMOS with $Z > 5$ have been studied in this work. In order to reconstruct the charge, Z_{QP} , mass, A_{QP} , and momentum vector \mathbf{p}_{QP} , of the QP, particles with $Z = 1, 2$ and $Z \geq 3$, detected by INDRA were attributed to QP decay when their longitudinal velocities lay within the range of $\pm 65\%$, $\pm 60\%$, $\pm 45\%$, respectively, of the coincident QP residue velocity. In order to shed more light into these observations, we try to separate bosonic-like events and fermionic-like events by means of the following event-by-event quantity:

$$b_j = \frac{1}{M} \sum_{i=1}^M \frac{(-1)^{N_i} + (-1)^{Z_i}}{2}$$

where M is the event multiplicity and Z_i and N_i are the charge and neutron numbers of the i^{th} fragment, respectively. b_j is equal to 1, -1 and 0 when all fragments emitted in the event are Z even- N even, Z odd N odd, and A -odd, respectively. The temperatures and local volumes of the produced systems can then be estimated by studying the measured particle quadrupole momentum and multiplicity fluctuations, as well as mean multiplicities, according to the quantum fluctuation analysis techniques. In Fig.1, we showed the critical temperature T_0 as function of density for both mixture and boson-like events (the lines indicate the ideal boson gas result). Values of the order of few MeV are obtained for both particles, in agreement with theoretical predictions. The experimentally derived values are systematically higher both for d and α as compared to the ideal case. This is expected because the Coulomb repulsion enhances the condensate. It is important to remark that at high density, and especially for the case (d displays unfortunately large

error bars due to poor statistics), the data are closer to the ideal case. This is due to the increased importance of the nuclear force which reduces the Coulomb repulsion.

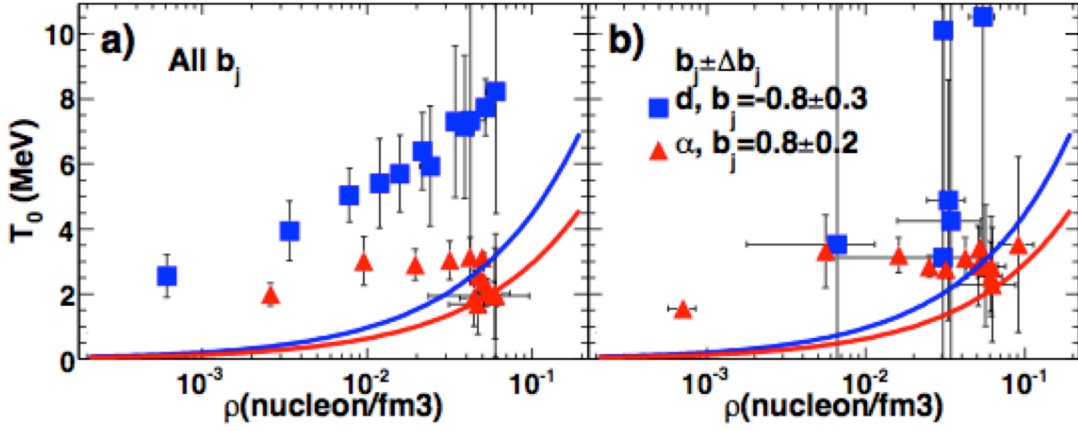


FIG. 1. Critical temperature vs local density for (a) mixture and (b) boson-like events.

In summary we have studied the decay of ex-cited quasi-projectile systems produced in mid-peripheral Ca40+Ca40 collisions at $E/A = 35$ MeV with the INDRA-VAMOS setup. Within the selected events, mean partial volumes per particle and temperatures, probed by bosons (deuterons and alphas) and by fermions (protons) in the low density gas-like phase have been estimated with quantum fluctuation methods. The observed results show that bosons experience a smaller volume and a higher energy density than fermions. These results may be associated to the presence of boson condensation and fermionic quenching phenomena in nuclear systems. Condensation temperatures are in agreement with theoretical predictions. These phenomena are observed even in events where mixtures of bosons and fermions coexist, suggesting that they are not reduced by boson-fermion interactions. The results of this work recall closely similar phenomena observed in atomic systems where the coexistence of a quasi-pure Bose Einstein condensate of Li7 atoms (bosons) in a Fermi sea of Li6 (fermions) was observed [2]. This interdisciplinary analogy seems to indicate a similar nature for processes occurring in atomic scale and nuclear scale quantum systems, regardless of their different sizes and characteristic interactions. Future investigations on implications of these phenomena on α clustering and symmetry energy at low density also stimulate using particle-particle correlations to estimate emission densities and volumes.

[1] P. Marini *et al.*, arXiv: 1501.00595.

[2] F. Schreck, L. Khaykovich, K.L. Corwin, G. Ferrari, T. Bourdel, J. Cubizolles, and C. Salomon, Phys. Rev. Lett. **87**, 080403 (2001).

Toward understanding relativistic heavy-ion collisions with the STAR detector at RHIC

M. Cervantes, Y. Liu, S. Mioduszewski, N. Sahoo, and the STAR Collaboration

The focus of this project is the study of high-energy heavy-ion collisions at the Relativistic Heavy Ion Collider (RHIC). Two valuable probes of the matter created in these collisions are direct-photon-triggered (jet) correlations and heavy-quarkonium production.

Measurement of γ -Jet at low z_T and high trigger p_T

Direct photons produced in hard collisions, early in the evolution of a heavy-ion collision, are promising probes [1], as they do not interact via the strong force. Jet correlations (of the recoiling parton) with a direct-photon trigger can give information about the parton energy loss in the medium. The correlations with a photon trigger are compared to those measured with a π^0 trigger because of the difference in expected surface biases. While direct photons are not affected by the medium and can originate from anywhere in the medium without bias, π^0 triggers are likely to have a bias of production near the surface of the medium. Therefore, on average, one would expect that the away-side jet for a π^0 trigger has a larger path length to traverse and experiences larger energy loss than the away-side jet of a γ^{dir} trigger. Because of the increased sensitivity to the path-length dependence of partonic energy loss at low fractional jet momentum z_T ($z_T = p_T^{\text{assoc}}/p_T^{\text{trig}} < 0.4$, according to theoretical predictions [2]), we have extended the kinematic reach of our previous measurement [3] to lower z_T . In the past year, we carried out the analysis with higher statistics data sets: Run-11 Au+Au data and Run-9 p+p data. We lowered the $p_{T,\text{assoc}}$ cut down to 1.2 GeV/c, and raised the $E_{T,\text{trig}}$ cut to 12 GeV. This extended our z_T down to 0.1.

Fig. 1 shows the latest result for I_{AA} as a function of z_T . A full systematic study has been performed for these data points, and the derived uncertainties are included in this plot. This result is expected to be close to final. A manuscript presenting these results is in preparation. Although the uncertainties are large, there does seem to be a hint of less suppression at low z_T . This may indicate the recovery of lost energy when including the lower momentum particles in the jet. However, the difference expected in π^0 -triggered away-side suppression and γ^{dir} -triggered away-side suppression, due to geometry, is not seen within our uncertainties.

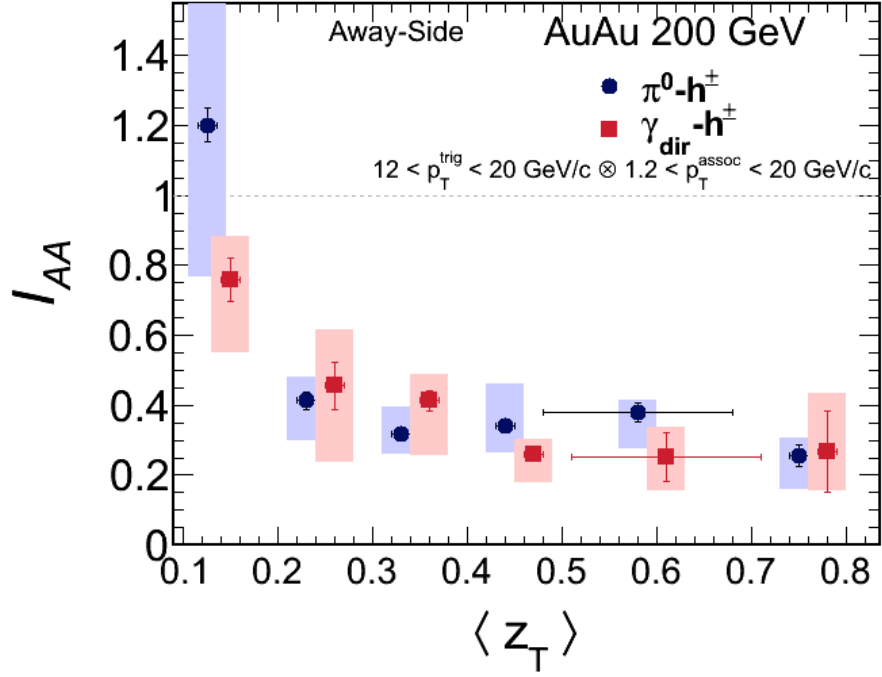


FIG. 1. I_{AA} vs. z_T for π^0 -triggered away-side yields (blue) and γ^{dir} -triggered away-side yields (red) from Run-9 p+p and Run-11 central Au+Au data.

Upsilon (Υ) Production Mechanism through Spin-Alignment (“Polarization”) Measurement

We are interested in studying heavy quarkonium production in p+p collisions. The systematics of prompt production of heavy quarkonium is not fully described by common production models, e.g. the Color Singlet Model (CSM) and the Color Octet Model (COM). Historically, CSM calculations grossly under-predicted production cross-sections of heavy quarkonium, but recent development with higher-order corrections can describe data better [4]. The COM can describe the p_T spectra of heavy quarkonia, but the spin-alignment (“polarization”) prediction disagrees with experimental data from Fermilab experiments [5].

A measurement that puts constraints on theoretical models of the production mechanism is the spin-alignment (or “polarization”) of the Υ . Here, the angle between the direction of the e^+ momentum is measured in the Υ ’s rest frame with respect to the Υ ’s direction of motion, i.e. the “polarization axis”. The distribution of Υ ’s as a function of this angle θ is then fit with the function $dN/d\cos\theta = A(1 + \lambda_s \cos^2\theta)$, where λ_s is the polarization. The value of λ_s can vary from -1 to 1; with -1 corresponding to a fully longitudinal polarization, 0 no polarization, and +1 fully transverse polarization.

The most difficult part of the analysis has been removing the backgrounds due to Drell-Yan and $b\bar{b}$ production, which may have their own polarization (i.e. θ dependence) and their

own acceptance corrections. We have made significant progress on this task in the past year. From simulation/theory studies, as well as a fit to the mass line-shape, we concluded that, while at $\sqrt{s}=200$ GeV the backgrounds from Drell-Yan and $b\bar{b}$ are comparable, at $\sqrt{s}=500$ GeV the background is dominated by (open) $b\bar{b}$ pair production. This background has now been carefully subtracted, and the systematic uncertainties have been assessed. The systematic uncertainties include the simulation of the trigger cuts, the input polarization for the embedded Y's used for the acceptance correction, and the particle-identification cuts (which affect the purity of the electrons).

The finalized physics result is shown in Fig. 2. This result will be included in a manuscript that also includes additional physics results from other groups in the STAR experiment that are not yet finalized. Therefore, publication of the result will wait for the completion of the other corresponding analysis.

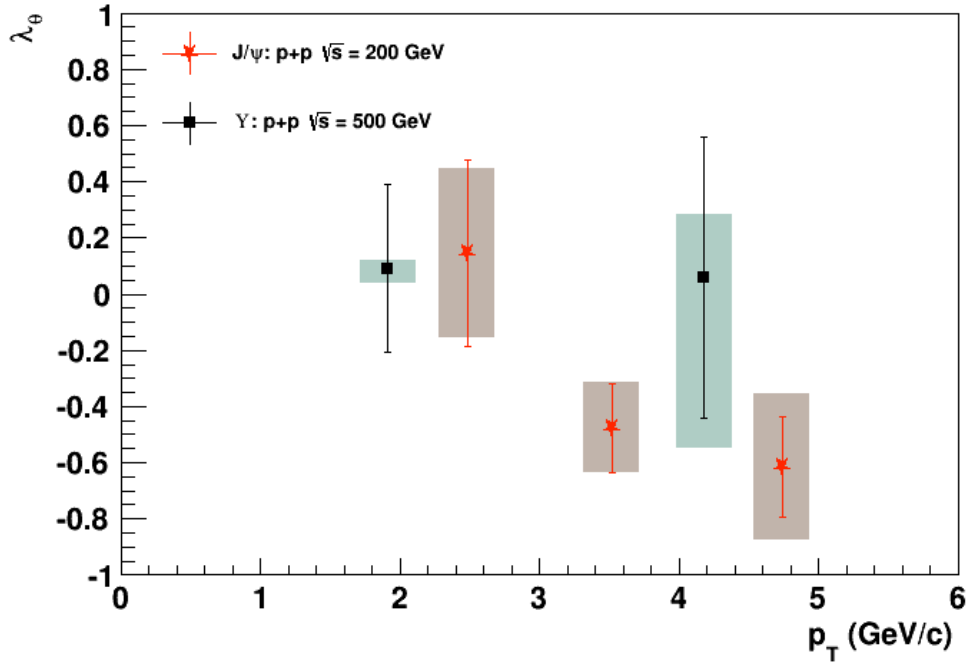


FIG. 2. Polarization parameter λ_θ as a function of p_T , measured in Run-11 500-GeV p+p collisions, for Y particles (our results), compared to J/ψ particle measured in 200-GeV collisions (another STAR group's published results [6]).

- [1] X.N. Wang, Z. Huang, and I. Sarcevic, Phys. Rev. Lett. **77**, 231 (1996).
- [2] H. Zhang, J.F. Owens, E. Wang, and X.-N. Wang, Phys. Rev. Lett. **103**, 032302 (2009).
- [3] B.I. Abelev *et al.* (STAR Collaboration), Phys. Rev. C **82**:034909, 2010.
- [4] J.P. Lansberg, Eur. Phys. J. C **60**, 693 (2009).
- [5] A. Abulencia *et al.* (CDF Collaboration), Phys. Rev. Lett. **99**, 132001 (2007).
- [6] L. Adamczyk *et al.* (STAR Collaboration), Phys. Lett. B **739**, 180 (2014).

Inelastic scattering of alphas on ^{24}Mg as a surrogate for stellar carbon burning

J.M. Munson,¹ E.B. Norman,¹ J.T. Burke,² R.J. Casperson,² E. McCleskey,
M. McCleskey, R. Hughes,² S. Ota,² A. Czeszumski,¹
A. Saastamoinen, and A. Spiridon

¹University of California-Berkeley, Berkeley, California

²Lawrence Livermore National Laboratory, Livermore, California

The carbon burning nuclear reactions $^{12}\text{C}(^{12}\text{C},\alpha)^{20}\text{Ne}$, $^{12}\text{C}(^{12}\text{C},\text{p})^{23}\text{Na}$, and $^{12}\text{C}(^{12}\text{C},\text{n})^{23}\text{Mg}$ are important during supernova explosions as well as in the later stages of evolution for larger stars. The Gamow window for these reactions is typically around 1.5 MeV, however direct measurements at energies in this range are very difficult due to the large coulomb barrier. A surrogate measurement was made by inelastically scattering alpha particles on ^{24}Mg . This allows the relative reaction rate for each reaction channel to be investigated in an energy region inaccessible to direct measurement.

The final measurement for this project was made at the TAMU Cyclotron Institute using the K150 Cyclotron and the STARLiTeR target chamber and detector system. This run, not including setup, ran from November 11, 2014 until November 18, 2014. A 40 MeV alpha beam was directed at a thin enriched ^{24}Mg target, and the emitted particles and gammas were detected by two “S2” type silicon detectors and six “Clover” germanium detectors respectively.

Fig.1 is the result of coincidence measurements in the silicon detectors for the scattered alpha and the ejected particle. Horizontal bands indicate states in the daughter nuclei. For excited states of the daughter the coincident emitted gamma was used in the identification of an event as well.

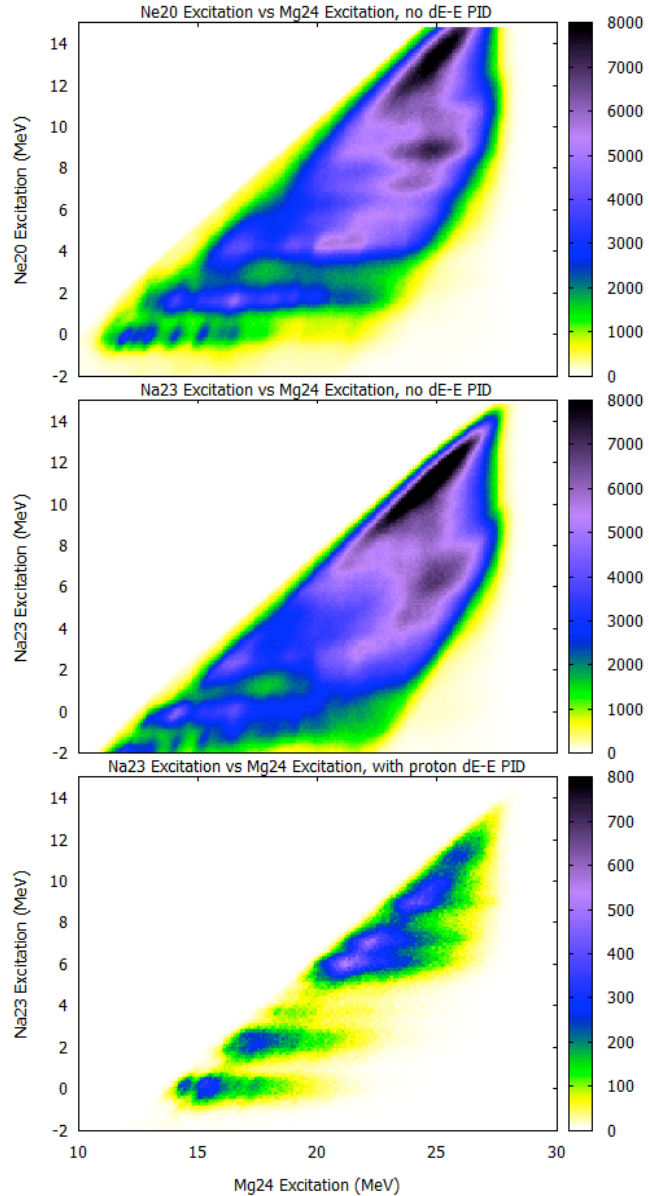


FIG. 1. ^{24}Mg and product nucleus excitation.

The alpha and proton branching ratios, including separate branches for the ground and excited states of the resulting ^{20}Ne and ^{23}Na , as well as the neutron channels populating the first state of ^{23}Mg were successfully measured for the excitation range of interest for a $^{12}\text{C}+^{12}\text{C}$ compound nucleus in stellar environments. These measurements are shown in Fig. 2. The

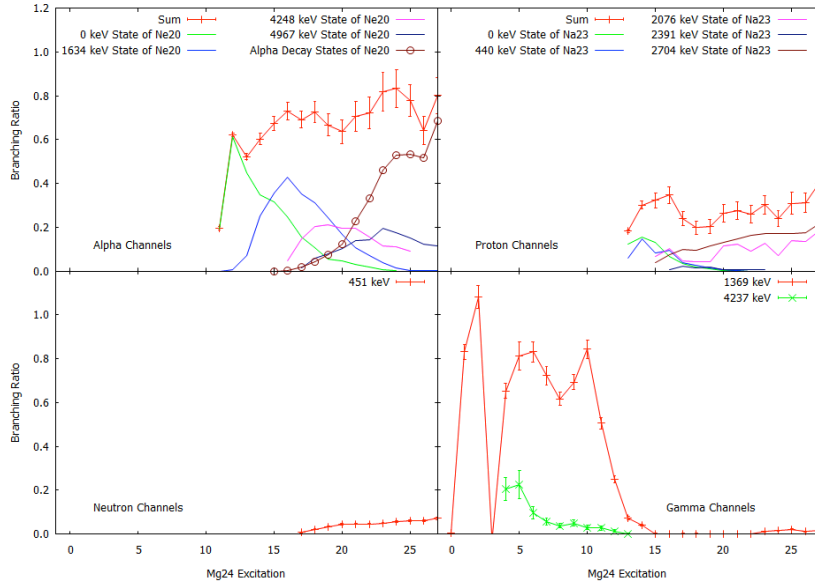


FIG. 2. Branching Ratios.

summed branching ratios for the alpha,

proton, and neutron channels are shown in Figure 3, and are normalized such that the total of all measured branches is 1. Prior to normalization, the sum of all branching ratios in the energy range of interest was close to 1.

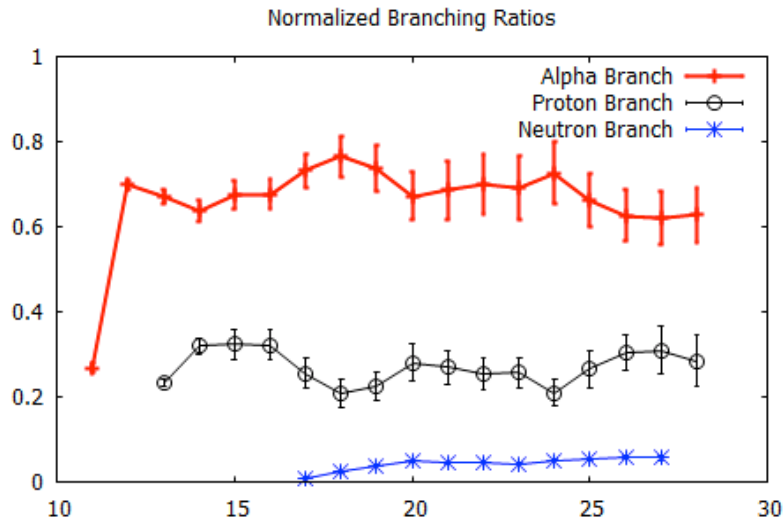


FIG. 3. Normalized Branching Ratios.

Additionally, angular scattering cross sections for a 40 MeV beam on ^{24}Mg were determined for several excited states using the same data. These measurements are shown in Fig.

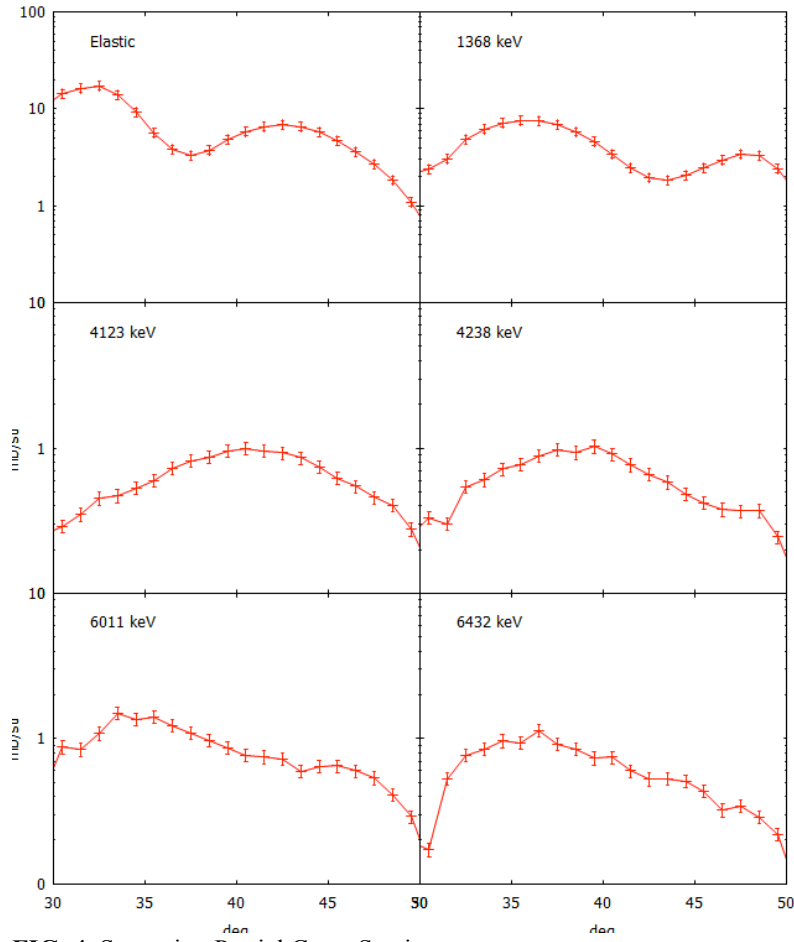


FIG. 4. Scattering Partial Cross Sections.

4.

SECTION III
NUCLEAR THEORY

Neutron stars in the framework of Landau's theory

H. Zheng, J. Sahagun, and A. Bonasera

A general formula of the symmetry energy for many-body interaction is proposed and the commonly used two-body interaction symmetry energy is recovered. Within Landau's theory (Lt), we generalize two equations of state (EoS) CCS δ 3 and CCS δ 5 to asymmetric nuclear matter. We assume that the density and density difference between protons and neutrons divided by their sum are order parameters. We use different EoS to study neutron stars by solving the TOV equations. We demonstrate that different EoS give different mass and radius relation for neutron stars even when they have exactly the same ground state (gs) properties (E/A , ρ_0 , K , S , L and K_{sym}). Furthermore, for one EoS we change K_{sym} and fix all the other gs parameters. We find that for some K_{sym} the EoS becomes unstable at high density even for neutron matter. This suggests that a neutron star (NS) can exist below and above the instability region but in different states: a quark gluon plasma (QGP) at high density and baryonic matter at low density [1].

We fix incompressibility $K=225$ MeV, symmetry energy $S=28.5$ MeV, and the slope of symmetry energy $L=73$ MeV from Skyrme EoS CK225 $_1$ [1]. In this case, EoS CK225 $_1$, CK225 and CCS δ 3 have the same values for K , S , L and K_{sym} . This motivates us to fix the same values of S , L and K_{sym} for EoS CCS δ 5. For the four EoS, CK225 $_1$, CK225, CCS δ 3 and CCS δ 5, we solve the TOV equations for the PNM to obtain the mass-radius relation of neutron stars. The results are shown in Fig. 1.

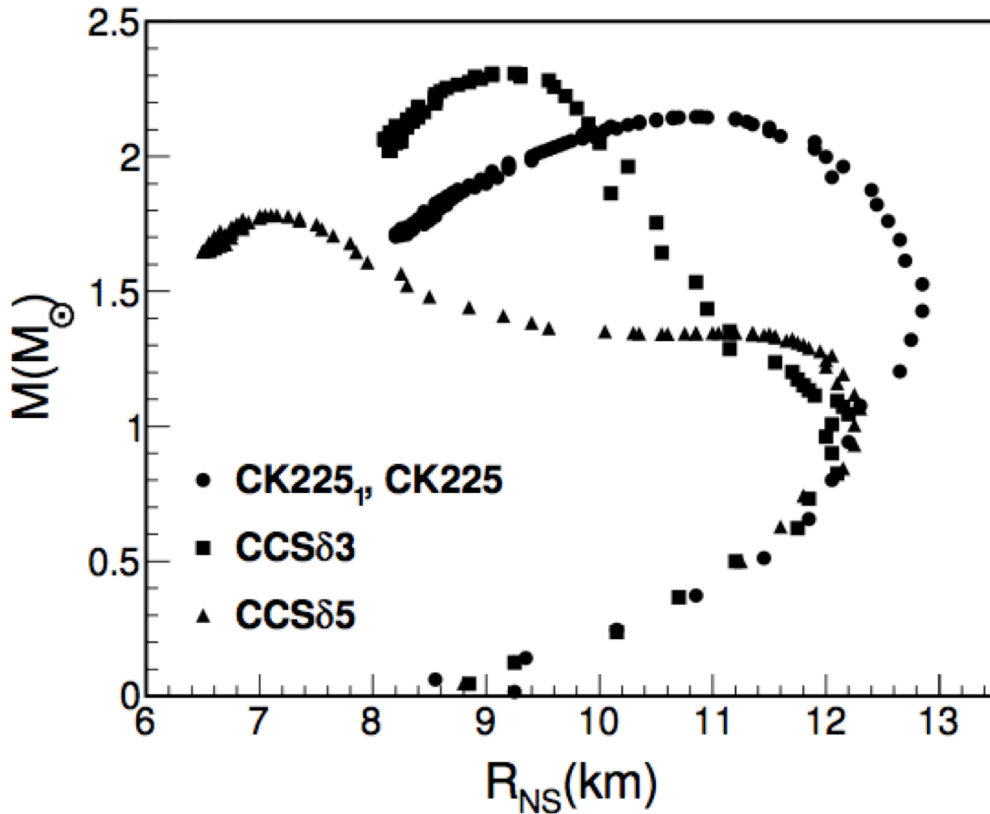


FIG. 1. The NS mass-radius relation for CK225 $_1$, CK225, CCS δ 3 and CCS δ 5 with same values of $K=225$ MeV, $S=28.5$ MeV, $L=73$ MeV and $K_{\text{sym}} = -25$ MeV.

We can see that the mass-radius relations for the neutron stars are different for the four EoS (CK225₁ and CK225 are the same in this case) even though they have the same values of K , S , L and K_{sym} . This indicates that the mass-radius relation of the NS is not only determined by K , S , L and K_{sym} , but the high density dependence of the EoS is crucial. We also notice that there are wiggles in the mass-radius relation of PNM NS for CCS δ 3 and CCS δ 5 rather than CK225₁ and CK225 because of a cross-over at high density for the two EoS. Thus, the second order PT assumed in deriving CCS δ 3 and CCS δ 5 becomes cross-over for these parameters choice. The maximum mass of the NS for CCS δ 3 is larger than the one for CK225₁ or CK225. The reason for this is because of the higher power of ρ in CCS δ 3 compared to CK225. But the maximum mass of the NS for CCS δ 5 (which contains even higher power density values) is lower than the one for CCS δ 3. The ‘missed phase transition’ or cross-over softens the EoS and causes the pressure for CCS δ 5 to decrease compared to the one for CCS δ 3 at the same density.

The EoS CCS δ 5 displays an instability when $K_{\text{sym}} = -215 \text{ MeV}$ corresponding to a first order PT. In this case the TOV equations cannot be solved in the instability region. We have used the Maxwell construction to determine the densities where the two phases (which we call phase A and B) are separated. In Fig. 2, we plot the results obtained solving the TOV equations when the central density is $10\rho_0$.

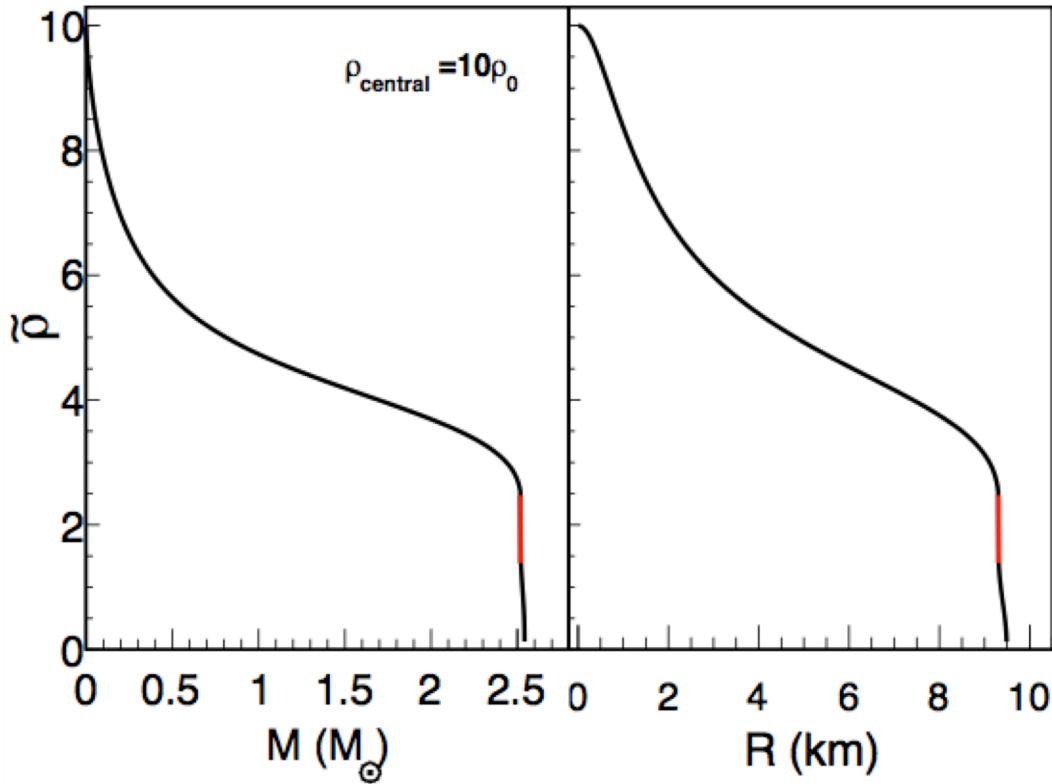


FIG. 2. The density profiles of a neutron star with central density $10\rho_0$ for EoS CCS δ 5 when $S = 28.5 \text{ MeV}$, $L = 50 \text{ MeV}$ and $K_{\text{sym}} = -215 \text{ MeV}$. The red lines are the Maxwell construction in the instability region.

[1] H. Zhang, J. Sahagun, and A. Bonasera, arXiv: 1411.3030.

Asymptotic normalization coefficients and spectroscopic factors from deuteron stripping reactions

D.Y. Pang and A.M. Mukhamedzhanov

We present the analysis of three deuteron stripping reactions, $^{14}\text{C}(d,p)^{15}\text{C}$, $^{58}\text{Ni}(d,p)^{59}\text{Ni}$ and $^{116}\text{Sn}(d,p)^{117}\text{Sn}$ using the combined method [1], in which each reaction is analyzed at low and significantly higher energies. At low energies all these reactions are peripheral and the experimental asymptotic normalization coefficients (ANCs) are determined with accuracy about 10%. At higher energies we determine the spectroscopic factors (SFs) by fixing the normalization of the peripheral parts of the reaction amplitudes governed by the ANCs found from the low-energy data. The combined method imposes a strict limitation on the variation of the geometrical parameters of the single-particle potential, which can be arbitrarily taken in the standard approach. By checking the compatibility of the ANCs and SFs using the combined method we reveal the flaw in the contemporary nuclear reaction theory in treating the nuclear interior, which is the most crucial part in the determination of the SFs.

The work has been published in Phys. Rev. C 90, 044611 (2014).

[1] A.M. Mukhamedzhanov and F.M. Nunes, Phys. Rev. C **72**, 017602 (2005)

Big bang nucleosynthesis revisited via Trojan Horse method measurements

R.G. Pizzone, R. Spartá, C.A. Bertulani, C. Spitaleri, M. La Cognata, J. Lalmansingh, L. Lamia,
A. Mukhamedzhanov, and A. Tumino

Nuclear reaction rates are among the most important input for understanding the primordial nucleosynthesis and therefore for a quantitative description of the early Universe. An up-to-date compilation of direct cross sections of ${}^2\text{H}(d,p){}^3\text{H}$, ${}^2\text{H}(d,n){}^3\text{He}$, ${}^7\text{Li}(p,\alpha){}^4\text{He}$ and ${}^3\text{He}(d,p){}^4\text{He}$ and reactions is given. These are among the most uncertain cross sections used and input for Big Bang nucleosynthesis calculations. Their measurements through the Trojan Horse Method are also reviewed and compared with direct data. The reaction rates and the corresponding recommended errors in this work were used as input for primordial nucleosynthesis calculations to evaluate their impact on the ${}^2\text{H}$, ${}^3,4\text{He}$ and ${}^7\text{Li}$ primordial abundances, which are then compared with observations.

This work has been published in the *Astrophys. J.* **786**, 112 (2014).

Constraining the 6.05 MeV 0^+ and 6.13 MeV 3^- cascade transitions in the $^{12}\text{C}(\alpha,\gamma)^{16}\text{O}$ reaction using the asymptotic normalization coefficients

M.L. Avila, G.V. Rogachev, E. Koshchiy, L.T. Baby, J. Belarge, K.W. Kemper, A.N. Kuchera, A.M. Mukhamedzhanov, D. Santiago-Gonzalez, and E. Uberseder

The $^{12}\text{C}(\alpha,\gamma)^{16}\text{O}$ reaction plays a fundamental role in astrophysics and needs to be known with accuracy better than 10%. Cascade γ transitions through the excited states of ^{16}O are contributing to the uncertainty. We constrained the contribution of the 0^+ (6.05 MeV) and 3^- (6.13 MeV) cascade transitions by measuring the asymptotic normalization coefficients for these states using the α -transfer reaction $^6\text{Li}(^{12}\text{C},d)^{16}\text{O}$ at sub-Coulomb energy. The contribution of the 0^+ and 3^- cascade transitions at 300 keV is found to be 1.96 ± 0.3 and 0.12 ± 0.04 keVb for destructive interference of the direct and resonance capture 4.36 ± 0.45 and 1.44 ± 0.12 keVb for constructive interference, respectively. The combined contribution of the 0^+ and 3^- cascade transitions to the $^{12}\text{C}(\alpha,\gamma)^{16}\text{O}$ reaction cross section at 300 keV does not exceed 4%. Significant uncertainties have been dramatically reduced.

The work has been published in Phys. Rev. Lett. **114**, 071101 (2015).

Determination of the asymptotic normalization coefficients for the $^{14}\text{C} + n \leftrightarrow ^{15}\text{C}$, $^{14}\text{C}(n,\gamma)^{15}\text{C}$ reaction rate and evaluation of a new method to determine spectroscopic factors

M. McCleskey, A.M. Mukhamedzhanov, L. Trache, R.E. Tribble, A. Banu, V. Eremenko, V.Z. Goldberg, Y.-W. Lui, E. McCleskey, B.T. Roeder, A. Spiridon, F. Carstoiu, V. Burjan, Z. Hon, and I.J. Thompson

The $^{14}\text{C} + n \leftrightarrow ^{15}\text{C}$ system has been used as a test case in the evaluation of a new method to determine spectroscopic factors that uses the asymptotic normalization coefficient (ANC). The method proved to be unsuccessful for this case. As part of this experimental program, the ANCs for the ^{15}C ground state and first excited state were determined using a heavy-ion neutron transfer reaction as well as the inverse kinematics (d,p) reaction, measured at the Texas A&M Cyclotron Institute. The values $C_{2s1/2}^2 = 1.88 \pm 0.18 \text{ fm}^{-1}$ for the ground state and $C_{1d5/2}^2 = (4.25 \pm 0.38) \times 10^{-3} \text{ fm}^{-1}$ for the first excited state ($E_{exc} = 740 \text{ keV}$) were obtained. The ANCs were used to evaluate the astrophysical direct neutron capture rate on ^{14}C , which was then compared with the most recent direct measurement and found to be in good agreement. A study of the ^{15}C spectroscopic factor via its mirror nucleus ^{15}F and a new insight into deuteron stripping theory are also presented.

This work has been published in Phys. Rev. C **89**, 044605 (2014).

Indirect techniques in nuclear astrophysics: A review

R.E. Tribble, C.A. Bertulani, M. La Cognata, A.M. Mukhamedzhanov, and C. Spitaleri

In this review, we discuss the present status of three indirect techniques that are used to determine reaction rates for stellar burning processes, Asymptotic Normalization Coefficients, the Trojan Horse Method, and Coulomb Dissociation. A comprehensive review of the theory behind each of these techniques is presented. This is followed by an overview of the experiments that have been carried out using these indirect approaches.

The techniques are now well established tools in nuclear astrophysics. As rare isotope beam facilities are developed around the world, indirect methods will play a major role in determining rates for reactions that occur on short lived isotopes. The work that has been done to date with rare-isotope beams represents only the first steps in this effort. Beam intensities and beam species will expand dramatically by the end of this decade opening up many new opportunities to further utilize indirect tools to learn about the nuclear reactions that drive the cosmos.

This work has been published in *Rep. Prog. Phys.* **77** 106901 (2014).

Low-energy R-matrix fit for the ${}^6\text{L}(d,\alpha){}^4\text{He}$ S factor

J. Grineviciute, L. Lamia, A.M. Mukhamedzhanov, C. Spitaleri, and M. La Cognata

Information about the ${}^6\text{L}(d,\alpha){}^4\text{He}$ reaction rates of astrophysical interest can be obtained by extrapolating direct data to lower energies, or by indirect methods. The indirect Trojan Horse method, as well as various R-matrix and polynomial fits to direct data, estimate electron screening energies much larger than the adiabatic limit. The astrophysical S factor for the low energy ${}^6\text{L}(d,\alpha){}^4\text{He}$ reaction dominated by broad subthreshold resonances has been analyzed using the single, two and three level R-matrix fits. For the low energy R matrix we use the s-wave approximation for the deuteron. The resulting ambiguity due to the choice of channel radii is large in a single-level fit as well as in the fit that considers three subthreshold resonances. Our goal is to check possibility of determination of the electron screening potential from the low energy astrophysical S factors. We find that parameters depend on the number of the subthreshold states involved in the fitting. We consider the fit with three subthreshold states as the most reliable. We find that the extracted screening potential depends on the used procedure. If we first fit the S factor varying all the parameters at energies above 60 keV, at which the electron screening potential can be neglected, and then fixing all the parameters and varying only U_e to fit the astrophysical factor at energies below 1 MeV, we obtain $U_e = 71.4$ eV. However, if we fit the S factor at energies below 1 MeV varying all the parameters simultaneously including U_e , we get $U_e = 149.5$ eV. Thus, the result strongly depends on the fitting procedure. We may conclude that the assumption that electron screening effects are negligible at energies above 50 keV is not valid and our recommended value is $U_e = 149.5$ eV. Note, that other obtained fitting parameters are also sensitive to the fitting procedure.

The work has been published in Phys. Rev. C **91**, 014601 (2015).

Measurement of the 10 keV resonance in the $^{10}\text{B}(p, \alpha_0)^7\text{Be}$ reaction via the Trojan Horse method

C. Spitaleri, L. Lamia, S.M.R. Puglia, S. Romano, M. La Cognata, V. Crucilla, R.G. Pizzone, G.G. Rapisarda, M.L. Sergi, M. Gimenez Del Santo, N. Carlin, M.G. Munhoz, F.A. Souza, A. Szanto de Toledo, A. Tumino, B. Irgaziev, A. Mukhamedzhanov, G. Tabacaru, V. Burjan, V. Kroha, Z. Hons, J. Mrazek, Shu-Hua Zhou, Chengbo Li, Qungang Wen, Y. Wakabayashi, H. Yamaguchi, and E. Somorjai

The $^{10}\text{B}(p, \alpha_0)^7\text{Be}$ bare nucleus astrophysical $S(E)$ factor has been measured for the first time at energies from about 100 keV down to about 5 keV by means of the Trojan Horse method (THM). In this energy region, the $S(E)$ factor is strongly dominated by the 8.699 MeV ^{11}C level ($J^\pi = 5/2^+$), producing an s-wave resonance centered at about 10 keV in the entrance channel. Up to now, only the high-energy tail of this resonance has been measured, while the low-energy trend is extrapolated from the available direct data. The THM has been applied to the quasifree $^2\text{H}(^{10}\text{B}, \alpha_0^7\text{Be})n$ reaction induced at a boron-beam energy of 24.5 MeV. An accurate analysis leads to the determination of the $^{10}\text{B}(p, \alpha_0)^7\text{Be}$ $S(E)$ factor and of the corresponding electron screening potential U_e , thus giving for the first time an independent evaluation of it.

This work was published in *Phys. Rev. C* **90**, 035801 (2014).

New determination of the ${}^2\text{H}(\text{d,p}){}^3\text{H}$ and ${}^2\text{H}(\text{d,n}){}^3\text{He}$ reaction rates at astrophysical energies

A. Tumino, R. Spartà, C. Spitaleri, A.M. Mukhamedzhanov, S. Typel, R.G. Pizzone, E. Tognelli, S. Degl'Innocenti, V. Burjan, V. Kroha, Z. Hons, M. La Cognata, L. Lamia, J. Mrazek, S. Piskor, P.G. Prada Moroni, G.G. Rapisarda, S. Romano, and M.L. Sergi

The cross-sections of the ${}^2\text{H}(\text{d,p}){}^3\text{H}$ and ${}^2\text{H}(\text{d,n}){}^3\text{He}$ reactions have been measured via the Trojan Horse method applied to the quasi free ${}^2\text{H}({}^3\text{He},\text{p}){}^3\text{H}$ and ${}^2\text{H}({}^3\text{He},\text{n}){}^3\text{He}$ processes at 18 MeV off the proton in ${}^3\text{He}$. For the first time, the bare nucleus $S(E)$ factors have been determined from 1.5 MeV, across the relevant region for standard Big Bang nucleosynthesis, down to the thermal energies of deuterium burning in the pre main sequence (PMS) phase of stellar evolution, as well as of future fusion reactors. Both the energy dependence and the absolute value of the $S(E)$ factors deviate by more than 15% from the available direct data and existing fitting curves, with substantial variations in the electron screening by more than 50%. As a consequence, the reaction rates for astrophysics experience relevant changes, with a maximum increase of up to 20% at the temperatures of the PMS phase. From a recent primordial abundance sensitivity study, it turns out that the ${}^2\text{H}(\text{d,n}){}^3\text{He}$ reaction is quite influential on ${}^7\text{Li}$, and the present change in the reaction rate leads to a decrease in its abundance by up to 10%. The present reaction rates have also been included in an updated version of the FRANEC evolutionary code to analyze their influence on the central deuterium abundance in PMS stars with different masses. The largest variation of about 10%–15% pertains to young stars (≤ 1 Myr) with masses $\geq 1M$. This work has been published in *Astrophys. J.* **785**, 96 (2014).

Optical model potential of $A = 3$ projectiles for 1p-shell nuclei

D.Y. Pang, W.M. Dean, and A.M. Mukhamedzhanov

A set of global optical potential parameters describing the elastic scattering of $A = 3$ particles ${}^3\text{He}$ and ${}^3\text{H}$ from 1p-shell nuclei, HT1p, is obtained by simultaneously fitting 118 sets of experimental data of ${}^3\text{He}$ and ${}^3\text{H}$ elastic scattering from ${}^9\text{Be}$, ${}^{10}\text{B}$, ${}^{11}\text{B}$, ${}^{12}\text{C}$, ${}^{13}\text{C}$, ${}^{14}\text{C}$, ${}^{14}\text{N}$, ${}^{15}\text{N}$, ${}^{16}\text{O}$, ${}^{17}\text{O}$, and ${}^{18}\text{O}$ within the incident energy interval $4 \leq E \leq 118.5$ MeV and 25 sets of elastic scattering data on ${}^6\text{Li}$ and ${}^7\text{Li}$ targets from $3 \leq E \leq 44$ MeV. HT1p is found to be superior to GDP08 [1], which is a systematic potential designed for the heavy-target region, in reproduction of the angular distributions of elastic scattering cross sections of ${}^3\text{He}$ and ${}^3\text{H}$ from 1p-shell nuclei at energies below 100 MeV. Above 100 MeV GDP08 is found to be better than HT1p.

This work has been published in Phys. Rev. C **91**, 024611 (2015).

[1] D.Y. Pang, P. Roussel-Chomaz, H. Savajols, R.L. Varner, and R. Wolski, Phys. Rev. C **79**, 024615 (2009)

Surface-integral formalism of deuteron stripping

A.M. Mukhamedzhanov, D.Y. Pang, C.A. Bertulani, and A.S. Kadyrov

The purpose of this paper is to address an alternative theory of deuteron stripping to resonance states, which is based on the surface integral formalism and continuum discretized coupled channels (CDCC) [1, 2].

First we demonstrate how the surface integral formalism works in the three-body model and then we consider a more realistic problem in which a composite structure of target nuclei is taken into account via optical potentials. We explore different choices of channel wave functions and transition operators and show that a conventional CDCC volume matrix element can be written in terms of the surface-integral matrix element, which is peripheral, and the auxiliary matrix element, which determines the contribution of the nuclear interior over the variable r_{nA} . This auxiliary matrix element appears due to the inconsistency in treating of the n - A potential: this potential should be real in the final state to support bound states or resonance scattering and complex in the initial state to describe n - A scattering.

Our main result is formulation of the theory of the stripping to resonance states using the prior form of the surface integral formalism and CDCC method. It is demonstrated that the conventional CDCC volume matrix element coincides with the surface matrix element, which converges for the stripping to the resonance state. Also the surface representation (over the variable r_{nA}) of the stripping matrix element enhances the peripheral part of the amplitude although the internal contribution doesn't disappear and increases with increase of the deuteron energy.

Although the code for the surface-integral formalism in the CDCC approach is not yet available, we presented many calculations corroborating our findings both for the stripping to the bound state and the resonance.

This work has been published in Phys. Rev. C **90**, 034604 (2014).

[1] A.S. Kadyrov *et al.*, Ann. Phys. **324**, 1516 (2009).

[2] I. Bray *et al.*, Phys. Rep. **520**, 135 (2012).

Trojan Horse particle invariance in fusion reactions

R.G. Pizzone, C. Spitaleri, C. Bertulani, A. Mukhamedzhanov, L. Blokhintsev, M. La Cognata,
L. Lamia, R. Spartá, and A. Tumino

Trojan Horse method plays an important part for the measurement of several charged particle induced reactions cross sections of astrophysical interest. In order to better understand its cornerstones and the related applications to different astrophysical scenarios several tests were performed to verify all its properties and the possible future perspectives. The Trojan Horse nucleus invariance for the binary reactions $d(d,p)t$,

${}^6,7\text{Li}(p,\alpha){}^3,4\text{He}$ was therefore tested using the appropriate quasi free break-ups, respectively. In the first cases results from ${}^6\text{Li}$ and ${}^3\text{He}$ break up were used, while for the lithium fusion reactions break-ups of ${}^2\text{H}$ and ${}^3\text{He}$ were compared. The astrophysical $S(E)$ -factors for the different processes were then extracted in the framework of the Plane Wave Approximation applied to the different break-up schemes. The obtained results are compared with direct data as well as with previous indirect investigations. The very good agreement between data coming from different break-up schemes confirms the applicability of the plane wave approximation and suggests the independence of binary indirect cross section on the chosen Trojan Horse nucleus also for the present cases. Moreover the astrophysical implications of the results will also be discussed in details.

The work has been published in Eur. Phys. J. Web of Conferences **86**, 00034 (2015),

Investigating discrepancy of the isoscalar giant octupole resonance in ^{92,96,98,100}Mo

D.H. Youngblood, Y.-W. Lui, Krishichayan,¹ J. Button, G. Bonasera, and S. Shlomo

¹*Department of Physics, Duke University, and Triangle Universities Nuclear Laboratory, Durham, North Carolina*

The microscopic mean-field based Random Phase Approximation (RPA) theory provides a good description of collective states in nuclei. It is common to calculate the RPA states $|n\rangle$ with the corresponding energies E_n , and obtain the strength function

$$S(E) = \sum_n |\langle 0|F|n\rangle|^2 \delta(E-E_n), \quad (1)$$

for a certain single particle scattering operator $F = \sum f(i)$, and then determine the energy moments

$$m_k = \int E^k S(E) dE. \quad (2)$$

The constrained energy, E_{con} , centroid energy, E_{cen} , and the scaling energy, E_s , of the resonance are then obtained from:

$$E_{\text{con}} = (m_1/m_{-1})^{1/2}, \quad E_{\text{cen}} = m_1/m_0, \quad E_s = (m_3/m_1)^{1/2}. \quad (3)$$

In a fully self-consistent mean-field calculation of the response function, one adopts an effective two-nucleon interaction V , usually fitted to ground states properties of nuclei, and determines the HF mean-field. Then, the RPA calculation is carried out with all the components of the two-body interaction using a large configuration space. In this sense, the calculations are fully self-consistent.

Recently a paper [1] found the Isoscalar Giant Octupole Resonance at ~ 21.5 MeV, about 5 MeV below the prediction of the KDE0v1 Skyrme effective nucleon-nucleon interaction in ^{92,96,98,100}Mo and ^{90,92,94}Zr. We carried out HF-RPA calculation of the centroid energy for many different Skyrme interactions found in the literature, using an occupation approximation for the single particle orbits of the open shell nuclei. As can be seen in Figs.1 and 2 we find that all the interactions considered predict the Octupole resonance to be above the experimental value. We also see a strong dependence of the Centroid Energy on the effective mass. The reason for the discrepancy between theory and experiment currently under investigation [2].

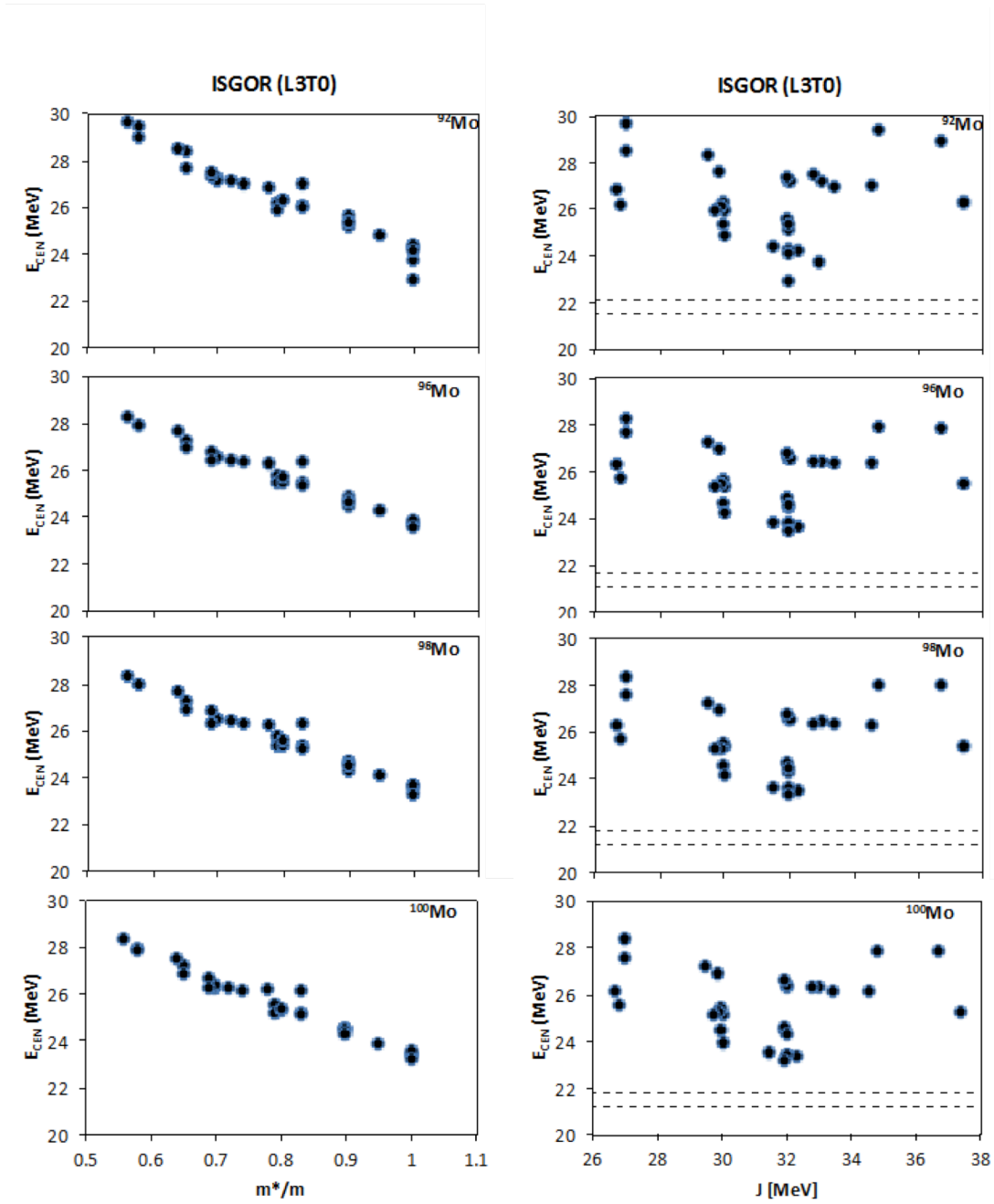


FIG. 1. Results of the HF-RPA calculations, each point is a different Skyrme interaction. Plotted are the centroid energies, E_{cen} , of the ISGOR for $^{92,96,98,100}\text{Mo}$ as a function of the effective mass (left) and the Symmetry Energy coefficient (right).

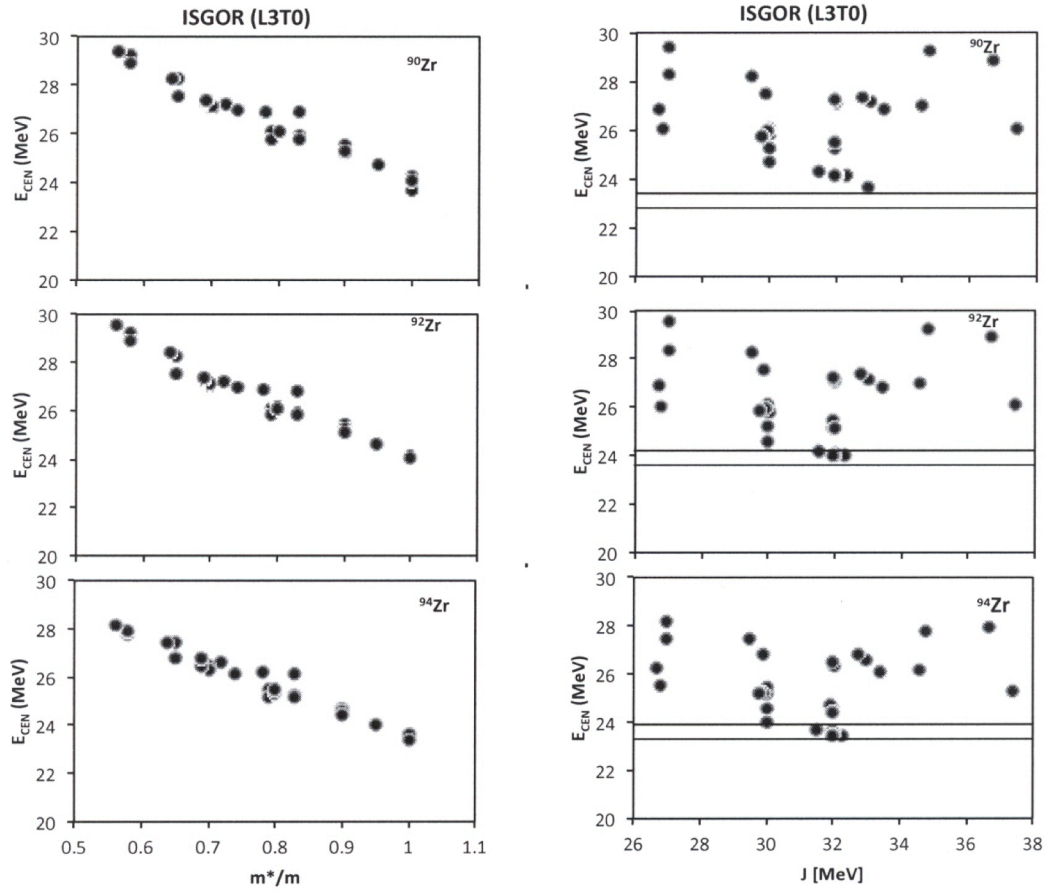


FIG. 2. Results of the HF-RPA calculations, each point is a different Skyrme interaction. Plotted are the centroid energies, E_{cen} , of the ISGOR for $^{90,92,94}\text{Zr}$ as a function of the effective mass (left) and the Symmetry Energy coefficient(right).

- [1] D.H. Youngblood *et al.*, Phys. Rev. C (submitted).
- [2] G. Bonasera *et al.*, in preparation.

Isoscalar giant quadrupole resonances in select spherical nuclei and the effective mass

M.R. Anders, G. Bonasera, and S. Shlomo

We carried out fully self-consistent Hartree-Fock based Random Phase Approximation (HF-RPA) calculations of the centroid energies of Isoscalar and Isovector resonances up to $L=3$. We selected various spherical nuclei over a wide range of mass. We perform very precise calculations using over 30 commonly employed Skyrme-type effective nucleon-nucleon interaction found in the literature.

Pearson Correlation function is also calculated for every Nuclear Matter property and each resonance. By looking at which interactions predict correctly the experimental value, and if we have a high correlation, we can set limits on the values of Nuclear Matter. For example Fig. 1 shows the

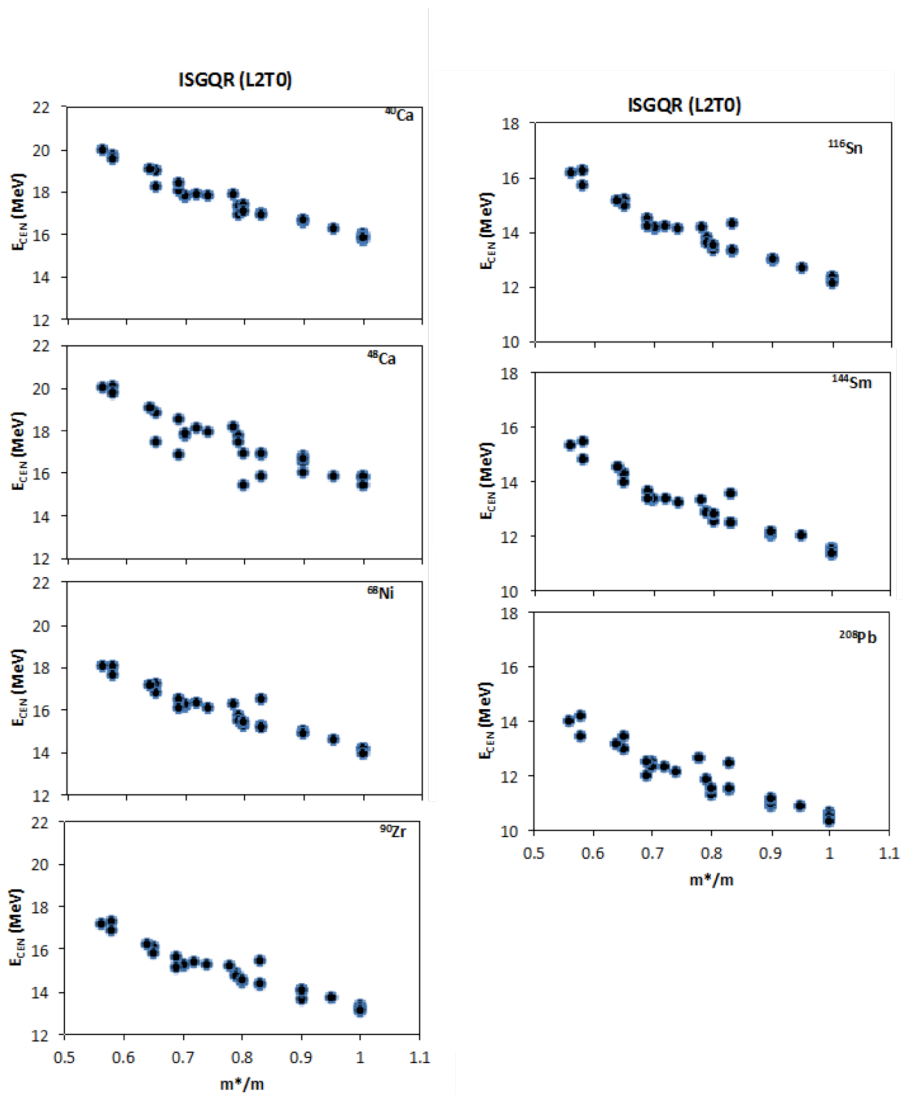


FIG. 1. Results of the HF-RPA calculations, each point is a different Skyrme interaction. Plotted are the centroid energies, E_{cen} , of the ISGQR for ^{40}Ca , ^{48}Ca , ^{68}Ni , ^{90}Zr , ^{116}Sn , ^{144}Sm , ^{208}Pb as a function of the effective mass. The dashed line represent the experimental error range.

calculated Centroid Energies of the Isoscalar Giant Quadrupole Resonance plotted against the effective mass, here we see a trend of decreasing Energy with increasing effective mass. We also see that the interactions with effective mass between 0.7-0.9 reproduce the data better. Similar analysis is performed for other quantities [1] and these results will be used to fit a new interaction with improved predictive power.

[1] G. Bonasera *et al.*, in preparation for publication.

Measured difference between ^{206}Pb , ^{205}Tl charge distributions and the proton $3s_{1/2}$ wave function

M.R. Anders, S. Shlomo, and I. Talmi¹

¹*The Weizmann Institute of Science, Rehovot 76100, Israel*

The difference between the charge distributions of ^{206}Pb and ^{205}Tl , $\Delta\rho_c$, was measured many years ago [1, 2]. It offers a good opportunity to study possible effects of short range correlations on the shell model wave function of a proton in the $3s_{1/2}$ orbit. Effects of this kind were estimated by comparing measured cross sections of various reactions to those calculated using shell model wave functions. Usually, the measured values were lower than the calculated ones. The difference between the charge distributions considered here cannot be depleted. The integrated difference must be exactly equal to the charge difference between the two isotones, 1 proton charge. The effects of short range correlations in this case can only change the *shape* of the difference between the charge distributions.

The corresponding single particle potential for a nucleon is

$$V_{cen}(r) = E + \frac{\hbar^2}{2m} S(r) - V_{coul}(r), \quad S(r) = \frac{d^2 R}{dr^2} \frac{1}{R(r)}, \quad (1)$$

where $V_{coul}(r)$ is the Coulomb potential and $R(r)$ is related by $\psi_{nlj}(\vec{r}) = \frac{R_{nlj}(r)}{r} Y_{lj}$.

The single particle radial density $\rho(r)$ is related to the square of the radial wave function R by

$$R^2(r) = 4\pi r^2 \rho(r). \quad (2)$$

From (2) it is possible to extract the wave function $R(r)$ and use Eq. (1) to deduce the corresponding single particle potential, but this leads to numerical complications. Therefore, we developed a method to determine the potential directly from the density and its first and second derivatives. Using the Schrodinger equation for the radial wave-function $R(r)$, we obtain the simple relations

$$S(r) = \frac{1}{2R^2} \left[\frac{d^2(R^2)}{dr^2} - \frac{1}{2} \left[\frac{1}{R} \frac{d(R^2)}{dr} \right]^2 \right], \quad (3)$$

and

$$S(r) = \frac{1}{2\rho} \left[\frac{d^2\rho}{dr^2} + \frac{2}{r} \frac{d\rho}{dr} - \frac{1}{2\rho} \left(\frac{d\rho}{dr} \right)^2 \right]. \quad (4)$$

The experimental values of that difference have features which are very similar to those due to the wave function of a proton in a $3s_{1/2}$ orbit. Within the experimental error bars, all its values are non-negative and there are two zero values for $r > 0$ which correspond to the two nodes of the $3s$ wave function $R_p(r)/r$. If the point proton distribution $\Delta\rho_p(r)$ is due to a $3s$ wave function, two more

conditions should be satisfied, in addition to its having first and second derivatives for all r values. At r where $\Delta\rho_p(r) = 0$, also its first derivative should vanish. The condition that if $R_p(r) = 0$, also its second derivative must vanish at that r leads to the other condition. Where the point proton distribution $\Delta\rho_p(r) = 0$, the corresponding expression in the square brackets on the right hand side of (4) should vanish. These conditions are necessary for deriving the single particle potential V , using Eqs. (1) and (3) or (4), from a parametrized point proton distribution $\Delta\rho_p(r)$ fitted to the experimental data. It is difficult to see whether these conditions are satisfied by the measured difference of charge distributions. The experimental accuracy is not sufficient, especially near the zero values.

We started by deriving and employing a new relation [3] between the potential V and the single particle density and its first and second derivatives, Eqs. (1), (3) and (4). Around its minima, the experimental uncertainty in $\Delta\rho_c(r)$ is larger than its value. Hence, no reliable potential can be obtained.

In view of this situation, we tried to construct nuclear single particle potentials V whose proton $3s_{1/2}$ orbit in ^{206}Pb yield charge distributions which best fit the electron scattering data. We found several potentials which yield fair fits to the data (Fig. 1). The fair agreement with fitted potentials may be an

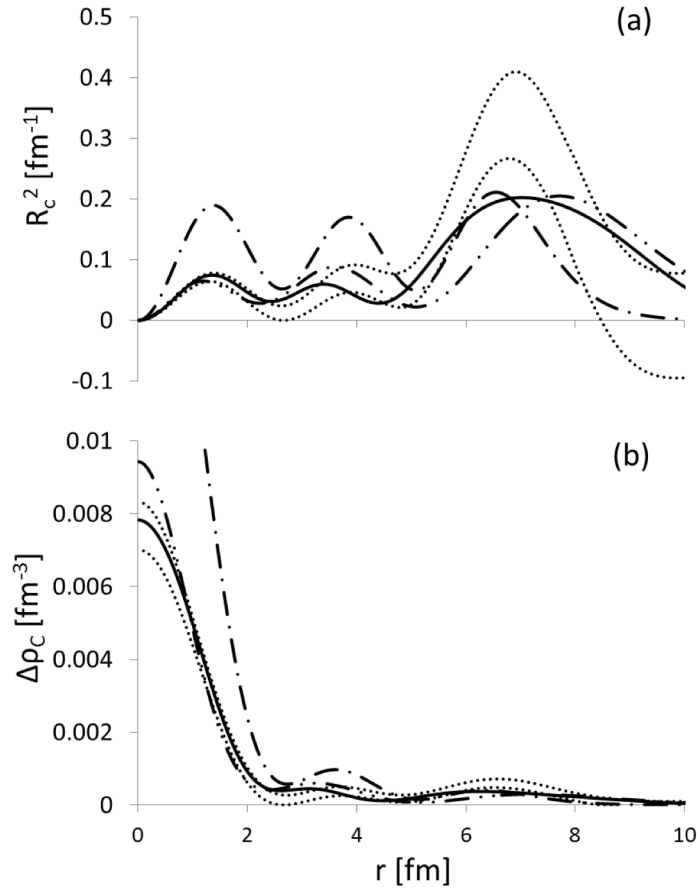


FIG. 1. Experimental values of $R_c^2(r) = 4\pi r^2 \Delta\rho_c(r)$ (a) and $\Delta\rho_c(r)$ (b) plotted between dotted lines of error limits. They are compared to calculated charge distributions due to the $3s_{1/2}$ wave functions of the fitted $V_F(r)$ potential (solid lines), the fitted Wood-Saxon $V_{FWS}(r)$ potential (double dotted-dashed lines) and the conventional $V_{WS}(r)$ potential (dashed-dotted lines).

indication that effects of short range correlations on charge distributions due to shell model wave functions are not significant. More accurate experimental data for $\Delta\rho_c(r)$ with uncertainty smaller by a factor of two or more may answer the question how well can the data be reproduced by a calculated $3s_{1/2}$ wave function.

[1] J.M. Cavedon *et al.*, Phys. Rev. Lett. **49**, 978 (1982).

[2] B. Frois *et al.*, Nucl. Phys. A396, 409c (1983).

[3] M.R. Anders *et al.*, to be published.

Properties of high-energy isoscalar monopole excitations in medium-heavy mass spherical nuclei

M.L. Gorelik,¹ S. Shlomo, B.A. Tulupov,^{1,2} and M.H. Urin¹

¹*National Research Nuclear University «MEPhI», Moscow, 115409 Russia*

²*Institute for Nuclear Research, RAS, Moscow, 117312 Russia*

Continued interest in experimental and theoretical studies of high-energy particle-hole-type isoscalar monopole (ISM) excitations in medium-heavy mass nuclei is mainly due to the possibility of determining of the nuclear matter incompressibility coefficient, a fundamental physical quantity. The value of this coefficient depends on the mean energy of the strength distribution, corresponding to the ISM external field r^2Y_{00} (in other words, on the energy of the isoscalar giant monopole resonance (ISGMR)). To deduce the ISGMR strength distribution from experimental data of (α, α') -inelastic scattering cross sections at small angles, it is usually assumed that the properly normalized quasi-classical collective model transition density of the ISGMR can be used within the folding model distorted wave Born approximation (FM-DWBA). It is important to point out that the quasi-classical collective model transition density is independent on the excitation energy.

In a microscopic approach, the input quantity for the analysis of the (α, α') -reaction cross section should be the energy-averaged double transition density (i.e. the energy-averaged product of energy dependent transition densities taken in different points). Being considered in a wide excitation-energy interval, this quantity is expected to be different from the product of the quasi-classical collective model transition densities or the product of microscopic transition densities, due to proper treatment of the shell structure of nuclei (i.e. the Landau damping) and also of the spreading effect. Developed recently, the particle-hole (p-h) dispersive optical model (PHDOM) [7,8] allows one to describe the energy-averaged double transition density at arbitrary (but high-enough) excitation energy and, in particular, to trace the change of this quantity from the ISGMR to ISGMR2.

Being an extension of the continuum-RPA, the PHDOM accounts for the Landau damping, coupling of high-energy (p-h)-type states to the single-particle (s-p) continuum and to many-quasiparticle configurations (the spreading effect). Within the model, Landau damping and coupling of high-energy (p-h)-type states to the s-p continuum are described microscopically in terms of the Landau-Migdal p-h interaction and a phenomenological mean field, partially consistent with this interaction. The spreading effect is treated phenomenologically in terms of the imaginary part of an effective s-p optical-model potential. The imaginary part also determines the corresponding real part via the proper dispersive relationship.

In this work we have carried out first evaluation of the energy-averaged double p-h transition density within the PHDOM. The calculations are performed for ISM excitations in ^{208}Pb . A wide excitation-energy interval is considered which includes the ISGMR and ISGMR2. The fractions of the energy-weighted sum-rule (EWSR) associated with the strength functions of these resonances, i.e. the energy-weighted strength functions divided by the corresponding EWSR, were also analyzed.

In Fig. 1 we show the calculated fractions of the energy-weighted strength functions $y_i(\omega) = \omega S_{V_{0,i}}(\omega)/(EWSR)_i$, obtained within the PHDOM for the external fields $V_{0,i}$, which are associated with the ISGMR ($i = 1$) and the ISGMR2 ($i = 2$), respectively. The fractions $y_i^{cRPA}(\omega)$ calculated within the RPA continuum version, i.e. in the approximation $W(\omega) = P(\omega) = 0$, are also shown in Fig. 1. As follows from the results presented in Fig. 1, the ISGMR in such heavy nucleus as ^{208}Pb exhibits (after taking the spreading effect into account) a well-formed resonance. The centroid energy ω_1 and total width Γ_1 (FWHM) of 13.8 MeV and 2.9 MeV, calculated within the used model for the excitation energy interval 10-35 MeV, are in agreement with experimental quantities of 13.96 MeV and 2.88 MeV, respectively. In contrast to the ISGMR its overtone does not exhibit a well-formed resonance. The energy centroid $\omega_1 = 22.7$ MeV calculated for the excitation energy interval 5-45 MeV is markedly less than the peak energy $\omega_{1,\text{peak}} = 31$ MeV of the main ISGMR2 maximum. The ISGMR2 width evaluated as $\Gamma = 2.35\sigma$ (σ^2 is the squared energy dispersion), $\Gamma = 22.8$ MeV, is markedly larger than the FWHM = 10 MeV found for the main ISGMR2 maximum. Concluding the description of the energy-weighted strength functions, we note that the calculated fractions $y_1(\omega)$ well exhaust the corresponding $EWSR_i$. Being calculated for the excitation energy intervals 5-35 MeV and 5-45 MeV, the quantities $N_i = \int y_i(\omega)d\omega$ are found close to unity: $N_1 = 0.986$ and $N_2 = 0.98$, respectively

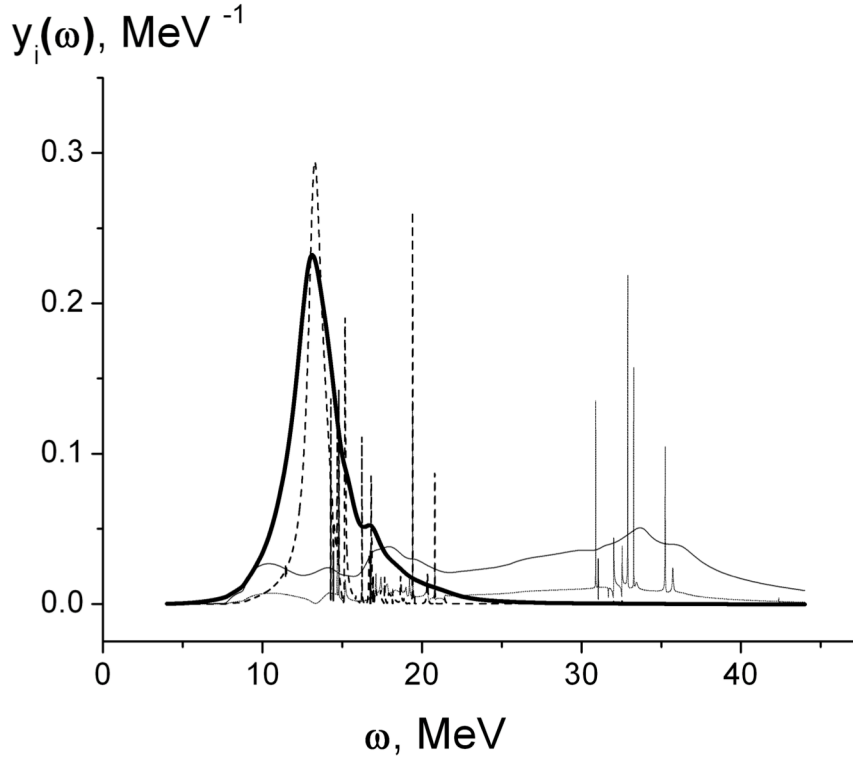


FIG. 1. Fractions of the energy-weighted strength functions, $y_i(\omega) = \omega S_{v_{0,i}}(\omega)/(EWSR)_i$ calculated within the PHDOM, ($y_1(\omega)$ – the thick solid line, $y_2(\omega)$ – the thin solid line) in comparison with $y_i^{cRPA}(\omega)$, calculated within the continuum-RPA ($y_1^{cRPA}(\omega)/2$ – thin dotted line, $y_2^{cRPA}(\omega)/4$ – thin dashed line).

[1] M.H. Urin, Phys. At. Nucl., **74**, 1189 (2011); M.H. Urin, Phys. Rev. C **87**, 044330 (2013).

Unitarity of the particle-hole dispersive optical model

M.L. Gorelik,¹ S. Shlomo, B.A. Tulupov,² and M.H. Urin¹

¹*National Research Nuclear University "MEPhI", Moscow Russia*

²*Institute for Nuclear Research, RAS, Moscow, Russia*

Within a recently developed particle-hole dispersive optical model (PHDOM) the main relaxation modes of high-energy particle-hole-type nuclear excitations are commonly taken into account [1]. In connection with the description of isoscalar monopole (ISM) excitations within the PHDOM (first results are obtained in [2]) the question of violation of the model unitarity arises. The source of the violation is the use of the optical-model Green functions. The latter satisfy equations that contain an optical-model energy-dependent term (having imaginary and real parts) which is added to the nuclear mean field. The signatures of violation are: (i) a non-zero value of the calculated strength function $S_1(\omega)$, corresponding to the "spurious" external field $V_1(r) = 1$ (the general expression for an isoscalar monopole (ISM) external field is $V(\vec{r}) = V(r)Y_{00}(\vec{n})$); (ii) negative values of the strength function $S_{r,2}(\omega)$ at high excitation energies ω , that leads to underestimation of the corresponding energy-weighted sum rule.

To restore unitarity of the model, we properly modify the energy-averaged ISM double transition density by adding to it a term involving the ground-state density normalized to unity. As a result, we get: (i) the zero value for the modified "spurious" strength function; (ii) the modified ISM strength functions, which are now evaluated for the modified external field $V(r) - \bar{V}$, with averaging over the ground-state density. Calculations are being performed for ^{208}Pb .

[1] M.H. Urin, Phys. At. Nucl. 2011. V.74. p.1189; Phys. Rev. C. **87**, 044330 (2013).

[2] M.L. Gorelik, S. Shlomo, B.A. Tulupov, and M.H. Urin, NUCLEUS 2014, Books of Abstracts, p.143; Phys. At. Nucl. 2015 (in press).

Jet fragmentation via recombination of parton showers in vacuum

K. Han, R. Fries, and C.M. Ko

We have devised a model to hadronize perturbative parton showers in jets based on quark recombination [1]. This is achieved by turning perturbative parton showers into showers of constituent quarks and antiquarks by gluon decay, and then applying Monte Carlo methods to recombine quarks and antiquarks using probabilities given by the overlap integrals of their Gaussian wave packets with meson and baryon Wigner functions [2]. For remnant quarks and antiquarks that are not used for recombination, they are connected to form short strings and subjected to the usual string fragmentation procedure in PYTHIA [3]. As an example, we have studied hadron production from e^+e^- collisions at center of mass energy of 200 GeV using shower partons generated from PYTHIA. Fig. 1 shows the longitudinal (through the momentum fraction z of the jet) and transverse momentum spectrum p_T of pions, kaons, protons, and Lambdas obtained from recombination, remnant fragmentation, and their sum. For the recombination contribution, we fix the cutoff parameters in meson and baryon Wigner functions by the charge radii of pion, kaon, and proton, and also include decays of excited states from recombination. It is seen that low momentum hadrons are mainly produced from recombination while high momentum ones are dominated by string fragmentation of remnant partons, reflecting the decreasing recombination probability of shower partons with their momentum. The sum of the recombination and short-string fragmentation qualitatively reproduces the results from PYTHIA string fragmentation of original parton showers. Our study differs from early works using quark recombination for hadronization of jets [4] in

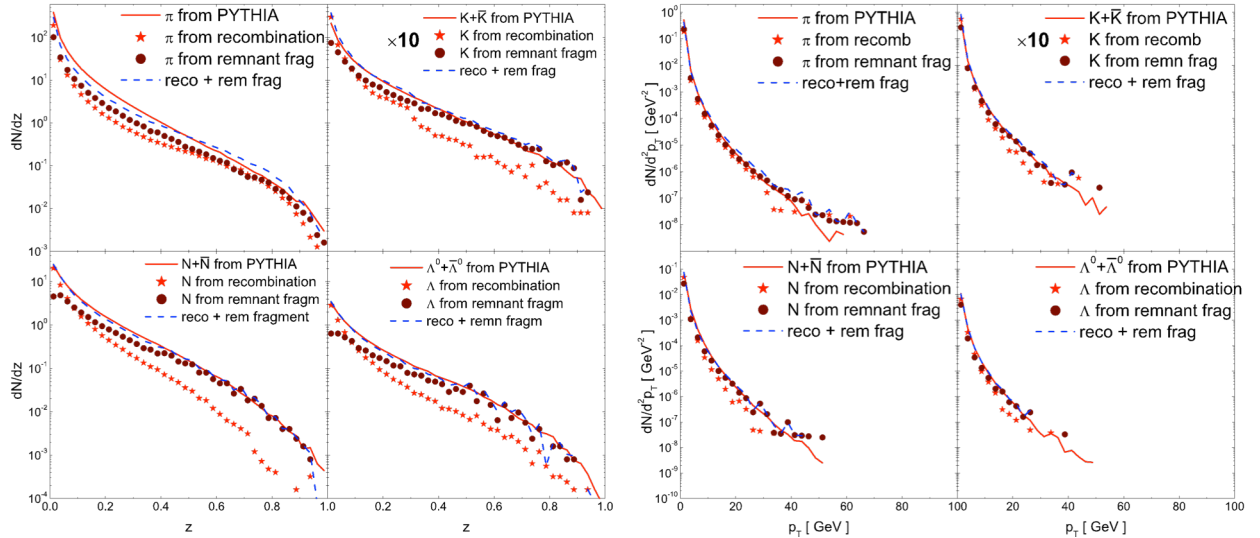


FIG. 1. Longitudinal momentum fraction dN/dz (left window) and transverse momentum p_T spectrum (right window) of pions (upper left panel), kaons (upper right panel), nucleons and antinucleons (lower left panel), and Lambdas and antilambdas (lower right panel) from the recombination of shower partons (stars), fragmentation of remnant partons (circles), and their sum (dashed lines), compared with results from PYTHIA string fragmentation (solid lines) for jets produced in e^+e^- collisions at center of mass energy of 200 GeV.

that parton showers in our study are obtained from the sophisticated parton Monte Carlos available today instead of from fitting to data or from specific models. In addition, earlier works used event-averaged spectra, ignoring fluctuations coming from the small number of partons in each jet. Work is in progress to generalize present approach to include partons from an ambient medium such as the quark-gluon plasma (QGP) produced in relativistic heavy ion collisions by allowing shower partons to recombine with thermal partons at phase transition temperature.

- [1] K.C. Han, R. Fries, and C.M. Ko, to be published.
- [2] V. Greco, C.M. Ko, and P. Levai, Phys. Rev. Lett. **90**, 202302 (2003); Phys. Rev. C **68**, 034904 (2003).
- [3] T. Sjostrand, S. Mrenna, and P.Z. Skands, JHEP **0605**, 026 (2006).
- [4] R.C. Hwa and C.B. Yang, Phys. Rev. C **70**, 024904 (2004).

Quarkonium formation time in relativistic heavy ion collisions

T. Song,¹ C.M. Ko, and S.H. Lee²

¹*Frankfurt Institut for Advanced Studies and Institute for Theoretical Physics, Johann Wolfgang Goethe Universitat, Frankfurt am Main, Germany*

²*Institute of Physics and Applied Physics, Yonsei University, Seoul 120-749, Korea*

The formation time of quarkonium is one of essential ingredients used in studies on quarkonium production in relativistic heavy-ion collisions. Based on the space-time correlator of heavy quark vector currents [1,2] in a hydrodynamics background with the initial nonequilibrium stage expanding only in the longitudinal direction, we have calculated the quarkonium formation time in relativistic heavy-ion collisions [3]. Using in-medium quarkonia properties determined with the heavy quark potential taken to be the free energy from lattice calculations [4] and the fact that quarkonia can only be formed below their dissociation temperatures due to color screening, we have found that $\Upsilon(1S)$, $\Upsilon(2S)$, $\Upsilon(3S)$, J/ψ and ψ' are formed, respectively, at 1.2, 6.6, 8.8, 5.8, and 11.0 fm/c after the quark pair are produced in central Au+Au collisions at the top energy of Relativistic Heavy Ion Collider (RHIC), and these times become shorter in semi-central collisions. These results are shown in Fig. 1 for charmonia (left window) and bottomonia (right window). We have further found that including the effect of formation time enhances appreciably the survivability of quarkonia in the produced hot dense matter.

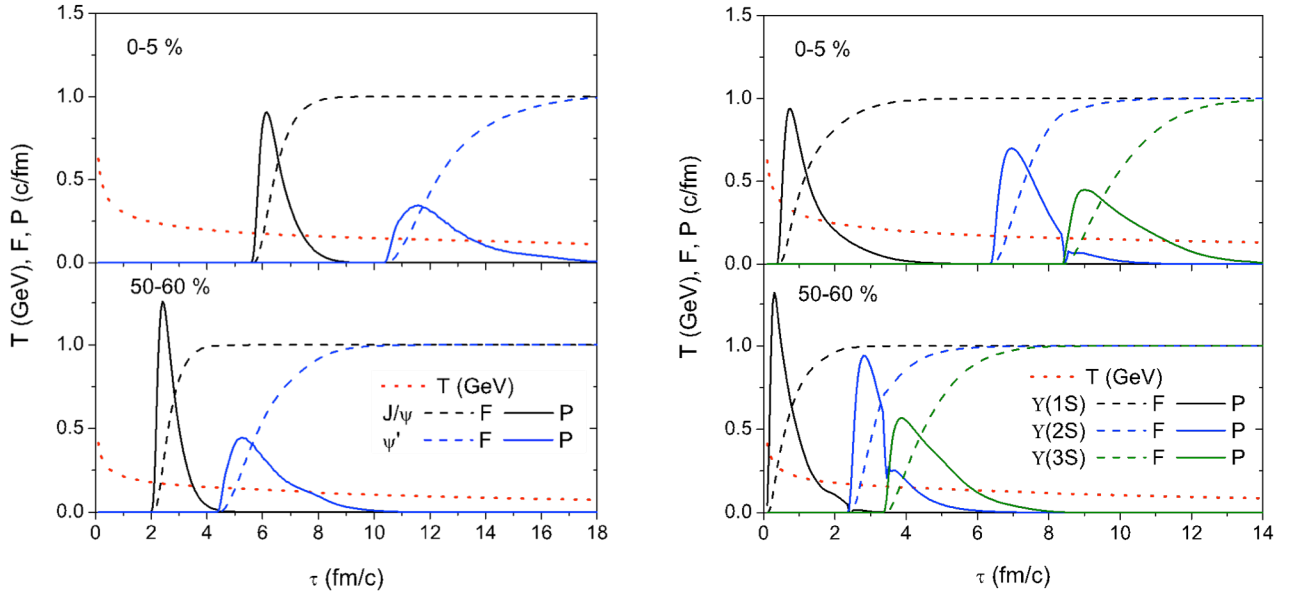


FIG. 1. Average temperature T , the fractions of quarkonium states F in the heavy quark vector current correlation function, and their time derivatives P as functions of time in Au+Au collisions at $\sqrt{s_{NN}} = 200$ GeV for the 0-5% (upper panel) and 50-60% (lower panel) centralities. Left and right windows are for charmonia and bottomonia, respectively.

- [1] D. Kharzeev and R.L. Thews, Phys. Rev. C **60**, 041901(R) (1999)
- [2] T. Song, C.M. Ko, and S.H. Lee, Phys. Rev. C **87**, 034910 (2013).
- [3] T. Song, C.M. Ko, and S.H. Lee, Phys. Rev. C **91**, 044909 (2015).
- [4] S.H. Lee, K. Morita, T. Song, and C.M. Ko, Phys. Rev. D **89**, 094015 (2014).

Spinodal instability in baryon-rich quark matter

F. Li and C.M. Ko

The baryon-rich quark matter is expected to undergo a first-order phase transition at finite baryon density. Using the Polyakov Nambu-Jona-Lasinio (PNJL) model [1], which shows both the deconfinement and chiral phase transitions of quark matter at high temperature and density, we have studied the spinodal instability in a baryon-rich quark matter [2]. Shown in Fig. 1 is the spinodal boundary in the temperature and density plane for different values of the wave number k of the unstable mode with (right window) and without (left window) the repulsive quark interaction. It is seen that the boundary of the spinodal region shrinks with increasing wave number, and for the same wave number, it is reduced by the repulsive quark vector interaction.

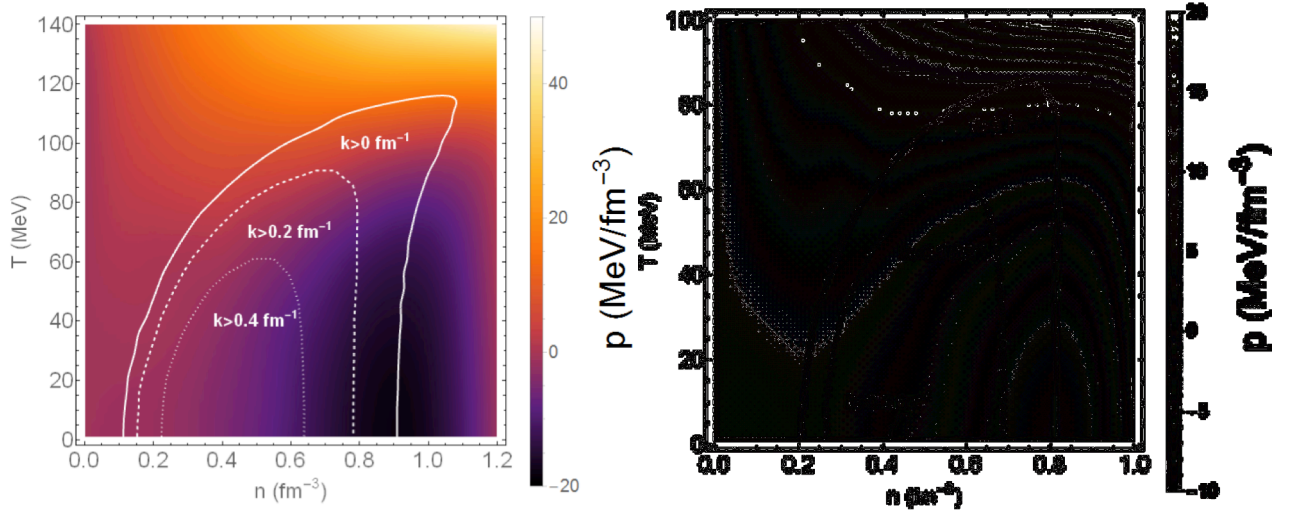


FIG. 1. Spinodal boundaries in temperature and net quark density plane for different wave numbers with quark vector interaction $G_V = 0$ (left window) and $G_V = 0.2$ GS (right window).

Using the linear response theory, we have also calculated the growth rate of the unstable mode, which is given by the imaginary part of its dispersion relation, as a function of the wave number. Fig. 2 shows that for quark matter at temperature $T = 70$ MeV and net quark density $n_q = 0.7$ fm^{-3} , the growth rate of the unstable model in the absence of vector interaction first increases and then decreases with the wave number after reaching a peak value of about 0.01 fm^{-1} at $k \sim 0.15$ fm^{-1} . The growth rate is, however, significantly reduced after including the quark vector interaction, resulting in a suppression of the spinodal instability that is greater for unstable modes of shorter wavelength.

We have further studied how density fluctuations develop in a baryon-rich quark matter inside the spindodal region by numerically solving the Vlasov equation derived from the PNJL model for the quark distribution function inside a box of periodic boundary conditions. With an initial net quark density of $n_q = 0.6$ fm^{-3} and temperature of $T_0 = 70$ MeV, the quark density distributions in the x-y plane at later times

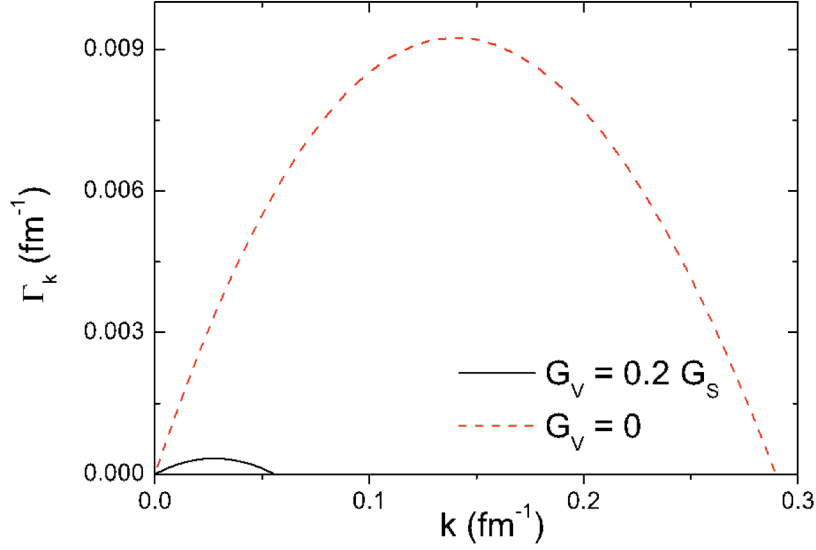


FIG. 2. Growth rate of unstable modes in quark matter of net quark density $n_q = 0.7 \text{ fm}^{-3}$ and at temperature $T = 70 \text{ MeV}$ for quark vector interaction $G_V = 0$ and $G_V = 0.2 G_S$.

of 20 fm/c and 70 fm/c are shown in the left and right windows of Fig. 3, respectively. Density fluctuations are seen to appear already at 20 fm/c and become very large at 70 fm/c.

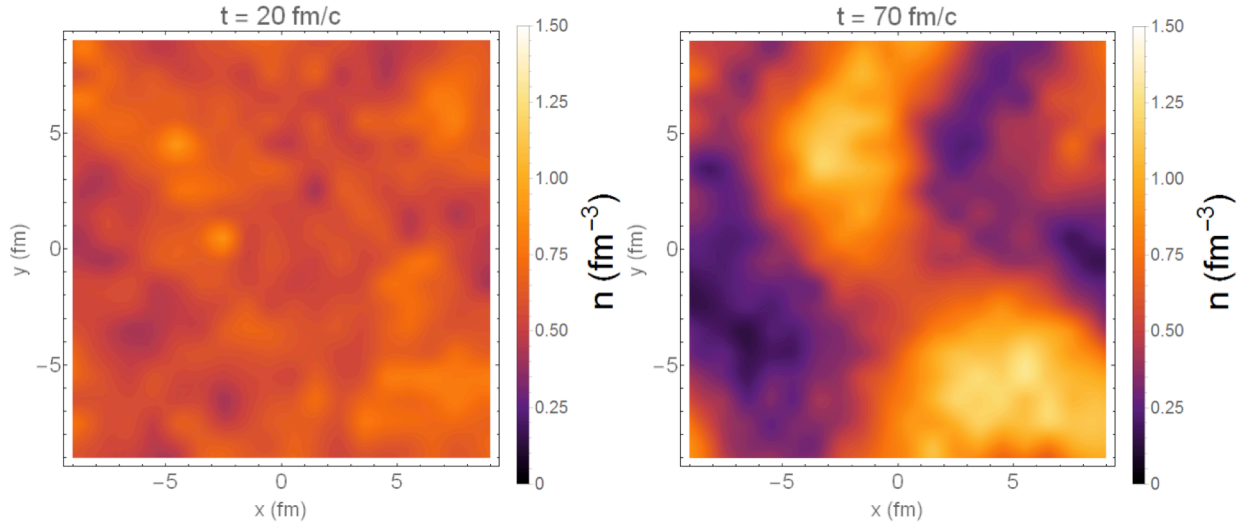


FIG. 3. Density distributions at $t = 20 \text{ fm/c}$ (left window) and 70 fm/c (right window) on the plane $z = 0$ of a quark matter with initial uniform density of $n_q = 0.6 \text{ fm}^{-3}$ and temperature $T_0 = 70 \text{ MeV}$.

To quantify the density fluctuations, we have calculated the density moments $\langle \rho^N \rangle$ of all quarks in the box [3]. Shown in Fig. 4 is the time evolution of scaled density moments $\langle \rho^N \rangle / \langle \rho \rangle^N$ for $N = 2, 4$, and 6. All are seen to increase with time, and the higher the moment, the larger its magnitude is.

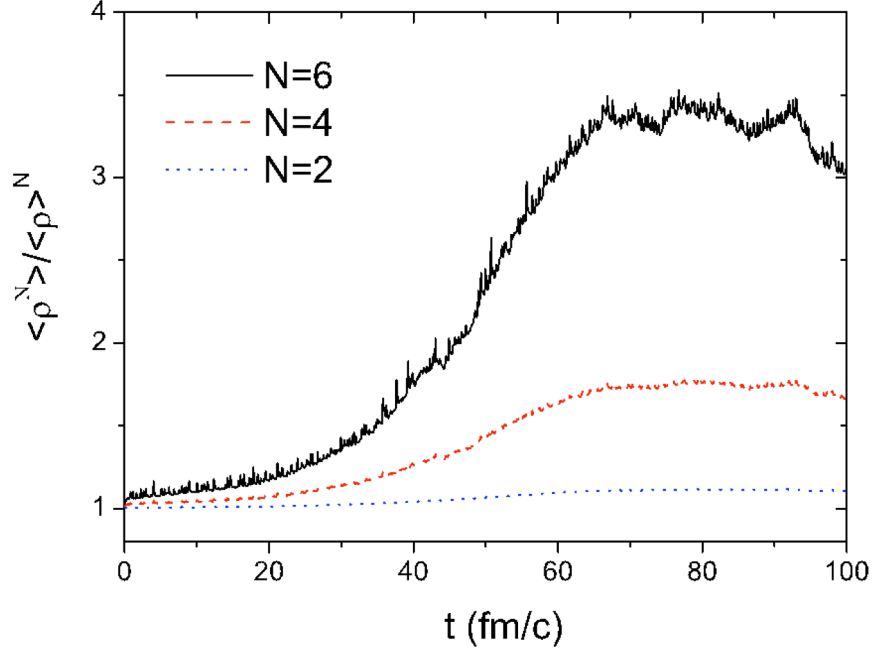


FIG. 4. Time evolution of density moments of a quark matter with initial density $n_q = 0.6 \text{ fm}^{-3}$ temperature $T_0 = 70 \text{ MeV}$.

Work is in progress to study the density fluctuations of an expanding fireball to investigate if they can still be developed before the system disintegrate due to expansion. Also, physical observables that are sensitive to density fluctuations are being studied.

[1] K. Fukushima, Phys. Lett. B **591**, 277 (2004).

[2] F. Li and C.M. Ko, to be published.

[3] J. Steinheimer and J. Randrup, Phys. Rev. C **87**, 055903 (2013).

Medium modification of pion production threshold in heavy ion collisions and the nuclear symmetry energy

T. Song¹ and C.M. Ko

¹*Frankfurt Institut for Advanced Studies and Institute for Theoretical Physics, Johann Wolfgang Goethe Universitat, 60438 Frankfurt am Main, Germany*

Using the relativistic Vlasov-Uehling-Uhlenbeck (RVUU) equation [1,2] based on mean fields from the nonlinear relativistic NL ρ and NL $\rho\delta$ models [3], which have same nuclear equation of state and symmetry energy but different symmetry energy slope parameters of 83 MeV and 98 MeV, respectively, we have studied the effect of medium modification of the pion production threshold on the total pion yield and the π^-/π^+ ratio in Au+Au collisions [4]. We have found that the in-medium threshold effect enhances both the total pion yield and the π^-/π^+ ratio, compared to those without this effect. Furthermore, including the medium modification of the pion production threshold leads to a larger π^-/π^+ ratio for the NL $\rho\delta$ model with a larger symmetry energy parameter than the NL ρ model with a smaller symmetry energy parameter, opposite to that found without the in-medium threshold effect. To reproduce the total pion yield measured by the FOPI Collaboration [5], we have introduced a density-dependent cross section for Delta baryon production from nucleon-nucleon collisions [6], which suppress the total pion yield but hardly changes the π^-/π^+ ratio. Because of the small difference in the stiffness of their symmetry energies, the π^-/π^+ ratios obtained from both the NL ρ and NL $\rho\delta$ models are consistent with the FOPI data within the experimental errors as shown in Fig.1.

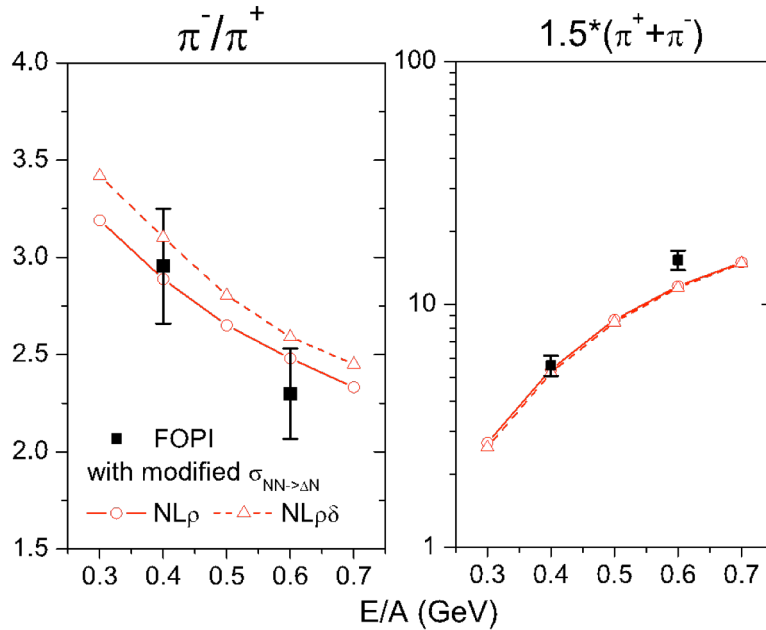


FIG. 1. π^-/π^+ ratio (left panel) and total pion yield (right panel) as functions of the collision energy obtained with the threshold effect and the density-dependent Delta production cross section in Au+Au collisions at impact parameter of 1 fm for both the NL ρ and NL $\rho\delta$ models. Experimental data are from the FOPI Collaboration [6].

- [1] C.M. Ko, Q. Li, and R.C. Wang, Phys. Rev. Lett. **59**, 1084 (1987).
- [2] C.M. Ko and Q. Li, Phys. Rev. C **37**, 2270 (1988).
- [3] T. Gaitanos, M. Di Toro, S. Typel, V. Baran, C. Fuchs, V. Greco, and H.H. Wolters, Nucl. Phys. **A732**, 24 (2004).
- [4] T. Song and C.M. Ko, Phys. Rev. C **91**, 014901 (2015).
- [5] W. Reisdorf *et al.*, Nucl. Phys. **A781**, 459 (2007).
- [6] A.B. Larinov and U. Mosel, Nucl. Phys. **A728**, 135 (2003).

Dilepton production from quark-gluon plasma in the PNJL model

Y.F. Sun and C.M. Ko

Using the Polyakov Nambu-Jona-Lasinio model (PNJL) [1], we have studied dilepton production from a quark-gluon plasma (QGP) [2]. Because the PNJL model allows the existence of pions in a QGP, dileptons can be produced not only from quark-antiquark annihilation but also from pion-pion annihilation to a dilepton pair in the final state. Besides these leading-order processes, dileptons can be further produced from next-to-leading-order processes involving an additional pion in the final state of quark-quark annihilation and from quark or antiquark scattering with pions. We have calculated the dilepton production rates from these processes using the medium-dependent quark and pion masses, which respectively decreases and increases with the temperature of the QGP and the quark-pion coupling constant as well as the modified quark Fermi distributions due to the Polyakov loop.

Fig.1 shows the various dilepton production rates in a QGP of zero quark baryon chemical potential for two different temperatures. For the temperature $T = 140$ MeV (left window), which is below the phase transition temperature $T_C = 212$ MeV, dileptons of small invariant mass are produced from processes involving pions, while dileptons of large invariant mass are dominately produced from quark-antiquark annihilation, as a result of the large quark constituent mass compared to the small pion mass below T_C . For $T = 212$ MeV, the relative importance of processes with and without pions is reversed as shown in the right window of Fig. 1, except for dileptons of very small invariant mass, which is always dominated by next-to-leading-order processes. Increasing the quark chemical potential does not change much the production rate of dileptons of large invariant mass, although that of small invariant mass is slightly reduced.

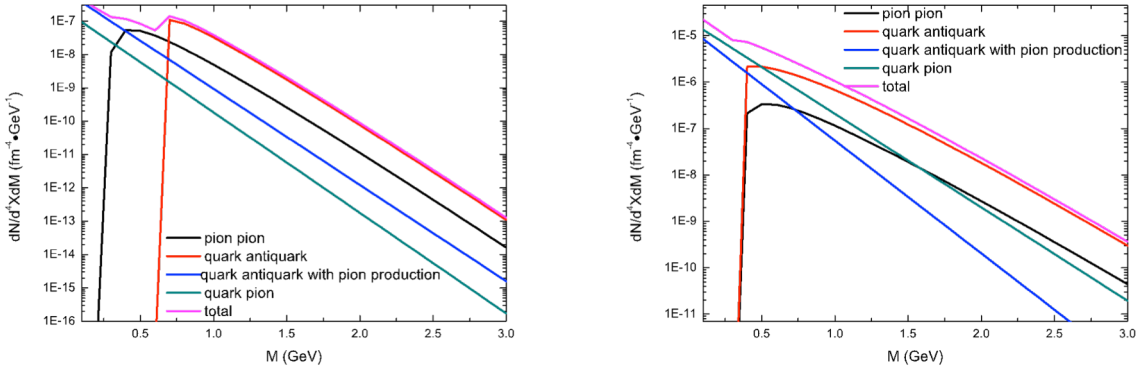


FIG. 1. Dilepton production rates in a QGP of temperature 140 MeV (left window) or 212 MeV (right window) and zero quark baryon chemical potential.

Fig. 2 shows the production rates of dileptons of zero momentum produced from a QGP at temperature $T = 240$ MeV and zero quark baryon chemical potential, for which results from lattice calculations are available as shown by the black line [3]. Since this temperature is above the Mott

temperature $T_M = 230$ MeV at which the decay of pion to quark and antiquark becomes possible in the QGP, leading to the disappearance of pions, only quark-antiquark annihilation with and without a pion in the final state contribute to dilepton production.

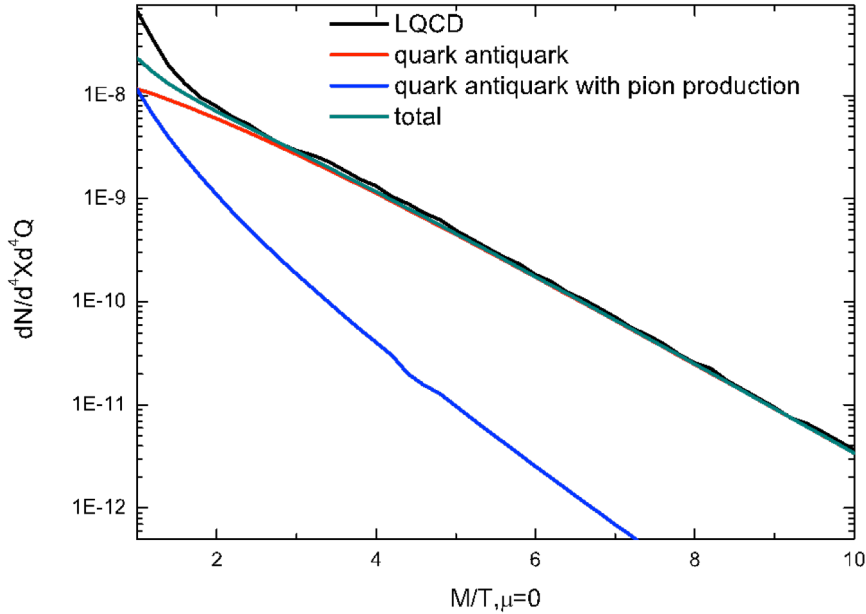


FIG. 2. Production rates of dileptons of zero momentum in a QGP of temperature $T = 240$ MeV and zero quark baryon chemical potential. Results from lattice QCD calculations are from Ref.[3].

The hot dense matter described by the PNJL model below the Mott temperature, especially around the transition temperature, consists of both quarks and pions as in the quarkyonic matter discussed in Ref. [4]. Since the dilepton production rates calculated with and without the contribution from pions can differ considerably, it can be used as a signature for the quarkyonic matter produced in a heavy ion collision.

- [1] K. Fukushima, Phys. Lett. B **591**, 277 (2004).
- [2] Y.F. Sun and C.M. Ko, to be published.
- [3] H.T. Ding, A. Francis *et al.*, Phys. Rev. D **83**, 034504 (2011).
- [4] L. McLerran and R.D. Pisarski, Nucl. Phys. **A796**, 83 (2007).

Heavy quark correlations and the effective volume for quarkonia production in heavy ion collisions

J.P. Liu,¹ C.M. Ko, and F. Li

¹*Physics Department, Tianjian University, Tianjin, China 300072*

Using the Boltzmann transport approach, we have studied the effect of initial spatial and momentum correlations between a heavy quark pair, such as that produced from a $p + p$ collision, on their collision rate in a partonic medium [1] that is relevant for their thermalization and the production of quarkonium from regeneration [2]. Characterizing this effect by an effective volume given by the inverse of the ratio of their collision rate to the collision rate of a thermally equilibrated and spatially uniformly distributed heavy quark pair in a unit volume, we have found that the effective volume is finite and depends sensitively on the momentum of the heavy quark and the temperature of the medium. Generally, it increases linearly with time t at the very beginning, thus an enhanced collision rate, and the increase then becomes slower due to multiple scattering, and finally it increases as $t^{3/2}$ as shown in Fig.1. Consequently, the chance for a heavy quark pair to collide with each other per unit time decreases monotonically with time. Also, heavy quarks of lower initial momentum in a medium of higher temperature have a larger chance to collide. Furthermore, the distribution of the center of mass energy of the heavy quark pair is found to correspond to an effective temperature that is lower than the actual temperature of the medium. All these properties are important for quarkonium regeneration in collisions where heavy quarks are rarely produced.

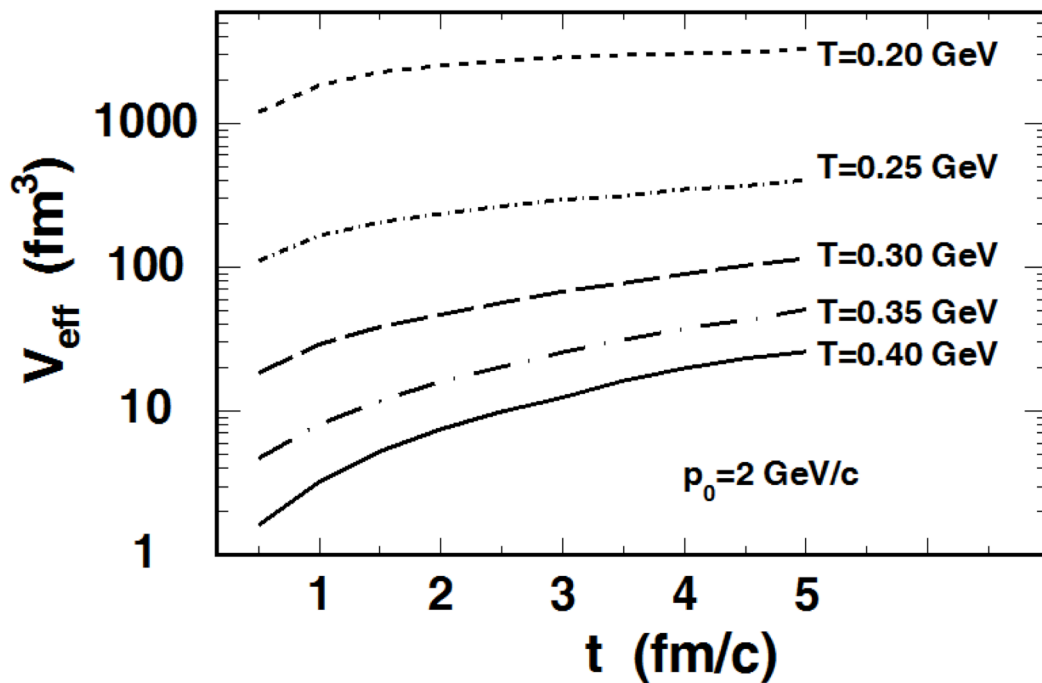


FIG. 1. Time evolution of the effective volume V_{eff} of heavy quarks with initial momentum $p_0 = 2$ GeV/c for different medium temperatures.

- [1] Y.P. Liu, C.M. Ko, and F. Li, Phys. Rev. C (submitted).
- [2] M.I. Gorenstein, A. Kostyuk, H. Stoecker, and W. Greiner, Phys. Lett. B **509**, 277 (2001).
- [3] A. Andronic, P. Braun-Munzinger, K. Redlich, and J. Stachel, Nucl. Phys. **A789**, 334 (2007).

Searching for photons from jets in quark gluon plasma using jet triggers

R.J. Fries and Collaborators

Quark gluon plasma (QGP) is routinely created in collisions of large nuclei at very high energies, for example at the Relativistic Heavy Ion Collider (RHIC) and the Large Hadron Collider (LHC). Experiments at both colliders are collecting data to quantitatively characterize the properties of quark gluon plasma. Photons and jets are both important probes of QGP. Photons, once created, can escape the strongly interacting plasma due to their long mean free path and thus give unobstructed information about their origin. Very high energy quarks and gluons can also leave QGP but due to their color charge they interact strongly with the quarks and gluons in the plasma. They suffer from energy loss, mostly due to induced radiation of gluons, but the mechanism is still not fully understood. High energy quarks and gluons eventually form jets, i.e. sprays of hadrons, in the detectors.

Progress could be made if the process of energy loss of quarks and gluon due to *photon* emission could be studied with precision. This is a small fraction of the total energy loss, but because photons escape QGP unscathed the induced radiation spectrum could in principle be measured. However, there are many sources of photons in nuclear collisions and so far we have been unable to separate photon radiation induced by jets from other sources. In this project, we have looked at the possibility to detect photons from a very specific kinematic situation, namely Compton back scattering. In this process basically all the energy of the fast quark or gluon is transferred onto the radiated photon. We have studied the possibility to detect such photons using a jet on the away side (~ 180 degrees from the detected photon around the beam axis) as a trigger [1]. The underlying process is thus a pair of partons (quarks, gluons) created back to back with high energy. One parton escapes QGP and forms a jet which serves as a trigger. The other parton undergoes Compton back scattering with QGP and converts into a high energy photon.

We have calculated this process in various approximations, taking into account energy loss of both the trigger jet, and the parton entering the Compton process [1]. We have also computed the background from other processes, for example from jet-photon pairs created directly. We find that the signal can amount to a visible excess of photon yield for photon energies just below the window chosen for the energy of the trigger jet. The excess can be as large as 30-40%. Fig. 1 shows a typical situation for LHC energies. However, energy loss of the trigger jet can dilute the signal significantly. For realistic values of jet radii used today this makes the signal much less compelling.

Our calculation uses several conservative estimates, and it also focuses exclusively on Compton back scattering kinematics, thus ignoring part of the induced photon yield. An improved calculation, which should use a jet shower Monte Carlo as they are currently being developed, could clarify the situation.

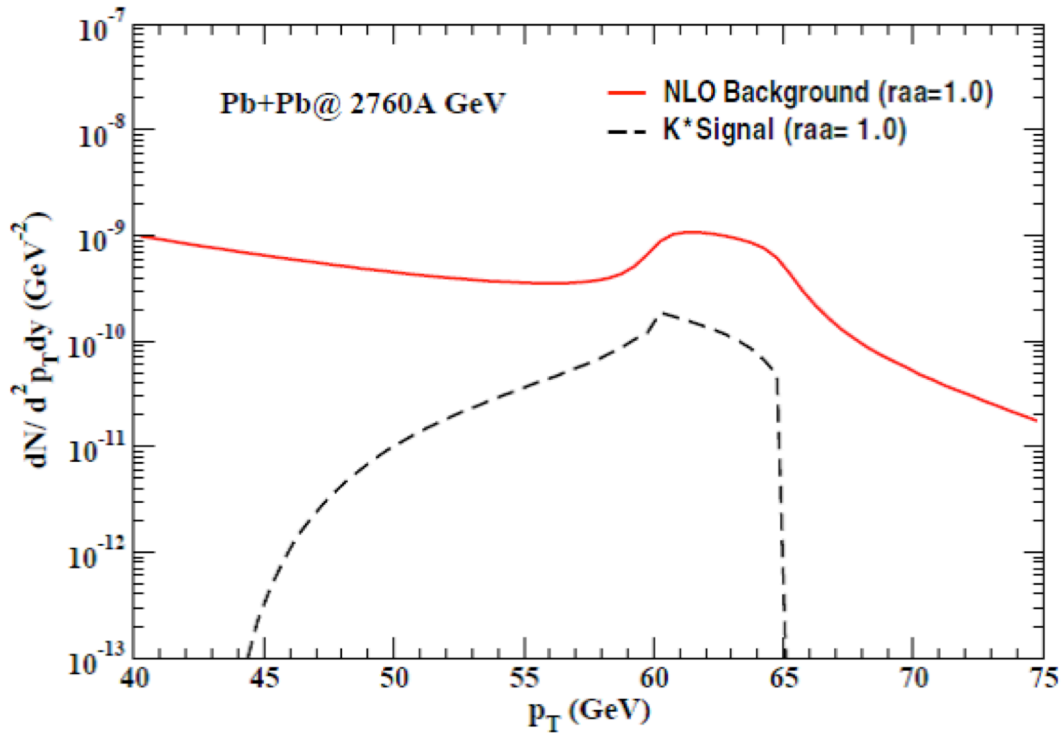


FIG. 1. The yield of photons opposite of trigger jets with an energy between 60 and 65 GeV/c for central Pb+Pb collisions at 2.76 TeV center of mass energy per nucleon-nucleon pair. Photons from Compton back scattering (black dashed line) compete with the background of photons from other processes (red solid line).

[1] Somnath De, Rainer J. Fries, Dinesh K. Srivastava, Phys. Rev. C **90**, 034911 (2014).

Heavy flavor at the large hadron collider in a strong coupling approach

M. He, R.J. Fries, and R. Rapp

Heavy charm and bottom quarks are powerful probes of the hot matter created in collisions of nuclei at high energies. Due to their large mass and the relatively short lifetime of the fireball they are not expected to reach full kinetic equilibrium. However, their approach to thermalization encodes valuable information about the strength of the heavy-quark coupling to the medium.

Previously we have reported the development of a comprehensive formalism to calculate heavy-quark (HQ) diffusion in quark-gluon plasma (QGP), HQ hadronization with recombination and fragmentation, and subsequent diffusion of heavy mesons in hot hadronic matter [1]. Heavy-flavor (HF) relaxation rates are obtained from non-perturbative T-matrix calculations [2] in the QGP and phenomenological cross sections of D-mesons in the hadronic phase [3]. The background medium is modeled through ideal hydrodynamics carefully fitted to bulk-hadron observables.

In the current reporting period we have conducted a systematic study of HF probes in Pb+Pb collisions at LHC energies (2.76 TeV per nucleon pair) [4]. We have tuned our hydrodynamic simulation to fit data on bulk-hadron spectra and elliptic flow at the LHC. We have run our strong-coupling HF formalism [1], which does not have any tunable parameters, within the fluid-dynamic simulation. Similar to our previous results at RHIC energies we find a characteristic “flow bump” in the nuclear modification factor of D mesons, indicating that HF particles are dragged along with the collective flow of the expanding fireball in central collisions, due to their strong coupling to the medium. The ALICE data for the D meson nuclear modification factor, R_{AA} , are reasonably well reproduced (see Fig. 1), but they

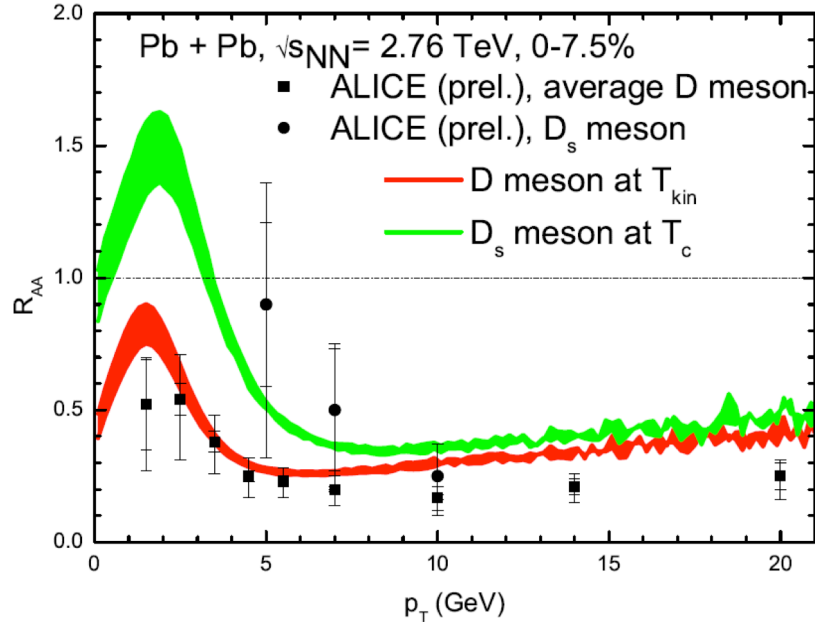


FIG. 1. Nuclear modification factor R_{AA} for D mesons at kinetic freeze-out and D_s mesons assumed to freeze-out just after hadronization in central Pb+Pb collisions at a center of mass energy of 2.76 TeV per nucleon pair, compared to preliminary data from the ALICE experiment [6]. The bands indicate uncertainties due to shadowing effects in the initial charm production.

currently do not extend to low enough momentum to fully resolve the predicted structure of the “flow-bump”.

Recently, we predicted that the D_s meson (a bound state of a charm and strange quark) is a unique tool to disentangle effects from the HQ hadronization mechanism, and the impact of the hadronic phase on HF diffusion [5]. We had found that the R_{AA} of the D_s , when compared to the R_{AA} of the D meson, exhibits the influence of charm-quark recombination with thermal strange quarks whose production is well known to be enhanced in the fireball of high-energy heavy-ion collisions. We have implemented this mechanism into our calculation at LHC energies. First data on the D_s R_{AA} are now available from the ALICE experiment and indeed indicate a notable enhancement (see Fig. 1), in qualitative agreement with our prediction. More precise data on this observable are expected soon from RHIC and LHC.

We have also evaluated the sensitivity of open HF transport properties to the azimuthal anisotropy in semi-central Pb+Pb collisions, by comparing our calculations to data for the R_{AA} in- and out-of-plane (see Fig. 2) and the elliptic flow (v_2) of D mesons and HF decay electrons. A fair overall description of ALICE data on in- vs. out-of-plane suppression, the resulting v_2 for D -mesons (which tends to be somewhat underestimated) and HF leptons, as well as CMS data on non-prompt J/ψ R_{AA} from B meson decays emerges. This provides a significant improvement on the challenge of simultaneously describing HF R_{AA} and v_2 data at the LHC.

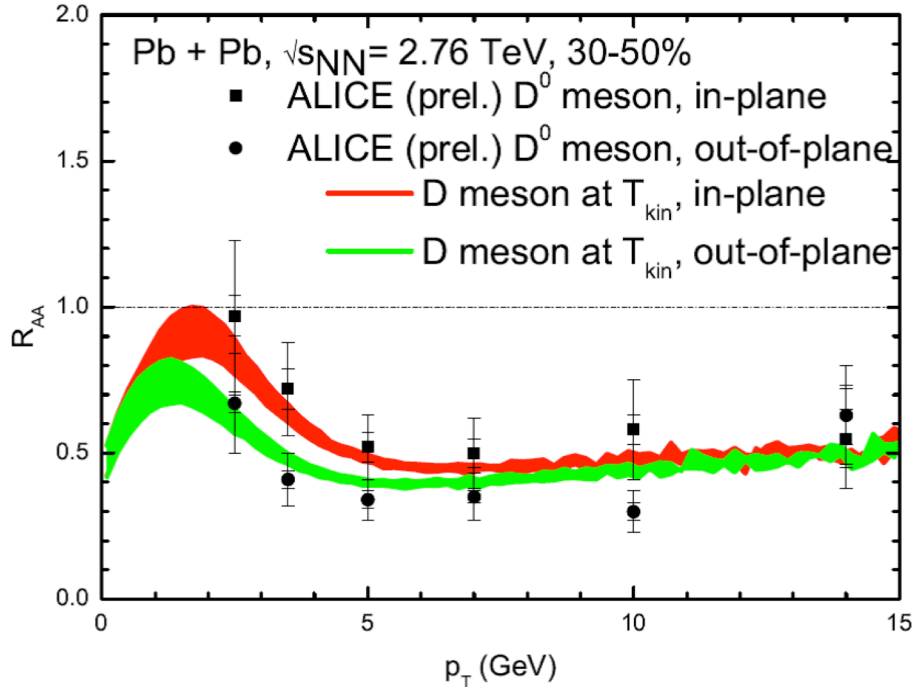


FIG. 2. Nuclear modification factor R_{AA} for D mesons at kinetic freeze-out in the reaction plane and out of the reaction plane for semi-central (30-50%) Pb+Pb collisions at a center of mass energy of 2.76 TeV per nucleon pair, compared to preliminary ALICE data [7].

- [1] M. He, R. J. Fries and R. Rapp, Phys. Rev. C **86**, 014903 (2012).
- [2] F. Riek and R. Rapp, Phys. Rev. C **82**, 035201 (2010).
- [3] M. He, R.J. Fries, and R. Rapp, Phys. Lett. B **701**, 445 (2011).
- [4] M. He, R.J. Fries, and R. Rapp, Phys. Lett. B **735**, 445 (2014).
- [5] M. He, R.J. Fries, and R. Rapp, Phys. Rev. Lett. **110**, 112301 (2013).
- [6] G.M. Innocenti *et al.* (ALICE Collaboration), Nucl. Phys. **A904-905**, 433 (2013).
- [7] D. Caffarri *et al.* (ALICE Collaboration), Nucl. Phys. **A904-905**, 643 (2013).

Pseudo-critical enhancement of thermal photons in relativistic heavy-ion collisions?

H. van Hees, M. He, and R. Rapp

The radiation of photons from the fireballs created in high-energy collisions of heavy nuclei has long been suggested as an observable to extract the temperatures of the strongly interacting medium in its early (hottest) evolution phases. It thus came as a surprise when the PHENIX collaboration reported a large elliptic flow of “direct photons” in Au-Au($\sqrt{s}=200\text{GeV}$) collisions, indicating a rather late emission of these photons, together with an “effective temperature” (or inverse slope parameter) of about $T_{\text{eff}} = 220 \pm 30 \text{ MeV}$ [1]. In our previous work [2] we have shown that these observations can be reconciled with an emission of thermal photons with large contributions from the hadronic phase, where the elliptic flow of the expanding fireball is large and the local emission temperature of $T < 180 \text{ MeV}$ is Doppler blue-shifted to produce the experimentally observed value for T_{eff} .

In the present work [3] we have scrutinized the above findings by implementing an updated equation of state (using lattice-QCD data) and cross-checking our expanding fireball model against a hydrodynamic evolution of the medium. Both evolution models have been tuned to reproduce the bulk-hadron spectra and their elliptic flow at both RHIC and LHC energies.

In Fig. 1 (left) we compare the temperature emission profile of thermal photons at given transverse momentum of $q_T = 2 \text{ GeV}$ for both evolution models, clearly indicating that in both cases a maximum of the emission occurs around the pseudo-critical temperature of $T_{\text{pc}} \sim 170 \text{ MeV}$. However, the hydrodynamic model radiates significantly less photons from the hadronic phase, which can be understood by its continuous freeze-out throughout the lifetime of the fireball, leading to a gradual decrease of the “active” matter elements, see right panel of Fig. 1.

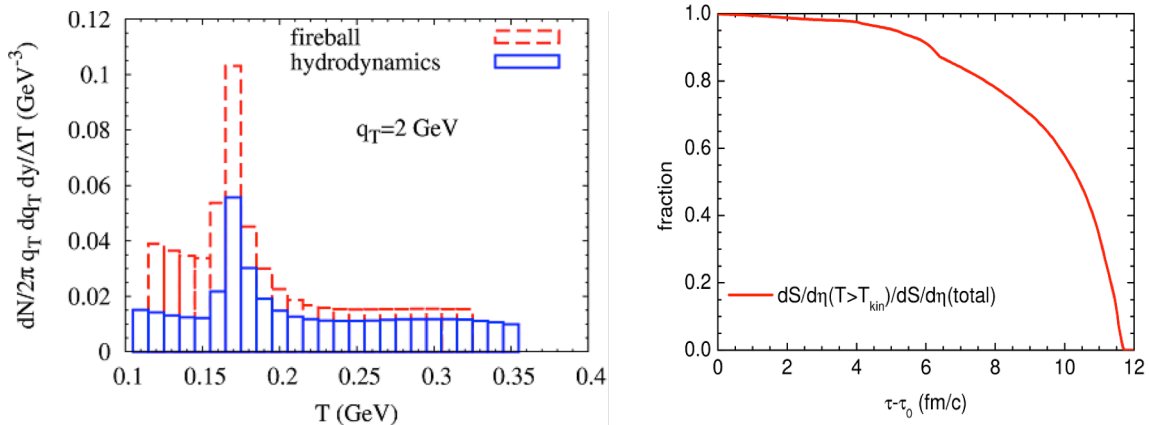


FIG. 1. Left: Emission profile of thermal photons as a function of temperature. Right: fraction of the entropy at temperatures above the kinetic freeze-out temperature to the total entropy in the hydrodynamic evolution model as a function of proper time in the rest frame of the fluid cells.

A comparison of the final photon spectra and elliptic flow from both evolution models is displayed in Fig. 2 for central Au-Au collisions at RHIC. Overall, there is a fair agreement in the photon observables between the two evolution models. Upon closer inspection one finds that the larger hadronic emission contribution from the fireball expansion leads to slightly higher spectral yields and elliptic flow. Since both evolution models tend to under-predict the experimental data at low q_T , an increased thermal photon emission rate seems to be required to help resolve the discrepancies. Investigations of hitherto unaccounted for photon sources in the hadronic phase are ongoing [4].

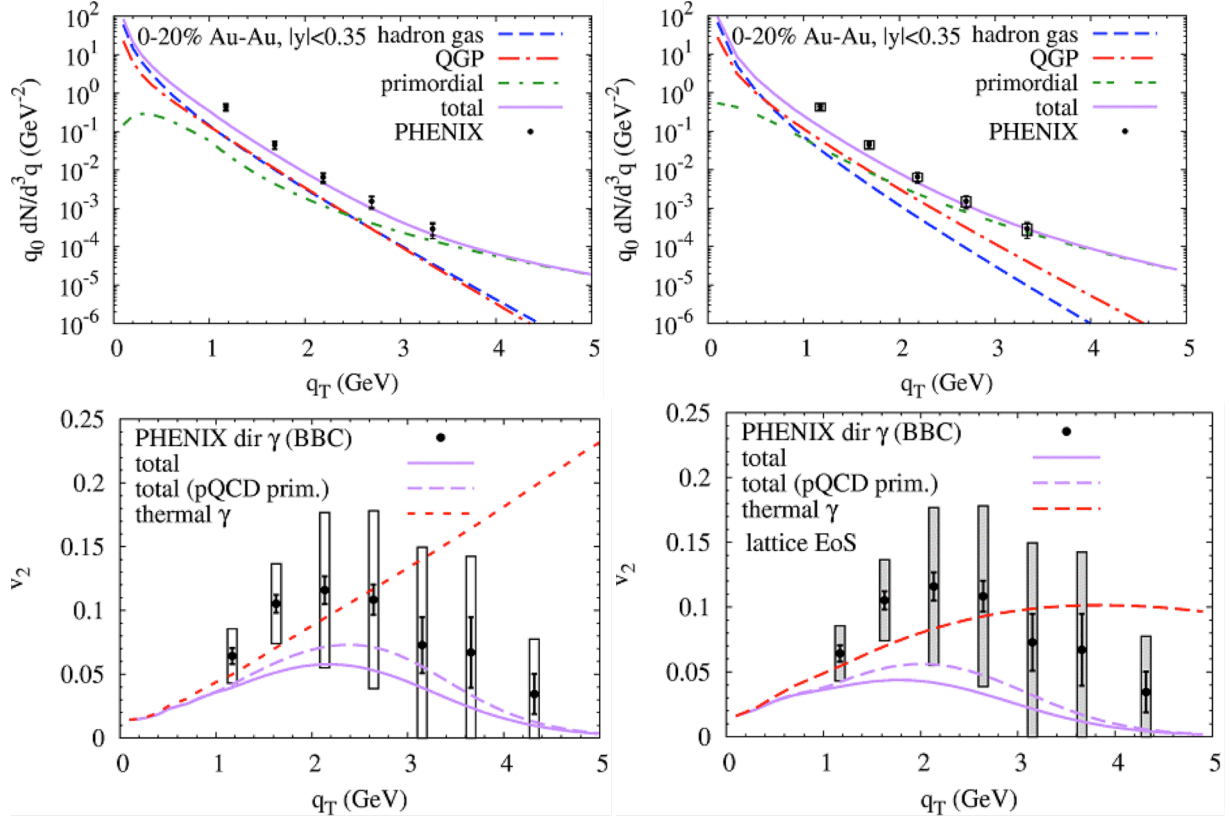


FIG. 2. Comparison of our calculations [3] for direct-photon spectra (upper panels) and their elliptic flow (lower panels) to PHENIX [1] data in 0-20% Au-Au collisions at $\sqrt{s}=200$ AGeV, using either an isotropically expanding fireball model (left column) or ideal hydrodynamics (right column).

- [1] A. Adare *et al.*, Phys. Rev. Lett. **103**, 132301 (2010); *ibid.* **109**, 122302 (2012).
[2] H. van Hees, C. Gale, and R. Rapp, Phys. Rev. C **84**, 054906 (2011).
[3] H. van Hees, M. He, and R. Rapp, Nucl Phys. **A933**, 256 (2015); *ibid.* **A931**, 696 (2014).
[4] N. Holt, P. Hohler, and R. Rapp, in preparation (2015).

Universal parameterization of thermal photons in hadronic matter

M. Heffernan, P. Hohler, and R. Rapp

The emission of thermal photon radiation from hadronic matter plays an important role in the understanding of direct-photon observables in high-energy heavy-ion collisions [1]. In particular, the soft spectral slopes and large elliptic flow of photon radiation observed by the PHENIX collaboration in Au-Au($\sqrt{s}=200\text{GeV}$) collisions at RHIC [2] suggest important emission sources from the later hadronic phases of the expanding fireball formed in these collisions, based on our previously calculated emission rates from hot and dense hadronic matter including the effects of baryons and anti-baryons [3].

To render the rather involved microscopic rate calculations widely available for phenomenological applications in heavy-ion collisions, we have in the present work [4] developed a universal parameterization of the photon emissivity valid over a broad range of temperatures, $T = 100\text{--}180\text{ MeV}$, and baryon chemical potentials, $\mu_B = 0\text{--}400\text{ MeV}$, and for photon energies from $q_0 = 0.2\text{--}5\text{ GeV}$. While parameterizations of the emission rates from the $\pi\rho a_1$ system have been provided earlier [3], the effects of higher mesonic resonance and baryon-induced emission (as encoded in the in-medium ρ -meson spectral function of Ref. [5]) have not been readily available through a compact parameterization thus far. Here, we have constructed such a parameterization in the 3 variables (q_0, μ_B, T) using nested fitting techniques, resulting in an overall accuracy of within 20% over more than 10 decades in the emission

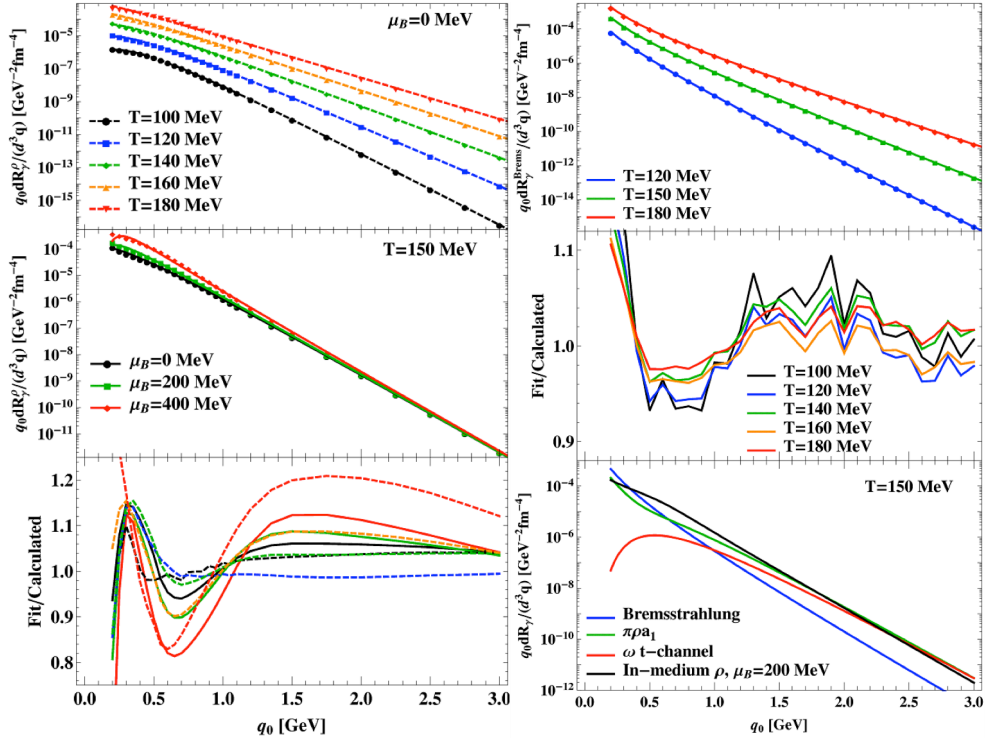


FIG. 1. Parameterizations (lines) of thermal photon emission rates from hot and dense hadronic matter (symbols). Left column: for the in-medium ρ -meson spectral function [5] at the photon point at vanishing (upper panels) and finite (middle panel) baryon chemical potential, with pertinent relative error plot (lower panel). Right column: for $\pi\pi \rightarrow \pi\pi\gamma$ Bremsstrahlung [6] (upper panel) with corresponding relative error plot (middle panel), and an overview plot of different sources (lower panel).

rate, cf. Fig. 1 left. Note that even at vanishing chemical potential, the (equal) contributions of baryons and anti-baryons do not vanish but add up.

In addition, we have revisited the role of $\pi\pi \rightarrow \pi\pi\gamma$ and $\pi K \rightarrow \pi K\gamma$ Bremsstrahlung, by extending the calculations of Ref. [6] to high energies and providing pertinent parameterizations as well, cf. Fig. 1 right. The lower right panel of Fig. 1 summarizes the various sources of thermal hadronic photon emission, indicating the importance of anti-/baryonic and mesonic-resonance sources while the Bremsstrahlung off light meson scattering comes in at the $\sim 10\%$ level.

- [1] H. van Hees, C. Gale and R. Rapp, Phys. Rev. C **84**, 054906 (2011).
- [2] A. Adare *et al.*, Phys. Rev. Lett. **103**, 132301 (2010); *ibid.* **109**, 122302 (2012).
- [3] S. Turbide, R. Rapp, and C. Gale, Phys. Rev. C **69**, 14903 (2004)
- [4] M. Heffernan, P. Hohler, and R. Rapp, Phys. Rev. C **91**, 027902 (2015).
- [5] R. Rapp and J. Wambach, Eur. Phys. J. A **6**, 415 ((1999).
- [6] W. Liu and R. Rapp, Nucl Phys. **A796**, 101 (2007).

Realistic implementation of massive Yang-Mills theory for ρ and a_1 Mesons

P.M. Hohler and R. Rapp

Local gauge theories are a central guiding principle in describing elementary particle interactions. Among its attractive features is the use of a universal gauge coupling constant to characterize the interactions. The massive Yang-Mills approach embodies this principle by implementing axial-/vector mesons into the chiral pion Lagrangian, but in the past it had difficulties in describing experimentally measured spectral functions.

In this work [1] we have advanced the massive Yang-Mills framework for hadronic interactions in vacuum by implementing a dressed ρ -meson propagator into the self-energy of its chiral partner, the $a_1(1260)$ meson. The main achievement in this procedure is the preservation of chiral symmetry of the low-energy strong interaction, made possible by an identification of suitable vertex corrections in the pi-rho loop of the a_1 self-energy while rendering loop integrals finite through suitable counter-terms based on the Lagrangian interactions, see Fig. 1.

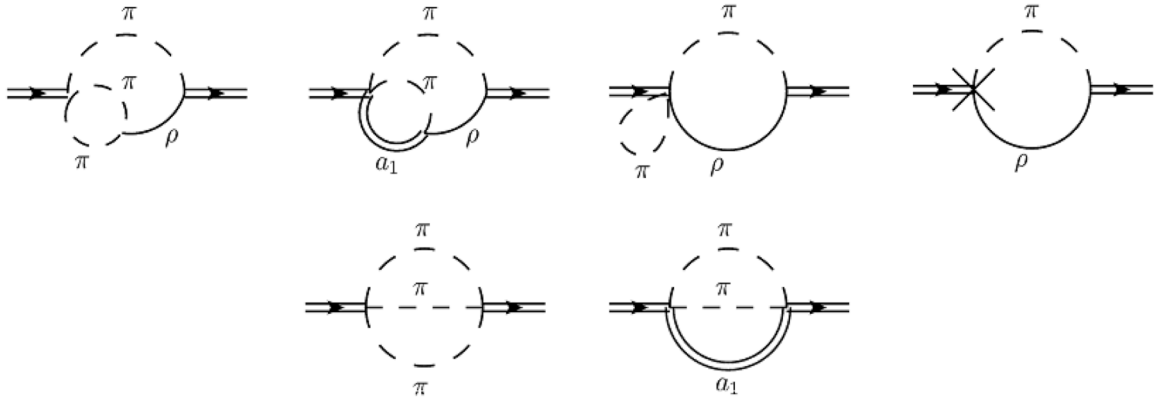


FIG. 1. Diagrammatic representation of the corrections to the $\pi\rho a_1$ vertex necessary to preserve chiral symmetry when utilizing a fully dressed ρ propagator in the a_1 selfenergy.

When attempting a fit to the vector and axialvector spectral functions, as accurately measured in hadronic decays of the τ lepton [2], the concept of a universal high-energy continuum in both channels [3] has been employed, based on the notion that the effective theory decouples at sufficiently large masses, here somewhat above the a_1 resonance, $M > 1.4$ GeV. Together with the broad ρ propagator in the axialvector spectral function, this enabled a fair agreement with experimental data, see Fig. 2.

Our framework re-establishes the local gauge principle as a viable description of axial-/vector mesons in the chiral pion lagrangian. It also provides a realistic basis for future investigations of the long-standing question of chiral symmetry restoration in the context of dilepton data in heavy-ion collisions [4].

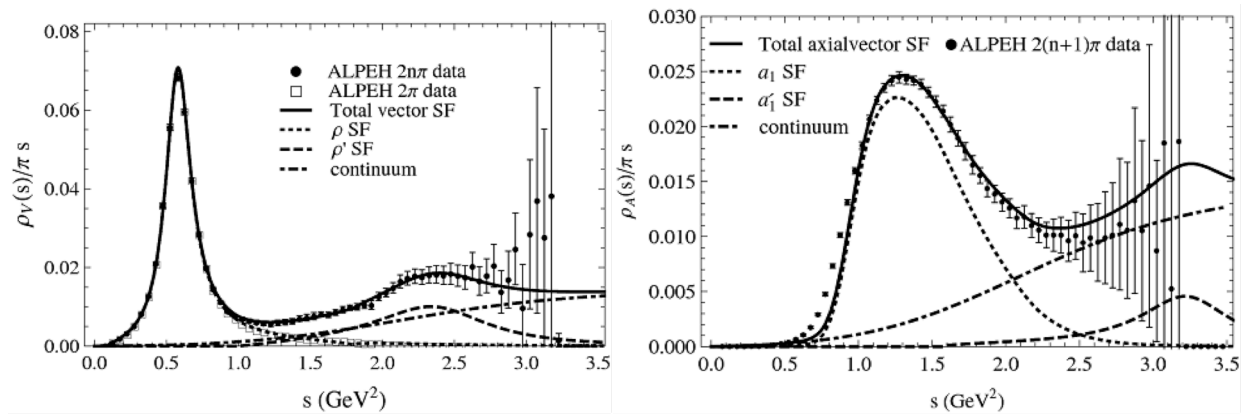


FIG. 2. Our fit to the vacuum vector (left) and axial-vector (right) spectral functions as measured in hadronic decays of the τ lepton [2] into an even or odd number of pions, respectively.

- [1] P.M. Hohler and R. Rapp, Phys. Rev. D **89**, 125013 (2014)
- [2] R. Barate *et al.* (ALPEH Collaboration), Eur. Phys. J. C **4**, 409 (1998); K. Ackerstaff *et al.* (OPAL Collaboration), Eur. Phys. J. C **7**, 571 (1999).
- [3] P.M. Hohler and R. Rapp, Nucl Phys. **A892**, 58 (2012).
- [4] R. Rapp, J. Wambach, and H. van Hees, in *Relativistic Heavy-Ion Physics (R. Stock, ed.)*, Landolt-Börnstein (Springer) **23**, 134 (2010) [e-print arXiv:0901.3289 [hep-ph]].

Weak branches in ^{34}Ar and ^{38}Ca β^+ decay

I.S. Towner and J.C. Hardy

In the β^+ decay of ^{34}Ar and ^{38}Ca , precisely-calibrated γ -ray yields have been measured and corresponding β branches determined. The Q_{EC} for these decays are 6.0 and 6.6 MeV respectively. Gamma rays with energy less than 3.5 MeV in ^{34}Cl and 4.0 MeV in ^{38}K have been identified [1, 2]. There is a small probability that not all the possible β -branches have been observed. How many 1^+ states are there in ^{34}Cl with an excitation energy between 3.5 and 6.0 MeV, or in ^{38}K between 4.0 and 6.6 MeV that could in principle be fed by a Gamow-Teller transition? These transitions would be very weak, too weak to be measured individually, but if there are sufficient of them they could cumulatively sum to a fraction of a percent of the total β strength. In precision work, a fraction of a percent could represent an important correction.

To answer the question, we performed some shell-model calculations. For ^{34}Cl , the model space is the full s, d shell with effective interactions USD of Wildenthal [3] and two more recent updates, USD-A and USD-B, of Brown and Richter [4]. These calculations identify four 1^+ states in the excitation energy window of 3.5 to 6.0 MeV with a β -decay feeding fraction greater than one part per million (ppm). We further calculated the γ -ray de-excitation of these states to identify how much of their feeding strength would have been measured in the experiment and how much would have been missed.

In the upper half of Table I we present some shell-model results. In the left two columns are the previous experimental results as recorded in the Evaluated Nuclear Structure Data File (ENSDF) [5] that show four 1^+ states at excitation energies below 3.5 MeV populated in β decay. The remainder of the Table shows three shell-model calculations that each predict four additional 1^+ states at excitation energies above 3.5 MeV that have weak β feeding strengths at the ppm level. The average sum of such feeding from the three calculations is 0.0045(16)%. Some fraction of this feeding would be counted in the β -decay experiment: the part that de-excites through one of the four lower-lying 1^+ states. However, most of the de-excitation does not proceed that way. Most de-excites by high-energy γ rays directly to the ground state or the first excited 3^+ state. This we call the missing strength as it remains unobserved in the experiment. The average missing strength from these calculations is 0.0036(13)%. The goal of the experiment is to measure and sum all the Gamow-Teller β branches and subtract the total from 100%. This yields the sought superallowed Fermi branch to the ground state in the daughter nucleus. The missing strength the shell-model calculations identify of 0.0036(13)% would be a correction to the superallowed Fermi branching ratio. In this case the correction is too small to be of any significance.

Similar calculations for ^{38}K are more difficult to complete. With a USD interaction only a few of the known states are described as the model space is very small: just two holes in a closed shell at $A = 40$. What is needed is a calculation that includes 4-hole, 2-particle configurations. Effective interactions for such model spaces are not under good control. We use a Millener-Kurath interaction [6] for the cross-shell Hamiltonian matrix elements and keep the

model space to just three orbitals, $s_{1/2}$, $d_{3/2}$ and $f_{7/2}$. In the bottom half of Table I we give the results. As before, the left two columns give the previous results recorded in ENSDF [5],

Table I. Branching ratios, R, to 1^+ states in the β decay of ^{34}Ar (upper half) and ^{38}Ca (lower half) from experiment, ENSDF, and from shell-model calculations with USD (upper half) and Millener-Kurath (MK) (lower half) effective interactions.

ENSDF			USD		USD-A		USD-B	
E_x	R(%)	State	E_x	R(%)	E_x	R(%)	E_x	R(%)
0.46	0.91	$1^+; T = 0$	0.32	0.28	0.55	0.47	0.33	0.26
0.67	2.49	$1^+; T = 0$	0.66	2.24	0.27	2.09	0.52	0.42
2.58	0.86	$1^+; T = 0$	2.52	0.69	2.26	0.92	2.37	0.28
3.13	1.30	$1^+; T = 0$	3.25	0.85	3.15	0.93	3.05	0.90
		$1^+; T = 0$	3.88	0.0003	4.06	0.0022	3.73	0.0010
		$1^+; T = 1$	3.95	0.0017	3.69	0.0028	3.80	0.0015
		$1^+; T = 0$	4.98	0.0008	4.83	0.0015	4.88	0.0008
		$1^+; T = 0$	5.11	0.0005	5.17	0.0000	5.02	0.0006
feeding to states above 3.5 MeV				0.0032		0.0065		0.0039
feeding unobserved				0.0025		0.0052		0.0032

ENSDF			MK	
E_x	R(%)	State	E_x	R(%)
0.46	2.81	$1^+; T = 0$	0.47	3.94
1.70	20.00	$1^+; T = 0$	1.26	15.70
3.34	0.50	$1^+; T = 0$		
3.86	0.50	$1^+; T = 0$	3.79	0.01
3.98	0.12	$1^+; T = 0$	4.08	0.04
		$1^+; T = 1$	4.78	0.0000
		$1^+; T = 0$	5.71	0.0002
		$1^+; T = 0$	5.80	0.0000
feeding to states above 4 MeV				0.0002

showing five 1^+ states populated at excitation energies below 4 MeV. The shell-model calculation only matches four of them. At higher excitation energy, the shell model predicts a further three 1^+ states between 4 and 6 MeV, but with very small β feeding of 0.0002% in total. Thus the missing strength is completely negligible and no correction is required for the superallowed Fermi branching ratio.

- [1] V.E. Jacob *et al.*, *Progress in Research*, Cyclotron Institute, Texas A&M University (2013-2014), p. I-20.
- [2] H.I. Park *et al.*, *Phys. Rev. C* (to be published).
- [3] B.H. Wildenthal, *Prog. Part. Nucl. Phys.* **11**, 5 (1984).
- [4] B.A. Brown and W.A. Richter, *Phys. Rev. C* **74**, 034315 (2006).
- [5] Evaluated Nuclear Structure Data File (ENSDF), [www.nndc.bnl.gov].

[6] D. Millener and D. Kurath, Nucl. Phys. **A283**, 315 (1975).

Spectrum shape functions in first-forbidden beta transitions

I.S. Towner

The beta-decay differential decay rate is written in Behrens and Bühring [1] (called BB) as

$$d^5\Gamma = \frac{G^2}{(2\pi)^5} F_0 L_0 (W_0 - W)^2 p W dW d\Omega_e d\Omega_\nu \left(C(W) + D(W) \frac{p}{W} \hat{\mathbf{p}} \cdot \hat{\mathbf{k}} + \dots \right) \quad (1)$$

where $\hat{\mathbf{p}}$ and $\hat{\mathbf{k}}$ are unit vectors in the directions of the electron and neutrino respectively. Here W_0 is the maximum value of the electron total energy W , p is the electron momentum, $p^2 = W^2 - 1$ in electron rest-mass units, and $F_0 L_0$ is the Fermi function as defined by BB. The spectrum shape functions of interest here are denoted $C(W)$ and $D(W)$ and their ratio defines the beta-neutrino angular-correlation coefficient

$$a_{ev}(W) = \frac{D(W)}{C(W)}. \quad (2)$$

Starting from the BB formalism and invoking the impulse approximation, we have derived simple expressions for the spectrum shape functions in terms of six nuclear matrix elements characterizing the parity-changing nature of first-forbidden beta decay. To display these expressions, we define

$$\begin{aligned} C(W) &= \sum_K k_1^{(K)} \left(1 + A_1^{(K)} W + \frac{B_1^{(K)}}{W} + C_1^{(K)} W^2 \right) \\ D(W) &= \sum_K k_2^{(K)} \left(1 + A_2^{(K)} W + \frac{B_2^{(K)}}{W} + C_2^{(K)} W^2 \right) \end{aligned} \quad (3)$$

Where K is the multipolarity of the beta transition, which for first-forbidden decays has the value $K = 0$ and 1 for non-unique transitions and $K = 2$ for unique transitions. Expressions for the coefficients $k^{(K)}$, $k^{(K)} A^{(K)}$, $k^{(K)} B^{(K)}$ and $k^{(K)} C^{(K)}$ are given in Table I. They depend on the six nuclear matrix elements, on W_0 the maximum electron energy, and on $\xi = \alpha Z/2R$, where R is the radius of a uniformly charged sphere approximating the nuclear charge density distribution. The six nuclear matrix elements are defined schematically by

$$x = -g_V \langle ir C_1 \rangle \quad (4)$$

$$\begin{Bmatrix} W \\ u \\ z \end{Bmatrix} = g_A \begin{Bmatrix} \sqrt{3} \\ \sqrt{2} \\ -2 \end{Bmatrix} \langle ir [C_1 \times \sigma]^{(K)} \rangle \quad (5)$$

$$\xi'v = -\frac{g_A}{M}\sqrt{3}\langle[\mathbf{p}\times\sigma]^{(0)}\rangle \quad (6)$$

$$\xi'y = -\frac{g_V}{M}\langle\mathbf{p}\rangle \quad (7)$$

Table I. Expressions for the parameters introduced in the spectral function, Eq. (3), in terms of the nuclear matrix elements.

		$K = 0$	$K = 1$	$K = 2$
$C(W)$	$k_1^{(K)}$	$\zeta_0^2 + \frac{1}{9}w^2$	$\zeta_1^2 + \frac{1}{9}(u+x)^2 - \frac{2}{9}u(u+x) + \frac{1}{18}W_0^2(2x+u)^2 - \frac{1}{18}(2x-u)^2$	$\frac{1}{12}(W_0^2 - 1)z^2$
	$k_1^{(K)} A_1^{(K)}$	0	$-\frac{4}{3}\zeta_1 u - \frac{1}{9}W_0(2x+u)^2$	$-\frac{1}{6}W_0 z^2$
	$k_1^{(K)} B_1^{(K)}$	$-\frac{2}{3}\zeta_0 w$	$\frac{2}{3}\zeta_1(u+x)$	0
	$k_1^{(K)} C_1^{(K)}$	0	$\frac{4}{9}u^2 + \frac{1}{18}(2x+u)^2 + \frac{1}{18}(2x-u)^2$	$\frac{1}{6}z^2$
$D(W)$	$k_2^{(K)}$	$\zeta_0^2 - \frac{1}{9}w^2$	$-\frac{1}{3}\zeta_1^2 + \frac{1}{27}(u+x)^2 - \frac{4}{9}W_0\zeta_1(2x+u) - \frac{4}{27}(u+x)(2x-u) + \frac{1}{54}W_0^2(2x+u)^2 - \frac{1}{54}(2x-u)^2$	$-\frac{1}{60}(W_0^2 - 1)z^2$
	$k_2^{(K)} A_2^{(K)}$	0	$\frac{4}{3}\zeta_1 u + \frac{8}{27}W_0 u(2x+u) + \frac{1}{27}W_0(4x^2 - u^2) - \frac{1}{27}(2x+u)^2$	$\frac{1}{5}W_0 z^2$
	$k_2^{(K)} B_2^{(K)}$	0	0	0
	$k_2^{(K)} C_2^{(K)}$	0	$-\frac{20}{27}u^2 + \frac{8}{27}x^2$	$-\frac{1}{5}z^2$

Here the spherical harmonic of rank L is written $C_L(\hat{\mathbf{r}}) = (4\pi/(2L+1))^{1/2} Y_L(\hat{\mathbf{r}})$. Further, \mathbf{p} is the momentum operator, which in coordinate space is taken as a symmetrized derivative operator $-i\frac{1}{2}(\vec{\nabla} + \vec{\nabla})$. Lastly, g_V and g_A are the vector and axial-vector coupling constants of the weak interaction, and M is the nucleon mass in electron rest-mass units. We have also introduced ζ_0 and ζ_1 as specific combinations of nuclear matrix elements:

$$\begin{aligned} \zeta_0 &= \xi'v + \xi\omega' + \frac{1}{3}\omega W_0 \\ \zeta_1 &= \xi'y - \xi(u' + x') + \frac{1}{3}(u-x)W_0 \end{aligned} \quad (8)$$

Most first-forbidden non-unique decays studied have been low-energy transitions in heavy nuclei for which the inequality $\xi \gg W_0$ holds. In this limit the coefficient $k^{(K)}$ is of order ξ^2 , coefficients $k^{(K)} A^{(K)}$ and $k^{(K)} B^{(K)}$ are of order ξ and coefficient $k^{(K)} C^{(K)}$ is of order one. Thus in the ξ -approximation (in which only terms in the leading power of ξ are retained), the spectral functions $C(W)$ and $D(W)$ both become energy independent, and the beta spectrum has the allowed shape. The effect is independent of the nuclear matrix elements and thus little nuclear-structure information may be

determined from shape measurements alone. The beta-neutrino correlation coefficient in the ξ -approximation becomes energy independent and takes a simple form

$$a_{ev} = \frac{\zeta_0^2 - \frac{1}{3}\zeta_1^2}{\zeta_0^2 + \zeta_1^2} \quad (9)$$

Thus in a $0^+ \rightarrow 0^-$ transition in which only the rank-0 multipole enters, $a_{ev} = +1$, while in a $0^+ \rightarrow 1^-$ transition in which only rank-1 multipole enters, $a_{ev} = -1$. This is exactly the same situation that exists in allowed decays: $a_{ev} = +1$ for pure Fermi transitions and $a_{ev} = -1$ for pure Gamow-Teller transitions. Only for transitions for which both multipolarity 0 and 1 contribute is there any likelihood there will be any significant dependence on the details of nuclear matrix elements.

To test our coding, we have recomputed shell-model estimates of first-forbidden β -decay matrix elements for a few cases in light nuclei that are available in the literature. We start with a 1972 calculation of Towner and Hardy [2] for the $\frac{1}{2}^+ \leftrightarrow \frac{1}{2}^-$ transitions in ^{15}C , ^{17}N and ^{17}Ne . We compute the integrated spectrum shape function, f , defined as

$$f = \int_1^{W_0} W p(W_0 - W)^2 F_0 L_0 C(W) dW. \quad (10)$$

Since this latter quantity includes all the matrix-element information, first forbidden ft values (up to radiative and isospin-symmetry-breaking corrections) are all equal to a universal constant established from the average corrected $\mathcal{F}t$ value from superallowed beta decay: i.e.

$$ft = 2\mathcal{F}t = 6145 \text{ s}. \quad (11)$$

Thus an experimental value for f can be deduced from the measured partial half-life via Eq. (11). The results are listed in Table II. Our calculated matrix elements and the integrated spectrum shape function are in very good agreement with the published values. The experimental values for f obtained from the ENSDF [3] listings of partial half-lives are in excellent agreement with the shell-model results.

The other literature values we compare with are those of Millener *et al.* [4] for the β decay of ^{11}Be ($\frac{1}{2}^+$) to the ground state ($\frac{3}{2}^-$) and first excited state ($\frac{1}{2}^-$) in ^{11}B . Millener's shell-model calculation is based on six valence orbitals: $1s_{1/2}$, $p_{3/2}$, $p_{1/2}$, $d_{5/2}$, $2s_{1/2}$, and $d_{3/2}$ using the Cohen-Kurath [5] effective interaction for p -shell interactions, and the Millener-Kurath [6] effective interaction for the cross-shell interactions. No more than one nucleon occupies the sd -shell orbitals in the $1 \rightarrow 0\hbar\omega$ calculation, and no more than two in the $1 \rightarrow (0 + 2)\hbar\omega$ calculation. The inclusion of the lowest $1s_{1/2}$ orbital is essential for the $2\hbar\omega$ calculation, in order that the spurious centre-of-mass motion could be correctly removed. In our

work, we only use five orbitals, $p_{3/2}$, $p_{1/2}$, $d_{5/2}$, $2s_{1/2}$ and $d_{3/2}$, and do not remove the spurious centre-of-mass component.

Table II. Nuclear matrix elements (in fm units) for $\frac{1}{2}^+ \rightleftharpoons \frac{1}{2}^-$ transitions in the β decay of ^{15}C , ^{17}N and ^{17}Ne from the published values of Towner and Hardy [2] and the present work. Also given is the integrated spectrum shape function f and its current experimental value.

	$^{15}\text{C}(\beta^-)^{15}\text{N}$		$^{17}\text{N}(\beta^-)^{17}\text{O}$		$^{17}\text{Ne}(\beta^+)^{17}\text{F}$	
	TH72	this work	TH72	this work	TH72	this work
w	-1.854	-1.882	0.734	0.777	-0.734	-0.777
$\xi'v$	46.454	47.051	-16.025	-16.993	14.596	15.422
x	0.927	0.930	0.425	0.438	0.425	0.438
u	2.085	2.099	0.850	0.904	-0.850	-0.904
$\xi'y$	23.130	23.238	9.190	9.582	8.341	8.696
f	841	873	34	39	402	441
Expt.[3]	$f = 935 \pm 20$		$f = 45 \pm 7$		$f = 350 \pm 60$	

Our results are shown in Table III. For the small space $1 \rightarrow 0 \hbar\omega$ calculation, our values of the coordinate matrix elements, w , x , u , z , agree quite well with Millener's values, but we are less successful in the $1 \rightarrow (0+2) \hbar\omega$ calculation. This is probably due to our failure to remove the spurious centre-of-mass component from the $2\hbar\omega$ wave functions. For the relativistic matrix elements, we have used Siegert's theorem for both ξv and ξy . Millener uses a similar but not identical CVC relation for ξy and derivatives of oscillator functions for ξv . So our results differ from Millener's on the value of the

Table III. Nuclear matrix elements (in fm units) for the β decay of $^{11}\text{Be}(\frac{1}{2}^+)$ to the ground state ($\frac{3}{2}^-$) and first excited state ($\frac{1}{2}^-$) in ^{11}B from the published values of Millener *et al.*[4] and the present work in a small shell-model space, $1 \rightarrow 0 \hbar\omega$ and a large space $1 \rightarrow (0+2) \hbar\omega$. Also given is the integrated spectrum shape function for each multipole, $f^{(K)}$, and their sum: $f = \sum_K f^{(K)}$.

Final state		Millener <i>et al.</i>	present work	Millener <i>et al.</i>	present work
		$1 \rightarrow 0 \hbar\omega$	$1 \rightarrow 0 \hbar\omega$	$1 \rightarrow (0+2) \hbar\omega$	$1 \rightarrow (0+2) \hbar\omega$
$\frac{1}{2}^-$	w	-1.206	-1.243	-1.178	-1.023
	$\xi'v$	35.840	27.417	30.160	22.569
	x	0.456	0.462	0.453	0.313
	u	1.387	1.404	1.350	0.969
	$\xi'y$	9.305	10.184	9.244	6.907
	$f^{(0)}$	465	206	293	140
	$f^{(1)}$	38	42	37	20
	f	503	248	330	160
	Expt. [4]	$f^{(0)} = 115 \pm 18$	$f^{(1)} < 35$	$f = 140 \pm 8$	
	$\frac{3}{2}^-$	x	0.532	0.535	0.544
u		-1.054	-1.027	-0.971	-0.755
$\xi'y$		13.080	14.015	13.360	10.624
z		1.816	1.977	1.900	1.520
f		415	476	425	274
Expt. [4]		$f = 244 \pm 9$			

relativistic matrix elements and hence on the integrated spectrum shape, f . Both calculations in the small space, $1 \rightarrow 0 \hbar\omega$, find f values much larger than the experimental value. In the larger space, $1 \rightarrow (0 + 2) \hbar\omega$, our results are closer to experiment than Millener's because our relativistic matrix elements are smaller. This result gives some support for the use of Siegert's theorem in the evaluation of relativistic matrix elements.

[1] H. Behrens and W. Bühring, *Electron Radial Wave Functions and Nuclear Beta-decay* (Clarendon Press, Oxford, 1982).

[2] I.S. Towner and J.C. Hardy, *Nucl. Phys.* **A179**, 489 (1972).

[3] Evaluated Nuclear Structure Data File (ENDSF), [www.nndc.bnl.gov].

[4] D.J. Millener, D.E. Alburger, E.K. Warburton, and D.H. Wilkinson, *Phys. Rev. C* **26**, 1167 (1982).

[5] S. Cohen and D. Kurath, *Nucl. Phys.* **73**, 1 (1965).

[6] D. Millener and D. Kurath, *Nucl. Phys.* **A283**, 315 (1975).

SECTION IV

SUPERCONDUCTING CYCLOTRON AND INSTRUMENTATION

K500 operations and development

D.P. May, G.J. Kim, B.T. Roeder, H.L. Clark, and F.P. Abegglen

Introduction

During the 2014-2015 reporting period a total of 29 different beams, including 15 newly developed beams, were used for experiments, and there were a total of 37 beam tunings for these experiments. The SEE program and the charge-breeding effort are treated separately in this progress report.

Ion Sources

During the shutdown ECR1 was opened for examination, and it was found that there had been no further deterioration in the damaged spot that had developed over a plasma flute on the aluminum wall.

Cyclotron Beams

New beams of ^{10}B at 31 AMeV, ^{12}C at 2.7 AMeV and 7.0 AMeV, ^{15}N at 7.0 AMeV, ^{16}O at 3.5 AMeV and 40 AMeV, ^{18}O at 40 AMeV, ^{22}Ne at 31 AMeV, ^{24}Mg at 24.0 AMeV, ^{25}Mg at 13 AMeV, ^{31}P at 30 AMeV and ^{36}Ar at 17 AMeV and 36 AMeV, ^{40}Ca at 40 AMeV and ^{44}Ca at 4.9 AMeV were developed for experiments.

Operations

For the period April 1, 2014 through March 31, 2015, the operational time is summarized in Table I, while Table II lists how the scheduled time was divided. A water-leak in a lower dee-stem occurred five days before the December shut-down, which accounted for the bulk of the unscheduled maintenance. Most of the repair for this leak occurred during the shutdown. Scheduled maintenance occurred mainly in the January-February shut-down.

Table I. 2014-2015 operational time.

Time	Hrs.	%Time
Beam on target	6283	71.9
Beam development	722	8.3
Scheduled maintenance	1456	16.7
Unscheduled maint	275	3.1
Total	8736	100.0

Table II. 2014-2015 Scheduled Beam Time.

Time	Hrs.	%Time
Nuclear physics	1469.5	21.0
Nuclear chemistry	1560	22.3
Outside collaboration	0	0.0
Outside users	3253.5	46.4
Beam development	722	10.3
Total	7005	100.0

Texas A&M cyclotron radiation effects facility
April 1, 2014 – March 31, 2015

H.L. Clark, J. Brinkley, L. Chen, G. Chubarian, V. Horvat, B. Hyman, B. Roeder, and G. Tabacaru

The activity of the Radiation Effects Facility (REF) increased over the previous reporting year. In this reporting period, the facility was used for 3,024 hours, which is a ~26% increase over the 2,399 hours used in the 2013-2014 reporting period and was the second highest usage year ever (3,042 in reporting year 2010-2011). Users of the facility (and hours used) over the past year were: Sandia National Laboratory (287), NASA GSFC (274.5), NASA JPL (208), Honeywell (181), International Rectifier (156), Intersil (152.5), SEAKR (152), Aeroflex (140.25), HIREX-France (136), NAVSEA (117), Microsemi (115.75), Lockheed Martin (96), BAE Systems (86), Ryoei-Japan (84), Defense Threat Reduction Agency (80), IMT-Italy (68.5), Johns Hopkins (62.5), Texas Instruments (56), Boeing Satellite Systems (48.5), Ball Aerospace (48), Northrop Grumman (47.5), L-3 Communications (44), ATMEL-France (30.5), GNSS-Norway (24), Scientic (24), Thales Alenia-France (24), VPT Inc (23.5), DSO-Singapore (22.5), Raytheon (22.5), Maxwell (16.5), InnoFlight (16.25), Cisco (16), General Dynamics (16), Harris (16), Signal Analysis (16), Save Inc (14), Peregrine (13.5), ICs LLC (12), Blue Line Engineering (12), IBM Corporation (12), ARIA (9.5), University of Saskatchewan-Canada (9.5), SwRI (9), University of Colorado/LASP (8), RES LLC (8), T2 Research (8). New users included Ryoei-Japan, IMT-Italy, GNSS-Norway, DSO-Singapore, InnoFlight, Signal Analysis, ICs LLC, Blue Line Engineering, ARIA, University of Saskatchewan-Canada, University of Colorado/LASP and RES LLC .

Table I compares the facility usage by commercial and government customers. The ratio from

Table I. Radiation Effects Facility usage by commercial and government customers for this and previous reporting years.

Reporting Year	Total Hours	Commercial Hours (%)	Government Hours (%)
2014-2015	3,024	1,975 (65%)	1,049 (35%)
2013-2014	2,399	1,517 (63%)	882 (37%)
2012-2013	2,626	1,856 (71%)	770 (29%)
2011-2012	2,673	1,630 (61%)	1,043 (39%)
2010-2011	3,042	1,922 (63%)	1,121 (37%)
2009-2010	2,551	1,692 (66%)	859 (34%)
2008-2009	2,600	1,828 (70%)	772 (30%)
2007-2008	2,373	1,482 (62%)	891 (38%)
2006-2007	2,498	1,608 (64%)	890 (36%)
2005-2006	2,314	1,314 (57%)	1,000 (43%)
2004-2005	2,012	1,421 (71%)	591 (29%)
2003-2004	1,474	785 (53%)	689 (47%)
2002-2003	1,851	1,242 (67%)	609 (33%)
2001-2002	1,327	757 (57%)	570 (43%)
2000-2001	1,500	941 (63%)	559 (37%)
1999-2000	548	418 (76%)	131 (24%)
1998-1999	389	171 (44%)	218 (56%)
1997-1998	434	210 (48%)	224 (52%)
1996-1997	560	276 (49%)	284 (51%)
1995-1996	141	58 (41%)	83 (59%)

this reporting year (65% to 35%) is similar to the trend seen in previous reporting periods and commercial hours still dominate (see Fig 1). Commercial hours increased by 30% and government hours increased by 19% over hours from 2013-2014. 15 MeV/u ions were the most utilized and especially 15 MeV/u Au. No new beams were added to SEELine users list. Much of the testing conducted at the facility continues to be for defense systems by both government and commercial agencies. Almost 17% (340 hours) of the commercial hours were for foreign agencies from Canada, France, Italy, Japan, Norway and Singapore. It is expected that the facility will continue to be as active in future years.

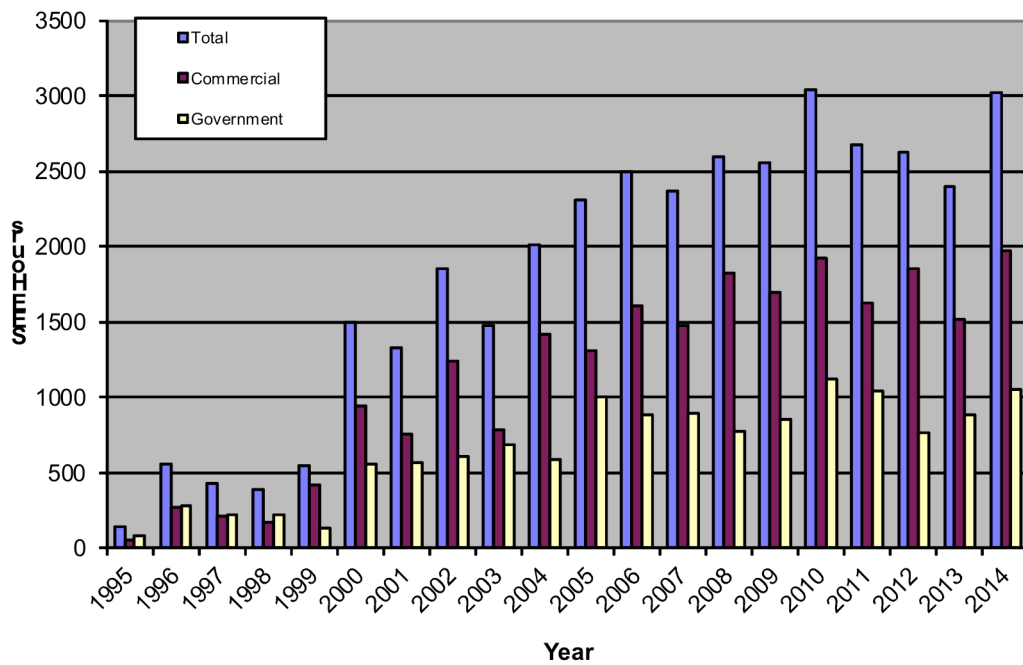


FIG. 1. Radiation Effects Facility usage by commercial and government customers for this and previous reporting years. The ratio from this reporting year (65% to 35%) is similar to the trends seen in previous reporting periods where commercial hours still dominate. About 17% (340 hours) of the commercial hours were from foreign agencies from Canada, France, Italy, Japan, Norway and Singapore.

Plans for new ECR4 ion source

D.P. May and L.E. Henderson

Introduction

A new electron-cyclotron-resonance source (ECRIS), designated ECR4, is being designed as a supplement to the ECR1 ion source currently injecting the K500 cyclotron. The new source will use 6.4 GHz microwave heating and its design will incorporate the successful magnetic field structure of ECR1.

Ion Source Design

The magnetic fields for ECR4 were optimized using the POISSON-SUPERFISH software. The specifications for the NdFeB permanent magnets in the hexapole structure, including the residual magnetization (B_r), coercivity (H_c) and dimensions were determined via the PANDIRA tool of the software (Fig. 1). The yoke and coil geometry was determined using the POISSON tool (Fig. 2). This hexapole structure for ECR4 is almost identical to that of ECR1, with the exception of somewhat higher B_r and H_c for ECR4. The yoke-coil structure was simplified from ECR1 so that only seven identical coils are incorporated; no steel connects the two ends of the yoke; and the injection-end, steel plug is shorter. This optimization is possible because the ideal magnetic field profile was retrofitted to ECR1 which uses a nine-coil (eight identical and one larger) yoke structure.

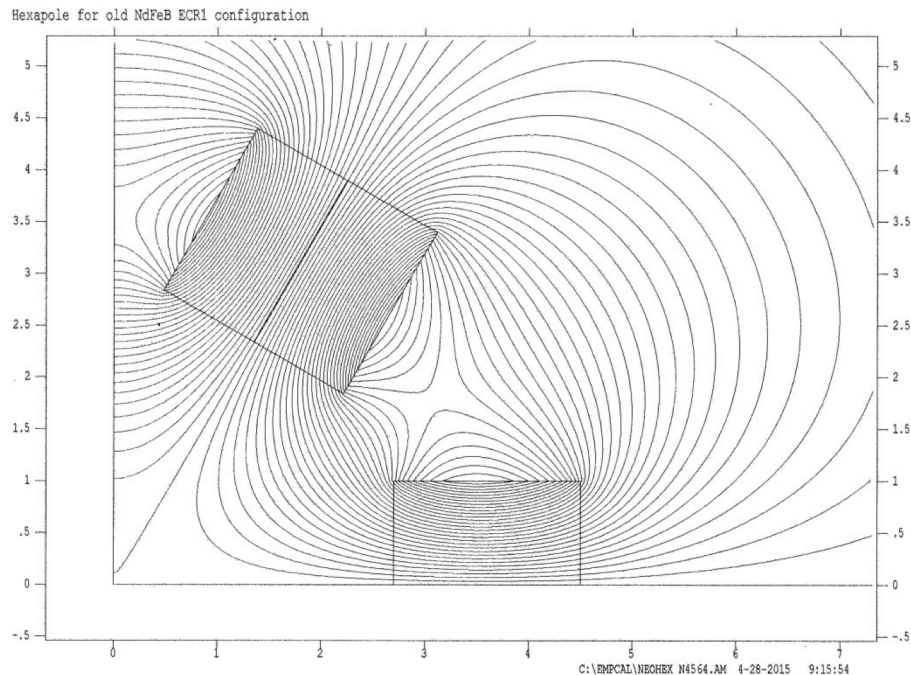


FIG. 1. PANDIRA simulation of the hexapole design.

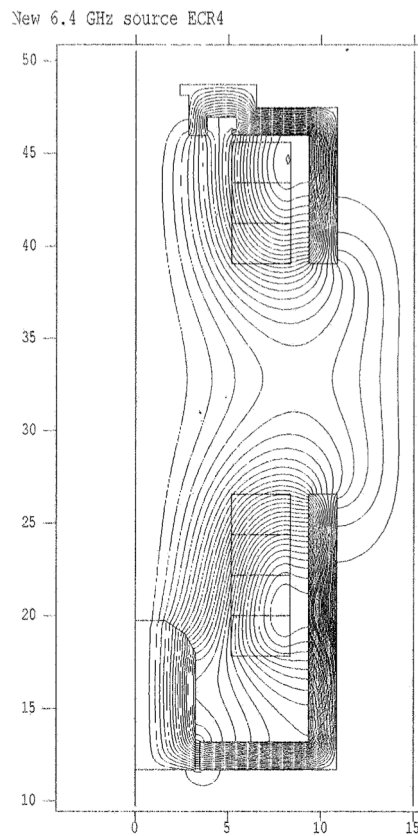


FIG. 2. POISSON simulation of the steel yoke and coil assembly.

Plans

The mechanical drawings for ECR4 are currently being made. The plasma chamber will feature more water-cooling for the permanent magnets. The source will also accommodate studies of the ECR plasma that relate to the beam properties, including charge-state distribution, stability and emittance. These studies will include x-ray spectroscopy of the plasma and will constitute a thesis project for L. E. Henderson.

Axially-mounted, high-temperature oven for ECR2

H. Peeler, F.P. Abegglen, B.T. Roeder, and D.P. May

The high-temperature oven for axial mounting on ECR2 described in the last progress report has been tested, producing beams of both titanium and aluminum. The oven was modelled on the design of an oven for the production of uranium for the ECR ion sources at the LBL 88" Cyclotron [1].

First the power supply was mounted on an insulated platform above the source (Fig. 1) and powered through an isolation transformer. Natural titanium in powder form was loaded into the tantalum crucible and the crucible clamped between the two current leads. The back-plate-oven-assembly was then inserted into the injection end of ECR2. After pumping and rf-conditioning of the ion source the oven

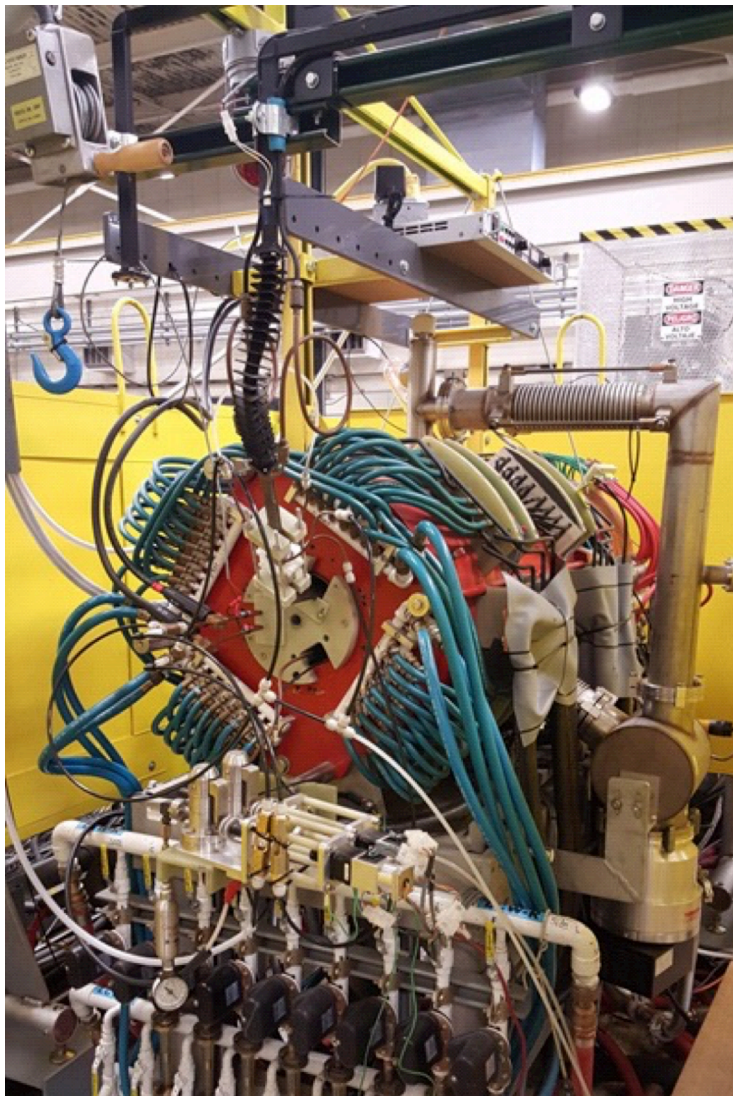


FIG. 1. The high-current supply mounted above ECR2. The water-cooled leads for the oven enter on the left-hand side of the center G-10 disk that mounts the steel plug.

current was slowly raised until a charge-state spectrum of titanium appeared. This spectrum shifted to more intensity in the higher charge-states over the course of several hours. The oven current was optimum at 130 A at 1.6 V. Before in the test chamber, titanium was observed to be depositing when the current reached 110 amperes at 1.2 volts. The temperature for a vapor pressure of 10^{-6} torr for titanium is about 1220 °C. Fig. 2 shows one of the charge-state scans from the test.

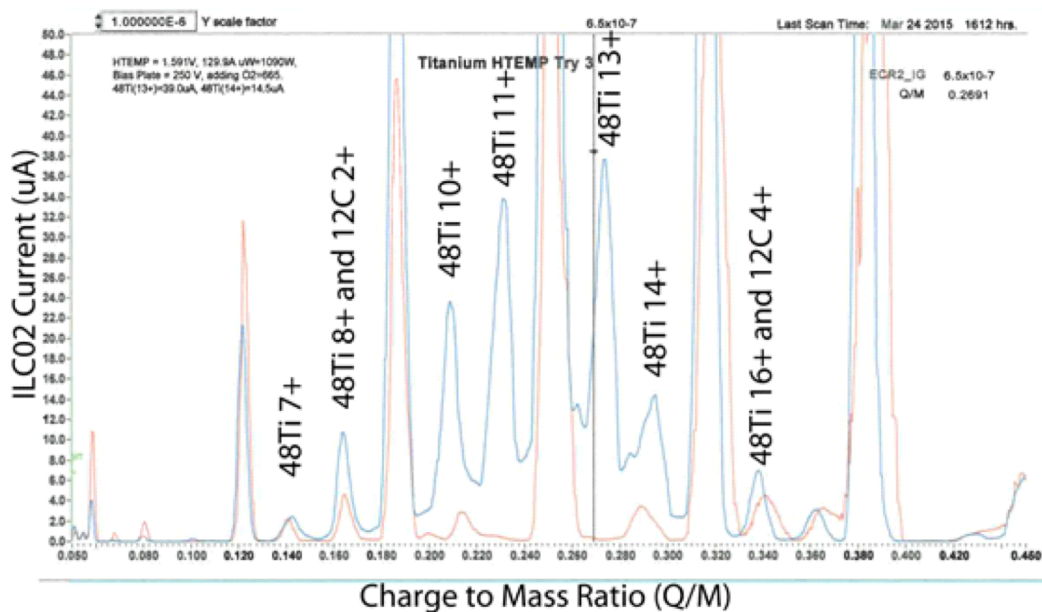


FIG. 2. Scan showing the titanium spectrum superimposed over the spectrum taken before the oven was turned on.

In another test aluminum wire was loaded into a different tantalum crucible. An aluminum charge-state spectrum was observed, but at a much higher oven current than predicted. Withdrawing the oven it was found that liquid aluminum was migrating from the crucible onto the oven heat-shields and onto the wall of the plasma chamber. Unlike titanium and many other metals, aluminum has a lower melting temperature (660 °C) than its temperature (820 °C) for a sufficient vapor pressure for the source. In a subsequent test, tungsten screen was inserted blocking the exit hole of the crucible, interfering with leakage of the liquid aluminum but allowing aluminum vapor to pass through. Leakage of aluminum was much reduced as was the required oven current. Fig. 3 shows the oven after removal immediately after this test. With the tungsten screen, aluminum was observed in the charge-state spectrum with oven settings as low as 106 A and 1.0V. The optimum aluminum output was observed with 110.7 A and 1.2V over the course of several hours.

Eventually the oven will be tested in the production of beams requiring even higher vaporization temperatures.

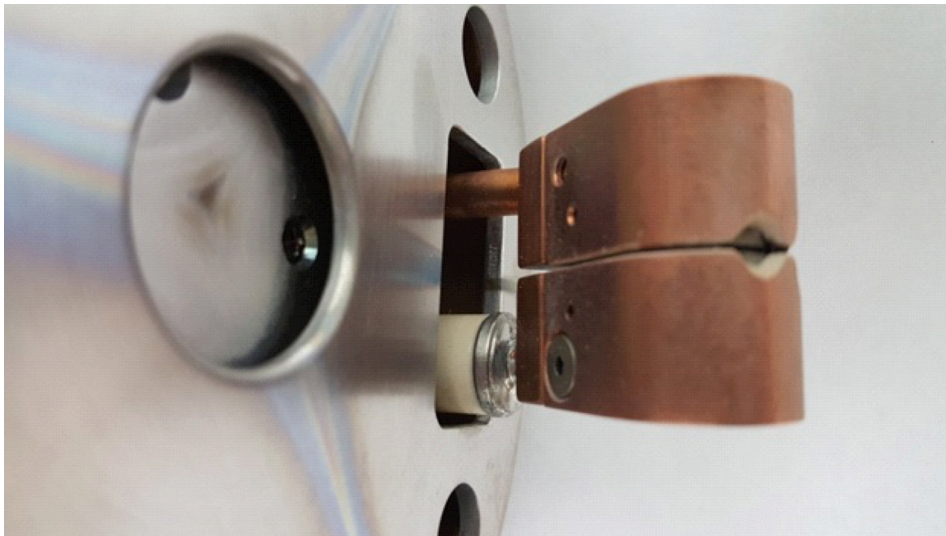


FIG. 3. The oven on the injection plate immediately after the aluminum test.

- [1] T. Loew, S. Abbott, M. Galloway, D. Leitner, and C.M. Lyneis, Proceedings of the Particle Accelerator Conference, Albuquerque, NM, USA (2007), p. 1742.

Texas A&M cyclotron K150 broad beams for foil irradiation

L.E. Henderson and H.L. Clark

The Broad Beam project aims to deliver a uniform, narrow, 35 cm wide beam spot to customers who will contract beam time on the K150 Cyclotron for the production of ultrafine filters. The broad beams will be produced electromagnetically by setting the final quadrupole magnet to defocus in one plane thus allowing the beam to grow to 35 cm as it drifts down the beamline (Fig. 1). Existing hardware has been used where possible to speed up construction and reduce cost.

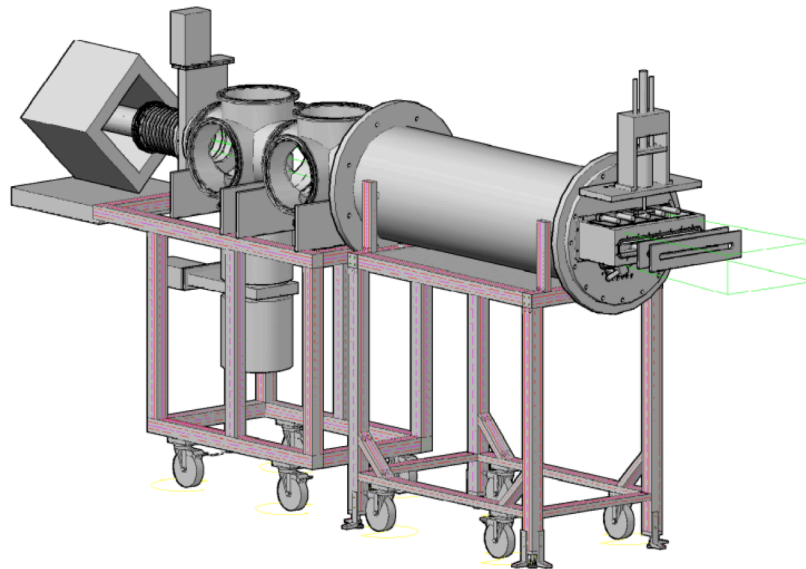


FIG. 1. Simplified beamline after the defocusing quadrupole magnet.

The most recently completed part, the “duckbill” (Fig. 2), completes the outer mechanical structure of the beamline. However, mounting assemblies are still being made for the scintillator detectors and filter foil samples. The duckbill provides the beam window for in-air delivery of the beam and housing for detectors used to monitor the beam in vacuum. Existing scintillators from SEELine will be used as the detectors, which will be monitored and logged by a system of National Instruments PCI/PCIe cards, NIM units, and other electronics. This experiment will serve as an evaluation for the use of similar cost-saving electronics in other applications. Equipment such as vacuum pumps, cabling, and NIM electronics is shared with the SEELine proton irradiation setup in the 88” Vault. A minimal-setup test run in December 2014 demonstrated the expected beam profile, but issues with the electronics prevented an exact measurement of beam uniformity. A test run is expected in the summer of 2015.



FIG. 2. Duckbill, detector mounting plate, two interchangeable beam windows, beam window transition plate and Duckbill mounting flange with feedthrough holes.

A new radiation effects facility beam line

B. Hyman, H.L. Clark, G.J. Kim, B. Roeder, and S. Russell

A new Radiation Effects Facility beam line has been developed for the K150 Cyclotron. The anticipated primary use for the beam line will be for space electronics and materials testing with proton beams, although heavy ion beams will also be available. While the beam line has initially been installed in the K150 vault (see Fig. 1), it has been designed such that it can be relocated to other experimental areas within the building as needed. The new beam line has all of the features of the existing K500 Radiation Effects beam line with the exceptions of a vacuum chamber and a beam energy degrader system. Unique to the new beam line is an actuated aluminum shield to protect the scintillator detectors during high intensity proton exposures. As much as possible, hardware and electronics have been duplicated with equipment currently used with the existing K500 Radiation Effects Facility beam line. Beam uniformity of >90% has been achieved using 12 MeV/u ^{16}O . A first external customer has been scheduled to test on the new beam line in June 2015 using 40 MeV protons.

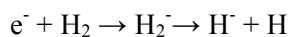


FIG. 1. New Radiation Effects Facility beam line developed for use with the K150 Cyclotron.

Repair of the H⁻ ion source

H. Clark, B.T. Roeder, D.P. May, G. Kim, F. Abegglan, H. Peeler, and G. Tabacaru

The H⁻ ion source has been providing high-intensity H⁻ and D⁻ ions to the K150 cyclotron since 2008. The H⁻ source is a magnetically filtered multicusp volume ion source [1] and operates in two stages. In the first stage, a hot filament of tantalum ionizes hydrogen gas into H⁺ and e⁻. The resulting plasma is confined by permanent magnets positioned around the ion source chamber (the “multicusp” field). In the second stage, near the exit of the ion source, but before the extraction region, there is a magnetic filter stage that also consists of permanent magnets. The magnetic filter serves two purposes. First, the field in the magnetic filter region is strong enough to prevent all energetic electrons from escaping the plasma chamber of the ion source in the first stage. Second, the magnetic filter captures low energy electrons which are capable of dissociating H₂ molecules in the following process:



which is the main method of producing H⁻ (or D⁻) ions in the ion source. The resulting negative ions are then extracted with a voltage of 8-10 kV and injected into the K150 cyclotron for acceleration.

In December 2014, a water leak was discovered in the H-minus ion source. The source of the water leak was a small hole in one of the water cooling lines that make up the magnetic filter part of the source mentioned above. A picture of the magnetic filter region of the ion source before the repair is shown in Fig. 1.

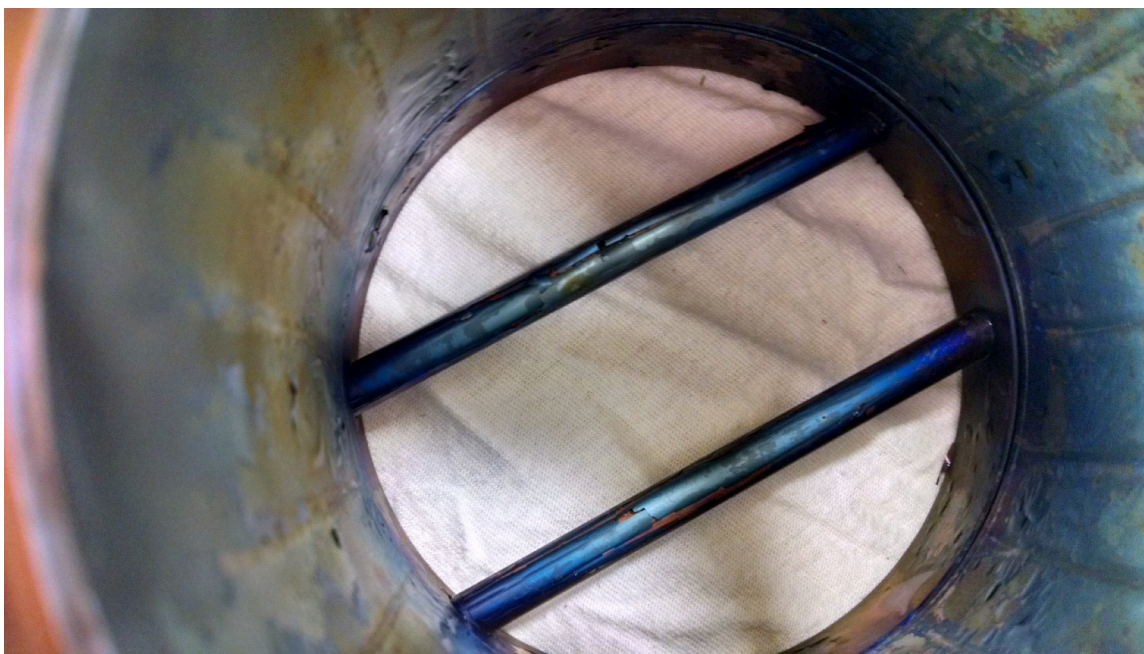


FIG. 1. Picture of the inside of H⁻ ion source plasma chamber with the tantalum filament removed. The magnetic filter region is formed by the field from small permanent magnets housed in the two copper water cooling lines that pass through the middle of the chamber near the source exit. The damaged water cooling line is the upper pipe in the picture.



FIG. 2. The new cooling line installed in the magnetic filter region of the H^- source. The north poles of the permanent magnets are aligned perpendicular to the path of the extracted beam as shown above.

To repair the leak, the upper cooling line shown in the figure was removed. The first idea for the repair was to try to plug the hole with solder or similar material, but the heating process would likely damage the permanent magnet that was housed on the inside of the cooling line. Also, when the magnet was removed from the damaged copper line, it was found to be broken and severely corroded. In the end, it was decided to make a new cooling line with a new permanent magnet embedded in the middle. We found that we had purchased some replacement permanent magnets during the original installation of the ion source. The magnets are made of $SmCo_5$, and are held in place in the middle of the cooling line where they are kept cool with low-conductivity water. The new cooling line consists of two of the replacement $SmCo_5$ magnets super-glued together pole to pole on a thin rod of Inconel. The resulting rod was then mounted in the middle of the new copper cooling line and reinserted into the plasma chamber of the H^- ion source. Finally, the north poles of both of the magnetic filter permanent magnets were aligned in the same direction and perpendicular to the path of the extracted H^- beam. The new cooling line installed in the magnetic filter region of the source is shown in figure 2. When the ion source was reassembled, the inside of the plasma chamber was also thoroughly cleaned to remove the deposits that had built up on the walls.

As a result of the repair, the H^- ion source is again operational and is producing H^- ions with intensities similar to those observed previously. However, the extraction optics of the ion source have changed slightly now that the new permanent magnet has been installed. This slight change does not significantly affect the performance of the ion source.

[1] H. Zhang, Ion Sources, (Science Press, Beijing, 1999). Section 8.6.3, p. 364-368.

Cyclotron Institute upgrade project

H.L. Clark, F. Abegglen, G. Chubaryan, G. Kim, D.P. May, B. Roeder, and G. Tabacaru

On January 3, 2005 the Cyclotron Institute Upgrade Project (CIUP) began with the approval of the CIUP management plan by the Department of Energy Nuclear Physics Office. The project will extend at least to the second quarter of calendar year 2016. When completed, the upgraded facility will provide high-quality re-accelerated secondary beams in a unique energy range in the world. Funding for the upgrade comes from several sources: the Department of Energy, matching support from TAMU, the Robert A. Welch Foundation and beam time sales for testing electronics components at the Cyclotron Institute.

The CIUP is divided into three major tasks: (1) Re-commission of the existing K150 (88") cyclotron and refurbish beam lines; (2) Construct light-ion and heavy-ion guides and produce 1+ radioactive ions; (3) Transport and charge boost radioactive ions and accelerate in the K500 cyclotron.

Effort made during this year included beam development of the K150 cyclotron, testing and development of the Light Ion Guide (LIG) gas cell and assembly of the Heavy Ion Guide (HIG) transport system equipment. Below we report on a few of the accomplishments listed above.

I. K150 Cyclotron Development

In the past year, we provided eleven beams, proton to silicon, using the H^- and the ECR ion sources, for in-house groups and one alpha beam for the STAR/LIBERACE collaboration. The late start for the beams and a water leak in the 88 LCW heat exchanger limited the time available for the experiments. The efficiency for the proton beams from the H^- source continues to be very high, up to 50% throughput (the ratio of beam currents on FC02 divided by ILC02). For the ECRIS beams, about 10% for the 1st harmonic beams and about 3% for the 3rd harmonic beams were obtained for the throughput. We continue to strive to improve the beam tune.

The installation of a new "target probe", which measured the beam current very close to the inflector, and the complete replacement of the deflector spark shields took a long time to complete. The old deflector spark shield plates were found to be heavily damaged and had to be replaced; most of the plates were made of stainless steel except for a few plates near the deflector entrance which were made of tungsten. Due to the expense of making a complete new set of tungsten plates, the newly installed plates consist of new tungsten plates near the deflector entrance and a mix of new and used stainless steel plates for the middle and exit sections of the deflector. Even after the spark shield replacement, the difficulties with the deflector conditioning and necessary beam studies with the new target probe further delayed the start of beams for experiments to late July. Also, we moved the deflector power supply from the basement to above the deflector cage (at near the height of the top of the cyclotron yoke), (Fig. 1), bringing it close to the deflector and minimizing the HV cable length (from 75 ft to 8 ft), this in turn reduced the stored energy in the cable substantially. This reduction in the stored energy should help with controlling damage to the deflector spark plates. The power supply relocation also in resulted in much

calmer operations for the former neighbors of the deflector supply, such as Sol 3, which used to regularly fault off due to sparking from the deflector.



FIG. 1. The deflector power supply was relocated closer to the deflector above of the deflector cage. The supply is shielded from neutrons inside a box with 3 layers of 1" borated polyethylene panels.

II. Target Probe Measurements

The motivation for the target probe measurements was to study how and where the beam losses occur, especially for the 3rd harmonic beams. (The 3rd harmonic beams are beams with the final energies less than 6 AMeV, where the RF runs at 3 times the orbital frequency of the beam.) The target probe was temporary installed using the same port in the dee tank that is normally used for the stripper foil

mechanism for the H- extraction. The probe ran radially and it reached just 0.4" outside the inflector on the dummy dee side, intercepting the beam as it exited from the inflector. The probe was fitted with two heads, flat 5/8" wide copper paddles, oriented radially and perpendicular to the beam. One head was made 1/8" longer than other one in order to resolve the radii of the first few orbits at the cyclotron center, see Fig. 2.



FIG. 2. Target probe runs radially from the dummy dee side.

We used several ^{16}O and one ^{40}Ar beams from 5 to 10 AMeV to look at beam transmissions from ILC02 to FC02, with interests in beam losses and the RF acceptance at the center of the cyclotron; these measurements were then compared with the center region particle tracking calculations. The most radially inward position of the target probe was 0.9" from the center of the cyclotron, and 0.4" away from the inflector. At this radius, the transmission efficiency with respect to the current on ILC02 was about 35%, it was the same for the 1st and the 3rd harmonic beams. This number depends mainly on the injection line optics to focus the beam onto the mirror inflector; higher extraction voltages on the ECR ion source gave slightly better numbers. Since this was before any acceleration, the beam bunchers did not affect the measurement at 0.9". The transport efficiency from ILC02 to the inflector was about 65%, and it seemed that about half of the beam made it through the mirror inflector. Next, the beam transmission from 0.9" to 5", which is after 7 to 8 turns for the 1st harmonic beams and 6 to 7 turns for the 3rd harmonics beams, was about 60% for the 1st harmonic beams and about 35 to 50% for the 3rd harmonic beams. The probe readings were obtained with the bunched beams using both the 1st and 2nd harmonics bunchers. The lower numbers for the 3rd harmonic beams seemed to be due to a smaller RF acceptance

compared with the 1st harmonic beams. Also, the 2nd harmonic buncher was not always effective for the 3rd harmonic beams. Interestingly the 2nd harmonic buncher for the K150 cyclotron is much more effective than that for the K500. For example, for one 1st harmonic beam from the K150, the 1st harmonic buncher increased the beam intensity (on FC02) by a factor of 3.6 and then the 1st and 2nd harmonic bunchers together increased the beam by another factor of 1.7, for the total 6. On the K500, the 1st harmonic buncher boosts the beam by a factor of 2 to 4 and then the addition of the 2nd harmonic buncher helps only about 10% more. From $R = 5''$ to $15''$, all beams had better than 85% transmission, except the 5 AMeV $^{40}\text{Ar}^{12+}$ only 65%.

Comparing with the center region calculations, a typical orbit of a 1st harmonic beam is shown in Fig. 3. Looking at the turn-to-turn radius of the orbits at 110 deg, which is the location of the target probe, for turns 1 to 6 the radii of the orbits are at 2.3'', 3.1'', 3.8'', 4.4'', 4.9'', and 5.3''. These numbers compare very well with the measured radii of 2.5'', 3.2'', 3.9'', 4.4'', 4.9'', and 5.3''. The agreement gives confidence to the dee voltage that was used. This dee voltage translates into about 340 turns inside the cyclotron for the 1st harmonic beams. Also, from the orbit calculations, about 40 degree width (out of 360) for the RF acceptance was found for proper accelerations, and this gives $6 \times 40/360 = 0.67$ (including 6 for the bunching factor) and this compares well with 60% efficiency measured for the 0.9'' to 5'' transmission. Thus, the overall 10% throughput may be understood by $0.1=0.35$ (injection) \times 0.6 (RF acceptance) \times 0.85 (internal transmission) \times 0.6 (extraction).

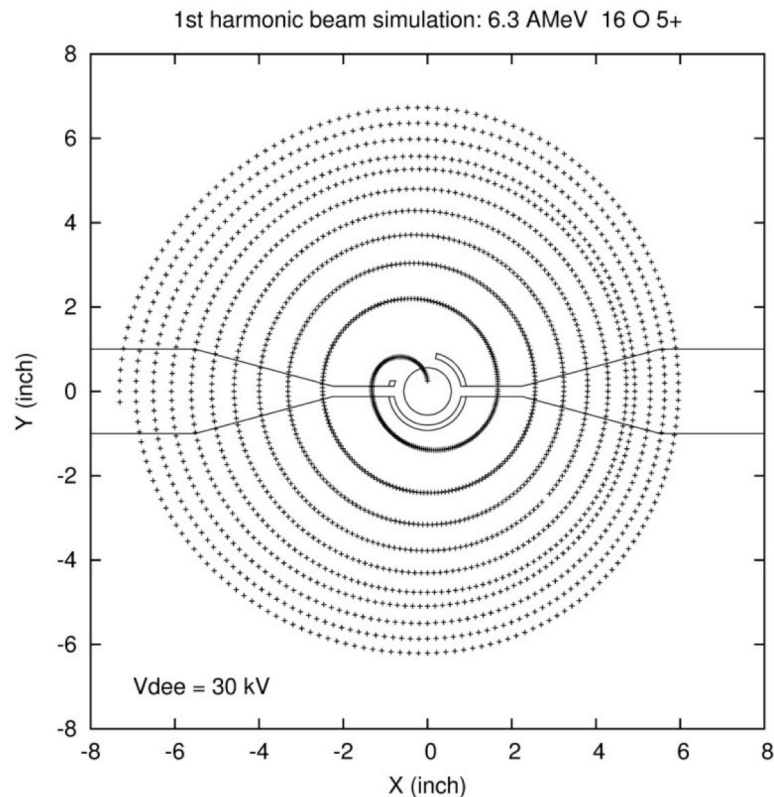


FIG. 3. First ten orbits of a 1st harmonic beam, specifically 6.3 AMeV $^{16}\text{O}^{5+}$, are shown. The beam exits from a mirror inflector at the center and into the dummy dee side before the acceleration begins.

Next, the 3rd harmonic beam data are compared with the center region calculations. A typical 3rd harmonic orbit is shown in Fig. 4. The radii of the first few orbits are at: 2.4", 3.5", 4.3", 5.0" and 5.6", which shows a little larger steps than the probe measurements of: 2.4", 3.1", 3.7", 4.3", 4.6", 5.1", and 5.4". Thus, it seems that the dee voltage used for the experimental measurements was less than the voltage for the calculation. Using a lower dee voltage in the calculation would have brought the orbit radii closer to the experimental numbers, however, it would have resulted in a smaller RF width for the acceptance. A computer simulation showed a 25 degree (out of 3×360 , but 3 bunches per orbit) RF acceptance (using a 224 turn scheme) for the 3rd harmonics beams. The RF acceptance is then $6 \times 25/360 = 0.4$ (using the same bunching factor of 6), and this number is compatible with the measured 35 to 50% efficiency for the 0.9" to 5" transmission. There is undoubtedly some vacuum attenuation, especially for the slower 3rd harmonic beams, but it is not possible to separate out this effect from the RF acceptance at this time.

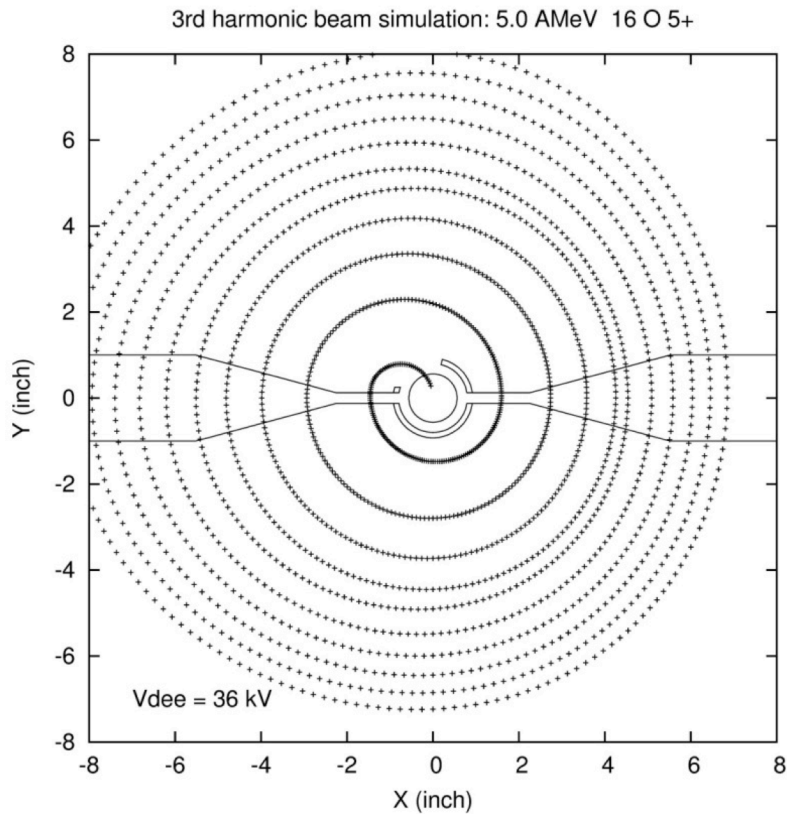


FIG. 4. 3rd harmonic beam simulation, specifically 5 AMeV $^{16}\text{O}^{5+}$ beam.

III. New Beam Tuning Scheme using VC04

For some beams a rapid intensity loss close to the extraction radius was observed. A new way of using VC04 (valley coil 4) was tried to reduce the beam loss near the extraction. In the past VC04 did not help to increase the beam current on FC02, and so it was usually not used. However, this time we tried to

peak the beam current at the extraction radius with VC04 turned on and VC05 off. After that, we turned on VC05 to extract the beam onto FC02. The required VC05 bump was less and the bump angle was also different than if the beam was tuned without VC04. With the use of VC04, the beam loss at the extraction was reduced and the extraction efficiency improved. Using VC04 this way, we were able to tune out a few more (1st harmonic) beams in the fall of 2014 to get close to the desired 10% mark for the throughput.

IV. Light Ion Guide

The Light Ion Guide project continued to advance in the last year with the coupling of the Roots pumps chambers to the Charge Breeding-ECR Ion Source (CB-ECRIS). As explained previously [1], a campaign of experiments were performed in order to better characterize the device. Proton beams of 15 MeV and a natural zinc target were used to produce ^{64}Ga and ^{66}Ga as radioactive ion beams. The production cross-section for ^{64}Ga ($T_{1/2}=2.6$ min) is about 170 mbarn for 14.1 MeV, the final energy after passing through Havar windows in the target chamber. At this cross-section, sufficient products are stopped and extracted from the gas cell, as seen in the previous report. The 1 meter long RF-only sextupole was replaced by a shorter and larger one with the following characteristics: 2 sections of approximately 8 cm each long, with 4 mm diameter rods and the inner diameter of 8 mm (Fig. 5). This design is similar to the one presented in reference [2], although adapted to our chamber. The second section was replaced later with a longer one, double in length, in order to provide a better transport through the region of poor vacuum.

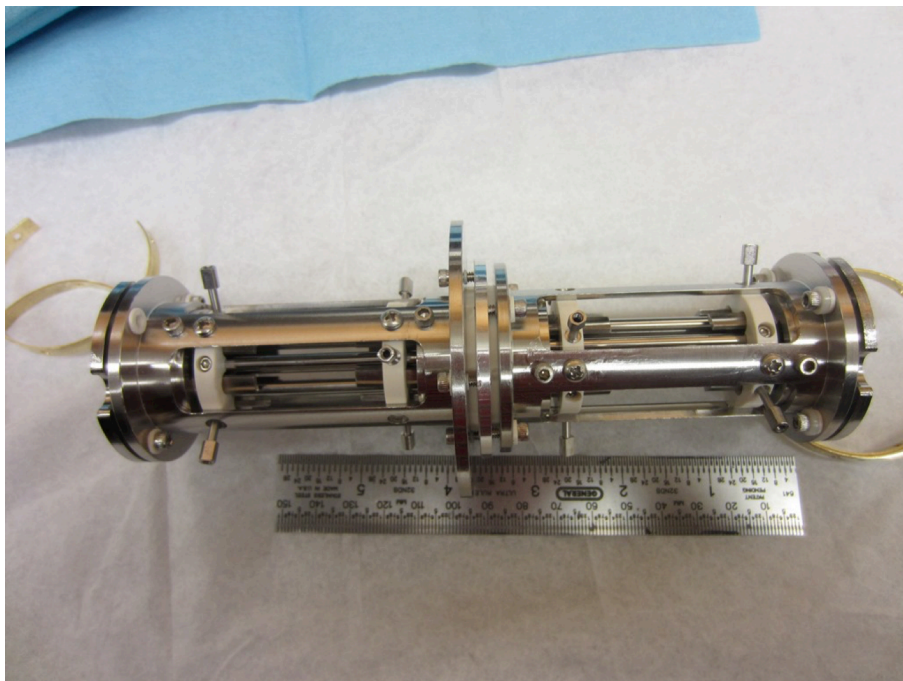


FIG. 5. The new RF-only sextupole before installation in the Light-Ion-Guide

The radioactive products are transported through the RF-only sextupole in the second Roots chamber where a grounded extraction tube was installed to provide the final acceleration (see Fig. 6). The region between the exit of the sextupole and the entrance to this tube should have good vacuum, so

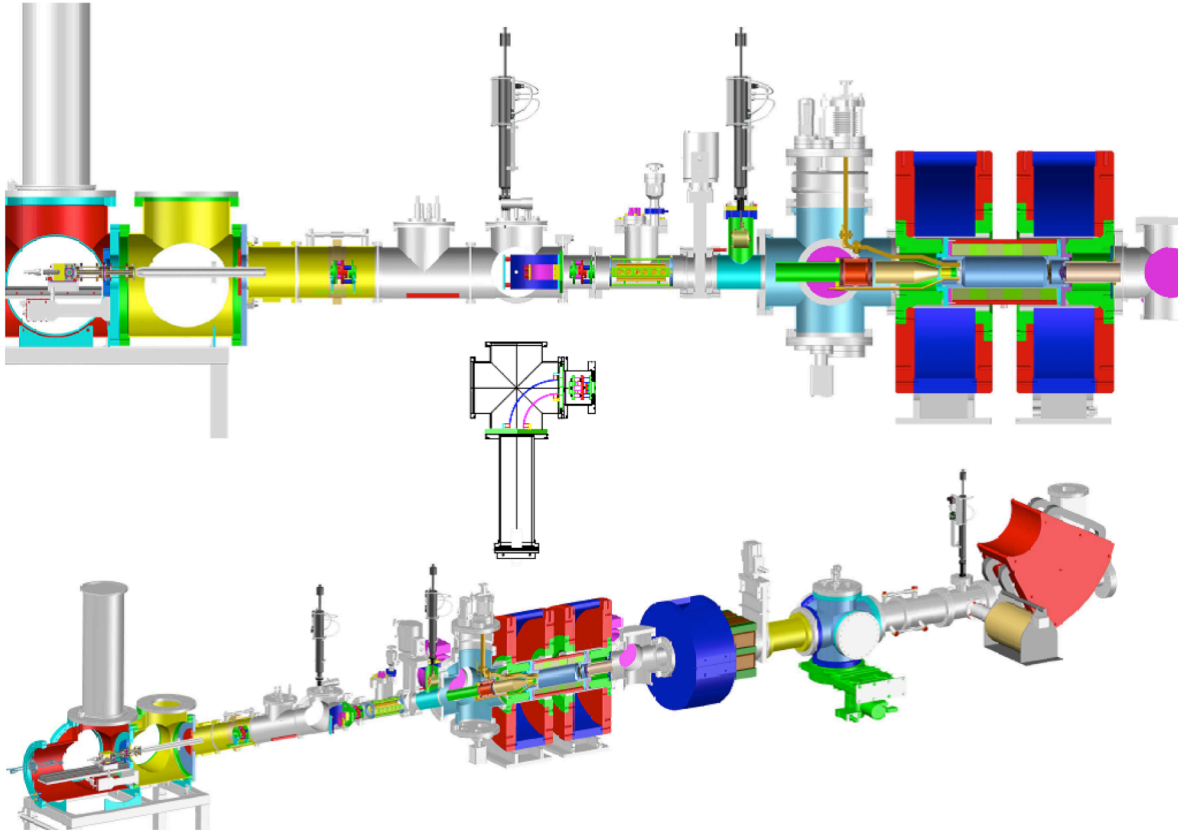


FIG. 6. Drawing of the Light Ion Guide coupled with the CB-ECRIS.

different strategies were tested and checked. Finally a turbo-molecular pump with 700 l/s pumping speed and a backing Roots blower of 1000 m³/h pumping speed were chosen. A compromise in the vacuum design of the whole system, the Light Ion Guide plus CB-ECRIS, must be made: good vacuum in the sextupole-to-ground acceleration region and excellent vacuum (10^{-7} torr range) in the CB-ECRIS injection region in order not to overload the ion source. The acceleration tube has an inner diameter of 19 mm and various apertures can be mounted at its entrance. An aperture of 6 mm diameter was the best choice to provide good vacuum at the extraction end and 10^{-7} torr range at the CB-ECRIS injection region. Another important parameter to be selected is the distance from the exit of the sextupole and the extraction tube. Various tests were performed, using the ²²⁸Th open source, and a distance of 25 mm was chosen as optimal. A shorter distance leads to the majority of the ions colliding inside the acceleration tube, and a larger distance leads to the ions being neutralized or scattered in the poor vacuum region. Simulations made with SIMION ion optics software show that for larger distances, better transmission is achieved, but the software does not take into account the transport through a poor vacuum region, so the direct comparison of SIMION with the experiment is not adequate.

The new set-up was tested first with the radioactive ^{228}Th open source and online with the proton beam on the zinc target. The tests performed using the ^{228}Th open source used a helium pressure of 28 mbar in the target chamber, consequently good vacuum was achieved along the beam line. However the on-line p+Zn tests use a helium pressure of 130 mbar and the transport of the radioactive ^{64}Ga was very sensitive to the vacuum conditions. With the choices mentioned previously we were able to find stable conditions and collect ^{64}Ga at the entrance of the CB-ECRIS. No transport efficiency was measured due to the difficulty of the measurements.

The next step was to transport ^{64}Ga through the CB-ECRIS and turn on the microwave power. The energy of the injected ^{64}Ga should be slightly above the CB-ECRIS plasma potential in order to achieve charge breeding. Multiple tunings were made to achieve the good transport settings, but due to the small amount of radioactivity involved and the difficulty of the measurements we only found settings with the energy of ^{64}Ga 3.5 keV higher than the CB-ECRIS potential. This energy difference is too big to achieve charge breeding, however interesting results were found: the radioactivity collected with the microwave turned on is higher than the case of the microwave turned off. Possible explanations for this behavior are either better focusing is achieved inside the plasma chamber, or more ions are produced by stripping or breaking complex molecules with radioactive products attached to it. In the Fig. 7 is represented the ratio of the number of counts from 991 keV line (^{64}Ga) to the Background for eight runs where the CB-ECRIS microwave power was turned on with different power settings and subsequently off.

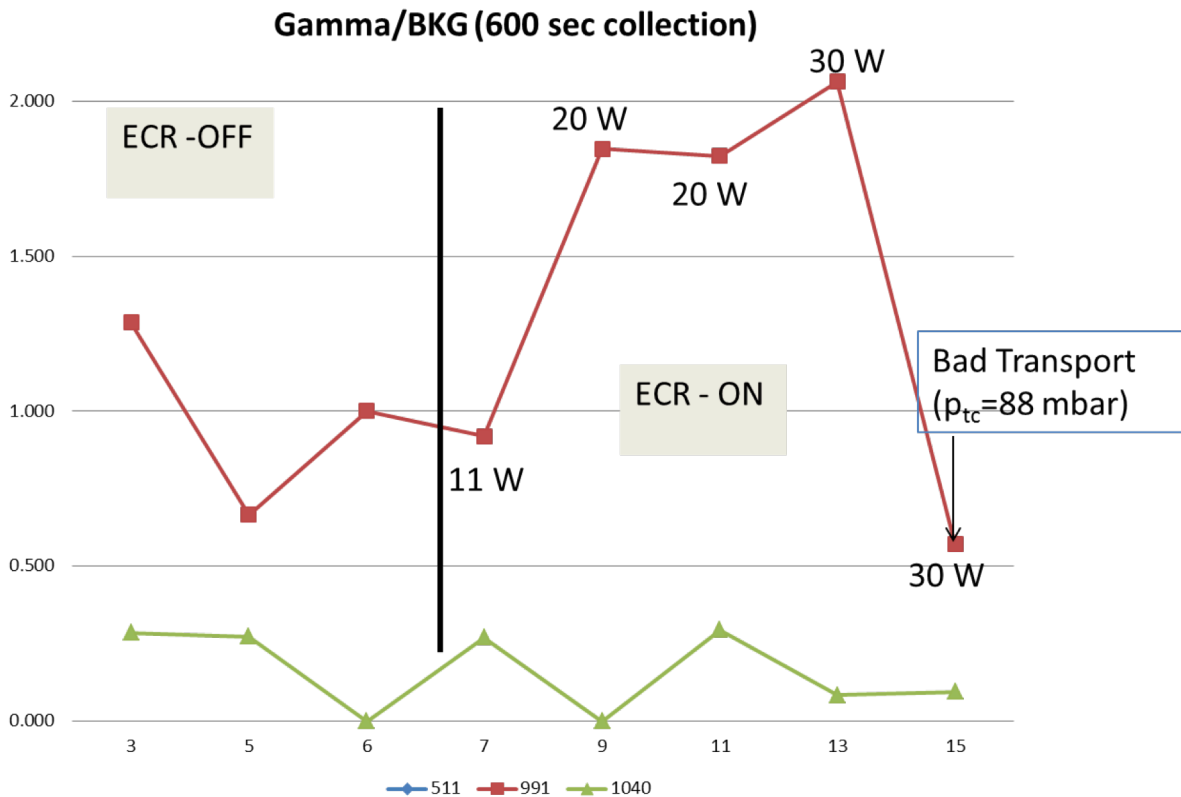


FIG. 7. Ratio of number of counts from 991 keV line (^{64}Ga) to the background for different runs with **microwave**

The lack of an efficient diagnostic system make the fine-tuning of the device very difficult. In the future our efforts will be directed towards improving the vacuum conditions in the second Roots chamber, finding better transport conditions for the radioactive products and developing an efficient diagnostic system for low intensity and low energy radioactive beams.

V. Heavy Ion Guide

The main components of the heavy-ion guide including the gas catcher and multi-RFQ have been assembled (see Fig. 8). Testing with a Cf source will begin in the fall.



FIG. 8. Heavy ion guide gas catcher (left) and multi-RFQ (right).

- [1] G. Tabacaru *et al.*, *Progress in Research*, Cyclotron Institute, Texas A&M University (2013-2014), p. IV-9. http://cyclotron.tamu.edu/2014%20Progress%20Report/cyclotron_progress_2014.pdf
- [2] P. Karvonen *et al.*, *Nucl. Instrum. Methods Phys. Res.* **B266**, 4794 (2008).

Cyclotron computing

R. Burch and K. Hagel

Cyclotron research programs require stable, fast, and secure computational and network resources. To that end, we continued to add infrastructure to accommodate the growing need for cpu power, storage, and network throughput. We also migrated our mail users to the University mail server as required by the recent decision of TAMU to consolidate email services.

The majority of our mail users have been successfully migrated from our departmental mail server to the TAMU central server. This enables us to eliminate headaches having to do with operating a mail server and transfers the responsibility of implementing University policy requirements for confidential data inherent in email as well as mail archiving requirements.

We added two powerful new computational servers, each with the ability to run 40 jobs concurrently, to the lab's general computational cluster. Additionally we provisioned for one particular group a computational docker grid comprised of 1 master node and 4 compute nodes capable of running a total of 48 jobs concurrently. This gives the lab a total of 53 computational servers capable of running 768 jobs concurrently.

Four new DAQ front-ends were brought online. Two small form-factor pc's for USB to VME crate readout and one larger with a PCE slot enabling it to utilize a PCE to VME fiber link for VME crate readout were implemented. We also implemented a Raspberry-Pi (\$50 credit card sized unix pc) to test the feasibility of utilizing it as a DAQ frontend for USB to VME crate readout.

A new backup server which has a capacity of 11 terabytes of storage was provisioned and put into production. It is currently at 8% storage utilization and has 8 free slots for an additional 32 terabytes of backup storage. We also added 32 terabytes of disk space to one group data file server and added 4 terabytes of disk space to the data file server for another group.

All aging 3COM 100 megabit network switches were replaced with new 1 gigabit switches to facilitate data analysis and network reliability since we were seeing switch lockups which resulted in loss of internal access for some users. We are continuing the process of recovering network addresses from devices which do not require outside internet interaction and reassign these addresses to devices that do.

MARS status report for 2014-2015

B.T. Roeder, A. Saastamoinen, and A. Spiridon

This year we produced and separated several radioactive beams for the physics program at the Cyclotron Institute at Texas A&M University with the Momentum Achromat Recoil Separator (MARS) [1]. Some of the beams in this report were developed during previous years [2]. A new, low energy ^{16}N beam was also developed (see below in section IV).

I. Production of radioactive beams for superallowed β -decay measurements

During 2014-2015, we tuned several radioactive beams with MARS for the group of Prof. J.C. Hardy with the (p, 2n) fusion-evaporation reaction. Nearly pure beams of ^{30}S , ^{26}Si , and ^{34}Ar were produced. These beams were needed as part of Prof. Hardy's research group's continuing studies of the lifetime and branching ratios for superallowed β -decays.

The ^{30}S beam was produced with the $p(^{31}\text{P}, ^{30}\text{S})2n$ reaction. A primary beam of $^{31}\text{P}^{10+}$ at 30 MeV/u from the K500 cyclotron bombarded the MARS gas cell target to produce the ^{30}S . The target was filled with 2 atm of H_2 gas cooled to 77K. After optimizing the tune of MARS, we obtained 90 eV/nC, or about 18,000 particles/sec of ^{30}S at the end of MARS with the full primary beam intensity. The total impurity rate was about 1.3%, with the main contribution coming from ^{27}Si at about 0.4%.

The ^{26}Si beam was produced with the $p(^{27}\text{Al}, ^{26}\text{Si})2n$ reaction. A primary beam of $^{27}\text{Al}^{8+}$ at 30 MeV/u from the K500 cyclotron bombarded the MARS gas cell target to produce the ^{26}Si . The target was filled with 2 atm. of H_2 gas cooled to 77K. After optimizing the tune of MARS, we obtained 240 eV/nC, or about 22,000 particles/sec of ^{26}Si at the end of MARS with the full primary beam intensity. The total impurity rate was about 1.6%, with the main contribution coming from ^{23}Mg at about 0.8%.

The ^{34}Ar beam was produced with the $p(^{35}\text{Cl}, ^{34}\text{Ar})2n$ reaction. A primary beam of ^{35}Cl at 30 MeV/u from the K500 cyclotron bombarded the MARS gas cell target to produce the ^{34}Ar . The target was filled with 2 atm of H_2 gas cooled to 77K. After optimizing the tune of MARS, we obtained 51 eV/nC, or about 20,400 particles/sec of ^{34}Ar at the end of MARS with the full primary beam intensity. The total impurity rate was about 1.1%, with the main contribution coming from ^{31}S at about 0.2%.

II. ^{35}K secondary beam

In March 2014, we produced and separated ^{35}K with MARS [2]. Following this successful test run, the ^{35}K β -delayed proton decay experiment was conducted in June 2014. Details of the measurement are given in a separate report [3]. For this measurement, the ^{35}K was produced with the fusion-evaporation reaction (p,2n) in inverse kinematics with ^{36}Ar primary beam at 36 MeV/u. Hydrogen gas at a pressure of 2 atm and at a temperature of 77K was used in the MARS gas cell target.

In the experiment, the ^{35}K secondary beam was slowed down and implanted into a thin silicon strip detector that is only ~ 45 μm thick. Thus, the ^{35}K secondary beam must have a small momentum spread such that all the nuclei produced are implanted into the detector. For the ^{35}K production test, we set

the MARS momentum slits (the “coffin slits”) to ± 0.5 cm, which corresponds to a momentum spread of the secondary beam of $\Delta P/P \approx \pm 0.3\%$. With this momentum slit setting, we produced ^{35}K at a rate of about 3.0 events/nC. This gave a rate of about 450 particles/sec for the ^{35}K (using 150 nA of ^{36}Ar primary beam) with about 40% impurities. The largest impurity contribution came from ^{32}Cl , but this did not significantly affect the experiment. The ΔE vs. Y-position spectrum on the MARS target detector showing the resulting secondary beam for the ^{35}K is shown in Fig. 1.

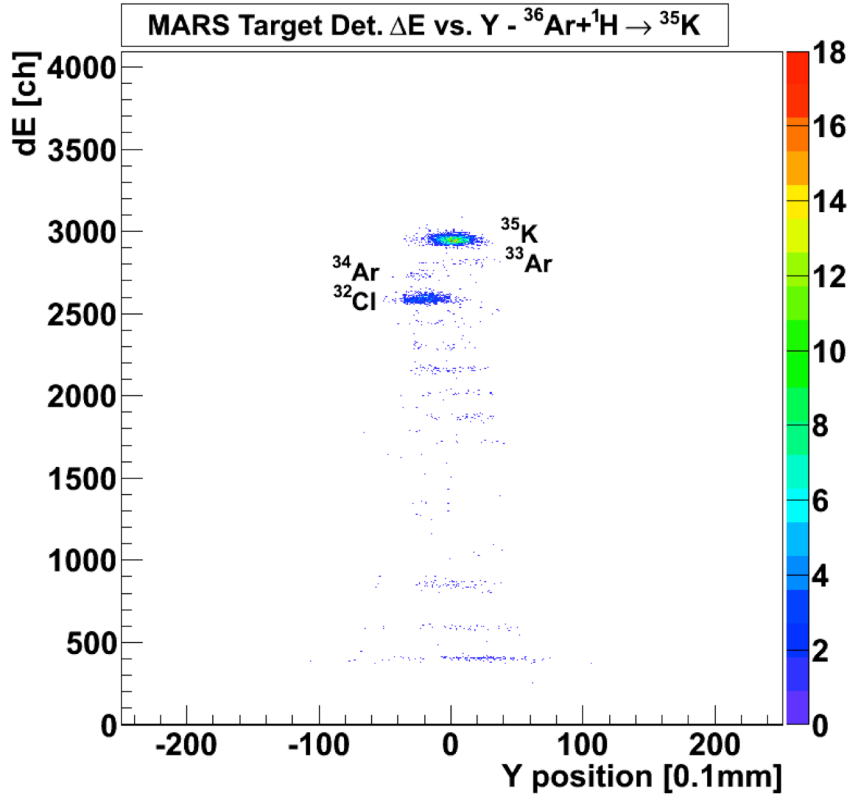


FIG. 1. Results of the ^{35}K MARS tuning for the June 2014 experiment.

III. ^9C secondary beam

Also in March 2014, we produced and separated ^9C with MARS [2]. ^9C was needed by the group of Prof. G. Rogachev for their experiment with resonant elastic proton scattering using the Thick Target Inverse Kinematics (TTIK) method. The ^9C secondary beam was employed to study the unbound ^{10}N nucleus. The experiment was conducted in October 2014.

For the ^9C experiment, a ^{10}B primary beam at 31 MeV/u bombarded the MARS gas cell target. The gas cell target was filled with 3 atm of hydrogen gas at a temperature of 77K. The ^9C was produced with the fusion-evaporation reaction (p,2n) in inverse kinematics. The Q-value for the $p(^{10}\text{B},^9\text{C})2n$ reaction is -25.7 MeV. Thus, 31 MeV/u was chosen for the primary beam energy as a compromise

between the production rate for ${}^9\text{C}$, which is better at higher primary beam energies, and the desire to have the ${}^9\text{C}$ at the lowest possible energy. For the experiment, the ${}^9\text{C}$ energy was reduced to ~ 11 MeV/u with degraders and a thick scintillator foil at the entrance of their scattering chamber.

The optimized production rate for the ${}^9\text{C}$ secondary beam was about 7.0 events/nC with the 3 atm of gas in the target, which gave \sim about 1.4×10^3 particles/sec with 200 nA of ${}^{10}\text{B}$ beam on target. The ${}^9\text{C}$ secondary beam was relatively pure, although there was some contamination in the beam from α -particles and ${}^3\text{He}$. Some of this contamination from the α -particles was removed in the experiment by closing the slits of MARS. The resulting ${}^9\text{C}$ secondary beam as measured by the MARS target detector is shown in Fig. 2.

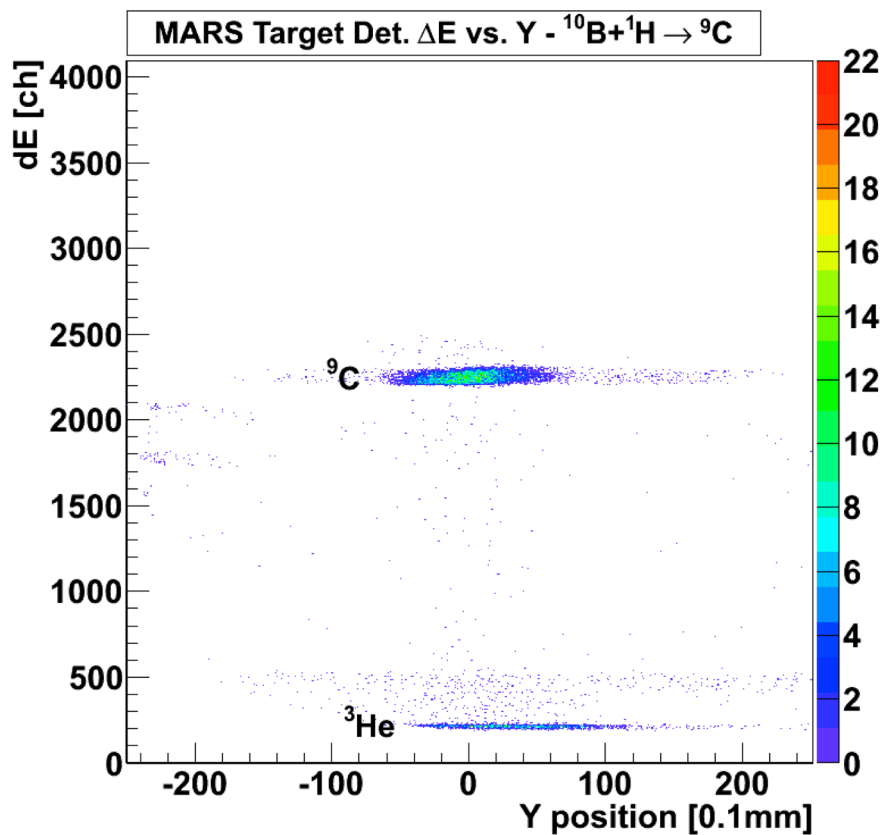


FIG. 2. Result of the ${}^9\text{C}$ production with MARS. The main contaminant of the secondary beam is from ${}^3\text{He}$.

IV. Production of ${}^{16}\text{N}$ secondary beam

${}^{16}\text{N}$ secondary beam was produced with MARS at low energy in preparation for upcoming experiments to study the pionic fusion reaction mechanism with Prof. Yennello's group.

In the test, a $^{15}\text{N}^{2+}$ primary beam at 7 MeV/u from the K500 cyclotron bombarded the MARS gas cell target. The gas cell was filled with $^2\text{H}_2$ (deuterium) gas at a pressure of 948 torr and a temperature of 77K. The reaction $d(^{15}\text{N}, ^{16}\text{N})p$ was used to produce the ^{16}N . However, ^{16}O was also produced with high cross section at this energy from the $d(^{15}\text{N}, ^{16}\text{O})n$ reaction. It is possible for the ^{16}O ions to be produced in other charge states besides $^{16}\text{O}^{8+}$. Thus if $^{16}\text{O}^{7+}$ is produced, it is indistinguishable from $^{16}\text{N}^{7+}$ in MARS unless a thin silicon detector or degrader foil is employed to separate the two secondary beams by their different energy losses in the materials. Since a thin silicon detector was not available for the experiment, a thin Al degrader foil with areal density 4.4 mg/cm^2 was inserted in front of the MARS target detector. To optimize the production of $^{16}\text{N}^{7+}$ vs. $^{16}\text{O}^{7+}$, the MARS magnet settings were kept constant ($D1-2 = 255.2 \text{ A}$, or $B\rho = 0.60 \text{ T}\cdot\text{m}$) while the gas cell pressure was varied from 1220 torr to 777 torr in steps of about 50 torr. We found the optimized $^{16}\text{N}^{7+}$ production with 948 torr, $^{16}\text{O}^{7+}$ at 832 torr, and some mixture of the two elements at the settings in-between.

Depending on the MARS quadrupole settings used, the production rate for $^{16}\text{N}^{7+}$ varied between 900 events/nC and 2200 events/nC. With $\sim 100 \text{ nA}$ of primary beam on target, this implies that production rates of greater than 10^5 particles/sec are available for this beam at this energy. This relatively intense ^{16}N beam may be employed in future nuclear astrophysics experiments.

- [1] R.E. Tribble, R.H. Burch, and C.A. Gagliardi, Nucl. Instrum. Methods Phys. Res. **A285**, 441 (1989).
- [2] B.T. Roeder *et al.*, *Progress in Research*, Cyclotron Institute, Texas A&M University (2013-2014), p. I-48; [http://cyclotron.tamu.edu/2014 Progress Report/index.html](http://cyclotron.tamu.edu/2014%20Progress%20Report/index.html).
- [3] A. Saastamoinen *et al.*, *Progress in Research*, Cyclotron Institute, Texas A&M University (2014-2015), [http://cyclotron.tamu.edu/2015 Progress Report/index.html](http://cyclotron.tamu.edu/2015%20Progress%20Report/index.html).

Update on the upgrade of the Oxford detector

A. Spiridon, R. Chyzh, M. Dag, E. McCleskey, M. McCleskey, B.T. Roeder, A. Saastamoinen, R.E. Tribble, L. Trache,¹ E. Pollacco,² and G. Pascovici¹

¹ *National Institute of Physics and Nuclear Engineering, Bucharest-Magurele, Romania*

² *IRFU, CEA Saclay, Gif-sur-Yvette, France*

The Oxford detector [1] is one of the two focal plane detectors of the Multipole-Dipole-Spectrometer (MDM). In the nuclear astrophysics group, this setup has been used primarily to study scattering and transfer reactions involving nuclei with $A \leq 26$. However at higher masses than that, we found that we are having significant difficulties in particle identification due to the insufficient resolution of both the dE and E signals. The upgrade was focused on improving the resolution of both of these signals. For details on the project see ref [2] and [3]. We proposed to improve the dE signal by introducing Micromegas [4], a new technology shown to provide gains of $\sim 10^4$, as well as very good energy resolution.

Over the last year, we finished the modifications to the Oxford detector chamber to include 2 flanges with one D-Sub 25 feedthrough each. We received the Micromegas anode from the manufacturer and installed it in the Oxford. As seen in Fig. 1 the new anode consists of 28 pads, each 3.25 cm by 4.4 cm in size. The amplification gap is 256 μm thick. We collect the 28 energy signals through two D-Sub 25 connectors as seen in Fig. 2.



FIG. 1. The Micromegas Anode.



FIG. 2. Oxford detector with the new Anode mounted.

We first tested the upgraded detector with a 4-peak mix alpha source. Unfortunately, due to the design of the Oxford, the closest we could place the source was ~ 4 cm from the

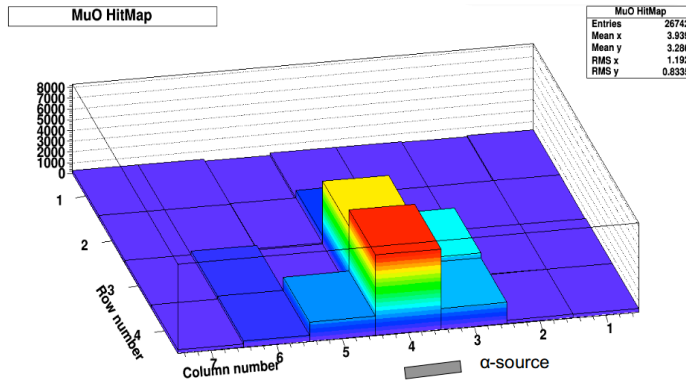


FIG. 3. Micromegas Pad Map showing the pads that detect alpha particles.

Micromegas anode. With an isobutane gas pressure of 100 Torr, we could only test a limited number of pads (Fig.3). However, it was enough as it showed that the new component works (Fig.4).

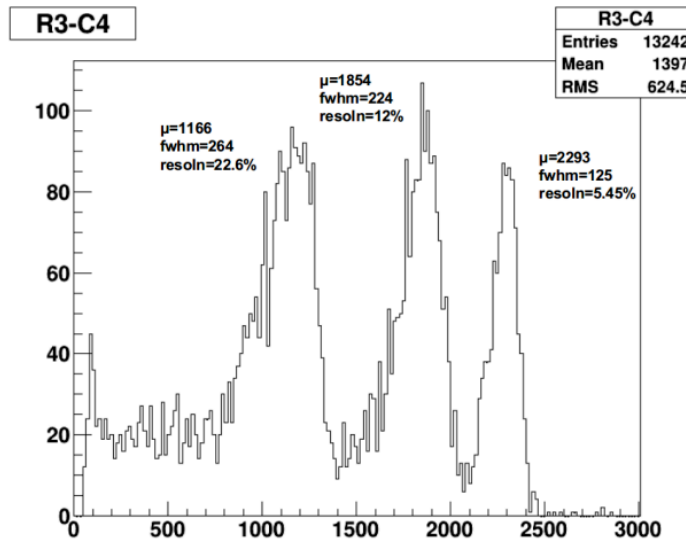


FIG. 4. Energy spectrum detected by pad R3-C4 (Row 3, Column 4).

Next, we tested the detector with beams in two separate experiments. In the first, we used ^{16}O at 12 MeV/u. In the second, we used ^{22}Ne and ^{28}Si , each at 12 MeV/u. We focused on elastic scattering on gold foil (Fig. 5) in all measurements, and the reaction products were collimated with a narrow slit. We observed the detector response under these conditions for different bias voltages, gas pressures, and electronic gains.

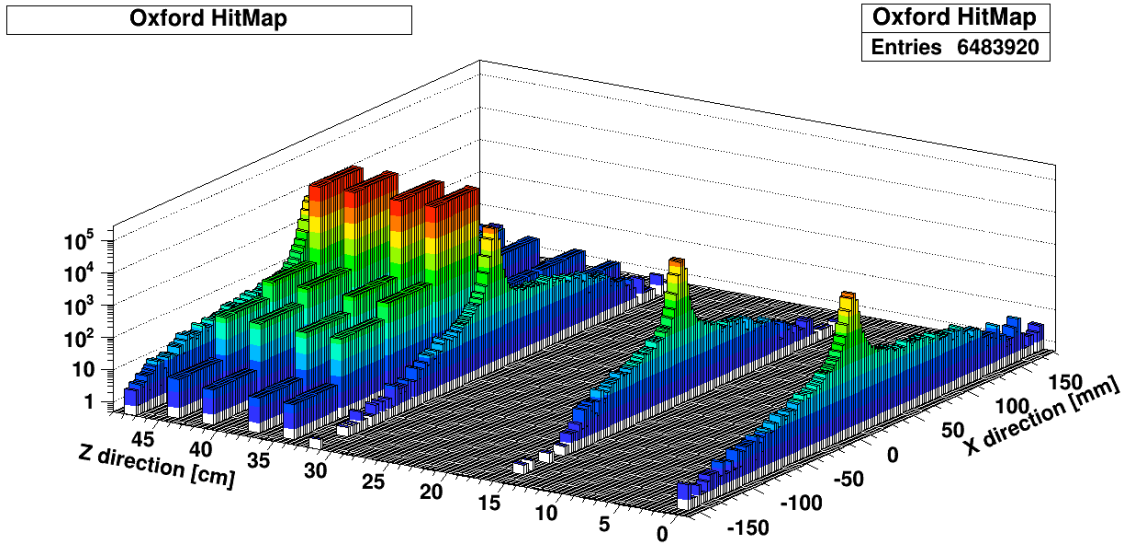


FIG. 5. A map of the Oxford detector showing the 4 position-sensitive avalanche counters and the Micromegas pads. The peaks show that the beam is passing through the center of the detector highlighting predominantly column 4 (central) of the Micromegas anode.

We obtained energy resolutions for the individual pads in the range of 5.5-6.5% for 100 Torr and 85 Torr, 5.5-6% for 70 Torr, 6.5-7% For 50 Torr and 8-9% for 30 Torr. Averaging the energy over all the pads gave us significantly better resolution (Fig. 6).

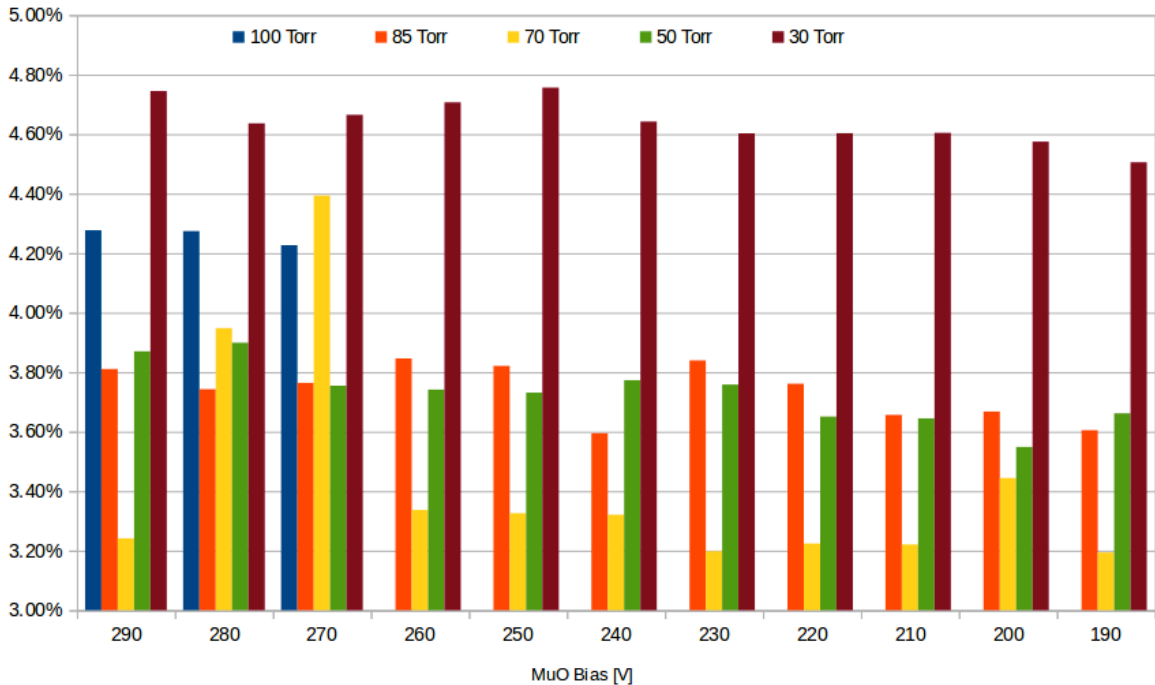


FIG. 6. Plot showing the energy loss resolution for the Micromegas anode (averaged over the 28 pads) for different bias voltages of the Micromegas and different gas pressures.

Last but not least, we analyzed reaction products of the beam ions interaction with a ^{13}C target at different MDM angles. We compared the new PID spectra with the spectra obtained with the original design. Fig. 7 shows one such comparison for ^{22}Ne at 5 deg and 30 Torr.

It can be easily seen in this figure that the resolution is much better with the Micromegas than the ionization chamber. The upgrade was considered successful so the modified detector is going to be used in nuclear physics experiments. As suggested by our collaborators, when the beam schedule allows for it, there will be further tests done with beams at much higher energies.

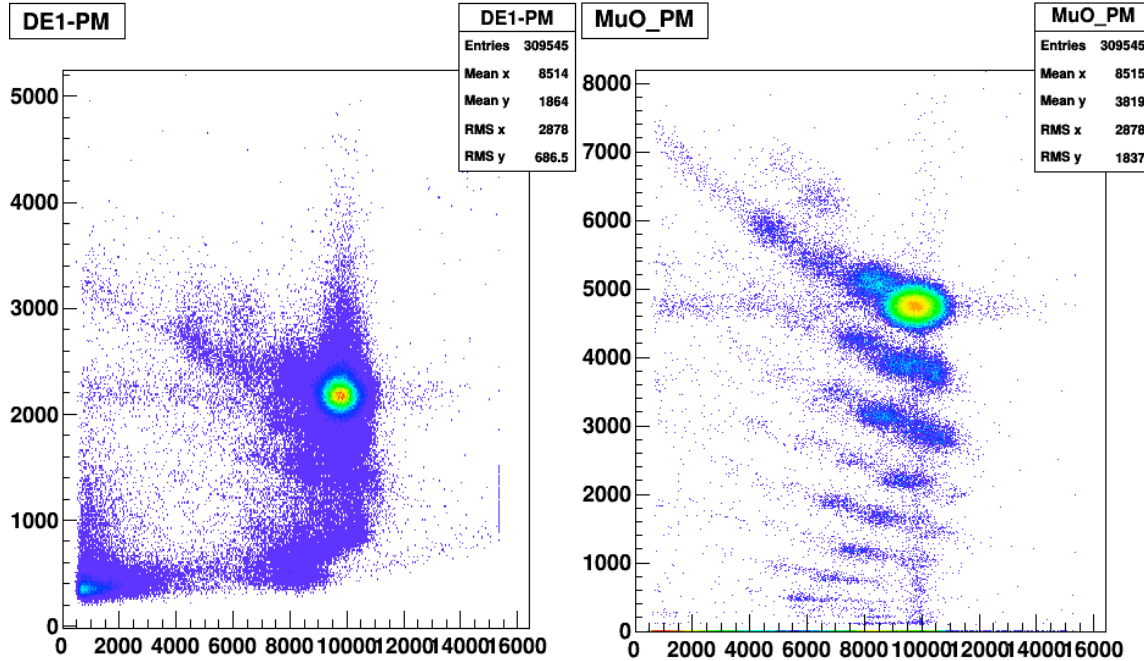


FIG. 7. Spectrum on left shows energy detected by the ionization chamber, dE1, versus residual energy detected by the scintillator. Spectrum on right shows energy detected by the Micromegas versus same residual energy.

For information on improving the residual energy signal, see part 2 of this paper in the same annual report.

[1] D.H. Youngblood *et al.*, Nucl. Instrum. Methods Phys. Res. **A361**, 359 (1995); M. McCleskey, Ph.D Thesis, Texas A&M University (2011)
 [2] A. Spiridon *et al.*, *Progress in Research*, Cyclotron Institute, Texas A&M University (2012-2013), p. IV-50
 [3] A. Spiridon *et al.*, *Progress in Research*, Cyclotron Institute, Texas A&M University (2013-2014), p. IV-45.
 [4] Y. Giomataris *et al.*, Nucl. Instrum. Methods Phys. Res. **A376**, 29 (1996).

Construction and commissioning of the AstroBox2 detector

A. Saastamoinen, B.T. Roeder, A. Spiridon, R.E. Tribble, E. Pollaco,¹ L. Trache,² and G. Pascovici²

¹IRFU, CEA Saclay, Gif-sur-Yvette, France

²National Institute of Physics and Nuclear Engineering, Bucharest-Magurele, Romania

In past years we have done several studies of beta-delayed proton emitters of astrophysical interest by implantation technique [1-5]. It was realized rather soon that shrinking the physical detection volume of elements in Si detector did not reduce the beta-background enough to create background free spectrum in the typical energy range of astrophysically interesting decays

($E_p \sim$ few hundred keV). To further reduce the beta-background a novel detector, AstroBox, based on Micro Pattern Gas Amplifier Detector (MPGAD) was developed [6].

We have built an upgraded version, AstroBox2, described in the previous annual report [7]. The design of the detector field cage and other related components, as well as the custom vacuum chamber was completed and the chamber was built at the Cyclotron Institute in spring/summer 2014. The detector chamber includes many novel features, including possibility to scan all the detector pads with an X-ray source while keeping the system under clean conditions.

In October we received three detector elements, two 256 μm thick and one 128 μm thick. The first 256 μm element, shown in Fig. 1., has been thoroughly characterized with ^{55}Fe X-ray

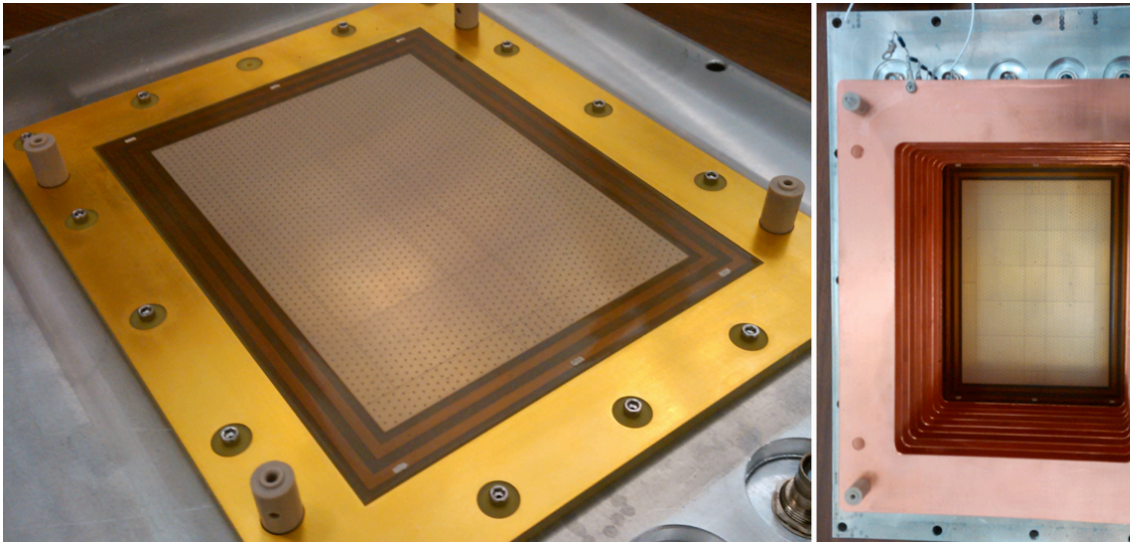


FIG. 1. Left: The first AstroBox2 MicroMEGAS detector element mounted into the detector flange. Right: The detector and the field cage from top (cathode removed for visibility)

source, a

mixed alpha source (^{148}Gd , ^{239}Pu , ^{241}Am , ^{244}Cm), and a pulser. Typical resolution of 13% is achieved for the 6 keV X-ray from ^{55}Fe (Fig. 2.), and about 3% for the 5.5 MeV alphas from ^{241}Am (Fig. 3). The detector will be tested online in April 2015.

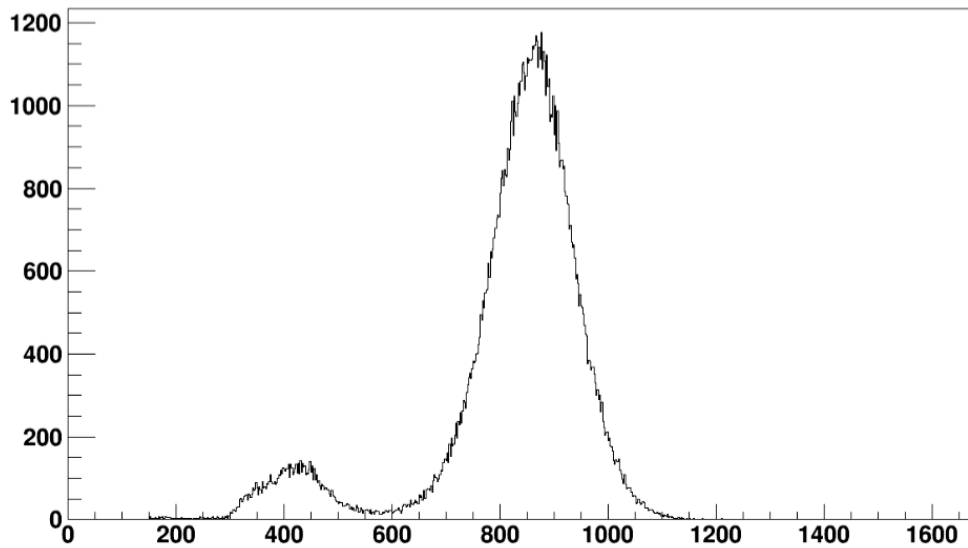


FIG. 2. An X-ray spectrum from ^{55}Fe source.

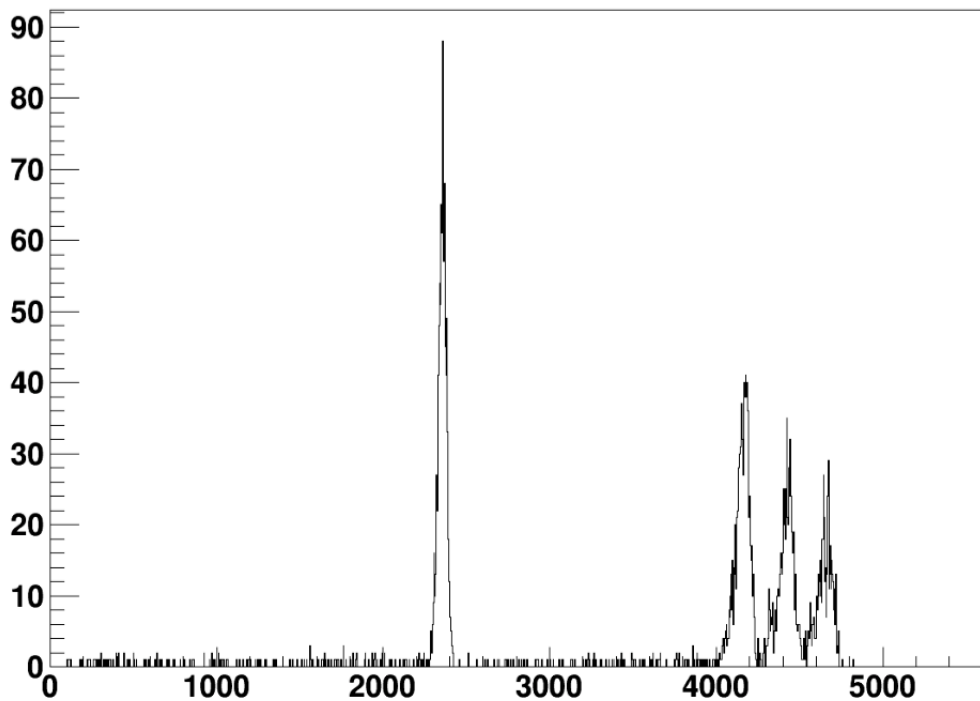


FIG. 3. Spectrum from a tightly collimated, mixed (^{148}Gd , ^{239}Pu , ^{241}Am , ^{244}Cm) alpha source.

- [1] A. Saastamoinen *et al.*, Phys. Rev. C **83**, 044808 (2011).
- [2] L. Trache *et al.* PoS (NIC X), 163 (2008).
- [3] A. Saastamoinen *et al.*, AIP Conf. Proc. **1409**, 71 (2011).
- [4] J. Wallace *et al.*, Phys. Lett. B **712**, 59 (2012).
- [5] M. McCleskey *et al.*, Nucl. Instrum. Methods Phys. Res. **A700**, 124 (2013).
- [6] E. Pollaco *et al.*, Nucl. Instrum. Methods Phys. Res. **A723**, 102 (2013).
- [7] A. Saastamoinen *et al.*, *Progress in Research*, Cyclotron Institute, Texas A&M University (2013-2014), p. IV-55.

Commissioning the TAMUTRAP RFQ cooler/buncher

E. Bennett, R. Burch, B. Fenker, M. Mehlman, D. Melconian, and P.D. Shidling

In order to efficiently load ions into a Penning trap, the ion beam should be bunched and have a low energy with sufficiently small time and energy spread. A gas-filled linear RFQ Paul trap cooler and buncher is particularly adept at such beam preparation, and has been developed and characterized for use at TAMUTRAP. This work is described in detail in the PhD thesis of Michael Mehlman.

An approximately 5m section of horizontal beamline (see Fig. 1) has been installed at the TAMUTRAP facility to facilitate the commissioning and characterization of the RFQ cooler and buncher, the pulsing cavity, and the diagnostic stations, among other beamline elements. In addition, though, it will be carried over to the final TAMUTRAP facility with very little changes to its current configuration. The most important elements in this set up are, in order: the Heat Wave Labs ion source followed by a 2mm collimator, Einzel lens, 2-axis beam steerer, 10mm collimator, diagnostic station, 2-axis beam steerer, injection optics, 6mm entrance diaphragm, RFQ electrode structure, 6mm exit diaphragm, extraction optics, 2-axis beam steerer, and diagnostic station, respectively. To achieve the required vacuum, turbo pumps with pumping speeds of 1000L/s and backed by dry scroll roughing pumps are placed at the locations of the diagnostic stations.

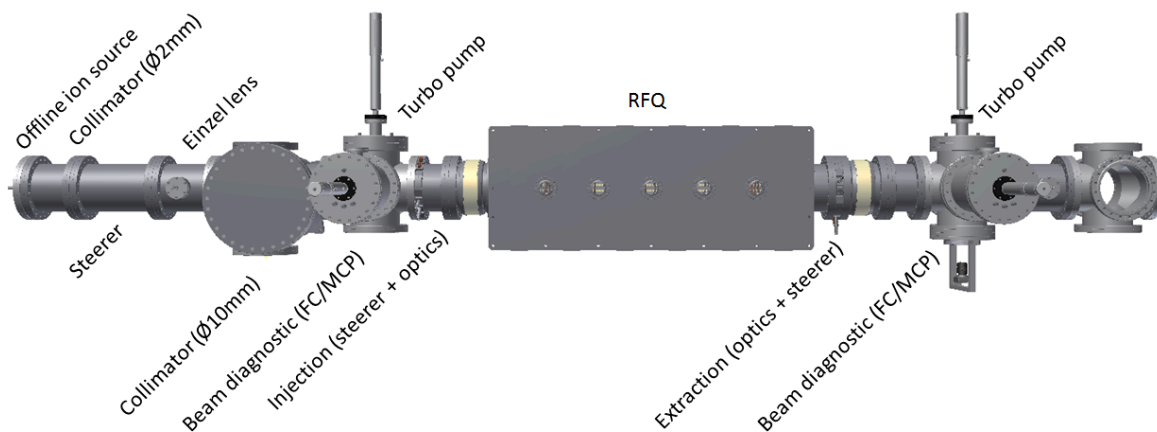


FIG. 1. The test line for commissioning the RFQ, pulsing cavity, diagnostic stations, and other beam elements.

Alignment of the RFQ cooler/buncher test line was performed via optical transit. The optical axis has been recorded by two targets on the high bay floor (one on a shielding block and one on a fixed cement wall), and one midplane mark on a nearby steel I-beam. The optical transit that was used to generate the axis to which all elements were aligned can be replaced by re-aligning to these targets.

Once the optical axis had been established, centers of the flanges that are used to support the beam line were forced into alignment via 1/2-13 set screws located on the beam supports (as discussed in a previous annual report). The center of the flange was located by threading a thin (diameter approximately 0.2mm) red thread that was wound between pins located in bolt holes of the flange separated by 90 degrees. The location at which the threads crossed was considered the flange center to within about the diameter of the thread. Several elements were further aligned

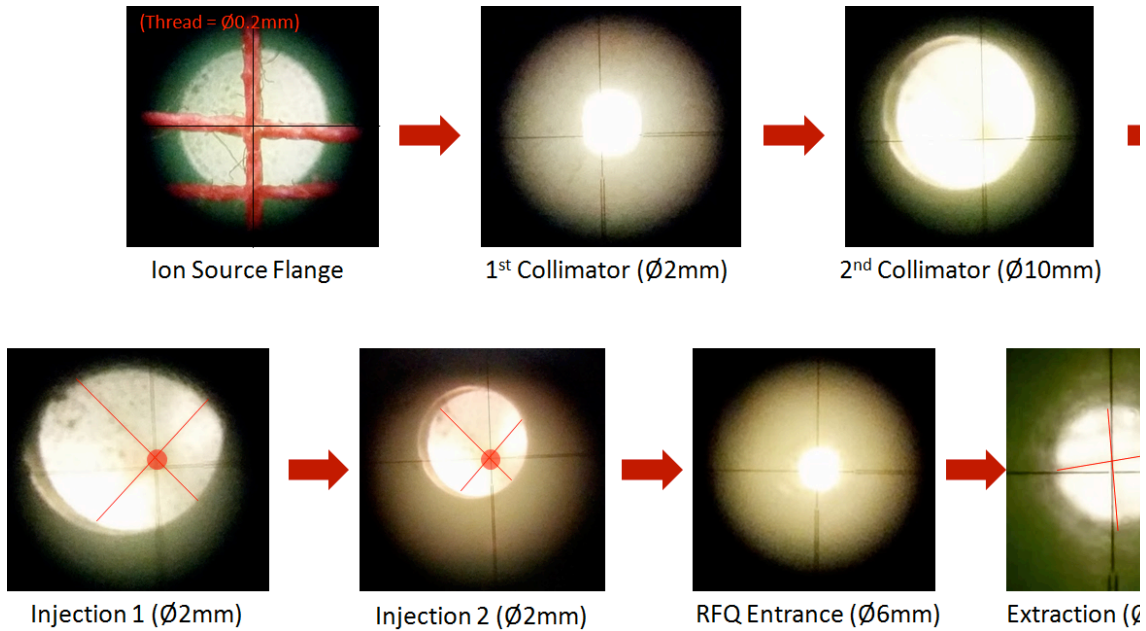


FIG. 2. Final Alignment of the test beamline.

within the centered flanges via set screws on individual electrodes. In general, the process was performed on elements in sequence, beginning with the ion source flange. Results at the seven locations of beam alignment can be seen in Fig. 2.

After the alignment procedure was completed, the vacuum chamber was sealed on each end, and pumped down. Overall, critical elements were aligned to within 1mm in any direction by this process, with the majority of elements centered to the arbitrary optical axis to within 0.5mm, which should be sufficient for TAMUTRAP.

The electrode structure of the TAMUTRAP RFQ cooler and buncher (see Fig. 3) is

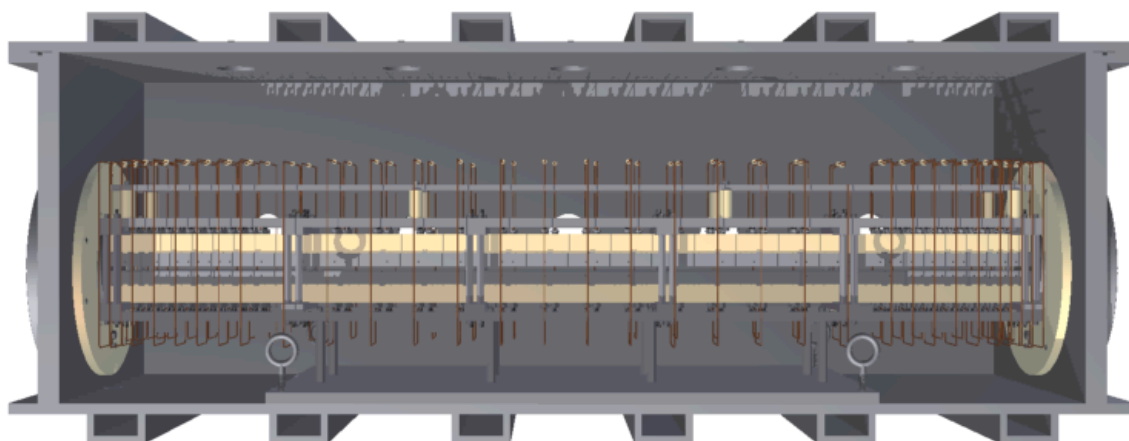


FIG. 3. The mechanical structure of the RFQ cooler/buncher

composed of four rods with radius of curvature $r=7\text{mm}$ that are rigidly held at a surface-to-surface rod spacing of $2r_0=12\text{mm}$ for opposite rods, yielding a characteristic ratio of $r/r_0=1.16$. The structure is approximately 87cm in length, and is separated axially into 33 segments to enable the application of a linear drag potential.

The device has been optimized to ensure mechanical rigidity, hide dielectrics, and achieve the minimum gap between adjacent segments. Care has also been taken to minimize electrical impedance by minimizing material in critical locations. The main structure is composed of 8 custom fabricated parts, with the remainder of the assembly coming from precision stock components. Apart from electronics, all components used are made of aluminum, stainless steel, or ceramic for vacuum considerations.

Analog electronics have been developed to drive the device, with each segment receiving a unique adjustable DC potential for fine-tuning of the axial electric field. RF is coupled to the segments in vacuum using vacuum safe ceramic capacitors and resistors (Fig. 4), ensuring a minimum of line-impedance. Switching of the final segments during ejection is accomplished by a single Behlke HTS 31-03-GSM high voltage, ultra fast solid-state switch. The switch itself demonstrates a switching time on the order of 500ns , which is slowed to approximately $50\mu\text{s}$ due to the RC circuit attached to each electrode that is used to protect the DC power supply. Despite the relatively slow switching time, satisfactory bunch characteristics have been observed, as will be discussed.



FIG. 4. A photo of the TAMUTRAP RFQ with in-vacuum electronics attached.

The cooler/buncher device has been assembled, and initial commissioning has been completed. Continuous mode efficiencies are calculated as the ratio of the beam current measured on Faraday cups located prior to the injection optics and after the extraction optics of the cooler/buncher, as in Fig. 1. Preliminary results are shown in Fig. 5, and all efficiencies are reported at 0V/mm drag potential. The efficiency for each energy and pressure combination was found to be optimized by a distinct drag potential setting, so the decision was made to facilitate comparison by choosing a constant 0V/mm rather than possibly introducing additional error into the measurements by choosing a sub-optimal drag potential. As a result, all efficiencies should

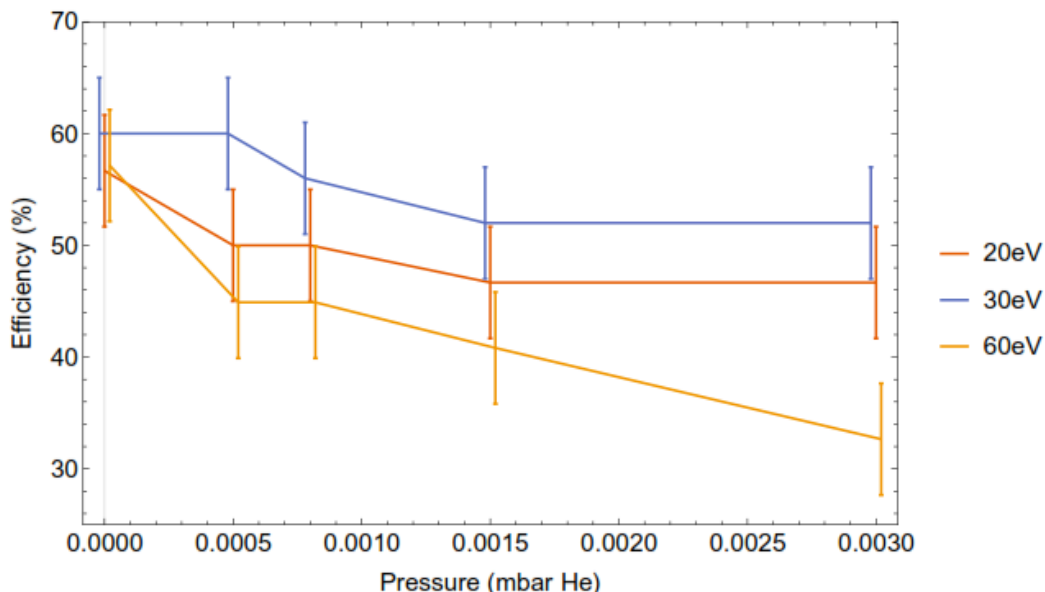


FIG. 5. Efficiency as a function of pressure at three different incident beam energies for the TAMUTRAP RFQ cooler/buncher.

be able to be improved to some degree by adjusting the drag potential. The peak efficiency of around 60% a great improvement over the approximate 13% efficiency of the prototype device and comparable to efficiencies achieved at existing world-class facilities.

In normal use, the TAMUTRAP RFQ cooler/buncher will be operated in bunched mode, collecting ions of interest for some set amount of time, bunching, and ejecting them in a tight packet. Individual ions are detected by a 40mm Beam Imaging Solutions MCP detector. The resulting time-spectrum relative to the ejection signal generated by the control system was fit by a skewed Gaussian, as in Fig. 6, yielding a Full Width at Half Max (FWHM) characterizing the time-spread of the bunch and the integrated number of counts per bunch (up to an arbitrary constant dependent on acquisition and analysis). It should be noted when comparing bunch characteristics to other facilities that fitting with a standard Gaussian resulted in a poorer fit, but also significantly reduced the observed FWHM due to exclusion of the low-count large-time tail of the distribution. Caution should be observed when comparing integrated number of counts between data points, as fluctuation of up to 10% in ion source current was observed on a several minute time scale.

The operation of the RFQ in bunched mode was investigated systematically by testing the effect of adjusting one operating parameter at a time. While it is true that various parameters are no-doubt

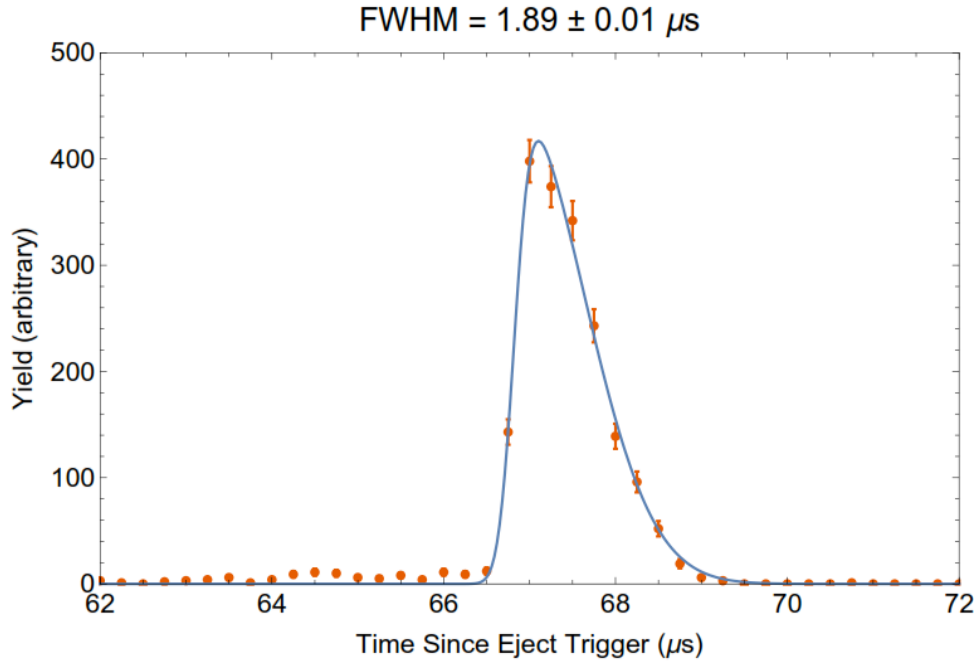


FIG. 6. Time spectrum of bunched ions. Plotted are the counts as a function of time since eject-trigger along with a skewed Gaussian fit.

correlated, the parameter space was too large to evaluate the variables co-dependently. A small subset of the operating parameters tested systematically is presented here.

At the pressures available for operation at TAMUTRAP, bunch characteristics have proven to be largely independent of gas-pressure. At the low-pressure extreme, the integrated number of counts begins to fall off, since there is a minimum amount of buffer-gas required for successfully cooling and bunching the incoming ions. This makes no comment on the effect gas pressure has on transverse emittance, which could worsen to some degree with increasing pressure due to gas collisions after ejection. FWHM and number of ions per bunch as a function

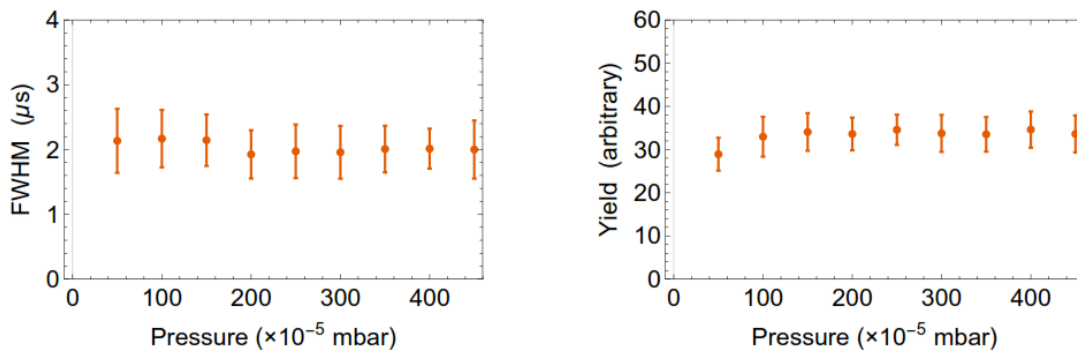


FIG. 7. FWHM and yield as a function of He gas pressure.

of gas pressure can be seen in Fig. 7.

A 30eV incident beam energy demonstrated the greatest continuous mode transmission efficiency of all incident energies tested for an uncooled beam. Since the TAMUTRAP RFQ will be employed exclusively as a cooler/buncher, it is more critical to determine what beam energy to use in bunched mode in order to obtain bunches with the smallest FWHM time spread and greatest yield (Fig. 8). This was accomplished by raising and lowering the voltage at which the RFQ platform is floated in order to achieve the desired potential difference from the ion source, which was held at approximately 10kV. The FWHM of the bunch's time spread is rather insensitive to the incident beam energy (phase space is reset in the device), while the overall yield degrades slightly at higher incident energies. In this regime, the number of counts per bunch decreases slightly, likely due to a reduced initial capture efficiency of the Paul trap for more energetic ions.

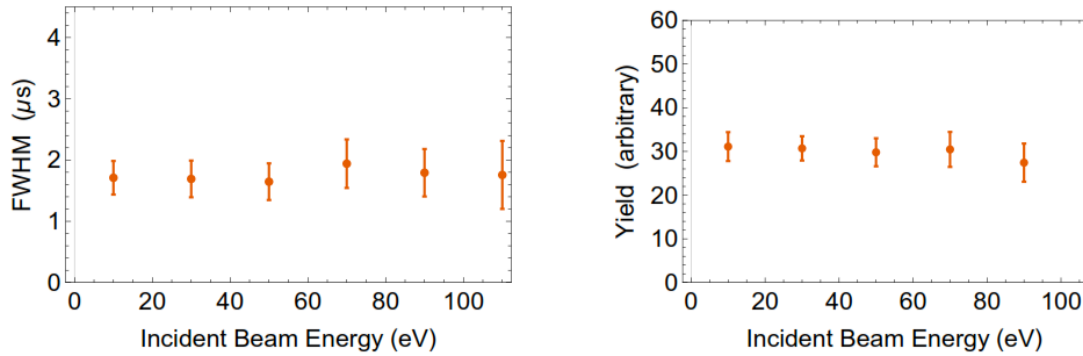


FIG. 8. FWHM and yield as a function of incident beam energy.

Additional systematic tests of the device have been performed, measuring bunch FWHM and yield as a function of eject duration, RF properties (frequency and voltage), incident beam current, and DC drag potential, and will be presented in detail in future work.

Texas active target (TexAT) detector – part 1: Design and construction progress

E. Koshchiy, G.V. Rogachev, E. Uberseder, and E. Pollacco¹

¹ IRFU, CEA Saclay, Gif-Sur-Ivette, France

Construction of a general purpose active target detector - Texas Active Target (TexAT) for experiments with rare isotope beams at the Cyclotron Institute is in progress. TexAT will be used for wide variety of experiments to detect the charged products of nuclear reactions with rare isotope beams. Resonance elastic and inelastic scattering of protons and α -particles, (α ,p) and (p, α) reactions, nucleon-transfer reactions, such as (d,p), (d, ^3He), (p,d), (p,t), (^4He ,t) and decay spectroscopy studies are the examples of the experiments that can be performed with TexAT. The Monte Carlo simulation package has been developed to guide the design of the layout of TexAT and to evaluate the reliability of tracks reconstruction, energy and position resolution. More details on the Monte Carlo simulation package are given in a separate report.

The general layout of the TexAT detector is shown in Fig. 1. Setup contains a Time Projection Chamber (TPC) with a high level of segmentation in the readout plane, surrounded by array of 58 Si detectors backed with an array of up to 58 CsI detector. The length of an active area is 224 mm and it covers solid angle of about 3π , providing high efficiency for experiments with low intensity exotic beams.

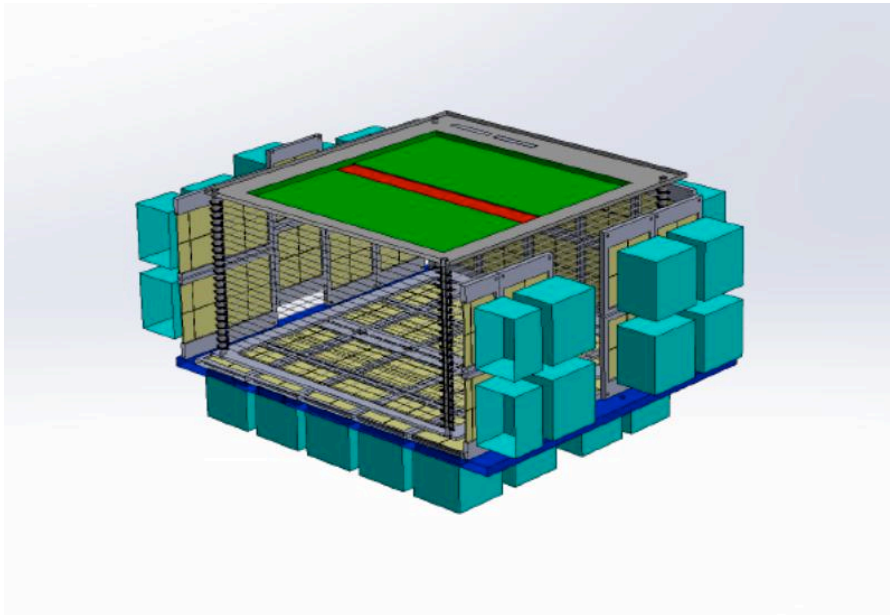


FIG. 1. TexAT assembly (one side of array is removed to show details).

I. Time projection detector.

The key component of TexAT is a time projection chamber with a readout based on Micromegas (Micro-MESH Gaseous Structure) technology [1]. The mesh and the readout pads are mounted on PC board plate that covers active area of 224mm x224 mm. A Field Cage provides a uniform electric field that generates a drift of electrons produced by the ionization of incoming ions and recoils. The total number of readout channels is 1024. The board is divided into three areas as shown in Fig.2: the zone to the left of a beam axis (L), the beam axis zone (C) and the zone to the right of the beam axis (R). Central part along the beam axis (21 mm wide) has high segmentation: $128 \times 6 = 768$ individual pads (the pad size is 1.75mm x 3.5 mm). The pads are arranged so that there are 128 pads in the direction of the beam (long 224 mm side) and 6 pads in the direction perpendicular to the beam (21 mm long side). The left (L) and right (R) areas are identical and have dimensions 224 mm x 101.5 mm. Each one consists of 64 strips, perpendicular to the beam axis. The strip is 1.75mm x101.5mm. There is 1.75mm space between strips to allow for an individual pad to be placed between the strips. Distance between the centers of the strips is 3.5 mm. There are 64 individual 1.75mm x 1.75 mm pads between each two strips. These pads are not connected between each other. However, each pad is connected to the corresponding pads placed between other strips, so that there are 64 “chains” of pads arranged in the direction parallel to the beams axis.

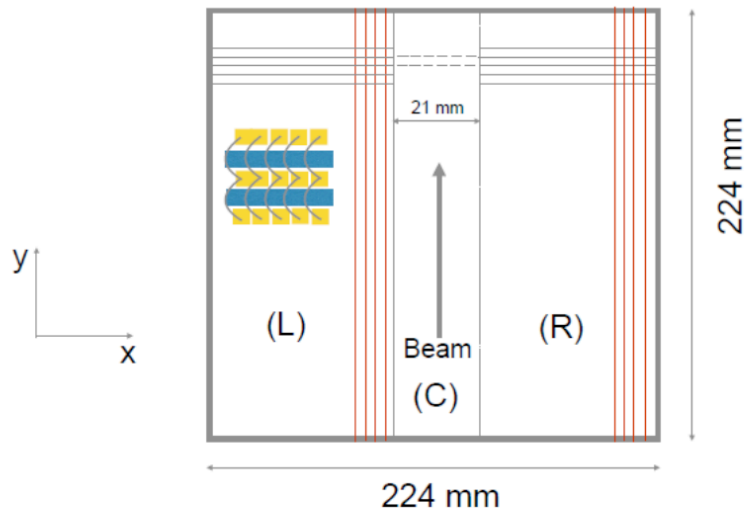


FIG. 2. Micromegas PC board design.

Optimized channel map has been designed to provide for a more uniform expected readout rate for different AGET chips. After fabrication at CERN Micromegas PC-board and bulk

detector (PC board and installed mesh) has to be fully tested at IRFU (Saclay, France) and sent to Cyclotron Institute. Expected lead time: Fall of 2015.

II. Field cage design.

Field cage must generate the uniform electric field for time projection volume with sufficient field strength to provide constant electron drift velocity. Besides, the cage has to be as transparent as possible for the reaction products escape the field cage and be detected in Si array with minimal losses. The geometry of field cage is specified by Micromegas detector and Si detectors design: 260 mm x 260 mm x 150mm; a 50 micron thick gold plated tungsten wire has been chosen as an element to create transparent cage.

To optimize geometry of field cage the simulations with computer codes GARFIELD [2], GMSH [3], ElmerFEM [4] have been performed to estimate electric field uniformity for different wires spacing, and create the best condition for electron drift inside the active target. It was shown (see Fig.3) that the field fluctuations appear to be around 10% which leads to less than 1% change in velocity if we run with correct field strength. The sufficient spacing between field cage wires is about 5 mm, that allow us to load wires with extension springs to avoid wire sagging.

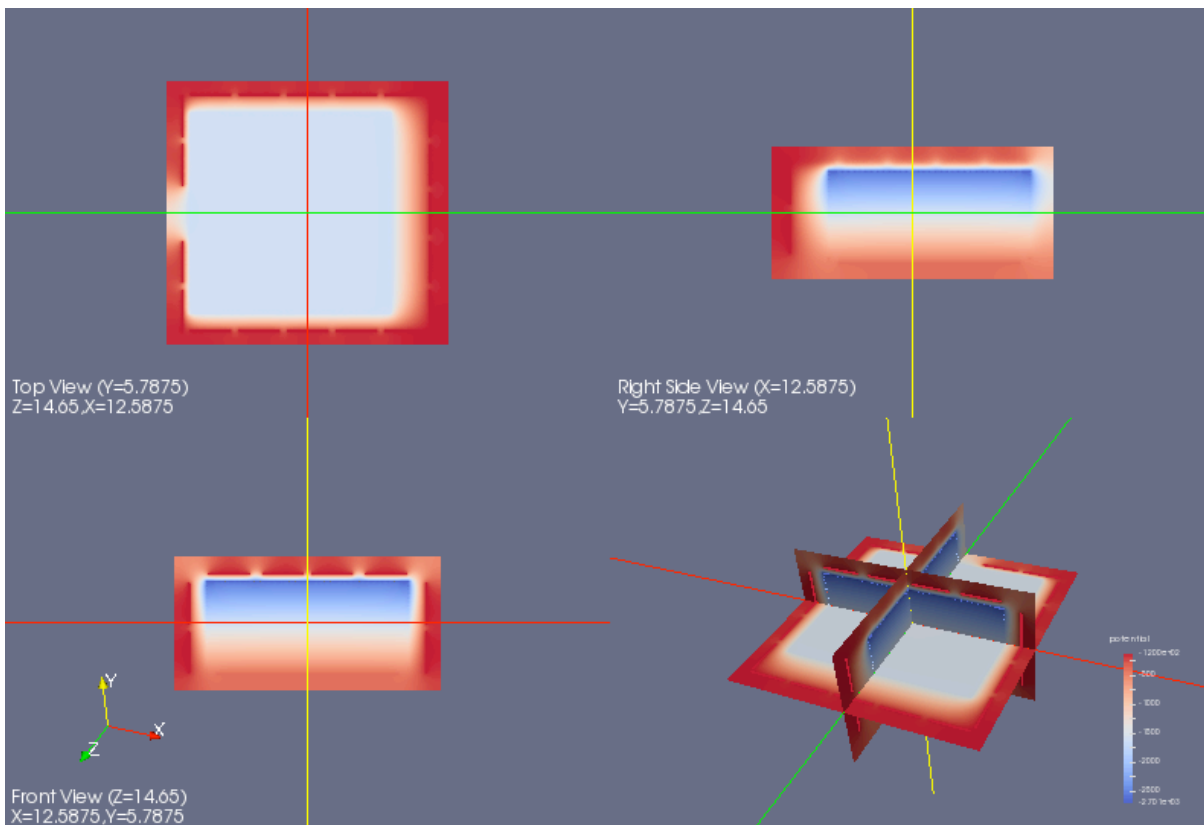


FIG. 3. TexAT electric field simulations.

III. Solid state detectors array.

Quad-segmented Si detectors (58 total) will surround bottom and four sides of TPC independently, providing an easy access to any component of detector array. Geometry of side, upstream and downstream arrays are slightly different, allowing entrance for incoming beam in upstream wall. We received a first set of five Si- detectors, designed at BIT Ltd (Kiev, Ukraine). These detectors have been tested with alpha- source, and the performance has been found to meet expectations (an average energy resolution of all detectors is less than 50 keV). The remaining detectors will be ordered at the same company. A set of first five custom scintillation CsI(Tl) detectors with scintillator dimensions 50x50x40 mm³ was produced by SCIONIX (Netherlands). They will be tested after shipping (expected by the end of May, 2015).

IV. Scattering Chamber.

A custom vacuum and target gas chamber has been designed to hold the detector array and to maintain the workable conditions for both gaseous and solid state (silicon and scintillation) detectors. It provides an easy access to any component of the detector array and versatile installation at any beam line (either the beam line at the end of the MARS separator or a future designated beam line). Chamber meets the stringent requirements for steady operation of impurities-sensitive Micromegas detector, namely: clean vacuum/gas (avoid as much as possible

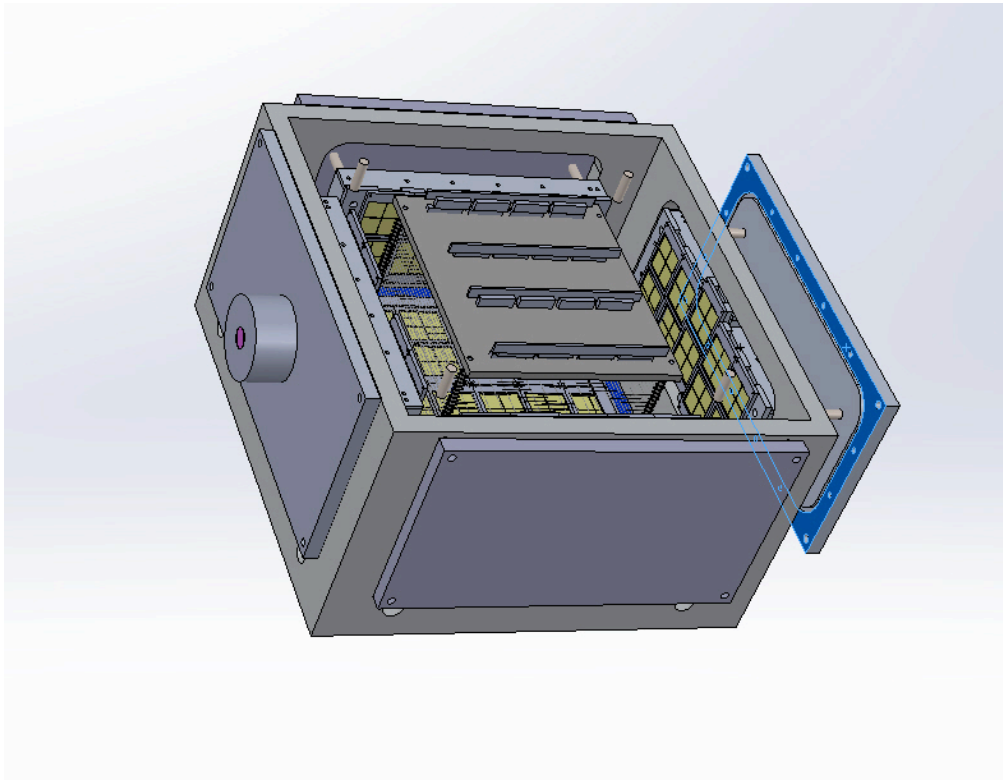


FIG. 4. TexAT design (general view).

outgassing from the chamber walls and a vacuum leak rate at the range of $10E-8$ atm-cc/sec). It has aluminum body cuboid shape: 20" x 20" x 13.5" with lids and all necessary ports for vacuum/gas handling installation and signal feedthroughs. A fabrication order has been submitted to A&N Corporation and it has to be complete at the end of May, 2015. The general view of TexAT setup is shown in Fig.4. Most of the major components of TexAT have been designed and ordered and now they are nearing completion on schedule. We expect that the first commissioning run with TexAT will take place at the end of 2015.

[1] Y. Giomataris *et al.*, Nucl. Instrum. Methods Phys. Res. **A376, 29** (1996).

[2] <http://garfield.web.cern.ch/garfield/>

[3] <http://www.geuz.org/gmsh>

[4] <http://elmerfem.org/>

Texas active target (TexAT) detector - part 2: Monte Carlo simulations

E. Uberseder, G.V. Rogachev, E. Koshchiy, and E. Pollacco¹

¹*IRFU, CEA Saclay, Gif-sur-Yvette, France*

The TexAT (Texas Active Target) detector is a new active-target time projection chamber (TPC) that will reside at the Cyclotron Institute. The detector is designed to be of general use for experiments relevant to nuclear astrophysics and nuclear structure. The details of the design are described in the previous report [1]. Time projection chambers allow for the 3D track reconstruction of the incoming and outgoing particles involved in a reaction. Ionization electrons from interactions of the particle with the gas volume drift at a uniform velocity to the readout plane, which in this present case is a highly segmented MicroMegas board. The point of detection of the electrons on the readout plane determines two coordinates of the tracks, while the drift time yields the third dimension. In addition to the TPC component, the TexAT tracking volume is also surrounded on five sides by CsI-backed Silicon detectors. See [1] for more details on the design of TexAT.

To reduce the total number of channels on the TexAT MicroMegas board, a unique segmentation scheme was conceived, consisting of rectangular pads in the beam region and overlapping strips and chains to the left and right of the central region. To verify that the chosen pad segmentation would allow for the required vertex and angular resolution, detailed Monte Carlo simulations were performed. These simulations utilized the Geant4 [2] and Garfield++ [3] packages for ion and electron transport, respectively. Two reactions were studied as the test case: $^{12}\text{C}(p,p)^{12}\text{C}$ and $^{18}\text{Ne}(a,p)^{21}\text{Na}$. In the latter, residual ^{21}Na nuclei in both the ground state and first excited state were populated. In the simulation, the incoming ions were forced to undergo the reaction of interest at a random point within the TPC using realistic reaction kinematics. At each step of an incoming or product track, the total ionization energy was converted to a number of electron and ion pairs, and each electron was drifted under a constant electric field to the MicroMegas board. Time-dependent histograms of the number of detected electrons for each pad of the MicroMegas board were generated and stored for offline processing. Additionally, the energy collected in each detector of the Silicon array was also recorded per event. Fig. 1 shows an example event visualized in Geant4.

Custom track reconstruction routines have been developed for the TexAT detector. For particles traversing the left and right regions, X-Y coordinates are determined by matching strips to chains (or vice versa) using the average recorded drift time. In the central region, the X-Y coordinates of a track are determined solely from the position of the rectangular pad with the highest electron count per row. Such a procedure yields two tracks: one for the light product and one combined track for the incoming ion and heavy recoil. By finding the point of closest approach of the fitted light product and the heavy ion tracks, the heavy ion track in the central region can be split into separate incoming and recoil tracks. Finally, the three tracks are re-fit simultaneously to find the vertex of the interaction and the relative angles of the reaction

products. Fig. 2 shows an example of the track reconstruction. The blue points are the simulated interaction points, while the yellow, purple and green points are reconstructed from the

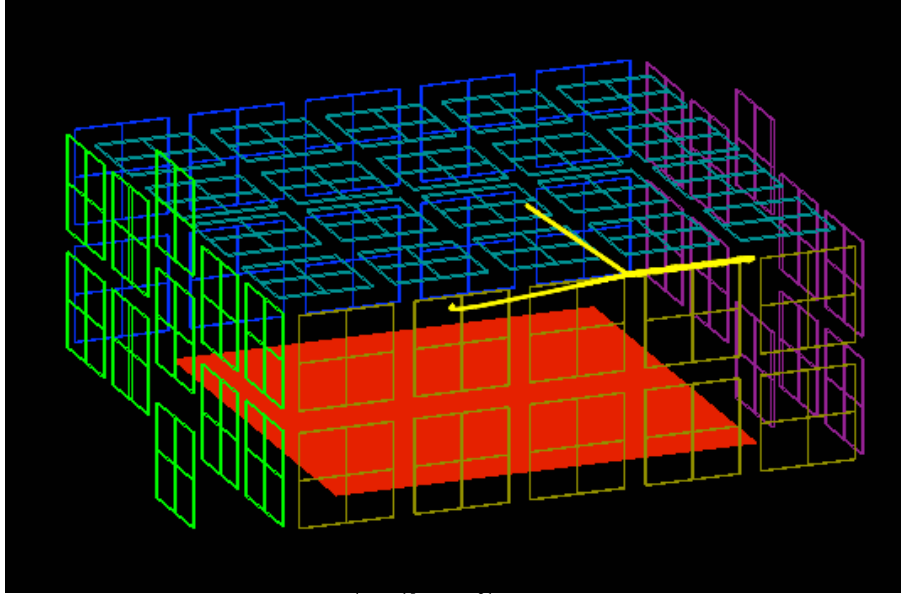


FIG. 1. Example track for the ${}^4\text{He}({}^{18}\text{Ne},\text{p}){}^{21}\text{Na}$ reaction in the TexAT detector as visualized in Geant4. The light recoil (proton) hits the Si detector on the top plate and the heavy recoil (${}^{21}\text{Na}$) stops in the gas volume.

information recorded from the simulation for the MicroMegas board. The black lines are the fitted tracks, and the teal point indicates the fitted reaction vertex. For the reactions of interest, the vertex reconstruction error was found to be approximately 1.5 mm on average, with a distribution that peaked below 1 mm. The angular resolution determined from the simulation was approximately 3 degrees at FWHM. If the Q-value of the reaction is unknown, the center of mass

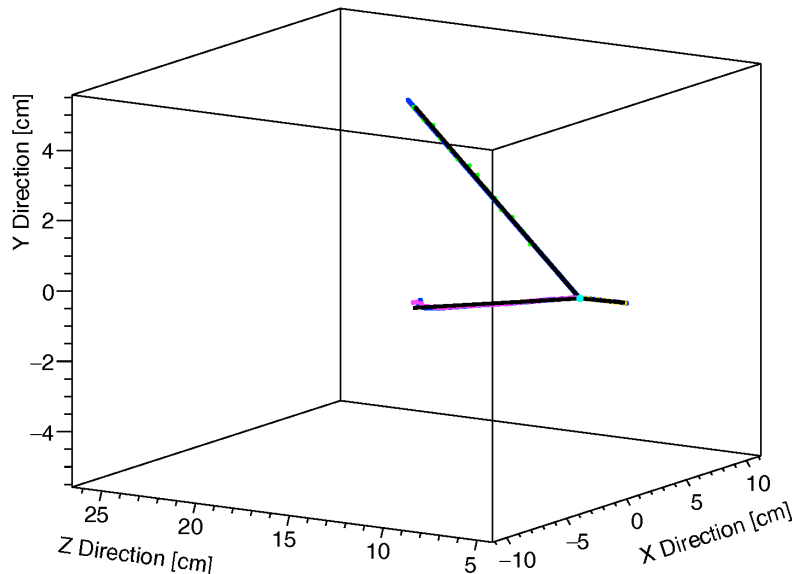


FIG. 2. Same track as in Fig. 1, but reconstructed from drifted electrons detected by the MicroMegas pads.

energy of the interaction can only be reconstructed from the vertex position and the average energy loss in the gas, and is limited by energy straggling effects. For the incoming ^{18}Ne ions, this yielded a center of mass energy resolution of 190 keV at FWHM. Using the interaction energy as provided by the vertex, in addition to the angle and energy (measured in Si detectors) of the light product, the Q-value can be reconstructed. In the case of the $^{18}\text{Ne}(a,p)^{21}\text{Na}$ reaction, transitions to the ground and first excited states of ^{21}Na (separated by only 330 keV) could be well resolved (see Fig. 3). Once the reaction mechanism is identified (e.g. elastic or inelastic scattering), the c.m. energy resolution can be improved by recalculating using the Q-value, the detected energy in the Si detector, and emitted light product angle. In the present study, the center of

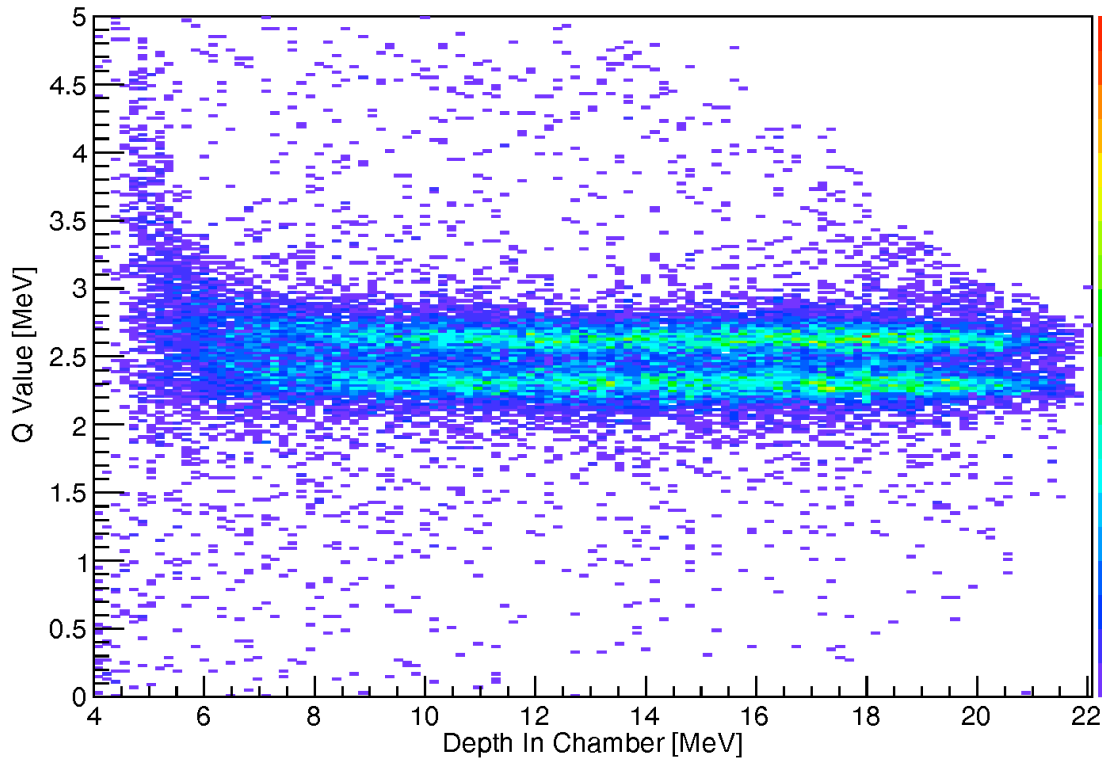


FIG. 3. Reconstructed Q-value vs. chamber depth for the simulated $^{18}\text{Ne}(a,p)^{21}\text{Na}$ reaction.

mass energy resolution for these events was found to be 40 keV at FWHM (see Fig. 4). Additionally, these energy and angle resolutions were found to be mostly insensitive to the depth within the scattering chamber and therefore interaction energy and scattering angle.

In summary, detailed Monte Carlo simulations of the TexAT detector have been performed to test the design characteristics against relevant example reactions. Algorithms have been developed for the reconstruction of the tracks within the TPC volume and the resulting

reaction kinematics. With the current segmentation, the observables can be reconstructed with enough precision to separate two closely spaced excited states for a relevant inelastic two-body reaction. It was shown that track reconstruction allows for excellent energy and angular resolution over wide range of excitation energies and scattering angles for various reaction types.

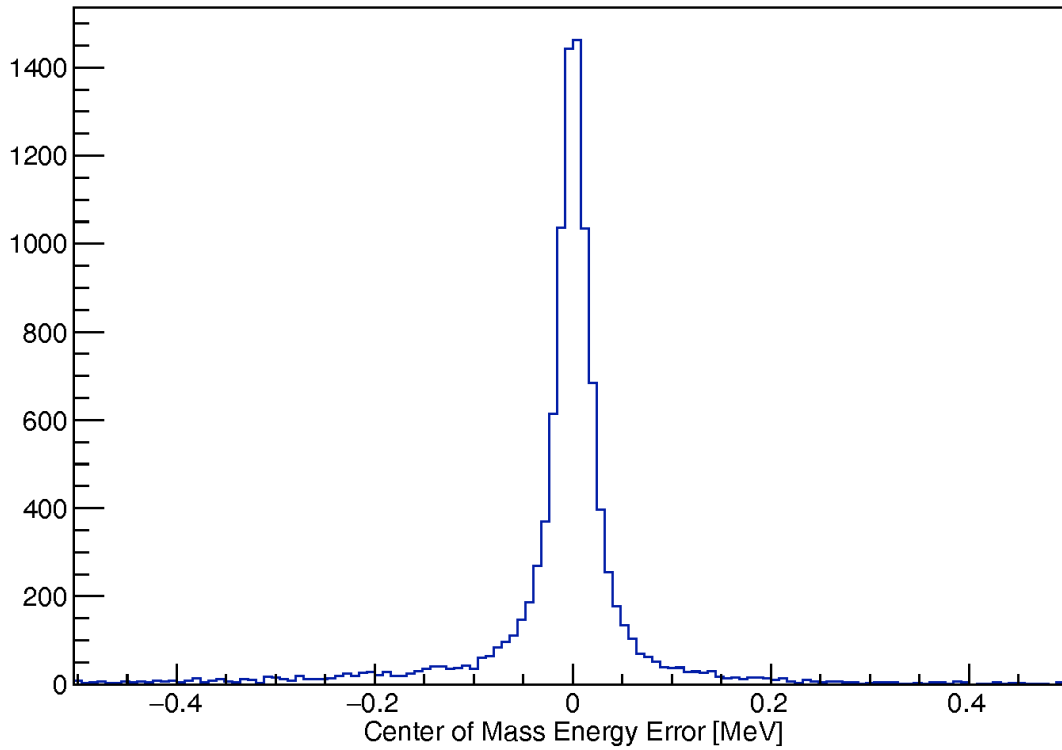


FIG. 4. Center of mass energy resolution for the simulated $^{12}\text{C}(p,p)^{12}\text{C}$ reaction.

- [1] E. Koshchiy, G.V. Rogachev, E. Uberseder and E. Pollacco, *Progress in Research*, Cyclotron Institute, Texas A&M University (2014-2015), p.IV-42.
- [2] S. Agostinelli *et al.*, Nucl. Instrum. Methods Phys. Res. **A506**, 250 (2003).
- [3] <http://garfieldpp.web.cern.ch/>

Texas active target (TexAT) detector - part 3: Acquisition and analysis infrastructure

E. Uberseder, G.V. Rogachev, E. Koshchiiy, and E. Pollacco¹

¹IRFU, CEA Saclay, Gif-sur-Yvette, France

The TexAT (Texas Active Target) detector under development at the Cyclotron Institute will contain a Time Projection Chamber (TPC) with a high level of segmentation in the readout plane. Additionally, the tracking volume will be surrounded by 58 quad-segmented Si detectors backed with an additional CsI detector. All together, the TexAT detector consists of 1024 MicroMegas, 232 Silicon, and 58 CsI readouts for a total 1314 channels. Such a large number of channels, if analyzed using traditional electronics, would lead to an extreme cost for the acquisition system. With the increasing use of TPCs in nuclear physics, the problem of large channel numbers has been addressed by the community. A collaboration of CENBG, GANIL, IRFU, NSCL and RIKEN has developed a low-cost high-fidelity data acquisition system, known as GET, for use with highly segmented TPCs [1].

The GET system is built upon individual “AGET” ASIC chips of 64 channels each. These chips provide, on a per channel basis, customizable pre-amplification and shaping of each signal. Additionally, the analog signal is stored over 512 sequential time bins via a switched capacitor array (SCA) with a selectable clock frequency. Four of these chips are loaded onto a single “AsAd” card (see Fig. 1), which samples and

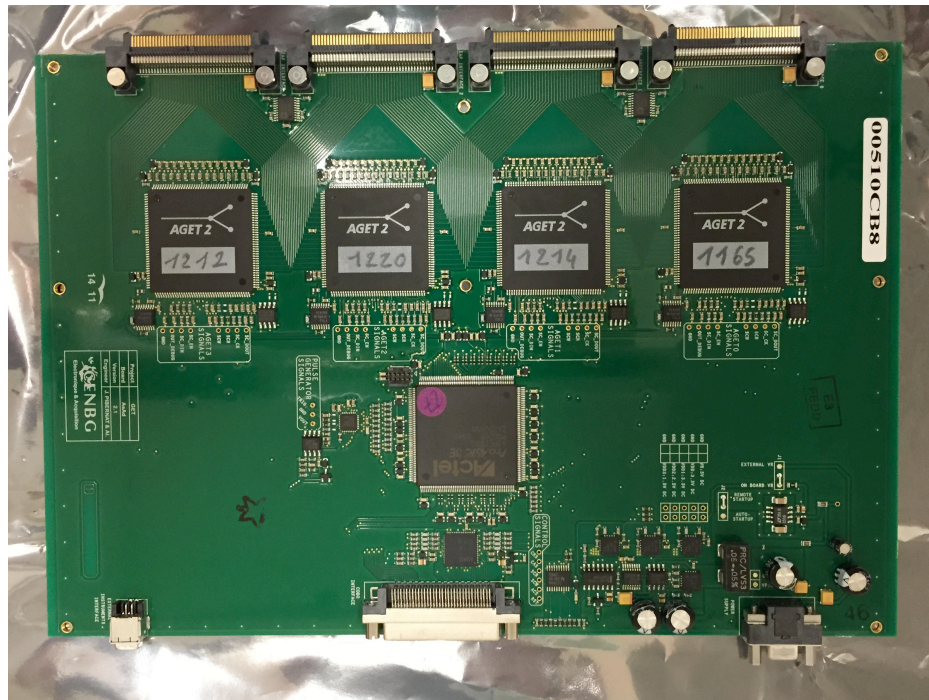


FIG. 1. Image of the AGET chips mounted on an AsAd board.

digitizes all 512 time bins for each of the 256 channels. These “AsAd” boards are read out by a MicroTCA module referred to as “CoBo” (see Fig. 2), which has the ability to package and send the data to a PC from four AsAd boards — a total of 1024 independent channels. The CoBo board has a theoretical throughput of 1 Gbps, and the MicroTCA architecture can transmit 10 Gbps through a fiber uplink, allowing for the operation of 10 CoBo boards, or 10240 channels, within a single crate. An additional MicroTCA board, called

“Mutant”, distributes the clocks to the CoBo boards and handles complex custom trigger decisions. The GET system has a specialized set of software tools for control, monitoring, and data offload, and the system has been integrated into the GANIL Narwal-based data acquisition package.



FIG. 2. Image of MicroTCA crate including the two CoBo cards

To date, we have procured five of the six necessary AsAd boards for the TexAT detector, as well as the two needed CoBo boards. The production run for the Mutant boards has not yet taken place, though one has been ordered. The MicroTCA architecture (crate, MCH, power supply, etc.) has also been delivered. The associated software has been preliminarily installed on a staging computer, and data generated via an onboard pulser on the AsAd cards has successfully been collected using the system. To attach the GET system to a detector, a customized “ZAP” board must be manufactured which allows for biasing and reverse-protection of the ASIC chips. These boards are currently under design. As the MicroTCA crate can offload up to 10 Gbps, the associated computing system must be capable of writing such a throughput to disk. The GANIL data acquisition system can operate across several distributed nodes, though also this requires synchronization of the experiment-specific configuration files across each node. Another solution is currently under consideration for the TexAT detector that would incorporate a single multi-processor multi-drive node as the backbone of the acquisition system.

To be performed in a timely manner, the analysis of the large data sets associated with TPC type detectors requires parallel data processing. We have conceived and tested a cluster design unique in nuclear physics, adopted from the data science industry, to fulfill the parallel processing needs for the TexAT

detector. The cluster is based on the open-source Hadoop Distributed File System (HDFS) [2], where each compute node contains several terabytes of data storage, and the files are distributed, with replication, across the nodes. This is in contrast to a traditional cluster, where most of the storage is centralized on a single file server and must be pulled to the computed node over the network. The open-source cluster engine used in the present case, Spark [3], is aware of the location of the data file on the cluster, and computations on that file occur locally on the particular node. As such, very little data needs to travel over network, and only a reduced set of histograms traverse the network to the master node, where they are reduced. The Python interface to the Spark API allows for very seamless integration of physics analyses through the Python hooks into the ROOT [4] analysis package (PyROOT). While the ROOT developers also have a parallel analysis system with data-local capabilities, PROOF, a large advantage of using Spark is found in generality of the cluster engine. The same cluster engine used for data-local analysis can be used to perform parallel batch computations, such as Geant4 calculations, with only a small python wrapper comparable in length to a Condor submit script.

To test the cluster design, we have purchased four data/compute nodes, and a single master node. Each compute node consists of six cores and four 2 Tb hard drives. The total configured space of the distributed file system is 32 Tb, with 24 cores available for computation. The nodes are connected through a 1 Gbps network backbone. The entire configuration has been built inside of a Docker [5] image, such that deployment on a new node takes only minutes after operating system installation. We have benchmarked the system against a data set of 30 GB. A serial analysis consisting of a simple *TSelector* processing a *TChain* on the master node, with no data-locality, took 870 seconds to run. The same analysis performed on 4 nodes with 24 cores and data locality preferred took only 40 seconds, which represents a 90% parallelization efficiency. Additionally, this represents a 6 Gbps data processing rate, a value that demonstrates the power of data locality, as it would ordinarily exceed the maximum possible network transfer rate for only four compute nodes on a 1 Gbps network (4 Gbps).

In summary, the TexAT detector will utilize an entirely new data acquisition system, GET, designed specifically for TPCs. This system allows for a high data throughput at a low cost per channel. We have obtained and tested nearly all of the hardware and software components of the system. To process the large amount of data that will be generated by the detector, a locality-aware parallel cluster design, utilizing software adopted from the data science industry, has been constructed and benchmarked. The parallel data processing efficiency is extremely good, with the data rate exceeding the network bandwidth thanks to the data-local feature of the design.

[1] E. Pollacco *et al.*, Physics Procedia **37**, 1799 (2012).

[2] <https://hadoop.apache.org/>

[3] <https://spark.apache.org/>

[4] R. Brun and F. Rademakers, Nucl. Instrum. Methods Phys. Res. **A389**, 81 (1997).

[5] <http://www.docker.com/>

FAUST upgrade (FAUSTUPS) for experimental proton-proton correlation functions

L. Heilborn, A.B. McIntosh, M. Youngs, K. Hagel, L. Bakhtiari, P.J. Cammarata, M. Chapman, A. Jedele, J. Mabilia, L.W. May, A. Zarrella, and S.J. Yennello

The proton-proton correlation function has been predicted to be sensitive to the asymmetry energy of nuclear matter [1]. We have taken data for reactions of 40 MeV/nucleon $^{40}\text{Ar}+^{58}\text{Fe}$, ^{70}Zn and $^{40}\text{Ca}+^{58}\text{Ni}$ at the Texas A&M Cyclotron Institute. After calibration, proton-proton correlation functions will be extracted. The data will then be compared to Constrained Molecular Dynamics (CoMD) [2] and isospin-dependent Boltzmann-Uehling-Uhlenbeck (iBUU) model[1] results, for the purpose of investigating the impact of the asymmetry energy term of the equation of state on the shape and magnitude of the correlation function. FAUST (Forward Array Using Silicon Technology) is comprised [3] of sixty-eight dE-E telescopes arranged to provide coverage of particles emitted from quasiprojectiles (QP, the excited source resulting from heavy ion reactions). Each telescope consists of a 2x2cm 300 μm thick silicon backed by a CsI(Tl)-photodiode detector. The array has been modified to include Upgraded Position Sensitivity, to complete the new acronym, FAUSTUPS. The successful upgrade and subsequent campaign and data collection are described here.

A precise knowledge of the point of detection of the particles is essential when measuring a correlation function, so satisfactory angular resolution is of paramount importance [4]. In order to increase the angular resolution of charged-particle detection, the FAUST array has been upgraded using Dual-Axis Dual-Lateral (DADL) Si detectors [5]. The DADLs have uniform resistance across the front and back of the detectors and employ charge-splitting to determine the position of the detected light charged particles to within 200 μm [5].

Fig. 1 illustrates the features of a DADL detector. A reverse bias is applied to the silicon semiconductor, which depletes the conduction band. Electrons and holes liberated by ionizing radiation migrate to opposite faces of the detector due to the bias voltage. Due to the resistive

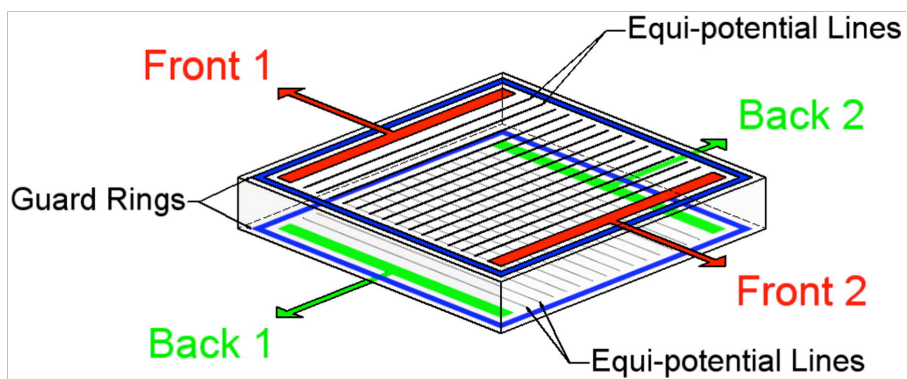


FIG. 1. Schematic of DADL, showing the equipotential lines on the uniformly resistive surface, which allows position to be determined by charge splitting [5].

surface across each

face of the detector, the electrons on the back of the detector split proportionally to the two back signals, while the holes are charge split proportionally to the two front signals. These four signals

allow the relative x and y position of the detected fragment to be determined. Guard rings and conductive equipotential strips ensure a uniform potential across the entire surface of the detector [5]. The additional signals on each Si-CsI(Tl) telescope resulted in an 150% increase in the number of channels processed, so Application-Specific Integrated Circuit (ASIC) Heavy Ion Nuclear Physics (HINP) chip electronics are used to deal with the increased number of signals [6].

As of fall 2014, all of the original silicon detectors of FAUST have been replaced with position-sensitive DADLs. Reactions of 40 MeV/nucleon $^{40}\text{Ar}+^{58}\text{Fe}$, ^{70}Zn and $^{40}\text{Ca}+^{58}\text{Ni}$ were measured, along with 10 MeV/nucleon proton- α and 15 MeV/nucleon α beams for energy and position calibrations. Particle identification (PID) and position of protons and other light charged particles produced in the reactions were measured in FAUSTUPS using high-gain CSAs (charge sensitive amplifier) developed by RIS Corporation [7]. The charge-splitting across the surface of the detector can result in a very small signal, which demands high-gain preamps. The total energy deposited in the Si wafer is determined by adding the two sides (Front 1 + Front 2 or Back 1 + Back 2). The separation of the LCPs is shown in an E-dE plot, derived from Si and CsI(Tl) signals, Fig. 2. The E-dE plot for the CsI energy calibration from 10 MeV/nucleon proton- α beam is shown in Fig. 3.

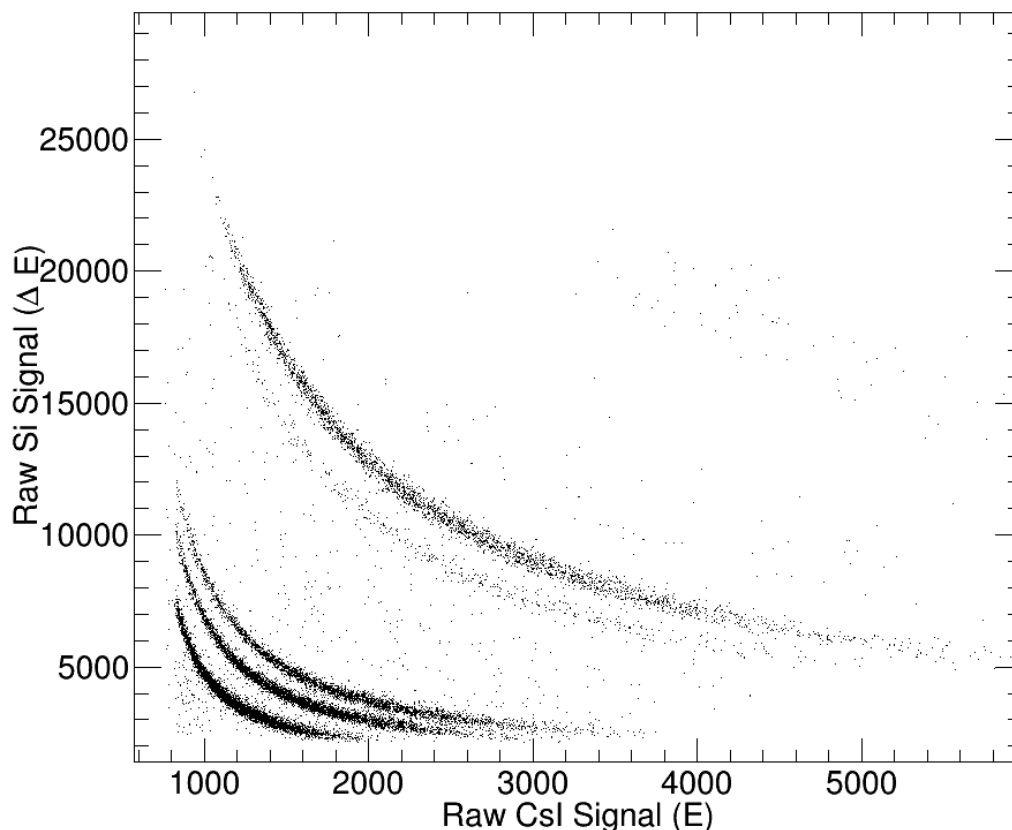


FIG. 2. Representative dE-E plot, from one of the detectors in Ring E for the reaction of 40A MeV $^{40}\text{Ar} + ^{58}\text{Fe}$, demonstrating the excellent p-d-t differentiation using the new silicons and electronics from the FAUSTUPS upgrade.

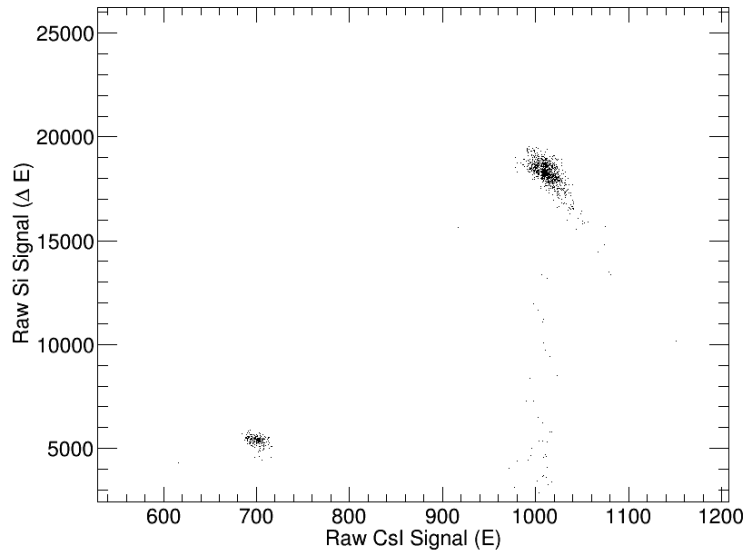


FIG. 3. Representative dE-E plot, from one of the detectors in Ring A for the calibration beam of 10 MeV/A proton and $\alpha + {}^{197}\text{Au}$, useful for a check of the energy calibration process.

In addition to high positional accuracy of a detected particle within a detector, the relative alignment from one detector to another must be known. In order to calibrate relative detector position, a mask of 0.040" tungsten was designed and produced. Slits of 0.010" were angled through the mask in order to allow α particles from a well-collimated source or elastically

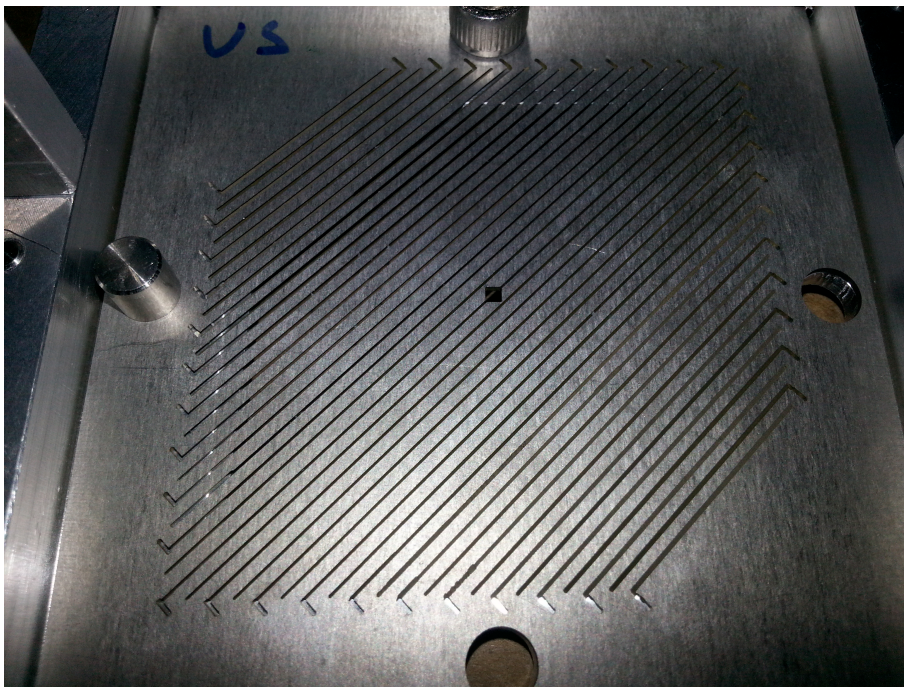


FIG. 4. Mask as machined by sinker and wire EDM at Reliable EDM. Square hole in the center allows the beam to pass through the mask, and deposit into a Faraday Cup after the FAUSTUPS array.

scattered off of a gold target to reach each ring of FAUSTUPS. To prevent the large beam spot from effectively scattering elastic alpha particles around the slits in the mask, an aluminum collimator was used to reduce the beam spot to 1 mm. The 0.0675" square cut through the center (see Fig. 4) allows the beam to pass through, reducing beam particle interactions with the tungsten mask. The stripes from the mask can be seen on the face of the detectors by gating on a single alpha energy from a thorium source or beam elastically scattered, the spectrum from a ^{228}Th high-energy alpha is shown in Fig. 5.

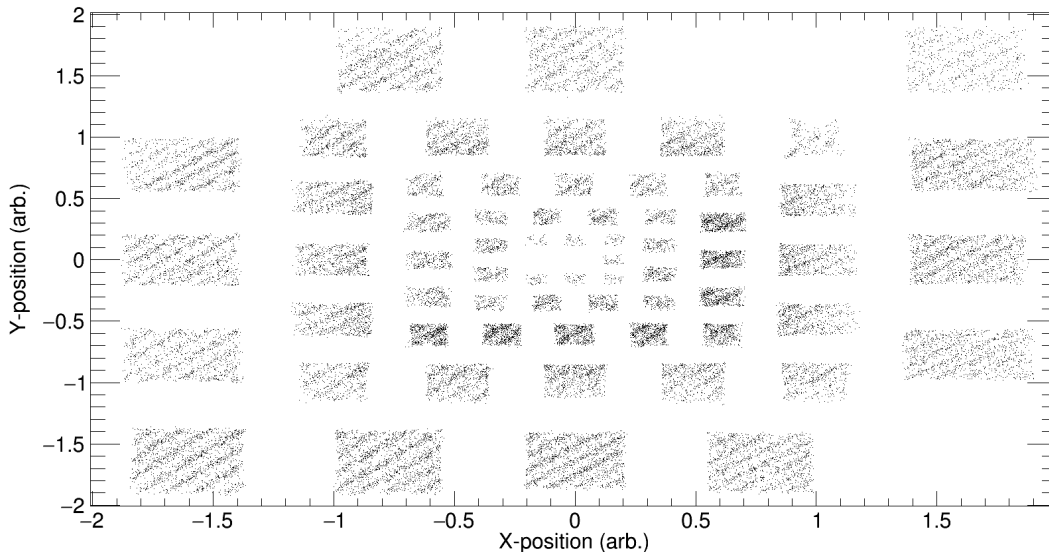


FIG. 5. Position spectra of detectors, cut on the E of the highest energy ^{228}Th α in the silicons, through the position-calibration mask.}

Based on previous successful test runs and preliminary analysis, excellent PID and position resolution are expected to be achieved. The systems were chosen to allow for comparisons of systems with varying N/Z asymmetry, but keeping constant either the total mass or Z of the system. Energy and position-calibrated multiple proton events will allow the correlation function to be extracted from the 40A MeV $^{40}\text{Ar}+^{58}\text{Fe}$, ^{70}Zn and $^{40}\text{Ca}+^{58}\text{Ni}$ reactions with different density-dependencies of the asymmetry energy in CoMD and iBUU simulations of the same reactions. For comparison between experimental data and results from simulations (CoMD and iBUU), a software filter of the geometric and energy acceptance of the FAUSTUPS array will be used event-by-event. The same data analysis performed upon the experimental results can then be compared to the simulations.

- [1] L.W. Chen, V. Greco, C.M. Ko, and B.A. Li, Phys. Rev. Lett. **90**, 162701 (2003).
- [2] M. Papa, G. Guiliani, and A. Bonasera, J. Computational Phys. **208**, 403 (2005).
- [3] F. Gimeno-Nogues *et al.*, Nucl. Instrum. Methods Phys. Res. **A399**, 94 (1997).
- [4] G. Verde *et al.*, Eur. Phys. J. A **30**, 81 (2006).
- [5] S. Soisson *et al.*, Nucl. Instrum. Methods Phys. Res. **A613**, 240 (2010).
- [6] G. Engel *et al.*, Nucl. Instrum. Methods Phys. Res. **A652**, 462 (2011).
- [7] R. Todd, RIS-Corp, 5905 Weisbrook Lane, Suite 102, Knoxville, TN 37909 (2013).

The ParTI array for studying pionic fusion

A. Zarrella, A. Bonasera, L. Heilborn, A. Jedele, L.W. May, A.B. McIntosh,
M. Youngs, and S.J. Yennello

Pionic fusion is the process by which two nuclei fuse during a collision and then deexcite by the exclusive emission of a pion. The resulting compound nucleus is left in or near its ground state [1]. The process requires that nearly all of the available kinetic and potential energy in the colliding system be concentrated into two degrees of freedom - the rest mass and kinetic energy of the emitted pion. Thus, the energy of the emitted pion is limited by the number of available final states of the fusion residue [2]. The combination of limited available energy and the extreme coherence required in the process ensures that the pionic fusion channel is greatly suppressed. Indeed, the measured pionic fusion cross sections range from hundreds of nanobarns for the lightest systems (He + He) to hundreds of picobarns as one moves to larger systems ($A_{\text{tot}} = 6 - 24$) [2-12].

During this past year we have continued progress towards measuring pionic fusion cross sections using the Momentum Achromat Recoil Spectrometer (MARS) [13]. In May of 2014 we conducted an experiment in MARS to measure the transmission efficiency of our pionic fusion residues of interest through the spectrometer. In August of that year, prototype phoswich detectors were tested in beam as a proof of concept for fast vs. slow light charged particle identification and digitizer waveform readout. Following the results of the August experiment, the design for the Partial Truncated Icosahedron (ParTI) phoswich array was finalized and the array was constructed in the winter of 2014. The phoswich detectors will be used to detect the charged pions resulting from pionic fusion reactions. They have been built and are currently in the process of being tested. The GANDALF digitizer module [14] will be used to identify the charged particle events and is currently in the process of being ported into CycApps for use in our standard ROOT environment.

From the MARS transmission efficiency test experiment we were able to determine the optimum MARS settings for the residues of interest and we achieved a transport efficiency of approximately 61%. A beam of ^{16}O was produced by the K500 cyclotron at the Cyclotron Institute at the predicted energy of the pionic fusion recoils, stripped of electrons using a mylar foil and transported through MARS. Faraday cups were used to measure the beam intensity before and after the spectrometer. The ratio of the intensity measured at the back of MARS to the intensity measured before MARS is the transport efficiency. A semi-empirical formula [15] was used to predict equilibrium charge state distributions of the ^{16}O beam leaving the mylar foil. We produced ^{16}N in the $^{15}\text{N}(d,p)^{16}\text{N}$ reaction to determine optimum MARS settings for these residues as well.

During the test experiment in August we tested prototype phoswich detectors of two types: fast plastic/slow plastic (EJ-212 and EJ-240, respectively purchased from Eljen Technologies) and fast plastic/CsI(Tl) where the fast plastic in both cases produces a dE, short emission time component to the produced signal and the slow plastic and CsI(Tl) produce long

emission time components proportional to the total energy. Fast vs. slow pulse shape analysis was performed on the signals produced by both types of phoswich and it was decided that the CsI(Tl) type detectors will be the design moving forward as particle identification was never achieved with the plastic/plastic units. Fig. 1 is an example of the fast vs. slow pulse shape discrimination for a fast plastic/CsI(Tl) phoswich. The vertical axis is the integrated fast

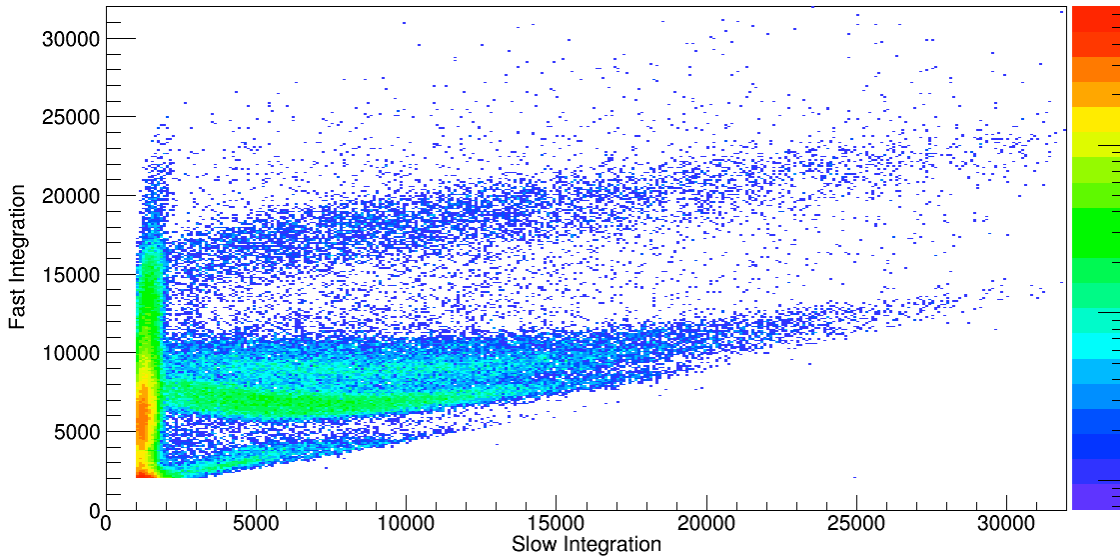


FIG. 1. A fast vs. slow particle identification plot for a fast plastic/CsI(Tl) phoswich detector. Moving up from the bottom of the plot, there is a straight line corresponding to neutron and gamma event, at least two particle identification lines for $Z = 1$ isotopes and, lastly, a thick line corresponding to $Z = 2$ isotopes. Pions are expected to mostly populate the area between the neutron/gamma line and protons.

component and the horizontal axis is the integrated slow component of the waveforms. We see particle identification lines for $Z = 1$ and $Z = 2$ isotopes. We expect pions to be located between the $Z=1$ and neutron/gamma lines in these plots.

Fig. 2 is a picture of the ParTI array fully built but not populated with the 15 total phoswich detectors. The design is also modular such that the array can be used in many different configurations in order to increase its utility in future experiments. The centers of each hexagonal detector are located on a sphere of radius 4.63 inches centered on the target position while the centers of each pentagonal detector are located 4.75 inches from the target position. Three partial hexagonal detectors will populate the center frame. These detectors will be positioned as a standard hexagonal unit with a hole through the center for beam to enter the chamber. For pionic fusion experiments, the array will be positioned backward of the target in order to minimize detection of background fragments produced by more standard reaction mechanisms while also taking advantage of the reported forward-backward peaked pion emission distribution that has been reported in previous pionic fusion experiments [2,3,4].

Fig. 3 is a picture of the pentagonal and hexagonal detector shapes. Moving backwards from the front face, these detectors consist of a 3 mm thick piece of EJ-212 fast scintillating

plastic, a 1 cm thick CsI(Tl) crystal and a 1 inch thick light guide which mates the face of the CsI to the face of a 1924a Hamamatsu photomultiplier tube (PMT). Aluminized mylar is wrapped around the front face of the detectors to protect them from delta rays and to provide a light-tight surface of uniform thickness for particles to pass through. The rest of the detector, from the sides of the fast plastic to the base of the



FIG. 2. The ParTI array in the configuration to be used in the coming pionic fusion experiments.

PMT, is wrapped with Teflon tape to provide a diffusely reflective and light-tight surface around

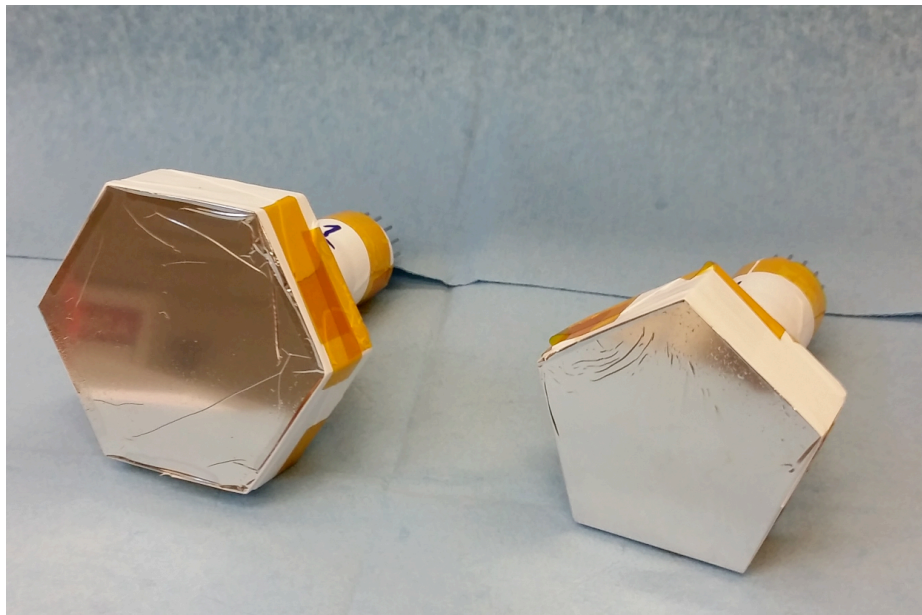


FIG. 3. A picture of the two regular polygon phoswiches that will populate the ParTI array. These detectors are 1.5" along each side

the detectors.

The GANDALF digitizer is a 16-channel (8 channel interleaved) fast sampling ADC with 12-bit resolution at approximately 500 MS/s (1 GS/s interleaved). The module also includes a customizable FPGA which will be used to perform real time pulse analysis of the phoswich waveforms with the intent of looking for particular shape characteristics consistent with pion decays. Using this method we believe we can suppress the recording of background events to increase the live time of our electronics. We are currently in the final stages of working the module into the ROOT environment. Once this is completed, work will begin on FPGA coding and testing.

In the coming summer of 2015 we will run two final test experiments. The first will be a calibration of the phoswich detectors. A phoswich will be mounted in the MARS detector chamber and secondary beams of light charged particles at known energies will be used to determine the shapes of particle identification lines for these detectors. We will also be able to test the position dependence of the phoswich performance. The second test will be of a fully populated ParTI array. In this test we will align the ParTI array inside the MARS production chamber and successfully read out all 15 phoswich detectors using the cube feedthrough chamber that was recently added to the line. Contingent upon these two successful tests, we expect to be able to begin measuring pionic fusion reactions in the fall of 2015.

[1] P. Braun-Munzinger and J. Stachel. *Ann. Rev. Nucl. Part. Sci.* **37**, 97 (1987).

[2] D. Horn, *et al.* *Phys. Rev. Lett.* **77**, 2408 (1996).

[3] Y. Le Bornec *et al.* *Phys. Rev. Lett.* **47**, 1870 (1981).

[4] L. Joulaeizadeh *et al.* *Phys. Lett. B* **694**, 310 (2011).

[5] W. Schott *et al.* *Phys. Rev. C* **34**, 1406 (1986).

[6] M. Andersson *et al.* *Nucl. Phys. A* **779**, 47 (2006).

[7] M. Andersson *et al.* *Phys. Lett. B* **481**, 165 (2000).

[8] M. Andersson *et al.* *Phys. Scr.* **T104**, 96 (2003).

[9] L. Bimbot *et al.* *Phys. Rev. C* **30**, 739 (1984).

[10] L. Bimbot *et al.* *Phys. Lett.* **114B**, 311 (1982).

[11] J. Homolka *et al.* *Phys. Rev. C* **38**, 2686 (1988).

[12] N. Willis *et al.* *Phys. Lett.* **136B**, 334 (1984).

[13] R.E. Tribble *et al.* *Nucl. Instrum. Methods Phys. Res.* **A285** 441 (1989).

[14] S. Bartknecht *et al.* *Nucl. Instrum. Methods Phys. Res.* **A623**, 507 (2010).

[15] G. Schiwietz and P.L. Grande, *Nucl. Instrum. Methods Phys. Res.* **B175-177**, 125 (2001).

Upgrades and characterization of the Texas A&M quadrupole triplet spectrometer (QTS)

A.B. McIntosh, L. Heilborn, M. Youngs, L.A. Bakhtiari, M. Chapman, A. Jedele, L.W. May,
E. McCleskey, A. Zarrella, and S.J. Yennello

The Quadrupole Triplet Spectrometer (QTS) [1] used in conjunction with FAUSTUPS [2-4] promises to be a powerful tool for studying low and intermediate energy heavy ion reactions. This report describes upgrades of the detector suite and the achieved results. Since the status of FAUSTUPS is being described elsewhere [4], this report will focus on the QTS detectors. The upgraded FAUSTUPS-QTS system is ready for experiments beginning this summer 2015 to measure fusion-evaporation reactions.

The upgraded QTS detector suite is designed to measure four essential pieces of information for heavy residues produced near $\theta=0^\circ$: the energy (E), the velocity (V), the atomic number (Z) and the mass number (A). To access this information, three measurements are necessary: the time-of-flight (TOF), the energy loss in a thin passage detector, and the remaining energy in a stopping detector. The addition of the dE measurement since prior experiments is critical to understanding and discriminating atomic processes from nuclear reactions.

The TOF is measured using two XY position sensitive PPACs (Parallel Plate Avalanche Counters), one on either end of the QTS magnets. Additionally, plastic scintillators can be inserted into the line to provide timing information for less ionizing particles (light and fast products). In our recent experiment, the results of which are shown below, we demonstrated that $^{86}\text{Kr} + \text{C}$ @ 35 MeV/nucleon and its reaction products are sufficiently heavily ionizing that the downstream PPAC provides reliable timing signals at the standard operating pressure of 6Torr and voltage of +530V. The dE-E measurement can be made with a thin silicon detector (58um) and a thick silicon detector (1000um). These two detectors comprise the Downstream Stack (DS).

The first data obtained using the full upgraded QTS suite including the dE information was obtained in run 041715 where the reaction system was $^{86}\text{Kr} + \text{C}$ @ 35 MeV/nucleon. Fig. 1 shows data obtained in the QTS detectors using the downstream (DS) stack as the trigger with the spectrometer tuned to 1.81Tm (84% of the rigidity of the beam) where fusion residues are expected to be found. A good signal in the three quantities is required: dE, E and TOF. The upper left panel shows the dE-E correlation. The elastic peak is clearly visible. Emanating from this peak are three rays of data. The long ray extending toward higher E and lower dE is consistent with channeling in the dE detector. The component tending to higher dE and lower E and having the same slope as the channeling component may be due to positive energy straggling in the dE. The component extending to lower E and constant dE is due to incomplete charge collection. A distribution of Z is visible at lower energies, consistent with fusion residues. At lower energy still is a thin band for only Z=36. A process that produces particles exclusively with the atomic number of the beam is an atomic process (i.e. slit scatter) rather than a nuclear process. The most likely edge for slit scatter is the Faraday cup just upstream of the QTS used to block unreacted beam inside of $\theta=0.9^\circ$.

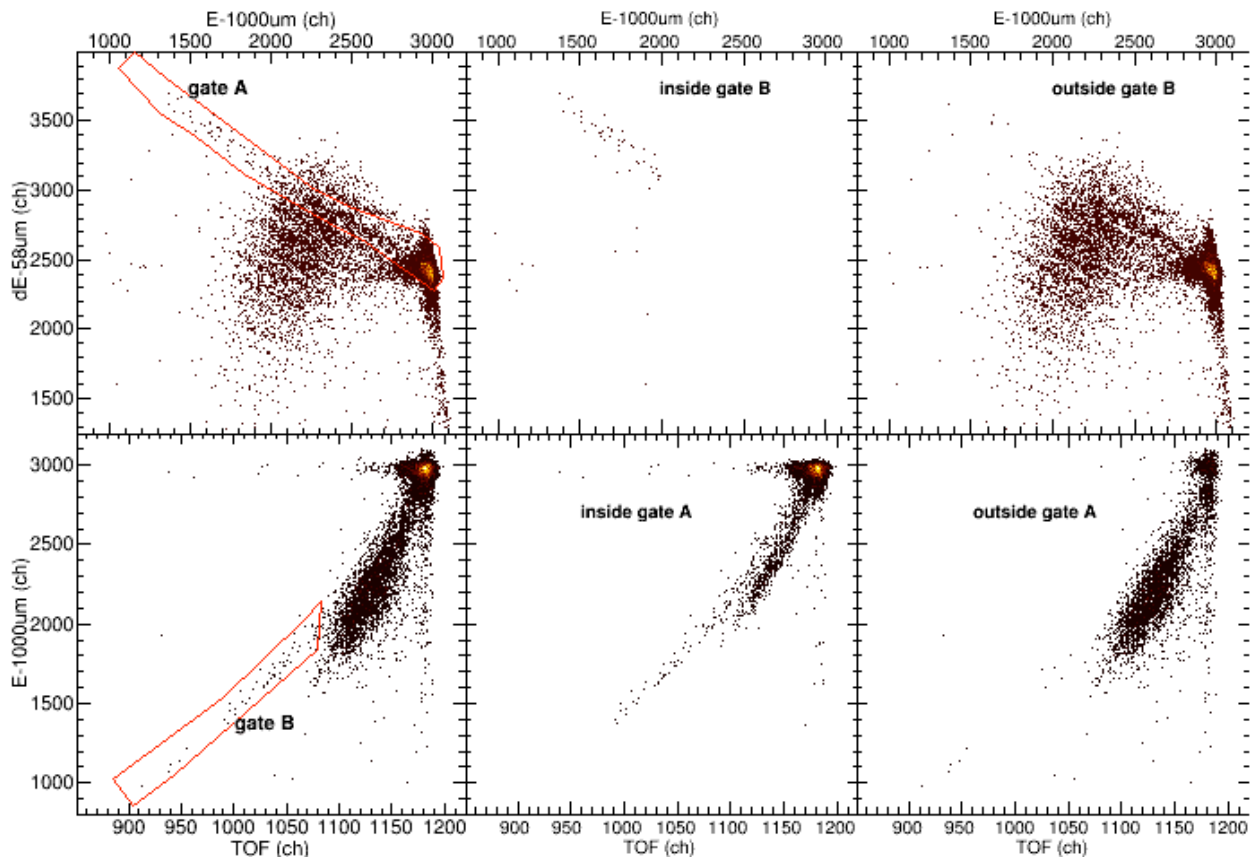


FIG. 1. Data from QTS detector array at $B\rho=1.81\text{Tm}$ with the downstream dE-E stack as the trigger. The top row shows dE-E correlations, which are sensitive to atomic number. The bottom row shows E-TOF correlations, which are sensitive to the mass number. The deviation of the residue band from the slit scatter band in the bottom middle indicates a decrease in the mass of the $Z=36$ residues with decreasing kinetic energy.

In the lower left panel of Fig. 1, the E-TOF correlation is shown. Short flight times appear on the right and longer flight times appear farther to the left. A significant distribution extends down from the elastic peak to about half the beam energy. A thin curve again extends through this yield and to lower energy still. To demonstrate the matching features between the two plots, a gate (B) is made on the thin curve in the E-TOF map. The dE-E map for data inside this gate is shown in the middle top panel; the data outside the gate is shown in the top right panel. The long thin curve in the E-TOF map is clearly associated with the long thin $Z=36$ band in the dE-E map, again consistent with slit scatter.

To further characterize the processes producing particles measured in the QTS detector suite, a gate (A) was defined around the $Z=36$ data in the dE-E map in the top right panel of Fig. 1. The E-TOF correlation for data inside (A) is shown in the bottom middle panel, and outside in the bottom right. The data outside the gate behaves as expected and does not exhibit the long slit scatter curve. The elastic peak is strongly suppressed, though remnants of the elastic peak exist. Most of the fusion residues in the E-TOF distribution lie outside the $Z=36$. Inside the $Z=36$ gate, we observe a high yield of the elastic peak, the long thin curve of slit scatter, and single narrow

band extending from the elastic and slightly sloping away from the slit scatter band. The slit scattered particles must have a constant mass of $A=86$. For $Z=36$ residues produced in nuclear reactions, the mass is not restricted to $A=86$. Higher masses are possible, but less likely since ^{86}Kr is already relatively neutron rich. Lower masses are possible and become increasingly likely with increasing excitation energy and thus increasing particle emission. In fact, this is what is observed – with increased kinetic energy loss, the residue distribution shifts to longer times than the slit scatter, implying a decreased residue mass. This is the first demonstration that the mass sensitivity that the QTS detector suite is expected to provide, and upon which we rely, is indeed realized.

Fig. 2 shows further data from the QTS detector suite also for $B_p=1.81\text{Tm}$ with FAUSTUPS CsI as the trigger. The requirement of a signal in FAUSTUPS strongly favors nuclear reactions over atomic interactions: the slit scatter line is gone and the elastic peak is highly suppressed as seen in the top left panel (dE-E) and the top right (E-TOF). Z identification

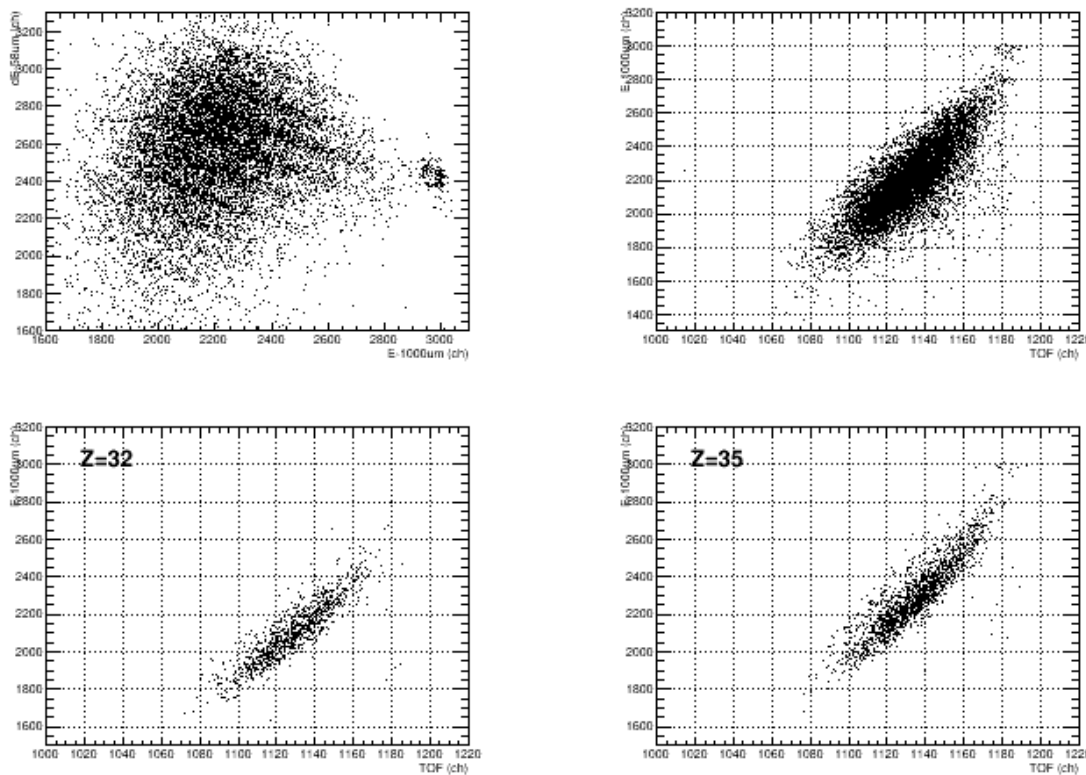


FIG. 2. Data from the QTS detector suite at $B_p=1.81\text{Tm}$ with FAUSTUPS CsI as the trigger. Slit scatter and elastic scatter are very strongly suppressed when FAUSTUPS is the trigger. Different Z are observed to populate different regions of the E-TOF map, further demonstrating the mass sensitivity of the QTS detector suite.

is achieved trivially from the dE-E map.

The lower two panels of Figure 2 display the E-TOF distribution for particles identified in the dE-E map as $Z=32$ (left) and $Z=35$ (right). The TOF range (and thus velocity) for the two

species are rather similar, while the $Z=35$ exhibits a significantly higher total energy than the $Z=32$ indicating significantly higher masses for $Z=35$ than for $Z=32$. This is the second demonstration of the mass sensitivity of the QTS detector suite. These two distributions are representative: for all atomic numbers identified, the velocity is not significantly affected by Z while the energy shifts to higher values with increasing Z .

This demonstrates that the QTS provides a clear method of separating atomic processes from the nuclear reactions of interest, and provides the information to characterize the nuclear residues in terms of Z , A , E , and V .

- [1] P. Cammarata *et al.*, Nucl. Instrum. Methods Phys. Res. **A** (accepted).
- [2] F. Gimeno-Nogues *et al.*, Nucl. Instrum. Methods Phys. Res. **A399**, 94 (1997).
- [3] S.N. Soisson *et al.*, Nucl. Instrum. Methods Phys. Res. **A613**, 240 (2010).
- [4] L.A. Heilborn *et al.*, *Progress in Research*, Cyclotron Institute, Texas A&M University (2014-2015), p. IV-54.

A LabVIEW solution for coupling an automated gamma-ray counter and software for spectra analysis

E.E. Tereshatov and C.M. Folden III

A simple approach to transfer data from a PerkinElmer[®] Wizard²[®] automatic gamma-ray counter to Canberra[®] Genie 2000[®] software for spectra analysis has been developed. The LabVIEW[®] graphical programming language has been utilized to collect data for automated ASCII file generation based on optical character recognition of information displayed by the Wizard². The results have been checked using spectra collected from an ⁸⁸Zr source. The system substantially increases the speed at which spectra can be analyzed while providing more flexibility to the user.

1. INTRODUCTION

Automation of any routine process allows one to manage time and efficiency more optimally. Radiochemical investigations often consist of numerous experiments in which scientists must check their hypothesis by varying one parameter at a time in a systematic way. This approach leads to large amounts of samples to be analyzed, and the most common and relatively simple means to treat samples with radioactive material is a gamma-ray detector. Compared to alpha detectors, gamma-ray detectors have substantially lower sample preparation requirements, but this comes at the expense of reduced detection efficiency. Long analysis times are typically required, but an automated gamma-ray detector helps to maximize throughput by allowing for sample set measurements to continue at night and on weekends. This implementation also helps to reduce dose rates on personal [1-3]. Thus, safety and speed of certain processes might be significantly enhanced. Also automation is very valuable in particular for radioimmunoassay [4-6], analysis of art objects [3,7], and environmental applications [8]. This explains the rise of the automatic γ -counters market worldwide [9-13].

Several years ago, PerkinElmer[®] designed and developed the Wizard²[®] automatic gamma-counter [14], which is actively used for radiometric detection in clinical and academic research labs around the world. These units are equipped with sodium iodide (NaI) gamma-ray detectors that have poor peak resolution (tens of keV FWHM) but very high efficiency (up to ~80%). Additionally, these units can be loaded with up to 1,000 samples, and options are available for up to 10 detectors. The Wizard² has built-in software to acquire and analyze spectra and to save summary information to a file. Although there are models that can track up to six energy regions of interest, usually a radionuclide has several emitted gamma-ray energies that would be useful to analyze. This problem is exacerbated if multiple radionuclides are studied simultaneously, such as when an element is present as multiple isotopes. Also, the unit does not allow the user to save a spectrum to a text file in order to store and analyze it independently.

In order to create a user-friendly device, the automated system is usually equipped with software to monitor parameters and control the process. Among numerous programming languages, LabVIEW[®] is one of the most popular and reliable. This National Instruments[®] product is a very well-known graphical medium for scientific and technical tasks. It has been widely used for instrument communication, data visualization and analysis, for example in food

inspections, wind turbine applications, spectrometry, optical character recognition, and many other fields [1,7,15-22].

As was mentioned above, the automation helps not only to physically replace samples on the counter, but also in data acquisition and analysis. Thus, the goal of the current work was to use LabVIEW[®] virtual instruments (VIs) from National Instruments[®] to save the raw spectrum data from a PerkinElmer[®] Wizard² automatic gamma-counter to a text file and then automatically analyze it using the Genie 2000 program from Canberra[®] [23], which is used worldwide for sophisticated analyses of gamma-ray spectra. The Wizard² model has a built-in computer with the Windows[®] operating system, so the LabVIEW program will be focused on calling Windows' functions for the reading the spectrum data. Thus, this procedure could be applied to any software capable of displaying spectra.

2. EQUIPMENT AND SOFTWARE

We used the PerkinElmer Wizard² automatic gamma-counter, model 2480 [24]. It has the capability to count vials or tubes of any shape up to 20 mL in volume and up to 95 mm in height (including cap). The maximum capacity is 1,000 tubes (up to 13 mm diameter) or 270 tubes (up to 28 mm diameter). The detector consists of a thallium-activated, NaI crystal with an end-well design. There are up to 6 simultaneous counting regions and its energy range is up to ~2,000 keV (2,048 channels). LabVIEW 2010 and Genie 2000 version 3.0 were used.

3. METHODS

Fig. 1 shows the Wizard² touchscreen when the system is collecting data from a sample of radioactive ⁸⁸Zr. (The radioactive decay daughter ⁸⁸Y is also present). The display resolution is 800 pixels x 600 pixels but the number of spectrum channels is 2,048, so simply digitizing the spectrum image will lead to errors because two neighboring channels cannot be distinguished. For convenience, the program has a moveable vertical marker, and the number of counts in the selected channel is displayed, so controlling the marker position and recording the associated marker counts was necessary. A subtask was to save the display information to a file, change the marker position, and repeat. This was accomplished using automated mouse control and the computer's "Print Screen" function.

The final executable file must access an image stored to the clipboard, so these tasks were realized via a .NET method. Fig. 2 shows an adapted code [25] that acquires image data and saves it to a PNG file. In order to synchronize our code with the beginning of the measurement, we use the Wizard² software principle that enables/disables buttons on the control panel during the

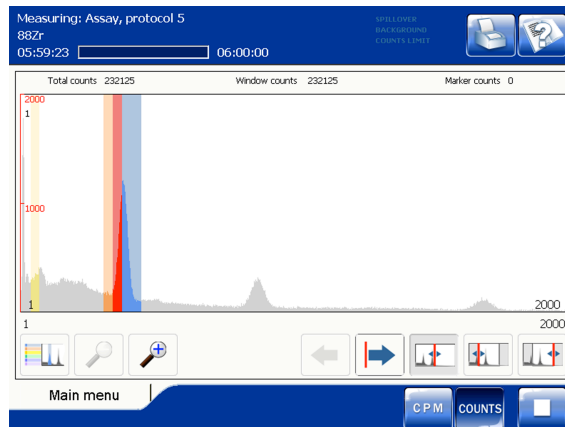


FIG. 1. Screenshot of the Wizard² display while the ⁸⁸Zr/⁸⁸Y sample was measured.

measurement and when samples are being changed, respectively. For example, in Fig. 1 one can see a number of active (colored) and inactive (grey) buttons underneath the spectrum.

The marker is moved by the user clicking the left or right arrow buttons on the touchscreen (see Fig. 1). Programmatically, this is accomplished by calling Windows' functions from the User32.dll library using a "Call Library Function Node" [26]. If the two approaches described here are combined together, then one can easily scan the entire spectrum by moving the marker from one side to another and saving the screenshots. In practice, this takes approximately 560 s, so the program must start approximately 10 min prior to the end of measurement. Usually energy lines of interest are in the first half of the spectrum (up to 1,000 keV), so the spectrum is scanned from right to left to get better statistics for the low-energy peaks. The data from each channel is recorded after a different counting time, so the data is normalized using the timestamps recorded by the "Get Date/Time In Seconds" function (Fig. 2, top left corner). This correction is trivial as long as the half-life of the nuclide(s) is/are long compared to the count time; this criterion is satisfied in the current work. The correction will be less with increased measurement time, so we recommend to measure each sample for at least 100 min in order to minimize error associated with the normalization.

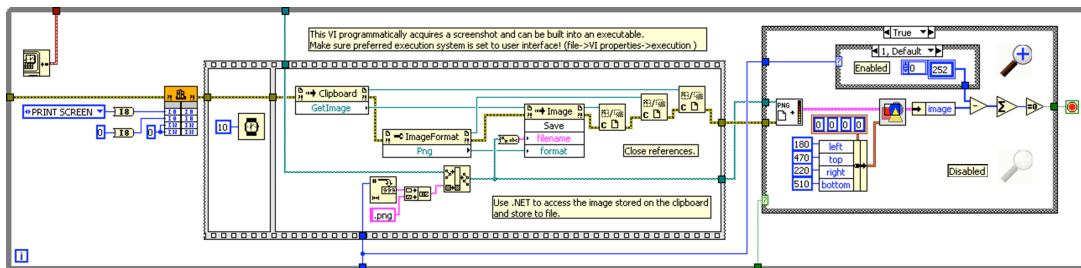


FIG. 2. .NET method to save screen images to PNG files with attention to the Wizard² touchscreen and the Print Screen button activities.

Implementation of the full code (shown in Fig. 3) results in ~2,000 screenshots collected with a different marker position for each PNG file, and the number of counts in the marker channel is shown on the top right of each screenshot. The timestamps can be used to correlate with the marker position on the screen.

Fig. 4 represents a code to read these data. A two dimensional array is a "library" of digits that has been created based on screenshots. A While Loop was implemented to identify all of the characters associated with marker counts and a positional notation method [27] has been applied afterwards. The one dimensional array near the top is the RGB background color we have used to determine if there is one more digit in the line. The accuracy of this procedure is 100%.

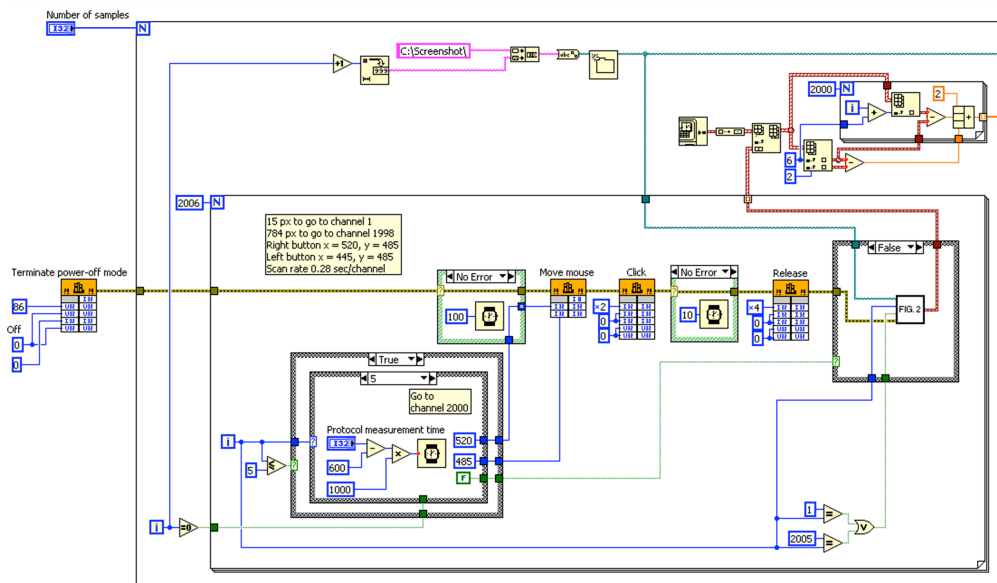


FIG. 3. Block-diagram to control the mouse position using left button clicks. SubVI in the False Case Structure represents the diagram shown in Fig. 2.

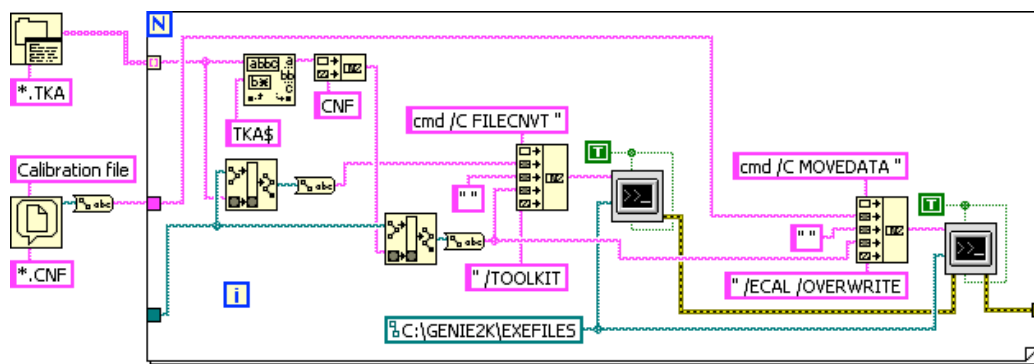


FIG. 4. Diagram to convert text files to Genie 2000 native formats with energy calibration.

The Wizard² automatic gamma-ray counter can handle up to 1,000 samples, so it is desirable to have all of the spectra analyzed automatically using Genie 2000 due to its sophisticated scripting and analysis capabilities. The ability to calibrate if needed and independently analyze the data provides substantial flexibility. The process consists of converting each spectrum's text file to a CNF file (a file format supported by Genie 2000), analyzing the

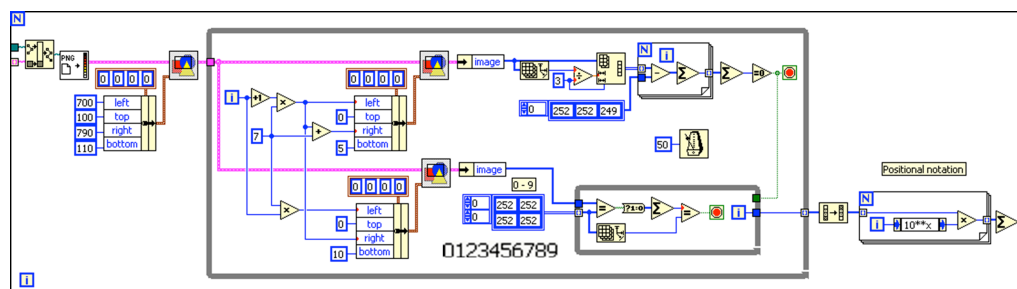


FIG. 5. Marker counts character recognition diagram.

spectrum, and extracting the data from “report” files. In order to run Genie 2000 via LabVIEW, we used commands one can find in the “S561 Batch Tools Support” and “Genie 2000 Customization Tools” PDF manuals co-installed by default with the software. Fig. 5 shows the code to convert each text file (file with a TKA extension) to a native Genie 2000 format (FILECNVT command with a TOOLKIT qualifier). It should be noted that TKA files do not contain energy calibration information. In order to calibrate the newly converted file, one should transfer such data from another CNF file prepared in advance by using the MOVEDATA command with the ECAL and OVERWRITE qualifiers. Thus, a set of energy-calibrated CNF files can be prepared.

Spectrum analysis is accomplished using the code shown in Fig. 6. A peak search command is required with established qualifiers such as threshold and number of channels. The PEAK_STD command performs an unidentified second difference peak locate followed by a pure

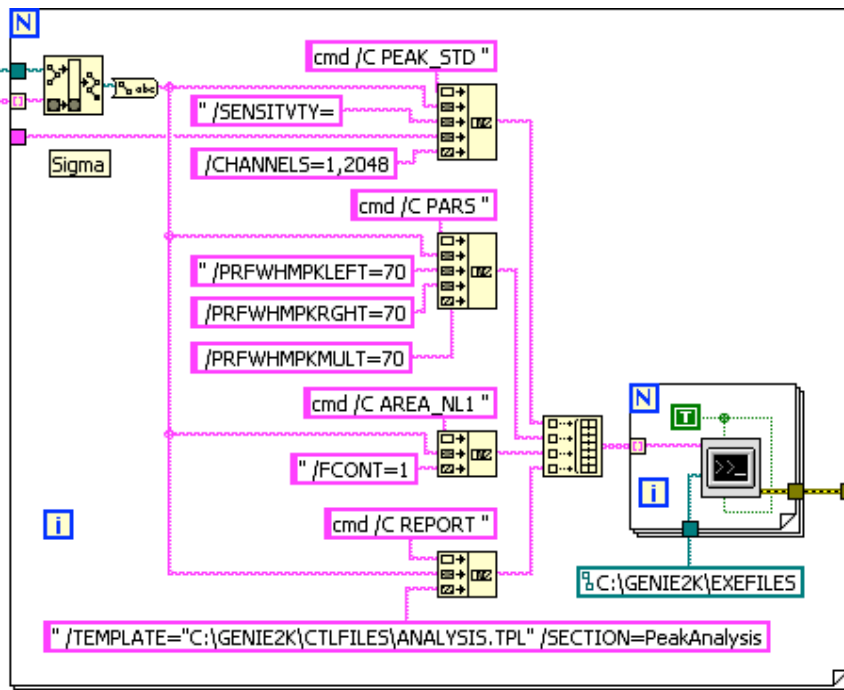


FIG. 6. Genie 2000 spectra analysis code.

gaussian peak fit phase of analysis on the specified datasource. The AREA_NL1 command is used to set the appropriate summation region, and the PARS command is used to modify the expected peak width to match the resolution of the detector. The Genie 2000 software has some analysis templates with access to a specific section. This is what has been used by the REPORT command and reference to a Peak Analysis section to save information generated to a report (RPT) file.

Genie 2000 produces one RPT file per spectrum, so the next step is to extract the data

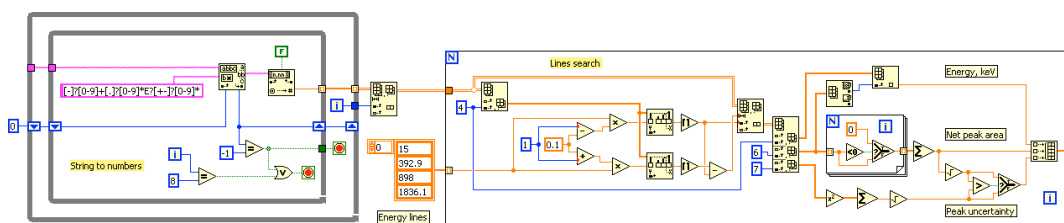


FIG. 7. Diagram to search for peaks of interest in Genie 2000 report files.

about the peaks of interest from all of the report files and combine these data together. The “Read From Spreadsheet File” virtual instrument can be easily used to open up report files if their extensions were previously changed from RPT to TXT. The report file contains a table, and the proper rows must be selected in order to keep track of the net peak area and associated uncertainty. Fig. 7 shows how report files can be treated in LabVIEW. The Match Pattern function with a corresponding regular expression has been used to create an array of numbers. Then, the search for energy lines of interest is performed using a For Loop. Genie 2000 works better with relatively small FWHM peaks, but the Wizard² peaks are very wide. To make the analysis procedure suitable for NaI detector data, a very small threshold for the peak search has been applied at a level of 0.5σ . This results in a large number of peaks, and summation of those that are close in energy to the known gamma-ray energy is required. A limit of 10% deviation from the known energy was chosen.

4. RESULTS AND DISCUSSION

Fig. 8 shows the spectrum extracted from the screenshot in Fig. 1, and qualitatively the two agree very well. In order to be sure that both methods (default and LabVIEW-based) give similar results, the Wizard² standard output file data (sum of counts in the desired range of channels) were compared to the results from the LabVIEW code. Table I gives the measurement time, ⁸⁸Zr gross peak area, and associated uncertainties obtained by each method. One can see that gross area values are close to each other. Despite the fact that all the corrections and background subtraction in the Wizard² software were disabled, the corresponding gross peak area number is not an integer, which suggests that some internal corrections were done. An interesting observation is that the relative uncertainties are significantly different; the Wizard² software overestimates the uncertainty by a factor of $t^{1/2}$, where t is the duration of the measurement in minutes. The statistical uncertainty in the net number of counts is

$$r = \frac{\sqrt{N}}{N} \cdot 100\% \quad (1)$$

where r is the relative uncertainty and N is the number of counts.

Table I. ⁸⁸Zr 392.87 keV gross peak area analysis.

Data source	Measurement Time (sec)	Gross Peak Area (counts)	Relative Uncertainty (%)
Wizard ²	21599.89	50532.26	8.44
LabVIEW	21600.00	50536.30	0.44

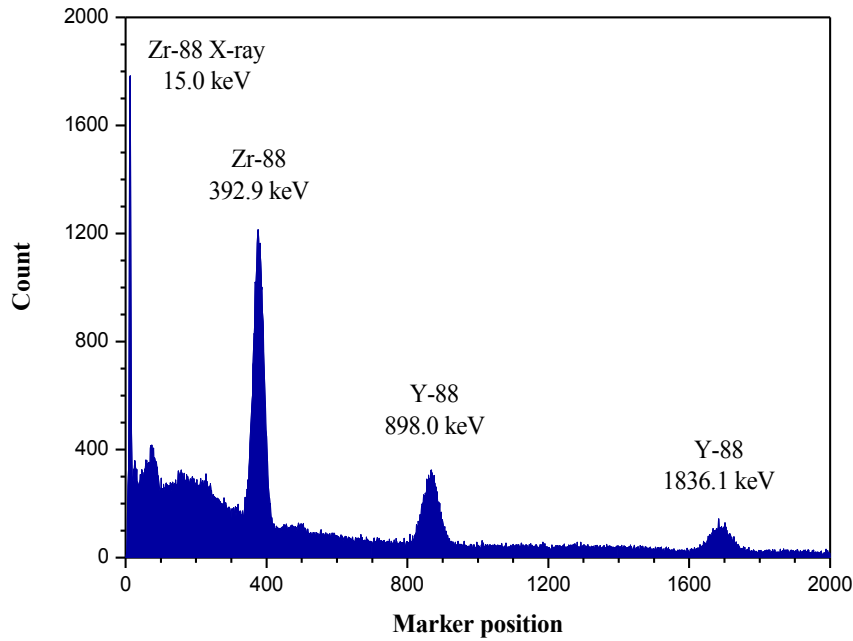


FIG. 8. Reconstituted spectrum from the Wizard² based on Fig. 1.

A section of the Genie 2000 report file for the spectrum shown in Fig. 8 is presented in

Table II. Selected lines from the Genie 2000 report file with an energy near the 392.87-keV gamma-ray from ⁸⁸Zr. The spectrum is shown in Fig. 8.

Peak No.	Peak Centroid (channels)	Energy (keV)	Net Peak Area (counts)	Net Area Uncertainty (counts)	Continuum (counts)
24	321.41	334.91	2.63E+002	58.58	1.54E+003
25	341.51	355.53	7.15E+002	61.69	1.52E+003
26	377.88	392.78	1.28E+004	359.37	1.34E+003
27	384.64	399.69	1.19E+004	335.75	1.28E+003
28	392.12	407.34	8.88E+003	253.50	1.22E+003
29	403.77	419.25	3.21E+003	107.78	1.16E+003
30	411.84	427.49	1.10E+003	64.55	1.14E+003
31	423.01	438.90	1.45E+002	54.05	1.23E+003

Table II.

Peaks that can be attributed to the ⁸⁸Zr gamma-ray with energy of 392.87 keV [28] lie in the range from 353.6 to 432.2 keV (lines 25 – 30 in Table II). Summing the net peak area from these lines and dividing the result by the measurement time gives the output shown in Table III. Finally, Table III gives the count rates of the four main peaks from the spectrum shown in Fig. 1 after applying the analysis described above.

Table III. Analysis of the spectrum shown in Fig. 1. Literature data are taken from [28].

Isotope	Measured Energy (keV)	Literature Energy (keV)	Counts per second
Zr X-ray	14.46	14.958	0.653 ± 0.022
^{88}Zr	392.78	392.87	1.787 ± 0.026
^{88}Y	897.01	898.042	0.677 ± 0.011
	1835.39	1836.063	0.343 ± 0.011

5. CONCLUSION

A LabVIEW-based system has been developed to save data from the Wizard² automated gamma-ray detector to a text file, convert them to a Genie 2000 native format spectrum, and automatically analyze that spectrum. LabVIEW was used to control a computer mouse and Print Screen button activity to move the Wizard² marker channel by channel and save a screenshot for each marker position. Optical character recognition was used on consecutive images in order to reconstitute the spectrum. Genie 2000 was chosen to work with spectra and a LabVIEW code helps with software communication and automated information extraction. This provides experimentalists significant flexibility in terms of independently analyzing the available data.

- [1] K.H. Chung, H. Kim, J.M. Lim, Y.Y. Ji, G.S. Choi, and M.J. Kang, "Rapid determination of radiostrontium in milk using automated radionuclides separator and liquid scintillation counter," *Journal of Radioanalytical and Nuclear Chemistry*, vol. **304**, no. 1, pp. 293-300, April 2015.
- [2] R. Marques, F. Bernardoni, S. Pollack, and R. Helmy, "Development of an automated system for preparation of liquid scintillation counting samples for radiolabeled pharmaceuticals," *Journal of Labelled Compounds and Radiopharmaceuticals*, vol. **57**, no. 3, pp. 121-124, March 2014.
- [3] C.R. Johnson, D.H. Johnson, N. Hamashima, H.S. Yang, and E. Hendriks, "On the utility of spectral-maximum-based automated thread counting from X-radiographs of paintings on canvas," *Studies in Conservation*, vol. **56**, no. 2, pp. 104-114, February 2011.
- [4] V. Dvorak, T. Vasek, K. Broj, and P. Temml, "Multidetector scintillation detection unit for the measurement of ^{125}I in an automatic gamma counter," *Isotopenpraxis*, vol. **26**, no. 2, pp. 54-56, February 1990.
- [5] I.S. Anand and R. Benzing, "A simple automatic gamma counter based upon the IAEA radioimmunoassay instrument," *Applied Radiation and Isotopes*, vol. **40**, no. 1, pp. 89-90, February 1989.
- [6] M. Regener, "Automated gamma-counters," *Proc. of the Conf. Antibiotics and Chemotherapy*, vol. **26**, pp. 61-66, 1979.
- [7] V. Desnica and M. Schreiner, "A LabVIEW-controlled portable X-ray fluorescence spectrometer for the analysis of art objects," *X-Ray Spectrometry*, vol. **35**, no. 5, pp. 280-286, August 2006.

- [8] M.J. O'Hara, S.R. Burge, and J.W. Grate, "Automated radioanalytical system for the determination of ^{90}Sr in environmental water samples by ^{90}Y Cherenkov radiation counting," *Analytical Chemistry*, vol. **81**, no. 3, pp. 1228-1237, February 2009.
- [9] Berthold Technologies, www.berthold.com.
- [10] Hidex, www.hidex.com.
- [11] Laboratory Technologies Inc, www.labtechinc.com.
- [12] Long Island Scientific, www.liscientific.com.
- [13] PerkinElmer, www.perkinelmer.com.
- [14] PerkinElmer automatic gamma counters,
<http://www.perkinelmer.com/catalog/family/id/wizard2%20automatic%20gamma%20counter>
- [15] Zh. Ding, R. Zhang, and Z. Kan, "Quality and safety inspection of food and agricultural products by LabVIEW IMAQ vision," *Food Analytical Methods*, vol. **8**, no. 2, pp. 290-301, February 2015.
- [16] B. Lin, L. Xiaofeng, and H. Xingxi, "Measurement system for wind turbines noises assessment based on LabVIEW," *Measurement*, vol. **44**, no. 2, pp. 445-453, February 2011.
- [17] S. Mu, D. Chen, H. Tang, J. Yang, and M. Huang, "Spectrum measurement network based on Labview," *Applied Mechanics and Materials*, vol. **239-240**, pp. 1356-1359, December 2012.
- [18] P. Novak, J. Navarik, J. Pechousek, V. Prochazka, L. Machala, and J. Tucek, "Development of fast pulse processing algorithm for nuclear detectors and its utilization in LabVIEW-based Mössbauer spectrometer," *Journal of Instrumentation*, vol. **9**, pp. T01001, January 2014.
- [19] N.C. Sahoo, A.S. Satpathy, N.K. Koshore, and B. Venkatesh, "D.C. motor-based wind turbine emulator using LabVIEW for wind energy conversion system laboratory setup," *International Journal of Electrical Engineering Education*, vol. **50**, no. 2, pp. 111-126, April 2013.
- [20] S.K. Singla and R.K. Yadav, "Optical character recognition based speech synthesis system using LabVIEW," *Journal of Applied Research and Technology*, vol. **12**, no. 5, pp. 919-926, October 2014.
- [21] P. Wrobel *et al.*, "LabVIEW control software for scanning micro-beam X-ray fluorescence spectrometer," *Talanta*, vol. **93**, pp. 186-192, May 2012.
- [22] F. Yuan, Y.Z. Li, and L.Y. Xie, "Design of gamma energy spectrometer based on the technology of LabVIEW and Bluetooth," *Advanced Material Research*, vol. 113-116, pp. 720-724, June 2010.
- [23] Canberra, Genie 2000 software,
http://www.canberra.com/products/radiochemistry_lab/genie-2000-software.asp.
- [24] PerkinElmer, 2480 WIZARD², <http://www.perkinelmer.com/catalog/product/id/2480-0010>.
- [25] National Instruments, *Programmatically acquiring a screenshot in a LabVIEW executable*,
<http://digital.ni.com/public.nsf/allkb/5AFA0CA7D031B05086257CC300430C28>.
- [26] National Instruments, *How can I programmatically simulate a mouse click?*
<http://digital.ni.com/public.nsf/allkb/0CC5602FE23E86DA86257350004E1B6A>.
- [27] D.E. Knuth, *The art of computer programming*, Addison-Wesley, Reading, 1985.
- [28] NNDC, Chart of the nuclides: basic properties of atomic nuclei, <http://www.nndc.bnl.gov>.

Shape discrimination of digitized pulses

V. Horvat, L. Chen, and J.C. Hardy

A data-acquisition system – both hardware and software – based on digital sampling of the pulses originating from a proportional counter has been developed for our high-precision measurements of nuclear beta decay. To eliminate the contributions from spurious pulses, a method for off-line shape discrimination of the pulses has been developed as well. This method was found to produce satisfactory results when applied to the data obtained in the proportional-counter plateau measurements and to the data obtained in the measurements of the ^{26m}Al half-life [1].

Here we report on our progress in the development of a different pulse-shape discrimination method, designed to be more intuitive, less sensitive to the conditions of the detector and the associated pulse-processing electronic equipment, and easier to apply. Upon completion of the project, the two methods will be compared in terms of their effectiveness and speed.

Various aspects of the new method are illustrated here by graphs. However, since the method is iterative in nature and has many variations and possible refinements that can yield similar results, the graphs shown should be regarded only as qualitative examples, not necessarily associated with any particular iteration, variation, refinement, or data set.

The new method begins with determination of an average pulse shape (APS) for the particular conditions of the proportional counter and the associated electronics. Initially, we do this by calculating the mean value for each sampling point, one-by-one, using all available pulses. With typically only a few percent of the pulses being spurious in nature [1], the average pulse shape obtained this way is expected to closely resemble that associated with a true beta-decay event.

Normally, each pulse is sampled by our wave-form digitizer (WFD) at the rate of one sample per nanosecond, for a period of 200 ns, starting 20 ns before the pulse exceeds the set threshold of 120 mV. The values measured at each sampling point are expressed as integers ranging from -127 to 127, corresponding to the range of -1 V to 1 V. An average pulse shape looks similar to that shown in Fig. 1 by the red line.

The next step in the method includes normalization of all pulse shapes, including that of the average pulse, to the same sum S of their respective sampling-point values s_i ($i = 1, 2, \dots, i_{\max}$), where initially i_{\max} is set to 200. This is followed by pulse shape "integration", in which the value of a sampling point s_i is replaced by the partial sum S_i of sampling point values from 1 to i . We set $S = 1$, so that $S_{i_{\max}} = 1$ as well. It should be noted that normalization to $S = 1$ is not possible for a very small fraction of the pulses for which the sum of sampling-point values is zero.

Finally, the "integrated" shapes of measured pulses are compared to that of the average pulse by calculating the root-mean-square deviation $D_{\text{rms}} = [\sum (S_i - S_i^{\text{av}})^2]^{1/2} / (i_{\max})^{1/2}$. A typical histogram of the D_{rms} values thus obtained looks similar to the one shown in Fig. 2. It features two distinct peaks. The

large peak, at low D_{rms} values, is due to true beta-decay events, while the small peak, at high D_{rms} values is due to pulses that do not resemble the shape of the average pulse very well and most

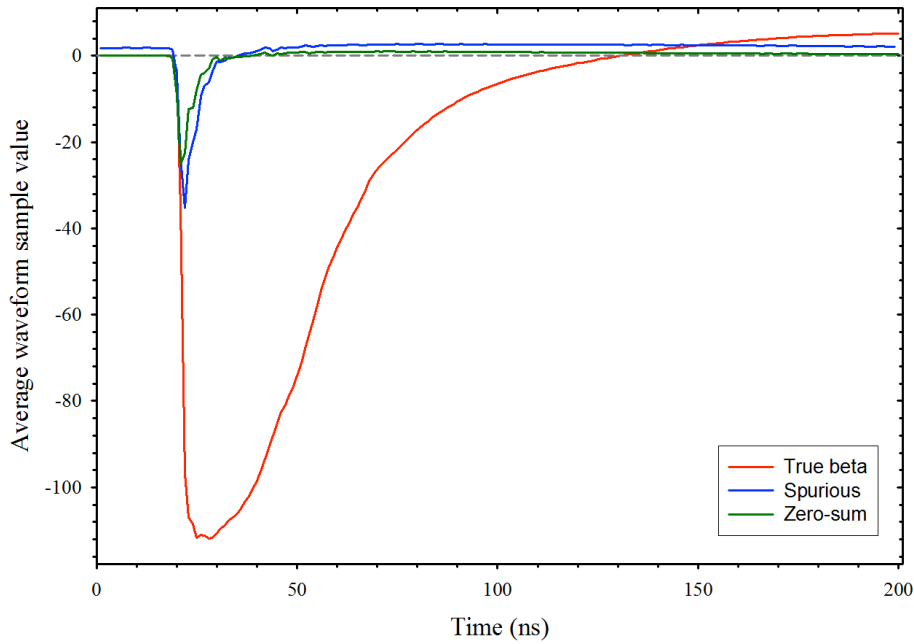


FIG. 1. Average shapes of the pulses originating from true beta-decay events (red line), spurious events (blue line), and pulses having the sum of their sample values equal to zero (green line).

likely are spurious

in nature. Since the two peaks are very well separated from each other, we conclude that the method reported here has very good selectivity.

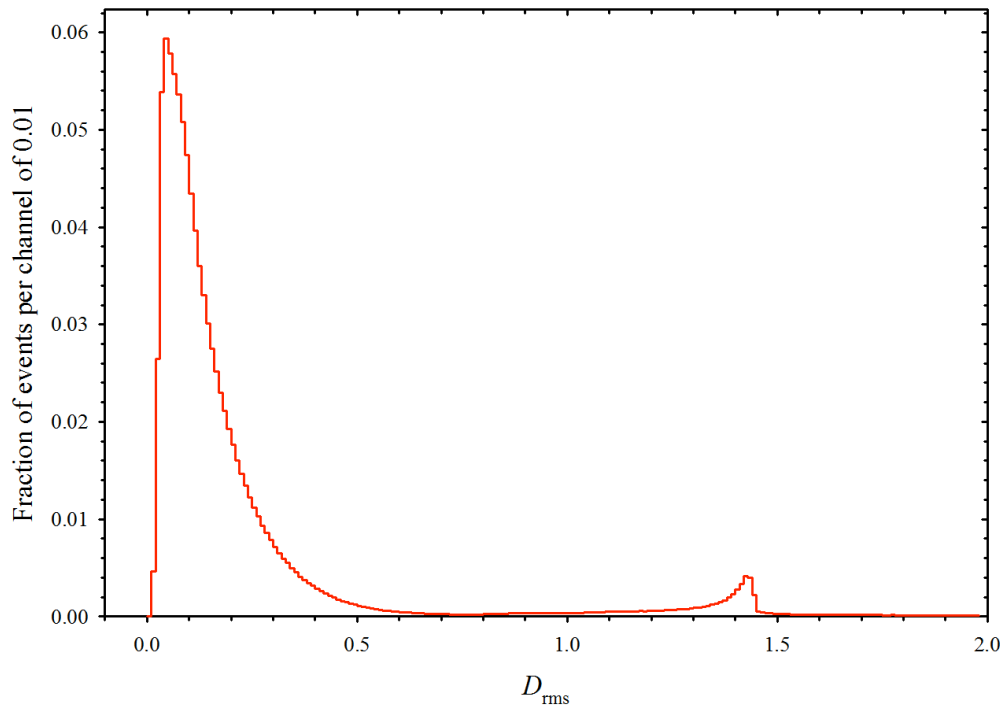


FIG. 2. Histogram of the root-mean-square deviation values from the comparison of the "integrated" individual pulses and the "integrated" average of the true beta-decay event pulses.

We can accomplish a further refinement of the method by using the histogram of D_{rms} values to select only the events contributing to the larger peak, and then use only their pulse shapes to determine a new APS, which leads to a refined histogram of D_{rms} values. The process can be repeated until it is determined that further iterations will not change the resulting histogram of D_{rms} values. Typically, only a few iterations are needed to accomplish this.

By using the final histogram of D_{rms} values to select the events contributing to the smaller peak we can determine the average of their pulse shapes, representing the typical shape of a spurious pulse. A typical result is shown in Figure 1 by the blue line. The green line in Figure 1 shows the average shape of the pulses whose sum of sampling-point values is equal to zero. Obviously, the shape of this average pulse is much closer to that of the average spurious pulse than it is to the average shape of true beta-decay pulses; therefore they should be treated as

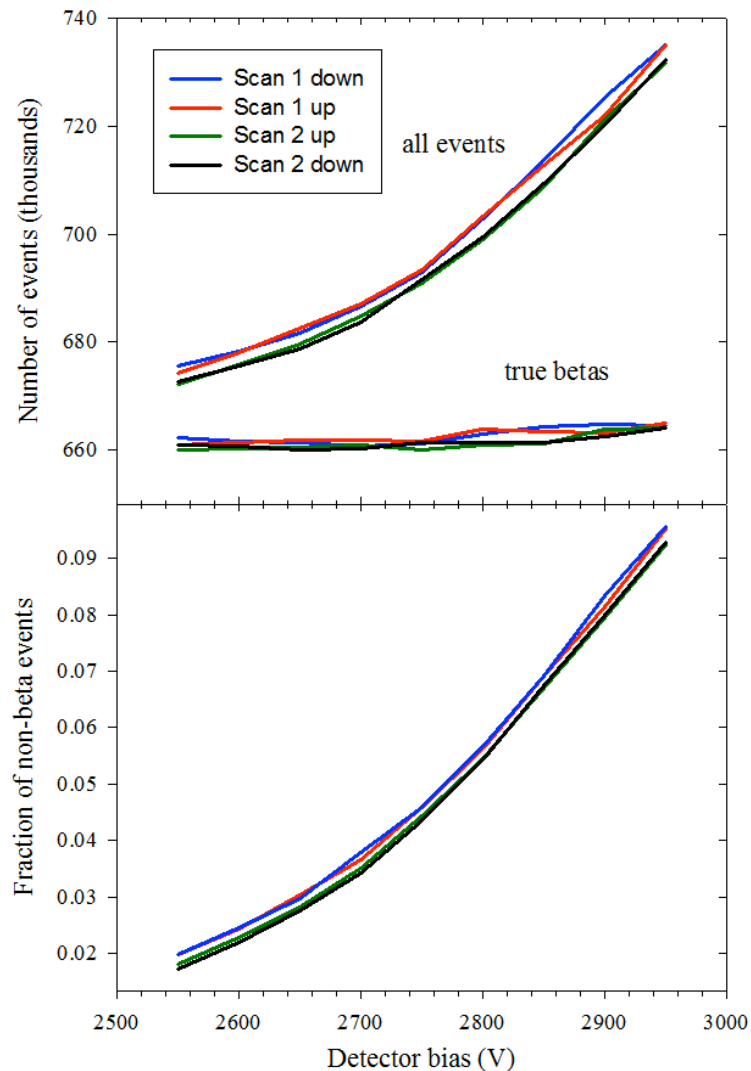


FIG. 3. Results of the proportional-counter plateau measurements (top) and the fraction if events that were determined not to originate from beta decay as a function of detector bias (bottom).

spurious.

Another refinement of the method can be applied based on the length of the APS, as shown by the red line in Fig. 1. Evidently, a typical beta-decay pulse returns to the baseline within the first 130 ns. Therefore, a better approach would be to use only the first 130 sampling points to determine the APS, i.e. to set i_{\max} to 130, rather than 200.

The APS was found to have negligible dependence on the counting rate. Also, it was found that the APS depends very little on the detector bias. The most notable feature is the increase of the fraction of spurious pulses as the detector bias increases (see Fig. 3). Consequently, elimination of spurious pulses significantly improves the plateau measured for the detector.

[1] L. Chen, J.C. Hardy, M. Bencomo, V. Horvat, N. Nica, and H.I. Park, Nucl. Instrum. Methods Phys. Res. **A728**, 81 (2013).

Tests on digital system for precise half-life measurement of ^{42}Ti

H.I. Park, L. Chen, and J.C. Hardy

Last year, we reported a successful test measurement of the half-life of ^{42}Ti [1]. Our results showed that we would be able to produce approximately 2000 particles/s of ^{42}Ti with 300 nA of primary ^{40}Ca beam at 32.4-MeV via the $^4\text{He}(^{40}\text{Ca}, 2n)^{42}\text{Ti}$ reaction. We also learned that quite pure ^{42}Ti samples could be obtained by setting tight extraction slits on the MARS recoil spectrometer and depositing ^{42}Ti samples near the back of the collection tape so that most produced impurities passed through the tape without stopping. For this test measurement, we used our digital data-acquisition system [2], which has prompted us to test this system more thoroughly and compare it with our standard analog system.

The first step was to verify the timing accuracy of our high-speed digitizer – a National Instruments PCI 5154 – in which the sample clock is set to 1 GS/s. We digitized sine and square waves generated from the Stanford Research Systems DS345 function generator [3] at 1 and 10 MHz respectively; and measured the frequency of these waveforms as a function of device temperature as read by the onboard sensor. The accuracy of the digitizer timebase was well within specs and sufficient for half-life measurements to 0.01% precision.

Our digital system was then connected to the gas proportional counter and used to measure the counts obtained from a 3.77-kBq $^{90}\text{Sr}/^{90}\text{Y}$ beta source as a function of the applied detector bias, from 2250 V to 2950 V in 50-V increments. Detector signals were processed through two cascaded fast amplification stages, the first a fast timing preamplifier, ORTEC VT-120A, and the second a SR445A amplifier from Stanford Research Systems. In the measurement we used the pre-triggered acquisition, with start and reference triggers. The start trigger, which the digitizer monitors for an acquisition arm-trigger, was specified as “immediate” and the recorded data consisted of a pre-defined number of pre-trigger and post-trigger samples relative to the reference trigger, which was an analog signal that passed the threshold level of 120 mV. The number of pre-trigger samples was set to 10% of the 200-ns recorded length. This configuration of our digitizer was identical to that used for the on-line test measurement of ^{42}Ti . The dead time of the system was 800 ns, dominated by the re-arming time of the digitizer.

Finally, for comparison, we repeated the $^{90}\text{Sr}/^{90}\text{Y}$ source measurement with our standard analog electronics. Signals from the detector were fed into a preamplifier followed by a fast timing amplifier (set to a gain of 500), a discriminator, a gate-and-delay generator (to impose a dominant dead-time) and a multichannel scalar. A 6- μs dominant dead time was imposed for measurements that we made with two different thresholds of 150 mV and 250 mV, respectively.

Fig. 1(a) displays the total number of counts recorded from the $^{90}\text{Sr}/^{90}\text{Y}$ β source as a function of detector bias between 2250 V and 2950 V, while the corresponding relative changes in slope per 100 V are plotted in Fig. 1b.. It is evident from the figure that fine discrimination between real beta events and spurious pulses for the digital system is critical to establishing a wide, flat plateau region, in which count rate is nearly independent of bias. A software filter that has already been developed for this purpose based on the pulse width and amplitude variability

offers rather good separation [2], but there is still room for further improvements. An independent approach to design an alternative filter is described elsewhere in this report [4].

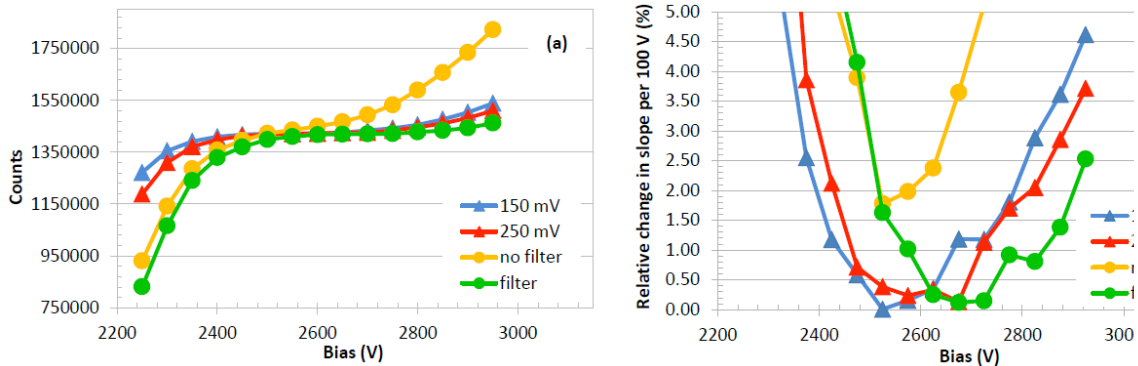


FIG. 1. (a) A total number of counts from the $^{90}\text{Sr}/^{90}\text{Y}$ β source were measured as a function of detector bias with digital and analog system. The points labeled with 150 mV and 250 mV correspond to the analog system; the other two sets of points refer to the filtered and unfiltered digital data. The count time for each data point was 300 seconds. (b) Relative change in slope per 100 V was calculated in % to define the plateau of our gas proportional counter.

Direct comparison of the flat plateau regions established by our two systems leads us to the conclusion that the gain of the digital system is likely insufficient for small but legitimate signals to be detected at lower bias voltages. Currently, we are evaluating the change in the plateau with different reference trigger thresholds in the digital system and applying those different threshold settings to the ^{42}Ti half-life analysis to see if the result shows any dependence on this threshold. The outcome from this test will guide us in improving the digital system.

- [1] H.I. Park *et al.*, *Progress in Research*, Cyclotron Institute, Texas A&M University (2013-2014), p. I-23.
- [2] L. Chen *et al.*, *Nucl, Instrum. Methods Phys. Res.* **A728**, 81 (2013).
- [3] SRS DS345 Function Generator: www.thinksrs.com/products/DS345.htm
- [4] V. Horvat *et al.*, *Progress in Research*, Cyclotron Institute, Texas A&M University (2014-2015), p. IV-75.

SECTION V
PUBLICATIONS

PAPERS PUBLISHED
April 1, 2014 – March 31, 2015

Determination of the asymptotic normalization coefficients for $^{14}\text{C} + n \leftrightarrow ^{15}\text{C}$, the $^{14}\text{C}(n,\gamma)^{15}\text{C}$ reaction rate, and evaluation of a new method to determine spectroscopic factors, M. McCleskey, A.M. Mukhamedzhanov, L. Trache, R.E. Tribble, A. Banu, V. Eremenko, V.Z. Goldberg, Y.-W. Lui, E. McCleskey, B.T. Roeder, A. Spiridon, F. Carstoiu, V. Burjan, Z. Hon, and I.J. Thompson, Phys. Rev. C **89**, 044605 (2014).

Peripheral elastic and inelastic scattering of $^{17,18}\text{O}$ on light targets at 12 MeV/nucleon, T. Al-Abdullah, F. Carstoiu, C.A. Gagliardi, G. Tabacaru, L. Trache, and R.E. Tribble, Phys. Rev. C. **89**, 064602 (2014).

Indirect techniques for nuclear astrophysics, R.E. Tribble, C.A. Bertulani, M. La Cognata, A.M. Mukhamedzhanov, and C. Spitaleri, Rep. Prog. Phys. **77**, 106901 (2014).

Further test of internal-conversion theory with a measurement in ^{119}Sn , N. Nica, J.C. Hardy, and V.E. Jacob, Nucl. Data Sheets **120**, 91 (2014).

The measurement and interpretation of superallowed $0^+ \rightarrow 0^+$ nuclear β decay, J.C. Hardy and I.S. Towner, J. Phys. G **41**, 114004 (2014).

The β decay of ^{38}Ca : sensitive test of isospin symmetry-breaking corrections from mirror superallowed $0^+ \rightarrow 0^+$ transitions, H.I. Park, J.C. Hardy, V.E. Jacob, M. Bencomo, L. Chen, V. Horvat, N. Nica, B.T. Roeder, E. Simmons, R.E. Tribble, and I.S. Towner, J. Phys. Soc J. (submitted).

Superallowed $0^+ \rightarrow 0^+$ nuclear β decays: 2014 critical survey, with precise results for V_{ud} and CKM unitarity, J.C. Hardy and I.S. Towner, Phys. Rev. C **91**, 025501 (2015).

Parameterization of the statistical rate function for select superallowed transitions, I.S. Towner and J.C. Hardy, Phys. Rev. C **91**, 015501 (2015).

Comment on “Atomic mass compilation 2012”, B. Pfeiffer, K. Venkataramaniah, U. Czok, C. Scheidenberger, G. Audi, K. Blaum, M. Block, G. Bollen, S. Goriely, J.C. Hardy, F. Herfurth, F.G. Kondev, H.-J. Kluge, D. Lunney, J.M. Pearson, G. Savard, K. Sharma, M. Wang, and Y.H. Zhang, At. Data Nucl. Data Tables **103-104**, 1 (2015).

Testing CVC and CKM unitarity via superallowed nuclear beta decay, J.C. Hardy, I.S. Towner, H.I. Park, V.E. Jacob, L. Chen, V. Horvat, N. Nica, and M. Bencomo, Eur. Phys. J. Web of Conferences **93**, 01001 (2015).

Precision half-life measurement of the β^+ decay of ^{37}K , P.D. Shidling, D. Melconian, S. Behling, B. Fenker, J.C. Hardy, V.E. Jacob, E. McCleskey, M. McCleskey, M. Mehlman, H.I. Park, and B.T. Roeder, Phys. Rev. C **90**, 032501(R) (2014).

Progress towards precision measurements of beta-decay correlation parameters using atom and ion traps, D. Melconian, R.S. Behling, B. Fenker, *et al.*, The Xth Latin American Symposium on Nuclear Physics and Applications (LASNPA), Proceedings of Science X LASNPA, 010 (2014); [arXiv:1408.1648](https://arxiv.org/abs/1408.1648).

Measurement of the half-life of the T=1/2 mirror decay of ^{19}Ne and its implications on physics beyond the standard model, L.J. Broussard, H.O. Back, M.S. Boswell, A.S. Crowell, P. Dendooven, G.S. Giri, C.R. Howell, M.F. Kidd, K. Jungmann, W.L. Kruithof, A. Mol, C.J.G. Onderwater, R.W. Pattie, Jr., P.D. Shidling, M. Sohani, D.J. van der Hoek, A. Rogachevskiy, E. Traykov, O.O. Versolato, L. Willmann, H.W. Wilschut, and A.R. Young, Phys. Rev. Lett. **112**, 212301 (2014).

Photoneutron cross sections for samarium isotopes: Toward a unified understanding of (γ, n) and (n, γ) reactions in the rare earth region, D.M. Filipescu, I. Gheorghe, H. Utsunomiya, S. Goriely, T. Renstrøm, H.-T. Nyhus, O. Tesileanu, T. Glodariu, T. Shima, K. Takahisa, S. Miyamoto, Y.-W. Lui, S. Hilaire, S. Péru, M. Martini, and A.J. Koning, Phys. Rev. C **90**, 064616 (2014).

Photoneutron cross sections for neodymium isotopes: Toward a unified understanding of (γ, n) and (n, γ) reactions in the rare earth region, H.-T. Nyhus, T. Renstrøm, H. Utsunomiya, S. Goriely, D.M. Filipescu, I. Gheorghe, O. Tesileanu, T. Glodariu, T. Shima, K. Takahisa, S. Miyamoto, Y.-W. Lui, S. Hilaire, S. Péru, M. Martini, L. Siess, and A.J. Koning, Phys. Rev. C **91**, 015808 (2015).

Energy calibration of the NewSUBARU storage ring for laser Compton-scattering gamma rays and applications, Hiroaki Utsunomiya, Tatsushi Shima, Keiji Takahisa, Dan Mihai Filipescu, Ovidiu Tesileanu, Ioana Gheorghe, Hilde-Therese Nyhus, Therese Renstrøm, Yiu-Wing Lui, Yasuhisa Kitagawa, Sho Amano, and Shuji Miyamoto, IEEE transactions on nuclear science **61**, 1252 (2014).

TRINAT: Measuring β -decay correlations with laser-trapped atoms, J.A. Behr, A. Gorelov, K.P. Jackson, *et al.*, ISAC and ARIEL: The TRIUMF Radioactive Beam Facilities and the Scientific Program, Hyperfine Interactions **225**, 115 (2014).

α -cluster asymptotic normalization coefficients for nuclear astrophysics, M.L. Avila, G.V. Rogachev, E. Koshchiy, L.T. Baby, J. Belarge, K.W. Kemper, A.N. Kuchera, and D. Santiago-Gonzalez. Phys. Rev. C **90**, 042801(R) (2014).

Alpha-cluster structure of ^{18}O , M.L. Avila, G.V. Rogachev, V.Z. Goldberg, E.D. Johnson, K.W. Kemper, Yu.M. Tchuvil'sky, and A.S. Volya, Phys. Rev. C **90**, 024327 (2014).

Near- and sub-barrier fusion of the ${}^7\text{Be}+{}^{58}\text{Ni}$ system, E. Martinez-Quiroz, E.F. Aquilera, D. Lizcano, P. Amador-Valenzuela, H. Garcia-Martinez, J.J. Kolata, A. Roberts, L.O. Lamm, G. Rogachev, V. Guimaraes, F.D. Becchetti, A. Villano, M. Ojaruega, M. Febraro, Y. Chen, H. Jiang, P.A. DeYoung, and G.F. Peaslee, Phys. Rev. C **90**, 014616 (2014).

Study of the excitation function for the ${}^{13}\text{C}+{}^4\text{He}$ elastic scattering with the thicktarget inverse kinematics method, N.A. Mynbayev, A.K. Nurmukhanbetova, V.Z. Goldberg, M.S. Golovkov, G.V. Rogachev, V.N. Dzyubin, M.V. Koloberdin, I.A. Ivanov, and R.E. Tribble, J. Exp. and Theor. Phys. **119**, 663 (2014).

Constraining the 6.05 MeV 0^+ and 6.13 MeV 3^- cascade transitions in the ${}^{12}\text{C}(\alpha,\gamma){}^{16}\text{O}$ reaction using the asymptotic normalization coefficients, M.L. Avila, G.V. Rogachev, E. Koshchiy, L.T. Baby, J. Belarge, K.W. Kemper, A.N. Kuchera, A.M. Mukhamedzhanov, D. Santiago-Gonzalez, and E. Uberseder, Phys. Rev. Lett. (Accepted 2014).

Clustering in non-self-conjugate nuclei ${}^{10}\text{Be}$ and ${}^{18}\text{O}$, G.V. Rogachev, M.L. Avila, A.N. Kuchera, L.T. Baby, J. Belarge, J. Blackmon, V.Z. Goldberg, E.D. Johnson, K.W. Kemper, E. Koshchiy, L. Linhardt, K. Macon, D. Santiago-Gonzalez, and I. Wiedenhoever, J. Phys.: Conf. Series **569**, 012004 (2014).

Test of modern theoretical approaches using modern experimental methods, V.Z. Goldberg, G.V. Rogachev, and R.E. Tribble, 33rd Mazurian Lakes Conference on Physics Proceedings, Acta Phys. Pol. B **45**, 309 (2014)

Studies of exotic nuclei at the RESOLUT facility of Florida State University, I. Wiedenhoever, L.T. Baby, D. Santiago-Gonzalez, A. Rojas, J.C. Blackmon, G.V. Rogachev, J. Blarge, E. Koshchiy, A.N. Kuchera, L.E. Linhardt, J. Lail, K.T. Macon, M. Matos, and B.C. Rascol, 5th Int. Conf. on Fission and Properties of Neutron-Rich Nuclei (ICFN5) Proceedings, 144 (2014).

New beta-delayed neutron measurements in the light-mass fission group, J. Agramunt, A.R. Garcia, A. Algora, J. Aysto, R. Caballero-Folch, F. Calvino, D. Cano-Ott, G. Cortes, C. Domingo-Pardo, T. Eronen, W. Gelletly, M.B. Gomez-Hornillos, J. Hakala, A. Jokinen, D. Jordan, A. Kankainen, V. Kolkinen, T. Martinez, P.J. Mason, I. Moore, H. Penttila, Z. Podolyak, M. Reponen, A. Riego, J. Rissanen, B. Rubio, A. Saastamoinen, J.L. Tain, and E. Valencia, Nucl. Data Sheets **120**, 74 (2014).

Measurement of the Am-240(n, f) cross section using the surrogate-ratio method, R.J. Casperson, J.T. Burke, N.D. Scielzo, J.E. Escher, E. McCleskey, M. McCleskey, A. Saastamoinen, A. Spiridon, A. Ratkiewicz, A. Blanc, M. Kurokawa, and R.G. Pizzone, Phys. Rev. C **90**, 034601 (2014).

Study of proton and He-3 induced reactions on U-235 at low energies, E. Gromova, V. Jakovlev, J. Aaltonen, K. Helariutta, S. Salminen-Paatero, J. Bergman, S.J. Heselius, H. Penttila, J. Rissanen, and A. Saastamoinen, Nucl. Data Sheets **119**, 237 (2014).

Coulomb displacement energies as a probe for nucleon pairing in the f(7/2) shell, A. Kankainen, T. Eronen, D. Gorelov, J. Hakala, A. Jokinen, V.S. Kolhinen, M. Reponen, J. Rissanen, A. Saastamoinen, V. Sonnenschein, and J. Aysto, Phys. Rev. C **89**, 051302 (2014).

Multiparticle emission in the decay of Ar-31, G.T. Koldste, B. Blank, M.J.G. Borge, J.A. Briz, M. Carmona-Gallardo, L.M. Fraile, H.O.U. Fynbo, J. Giovinazzo, B.D. Grann, J.G. Johansen, A. Jokinen, B. Jonson, T. Kurturkian-Nieto, J.H. Kusk, T. Nilsson, A. Perea, V. Pseudo, E. Picado, K. Riisager, A. Saastamoinen, O. Tengblad, J.C. Thomas, and J. Van de Walle, Phys. Rev. C **89**, 064315 (2014).

Sizeable beta-strength in Ar-31 (beta 3p) decay, G.T. Koldste, B. Blank, M.J.G. Borge, J.A. Briz, M. Carmona-Gallardo, L.M. Fraile, H. O.U. Fynbo, J. Giovinazzo, J.G. Johansen, A. Jokinen, B. Jonson, T. Kurturkian-Nieto, T. Nilsson, A. Perea, V. Pseudo, E. Picado, K. Riisager, A. Saastamoinen, O. Tengblad, J.C. Thomas, and J. Van de Walle, Phys. Lett. B **737**, 383(2014).

Transition from collectivity to single-particle degrees of freedom from magnetic moment measurements on Sr-82(38)44 and Sr-90(38)52, G.J. Kumbartzki, N. Benczer-Koller, S. Burcher, A. Ratkiewicz, S.L. Rice, Y.Y. Sharon, L. Zamick, K.H. Speidel, D.A. Torres, K. Sieja, M. McCleskey, A. Cudd, M. Henry, A. Saastamoinen, M. Slater, A. Spiridon, S. Yu Torilov, V.I. Zherebchevsky, G. Guerdal, S.J.Q. Robinson, S.D. Pain, and J.T. Burke, Phys. Rev. C **89**, 064305 (2014).

Improved measurement of the half-life of the J(pi)=8(-) nuclear isomer Eu-152m2, P. Humby, A. Simon, C.W. Beausang, T.J. Ross, R.O. Hughes, J.T. Burke, R.J. Casperson, J. Koglin, S. Ota, J.M. Allmond, M. McCleskey, E. McCleskey, A. Saastamoinen, R. Chyzh, M. Dag, K. Gell, T. Tarlow, and G. Vyas, Physical Review C **91**, 024322 (2015).

Measurement of the $^{13}\text{C}(\alpha, n)^{16}\text{O}$ reaction at astrophysical energies using the Trojan Horse Method focus on the -3 keV sub-threshold resonance, M. La Cognata, C. Spitaleri, O. Tripella, G.G. Kiss, G.V. Rogachev, A.M. Mukhamedzhanov, M. Avila, G.L. Guardo, E. Koshchiy, A. Kuchera, L. Lamia, S.M.R. Puglia, S. Romano, D. Santiago, and R. Sparta, International Nuclear Physics Conference (INPC-2013) Proceeding, Vol. 2, EPJ Web of Conferences **66**, 07010 (2014).

Measurement of the $^{13}\text{C}(\alpha, n)^{16}\text{O}$ reaction at astrophysical energies using the Trojan Horse Method. focus on the -3 keV sub-threshold resonance, M. La Cognata, C. Spitaleri, O. Tripella, G.G. Kiss, G.V. Rogachev, A.M. Mukhamedzhanov, M. Avila, G.L. Guardo, E. Koshchiy, A. Kuchera, L. Lamia, S.M.R. Puglia, S. Romano, D. Santiago, and R. Sparta, Origin of Matter and Evolution of Galaxies 2013 Proceedings, AIP Conference Proceedings **1594**, 206 (2014).

Constraining the 6.05 MeV 0^+ and 6.13 MeV 3^- cascade transitions in the $^{12}\text{C}(\alpha, \gamma)^{16}\text{O}$ reaction using the asymptotic normalization coefficients, M.L. Avila, G.V. Rogachev, E. Koshchiy, L.T. Baby, J. Belarge, K.W. Kemper, A.N. Kuchera, A.M. Mukhamedzhanov, D. Santiago-Gonzalez, and E. Uberseder, Phys. Rev. Lett. **114**, 071101 (2015).

Production cross sections of elements near the $N = 126$ shell in ^{48}Ca -induced reactions with ^{154}Gd , ^{159}Tb , ^{162}Dy , and ^{165}Ho targets, D.A. Mayorov *et al.*, Phys. Rev. C **90**, 024602 (2014).

Reconstructed primary fragments and symmetry energy, temperature, and density of the fragmenting source in $^{64}\text{Zn}+^{112}\text{Sn}$ at 40 MeV/nucleon, X. Liu, W. Lin, R. Wada *et al.*, Nucl. Phys. A**933**, 290 (2015).

Characterization of deuterium clusters mixed with helium gas for an application in beam-target-fusion experiments, W. Bang, H.J. Quevedo, A.C. Bernstein *et al.*, Phys. Rev. E **90**, 063109 (2014).

Experimental reconstruction of primary hot isotopes and characteristic properties of the fragmenting source in heavy-ion reactions near the Fermi energy, W. Lin, X. Liu, M.R.D. Rodrigues *et al.*, Phys. Rev. C **90**, 044603 (2014).

Exploring the alpha cluster structure of nuclei using the thick target inverse kinematics technique for multiple alpha decays, M. Barbui, K. Hagel, V.Z. Goldberg *et al.*, INPC 2013 - International Nuclear Physics Conference, EPJ Web of Conferences **66**, 03005 (2014).

Mass dependence of transverse flow in heavy ion collisions at intermediate energies, X. Liu, W. Lin, R. Wada *et al.*, Phys. Rev. C **90**, 014604 (2014).

Nucleation and cluster formation in low-density nucleonic matter: A mechanism for ternary fission, S. Wuenschel, H. Zheng, K. Hagel *et al.*, Phys. Rev. C **90**, 011601(R) (2014).

Primary isotope yields and characteristic properties of the fragmenting source in heavy-ion reactions near the Fermi energy, X. Liu, W. Lin, R. Wada *et al.*, Phys. Rev. C **90**, 014605 (2014).

Sifting through the remnants of heavy-ion collisions for observables sensitive to the nuclear equation of state, P. Cammarata, M. Colonna, A. Bonasera, A.B. McIntosh, Z. Kohley, L.W. May, M.B. Chapman, L.A. Heilborn, J. Mabila, A. Raphelt, A. Zarrella, and S.J. Yennello, Nucl. Instrum. Methods Phys. Res. **A761**, 1 (2014).

Coulomb corrections to the extraction of the density and temperature in non-relativistic heavy ion collisions, H. Zheng, G. Giuliani, and A. Bonasera, J. Phys. G **41**, 055109 (2014).

Coulomb corrections to experimental temperatures and densities in Fermi-energy heavy-ion collisions, J. Mabila, H. Zheng, A. Bonasera, P. Cammarata, K. Hagel, L. Heilborn, Z. Kohley, L.W. May, A.B. McIntosh, M.D. Youngs, A. Zarrella, and S.J. Yennello, Phys. Rev. C, **90**, 027602 (2014).

Isoscaling of heavy projectile residues and N/Z equilibration in peripheral heavy-ion collisions below the Fermi energy, G.A. Souliotis, P.N. Fountas, M. Veselsky, S. Galanopoulos, Z. Kohley, A. McIntosh, S.J. Yennello, and A. Bonasera, Phys. Rev. C, **90**, 064612 (2014).

Systematic study of neutron-rich rare isotope production in peripheral heavy-ion collisions below the Fermi energy, P.N. Fountas, G.A. Souliotis, M. Veselsky, and A. Bonasera, Phys. Rev. C, **90**, 064613 (2014).

Present capabilities and future plans of the Texas A&M Cyclotron Institute, S.J. Yennello, The VII International Symposium on EXOtic Nuclei (EXON- 2014) Conference Proceedings, 2014.

Study of the nuclear symmetry energy at $\rho \approx 2\rho_0$ with S π RIT-TPC, G. Jhang, R. Shane, A. McIntosh, T. Isobe, J. Barney, J. Estee, N. Nakatsuka, W. Powell, S. Tangwanchaoen, H. Baba, Z. Chajecki, M. Famiano, B. Hong, F. Lu, W.G. Lynch, T. Murakami, H. Sakurai, A. Taketani, M.B. Tsang, R. Wang, and S.J. Yennello, ARIS2014 Conference Proceedings, 2014.

Remarkable, delightful, awesome; it will change your life, not overnight, but over time, Mom the chemistry professor, R. Cole, C. Marzabadi, G. Webster, and K. Woznack (Eds.), Springer, 2014.

Density and temperature in heavy-ion collisions: A test of classical and quantum approaches, H. Zheng, G. Bonasera, J. Mabilia, P. Marini, and A. Bonasera, Eur. Phys. J. A **50**, 167 (2014).

Asymptotic normalization coefficients and spectroscopic factors from deuteron stripping reactions, D.Y. Pang and A.M. Mukhamedzhanov, Phys. Rev. C **90**, 044611 (2014).

Surface-integral formalism of deuteron stripping, A.M. Mukhamedzhanov, D.Y. Pang, C.A. Bertulani, and A.S. Kadyrov, Phys. Rev. C **90**, 034604 (2014).

Measurement of the 10 keV resonance in the $^{10}\text{B}(p,\alpha)^7\text{Be}$ reaction via the Trojan Horse method, C. Spitaleri, L. Lamia, S.M.R. Puglia, S. Romano, M. La Cognata, V. Crucilla, R.G. Pizzone, G.G. Rapisarda, M.L. Sergi, M. Gimenez Del Santo, N. Carlin, M.G. Munhoz, F.A. Souza, A. Szanto de Toledo, A. Tumino, B. Irgaziev, A.M. Mukhamedzhanov, G. Tabacaru, V. Burjan, V. Kroha, Z. Hons, J. Mrazek, S.-H. Zhou, C. Li, Q. Wen, Y. Wakabayashi, H. Yamaguchi, and E. Somorjai, Phys. Rev. C **90**, 035801 (2014).

Optical model potential of $A = 3$ projectiles for 1p-shell nuclei, D.Y. Pang, W.M. Dean, and A.M. Mukhamedzhanov, Phys. Rev. C **91**, 024611 (2015).

Trojan Horse particle invariance in fusion reactions, R.G. Pizzone, C. Spitaleri, C. Bertulani, A.M. Mukhamedzhanov, L. Blokhintsev, M. La Cognata, L. Lamia, R. Spartá, and A. Tumino, EPJ Web of Conferences **86**, 00034 (2015).

New determination of the ${}^2\text{H}(d,p){}^3\text{H}$ and ${}^2\text{H}(d,n){}^3\text{He}$ reaction rates at astrophysical energies, A. Tumino, R. Spartà, C. Spitaleri, A.M. Mukhamedzhanov, S. Typel, R.G. Pizzone, E. Tognelli, S. Degl'Innocenti, V. Burjan, V. Kroha, Z. Hons, M. La Cognata, L. Lamia, J. Mrazek, S. Piskor, P.G. Prada Moroni, G.G. Rapisarda, S. Romano, and M.L. Sergi, *Astrophys. J.* **785** 96 (2014); [doi:10.1088/0004-637X/785/2/96](https://doi.org/10.1088/0004-637X/785/2/96).

Big bang nucleosynthesis revisited via TROJAN HORSE method measurements, R.G. Pizzone, R. Spartà, C.A. Bertulani, C. Spitaleri, M. La Cognata, J. Lalmansingh, L. Lamia, A.M. Mukhamedzhanov, and A. Tumino, *Astrophys. J.* **786**, 112 (2014).

Low-energy R-matrix fit for the ${}^6\text{Li}(d,\alpha){}^4\text{He}$ S factor, J. Grineviciute, L. Lamia, A.M. Mukhamedzhanov, C. Spitaleri, and M. La Cognata, *Phys. Rev. C* **91**, 014601 (2015).

Heavy flavor at the large hadron collider in a strong coupling approach, M. He, R.J. Fries, and R. Rapp, *Phys. Lett. B* **735**, 445 (2014).

Jet-triggered photons from back-scattering kinematics for quark gluon plasma tomography, S. De, R.J. Fries, and D.K. Srivastava, *Phys. Rev. C* **90**, 034911 (2014).

Transverse flow of gluon fields in heavy ion collision, G. Chen and R.J. Fries, *J. Phys. Conf. Ser.* **535**, 012014 (2014).

Modifications of heavy-flavor spectra in $\sqrt{s_{NN}} = 62.4$ GeV Au-Au collisions, Min He, Rainer J. Fries, and Ralf Rapp, *Phys. Rev. C* **91**, 024904 (2015).

Free energy versus internal energy potential for heavy quark systems at finite temperature, S.H. Lee, K. Morita, T. Song, and C.M. Ko, *Phys. Rev. D* **89**, 094015 (2014).

Partonic mean-field effects on matter and antimatter elliptic flows, C.M. Ko, F. Li, T. Song, V. Greco, and S. Plumari, *Nucl. Phys. A* **931**, 607 (2014).

Modification of pion production threshold in nuclear medium in heavy ion collisions and the nuclear symmetry energy, T. Song and C.M. Ko, *Phys. Rev. C* **91**, 014901 (2015).

Quarkonium formation time in relativistic heavy-ion collisions, T. Song, C.M. Ko, and S.H. Lee, *Phys. Rev. C* **91**, 044909 (2015).

Double ratio of charmonia in p+Pb collisions $\sqrt{s_{NN}} = 5.02$ TeV, Y.P. Liu, C.M. Ko, and T. Song, *Proceeding of 30th Winter Workshop on Nuclear Dynamics, Galveston, Texas, April 6-12, 2014*, edited by R. Bellwied, F. Geurts, and A. Timmins, *J. Phys. Conf. Ser.* **535**, 012011 (2014).

Realistic implementation of massive Yang-Mills for ρ and a_1 Mesons, P.M. Hohler and R. Rapp, Phys. Rev. D **89**, 125013 (2014).

Is rho-meson melting compatible with chiral restoration? P.M. Hohler and R. Rapp, Phys. Lett. B **731**, 103 (2014).

Pseudo-critical enhancement of thermal photons in relativistic heavy-ion collisions? H. van Hees, M. He, and R. Rapp, Nucl. Phys. A **933**, 256 (2015).

Universal parameterization of thermal photon rates in hadronic matter, M. Heffernan, P. Hohler, and R. Rapp, Phys. Rev. C **91**, 027902 (2015).

Properties of thermal photons at RHIC and LHC, R. Rapp, H. van Hees, and M. He, Nucl. Phys. A **931**, 696 (2014).

Probing chiral restoration with ρ -Meson melting through sum rules, P.M. Hohler and R. Rapp, J. Phys. Conf. Ser. **535**, 012024 (2014).

Development of forward calorimeter system for the STAR experiment, O.D. Tsai, E. Aschenauer, W. Christie, L.E. Dunkelberger, S. Fazio, C.A. Gagliardi, S. Heppelmann, H.Z. Huang, W. Jacobs, G. Igo, A. Kisilev, K. Landry, M. Mondal, Y.X. Pan, M. Sergeeva, E. Sichtermann, S. Trentalange, G. Visser, and S. Wissnik, J. Phys. Conf. Ser. **587**, 01205 (2015).

A search for two body muon decay signals, R. Bayes, J.F. Bueno, Yu.I. Davydov, P. Depommier, W. Faszler, M.C. Fujiwara, C.A. Gagliardi, A. Gaponenko, D.R. Gill, A. Grossheim, P. Gumplinger, M.D. Hasinoff, R.S. Henderson, A. Hillairet, J. Hu, D.D. Koetke, R.P. MacDonald, G.M. Marshall, E.L. Mathie, R.E. Mischke, K. Olchanski, A. Olin, R. Openshaw, J.-M. Poutissou, R. Poutissou, V. Selivanov, G. Sheffer, B. Shin, T.D.S. Stanislaus, R. Tacik, and R.E. Tribble (TWIST Collaboration), Phys. Rev. D **91**, 052020 (2015).

Transverse-energy distributions at midrapidity in $p + p$, $d + Au$, and $Au + Au$ collisions at $\sqrt{s_{NN}} = 62.4 - 200$ GeV and implications for particle-production models, PHENIX Collaboration (S.S. Adler *et al.*), Phys. Rev. C **89**, 044905 (2014).

Charged-to-neutral correlation at forward rapidity in $Au+Au$ collisions at $\sqrt{s_{NN}} = 200$ GeV, STAR Collaboration (L. Adamczyk *et al.*), Phys. Rev. C **91**, 034905 (2015).

The $\Lambda\Lambda$ correlation function in $Au+Au$ collisions at $\sqrt{s_{NN}} = 200$ GeV, STAR Collaboration (L. Adamczyk *et al.*), Phys. Rev. Lett. **114**, 022301 (2015).

J/psi polarization in p+p collisions at $\sqrt{s} = 200$ GeV in STAR, STAR Collaboration (L. Adamczyk *et al.*), Phys. Lett B **739**, 180 (2014).

Measurement of K_S^0 and K^{0S} in p+p, d+Au, and Cu+Cu collisions at $\sqrt{s_{NN}} = 200$ GeV, PHENIX Collaboration (A. Adare *et al.*), Phys. Rev. C **90**, 054905 (2014).

Measurement of longitudinal spin asymmetries for weak boson production in polarized proton-proton collisions at RHIC, STAR Collaboration (L. Adamczyk *et al.*), Phys. Rev. Lett. **113**, 072301 (2014).

Observation of D^0 meson nuclear modifications in Au+Au collisions at $\sqrt{s_{NN}} = 200$ GeV, STAR Collaboration (L. Adamczyk *et al.*), Phys. Rev. Lett. **113**, 142301 (2014).

Beam-energy dependence of charge separation along the magnetic field in Au+Au collisions at RHIC, STAR Collaboration (L. Adamczyk *et al.*), Phys. Rev. Lett. **113**, 052302 (2014).

Event-plane-dependent dihadron correlations with harmonic v_n subtraction in Au + Au collisions at $\sqrt{s_{NN}} = 200$ GeV, STAR Collaboration (H. Agakishiev *et al.*), Phys. Rev. C **89**, 041901 (2014).

Dielectron azimuthal anisotropy at mid-rapidity in Au + Au collisions at $\sqrt{s_{NN}} = 200$ GeV, STAR Collaboration (L. Adamczyk *et al.*), Phys. Rev. C **90**, 064904 (2014).

Beam energy dependence of moments of the net-charge multiplicity distributions in Au+Au collisions at RHIC, STAR Collaboration (L. Adamczyk *et al.*), Phys. Rev. Lett. **113**, 092301 (2014).

Calibration and performance of the STAR Muon Telescope Detector using cosmic rays, C. Yang *et al.*, Nucl. Instrum. Methods Phys. Res. **A762**, 1 (2014).

Beam-energy dependence of directed flow of protons, antiprotons, and pions in Au+Au collisions, STAR Collaboration (L. Adamczyk *et al.*), Phys. Rev. Lett. **112**, 162301 (2014).

Dielectron mass spectra from Au+Au collisions at $\sqrt{s_{NN}} = 200$ GeV, STAR Collaboration (L. Adamczyk *et al.*), Phys. Rev. Lett. **113**, 022301 (2014), Addendum-ibid. **113**, 049903 (2014).

Suppression of upsilon production in d+Au and Au+Au collisions at $\sqrt{s_{NN}} = 200$ GeV, STAR Collaboration (L. Adamczyk *et al.*), Phys. Lett. B **735**, 127 (2014).

System-size dependence of open-heavy-flavor production in nucleus-nucleus collisions at $\sqrt{s_{NN}} = 200$ GeV, PHENIX Collaboration (A. Adare *et al.*), Phys. Rev. C **90**, 034903 (2014).

J/psi production at low p_T in Au+Au and Cu+Cu collisions at $\sqrt{s_{NN}} = 200$ GeV at STAR, STAR Collaboration (L. Adamczyk *et al.*), Phys. Rev. C **90**, 024906 (2014).

Measurement of charge multiplicity asymmetry correlations in high energy nucleus-nucleus collisions at 200 GeV, STAR Collaboration (L. Adamczyk *et al.*), Phys. Rev. C **89**, 044908 (2014).

Recent results on event-by-event fluctuations from the RHIC Beam Energy Scan program in the STAR experiment, N.R. Sahoo (for the STAR Collaboration), J. Phys. Conf. Ser. **535**, 012007 (2014).

High- p_T direct photon azimuthal correlation measurements, A.M. Hamed (for the STAR Collaboration), Nucl. Phys. **A931**, 706 (2014).

SECTION VI

APPENDIX

TALKS PRESENTED
April 1, 2014 – March 31, 2015

*Charge and long range planning process, **J.C. Hardy, Invited Talk**, Joint DNP Town Meeting on Nuclear Structure and Nuclear Astrophysics, Texas A&M University, College Station, Texas (August 2014).*

*Testing CVC and CKM unitarity via superallowed nuclear beta decay, **J.C. Hardy, Invited Talk**, 15th International Symposium on Capture Gamma-Ray Spectroscopy and Related Topics, CGS 15, Dresden, Germany (August 2014).*

*Testing CVC and CKM unitarity via superallowed nuclear beta decay, **J.C. Hardy, Invited Talk**, Solvay Workshop on Beta-decay Weak Interactions Studies in the Era of the LHC, Brussels, Belgium (September 2014).*

*Testing CVC and CKM unitarity via superallowed nuclear beta decay, **J.C. Hardy, Invited Talk**, Workshop on Fundamental Symmetry Tests with Rare Isotopes, Amherst Center for Fundamental Interactions, University of Massachusetts, Amherst, Massachusetts (October 2014).*

*Nuclear tests of the standard model: Vector current conservation and CKM unitarity, **J.C. Hardy, Colloquium**, National Superconducting Cyclotron Facility, Michigan State University, East Lansing, Michigan (September 2014).*

*Testing the standard model via superallowed nuclear beta decay, **J.C. Hardy Seminar**, Physics Division, Argonne National Laboratory, Argonne, Illinois (November 2014).*

*From estimates of the order of magnitude to sub-percent precision measurements: The case of superallowed beta emitters, **V.E. Iacob, Invited Talk**, Carpathian Summer School in Physics, Sinaia, Romania (July 2014).*

*The β decay of ^{38}Ca : sensitive test of isospin symmetry-breaking corrections from mirror superallowed $0^+ \rightarrow 0^+$ transitions, **H.I. Park**, 2nd International Conference on Advances in Radioactive Isotope Science, Tokyo, Japan (June 2014).*

*Precise test of internal-conversion theory: Transitions measured in five nuclei spanning $50 \leq Z \leq 78$, **N. Nica**, Town Meetings on Nuclear Structure and Nuclear Astrophysics, Texas A&M University, College Station, Texas (August 2014).*

*Another interesting case of ICC measurement: The 88-keV, M4 transition in ^{127m}Te , **N. Nica**, the 5th Workshop of the Decay Data Evaluation Project (DDEP-2014), Bucharest, Romania (October 2014).*

*Comments on RULER: Contribution of branching ratio uncertainties $\Delta B R_i$ to reduced gamma-ray matrix elements uncertainty $\Delta B(\sigma\lambda)$, **N. Nica**, United States Nuclear Data Program Annual Meeting, Brookhaven National Laboratory, New York (November 2014).*

*New ICC precision measurement: The 150.8-keV, E3 transition in ^{111m}Cd , **N. Nica**, United States Nuclear Data Program Annual Meeting, Brookhaven National Laboratory, New York (November 2014).*

Nucleon structure from high-energy polarized proton collisions, **C.A. Gagliardi, Invited Talk**, 7th Int. Conf. Quarks Nucl. Phys. (QNP 2015), Valparaiso, Chile (March 2015).

RHIC spin in the next decade, **C.A. Gagliardi, Invited Talk**, 4th Joint Meet. Nucl. Phys. Div. APS JPS (HAWAII 2014), RHIC Town Meeting, Waikoloa, Hawaii (October 2014).

Gluon polarization and inclusive jet measurements with STAR, **C.A. Gagliardi** (for the STAR Collaboration), 4th Joint Meet. Nucl. Phys. Div. APS JPS (HAWAII 2014), Waikoloa, Hawaii (October 2014).

Exploring gluon and antiquark polarization in the proton with STAR, **C.A. Gagliardi** (for the STAR Collaboration), 20th Part. Nucl. Int. Conf.. (PANIC 2014), Hamburg, Germany (August 2014).

Giant monopole resonance: Present and future, **Y.-W. Lui, Invited Talk**, Lanzhou, China (October 2014).

Alpha clusters in nuclear physics and astrophysics, **V.Z. Goldberg, Invited Talk**, Carpathian Summer School of Physics 2014 "From nuclei to stars," Sinaia, Romania (July 2014).

Why modern theory of nuclear structure needs results of exotic experiments, **V.Z. Goldberg, Invited Talk**, VII Traditional International Symposium on Exotic Nuclei (EXON-2014), Kaliningrad, Russia (September 2014).

The most acute problems of the structure of the light exotic nuclei, **V.Z. Goldberg, Invited Seminar**, Lomonosov Moscow University, Russia (July 2014).

TTIK approach in resonance reactions and applications, **V.Z. Goldberg, Invited Seminar**, Nazarbayev University, Astana, Kazakhstan (August 2014).

Transverse single-spin asymmetries for jet-like events at forward rapidities in $p+p$ collisions at $\sqrt{s} = 500$ GeV with the STAR experiment, **M.M. Mondal** (for the STAR Collaboration), APS April Meeting, contributed, Savannah, Georgia (April 2014).

Measurement of the transverse single-spin asymmetries for π^0 and jet-like events at forward rapidities at STAR in $p+p$ collisions at $\sqrt{s} = 500$ GeV, **M.M. Mondal, Invited Talk**, (for the STAR Collaboration), XXII Int. Workshop Deep Inelastic Scatt. (DIS 2014), Warsaw, Poland (April 2014).

Gluon polarization in longitudinally polarized pp collisions at STAR, **Z. Chang, Invited Talk**, (for the STAR Collaboration), 21st Int. Symp. Spin Phys. (SPIN 2014), Beijing, China (October 2014).

Studies of excited states of ^{31}S via beta-decay of ^{31}Cl for $^{30}\text{P}(p,\gamma)^{31}\text{S}$ in ONe novae, **A. Saastamoinen**, Classical Novae in the Cosmos — satellite workshop of Nuclei in the Cosmos XIII, Debrecen, Hungary (July 2014).

Study of excited states of ^{35}Ar through beta-decay of ^{35}K for nucleosynthesis in novae and X-ray bursts, **A. Saastamoinen**, Carpathian Summer School of Physics, Sinaia, Romania (July 2014).

Developing surrogate reaction techniques to determine neutron capture rates, **A. Saastamoinen**, The Stewardship Science Academic Alliance annual symposium, Santa Fe, New Mexico (March 2015).

Upgrade of the TAMU MDM-focal plane detector with MicroMegs technology, **A. Spiridon**, 12th Russbach School on Nuclear Astrophysics, Russbach, Austria (March 2015).

Current status of the TAMUTRAP facility, **M. Mehlman**, 6th International Conference on Trapped Charged Particles and Fundamental Physics (TCP 2004), Takamatsu, Japan (December 2014).

A new correlation Penning trap for fundamental physics at Texas A&M, **D. Melconian, Invited Talk**, 6th International Conference on Trapped Charged Particles and Fundamental Physics (TCP 2004), Takamatsu, Japan (December 2014).

Current status of the TAMUTRAP Facility, **M. Mehlman**, American Physical Society - Texas Section 2014 Fall Meeting, College Station, Texas (October 2014).

Half-life and branching ratio measurements of $T=1/2$ mirror nuclei, **P.D. Shidling**, American Physical Society - Division of Nuclear Physics (APS-DNP) Conference, Waikoloa, Hawaii (October 2014).

TAMUTRAP: An ion trap facility for weak interaction and nuclear physics studies, **P.D. Shidling, Invited Talk**, American Physical Society - Division of Nuclear Physics (APS-DNP) Conference, Waikoloa, Hawaii (October 2014).

Measurement of the β -asymmetry in the decay of magneto-optically trapped, spin-polarized ^{37}K , **B. Fenker**, American Physical Society - Division of Nuclear Physics (APS-DNP) Conference, Waikoloa, Hawaii (October 2014).

Measurements of correlations in β -decay using laser and ion traps, **D. Melconian, Invited Talk**, Solvay Workshop on Beta-Decay Weak Interaction Studies in the Era of the LHC, Brussels, Belgium (September 2014).

β -decay correlation measurements using ion and laser traps, **D. Melconian, Invited Talk**, 15th International Symposium on Capture Gamma-Ray Spectroscopy and Related Topics (CGS15), Dresden, Germany (August 2014).

Clustering in non-self-conjugate nuclei ^{10}Be and ^{18}O , **G.V. Rogachev, Invited Talk**, SOTANCP3, Yokohama, Japan (May 2014).

Measurement of $p+^7\text{Be}$ elastic and inelastic excitation functions, **G.V. Rogachev, Invited Talk**, RIKEN Workshop on "Inelastic excitations in thick target inverse kinematics approach resonance," Waco, Japan (May 2014).

Recent progress in exotic nuclei studies using resonance scattering, **G.V. Rogachev, Invited Talk**, VII International Symposium on Exotic Nuclei EXON2014, Kaliningrad, Russian Federation (September 2014).

Nuclear structure with stable and rare isotope beams at TAMU, **G.V. Rogachev**, The meeting of the US Low Energy Nuclear Physics community, Preparation of the White Paper for the US Long Range Plan of nuclear physics research, College Station, Texas (August 2014).

Exploring reaction rates near $A=30$, **G.V. Rogachev**, The meeting of the US Low Energy Nuclear Physics community, Preparation of the White Paper for the US Long Range Plan of nuclear physics research, College Station, Texas (August 2014).

Indirect methods with stable beams, **G.V. Rogachev**, The meeting of the US Low Energy Nuclear Physics community, Preparation of the White Paper for the US Long Range Plan of nuclear physics research, College Station, Texas (August 2014).

Stable and γ beams, stars, stellar burning, Big Bang, sun, **G.V. Rogachev**, Summary of Working group, The meeting of the US Low Energy Nuclear Physics community, Preparation of the White Paper for the US Long Range Plan of nuclear physics research, College Station, Texas (August 2014).

Preliminary results of the S1264 experiment, **G.V. Rogachev**, Research seminar, TRIUMF, Vancouver, Canada (July 2014).

Recent results on event-by-event fluctuations from the RHIC beam energy scan program, **N.R. Sahoo, Invited Talk** (for the STAR Collaboration), the 30th Winter Workshop on Nuclear Dynamics, Galveston, Texas (April 2014).

Direct-photon+hadron correlations for the study of parton energy loss at the top RHIC energy, **N.R. Sahoo** (for the STAR Collaboration), the International Conference on Physics and Astrophysics of the Quark Gluon Plasma, Calcutta, India (February 2015).

High- p_T direct photon azimuthal correlation measurements, **A.M. Hamed** (for the STAR Collaboration), Quark Matter 2014 (XXIV International Conference on Ultrarelativistic Nucleus-Nucleus Collisions), Darmstadt, Germany (May 2014).

The quest to understand QCD matter using heavy nuclei in collisions, **S. Mioduszewski, Invited Talk**, Memorial Symposium in Honor of Dr. Richard Arnowitt, College Station, Texas (September 2014).

Heavy-ion collisions: Direct and indirect probes of the density and temperature dependence of E_{sym} , simulating the supernova neutrinosphere with heavy ion collisions, **S.J. Yennello, Invited Talk**, ECT* - European Centre for Theoretical Studies in Nuclear Physics and Related Areas, Trento, Italy (April 2014).

Stable & radioactive ion beams at the Texas A&M University Cyclotron Institute, **S.J. Yennello, Invited Talk**, The VII International Symposium on EXOTic Nuclei (EXON- 2014), Kaliningrad, Russia (September 2014).

How much cooler would it be with some more neutrons? Asymmetry dependence of the nuclear caloric curve, **S.J. Yennello, Invited Talk**, Triangle University National Laboratory, Durham, North Carolina (November, 2014).

Complex many body systems: Nuclei, nuclear science & Jolie, **S.J. Yennello, Invited Talk**, LBL, Berkeley, California (May 2014).

Educating the next generation of nuclear scientists, **S.J. Yennello, Invited Talk**, 248th ACS National Meeting, San Francisco, California (August 2014).

Structure of collaboration, **S.J. Yennello, Invited Talk**, 2014 SpiRIT Collaboration meeting, Riken, Japan (June 2014).

Equilibration between projectile and target in heavy-ion nuclear collisions, **L. May**, American Physical Society Spring 2015 Joint Meeting of the Texas Section of the APS, Texas Section of the AAPT, and Zone 13 of the Society of Physics Students, Baytown, Texas (March 2015).

*Third year site visits, **S.J. Yennello, Invited Talk***, ADVANCE Program Workshop, Alexandria, Virginia (March 2014).

*Remarkable, delightful, awesome; it will change your life, not overnight, but over time, **S.J. Yennello, Invited Talk***, 248th ACS National Meeting, San Francisco, California (August 2014).

*Advancing women in physics: Lessons learned from around the world, **S.J. Yennello, Invited Talk***, 4th Joint Meeting of the APS Division of Nuclear Physics and the Physical Society of Japan, Waikoloa, Hawaii (October 2014).

*Probing symmetry energy effects on reaction mechanisms using heavy-ion collisions below the Fermi energy, **P. Cammarata***, International Workshop on Multifacets of EoS and Clustering, Catania, Italy (May 2014).

*Stellar science, **S.J. Yennello, Invited Talk***, CUWIP, Brownsville, Texas (February 2015).

*Equilibration between projectile and target in heavy-ion nuclear collisions, **L. May***, American Physical Society Fall 2014 Joint Meeting of the Texas Section of the APS, Texas Section of the AAPT, and Zone 13 of the Society of Physics Students, Monmouth, Illinois (November 2014).

*Equilibration between projectile and target in heavy-ion nuclear collisions, **L. May***, Southwest Regional ACS meeting, Fort Worth, Texas (November 2014).

*Adventures with the heaviest elements: Chemistry and physics at the bottom of the periodic table, **Charles M. Folden III, Invited Talk***, University of Dallas Colloquium, Irving, Texas (November 2014).

*Prospects for production of new superheavy elements using projectiles with $Z > 20$, **Charles M. Folden III***, 4th Joint Meeting of the APS Division of Nuclear Physics and the Physical Society of Japan, Waikaloa, Hawaii (October 9, 2014).

*Online chemistry of superheavy elements, **Charles M. Folden III, Invited Talk***, The meeting of the US Low Energy Nuclear Physics community, Preparation of the White Paper for the US Long Range Plan of nuclear physics research, College Station, Texas (August 2014).

*Plutonium fingerprinting for forensics (PuFF) project: assessment of unique trace elements and isotope ratios in separated plutonium from low burnup nuclear fuel, **Charles M. Folden III***, and Sunil S. Chirayath, DNDO ARI Grantees Program Review, Leesburg, Virginia (June 25, 2014).

*Survival of excited compound nuclei and online chemistry experiments at Texas A&M, **Charles M. Folden III***, ARUNA Workshop, South Bend, Indiana (June 2014).

*Measuring cross-sections of astrophysical interest in a laser experiment, **M. Barbui***, The meeting of the US Low Energy Nuclear Physics community, Preparation of the White Paper for the US Long Range Plan of nuclear physics research, College Station, Texas (August 2014).

*Exploring the alpha cluster structure of nuclei using the thick target inverse kinematics technique for multiple alpha decays, **M. Barbui***, Simulating the Supernova Neutrinosphere with heavy Ion Collisions, ECT* workshop, Trento, Italy (April 2014).

*Measurement of the plasma astrophysical S factor for the ${}^3\text{He}(d, p){}^4\text{He}$ reaction in exploding molecular clusters, **M. Barbui, Invited Seminar***, Notre Dame University, South Bend, Indiana (February 2015).

*Measurement of the plasma astrophysical S factor for the ${}^3\text{He}(d, p){}^4\text{He}$ reaction in exploding molecular clusters, **M. Barbui, Invited Seminar**, NSCL, Michigan State University, East Lansing, Michigan (September 2014).*

*Clustering and medium effects in low density nuclear matter, **K. Hagel**, SSNHIC 2014, Trento, Italy (April, 2014).*

*Clustering in alpha conjugate nuclei, **K. Hagel**, IWMEC 2014, Catania, Italy (May, 2014).*

*Clustering in alpha conjugate nuclei, **K. Hagel**, Texas Section of the APS, Texas A&M University, College Station, Texas (October 2014).*

*Heavy ion collisions and the supernova equation of state, **K. Hagel**, ASY-EOS 2015, Piazza Armerina, Italy (March, 2015).*

*Sensitivities of energies of giant resonances to properties of the energy density functional, **S. Shlomo, Invited Talk**, International Conference “NUCLEUS-2014” on Fundamental Problems of Nuclear Physics, Atomic Power and Nuclear Technology, Minsk, Belarus (July 2014).*

*Modern energy density functional for nuclei and nuclear matter, **S. Shlomo, Invited Talk**, Workshop on Strongly Interacting Systems, Joint Institute for Nuclear Research, Dubna, Russia (July 2014).*

*Determining a modern energy density functional for properties of finite nuclei and nuclear matter, **S. Shlomo, Invited Talk**, The 60th Meeting of the Israel Physical Society (IPS), Ben-Gurion University of the Negev, Israel (December 2014).*

*Sensitivities of energies of giant resonances to properties of the energy density functional, **S. Shlomo, Invited Talk**, Tel Aviv University, Tel Aviv, Israel (December 2014).*

*Modern energy density functional for strongly interacting many body system, **S. Shlomo, Invited Lecture**, National Research Nuclear University MEPhI, Moscow, Russia (June 2014).*

*Properties of nuclei and nuclear matter within the mean-field approximation, **S. Shlomo, Invited Lecture**, National Research Nuclear University MEPhI, Moscow, Russia (June 2014).*

*Random-phase-approximation for the description of giant resonances, **S. Shlomo, Invited Lecture**, National Research Nuclear University MEPhI, Moscow, Russia (July 2014).*

*Distorted wave Born approximation and the folding model; hadron excitations of giant resonances, **S. Shlomo, Invited Lecture**, National Research Nuclear University MEPhI, Moscow, Russia (July 2014).*

*Sensitivities of giant resonances energies to properties of giant resonances, **S. Shlomo, Invited Lecture**, National Research Nuclear University MEPhI, Moscow, Russia (July 2014).*

*Current status of the nuclear matter equation of state, **S. Shlomo, Invited Lecture**, National Research Nuclear University MEPhI, Moscow, Russia (July 2014).*

*Modern energy density functional and the equation of state of symmetric and asymmetric nuclear matter, **S. Shlomo, Invited Talk**, International Workshop on Simulating the Supernova Neutrinosphere with Heavy Ion Collisions, The European Center for Theoretical Studies in Nuclear Physics and Related Areas (ECT*), Trento, Italy (May 2014).*

*On properties of high-energy isoscalar monopole (P-h)-type excitations in medium heavy mass nuclei, **M.L. Gorelik**, S. Shlomo, B.A. Tulupov, and M.H. Urin, **Invited Talk**, International Conference (NUCLEUS-2014) on Fundamenta Problems of Nuclear Physics, Atomic Power, and Nuclear Technology, Minsk, Belarus (July 2014).*

*Density and temperature from quantum fluctuations, **H. Zheng** and A. Bonasera, Nuclear Astrophysics town meeting, Texas A&M University, College Station, Texas (August 2014).*

*Can we constrain the EoS from NS observations? **H. Zheng** and A. Bonasera, Nuclear Astrophysics town meeting, Texas A&M University, College Station, Texas (August 2014).*

*Density and temperature from quantum fluctuations, **H. Zheng**, Laboratori Nazionali del Sud, via S. Sofia, Catania, Italy (October 2014).*

*Dalla dinamica delle stelle alle centrali nucleari a fusione, **A. Bonasera**, Laboratori Nazionali del Sud, via S. Sofia, Catania, Italy (December 2014).*

*Energy density, pressure and flow at early times, **Rainer J. Fries**, XXX Winter Workshop on Nuclear Dynamics, Galveston, Texas (April 2014).*

*Recombination MC for jet showers: Status and discussion, **Rainer J. Fries**, **Invited Talk**, 2014 JET Collaboration Meeting and Summer School, UC Davis, Davis, California (June 2014).*

*Hadronization for jet shower Monte Carlos, **Rainer J. Fries**, **Invited Talk**, Workshop on “Jet Modifications in the RHIC and LHC Era,” Wayne State University, Detroit, Michigan (August 2014).*

*In medium hadronization: Hadrons and jets, **Rainer J. Fries**, **Invited Talk**, Workshop on “Jet Modifications in the RHIC and LHC Era,” Wayne State University, Detroit, Michigan (August 2014).*

*The (3+1)-D structure of nuclear collisions, **Rainer J. Fries**, II. International Conference on the Initial Stages in High-Energy Nuclear Collisions (IS 2014), Napa, California (December 2014).*

*Quark recombination, **Rainer J. Fries**, **Invited Talk**, 7th International Conference on Physics and Astrophysics of Quark Gluon Plasma (ICPAQGP-2015), Kolkata, India (February 2015).*

*Jet fragmentation via shower parton recombination, **C.M. Ko**, **Invited Talk**, Third International Symposium on Non-Equilibrium Dynamics, Hersonissos, Crete, Greece (June 2014).*

*Effects of medium modification of pion production threshold in heavy ion collisions and the nuclear symmetry energy, **C.M. Ko**, **Invited Talk**, The 4th International Workshop on Nuclear Dynamics in Heavy-Ion Collisions, Lanzhou, China (August 2014).*

*Baryon-rich matter in heavy-ion collisions, **C.M. Ko**, **Invited Talk**, Workshop on High Temperature and High Density Nuclear Matter Study, Weihai, Shandong, China (August 2014).*

*Quarkonia production in relativistic heavy ion collisions, **C.M. Ko**, **Invited Talk**, 2014 JET Collaboration Meeting, Davis, California (June 2014).*

*Theoretical connections between dileptons and chiral symmetry, **P.M. Hohler**, 30th Winter Workshop on Nuclear Dynamics," Galveston, Texas (April 2014).*

Critical enhancement of thermal photons, **R. Rapp**, 24th Int. Conf. on Ultrarelativistic Nucleus-Nucleus Collisions “Quark Matter 2014,” Darmstadt, Germany (May 2014).

Heavy-flavor transport at FAIR, **R. Rapp, Invited Talk**, at HICforFAIR workshop on “Heavy-Flavor Physics with CBM”, FIAS, Frankfurt, Germany (May 2014).

In-medium quarkonia at RHIC and LHC, **R. Rapp, Invited Talk**, Workshop on “Newest Quarkonia Results,” RHIC & AGS Annual Users’ Meeting, BNL, Upton, New York (June 2014).

Theoretical overview of open heavy flavor at RHIC and LHC, **R. Rapp, Invited Talk**, Workshop on “Open Heavy Flavor,” RHIC & AGS Annual Users’ Meeting, BNL, Upton, New York (June 2014).

Vector meson spectral functions and chiral symmetry restoration, **P.M. Hohler, Invited Talk**, Int. RIKEN-BNL workshop on “Thermal photons and dileptons in heavy-ion collisions”, Brookhaven National Lab., Upton, New York (August 2014).

Dileptons and chiral symmetry restoration, **P. Hohler**, APS Division of Nuclear Physics Long-Range Plan Town Meeting, Temple University, Philadelphia, Pennsylvania (September 2014).

Thermal dileptons: Insights and prospects, **R. Rapp, Invited Talk**, Int. workshop on “BES-II at RHIC”, LBNL, Berkeley, California (September 2014).

Recent developments for quarkonia in medium, **R. Rapp, Invited Talk**, The INT program workshop on “Heavy Flavor and Electromagnetic Probes in Heavy-Ion Collisions,” INT, Seattle, Washington (September 2014).

Electromagnetic probes of QCD matter in heavy-ion collisions, **R. Rapp, Invited Plenary Talk**, Int. Conference on Science and Technology for FAIR in Europe, Worms, Germany (October 2014).

Hot nuclear correction to J/psi suppression in deuteron-gold collisions at 200 GeV, **X. Du**, Texas Section of APS 2014 fall meeting, Texas A&M University, College Station, Texas (October 2014).

A static potential from QQbar free energy lattice QCD data, **S. Liu**, Texas Section of APS 2014 Fall Meeting, Texas A&M University, College Station, Texas (October 2014).

What can electromagnetic probes reveal? **P.M. Hohler, Invited Talk**, STAR Collaboration meeting, Brookhaven National Lab., Upton, New York (November 2014).

Thermal EM radiation in AA and pA collisions, **R. Rapp, Invited Plenary Talk**, 2nd Int. Conference on “The Initial Stages in Heavy-Ion Collisions,” Napa, California (December 2014).

Heavy flavor in QCD matter, **R. Rapp, Invited Talk**, Sapore Gravis Workshop 2014, Padova, Italy (December 2014).

Heavy flavor interaction in hot QCD matter, **R. Rapp, Invited Talk**, Int. Workshop on Heavy-Flavor Production in High-Energy Collisions, LBNL, Berkeley, California (January 2015).

Heavy-flavor interactions in medium, **R. Rapp, Invited Talk**, Int. Workshop on Heavy-Quark Physics in Heavy-Ion Collisions, ECT*, Trento, Italy (March 2015).

RESEARCH PERSONNEL AND ENGINEERING STAFF

April 1, 2014 - March 31, 2015

Faculty and Research Group Leaders

Aldo Bonasera, Senior Scientist
Charles M. Folden III, Assist. Prof. of Nuclear Chemistry
Rainer Fries, Assist. Professor of Physics
Carl A. Gagliardi, Professor of Physics
John C. Hardy, Professor of Physics
Che Ming Ko, Professor of Physics
Dan Melconian, Assist. Professor of Physics
Saskia Mioduszewski, Assist. Prof. of Physics
J. B. Natowitz, Professor of Chemistry, Bright Chair (25%)
Ralf Rapp Associate Professor of Physics
Grigory Rogachev, Professor of Physics
Shalom Shlomo, Senior Scientist
Robert E. Tribble, Professor of Physics (20%)
Sherry J. Yennello, Professor of Chemistry, Director
Dave H. Youngblood, Professor of Physics
Akram M. Zhanov, Senior Scientist

Research Staff

Marina Barbui, Assist. Research Scientist
Henry Clark, Accelerator Physicist (50%)
Grigor Chubaryan, Research Scientist
Vladilen Goldberg, Research Scientist
John C. Hagel, Research Scientist (50%)
Vladimir Horvat, Research Scientist (50%)
Victor Iacob, Research Scientist
Yevgen Koshchiy, Assist. Research Scientist
Yiu-Wing Lui, Research Scientist
Ninel Nica, Associate Research Scientist
Alan McIntosh, Assist. Res. Scientist
George Souliotis, Associate Research Scientist

Visiting Scientists

Yu-Gang Ma – To 5/15/14
Yuri Oganessian – From 1/16/15
Dan-Yang Pang – To 3/1/15
Ian Towner – From 6/24/14 To 8/31/14

Accelerator Physics and Radiation Line Staff

Joseph Brinkley, Research Associate
Lixin Chen, Research Associate
Henry Clark, Accelerator Physicist (50%)
Vladimir Horvat, Research Scientist (50%)
Bruce Hyman, Research Associate
George Kim, Accelerator Physicist
Don May, Accelerator Physicist
Brian Roeder, Accelerator Physicist
Gabriel Tabacaru, Accelerator Physicist

Computer Systems Staff

Robert Burch, Jr., Lead Microcomputer/LAN Administrator
John C. Hagel, Research Scientist (50%)

Engineering Staff

Robert Olsen, Senior Mechanical Engineer

Postdoctoral Research Associates

Taun K. Bhardwaj
Xiguang Cao – From 1/14/15
Matthew Cervantes – To 1/14/15
Jerome Gauthier – From 10/06/14
Paul Hohler
Dario Lattuada – From 3/5/15
Yunpeng Liu - To 9/1/14
Ellen McCleskey
Mirganka Mondal
Hyo-In Park
Antti Saastamoinen
Nihar Sahoo
Praveen Shidling
Sara Wuenschel
Evgeny Tereshatov
Ethan Uberseder – From 4/28/14
Yi Xu – To 5/1/14
Michael Youngs

STUDENTS

April 1, 2014 - March 31, 2015

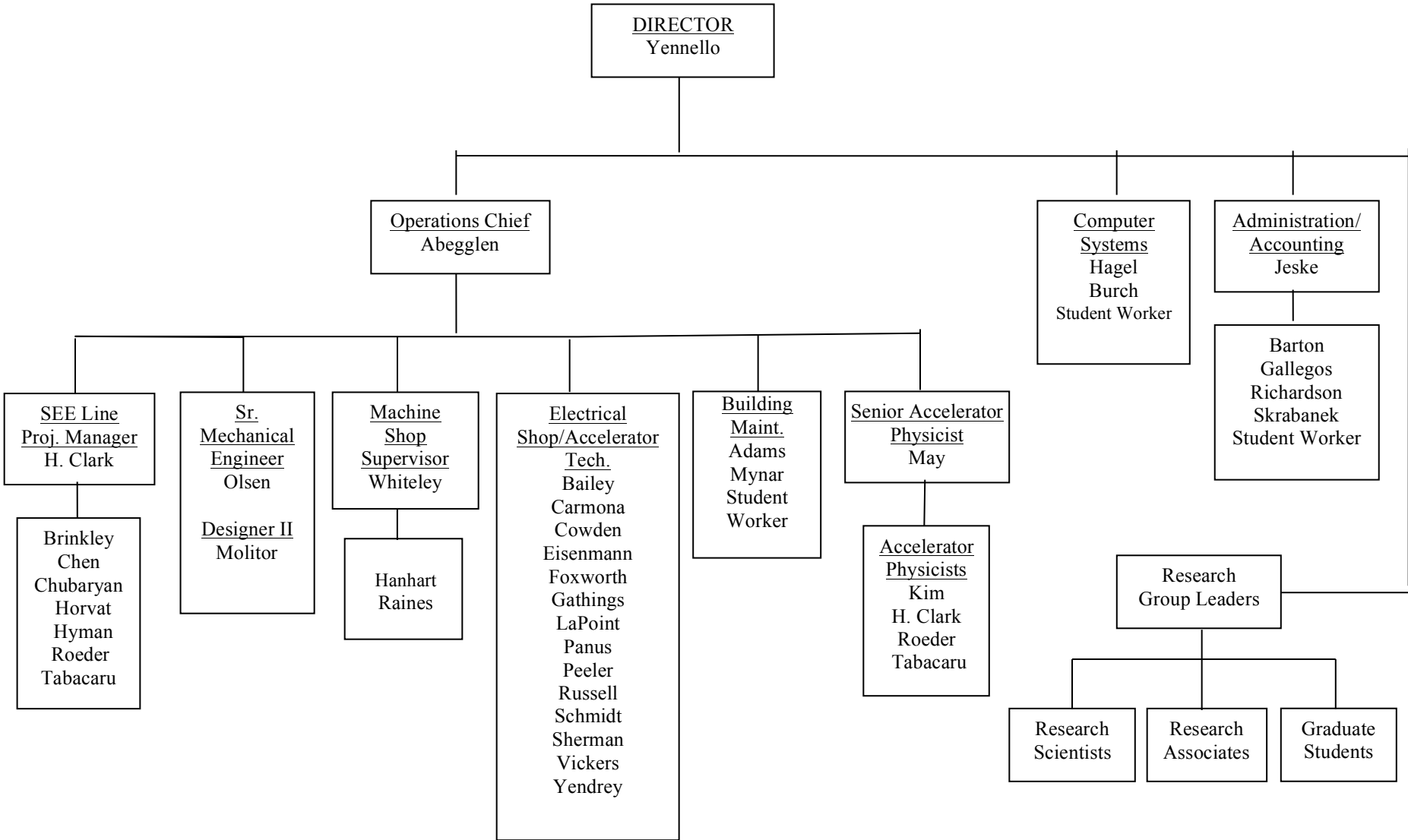
Graduate Students

Mason Anders
Marisa Alfonso
Joseph Atchison
Matteo Barbarino
Richard Spence Behling – To 1/16/15
Eames Bennett – From 1/15/15
Miguel Bencomo
Giacomo Bonasera – From 6/9/14
Jonathan Button
Paul Cammarata – To 12/31/14
Zilong Chang
Roman Chyzh
Murat Dag
Xiaojian Du
Benjamin Fenker
Kyong Choi Han
Lauren Heilborn
Laurence Henderson – From 6/1/14
Nathan Holt
Josh Hooker – From 6/1/14
Curtis Hunt – From 9/1/14
Heshani Jayatissa – From 6/1/14
Andrea Jedele – From 9/1/14
Feng Li
Shuai Liu
Yanfang Liu – From 9/1/14
Larry May
Demitri Mayarov
Michael Mehlman
Steven Rose
Issac Sarver
Alexandra Spiridon
Sidharth Somanathan
Sriteja Upadhyayula – From 1/15/15
Merinda Volia – From 1/16/15
Tyler Werke
Andrew Zarrella
Hua Zheng – To 12/31/14

Undergraduates and Student Technicians

Raymond Barringer – From 6/9/14
Robert Bordovsky – To 9/1/14
Nicolas Blando – To 8/18/14
Lindsey Bryce
Matthew Chapman
Zachary Gastony – To 10/16/14
Stephen Gerlt – From 6/1/14
Srivivas P. Harshal – From 1/12/15
Brook Johnson – To 6/25/14
Jesse Lopez – From 1/15/15
Magaret Moetteli
David Rosenbaum – From 1/15/15

ORGANIZATIONAL CHART - CYCLOTRON INSTITUTE



11-1A

**STUDENTS WHO RECEIVED GRADUATE DEGREES
FROM THESIS WORK CONDUCTED
AT
THE CYCLOTRON INSTITUTE**

April 1, 2014 – March 31, 2015

Name	Year	Thesis Title	Advisor	Present Position
Hua Zheng	2014	<i>Density and temperature in quantum nuclear systems</i>	A. Bonasera	Post Doc. at INFN - Laboratori Nazionali del Sud, Catania, Italy

**STUDENTS WHO RECEIVED GRADUATE DEGREES
FROM NON-THESIS**

April 1, 2014 – March 31, 2015

Name	Year	Advisor	Present Position
Issac Sarver	2014	R. Rapp	Continue to Ph. D. degree

INSTITUTE COLLOQUIA AND SEMINARS
April 1, 2014-March 31, 2015

2014

April 18	Prof. Madappa Prakash, Ohio University, Athens, Ohio	<i>The Neutron Star in Cassiopeia A and What It Is Telling Us?</i>
May 20	Prof. D. Bandyopadhyay, Saha Institute of Nuclear Physics, Kolkata, India	<i>Thermal Properties of Nuclear Surface</i>
June 24	Prof. Ushasi Datta Pramanik, Saha Institute of Nuclear Physics, Kolkata, India	<i>Coulomb Breakup as a Novel Spectroscopic Tool to Probe Directly the Quantum Numbers of Valence Nucleon of the Exotic Nuclei</i>
September 2	Dr. Boris L. Zhuikov, Laboratory of Radioisotope Complex, INR, Institute of Nuclear Research of Russian Academy of Science, Moscow, Russia	<i>Production of Medical Radioisotopes in Russia and Prospective Isotope Program in Institute of Nuclear Research</i>
October 8	Dr. Marion MacCormick, Institut de Physique Nucleaire d'Orsay, CNRS/IN2P3 – Universite Paris Sud, Orsay, France	<i>Evaluated Experimental Isobaric Analog States and the Isobaric Multiplet Mass Equation</i>
October 22	Prof. C.M. Ko, Cyclotron Institute, Texas A&M University, College Station, Texas	<i>Charge Pion Ratio in Heavy-Ion Collisions as a Probe of the Nuclear Symmetry Energy at High Density</i>
October 30	Prof. Niels Madsen, Department of Physics, Swansea University, Swansea, Wales, United Kingdom	<i>ALPHA: Antihydrogen and Fundamental Physics</i>
November 10	Dr. Dmitry K. Gridnev, Frankfurt Institute for Advanced Studies (FIAS), Johann Wolfgang Goethe University, Frankfurt, Germany	<i>Modern Expressions for Three-Body Forces Lead to the Collapse of Neutron Matter</i>
December 2	Prof. Romualdo de Souza, Department of Chemistry, Center for Exploration of Energy and Matter, Indiana University, Bloomington, Indiana	<i>Fusion of Neutron-Rich Light Nuclei: An Intersection of Nuclear Astrophysics and Nuclear Science</i>
December 10	Prof. Su Hounng Lee, Department of Physics, Yonsei University, Seoul, Korea	<i>Heavy Quark System in External Field</i>

December 16 Dr. A. Zhanov, Cyclotron Institute,
Texas A&M University, College
Station, Texas *ANC 20 Years at the Cyclotron Institute*

2015

February 13 Prof. D. Scott Wilbur, Department of
Radiation Oncology, University of
Washington, Seattle, Washington *The Promise and Challenges in Developing
Alpha-Emitting Radiopharmaceuticals*

March 9 Academician Professor Yuri
Oganessian, JJINR, Dubna, Russian
Federation and Cyclotron Institute,
Texas A&M University, College
Station, Texas *Super Heavy Elements*

March 24 Academician Professor Yuri
Oganessian, JJINR, Dubna, Russian
Federation and Cyclotron Institute,
Texas A&M University, College
Station, Texas *Exotic Nuclei and Astrophysics*

March 30 Dr. Bernard Laune, Institute de
Physique Nucléaire d'Orsay, Orsay,
France *Accelerator R&D in France*